Synthesis of Amphiphilic Glycomacromolecules and their Incorporation into Synthetic Membranes for Systematic Variation and Control of Membrane Dynamics

Inaugural Dissertation

for the attainment of the doctoral degree
in the Faculty of Mathematics and Natural Sciences
at the Heinrich Heine University Düsseldorf

presented by

Luca-Cesare Blawitzki

from Ratingen

Freiburg im Breisgau, February 2025

From the Institute of Organic Chemistry and Macromolecular Chemistry at the Heinrich Heine University Düsseldorf.

Published by permission of the

Faculty of Mathematics and Natural Sciences

Heinrich Heine University Düsseldorf

Supervisor: Prof. Dr. Laura Hartmann

Co-Supervisor: Prof. Dr. Cornelia Monzel

Date of oral examination: July 28, 2025

"We didn't have to play by the rules."

- Carolyn Bertozzi

Statuary declaration

I, Luca-Cesare Blawitzki, declare under oath that I have compiled my dissertation independently and without any undue assistance by third parties under consideration of the 'Principles for the safeguarding of good scientific practice at Heinrich Heine University Dusseldorf'.

Düsseldorf, 19.02.2025

_____

(Luca-Cesare Blawitzki)

Acknowledgements

First and foremost, I would like to thank my supervisor, Laura Hartmann. Thank you from the bottom of my heart for giving me this opportunity to do my doctorate in your group! Thank you for always supporting me and believing in me through the ups and downs. Thank you for all the opportunities you have given me! I enjoyed working together immensely and it made me grow a lot personally. I will always remember this time. I am forever grateful and I wish you all the best for your future.

I would also like to sincerely thank my mentor, Cornelia Monzel, and her group. You were an enormous help for our projects and you showed me a completely different world of scientific work, I learned a lot of new things from you. The work in your group was always very enjoyable and fruitful. Thank you, and all the best for your future!

Thank you very much, Stephan Schmidt. Thank you for always finding a sympathetic ear for problems of all kinds and always having a good idea ready when things got stuck.

I wish to thank Moniralsadat Tabatabai very much! You are the best of the best and I wish I had told you more often. The time we spent together in the *Makropraktikum* was incredibly exhausting, but also incredibly wonderful. Thank you for teaching me so much about polymers, for organizing everything so well and for always having my back. I wish you all the best for your future.

Many thanks also to Michaela Kitza and Stephanie Scheelen. Thank you for always keeping an eye on everything and pulling the right strings in the background to keep things running smoothly. I would also like to thank Sonja Coors, Birgit Ohler and Narges Irani for their support!

I am grateful for my graduates, Lina Charlotte Assenmacher (not once but twice!), Sören Nagel, Simon Weber, Sarah Schmitt and Angelina Brützel, who actively supported and promoted my research in the course of their theses.

Words cannot describe how grateful I am for the time I spent with my fellow doctoral students in Düsseldorf. Not only to my generation of fellow sufferers, but also to the old hands in the game. The time together with you was great! We spent many, many great moments together, laughed a lot, cried together and experienced growth together. All the *Klassenfahrten*, *Sozialraumparties* and extended coffee breaks are moments I wouldn't want to miss! I would also like to thank my new group in Freiburg for the wonderful time we had together. Even if it's hard sometimes, we still stick together well. Thanks especially to the *Bierlympische Komitee* (Ben, Jannis, Marcel) for the good cooperation, support and shared joy!

Dear Ulla, thank you so much for your support, input and friendship. You are not only a great colleague, but also a great roommate! Without you, the time in Freiburg would only be half as bearable and the evenings only half as cheerful!

Dear Nicholaaasch, Buuuuh, even if your standard is up there and mine is down here - on average it was always quite nice with you. Thanks for the productive exchange, the sass and the humor we shared. Last hopes. You know. Oh, and not to forget, thank you for your galactose! Even though you discarded it when we needed it the most! #NiLu #tirrrrred

Dear Meli, you not only have incredibly chic glasses but also a really great character. When we met over ten years ago, I could never have imagined that we would become such good friends. Thank you for your bottomless humor and your big heart.

Dear Mimi, honeyyyyyyyyyyy… For the fact that you didn't like me at all at the beginning, it worked out quite well with us; I would never have thought, not even in my Wildest Dreams! I was Enchanted to meet you and we will never go out of Style! And always remember: Ohana means family!

Dear Miriam, thank you for not only being a great supervisor for my master's thesis, a great colleague and collaborator, office buddy and fellow sufferer, but also for being a really good friend to me. Thank you for all the hilarious moments in the office, in the lab and elsewhere! OG Pupskopf!

Dear Lóránd, I don't know what cosmic coincidence brought us together, but I am so grateful. You have always been a great colleague, but you have become an even greater friend to me! Thank you for always being there for me, for bringing me back down to earth and thank you for all the beautiful moments that we have shared and will continue to share. It takes a Bubbele to know a Bubbele!

Last but not least, I would like to thank my loving parents from the bottom of my heart. Thank you for always caring for me so much, always supporting me, being there for me and believing in me. I wouldn't be where I am today without you!

Table of Contents

Abstract

The glycocalyx, a *sugary coat* that covers the plasma membrane on all eukaryotic cells, is a highly complex and heterogeneous entity, composed of glycolipids, glycoproteins and proteoglycans. This densely crowded ensemble of different constituents is highly dynamic, as it constantly adapts to external stimuli, and is intricately involved in manifold biological processes that unfold on the cell surface and are crucial for cellular function, such as pathogen infection, cancer progression, immune response and signaling. Consequently, elucidating these very mechanisms that are involved with the glycocalyx is highly desirable to properly comprehend cellular functions and to eventually progress targeted therapies, rendering the glycocalyx a subject of intensive research for decades.

Many of these glycocalyx-associated processes are closely connected to the interaction of membrane-presented glycans with specific receptor proteins, so called glycan binding proteins (GBPs). Since native glycans are highly challenging to isolate and characterize in pure forms, researchers have long employed synthetic mimics of naturally occurring glycans, so called glycomimetics, to study the interaction of proteinaceous receptors with these mimics in a precise setting. Though this approach gives valuable insights into macromolecular interactions, it does not mirror the immense complexity, dynamics and heterogeneity that is found on the cell surface. To overcome this limitation, glycocalyx models have been developed, that employ the incorporation of lipidated synthetic glycomimetics into phospholipid membranes to yield simplistic surrogates of native glycocalyces. Although these simple models are far from reflecting the complexity of eukaryotic cell membranes, they offer the potential to study glycocalyx-associated mechanisms in a very controlled and highly adjustable setting. To increase complexity and accuracy in these glycocalyx models, this thesis introduces a versatile platform to synthesize high-precision lipidated glycomimetics to construct more complex glycocalyx mimetics (cp. **Figure 1**).

In the first part of this thesis, four different cholesteryl-conjugated glycan mimetics are prepared by solid phase polymer synthesis (SPPoS) and a recently introduced new form of controlled radical polymerization (TIRP) in order to systematically investigate the influence of (hetero-) multivalently crowded surfaces of natural cell membranes on selective receptor binding. The combination of SPPoS and TIRP allows for a straightforward variation of key structural parameters, namely site-specific introduction of fluorophores and a cholesteryl-moiety, as well as a precise tuning of the glycan-head group in terms of glycosylation and valency. Employing SPPoS, established by *Hartmann et al.*, two tetravalent glycan mimetics are first synthesized that differ in their glycosylation (mannose (Man) or galactose (Gal)) and the attached fluorophore (Rhodamine B or Fluorescein). Both structures are linked

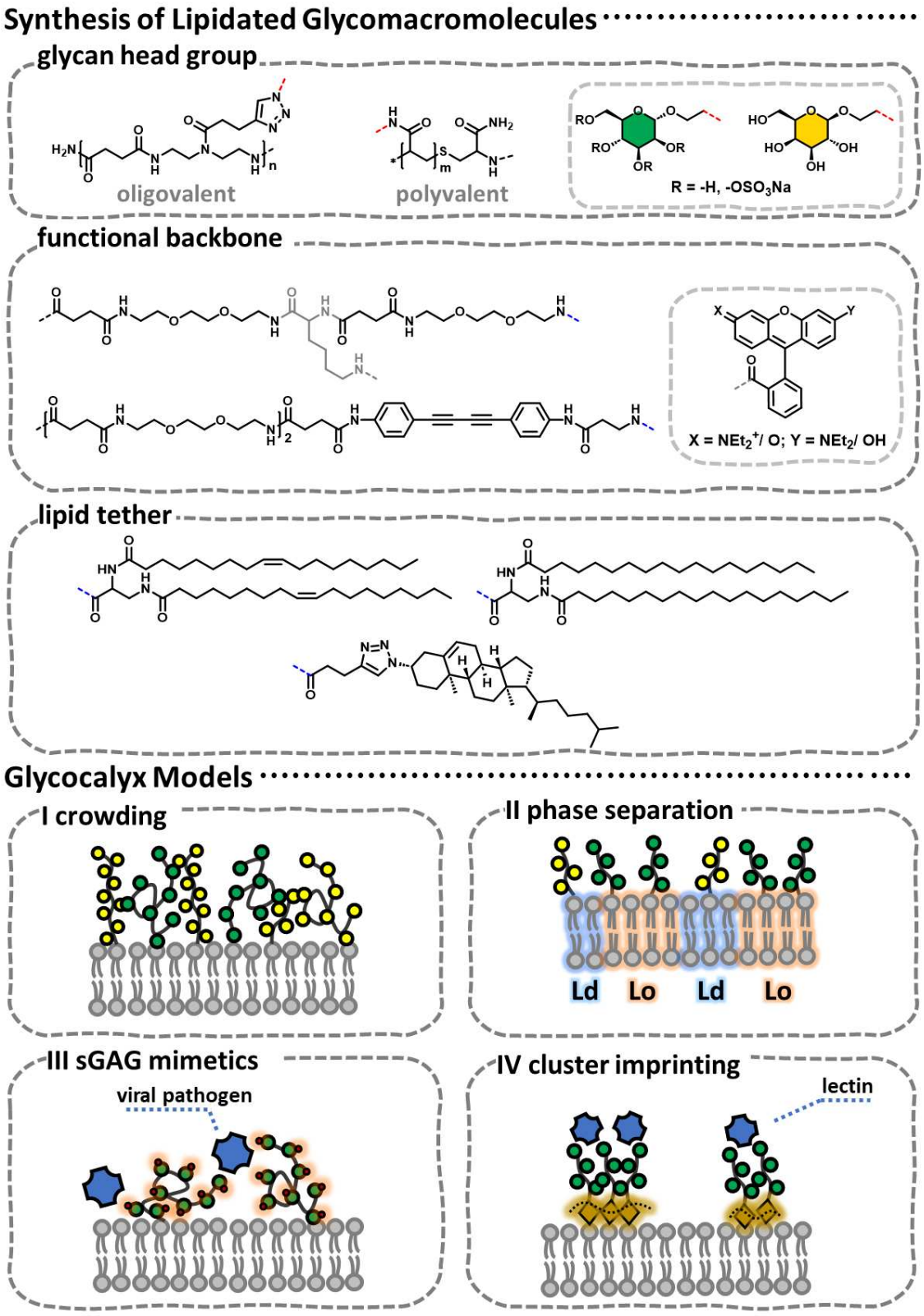

Figure 1. The further development of previously established SPPoS protocols now enables a facile synthetic platform to derive highly tailorable mimetics of lipidated glycans. These glycan mimetics are being employed to construct crowded glycocalyx mimetics (**I**), spatially resolved glycocalyx mimetics (**II**) and to derive sGAG mimetics to study membrane-virus interactions (**III**). Also, a polymerizable diacetylene building block, compatible with standard Fmoc-coupling protocols, is developed that can be used to imprint receptor-mediated glycan clusters within membranes (**IV**).

N-terminally to a cholesteryl anchor, which is later employed to introduce the ligands into giant unilamellar vesicles (GUVs) as model membrane systems. Since solid-phase synthesis is limited with regard to the achievable chain length, SPPoS is then combined with TIRP to obtain glycan mimetics with a polymeric glycan-head group. In this manner, SPPoS-derived macroinitiators are synthesized, equally featuring site-selective functionalization with a fluorophore and a cholesteryl-moiety, but bearing a *C*-terminal cysteine moiety.

The free thiol after isolation of the macroinitiators is then used as a grafting point for subsequent TIRP with Man- or Gal-functionalized acrylamide monomers to obtain the corresponding longer-chain glycan mimetics with narrow dispersities. The four different glycan mimetics (either functionalized with four or approximately forty Man- or Gal-moieties and a fluorophore, as well as a cholesteryl-anchor) are then incorporated into giant unilamellar vesicles. For this purpose, a protocol is developed that enables homogeneous anchoring of the derived structures in the membranes. The incorporation is demonstrated qualitatively by fluorescence microscopy and quantified by fluorescence correlation spectroscopy (FCS). Subsequently, the interaction of the glyco-decorated GUVs with Concanavalin A (Con A) -functionalized surfaces is investigated. It is shown that the Man-decorated vesicles adhere to the lectin surfaces, depending on the valency of the glycan-head group and the overall concentration of the incorporated ligands in the GUVs, whereas the Gal-functionalized vesicles show no interaction with the surfaces. The specificity of Con A-Man binding is confirmed by inhibition experiments. In a next step, mixtures of long and short, binding (Man) and non-binding (Gal) ligands are incorporated into the vesicles and characterized with regard to their interaction with the Con A surfaces, thereby focusing on the question, whether the non-binding glycan mimetics have an influence on the selective binding of the Man-ligands to the Con A surfaces, based on the dense and heteromultivalent presentation of glycans on natural cell surfaces (cp. **Figure 1** *Glycocalyx Models I*). In fact, this highly tunable model shows for the first time that depending on the valency (short vs. long) and the overall concentration of both, the Man-ligands and the Gal-ligands, three different scenarios can be identified: either the adhesion is not affected, the adhesion is significantly reduced or the adhesion of the vesicles on the Con A surfaces increases significantly. Generally, high concentrations of the long, non-binding ligands reduce adhesion, while the short, non-binding ligands have no effect. However, it is found that the long, non-binding crowding agents do not impact GUV adhesion when the vesicles contain low concentrations of the binding ligands. Notably, GUVs with low concentrations of the long, binding ligands adhere more strongly when doped with high concentrations of the short, non-binding ligands and low concentrations of the long, non-binding ligands.

The second part of the thesis focuses on reflecting naturally occurring lipid rafts in glycocalyx mimetics. Lipid rafts are dynamic and spatially localized agglomerates of glycolipids and various membrane

proteins in less mobile lipid domains. Although the exact function of lipid rafts is not yet fully understood, they are thought to play an important role in cellular interactions such as adhesion, communication or infection. The separation of a homogeneous lipid phase into ordered (Lo) and fluid (Ld) membrane domains is a phenomenon that is well researched in GUVs and is referred to as phase separation. Thereby unsaturated lipids form a fluid, disordered phase, while saturated lipids separate out with cholesterol into an ordered phase, which naïvely mirrors native lipid rafts. In order to reflect the local heterogeneities in the glycocalyx mimetics, four different glycan mimetics are synthesized, again employing SPPoS, differing in both, their respective glycosylation (Man or Gal) and their respective membrane anchor. The membrane anchors employed are derivatives of stearic acid and oleic acid, which differ significantly in their physico-chemical properties and are therefore expected to exhibit different behaviors in the phase-separating GUVs. Using a well-studied ternary lipid mixture and the glycan mimetics produced, phase-separating GUVs are prepared. Employing suitable lectin stainings, it is shown for the first time that the ligands preferentially insert into the ordered or disordered fluid domains of the vesicles according to their specific lipidic membrane-tether (cp. **Figure 1** *Glycocalyx Models II*). Based on these initial results, heteromultivalent systems are also produced that present different glycan mimetics in the ordered and disordered domains or different glycan mimetics in one domain. The influence of the membrane localization of the ligands on selective lectin binding is subsequently investigated. Astonishingly, it is shown that lectin recruitment associated with ligands in the ordered domains is considerably more efficient than with ligands in the disordered domains, which experimentally supports the idea that lipid rafts provide an important platform for vital processes in native cellular membranes and demonstrates that the developed model system enables for the first time the systematic study of raft-associated processes in glycocalyx mimetics.

Based on the first part of the thesis, the synthesis of lipid-functionalized and globally sulfated, so-called sulfated glycosaminoglycan (sGAG)-mimetics, is subsequently established. Virus-sGAG interactions on the glycocalyx are an important prerequisite to initiate viral infection and are, accordingly, important to study and comprehend in order to potentially inhibit viral infections therapeutically. Therefore, the previously established synthesis of long and short glycan mimetics is now expanded for sGAG mimetics to study virus-membrane interactions. For the sGAG mimetics, a combination of solid-phase synthesis and TIRP is again employed to obtain long and short glycan mimetics, site-selectively bearing a lipid moiety, as well as a fluorophore. The thusly derived glycan mimetics are then globally sulfated using established protocols to obtain a library of eight different short and long sGAG mimetics.

In a first series of experiments, one of the derived polymeric sGAG mimetics, functionalized with a cholesteryl-tether and Rhodamine B dye, is incorporated into GUVs and native cell membranes and the interaction with virus like particles (VLPs) is investigated (cp. **Figure 1** *Glycocalyx Models III*). It is

shown that some of the employed VLPs bind to the membrane tethered sGAG mimetics, demonstrating that the established synthesis platform enables structure-specific investigations with regard to virus binding on dynamic membrane model systems.

The final part of this thesis focuses on the dynamic clustering of glycan mimetics upon interaction with a multivalent receptor in glycocalyx models. Clustering of glycans in the glycocalyx is an important mechanism in biological systems, which appears to play an important role in a large number of processes. Clustering usually occurs very dynamically and is locally limited to a small area within the cell membrane. In order to emulate this dynamic clustering in glycocalyx mimetics, triggered by a ligand-receptor mediated binding, a novel SPPoS-compatible building block, featuring a polymerizable diacetylene-moiety, is developed that can be site-specifically incorporated into the backbone of the already established lipidated glycan mimetics. Diacetylenes can be topochemically polymerized under suitable conditions to generate a conjugated, fluorescent polydiacetylene backbone. In this manner, a first generation of diacetylene-functionalized glycan mimetics, bearing either a tetravalent Man- or Gal-head group, as well as a cholesteryl moiety, is synthesized and characterized. Subsequently, the self-assembly and polymerization of the diacetylene-functionalized glycan mimetics in aqueous solution is assessed, showing that the diacetylene-macromonomers polymerize upon irradiation and initial studies are executed to demonstrate the fixation and visualization of lectin-mediated clusters in GUVs (cp. **Figure 1** *Glycocalyx Models IV*).

In summary, the presented work offers several novel approaches for constructing glycocalyx mimetics that mirror more closely their natural analogues and, hence, enables the investigation of glycocalyx-associated phenomena in a simplified but highly tunable setting to further decipher the underlying biophysical and biochemical processes on cellular membranes.

List of Publications

Publications included in this Thesis

L.-C. Blawitzki, N. Bartels, L. Bonda, S. Schmidt, C. Monzel, L. Hartmann

'Glycomacromolecules to Tailor Crowded and Heteromultivalent Glycocalyx Mimetics'

Biomacromolecules **2024**, 25, 9, 5979–5994

L.-C. Blawitzki, S. Schmidt, C. Monzel, L. Hartmann

'Selective Glycan Presentation in Liquid-Ordered or -Disordered Membrane Phases and its Effect on Lectin Binding'

Angew. Chem. Int. Ed. **2025**, 64, e202414847

Publications not included in this Thesis

A. Banger, P. Pasch, L.-C. Blawitzki, S. Weber, M. Otten, C. Monzel, S. Schmidt, J. Voskuhl, L. Hartmann

'Detection of Lectin Clustering in Self-Assembled, Glycan-Functionalized Amphiphiles by Aggregation-Induced Emission Luminophores'

Macromol. Chem. Phys. **2023**, *224*, 2200314

Publications in Preparation

L.-C. Blawitzki‡, M. Hoffmann‡, L. Bonda, K. Schmidt, R. Groza, H. Ewers, L. Hartmann

‡ *authors contributed equally*

'Presentation of Sulfated Glycosaminoglycan Mimetics on Synthetic and Natural Membranes and their Interactions with Virus-Like Particles'

L.-C. Blawitzki‡, N. Jäck‡, L. C. Assenmacher, C. Monzel, S. Schmidt, L. Hartmann

‡ *authors contributed equally*

'Diacetylene-Functionalized Glycan Mimetics for Receptor-Mediated Cluster Imprinting in Model Membranes'

Conferences

M. Hoffmann, L. Bonda, L.-C. Blawitzki, R. Groza, H. Ewers, M. Schelhaas, N. L. Snyder, L. Hartmann

'Polymer Chemistry meets Virology – Sulfated Glycomacromolecules as GAG Mimetics'

Macromolecular Colloquium, February 23 - 25, 2022 – Freiburg im Breisgau, Germany

L.-C. Blawitzki, L. Bonda, S. Schmidt, C. Monzel, L. Hartmann

'The Impact of Crowding on Membrane-Associated Specific Binding Between Precision Glycomacromolecules and Lectins' – *awarded with poster price*

32nd Joint Glycobiology Meeting Glycans in health and disease, September 19 - 20, 2022 - Utrecht, The Netherlands

1. Introduction

1.1 The Cellular Membrane of Eukaryotes

The cellular membrane of eukaryotic cells is a complex entity composed of lipids, proteins, and carbohydrates, which forms a physical barrier to the cells' environment and maintains a non-equilibrium state between the cytoplasm and the extracellular space.[1,2]

The cell membrane primarily consists of a thin bilayer of lipids, which are essential for maintaining the integrity and functionalities of the cell membrane.[3] These lipids possess an amphiphilic nature, characterized by hydrophilic, usually charged, head groups and hydrophobic tail groups.[4,5] This amphiphilic property of the lipids enables them to self-arrange into a bilayer structure, with the hydrophobic tails facing inward and the hydrophilic heads facing outward towards the aqueous environment. This leads to the formation of a continuous, spherical lipid bilayer which is held together through non-covalent interactions between the hydrophobic tails.[1] Although this highly stabilizes the membrane, it is not rigidly fixed in place. Rather, lipids and integrated entities can rapidly diffuse laterally along the layer they reside in. In 1972 Singer and Nicholson proposed the nowadays widely agreed *Fluid Mosaic Model*, which describes the cell membrane as a dynamic and fluid arrangement of lipids and membrane-associated proteins.[6]

1.1.1 The Cellular Lipidome

Major lipid components of eukaryotic plasma membranes involve phospholipids, sphingolipids, and sterols, which are mainly synthesized in the endoplasmic reticulum (ER)(**Figure 2**).[3,7] The types of membrane lipids vary among species, tissues, and organelles, and are also known to be asymmetric in the outer and inner leaflets of a membrane.[8–11] Among the phospholipids, glycerophospholipids and sphingomyelins are the most common, with glycerophospholipids having a hydrophilic glycerol-3-phosphate backbone and sphingomyelins being derived from sphingosine.[7,12–14] To these backbones, hydrophobic long-chained fatty acids (the chain length of fatty acids generally falls within the range of 16–20 carbon atoms) are typically attached through ester linkages in 1- and 2-position (in case of glycerolipids) or through an amide bond with the primary amine of the sphingosine

backbone.[15,16] These fatty acids are straight-chained and display different levels of saturation, which regulates fluidity and structural integrity in the phospholipid membrane.

In biological membranes, most glycerophospholipids have polar head groups and only trace amounts are present as phosphatidic acid, which only comprises a phosphate in 3-position of the glycerol backbone and is an important intermediate in the synthesis of other phosphoglycerides. Phosphatidylcholine (PC) is the major component in eukaryotic membranes, followed by phosphatidylethanolamine (PE), phosphatidylglycerol (PG), phosphatidylserine (PS), and phosphatidylinositol (PI).[16,17]

Sphingomyelins mostly comprise phosphatidylcholine or phosphatidylethanolamine headgroups, while also hydrolyzed derivatives with a free terminal hydroxyl group (ceramides) are present in the plasma membrane. This enormous variation in head and tail groups enables the existence of more than 1000 distinct lipid species in eukaryotic cells.[11]

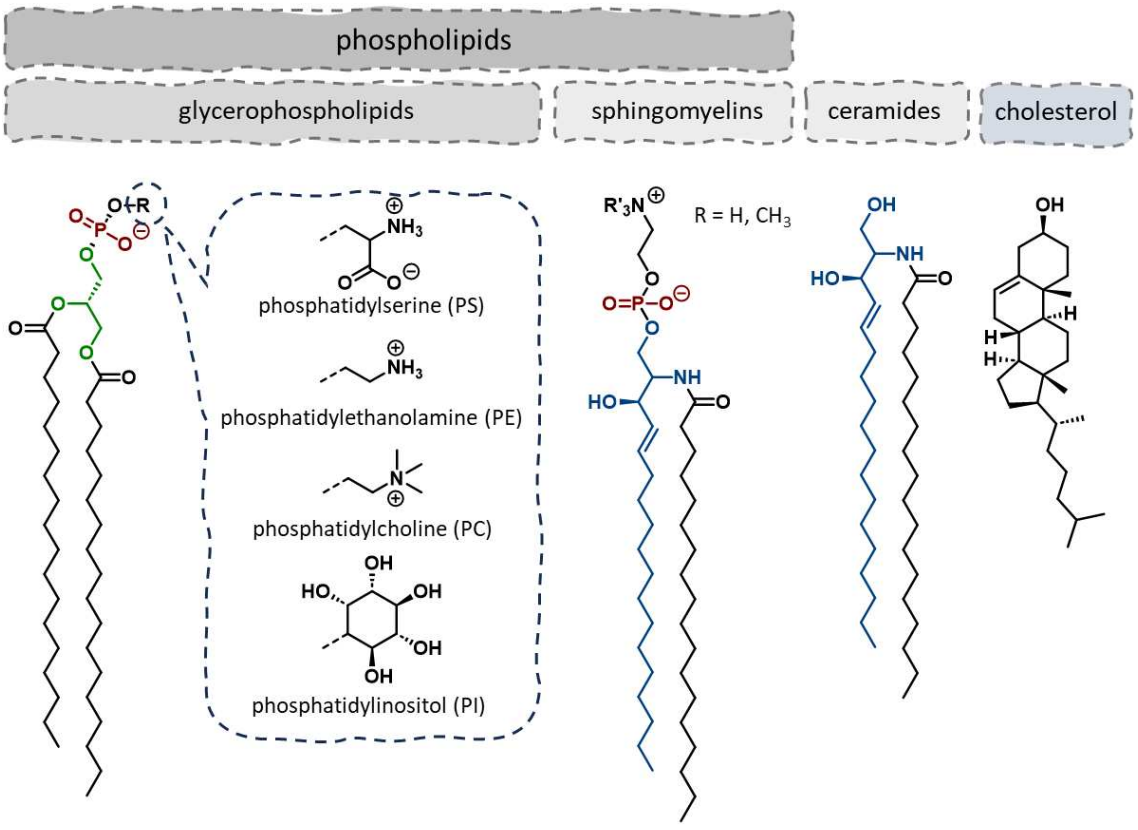

Figure 2. Schematic presentation of the prevalent lipids in mammalian cells.

Besides glycerophospholipids and sphingomyelins, cholesterol is the most important sterol in mammalian cells, making up about 30% of all cell membranes. It is necessary for membrane packing and fluidity maintenance, maintaining membrane integrity and allowing cells to change shape.[18] Its steroid backbone and hydrocarbon chain are embedded in the membrane along with the fatty acid chains of the other lipids, while its hydroxyl group is oriented towards the aqueous environment. The tetracyclic ring of cholesterol contributes to membrane fluidity and reduces permeability to neutral solutes and ions. The favorable interaction of cholesterol with sphingomyelins, which display a high level and saturation and can engage in intra- and intermolecular hydrogen bonding, mediates the formation of spatially fixed accumulations of lipids, which are referred to as lipid rafts.[3,7,18] These rafts are believed to fulfill important tasks, for instance trafficking and signaling through the recruitment and local concentration of protein complexes and binding motives.[19]

The large diversity of lipids, the lipid environment and the asymmetrical distribution across the inner and the outer leaflet of the membrane drastically influence microscale organization and function of the cell membrane and its enclosed entities.[20] It is, therefore, important to understand molecular details of membrane structure and mechanisms responsible for its dynamic organization. Furthermore, the lipid composition of the plasma membrane plays a crucial role in defining its physical properties, including mechanical and viscous characteristics.[21]

Besides being comprised of a plethora of different lipids, the cellular membrane also contains a large amount of membrane proteins, typically comprising around 50% of the membrane volume.[22] These proteins are crucial for the cellular function because they are responsible for the mediation of various biological processes as for instance trafficking, signaling, or adhesion.[23] Generally, there are two types of membrane proteins: peripheral membrane proteins, which are bound to the membrane surface, and integral membrane proteins, which are integrated into the lipid bilayer of the membrane with a hydrophobic component.[24,25]

Integral proteins or transmembrane proteins extend the whole lipid bilayer, comprising a hydrophilic cytosolic domain, which interacts with the cell's interior, a hydrophobic transmembrane domain that anchors it within the cell membrane, and a hydrophilic extracellular domain that interacts with the extracellular space. Peripheral membrane proteins do not establish a permanent connection with the cell membrane. Instead, they

engage with the cell membrane in a reversible manner through various interactions, such as electrostatic or hydrophobic connections with integral proteins or peripheral regions of the phospholipid bilayer, or by utilizing hydrophobic tails or glycophosphatidylinositol (GPI)-anchors directly.[24,26,27]

Both, lipids and membrane proteins on the surface of the cellular membrane, can be heavily decorated with carbohydrates to give glycolipids and glycoproteins, respectively (which together comprise 2-10% of the cellular membrane).[28] Glycoproteins are the predominant glycoconjugates, as approximately 80% of the cell surface located carbohydrates are glycoproteins.[29,30] The highly heterogenous and complex ensemble of glycosylated lipids and proteins within the cell membrane is essential for various biological events and is commonly referred to as the glycocalyx.

1.2 The Glycocalyx

The glycocalyx is a highly complex, dense layer of glycans linked to proteins and lipids on eukaryotic cells and is known to play a crucial part in a plethora of physiological and pathological processes (**Figure 4**). Since the glycocalyx is the first instance that gets into contact with a cell's adjacency, most biological processes are mediated by the interactions of proteins with carbohydrates presented on the glycocalyx, which renders the glycocalyx and thus the cell membrane a crucial entity for manifold biological processes.[31,32] In eukaryotic cells glucose (Glc), galactose (Gal), mannose (Man), fucose (Fuc), *N*-acetylgalactosamine (GalNAc), *N*-acetylglucosamine (GlcNAc), xylose (Xyl), glucuronic acid (GlcA), and *N*-acetylneuraminic acid (NeuAc) are the most abundant monosaccharide building blocks on the cellular membrane (**Figure 3**).[31]

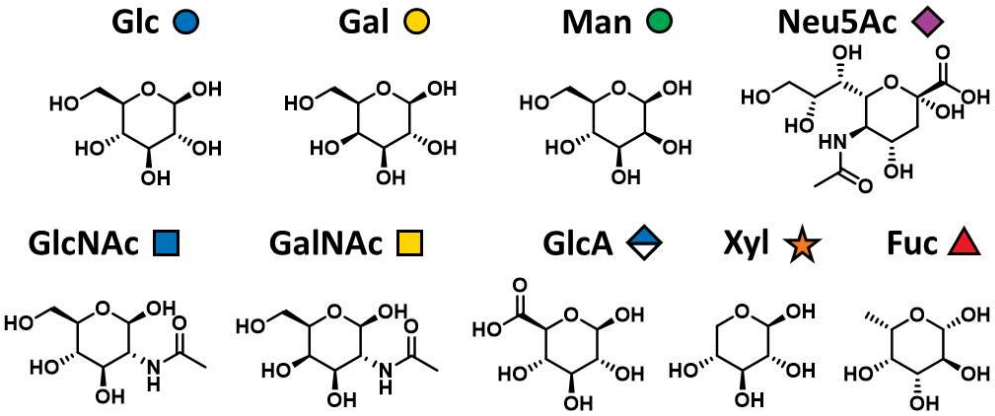

Figure 3. Chemical structures of the most abundant carbohydrates in eukaryotic glycocalyces and their denotation according to the Symbol Nomenclature For Glycans (SNFG).

Though only a few monosaccharide building blocks are available in nature, multiple enzymatic transformations enable the assembly of highly diverse and complex oligo- or polysaccharides in multiple regio- and stereochemical combinations, resulting in glycosylation patterns that vary in length, geometry, and composition and post synthetic functionalization with phosphates, sulfates or acetates.[36,37]

The dense ensemble of glycosylated proteins and lipids on the extracellular surface acts as a physiological barrier, regulating accessibility to adjacent entities, and plays a pivotal role in various cellular functions, including cell-cell-communication, adhesion, signaling and pathogen infection (**Figure 4**).[31,33–35] Consequently, understanding the diversity and roles of

these glycans is crucial for insights into cell biology, disease mechanisms, and the development of therapeutic strategies.

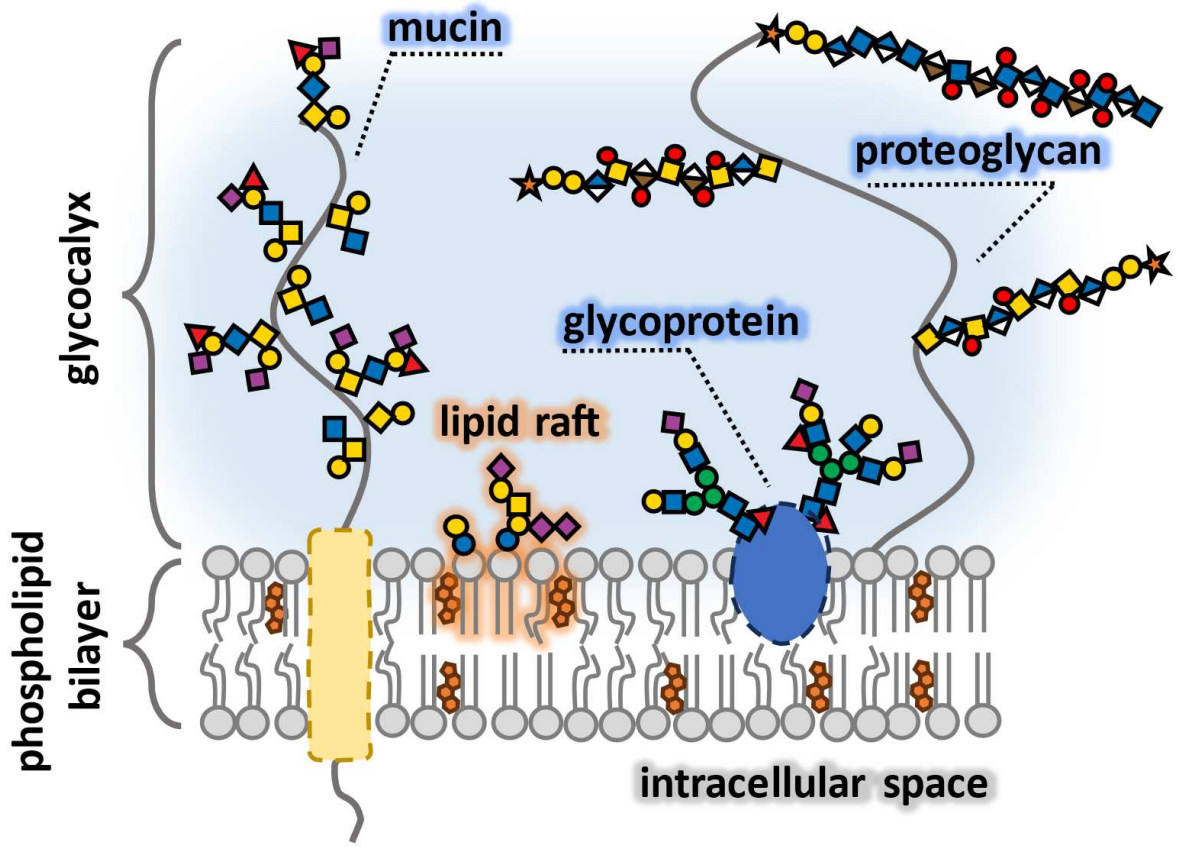

Figure 4. Schematic presentation of a eukaryotic glycocalyx. The plasma membrane consists of a phospholipid bilayer spiked with proteins. Both, lipids and proteins can be covalently functionalized with glycans that mediate a large number of biological mechanisms.

1.2.1 Glycan-Binding Proteins

Many biological processes that enroll on the cellular surface, such as cellular communication, immune responses or pathogen infections are mediated by the interaction of glycan-binding proteins (GBPs) and specific glycan-motives in the glycocalyx.[38,39] Generally, GBPs can be categorized into lectins and sulfated glycosaminoglycan-binding proteins (sGAG-binding proteins). Lectins can be further divided into different families, based on their carbohydrate-recognition domains (CRDs) and typically bind to terminal epitopes on cell surface associated glycans that fit well into their respective CRDs.[39]

Generally, the interaction between a particular carbohydrate epitope and a lectin is characterized by a relatively weak and reversible bond with binding constants ranging from micromolar to millimolar.[40–42] To address this issue, nature presents multiple copies of the same sugar or CRD, which is referred to as multivalency.[43,44] Ideally, this multivalent interaction results in an increase in binding avidity, where the overall binding enthalpy is stronger than the sum of the individual interactions (positive cooperativity).[42,43,45] The strengthened binding of multivalent ligands and CRDs can be attributed to four main factors that affect overall binding avidity. These factors include the chelate effect, the cluster-effect, statistical rebinding, and sterical shielding (**Figure 5**).[44,46]

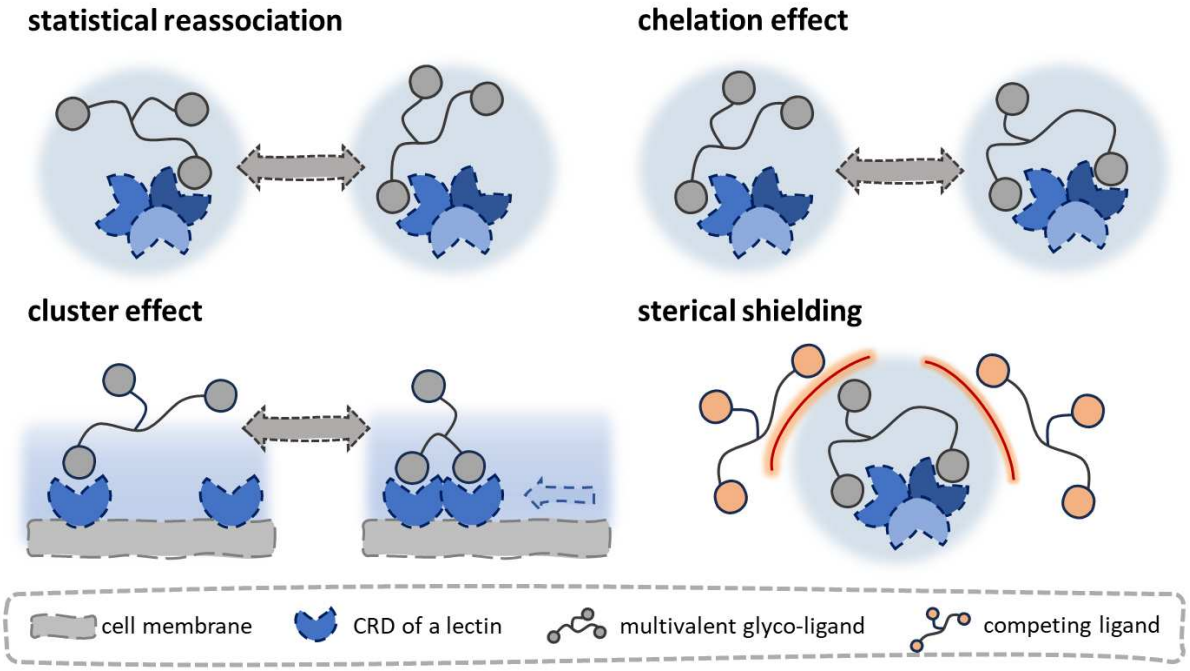

Figure 5. Schematic illustration of the multivalent effects increasing carbohydrate-lectin binding avidity.

Besides these homomultivalent effects on enhanced binding avidity, the influence of heteromultivalency, which involves the presentation of different carbohydrates on a single scaffold, can further lead to increased ligand-receptor binding and heightened specificity of the interaction.[47]

Two well-studied model lectins for lectin binding studies, that also have been employed in this work, are *Concanavalin A* (Con A) and *Ricinus communis agglutinin* (RCA). Both are plant-derived lectins and are well known for their specific carbohydrate-binding properties. Con A

is classified as a C-type lectin and exists as a dimer at acidic pH (below pH 5.5) or as a tetrameric form at neutral pH (between pH 5.8 and pH 7.0), with each subunit containing a CRD with high affinities for α-Man- and α-Glc-moieties.[48–50] The term C-type refers to a common CRD within this lectin family that requires divalent cations (especially Ca^{2+} and in the case of Con A Mn^{2+}) that stabilize the conformation of the lectin and enhance the interaction with Man- and Glc-glycans.[50,51]

By contrast, RCA is an R-type lectin and binds preferentially to terminal β-Gal-moieties in glycans.[52] R-type lectins are characterized by a conserved CRD that was originally identified in ricin, a very potent plant toxin and the first lectin to be discovered.[53] RCA is a tetramer consisting of two α- and two Gal-binding β-subunits that are non-covalently associated.[54]

Due to their specificity towards certain glycan-epitopes, lectins, such as the above-mentioned RCA and Con A, are often employed to analyze and enrich cell surface glycans.[55] Fluorescently labelled derivatives, for example, enable profiling of native glycans on cell surfaces and in other biological samples. Similarly, microarrays that employ lectins with different binding preferences allow for the simultaneous analysis of multiple glycan structures *in vitro*, providing a comprehensive analysis of glycan constitution and distribution.[56,57]

Another class of glycan-binding receptors that are preliminarily studied as part of this thesis and, hence, important to mention are sGAG-binding proteins. These do not have a specific CRD but rather bind through electrostatic interactions between negatively charged sulfate and uronic acid moieties in sGAGs and clusters of positively charged amino acids in their protein sequence.[38,58] Further secondary interactions, such as Van-der-Waals interactions or hydrogen bonding can also have an influence on the interaction with proteins. Besides cellular machineries, that rely on the interaction of sGAG binding proteins with cell surface glycans, many pathogens also make use of sGAGs in the glycocalyx to adhere to a host cell. For example, the viral spike protein of SARS-CoV-2 interacts with heparan sulfate on epithelial cells in the airways which mediates its transfer to host cell surface receptors, eventually resulting in infection of the cell.[38,59]

1.2.2 Glycolipids

Glycolipids are lipid molecules that have one or more carbohydrate groups attached and are mainly synthesized in the endoplasmatic reticulum (ER) and in the Golgi apparatus.[31] In a first step, the main lipid component is synthesized in the ER before it is transported to the golgi. Here, more complex structures are built up by stepwise addition of sugar residues by specific glycosyltransferases in an ordered sequence, before the final glycolipids are transported to the cell membrane.

The main types of glycolipids found in eukaryotic cells are glycosphingolipids and glycophosphatidylinositols (GPIs)(**Figure 6**).

Glycosphingolipids are the most common type of glycolipids in mammalian cells.[60] They consist of a ceramide backbone with one or more sugar residues attached and can be further subdivided into different classes.[61] Ceramides with neutral mono- or oligosaccharides bonded β-glycosidically to its terminal OH group are defined as cerebrosides, with galacto- and glucocerebrosides being the simplest ones. Cerebrosides can be sulfated, giving sulfatides or sialylated to yield gangliosides (**Figure 6B**).[62] Glycosphingolipids can excessively engage in intermolecular hydrogen bonding, resulting in tight packing of the lipid molecules, rendering glycosphingolipids highly common in lipid raft microdomains, along with cholesterol and sphingomyelins.[63] The presence of glycosphingolipids in lipid rafts, is crucial for cellular functions, such as signaling, adhesion and membrane protein trafficking.[64,65]

Besides their importance in native cellular mechanisms, also many pathogens exploit glycolipids to adhere to and invade host cells. For instance, certain polyomaviruses and influenza viruses bind to gangliosides in lipid rafts to initiate infection.[66,67]

Glycophosphatidylinositols (GPIs) are glycolipids where a conserved core structure consisting of Manα1→2Manα1→6Manα1→4GlcNα1 is linked to a *myo*-phosphatidylinositol.[68] GPIs serve as integral protein anchors on the extracellular membrane, known as GPI-anchored proteins, where the protein is conjugated via an amide bond between its *C*-terminus and a C6-phosphoethanolamine on the distal Man-moiety attached to the phosphatidylinositol backbone. The core structure of the GPI-anchor can be further functionalized with oligosaccharides and phosphates, depending on the type of cell (**Figure 6A**). Since the lipid moieties in GPIs generally display a high level of saturation, GPI-anchored proteins are also

found to especially associate with lipid rafts where they are essential in mediating cell-cell interactions and signal transduction (**Figure 6C**).[69–71]

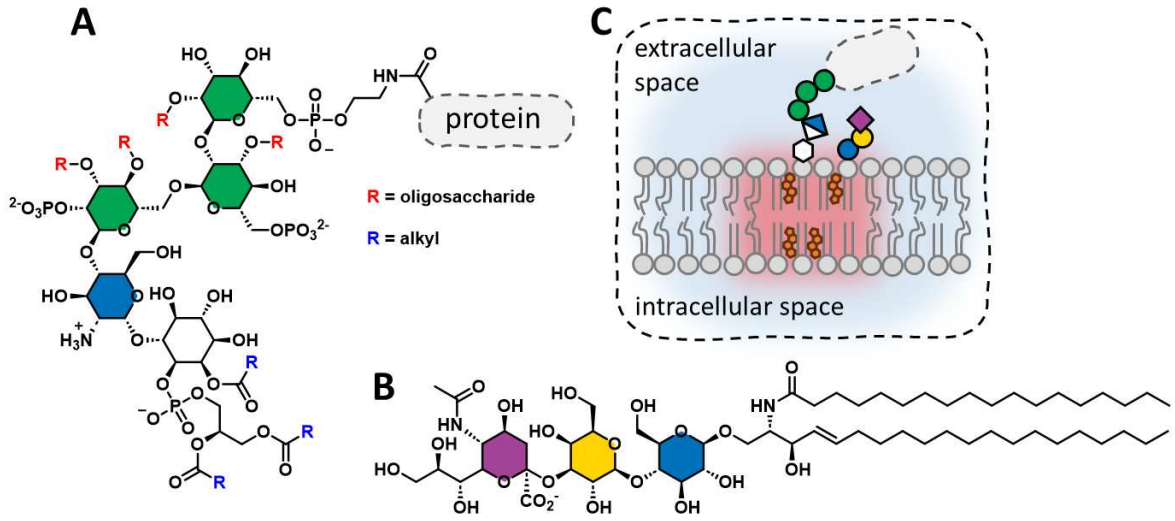

Figure 6. Chemical structures of an exemplary GPI-anchored protein (**A**) and the GM3 ganglioside (**B**). **C**: GPI-anchored proteins and glycosphingolipids, such as GM3, have high affinities towards lipid rafts (highlighted in red).

1.2.3 Glycoproteins

Glycoproteins are ubiquitous in nature. It is assumed that more than two thirds of the eukaryotic proteome is glycosylated, whereby the attachment of carbohydrates to a distinct protein core thereby significantly influences its structure, stability and function.[29,30,72] While there is a distinction to be made between soluble glycoproteins that circulate freely within the organism (e.g. certain antibodies, enzymes or hormones) and membrane associated glycoproteins, this chapter will focus only on the latter, which are embedded within the eukaryotic plasma membrane.[73,74]

Glycoproteins and proteoglycans, which are considered a subclass of glycoproteins, are two existential components of the glycocalyx (cp. **Figure 4**). While glycoproteins on the cell surface usually have short, branched glycans (approximately 3 to 20 monosaccharides) attached to their protein core, proteoglycans are made up of a core protein that is heavily decorated with one or more highly linear glycosaminoglycan (GAG) chains.[75,76] Glycosylation of proteins is a co- and posttranslational modification that is mediated by glycosyl- and oligosaccharyltransferases.[77] As a result, the modification produces a complex, covalently

bound glycosylation pattern due to the inherent molecular complexity of natural saccharides, as was discussed above.[78] Glycosylation of proteins promotes proper protein folding and increases protein stability by protecting against proteolysis.[79,80] Also, misregulation of glycosylation is closely linked to diseases.[77,81]

In glycoproteins, the linkage between the first sugar of a glycan and the protein defines its glycosylation class. The most prominent glycans found on eucaryotic plasma membranes are termed as *N*-linked and *O*-linked glycans. *N*-linked glycans are attached to the nitrogen atom of asparagine residues in proteins, while *O*-linked glycans attached through an oxygen atom of a serine or threonine moiety.[82] Glycoproteins, as are glycolipids, are biosynthesized in the ER and the Golgi apparatus. The core glycan in *N*-linked glycans is typically preassembled and transferred onto the protein inside the ER and can be further modified in the Golgi apparatus. For *O*-linked glycans, only a single carbohydrate-moiety is attached in the ER and the glycan is assembled iteratively in the Golgi apparatus.[60,82]

Over 90% of glycoproteins are *N*-linked glycoproteins. *N*-glycosylation is a co-translational process, i.e. the glycans are added to the protein while it is being biosynthesized, which ensures their proper folding and functioning. The biosynthetic *N*-glycosylation is initiated via the attachment of a high-mannose core structure, which is subsequently trimmed and sequentially connected with further monosaccharides, depending on the available glycosyltransferases.[83]

O-linked glycans typically begin with an *N*-acetylgalactosamine (GalNAc) moiety linked to serine or threonine residues in proteins and can be extended to different *O*-glycan core structures, which are then further elongated.[83,84] *O*-glycosylation, different to *N*-glycosylation, is a posttranslational process that occurs in the Golgi apparatus, i.e. the glycans are added to the protein after its being biosynthesized. They are especially important for structure, cellular protection, and cellular signaling. Prominent representatives of densely *O*-glycosylated proteins are mucins, large glycoproteins providing protective mucous barriers on epithelial surfaces.[85] Mucins are primarily classified into secreted mucins and transmembrane mucins. Secreted mucins, such as MUC2, form gel-like barriers around the cellular plasma membrane that trap pathogens and small particulates, while transmembrane mucins, like MUC1 and MUC4, are integral membrane proteins that contribute to the structural integrity of the glycocalyx.[86–88]

Glycosaminoglycans (GAGs) are long, unbranched and negatively charged polysaccharides consisting of repeating disaccharide units that form an extreme heterogeneity and structural complexity that is found on proteoglycans.[76] Except for hyaluronic acid (HA), GAGs are usually sulfated and comprise heparin sulfate, heparan sulfate (HS), chondroitin sulfate (CS), dermatan sulfate (DS) and keratan sulfate (KS) that are conjugated to a core protein.[89–93] GAGs are involved in many biological mechanisms, such as signaling, embryonic development or regulation of enzymes.[94] Especially HS proteoglycans are the most abundant GAGs on endothelial cells and make up more than 50% of the endothelial proteoglycans.[95,96]

1.3 Glycomimetics

Understanding the nature of carbohydrate-protein interactions is a fundamental step in order to fully comprehend the underlying mechanisms of glycocalyx-associated processes. The above-mentioned inherent complexity of natural glycans immensely complicates the investigation and understanding of such glycocalyx processes, since the isolation and proper characterization is often challenging. Additionally, the inhomogeneity of natural glycan presentation (e.g. the existence of different glycoforms) results in extraction of complex mixtures which can be difficult to separate. Therefore, researchers have developed simplified mimetics of naturally occurring glycans. The chemical synthesis of glycan mimetics requires a rational design of the target structure to present simple binding motives, usually terminal epitopes of glycans, to derive ligands with high affinity and selectivity that are more easily accessible.[97]

Multivalent presentation of carbohydrate motives is realized through covalent attachment of the respective carbohydrates onto a synthetic scaffold.[41,98] The employment of synthetic backbones provides a precise control over the architecture, density and composition of the glycan mimetics and also enables regulating the polarity and flexibility of the macromolecule in a highly reproducible manner. The employment of well-studied controlled polymerization techniques, such as reversible-addition-fragmentation chain-transfer polymerization (RAFT), ring opening metathesis polymerization (ROMP) or atom transfer radical polymerization (ATRP) in combination with post-polymerization modifications enables access to a wide series of well-defined glycan mimetics. In this manner, different synthetic strategies and scaffolds for the development of glycomimetics have been explored, such as linear glycopolymers[99–103], glycodendrimers[104], glyco-decorated micelles[105,106] or glyconanoparticles[107,108]. Also, the decoration of surfaces with glycomimetics has been demonstrated to be a suitable tool to study carbohydrate-protein interactions.[109,110] Some examples of different glycomimetics are shown in the following **Figure 7**. Typically, the resulting materials are characterized in terms of their binding affinity towards a suitable lectin. The respective binding affinity is often quantified through the dissociation constant (K_d) of the binding, which mirrors the strength of the interaction between the glycan-mimetic and the lectin.[111] Examples of suitable assays to quantify the interaction of glycan mimetics with lectins comprise surface plasmon resonance (SPR) studies, nuclear magnetic resonance (NMR) studies, isothermal titration calorimetry

(ITC) or fluorescence-based screening assays to identify suitable ligands for a target protein in terms of ligand density, architecture and multivalent presentation.[112–114]

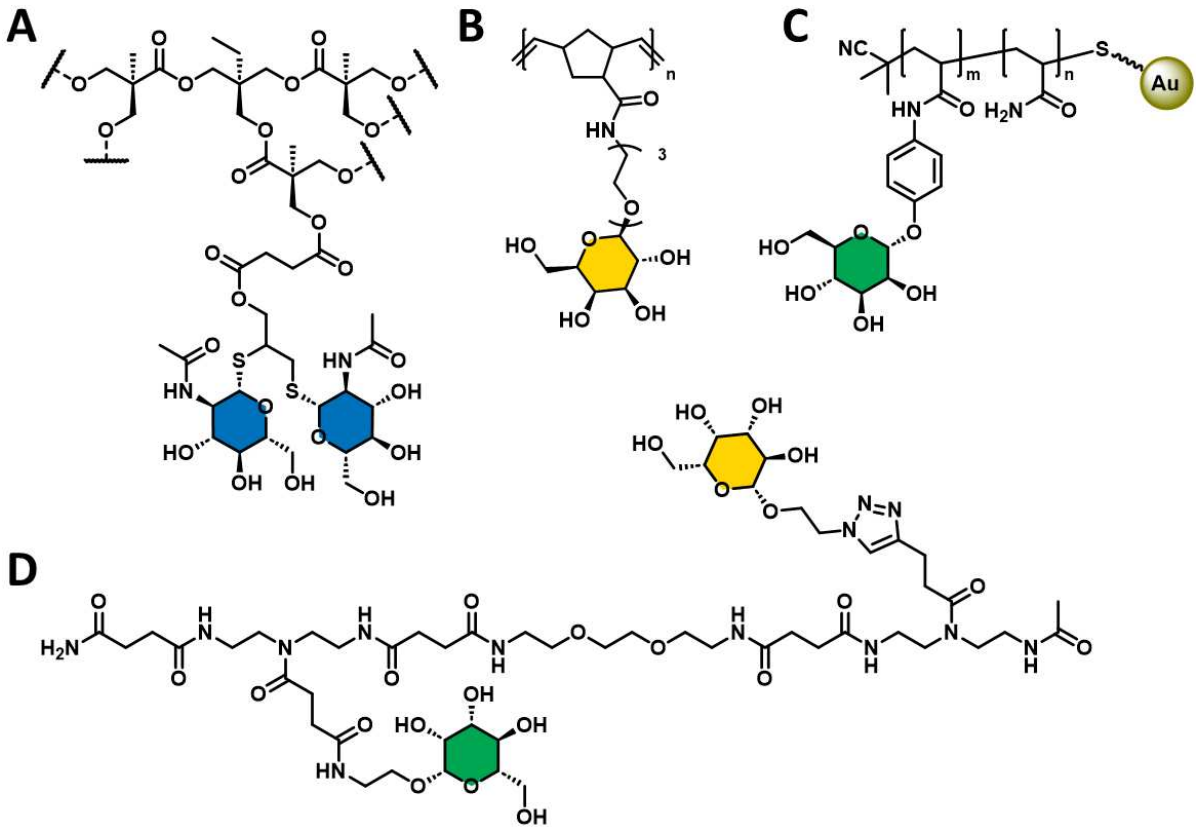

Figure 7. Chemical structures of exemplary glycan mimetics. **A**: A GlcNAc-terminated dendrimer.[104] **B**: Linear Gal-polymer derived via ROMP.[115] **C**: Gold-nanoparticles functionalized with a Man-copolymer derived via RAFT.[116] **D**: Sequence-defined, heteromultivalent glycooligo(amidoamine).[117]

While many of these systems have generally proven successful in generating high affinity glycan mimetics, the obtained materials still exhibit certain levels of dispersity, rendering it difficult to obtain proper structure-property correlations and compare results across different scaffolds and platforms.

A rather novel class of glycomimetics was introduced by *Hartmann and coworkers* trying to develop a platform that allows for a highly defined variation of the structural parameters of the synthetic scaffold and generate model compounds to investigate glycomimetic binding in a systematic fashion.[118,119] The approach is based on the solid-supported synthesis of sequence-defined glycooligo(amidoamines), which employs tailor-made synthetic building blocks in combination with already established solid-phase peptide synthesis protocols, enabling precise control over sequence, valency, inter-ligand spacing and architecture, which

are known to govern the specificity and avidity of lectin binding (cp. **Figure 7D**). Several examples demonstrate, that the thusly derived glycan mimetics have function as high-affinity glycomimetics in lectin binding studies as well as cell studies.[103,120,121]

1.3.1 Solid-Phase Polymer Synthesis of Sequence-Defined Glycooligo(amidoamines)

The employment of a solid support to derive sequence defined peptides was originally introduced by *Robert B. Merrifield* in 1963.[122] While conventional coupling reactions in solution require tedious purification steps, are rather time-consuming and low yielding, the iterative assembly of the peptide backbone on a solid phase allows for an efficient and reliable synthesis of sequence-defined peptides.[123]

Solid phase synthesis (SPS) employs three major steps to assemble sequence defined peptides on a solid support: 1.) functionalization of an insoluble carrier resin, 2.) deprotection of a temporary protecting group and 3.) coupling of a carboxy-functionalized, *N*-protected amino acid.[123] The iterative assembly of amino acid building blocks through repetitive coupling and deprotection steps eventually yields the sequence defined target peptide, assembled from the *C*- to the *N*-terminus (different than native protein biosynthesis).[123]

The employment of multifunctional building blocks (e.g. amino acids bearing a further functional group in their side chain, such as lysin (Lys) or cysteine (Cys)) requires a permanent protection of the side chain functionalities to prevent unwanted side reactions, while the α-amine that is required for the next coupling reaction is protected temporarily. Consequently, the temporal and the permanent protecting groups need to be orthogonal to one another, i.e. they are selectively cleavable in the presence of the other protecting groups.[124] Merrifield originally employed tert-butyloxycarbonyl (Boc) as temporary α-amino protecting group for the iterative scaffold elongation, while side chain functionalities were protected with benzyl protecting groups.[123] Boc chemistry requires acidic conditions for cleavage, while the benzylic protecting groups remain stable under these conditions and can subsequently be cleaved selectively via hydrogenolysis.

The choice of temporal and permanent protective groups depends on the chosen resin and its linker where the first building block is added.[123,125,126] The resin linkage critically dictates the cleavage conditions and the *C*-terminal functionality of the peptide after cleavage. Thus,

the choice of protective groups and the terminal linkage requirements prescribe the overall synthetic strategy.

While Merrifield originally employed a chloromethyl-linker functionalized polystyrene resin, which requires hard acidic cleavage conditions (HF) to give *C*-terminal carboxylates, today a commonly employed linker is the rink amide, giving a *C*-terminal primary amide after cleavage of the peptide.[123,127] Most current synthetic protocols rely on 9-fluorenylmethoxycarbonyl (Fmoc) as temporary protecting group, which is completely orthogonal to the acid-labile rink amide linker.[128,129] Cleavage of the Fmoc-group is achieved using secondary amines, such as piperidine, which releases a free amine and a dibenzofulvene derivative.[129] The use of piperidine as base promotes the formation of an adduct with the dibenzofulvene, which, on the one hand, prevents side reactions, such as Michael-addition of the N-terminal amine or polymerization of the dibenzofulvene and, on the other hand, enables monitoring of the conversion, since the chromophoric adduct can be detected via UV absorption.[128]

To increase the conversion rate after each coupling step, and eventually the yield and purity of the target peptide, excess building block is used along with coupling reagents, that promote the amide bond formation through activation of the free carboxylic acid. Excess reagent, as mentioned before, can easily be removed via filtration and washing and since the coupled building blocks remain protected during each coupling step, multiple couplings can be employed to ensure a complete conversion in each building block addition, rendering SPS more efficient than traditional solution-based coupling methods.

Merrifield employed dicyclohexylcarbodiimide (DCC) as coupling reagent, which converts the free carboxylic acid of the building block to couple into a reactive *O*-acylisourea, which is easily attacked by a nucleophilic amine to give an amide bond and release the respective urea derivative.[123] Nowadays, another commonly employed coupling reagent is PyBOP along with the sterically very demanding DIPEA.[130]

The reaction of the carboxylate of the building block to conjugate with the oxophilic phosphonium species gives an activated acyl phosphonium salt intermediate and thereby releases one equivalent of -OBt (1-hydroxybenzotriazole). The released OBt- can then attack the acyl oxophosphonium intermediate, resulting in a less-labile activated ester, which is prone to nucleophilic substitution with the free terminal amine on the solid support, giving

an amide bond. After removing the excess reagent through thorough washing of the resin, the Fmoc-protecting group of the new building block can be cleaved in order to couple the next building block.

For its general applicability and synthetic importance, SPS can nowadays be performed on automated peptide synthesizers, minimizing time effort and enabling an easier scale up. Modern synthesizers automatically measure the UV-absorbance after Fmoc-deprotection in order to ensure complete deprotection of the growing peptide before adding the next building block and further promote the conversion rate of each building block conjugation via microwave assistance, which results in less error sequences and thus higher overall purities and yields.[123,131]

The principle of SPS has proven so versatile and feasible that it is nowadays not only used for the synthesis of peptides, but also for the synthesis of other biopolymers such as nucleic acids and polysaccharides.[132,133] Furthermore, this approach is also suitable for the synthesis of mimetics of natural glycans. As mentioned above, *Hartmann et al.* have further developed solid-phase synthesis to create sequence-defined glycooligo(amidoamines) by means of solid phase polymer synthesis (SPPoS) to develop precision glycomimetics, enabling the systematic study of carbohydrate-lectin interactions.[118,119] While the fundamental principles of SPS remain the same, SPPoS employs tailor-made synthetic building blocks, which also bear an Fmoc-protected primary amine and a free carboxylic acid but additionally are designed in such a way, that their chemical structure meets the requirements of their respective purpose (**Figure 8**). Depending on their later function in the assembled scaffold, these building blocks are differentiated into functional building blocks and spacer building blocks.[134] Functional ones, based on a diethylenetriamine unit, conjugated to a succinic acid moiety, carry a side chain functionality on the secondary amine which can be used as functional handle for later modifications to the assembled backbone. As an example, the alkyne functionalized TDS building block (triple bond diethylenetriamine succinyl) or the azide functionalized BADS building block (benzyl azido diethylenetriamine succinyl) allow for a later conjugation of respectively functionalized motives (e.g. carbohydrates) via copper(I)-catalyzed azide-alkyne cycloaddition (CuAAC).[134]

The tailor-made spacer building blocks, on the other hand, allow for a rational modification of the backbone polarity as well as regulating the spacing between ligands and other

functionalities. The EDS building block (ethylene glycol diamine succinyl) is the most commonly employed building block to create a distinct spacing within the backbone and increase the hydrophilicity of the backbone altogether. The ODS building block (octamethylene diamine succinyl), on the other hand, increases the hydrophobicity of the backbone, while retaining the overall distance between ligands.[134]

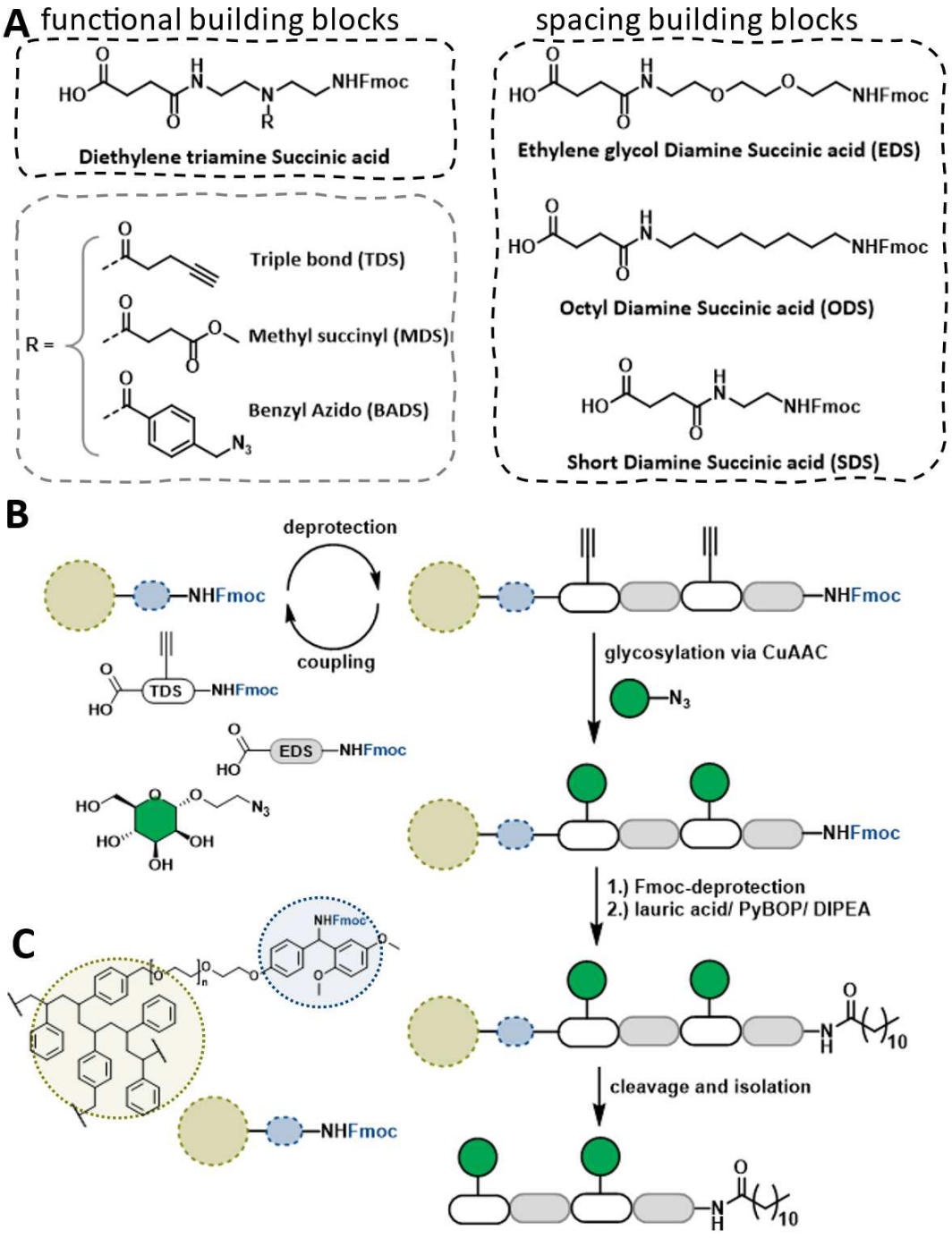

Figure 8. A: Chemical structures of tailor-made functional and spacing building blocks for SPPoS. **B:** Schematic illustration for the iterative assembly of an amphiphilic glycomacromolecule on the solid phase employing SPPoS. **C:** Chemical structure of the TentaGel resin (yellow) and the rink amide linker (blue).

While the usage of these tailor-made building blocks gives completely synthetic macromolecular scaffolds, a combination with natural or modified α-amino acids allows for the introduction, e.g. of short peptide motives or further functionalities, such as thiol-moieties through the introduction of Cys-units.[103] The introduction of multiple, orthogonally protected functional handles into the backbone allows for a site-specific functionalization, e.g. with fluorophores for fluorescence microscopy, or the introduction of branching points to tailor the architecture of the glycan mimetics.[135]

One major disadvantage employing SPPoS, is a limitation in accessible chain length. As the backbone grows on the solid support, secondary interactions between the backbone and the solid support lead to coiling and aggregation, which can impede quantitative coupling and deprotection of the growing backbone, leading to an increase in error sequences and, thus, reduced overall yields and purities.[136] To overcome this limitation, several methods have been employed to access higher molecular weight structures, for instance employing thiol-ene conjugation of solid phase derived segments.[103]

The solid-supported synthesis of mimics of naturally occurring glycans also offers the possibility to easily prepare amphiphilic structures. While classic conjugations of hydrophilic molecules to hydrophobic moieties faces certain difficulties, as solubility issues, tedious purifications, low coupling efficiencies or a lack of control of the position of the linkage, SPPoS enables the site-specific introduction of hydrophobic motives to the backbone. The only prerequisites that are important to meet is a good solubility of the hydrophobic motif to couple and a sufficient swelling behavior of the resin in the employed solvent, while the general solubility of the hydrophilic group is neglectable. In this manner, fatty acid conjugated glyco-mimetics have been prepared by means of solid-phase polymer synthesis, which self-assemble into micelles (cp. **Figure 8B**).[105] In the same manner, glycan mimetics can be prepared that are equipped with a cholesteryl moiety, which allows their stable introduction into phospholipid membranes to access natural mimics of glycocalyx constituents.[137]

In summary, this modular approach of SPPoS allows for the preparation of highly defined synthetic glycan mimetics, where valence and distance between ligands, flexibility and polarity of the backbone and the overall architecture of the structure, as well as the introduction of further functional handles can be precisely modified.

1.4 Glycocalyx Engineering

Analyzing carbohydrate-protein-interactions with synthetic glycan mimetics in solution or in highly simplified assays (e.g. with one of the components being fixed on a substrate) admittedly enables studying selective interactions between a protein of interest and its potential ligand. However, simple *in vitro* studies fundamentally lack the complexity and heterogeneity of native glycocalyces. *In vivo*, glycans interact in a densely crowded and highly inhomogeneous and dynamic context that simple binding assays cannot mirror properly.[35,138,139]

The glycocalyx of native cellular membranes is a densely crowded and highly heterogenous ensemble of glycoproteins and glycolipids whereby localization, dynamics and the manner of presentation of binding epitopes have a crucial influence on the interaction. To create a more realistic and adequate model of the natural environment and to draw fundamental conclusions about specific structure-impact-mechanisms, we need to conceptually recreate the three-dimensional complexity of native glycocalyces. To tackle this issue, researchers have developed different approaches that can be summarized under the term *glycocalyx engineering*.

1.4.1 Glycan Mimetics for Glycocalyx Engineering

One of the key aspects of *glycocalyx engineering* is the rational design and synthesis of lipidated mimetics of native glycocalyx constituents that can be introduced into biological or model cellular membranes to create models of or selectively alter cellular membranes and, thus, study molecular interaction in a more realistic setting.

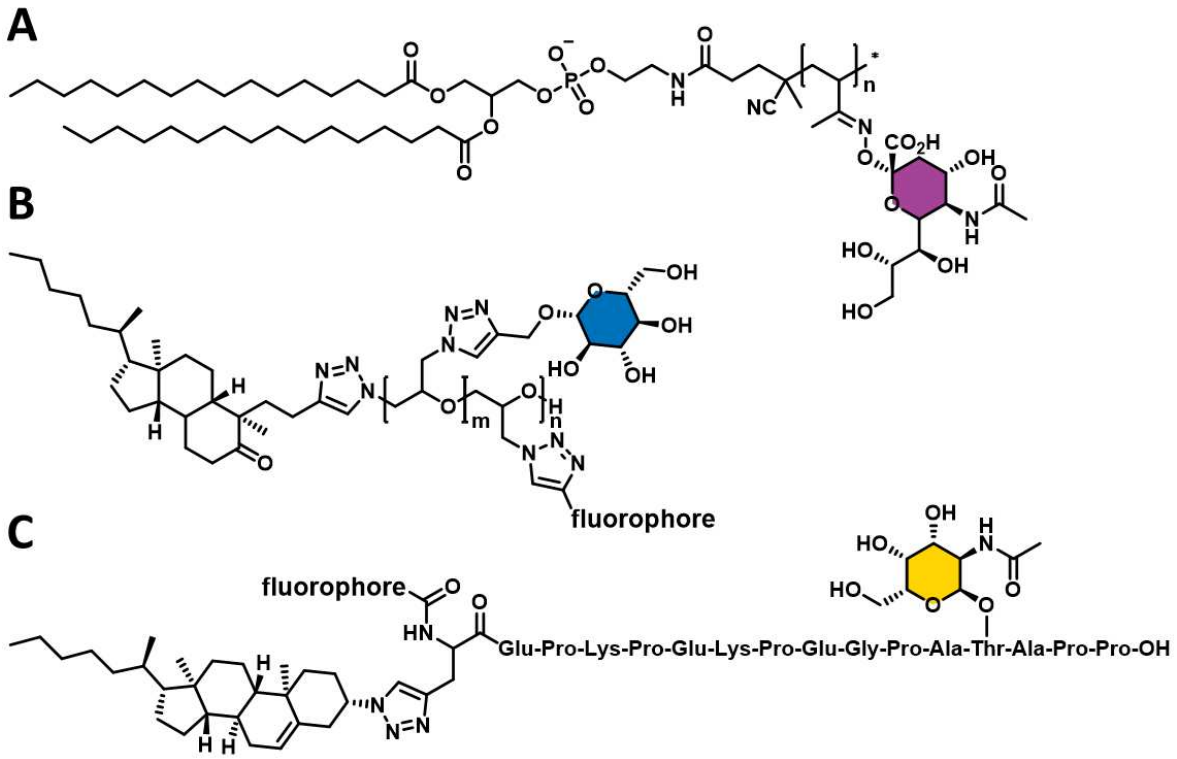

Figure 9. Chemical structures of exemplary lipidated glycan mimetics employed for glycocalyx engineering. **A**: DPPE-terminated pMVK post-functionalized with hydroxylamine functionalized sialic acids.[140] **B**: 4,5-Seco-cholesten-5-one functionalized PEG-backbone with glucose moieties and fluorescent dye.[139] **C**: Cholesteryl-substituted glycopeptide derived via SPS.[141]

To this day, various examples have been published, demonstrating the usefulness of such lipidated glycan mimetics. As for the soluble glycan mimetics that were covered in chapter 1.3, many approaches to obtain lipidated glycan mimetics rely on the employment of controlled polymerizations that enable narrow molecular weight dispersities and further functionalization of the polymers with lipids and fluorescent reporters. *Hudak et al.*, for example, employed a bivalently DPPE-functionalized 4,4'-azobis(4-cyanovaleric acid) initiator to polymerize methyl vinyl ketone. The resulting polymer, bearing free carbonyl-moieties along the backbone was subsequently functionalized with various aminooxy-functionalized glycan motifs via oxime formation to derive a library of glycan structures (cp. **Figure 9A**). Similarly, *Honigfort et al.,* employed controlled anionic ring-opening polymerization of epichlorohydrin with tetrabutylammonium azide to generate linear and hydrophilic, α-azido functionalized poly(epichlorohydrin) with narrow dispersities and high molecular weights. Subsequently, the azide moiety was reacted with a propargyl functionalized 4,5-seco-cholesten-5-one-moiety via copper-catalyzed azide alkyne cycloaddition (CuAAc) to introduce

a lipid-moiety into the polymer backbone, before the chlorine substituents were substituted with azide-functionalities, to introduce propargyl-functionalized Glc-motifs and fluorophores to the polymer (cp. **Figure 9B**). Besides the employment of controlled polymerizations, also solid-phase synthesis offers a convenient tool to synthesize highly defined, monodisperse glycan mimetics, with precise control over the glycosylation pattern and also offering the possibility to site-selectively introduce lipid moieties for membrane anchoring or functional handles, such as crosslinkers or fluorescent dyes for optical probing, which is highly desirable for the construction of high precision glycomimetics in the context of *de novo glycocalyx engineering*. *Stuhr-Hansen et al*., for instance, employed solid phase synthesis to derive sequence-defined GalNAc-glycopeptides, site-selectively functionalized with a cholesteryl-moiety for membrane-tethering and a Rhodamine B fluorophore for optical probing (cp. **Figure 9C**).[141] Similarly, *Banger et al.* have demonstrated the applicability of SPPoS (cp. chapter 1.3.1) to derive sequence-defined and cholesteryl-functionalized glyco(oligo(amidoamines)).[137]

1.4.2 *De Novo* Glycocalyx Engineering

Generally, the glycocalyces of native cells can be altered via chemo-enzymatic, genetic or metabolic approaches.[142–146] Oftentimes though, the resulting modifications occur globally and fundamentally lack precision regarding cell-surface presentation and spatial organization.[35] To circumvent these drawbacks, the so called *de novo glycocalyx engineering* has emerged, that enables controlled alterations to native glycocalyces in cells.[147,148] Through the passive introduction of lipid-anchored glycan mimetics into cellular membranes, existing glycocalyces can be edited or even completely reconstructed after removal of specific glycan motives on the cell. This top-down approach hence offers the possibility to study the effect of distinct changes to the glycocalyx of native cells with precision not achievable via conventional molecular biology tools.[35]

In this manner, *Hudak et al.* introduced sialylated glycopolymers (cp. **Figure 9A**) via a lipid moiety into cancerous cell lines and observed a protective effect of the increasingly sialylated cell surface on natural killer cell–mediated cytotoxicity.[140] A correlation between an upregulation in sialic acid in cancerous cells and a resulting protection from the immune system has been supposed but never been shown before. Similarly, the group of *Kamil Godula* has synthesized phospholipid-functionalized mucin-mimetic glycopolymers to derive a screening platform for inhibitors of the influenza A virus (IAV).[149] The synthesis of these mucin mimetics was later refined (cp. **Figure 9B**) to resemble the nanoscale architecture and properties of native mucins to employ them as glycocalyx spectators on the surface of red blood cells in order to study the effect of macromolecular crowding in the glycocalyx regarding the binding efficiency of glycan-binding proteins.[150] In another example, *Woods et al.* demonstrated that cholesteryl-substituted synthetic glycopolymers could be inserted into the cell membrane of zebrafish embryos, thereby displaying a prolonged residence time on the cell membrane, caused by a recycling mechanism of the endocytotically sequestered glycopolymers back to the cell surface for up to ten days. Also, these membrane-anchored glycopolymers demonstrated an increase in survival of non-malignant cells in a metastasis model.[151]

Altogether, the modification of native cells provides valuable insights into the molecular machinery that is associated with the glycocalyx in a highly genuine setting. However, this top-down approach is limited in unraveling single mechanistic principles, since the whole

ensemble is overwhelmingly complex and, thus, attributing a particular function to a single component remains challenging.[152] Instead, the isolation of single glycocalyx constituents and their study in an increasingly complex, well-defined set-up bears the potential to gain a better understanding of the function and cellular processes of certain glycocalyx constituents.[152] Thus, the construction of completely artificial glycocalyx models from the bottom up, termed as glycocalyx mimetics, has gained huge interest over the past few decades. [153] Examples show the application of fully synthetic lipid-tethered glycopolymers into model systems or cellular membranes to mimic natural glycan analogues in a highly controlled setting.[140,149,150]

1.4.3 Mimetics of the Glycocalyx

Glycocalyx mimetics offer a highly controlled environment to investigate the interplay between glycans, proteins, and phospholipid membranes in a more complex environment, mirroring native cellular glycocalyces.[35,153]

To generate such glycocalyx mimetics, mostly supported lipid bilayers (SLBs) or giant unilamellar vesicles (GUVs) are employed as simple phospholipid bilayer membranes to model native cellular membranes. These bilayers can then be decorated with lipid-anchored glycomimetics and proteins to gradually increase the complexity of the membrane models and to obtain very simplistic but highly precise surrogates of natural glycocalyces that capture the dynamics and heterogeneity of eukaryotic plasma membranes.

The advantage of such simple model membranes is that the highly heterogenous lipid composition of native cell membranes can be whittled down to a few, well studied lipids, that mirror the physico-chemical behavior of the cell membrane and allow to study membrane associated processes, such as phase separation, budding or membrane fusion, in a controlled environment.

SLBs are phospholipid bilayers that are supported on a fixed substrate, mirroring the physiology of native phospholipid membranes and allowing to study membrane-associated processes, such as ligand-receptor interactions or structure and mobility of constituents, in a reductionist, two-dimensional setting.[154] As solid support, mostly hydrophilic surfaces, such as glass or mica, are suitable, whereby the bilayer membrane is separated by a 10-20 Å layer

of water from the substrate, which retains the fluidity of the lower lipid leaflet.[154–157] Mainly three methods are commonly employed to formulate SLBs:

1.) the adsorption and fusion of preformed phospholipid vesicles from an aqueous suspension onto the substrate surface[158,159]
2.) a combination of the Langmuir-Blodgett and the Langmuir-Schaefer techniques, which involves the deposition of the lower lipid leaflet from an air water-interface on the substrate, followed by the introduction of the upper leaflet via horizontally dipping the lipid covered substrate on another air-water interface to create the bilayer[160]
3.) a combination of the first two methods, where the lower lipid leaflet is deposited on the support via the Langmuir-Blodgett technique, followed by fusion with preformed phospholipid vesicles to form the bilayer[161]

Especially the last two techniques allow for the preparation of asymmetric lipid bilayers, where the composition of lipids can vary between the two leaflets through the iterative assembly and additionally enables the incorporation of other membrane constituents, such as membrane proteins or glycan mimetics into the bilayer.[162]

Studying molecular interactions and dynamics in SLBs can be carried out employing several surface-sensitive techniques. Quartz crystal microbalancing (QCM), surface plasmon resonance (SPR), atomic force microscopy (AFM), and fluorescence microscopy have been employed to gather information on membrane interactions, morphology and mechanical properties.[163,164] Diffusion of membrane lipids or membrane constituents and lipid domain formation in SLBs can be examined, employing fluorescence recovery after photobleaching (FRAP) or fluorescence interference contrast (FLIC).[162,165] SLB experiments have been shown to enable insights into the effects of glycomimetic density and clustering upon interaction with lectins or pathogens.[166–168] Similarly, conformational changes from coiled to extended orientations in glycomimetics resulting from sterical repulsion in the membrane was examined.[169] As an example, *Delaveris et al.* incorporated lipid-functionalized mucin-mimetics along with the ganglioside receptor GD1a (that is known to interact with Influenza A virus (IAV)) into SLBs to create two-dimensional glycocalyx mimetics. Employing fluorescence interference contrast microscopy (FLIC) and dynamic light scattering (DLS), they found that the mucin-mimetics underwent a transition in conformation from a coiled to an extended conformation with increasing surface densities. Furthermore, they could demonstrate that

IAV binding to GD1a was only possible at low mucin-mimetic concentrations and inhibited at high mucin-mimetic concentrations at which the mimetics were in their extended conformation, likely forming a steric barrier and shielding the ganglioside from the virus particle.[170]

Although SLBs replicate the fluidity and dynamics of natural cell membranes, they lack the three-dimensional complexity of a cell, regarding membrane curvature and the ability to bud and fuse.[35,171]

Therefore, especially GUVs represent the most popular biomimetic systems to resemble eukaryotic cells.[35,153] GUVs are monolamellar, sperical phospholipid bilayer vesicles with sizes ranging from 5 to 50 µm that mirror the dimension of natural cells (1 – 100 µm). Similarly, GUVs reflect the attributes of native cellular membranes, such as mobility, curvature and flexibility, and thus enable the systematic study of key cellular functions, such as phase separation, membrane fusion and fission or membrane-associated interactions between ligands and receptors. These features and their facile studying via common microscopy techniques render GUVs very attractive and suitable model systems to study biophysical and -chemical events related to cellular functions.[153]

Just like for the preparation of SLBs, over the years several groups have presented and optimized various protocols to generate GUVs, with each technique bearing several advantages and disadvantages that must be considered and pondered for the respective purpose. The simplest and most conventional technique for the preparation of GUVs is the hydration method, which has been improved over the recent years through several other techniques to assemble more complex GUVs in a more efficient and precise fashion.[172] These techniques comprise electroformation[173–175], paper- and gel-assisted hydration[176,177], inverted emulsion[178] and microfluidics[179].

To formulate GUVs via hydration, the matrix lipids, dissolved in an organic solvent, such as chloroform, are spread on a substrate and dried to give multilamellar lipid bilayers on the substrate. Then the lipids are hydrated and swollen with an aqueous medium, whereby the lipid lamellae detach from the substrate and form mainly multilamellar vesicles.[172] Assisting support on porous and hydrophilic gel or fiber surfaces, such as dextran or polyvinyl alcohol (gel-assisted hydration) or application of an electric field during the hydration process

(electroformation) accelerates the vesicle formation and yields predominantly uniform and monolamellar GUVs. Especially the hydration of lipids via the electroformation technique is a widely employed methodology, giving rather uniform vesicles with a rather even lipid distribution and little defects, but no control over leaflet asymmetry.[175]

For the preparation of GUVs via electroformation, the matrix lipids, dissolved in a volatile organic solvent, are evenly spread on a conductive substrate, e.g. indium-tin-oxide coated glass (ITO) or Pt-wires, and dried. The multilamellar lipid film is then hydrated with an aqueous solution and an electric field with a set voltage and frequency is applied to the substrate, which facilitates the detachment of the lipids from the substrate (**Figure 10**).[175]

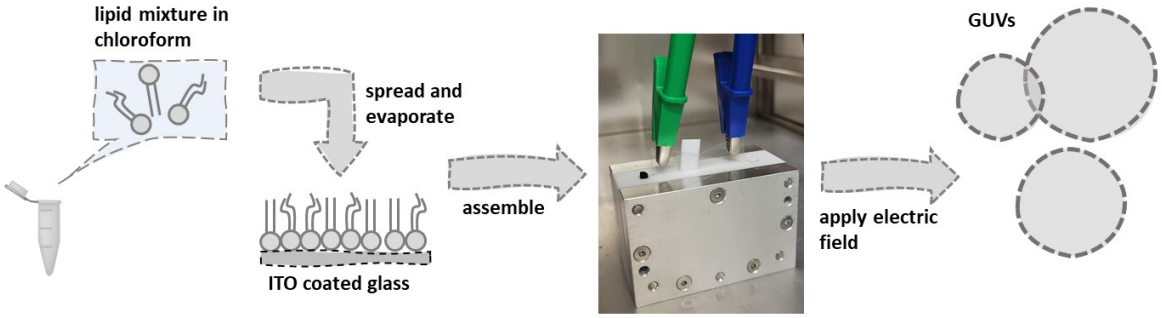

Figure 10. Schematic presentation of the electroformation procedure to form GUVs.

Common analytic techniques, such as FRAP, RICM, AFM, and FCS, enable a facile investigation of lipid (and other membrane constituent) dynamics, membrane properties, and molecular interactions on the vesicles. For example, reflection interference contrast microscopy (RICM) has been used to study the adhesion kinetics of functionalized GUVs on receptor surfaces providing quantitative information about different stages of adhesion.[180] Analysis of membrane dynamics can be performed by various fluorescence microscopy techniques, e.g. fluorescence recovery after photobleaching (FRAP) or fluorescence correlation spectroscopy (FCS)[181], while mechanical properties of the GUV lipid bilayer can be studied employing atomic force microscopy (AFM).[182]

Modifying existing protocols or spiking of preformed vesicles with lipidated glycomimetics enables the incorporation of membrane-anchoring glycan mimetics into GUVs to construct simple models of the glycocalyx in a highly controlled manner. For example, cholesterylated glycopeptides have been introduced into GUVs, thereby displaying different accessibilities

towards lectins, depending on the presentation of the glycopeptides on the membrane.[141] *Ewers et al.* employed GUVs to show that SV40-like particles induce the formation of tubular membrane invaginations upon interaction with certain GM1 gangliosides, which initiates infection of the targeted cells.[183] Similarly, glyco-decorated GUVs have been employed to study the interaction and uptake of the bacterial *Shiga toxin*.[184] In another example, cholesterylated peptides equipped with blood group glycans were incorporated into GUVs as mimetics of red blood cells to study the interaction with the malaria parasite *Plasmodium falciparum*, revealing the participation of blood group antigens O and A in infection.[185] *Villringer et al.* recently presented a novel approach to mimic the natural processes of cellular adhesion and organization using multivalent lectins that crosslink heteromultivalently glycan-mimetic functionalized GUVs, leading to the formation of protocellular junctions.[186]

In conclusion, the given examples underline the significance of glycan-lectin interactions in mediating essential cellular processes and demonstrate the broad applicability and suitability of glycan mimetics incorporated into GUVs as glycocalyx models for the systematic investigation of protein-carbohydrate interactions associated with the cellular glycocalyx. Consequently, further development of these model systems in terms of glycan-mimetic availability and customization holds the potential to yield valuable model systems for studying glycocalyx-associated interactions that are challenging, if not unfeasible, to examine systematically in native cellular membranes.

2. Aims and Outline

The glycocalyx of eukaryotic cells is a highly heterogenous and dynamic ensemble of densely glycosylated proteins and lipids that are associated with the plasma membrane. Today we know, that the glycocalyx is intricately involved in manifold biological processes that unfold on the cellular surface, such as cellular communication, adhesion or pathogen invasion.

The analysis of single ligand-receptor interactions *in vitro*, employing synthetic mimics of naturally occurring glycans, provides valuable insights on specific binding events, regarding avidity and specificity, that are associated with single constituents of native glycocalyces. However, such simple studies fundamentally lack the inherent complexity and dynamic nature of the eukaryotic cell surface. Natural binding events occur in densely crowded environments, where receptor-specific ligands are closely surrounded by non-binding constituents, or crowding agents, and the complex composition of the glycocalyx is not distributed homogenously along the membrane, but rather spatially organized into local domains.

To tackle this lack in complexity and dynamics, the field of glycocalyx engineering has emerged in the recent years, to provide more realistic images of the mechanisms that are involved with native glycocalyces. Alterations to native cellular glycans can be made metabolically, (chemo)enzymatically or through the introduction of synthetic, functional glycan mimetics into the plasma membrane. While these *in vivo* approaches yield results in living cells, alterations usually occur globally and lack precision.

Another promising approach is the construction of completely artificial mimetics of the glycocalyx from the bottom up. Here, phospholipid bilayers (usually GUVs or SLBs) are created from defined lipid mixtures and subsequently decorated with synthetic mimetics of natural glycans. Though far from mirroring native glycocalyces, these models resemble more closely the three-dimensional entity and presentation of ligands on a cellular surface than the analysis of ligand receptor interactions in solution or on immobilized surfaces.

Although the bottom-up construction of highly precise glycocalyx mimetics still lacks the inherent complexity of native cellular glycocalyces, this approach bears the potential to construct highly defined models of eukaryotic cell surfaces. Thus, the aim of this thesis is to contribute further to the existing work of creating glycocalyx mimetics by deriving (i) highly defined membrane-tethering mimetics of natural glycans and (ii) adding complexity to these

glycocalyx mimetics in terms of heterogenous membrane crowding, incorporation of sulfated glycans and spatial organization of glycans.

The first part of this thesis will focus on the development of crowded glycocalyx mimetics. To achieve this, a synthesis platform will be established, employing SPPoS and a novel type of controlled radical polymerization (TIRP, thiol-induced, light activated controlled radical polymerization), to obtain highly defined glycan mimetics with different glycosylation patterns and chain lengths. These structures shall comprise a membrane anchor and a fluorescence label, enabling their incorporation into model membranes and their detection via fluorescence microscopy.

Subsequently, the incorporation of the aforementioned structures into GUVs as model membrane systems shall be established to develop both homo- and heteromultivalent models of the glycocalyx employing the long and short glycan mimetics. These glycocalyx mimetics are supposed to mirror the natural, crowded surfaces of natural cellular membranes. Finally, the influence of these homo- and heteromultivalent systems on the interaction with the model lectin Concanavalin A will be investigated.

The second part of this work will focus on the creation of local glyco-heterogeneities in GUVs to mimic the inhomogeneous distribution of glycans in natural glycocalyces, e.g. via the formation of lipid rafts. Therefore, again employing SPPoS, sequence-defined glycan mimetics shall be derived, differing in glycosylation, as well in their type of membrane anchor. The different physico-chemical behaviors of these lipidated glycan mimetics shall enable a distinct allocation into different coexisting physical phases in phase separated GUVs (Ld or Lo), mimicking recruitment of natural glycans into lipid rafts or their remaining in more fluid parts of the membrane. In the next step, heteromultivalent glycocalyx models shall be constructed, thereby displaying different glycosylation patterns in the coexisting Ld and Lo phases of the GUVs according to the respective membrane anchor of the glycan mimetics. Finally, the impact of localization of Man ligands either in the Ld or Lo phase of the vesicles shall be examined regarding protein recruitment on the membrane.

In the third part of this work, the prior established synthesis of long and short precision glycan mimetics bearing membrane anchors shall be extended to now attain mimetics of naturally abundant sGAGs. These so-called sGAG mimetics shall be systematically investigated in GUVs

and first cell studies with regard to their interaction with virus-like particles (VLPs) to probe viral interactions with remodeled glycocalyces. Such studies have never before been conducted on completely synthetic sGAGs and bear the potential to study membrane-virus interactions in a highly controlled model system.

In the final part of this thesis, the objective is to develop a polymerizable diacetylene building block that is compatible with the established SPPoS protocols and enables the photo-induced crosslinking of adjacent ligands through irradiation. Clustering of glycans within the cell membrane has been described for its importance in cell surface interactions. Generally, cluster formation is a highly dynamic event and cannot be mirrored properly for instance via the presentation of glycan mimetics in preassembled membrane domains (as described in chapter 3.2). The employment of diacetylene functionalized glycan mimetics, however, potentially allows for direct visualization and fixation of ligand-receptor-mediated cluster formation.

Initially, the synthesis and conjugation of the building block will be established, followed by the synthesis of lipid-conjugated glycan mimetics with a polymerizable diacetylene moiety in their backbone. Subsequently, the derived ligands shall be investigated in terms of their self-assembly properties and their capability to polymerize upon irradiation. Finally, the ligands shall be incorporated into GUVs as simplistic glycocalyx models to demonstrate their efficacy as crosslinkers of ligand-receptor-mediated clusters, mimicking the spontaneous and dynamic clustering of glycans in native cellular membranes.

3. Results and Discussion

The following two chapters 3.1 and 3.2 will present two approaches to construct glycocalyx mimetics focusing on heteromultivalent, crowded glycocalyces and spatial arrangement of glycocalyx constituents to derive model systems that represent closer the natural inhomogeneity in natural glycocalyces.

Chapter 3.1 will present the published work on the synthesis of long and short precision glycomacromolecules with different glycosylation (Man or Gal) and their introduction into GUVs as model membrane systems to derive mimics of crowded, heteromultivalent glycocalyces. Key physical parameters are analyzed (incorporation efficiency, diffusion constants) and the impact of mixtures of long and short, binding and non-binding glycan mimetics on lectin binding are evaluated.

Chapter 3.2 will present the published work on lipidated, sequence defined glycomacromolecules, differing in their glycosylation and their lipid tether. The allocation of ligands into either Ld or Lo phases in phase separating GUVs, based on the employed lipid anchor, is established and yields the construction of heteromultivalent glycocalyx mimetics with distinct local glycosylation patterns. The effect of ligand allocation into either the Ld or the Lo phase on lectin recruitment will be analyzed quantitatively.

Chapter 3.3 will describe the development of sulfated mimetics of natural glycosaminoglycans (so called sGAG mimetics), based on the results of the previous chapters. Many viruses exploit the negatively charged GAGs on eukaryotic cells to adhere to and infect a host cell. The goal of the work presented in this chapter is the establishment of a synthetic route to access high precision mimetics of natural sulfated GAGs that can subsequently be incorporated into model membranes or native cellular membranes. This yields a platform to then study viral interactions in a very controlled setting, regarding the constitution of the employed sGAG mimetics.

The final chapter 3.4 will focus on the synthesis and establishment of a polymerizable diacetylene building block for SPPoS. Diacetylene-functionalized and lipid-tethered glycan mimetics are derived and characterized regarding their capacity to polymerize upon irradiation and their potential to fix and fluorescently display specific ligand-receptor clustering in model membranes will be explored.

3.1 Glycomacromolecules to Tailor Crowded and Heteromultivalent Glycocalyx Mimetics

Authors:	Luca-Cesare Blawitzki, Nina Bartels, Lóránd Bonda, Stephan Schmidt, Cornelia Monzel and Laura Hartmann
Journal:	Biomacromolecules
DOI:	10.1021/acs.biomac.4c00646
Impact Factor:	5.5 (as of 2024)

Contribution: Establishment of a synthetic route to synthesize dye-labelled and cholesteryl-functionalized precision glycomacromolecules and macroinitiators for TIRP. Synthesis and purification of glycooligomers and solid phase derived macroinitiators. Characterization of the derived compounds via RP-HPLC-MS, ^{1}H-NMR, HR-ESI-MS, SEC, UV-Vis and DLS. Collaborative establishment of a protocol to formulate glyco-decorated GUVs. Conduction of adhesion and inhibition experiments. Collaborative evaluation and interpretation of the measurements as well as visualization of the results. Collaborative writing of the manuscript.

pubs.acs.org/Biomac

Article

Glycomacromolecules to Tailor Crowded and Heteromultivalent Glycocalyx Mimetics

Luca-Cesare Blawitzki, Nina Bartels, Lorand Bonda, Stephan Schmidt, Cornelia Monzel, and Laura Hartmann*

Cite This: *Biomacromolecules* 2024, 25, 5979−5994

Read Online

ACCESS | Metrics & More | Article Recommendations | Supporting Information

ABSTRACT: The glycocalyx, a complex carbohydrate layer on cell surfaces, plays a crucial role in various biological processes. Understanding native glycocalyces' complexity is challenging due to their intricate and dynamic nature. Simplified mimics of native glycocalyces offer insights into glycocalyx functions but often lack molecular precision and fail to replicate key features of the natural analogues like molecular crowding and heteromultivalency. We introduce membrane-anchoring precision glycomacromolecules synthesized via solid-phase polymer synthesis (SPPoS) and thiol-induced, light-activated controlled radical polymerization (TIRP), enabling the construction of crowded and heteromultivalent glycocalyx mimetics with varying molecular weights and densities in giant unilamellar vesicles (GUVs). The incorporation and dynamics of glycomacromolecules in the GUVs are examined via microscopy and fluorescence correlation spectroscopy (FCS) and studies on lectin-carbohydrate-mediated adhesion of GUVs reveal inhibitory and promotional adhesion effects corresponding to different glycocalyx mimetic compositions, bridging the gap between synthetic models and native analogues.

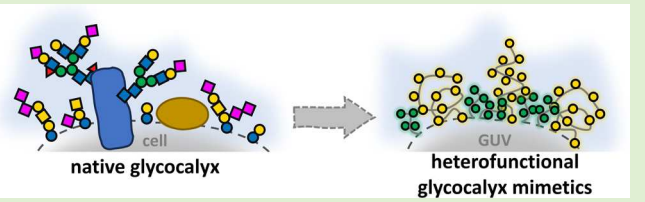

INTRODUCTION

The glycocalyx is a highly complex, dense layer of glycans on eukaryotic cells and is known to play a crucial part in a plethora of physiological and pathological processes such as cellular adhesion, pathogen infection and signaling, as the glycocalyx generally is the first instance of the cellular membrane that makes contact with its surroundings.[1−3] It is mainly composed of glycoproteins, proteoglycans, and glycolipids associated with the cell membrane and thereby forms a complex three-dimensional entity where both, the composition of glycans as well as their spatial distribution is known to critically affect its function.[3−8] Glycocalyx interactions are mainly driven by the recognition of glycans by glycan-binding proteins, such as lectins.[9,10] Glycan-lectin interactions are typically weak, but their binding avidity increases through multivalent interactions, such as multiple glycan ligands presented on a protein scaffold or glycan-conjugates forming clusters on the cell membrane.[9,11,12] Additionally, glycoheterogeneity in biological systems, i.e., the simultaneous adjacency of binding and nonbinding glyco motifs, has been shown to contribute to synergistic or antagonistic effects in glycan-lectin binding.[13] Besides their role in binding, glycans in the glycocalyx also affect biological processes through nonbinding effects like steric shielding and crowding.[14] The dense packing of glycans creates a crowded environment on the cell surface, occupying a distinct volume and limiting the accessibility and diffusion of membrane constituents. An important example is mucins, glycoprotein conjugates, that have been shown to assert a protective layer against the adhesion of viruses mediated through glycolipids, thus hindering viral infection. This is mainly assigned to the high molecular weight mucins stretching out from the membrane and thereby sterically shielding the glycolipids located closer to the membrane surface.[15] Furthermore, the dense packing induces steric pressure among the glycocalyx' constituents, leading to compartmentalization into clusters, alteration of the membrane morphology, fluid-crystallinity, and accessibility of constituents to their receptors, thus affecting selective binding processes.[16−18] For example, Godula and co-workers have shown that while mucin mimetics can slow down virus adhesion, they can also promote glycolipid cluster formation that enhances virus attachment, due to the lower unbinding rates of the virus attached to glycolipid clusters.[15]

Although it is generally recognized that the glycocalyx plays a pivotal role in biology, our understanding of its function is still evolving due to its complexity, heterogeneity, and highly dynamic nature. This is mainly due to our still limited access to fully characterizing and controlling the glycocalyx itself. Current biotechnological processes, such as metabolic

Received: May 13, 2024
Revised: July 31, 2024
Accepted: July 31, 2024
Published: August 9, 2024

https://doi.org/10.1021/acs.biomac.4c00646
Biomacromolecules 2024, 25, 5979−5994

strategies, genetic approaches addressing specific glycan enzymes, or using enzymes for chemoenzymatical changes, e.g., for removing specific glycan motifs, can be used to alter the glycocalyx compositions directly on living cells.[19] However, these methods affect the glycocalyx compositions globally, and lack spatial and dynamic control, and often result in unforeseen impacts like cellular lethality or protein misfolding.[2,20,21]

An alternative approach is to develop glycocalyx biomimetics consisting of synthetic cellular membranes functionalized with glycoconjugates. Here, the lipid membrane composition is well-defined and offers controlled reconstitution of glycoconjugates along with their structural and spatiotemporal variation within the membrane ensemble.[20,22] For example, Stuhr-Hansen et al. showed, that the different topological presentation of artificial glycopeptides on giant unilamellar vesicles (GUVs) dictates different accessibilities of *Vicia villosa* lectin to membrane-associated GalNAc moieties, due to the attachment of one or more membrane anchors along the backbone.[23] Furthermore, synthetic glycan mimetics such as glycopolymers are not only useful in developing glycocalyx mimetic systems but also allow for the so-called glycocalyx engineering by introducing synthetic glycoconjugates directly into cell membranes in a controllable manner.[24−26] For instance, Woods et al. demonstrated the efficient incorporation of cholesteryl-conjugated glycopolymers into cellular membranes that exhibit significantly prolonged cell-surface residence times facilitated by a continuous recycling process from internal reservoirs back to the cell surface, in contrast to native phospholipid-conjugated glycopolymers, which allowed the examination of longer-term biological processes.[26] In another example, Delaveris et al. revealed that the accessibility of Influenza A viruses to a glycolipid receptor at the membrane can be inhibited in the presence of synthetic mucin mimetics. This inhibition depends on the density, by means of molecular crowding, as well as on the architecture of the glycomimetics in the membrane.[27]

Thus, by the bottom-up development of glycocalyx mimetics from artificial membranes and the top-down introduction of glycan mimetics into cell membranes by glycocalyx engineering, we gain new insights into the role and function of the glycocalyx. In addition, to quantitatively understand and further emulate the biological context, we first need to characterize the individual glycocalyx constituents and their binding affinities and then successively increase the complexity within the membrane by the reconstitution of multiple glycoconjugates. Therefore, in this study, we present a toolbox of glycan mimetics that allows for the controlled variation of important structural parameters such as composition, molecular weight, and membrane tethering and then demonstrate their use in deriving increasingly complex glycocalyx mimetics. To the best of our knowledge, this is the first fully synthetic glycocalyx mimetic model that combines two different glycan mimetic structures to derive heteromultivalency.

Specifically, a series of long and short mannose (Man) or galactose (Gal) presenting glycomacromolecules is synthesized and then characterized with regard to their reconstitution efficiency into GUVs via FCS. The incorporation of mixtures of long and short Man and Gal presenting glycomacromolecules into GUVs allows us to reconstruct the complexity and heterogeneity of native glycocalyces in a reductionist fashion. We then study the binding behavior of our glycocalyx mimetics toward the model lectin Concanavalin A (ConA) to mimic glycocalyx-mediated adhesion processes (e.g., cellular adhesion or pathogen adhesion), where Man-functionalized glycomacromolecules act as binders while Gal-functionalized glycomacromolecules act as nonbinders or crowders. Applying optical microscopy and reflection interference contrast microscopy (RICM) we evaluate how changes in glycocalyx crowding fundamentally impact ligand−receptor binding. We observe that glycomacromolecular crowding can either render the binding unaffected, hinder, or even promote binding to lectin depending on the length and density of the membrane-tethered glycomacromolecules.

EXPERIMENTAL SECTION

Synthesis of Building Blocks and Monomers. The building blocks ethylene glycol diamine succinic acid (EDS) and triple bond diethylenetriamine succinic acid (TDS) were prepared as reported earlier.[28] Tetra-*O*-acetyl-azidoethyl-α-D-mannopyranoside, tetra-*O*-acetyl-azidoethyl-β-D-galactopyranoside, 2-acrylamidoethyl-α-D-mannopyranoside (ManHEAA), and 2-acrylamidoethyl-β-D-galactopyranoside (GalHEAA) were synthesized according to the literature protocols.[28−30] 3-β-Azidocholesterol was synthesized according to a protocol by Sun et al.[31]

Solid-Phase Synthesis of Cholesterylated Glycomacromolecules and Macroinitiators. *General Coupling Protocol.* All structures were prepared on Tentagel S RAM resin (batch size: 0.1 mmol). All washing steps were conducted with 4 mL of solvent. Polypropylene reactors equipped with polyethylene frits and closed with Luer-stoppers were used. For the short glycomacromolecules, the backbone sequence was first assembled, followed by glycoconjugation via CuAAC (copper(I)-catalyzed alkyne−azide cycloaddition), Lys-side chain deprotection (Boc), fluorescent dye conjugation, terminal Fmoc-deprotection, and capping with 4-pentynoic acid before conjugation of the cholesteryl tether via CuAAC. For the macroinitiators, the backbone sequence was first assembled, followed by Lys-side chain deprotection (Dde), fluorescent dye conjugation, terminal Fmoc-deprotection, and capping with 4-pentynoic acid before conjugation of the cholesteryl tether via CuAAC.

For all compounds, the resin was first swollen in 4 mL of dichloromethane (DCM) for 30 min, subsequently washed ten times with dimethylformamide (DMF), Fmoc-deprotected by treating with 25% piperidine in DMF (three times for ten min), and again washed 15 times with DMF. The employed building blocks were coupled to the *N*-terminus by adding the respective building block (5 equiv), PyBOP (5 equiv), and DIPEA (20 equiv) in 4 mL of DMF to the resin and shaking for 1 h. Then, the resin was washed 15 times with DMF and the *N*-terminus was again deprotected followed by the next coupling step.

Copper(I)-Catalyzed Alkyne−Azide Cycloaddition. For glycosylation, either azido-functionalized and peracetylated α-D-Man or β-D-Gal (2.5 equiv per alkyne) in DMF (4 mL) as well as sodium ascorbate (50 mol % per alkyne) and $CuSO_4$ (50 mol % per alkyne) each dissolved in water (0.25 mL) were added consecutively to the resin.

For *N*-terminal cholesterylation 3-β-azidocholesterol (2.5 equiv) was dissolved in 1,4-dioxan (4 mL) and added to the resin along with sodium ascorbate (50 mol % per alkyne) and $CuSO_4$ (50 mol % per alkyne) each dissolved in water (0.25 mL). The resin was shaken overnight, and subsequently, excessive reagents were removed by washing with a solution of sodium diethyldithiocarbamate (23 mM in DMF/water 1:1), water, DMF, and DCM.

Boc-Deprotection. The resin was washed five times with tetrahydrofuran (THF) before a solution of 4 M HCl in 1.4-dioxane was drawn into the syringe reactor. The resin was rocked for 5 min before the solution was discarded. The fresh solution was drawn into the reactor, and the resin was rocked for 30 min before the solution was discarded again. The resin was then washed ten times with DMF.

Dde-Deprotection. The Dde-side chain protective group was cleaved via treatment with a freshly prepared solution of 2% hydrazine hydrate in DMF (v/v). After rocking for 5 min, the solution was

https://doi.org/10.1021/acs.biomac.4c00646
Biomacromolecules 2024, 25, 5979−5994

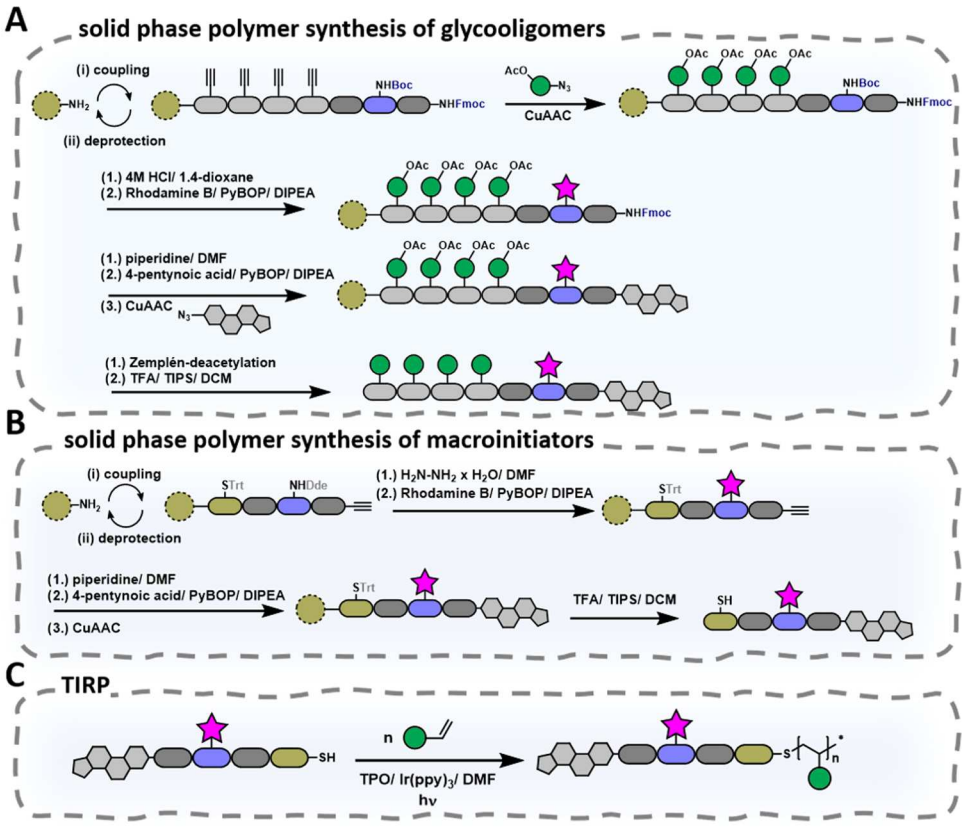

Figure 1. Schematic presentation of the solid-phase polymer synthesis of MC (A), macroinitiator synthesis (B), and TIRP of pMC (C). The synthesis of the Gal-functionalized macromolecules proceeds analogously, employing the respective Gal-functionalized building blocks and fluorescein as the fluorescent reporter.

discarded, and the resin was washed three times with DMF. The cleavage procedure was repeated twice.

On-Resin Acetyl Deprotection. Carbohydrate deacetylation was conducted under Zemplén conditions with 4 mL of a 0.2 M solution of sodium methoxide in methanol (two times for 30 min), followed by washing five times with methanol and ten times with DMF.

Cleavage from the Solid Support. Prior to the cleavage the resin was washed ten times with DCM. Then a cocktail of TFA, DCM, and TIPS (95:2.5:2.5, 4 mL) was drawn into the syringe reactor and the resin was rocked for 45 min. The glycomacromolecules were precipitated in diethyl ether and collected via centrifugation.

Purification. The short glycomacromolecules were purified by diafiltration with triethylamine in water and 0.5 M hydrochloric acid and three times with water in VIVASPIN 20 centrifugal concentrators from Sartorius (MWCO = 10 kDa). Macroinitiators were precipitated twice in 25% diethyl ether in hexanes. Afterward, the structures were lyophilized to obtain the pure product.

Thiol-Induced, Light-Activated Controlled Radical Polymerization (TIRP) of Macroinitiators. *Polymerization.* One equivalent of glyco-monomer (100 mol %) and 0.05 mol % $Ir(ppy)_3$ were dissolved in DMF (10 wt %), sealed in a 5 mL glass flask, and flushed with argon as inert gas for 10 min. In a second step, the macroinitiator (2.5 mol %) a tip of a spatula of tris(2-carboxyethyl)phosphine (TCEP) dissolved in a single drop of H_2O and equimolar amounts of TPO were also dissolved in DMF (10 wt %) and sealed in a 5 mL microwave reaction vial. The macroinitiator/TPO solution was flushed under an Ar atmosphere for 10 min and irradiated (UV-LED Spot P standard 405 nm, 2% intensity, Opsytec Dr. Gröbel GmbH, Germany) for 3 min. Subsequently, the monomer/$Ir(ppy)_3$ mixture was added to the TPO/thiol solution under an inert atmosphere, and the polymerization solution was irradiated further at an unchanged light intensity. After 1 h, the irradiation was stopped and the polymer solution was precipitated in diethyl ether.

Purification. The precipitated glycopolymer was dried under a gentle stream of nitrogen, dissolved in ultrapure water, and dialyzed via diafiltration against ultrapure water in five cycles (20 mL each, 1 M HCl was used in the first cycle). The dialyzed compounds were dissolved in fresh, ultrapure water and lyophilized.

Formulation of Giant Unilamellar Vesicles (GUVs). Custom-made Teflon swelling chambers and indium tin oxide (ITO)-coated glass coverslips (pgo GmbH, Iserlohn, Germany) were sonicated in 2% Hellmanex III in ultrapure water for 10 min. The solution was discarded, and the equipment was rinsed with ultrapure water, before sonicating in ultrapure water for 5 min twice. Afterward, the items were dried under a stream of nitrogen.

GUVs were assembled via electroformation. 25 μL of a mixture of DOPC (2 mg/mL) and 2 mol % 18:1 PEG_{2000}-PE in chloroform (all from Avanti Polar Lipids, Alabaster, AL) were mixed in a vial with the respective amount of cholesterylated glycomacromolecules (dissolved in 10% MeOH in chloroform (glycooligomers) or dimethyl sulfoxide (DMSO) (glycopolymers)). For biotin-functionalized vesicles, 1 mol % biotinyl CAP PE (Avanti Polar Lipids, Alabaster, AL) was also added to this mixture. The mixture was evenly spread onto a thin layer on the ITO-coated glass coverslips. The film was dried overnight in a vacuum chamber at 95 mbar. The coated glass slides were assembled in a tailored Teflon chamber, and the space between the coverslips was filled with 1400 μL of buffer solution (115 mOsM lactose to match the osmolarity of the measuring buffer: lectin binding buffer, 120 mOsM) to rehydrate the lipid film. An AC electric field (2.4 V, 89 Hz) was applied for 90 min at ambient temperature to generate the GUVs. The GUVs were transferred to a vial and stored at 4 °C before imaging.

Preparation of Measuring Chambers. 18-well slides (ibidi GmbH, Martinsried, Germany) were cleaned and activated by UV ozone treatment (UV Ozone Cleaner UVC-1014 from Nano-BioAnalytics) for 30 min. For surface passivation with ConA, the activated chambers were filled with 100 μL of ConA solution (1 mg/

https://doi.org/10.1021/acs.biomac.4c00646
Biomacromolecules 2024, 25, 5979−5994

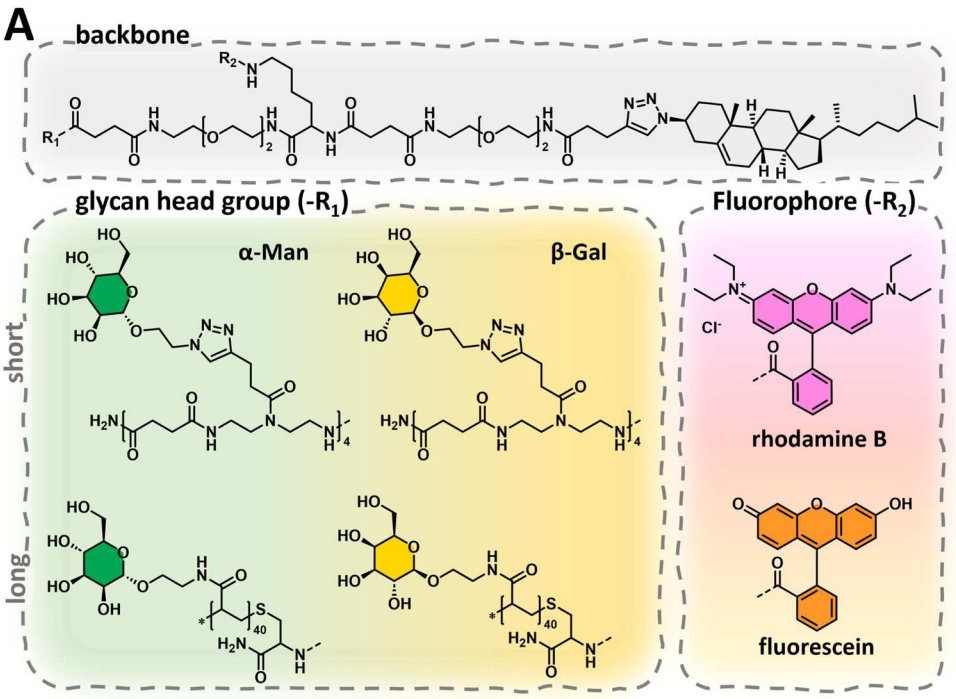

B

sample	glycosylation	valency	Đ	M_w [g/mol]	r_H [nm]
MC	Man	4 (short)	1.0[a]	3616.64	~ 1.5[d]
GC	Gal	4 (short)	1.0[a]	3469.94	~ 1.5[d]
pMC	Man	40 (long)[b]	1.08[c]	12800[c]	9.3 ± 0.2[e]
pGC	Gal	40 (long)[b]	1.38[c]	13400[c]	9.8 ± 0.1[e]

Figure 2. (A) Chemical structures of the synthesized cholesteryl-tethered glycomacromolecules. (B) Overview of the synthesized glycomacromolecules. [a] based on the synthetic pathway, [b] theoretical value (calculated), [c] via H_2O-size exclusion chromatography with multi-angle static light scattering (SEC-MALS), [d] based on literature values of similar structures,[36] [e] determined via dynamic light scattering (DLS).

mL in LBB) and incubated for 30 min. Thereafter, the solution was discarded, and the chambers were rinsed three times with LBB and filled with fresh LBB.

For NeutrAvidin passivated surfaces, the activated chambers were filled with 100 μL of NeutrAvidin in LBB (40 μg/mL) and incubated for 10 min. The solution was discarded, and the surfaces were rinsed three times with LBB, before incubating with bovine serum albumin (BSA) (5 mg/mL in LBB) for 20 min. Thereafter, the solution was discarded and the chambers were rinsed three times with LBB and filled with fresh LBB.

RESULTS AND DISCUSSION

Synthesis of Membrane Tethering Glycomacromolecules. In order to systematically evaluate the effects of chain length (molecular weight) and composition (binding and nonbinding glyco motifs) of membrane-tethered glycomacromolecules, we synthesized a first library of four glycomacromolecules site-specifically introducing a membrane anchor as well as an optical probe for visualization (Figure 1).

For the short-chain glycomacromolecules, we applied previously established SPPoS of precision glycooligomers.[30,32,33] In short, based on standard Fmoc-based peptide synthesis, the assembly of the macromolecular backbone is achieved through iterative coupling and deprotection steps of tailor-made building blocks on a solid support. Three different types of building blocks were used to assemble the glycooligomer scaffolds: (1) a functional building block (TDS) introducing an alkyne side chain. This alkyne moiety serves for the subsequent site-specific introduction of carbohydrate moieties; (2) lysine (Lys) with a Boc-protected side chain to conjugate the fluorophore via amide linkage; and (3) a spacer building block (EDS) introducing a short ethylene glycol unit. This unit enables to modulate the distance of the functional units and the overall chain length, while maintaining a hydrophilic backbone.[30] After assembly of the desired scaffold, on-resin glycosylation was achieved via copper-catalyzed azide−alkyne cycloaddition (CuAAC) between the alkyne-bearing TDS building block and 2-azidoethyl-carbohydrate (Man or Gal). Conjugation of a fluorescent reporter (Rhodamine B or Fluorescein) to the backbone was realized through the amide bond formation of the respective free dye and the primary amine of a Lys-side chain. Subsequent *N*-terminal capping of the backbone with 4-pentynoic acid allowed for the introduction of an azido-functionalized membrane tether again via CuAAC.[32] 3-β-Azidocholesterol was chosen as the membrane anchor, which is known from the literature to enable the installation of glycan mimetics into

https://doi.org/10.1021/acs.biomac.4c00646
Biomacromolecules 2024, 25, 5979−5994

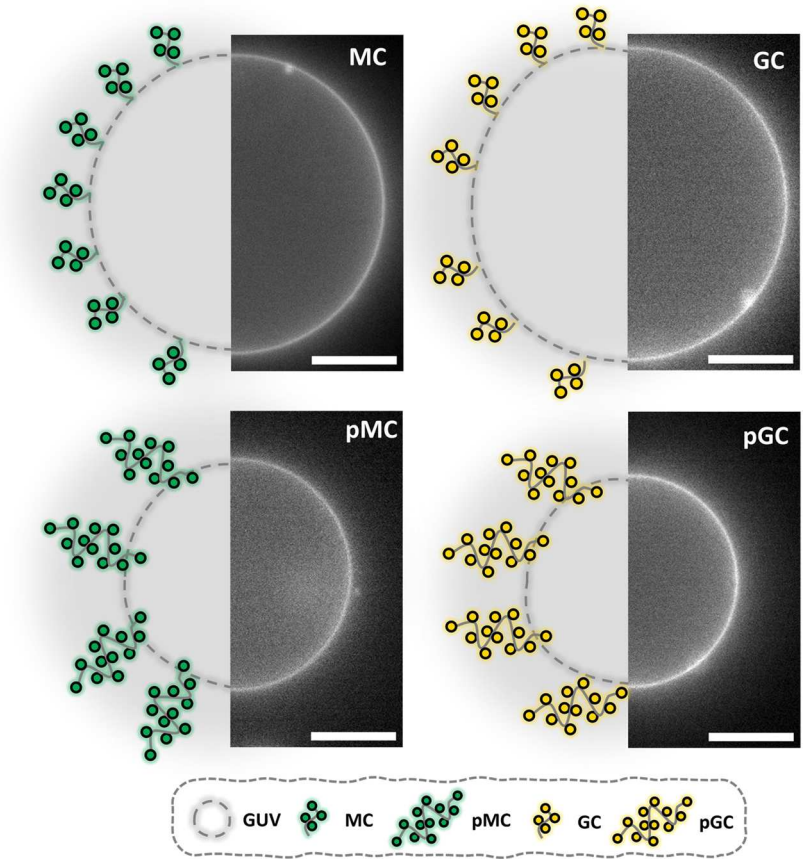

Figure 3. Fluorescence microscopy images of GUVs containing respectively 2 mol % cholesteryl-functionalized glycomacromolecules (right half) and schematic illustration of glycomacromolecule organization within the vesicle membrane (left half). Of note, for simplicity, glycomacromolecules are only depicted on the outer membrane leaflet. Contrast was adjusted for better visualization. Scale bar: 10 μm.

lipid membranes.[23,26] After Zemplén deacetylation of the sugar moieties, the structures were cleaved off the resin and isolated via precipitation. This approach enabled the synthesis of two short solid-phase derived glycooligomers termed MC (i.e., mannose-cholesteryl) and GC (i.e., galactose-cholesteryl) bearing four carbohydrate moieties each (Figure 2A).

Next, longer Man and Gal presenting glycomacromolecules with a cholesteryl unit were synthesized. These structures are not accessible by solid-phase assisted synthesis since high chain lengths often result in aggregation of the growing macromolecules, leading to incomplete coupling and deprotection steps and hence diminishing the overall purity and yield of longer chains.[34] To overcome this limitation, we present a novel approach that combines our recently developed TIRP polymerization and SPPoS.[35] We have demonstrated that TIRP as a controlled radical polymerization method is particularly suited for glycomonomers, enabling access to high molecular weight, low dispersity glycopolymers. First, applying SPPoS, we synthesized functional macroinitiators bearing the same fluorophore and cholesteryl tether on the macromolecular scaffold as used in the design of the first two glycomacromolecules, omitting the carbohydrate-presenting part of the construct. Instead, a cysteine (Cys) was introduced at the *C*-terminus, generating a free thiol group after cleavage from the resin. To ensure the stability of the Cys Trt-protecting group during assembly of the macroinitiator, a Dde-protected lysine was employed instead of a Boc-protected lysine.

This construct served as the macroinitiator in TIRP, where the polymerization of acrylamide-functionalized Man and Gal gave higher molecular weight glycomacromolecule constructs (Figure 1C). Through this approach, two glycopolymers termed pMC (i.e., polymannose-cholesteryl) and pGC (i.e., polygalactose-cholesteryl) with approximately 40 glyco moieties, respectively, were obtained. Thus, each glycomacromolecule/glycopolymer (in the following both are termed glycomacromolecule) is equipped with one cholesteryl anchor for membrane tethering and one fluorophore (either Rhodamine B for Man-ligands or Fluorescein for Gal-ligands) for optical probing (Figure 2A).

After isolation, all structures were purified via diafiltration and characterized by HRMS, reverse-phase high-performance liquid chromatography-mass spectrometry (RP-HPLC-MS), SEC, and ^{1}H NMR (see Supporting Information).

To further characterize the cholesteryl-tethered glycomacromolecules regarding their ability to act as crowding agents, we determined their hydrodynamic radii (r_H) via DLS. Higher molecular weight glycomacromolecules (pMC and pGC) showed a r_H of about 9.5 nm (see Supporting Information). Lower molecular weight glycomacromolecules with the membrane anchor showed a strong tendency to form aggregates in water, however, we have previously determined r_H of similar glycomacromolecules without the membrane anchor at approximately 1.5 nm (cp. Figure 2B).[36] For comparison, a frequently used macromolecule for studying crowding in phospholipid bilayers is PEG 6000, which has a hydrodynamic radius of about 2.5 nm.[18] Since our

https://doi.org/10.1021/acs.biomac.4c00646
Biomacromolecules 2024, 25, 5979−5994

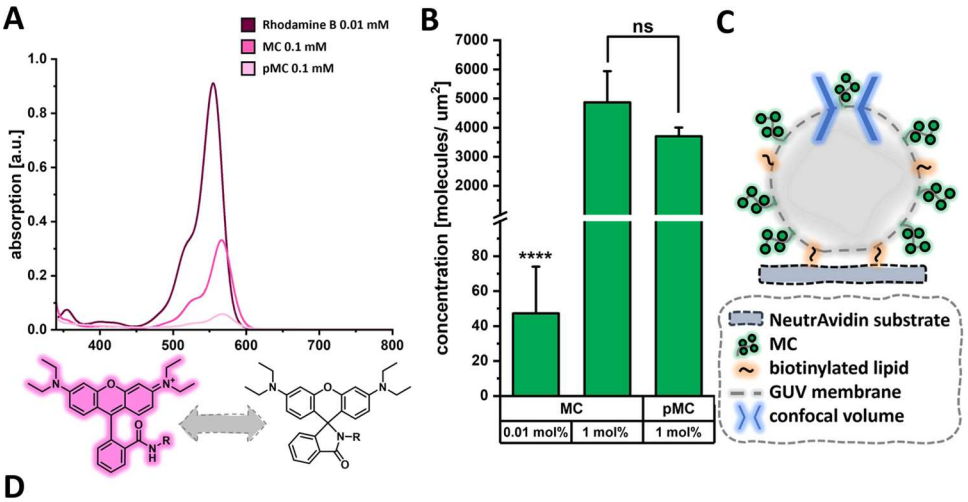

D

sample	$c_{applied}$ [mol%]	$c_{measured}$	$c_{corrected}$*	$c_{expected}$	D
		[molecules / µm²]			[µm² / s]
MC	0.01	2.0 ± 1.1	47.3 ± 26.7	286	7.6 ± 1.5
MC	1.0	207.3 ± 5.6	4867.8 ± 1070.3	28600	6.7 ± 0.6
pMC	1.0	51.5 ± 4.2	3701.4 ± 305.0	28600	6.6 ± 0.6

Figure 4. (A) Rhodamine B-labeled glycomacromolecules exhibit a significantly reduced absorption profile compared to the free dye. This is because the introduction of an amide bond shifts the equilibrium of the dye from its open (fluorescent) to closed (nonfluorescent) spiro-lactam form. (B) Determination of the glycomacromolecule concentration in the vesicle membrane via fluorescence correlation spectroscopy. Data are presented as mean + standard error of the mean (SEM) for 10 experimental replicates. Note that the glycomacromolecules exist on both sides of the membrane, therefore the surface concentration on the outer membrane side is half the value presented in (B). (C) Schematic presentation of the FCS measurement. (D) Summary of gathered FCS data. *measured concentrations were corrected by the determined DoALs.

glycomimetics differ considerably in size (oligomers vs polymers) and are in the same size range as other crowding agents, they are well suited for further testing as crowding agents in glycocalyx models.

Assembling Glyco-Decorated GUVs. After the successful synthesis of glycomacromolecules with varying ligand valency and glycosylation, their introduction into GUVs was established. To achieve this, we prepared GUVs via electroformation from mixtures containing DOPC, 18:0-PEG2000-PE, and the respective cholesteryl-tethered glycomacromolecules. While GUVs prepared from mixtures of charged and uncharged lipids via electroformation in equimolar media have been shown to display lipid asymmetries, accompanied by vesicle invaginations, vesicles prepared from pure DOPC exhibited no such inhomogeneities.[37] Since our vesicles are only composed of DOPC as the matrix lipid, we do not expect asymmetries in inner and outer leaflet composition and, hence, homogeneous incorporation of our glycomimetics into either leaflet.

The resulting vesicles ranging in diameter from 10 to 50 μm exhibited homogeneous fluorescence along their membranes (Figure 3). Though each glycomacromolecule was equipped with a hydrophobic cholesterol moiety, the majority of the structures are highly hydrophilic. Consequently, it is plausible that not all structures incorporate into the membrane but rather remain in the surrounding solution. We therefore sought to investigate how many of the glycomacromolecules are incorporated into the membrane.

Determination of Incorporation Efficiency. Fluorescence correlation spectroscopy (FCS) is a widely used method for studying the diffusion and concentration of fluorescent molecules in solution, and it also applies to analyze constituents within membranes.[38,39] To analyze the incorporation efficiency of our glycomacromolecules into the GUVs, we applied FCS to determine both diffusion constants and concentrations of the fluorescently labeled glycomacromolecules.

For reliable FCS results, a certain degree of labeling (DoL) is crucial. Our synthetic route ensures that each macromolecule is equipped with exactly one fluorophore. However, Rhodamine B, which is a commonly employed and a very affordable fluorescent reporter, can exist in an equilibrium between an open, fluorescent form and a closed, nonfluorescent form. Conjugation of the carboxylic acid moiety to a primary amine, results in the formation of a secondary amide which tends to favor cyclization into the nonfluorescent lactam form, a fact that is often overlooked.[40]

Thus, to take this effect into account, we determined the degree of active labeling (DoAL) for our Rhodamine B-labeled glycomacromolecules MC and pMC, i.e., measuring the amount of molecules that carry the fluorophore in its open, fluorescent form.

Since the cyclization of the dye is largely governed by changes in pH, a calibration curve for the absorption maxima at 555 nm against the concentration of Rhodamine B in lectin binding buffer (LBB) (10 mM HEPES, 50 mM NaCl, 1 mM $MnCl_2$, 1 mM $CaCl_2$, pH 7.4) was determined (Figures S19 and S20). MC and pMC were dissolved in LBB at a concentration of 0.1 mM, and the absorption maxima were used to determine the concentration of the fluorophore after calibration (Figure S21). The values obtained were then compared to the initially weighed concentrations to determine the degree of active labeling, i.e., the number of molecules that carry the fluorophore in its fluorescent form. In this manner,

https://doi.org/10.1021/acs.biomac.4c00646
Biomacromolecules 2024, 25, 5979−5994

we determined that in equilibrium only 4.3% of the glycooligomer MC and 1.4% of the glycopolymer pMC exist in their fluorescently active form (Figure 4A). These findings are in accordance with the literature and serve as the basis for calculating concentrations from the FCS measurements.[40] Of note, the percentage of fluorophores in the nonfluorescent lactam form should a priori be the same in the different glycomacromolecule samples. However, the absorbance of MC is about 250× smaller compared to the free dye, and the absorbance of pMC is 1000× smaller than the free dye. So pMC has a factor of 4 less active fluorophores than MC. We suppose that this discrepancy (i.e., the DoAL for the glycopolymers in comparison to the glycooligomers) is caused by photobleaching of the Rhodamine B-functionalized macroinitiators during the photopolymerization via TIRP.

Another possibility that might explain the lower concentrations of measured fluorophores is self-quenching or homo-Förster resonance energy transfer (FRET) effects. For this, the fluorophore can remain in an open form but needs to be in the vicinity of the second fluorphore, i.e., <10 nm.[41,42] FRET effects typically occur at molecular surface densities >1000 molecules/μm^2, which is the case for 1 mol % MC and pMC, respectively, while the 0.01 mol % MC sample is in the non-FRET regime. For a 100× higher concentration (i.e., 1 mol % MC) we observe that a 100-fold increase in concentration results likewise in a 100-fold increase in measured fluorophore concentration. Thus, we conclude that there is no significant self-quenching due to FRET in these systems. Based on the high structural similarity in the part of the molecule carrying the fluorophore between MC and pMC and the larger hydrodynamic radius of pMC, we assume that also for pMC potential self-quenching from FRET is neglectable.

To then quantify the incorporation efficiencies and the mobility of our glycomacromolecules via FCS, we prepared GUVs from DOPC, 18:0-PEG2000-PE, Biotin-CAP-PE and the respective glycomacromolecule. These GUVs were deposited on a NeutrAvidin-covered surface to prevent vesicle movement during FCS measurement. Diffusion coefficients and local concentrations were determined in the upper half of the vesicles. Of note, the glycomacromolecules are assumed to incorporate homogeneously into both leaflets of the phospholipid bilayer; hence, the surface concentrations on the outer leaflet are only half the value presented in Figure 4B,D. The diffusion constant D (Figure 4D) is very similar to the diffusion constant of native, pure DOPC (D = 8.4 ± 0.4 μm^2/s) in a GUV membrane, where the smaller values by 10−15% for the glycomacromolecule containing GUV, could arise from the comparatively large, hydrated glyco-head groups or other factors such as a different GUV lipid composition.[43] Although one might expect slower diffusion for the lower molecular weight glycomacromolecules, our results did not show significant differences in the diffusion coefficients of all of the studied glycomacromolecules. Similar observations were made e.g., in the study by Delaveris et al. on synthetic mucin mimetics in supported lipid bilayers where the diffusion coefficients of the mucin mimetics did not differ significantly from the diffusion of fluorescently labeled DOPC either, despite large differences in molecular weights and sizes of the glyco-head groups.[27] The membranes used in our study are composed only of DOPC, making them inherently more fluid, and measurements are performed in GUVs, which generally display higher diffusion values due to lower friction as compared with solid-supported lipid bilayers. This could explain the similar diffusion for all studied glycomacromolecules.[44,45]

The measured concentrations from the FCS experiments were corrected for the previously determined DoALs. Based on these corrected values, we observed that only about 15% of initially applied MC and pMC ligands incorporated into the vesicle membrane. For MC, this percentage of incorporation was observed for both glycomacromolecule concentrations, 0.01 and 1 mol %, respectively. We suspect that this is caused by sufficiently good water solubility of the glycomacromolecules and a stable equilibrium between dissociation and association at the membrane in the swelling solution during electroformation. As the formation of the vesicles using this method is quite complex, further investigations are required in the future.

Next, we examined membrane partitioning of our cholesteryl-tethered glycomacromolecules to ensure a stable insertion of our structures into the GUV membrane. GUVs containing either 2 mol % MC or pMC were mixed with non-functionalized GUVs in LBB and incubated for 18h at 4 °C. We found that the nonfluorescent control GUVs remained nonfluorescent after the incubation period, which indicated a stable insertion of our structures in the GUV membrane once installed (Figure S22). Of note, for each experiment, a small fraction of the initial vesicle solution is highly diluted in buffer; therefore, the concentration of any remaining nonincorporated or partitioning glycomacromolecules might be well below the detection limit. For convenience and in order to keep the nomenclature consistent, we will henceforward refer to the applied concentrations of ligands in the lipid mixtures instead of stating the corrected concentration value. In summary, FCS experiments show that about 15% of the ligand is incorporated stably into the vesicle membrane and that the ratios of incorporation do not change significantly at different concentrations. However, our data suggest that cholesterol as a membrane anchor might not function as efficiently as generally assumed to tether artificial glycan mimetics in phospholipid bilayers.

Lectin Binding to Homomultivalently Glyco-Decorated GUVs. Next, we aimed to show that glyco-functionalized GUVs are accessible for lectin binding. Our focus lies on investigating the glyco-mediated adhesion of the GUVs onto lectin-presenting surfaces, since the carbohydrate-lectin interaction resembles native cellular processes, e.g., pathogen-cell recognition and adhesion, and can thus serve as a simple model to provide insights into adhesion mechanisms that are associated with the glycocalyx.[6,46]

As lectin, we chose the commercially available and well-characterized plant lectin concanavalin A (ConA). ConA is a commonly employed model lectin in glyco-mediated binding assays, exhibiting high affinities for α-Man- and α-Glu-moieties, and lacking affinity toward Gal moieties. The native protein is a homotetramer at physiological pH with one binding site per subunit.[47] For our adhesion studies, ConA was immobilized on glass slides via physisorption following established protocols.[48]

We prepared homomultivalently glyco-decorated GUVs containing either 0.5 or 2 mol % of the short (MC) and long (pMC) binding macromolecules. To account for the 10-fold longer polymers, we also reduced the respective concentrations of pMC by a factor of 10 to present the same amount of carbohydrates as the short MC ligands but at an overall lower ligand density.

https://doi.org/10.1021/acs.biomac.4c00646
Biomacromolecules 2024, 25, 5979−5994

The adhesion of glyco-functionalized GUVs onto ConA surfaces was determined by RICM. To quantify the binding of the GUVs onto the surface, the adhesion area diameters (d_a) determined via RICM were related to the vesicle projection diameter of the whole vesicle (d_v, Figure 5). The ratio of d_a/d_v results in a unitless value that can theoretically range between 0 (no adhesion) and 1 (maximum adhesion) and serves as a qualitative indicator of the relative adhesion strength between the glyco-decorated GUVs and the ConA substrate.

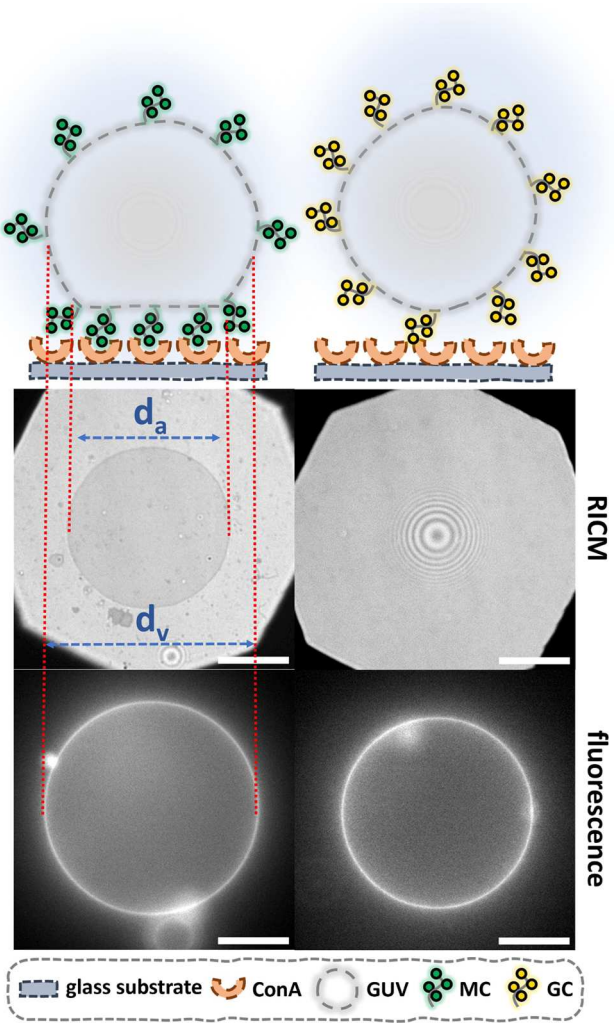

Figure 5. Glyco-decorated GUVs settle onto the ConA surfaces. Man-functionalized GUVs adhere to the substrate, whereas Gal-functionalized vesicles remain unbound. The ratio of the contact area diameter (d_a) to vesicle projection diameter (d_v) serves as a measure for the relative adhesion strength. Contrast of the images was adjusted for better visibility. Scale bar: 10 μm.

GUVs modified with Man groups demonstrated a notable behavior upon interaction with the lectin surface. Initially, they exhibited slight fluctuations on the ConA surface, followed by the rapid formation of an adhesive patch (Figure 5). Based on our FCS results, we assume that from a concentration of 0.2 mol % ligands upward, we exceed a local concentration of 1000 molecules per μm^2 in the adhesion area, rendering the resulting system crowded.[41] Crowding of the glycomacromolecules should increase the steric pressure on the membrane and hence alter the degrees of freedom of the macromolecules in terms of mobility and accessibility. Especially for the polymers, crowding, according to the brush polymer theory, should lead to polymer unfolding from a random coil to an extended conformation.[27]

Notably, regarding concentration and multivalency effects, the Man-functionalized homomultivalent binding systems containing either 2 mol % MC, 0.2 mol % pMC, 0.5 mol % pMC or 2 mol % pMC all exhibit similarly strong adhesion to the ConA surfaces. Although the systems vary in Man density, we noticed no significant differences in the relative adhesion strengths (Figure 6A). This could indicate that the density of Man units already exceeded the density of accessible ConA binding sites. For these Man-functionalized GUVs a rather homogeneous spherical contact area with a pronounced fluorescent halo at the edge of the adhesion zone was observed (Figure 6C). This increased fluorescence at the periphery of the contact area is due to either the projected fluorescent light of the membrane above the contact line or the accumulation of ligands. Intriguingly, for biotin/NeutrAvidin as a ligand/receptor system Schmidt et al. observed either ring-shaped or filled circular accumulations of the ligand, depending to the ligand/receptor density and the ligand mobility-dependent recruitment into the contact zone.[49] We only see filled circular adhesion patterns at any of the studied concentrations with no further growth over time (see Figures S23 and S34 for exemplary pictures). This suggests that due to the rather high ligand density the entire contact zone is saturated with ligand−receptor bonds in equilibrium. This agrees well with the fact that no differences in adhesion strength due to changes in valency and ligand density were observed. Accordingly, the saturated contact area may hinder the diffusion of ligands into the contact zone leading to an accumulation of ligands at the periphery of the contact area.

To substantiate this hypothesis, we conducted FCS measurements on 1 mol % MC-decorated vesicles on a ConA surface. The confocal volume was now focused on the top part of the vesicles and, subsequently, on the respective bottom part of the vesicles, where the membrane is in contact with lectin. From these two measurements, we observed a more than 2-fold decrease of Man-ligands on the upper part of the vesicles and an increase on the adherent membrane (Figure 6B) with surface concentrations in a similar range as obtained with the FCS for glyco-decorated GUVs adhered to a NeutrAvidin substrate. This coincided with a notable decrease in diffusion coefficients close to the substrate (D = 2.7 $\mu m^2/s$) compared to that of the free membrane part (D = 7.1 $\mu m^2/s$) (Figure 6B). Of note, the glycomacromolecules are assumed to incorporate homogeneously into both leaflets of the phospholipid bilayer; hence, the surface concentrations on the outer leaflet are only half the value presented in Figure 6B. We assume that the reduction of diffusivity is a result of the binding and unbinding events between ConA and ligands in the contact area, where receptor−ligand bonds form (im-)mobile obstacles in the membrane, as well as of the substrate proximity, which contributes additional friction. The whole contact area appears sealed and further ligands can only accumulate around the contact area forming a brighter fluorescent halo. Another possible explanation for the brighter fluorescent periphery of the contact area might be that our glycomimetics avoid positively curved areas of the vesicle membrane. Lu et al. have demonstrated, that MUC1 glycocalyx constituents (heavily glycosylated transmembrane proteins) tend to accumulate on negatively curved areas of the plasma membrane upon deformation of the latter and rather avoid

https://doi.org/10.1021/acs.biomac.4c00646
Biomacromolecules 2024, 25, 5979−5994

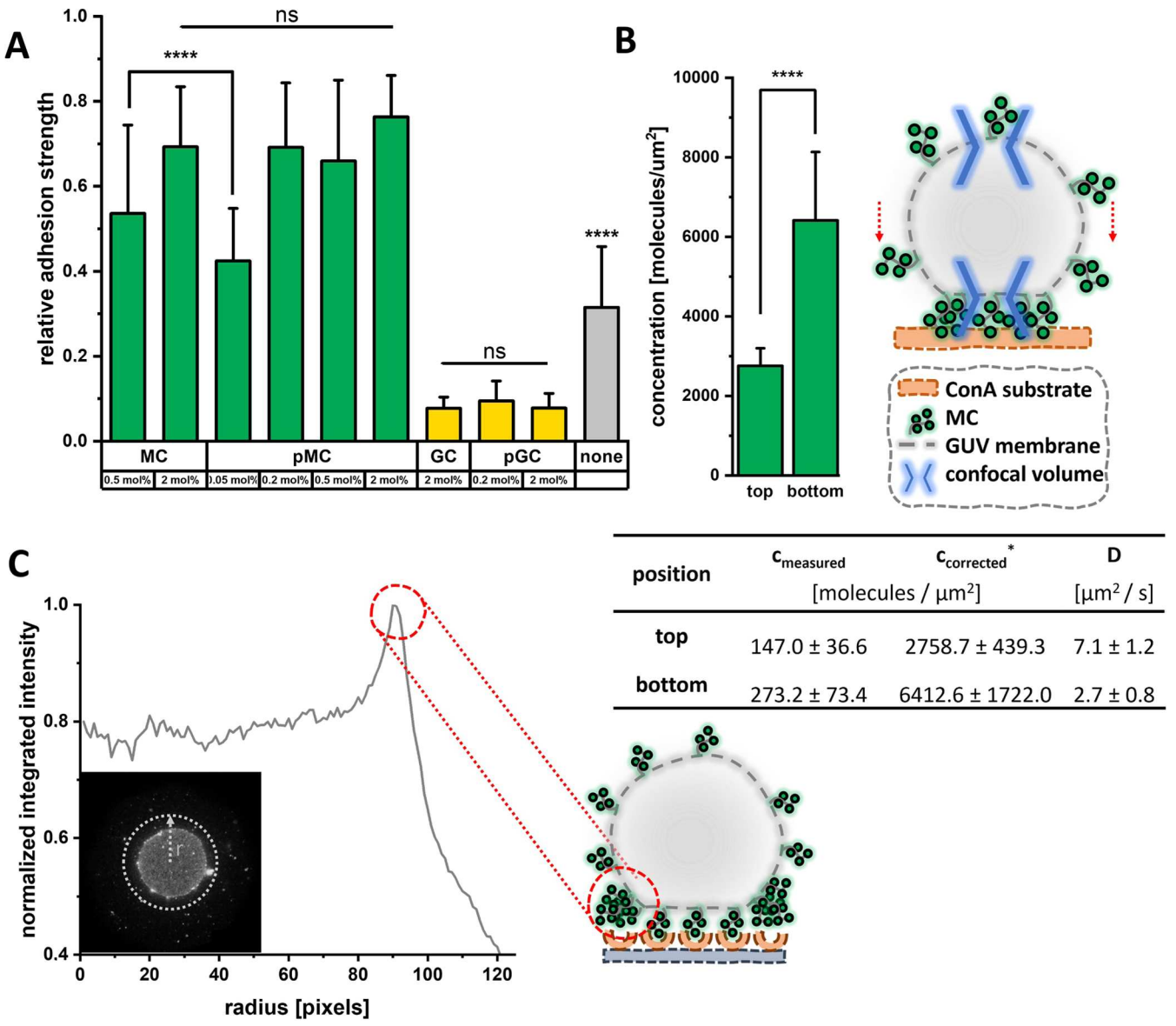

position	$c_{measured}$ [molecules / µm²]	$c_{corrected}$* [molecules / µm²]	D [µm² / s]
top	147.0 ± 36.6	2758.7 ± 439.3	7.1 ± 1.2
bottom	273.2 ± 73.4	6412.6 ± 1722.0	2.7 ± 0.8

Figure 6. (A) Relative adhesion strengths for GUVs decorated with binding (green) or nonbinding (yellow) glycomacromolecules and unfunctionalized GUVs (gray). Data are presented as mean + SEM for $n \geq 50$ experimental replicates and were evaluated using one-way analysis of variance (ANOVA) followed by Bonferroni correction (*: $p < 0.05$, **: $p < 0.01$, ***: $p < 0.005$, ****: $p < 0.001$, ns: not significant). (B) Data gathered via FCS of 1 mol % MC-vesicles adhered to ConA surfaces at the top and bottom of the vesicles. Schematic illustration of the experimental setup. Data are presented as mean + SEM for $n = 12$ experimental replicates. *Measured concentrations were corrected by the determined DoALs. Note that the glycomacromolecules are present on both sides of the membrane, therefore the surface concentration on the outer membrane side is half the value presented in (B). (C) Radial fluorescence intensity profile of the adhesion patch of GUVs functionalized with 2 mol % MC. Fluorescence intensity increases toward the rim of the adhesion area, likely due to an accumulation of ligands.

positively curved areas of the membrane to minimize steric repulsions and the overall free energy of the system.[50] However, the molecular weights of our glycomimetics are well below the molecular weights even of truncated forms of MUC1 and, thus, it remains debatable whether this also applies to our systems. Also, Callan-Jones et al. have shown that such sorting only occurs for curvatures >0.05 nm^{-1} and, accordingly, for GUVs of this size exhibiting only small curvature (10^{-4} nm^{-1}) no curvature-related sorting effect is known so far.[51]

GUVs decorated with 0.5 mol % MC and 0.05 mol % pMC exhibit a 30% reduced relative adhesion strength, which implies that in these systems the available ConA binding sites are not fully saturated. However, though theoretically presenting the same amounts of Man moieties, vesicles decorated with 0.5 mol % MC bind significantly stronger than those with 0.05 mol % pMC. We attribute this to the 10-fold higher local density and steric hindrance of Man moieties in the polymer chain for pMC, reducing the number of available Man moieties that can bind on average compared to the short MC chains. In addition, a pMC chain may bind to only a few ConA molecules at the same time, given a distance between ConA binding pockets of approximately 7.2 nm and the hydrodynamic radius of pMC of similar size (9.2 nm). Though we noticeably decreased the concentration of ligands in these systems, the resulting adhesion patches in RICM remained rather homogeneous and circular. This corresponds to the observation by Fenz et al., where biotinylated GUVs adhering to a NeutrAvidin substrate always exhibited circular and homogeneously filled

https://doi.org/10.1021/acs.biomac.4c00646
Biomacromolecules 2024, 25, 5979−5994

adhesion patches. The aforementioned ring-shaped partial adhesion would only arise, if the receptor concentrations on the substrate were $\lesssim$0.25 mol %.[52]

As a control, we also prepared vesicles with 2 mol % of either the short (GC) or longer (pGC) nonbinding ligands. Again, we also reduced the concentration of pGC by a factor of 10 to present the same amount of Gal moieties as the shorter nonbinding GC ligands, but at an overall lower ligand density (i.e., 0.2 mol % pGC). As anticipated, the Gal-decorated vesicles did not adhere to the ConA surfaces since the lectin has no affinity toward Gal moieties.

Strikingly, vesicles with no glycomacromolecules added also formed comparatively large contact areas on the ConA surfaces with a derived relative binding strength amounting to those previously measured for vesicles containing 0.5 mol % MC and 0.05 mol % pMC. We attribute this to unspecific interactions (electrostatic, hydrophobic) between membrane lipids and the ConA, which is well-known to occur in synthetic membrane systems if no blocking by a polymer such as polyethylene glycol is used.[53,54] Accordingly, nonbinding membrane constituents such as the Gal-glycomacromolecules seem to effectively block unspecific interactions between the membrane and protein surface as observed for the Gal moiety presenting GUVs.

To validate the specificity of the Man-mediated vesicle adhesion to the lectin surface, we performed inhibition assays in the presence of MeMan as an inhibitor that competitively binds to the lectin-covered surfaces (Figure 7).[55] Therefore,

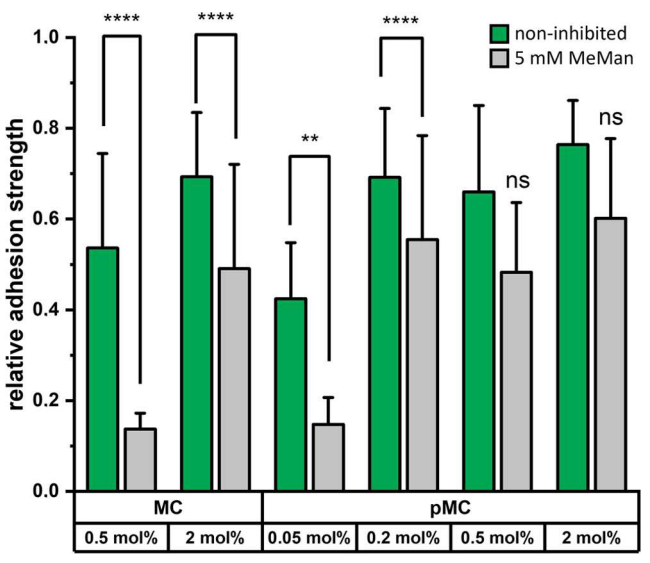

Figure 7. Derived relative adhesion strengths of Man-decorated GUVs on ConA surfaces in the absence (green) and presence (gray) of 5 mM MeMan. Data are presented as mean + SEM for $n \geq 20$ experimental replicates and were evaluated using one-way ANOVA followed by Bonferroni correction (*: $p < 0.05$, **: $p < 0.01$, ***: $p < 0.005$, ****: $p < 0.001$, ns: not significant).

the ConA surfaces were incubated with 5 mM MeMan for 30 min prior to vesicle addition. In the systems, where GUVs were decorated with only 0.5 mol % MC or 0.05 mol % pMC, respectively, incubation with 5 mM MeMan leads to inhibition of Man-mediated vesicle adhesion to the ConA surface. However, for the systems that we prior determined to saturate or exceed the available ConA binding sites on the substrate (i.e., 2 mol % MC, 0.2 mol % pMC, 0.5 mol % pMC, and 2 mol % pMC), vesicle adhesion was only reduced by approximately 25%. We then picked the systems employing 2 mol % MC and 2 mol % pMC as the extremes and tried to inhibit the adhesion. Indeed, for the shorter Man-ligand MC we required MeMan concentrations of 50 mM to inhibit vesicle adhesion. For the longer pMC ligand at 2 mol % even 50 mM MeMan did not lead to any significant decrease in adhesion (Figure S39). However, upon incubation with a multivalent glycopolymer (Man_{300}) inhibitor, vesicle adhesion was completely inhibited at 0.15 mM. With an average number of 300 Man units per polymer for the multivalent inhibitor, this translates to an effective concentration of carbohydrates of ~50 mM (Figure S40), comparable to the inhibition concentration used for monovalent MeMan.

In a previous study and similar RICM setup with Man-oligomer functionalized microgels, we observed that at a concentration of 50 mM MeMan particle adhesion to the ConA surfaces was completely inhibited.[48] The dissociation constant (K_D) of ConA for MeMan has been reported to be approximately 130 μM, as determined through ITC experiments.[56] Similarly, the K_D value for monovalently Man-functionalized oligoamidoamines was found to be approximately 200 μM, with decreasing values for higher valent structures.[57] Hence, despite ConA having a generally higher affinity for MeMan, the multivalent presentation of Man moieties compensates for the lower binding affinity, rendering the monovalent MeMan less competitive in binding to ConA. We attribute the difference and more challenging inhibition of the GUVs to the highly multivalent presentation and mobility of Man-ligands on the GUVs, which allows for the establishment and persistence of numerous simultaneous interactions with the lectin and enhances the overall binding avidity.

Especially the longer pMC ligands showing higher relative adhesion strengths under inhibitory conditions could be explained by multivalency and steric effects. The multivalent polymers can simultaneously engage in numerous binding events, resulting in an overall higher binding avidity, where parts of the ligand that are not actively engaged in binding may shield larger fractions of the immobilized ConA. As a result, the MeMan inhibitor is less able to compete for ConA binding sites, and accordingly, multivalent inhibitors are required to efficiently block the available binding sites from the Man-decorated GUVs. Moreover, the tight multivalent ensemble of bound ligands likely impedes the diffusion of inhibitors to the contact zone to compete for the ConA binding sites, consistent with our previous FCS results.

Heteromultivalently Glyco-Decorated GUVs to Mimic Glycocalyx Crowding. Glycocalyx crowding in cellular membranes is believed to exert both inhibitory as well as promotional effects on membrane constituents depending on the specific molecular interactions.[14,16,17] Modeling such a crowded environment of native cells in a very controlled setting can yield quantitative insights into the molecular interactions and the role of membrane-associated macromolecules that are not directly involved in a specific binding event.

To account for the heterogeneous and crowded nature of native glycocalyces and to determine the inhibitory or promotional effects of nonbinding membrane constituents, we next prepared vesicles with mixtures of either our short or long binding Man-ligands and the nonbinding Gal-structures to study the influence of nonbinding macromolecules on the specific binding of the Man-ligands to the ConA surfaces.

https://doi.org/10.1021/acs.biomac.4c00646
Biomacromolecules 2024, 25, 5979−5994

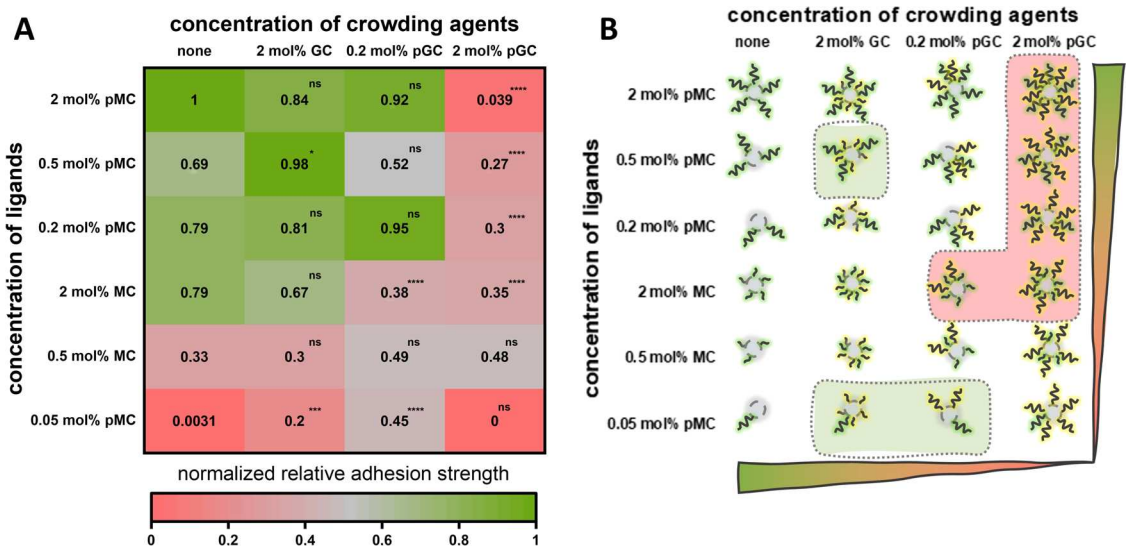

Figure 8. Direct binding experiments of heteromultivalently glyco-decorated GUVs. (A) Normalized relative adhesion strengths for the homomultivalent and heteromultivalent glycocalyx mimetics. Data are presented as mean for $n \geq 50$ experimental replicates and were evaluated using one-way ANOVA followed by Bonferroni correction (*: $p < 0.05$, **: $p < 0.01$, ***: $p < 0.005$, ****: $p < 0.001$, ns: not significant). (B) Schematic presentation of the experimental conditions. Systems highlighted in red undergo a decrease in relative adhesion strength, and those highlighted in green undergo an increase in relative adhesion strength upon crowding, when compared to the respective homomultivalent systems. Experimental conditions that are not highlighted remain unaltered in relative adhesion strength upon doping with crowding agents.

Therefore, we kept the same concentrations for the binding Man-ligands as before and doped the respective systems with different amounts (i.e., 2 mol % GC, 0.2 mol % pGC or 2 mol % pGC) of the nonbinding Gal-functionalized glycomacromolecules (i.e., crowding agents). The measured relative adhesion strengths were then normalized to compare the heteromultivalent glycocalyces with the corresponding homomultivalent systems (Figure 8).

From this systematic variation of molecular binding vs crowding ability, two fundamental trends were derived: (1) higher ligand concentration and valence lead to a stronger relative adhesion strength, and (2) higher concentrations of crowding agents decrease the adhesion strength.

In particular, incorporation of 2 mol % of the long crowding agent pGC to the homomultivalent systems leads to a significant reduction in the relative adhesion strengths of vesicles decorated with either 2 mol % MC, 0.2 mol % pMC, 0.5 mol % pMC, or 2 mol % pMC, i.e., the systems that in absence of any crowding agents showed to saturate the available ConA binding sites (see also Figure 6A). Here, it is hypothesized that crowding increases the steric repulsion within the vesicle−substrate contact zone to the extent that the accessibility of ConA for the Man-ligands is highly impaired. Polymeric crowders in the adhesion zone hence present obstacles that prevent some of the Man-ligand ConA bond formation. Also in the case of 2 mol % MC with 0.2 mol % of pGC a reduction in the relative adhesion strength is observed, whereas for the system with the same crowding agent (0.2 mol % of pGC) and the same amount of binding sites, but in polymeric form (0.2 mol % pMC), no significant change in the relative adhesion strength is found. This indicates that the long polymeric form is capable of competing with the long crowding agent.

Interestingly, GUVs with either 0.05 mol % pMC or 0.5 mol % MC are not negatively affected by doping with crowding agents in any scenario. Although these systems initially show the weakest relative adhesion strength due to their low ligand density, they exhibit equally strong adhesion strength under heavy crowding conditions (i.e., doping with 2 mol % pGC), displaying similar relative adhesion strengths as those systems with significantly higher concentrations of ligands. In this case, it is hypothesized that the lower concentration of ligands in the highly crowded heteromultivalent ensemble maintains the mobility of the Man-ligands and allows diffusion to the ConA binding sites. Potentially, interaction with the ConA could also be enhanced through the formation of local ligand clusters within the membrane, as has been reported by Shi et al. for the clustering of GM_1-gangliosides at high concentrations in phospholipid bilayers.[58]

Furthermore, doping of GUVs composed of 2 mol % MC, 0.2 mol % pMC, or 2 mol % pMC with 2 mol % of the short GC crowder has no statistically significant effect on the relative adhesion strength in comparison to the respective homomultivalent systems. Similarly, the addition of low concentrations of the long crowding agents (0.2 mol % pGC) to the homomultivalent systems (0.5 or 2 mol % pMC) does not impact the relative adhesion strength.

It is assumed that in these systems, the binding Man-ligands remain sufficiently mobile and accessible so that the interaction with ConA is not measurably impaired.

A small rise in adhesion strength is observed for the system 0.5 mol % pMC and 2 mol % GC, although the significance level is rather low ($p = 0.05$) and thus likely negligible. In contrast, a striking and progressive rise in the relative adhesion strength is observed for the system exhibiting the least amount of ligand density (i.e., 0.05 mol % pMC) upon the addition of 2 mol % short crowding agent GC and 0.2 mol % long crowding agent pGC.

As was shown via FCS before, in homomultivalent GUVs containing 0.05 mol % pMC, the concentration of polymeric ligands is below the threshold for crowding. However, upon the addition of further glycomacromolecules (i.e., 2 mol % GC or 0.2 mol % pGC), the concentration of macromolecules on

https://doi.org/10.1021/acs.biomac.4c00646
Biomacromolecules 2024, 25, 5979−5994

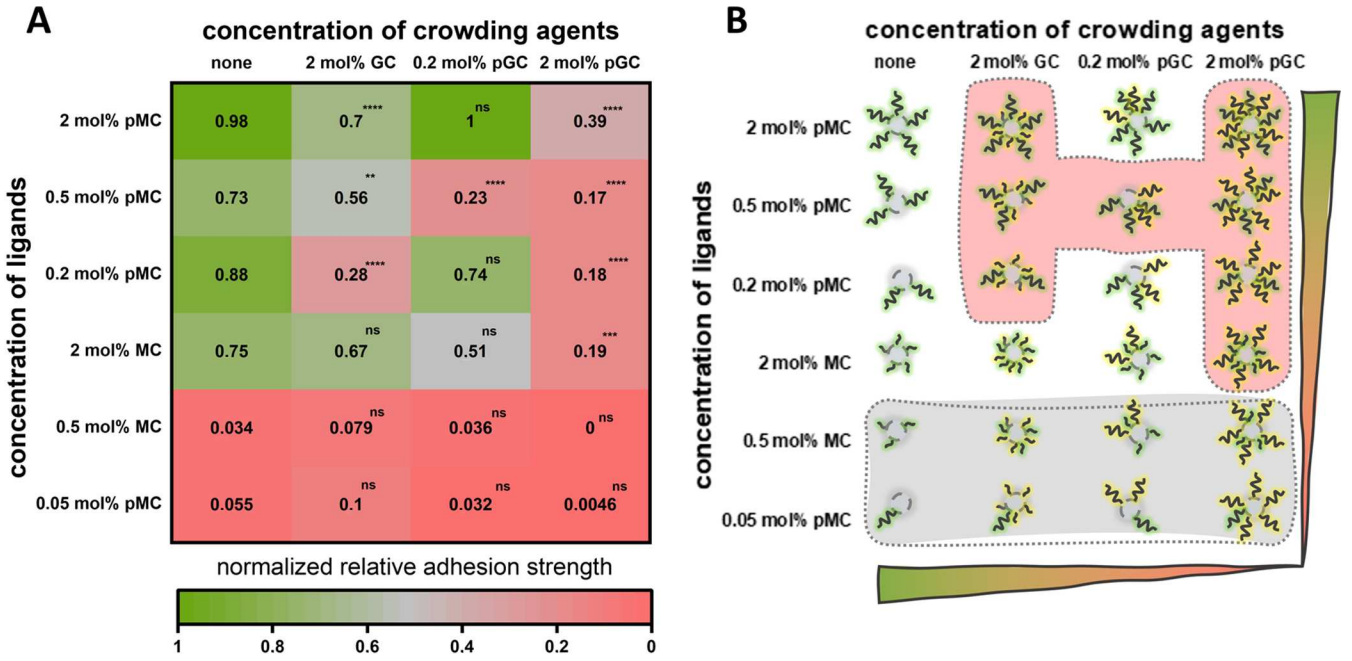

Figure 9. Inhibition/competition experiments of heteromultivalently glyco-decorated GUVs with 5 mM MeMan. (A) Normalized relative adhesion strengths for the homomultivalent and heteromultivalent glycocalyx mimetics in the presence of 5 mM MeMan inhibitor. Data are presented as mean for $n \geq 50$ experimental replicates and were evaluated using one-way ANOVA followed by Bonferroni correction (*: $p < 0.05$, **: $p < 0.01$, ***: $p < 0.005$, ****: $p < 0.001$, ns: not significant). (B) Schematic presentation of the employed experimental conditions. Systems highlighted in red undergo a decrease in relative adhesion strength compared with the respective homomultivalent systems. Experimental conditions that are highlighted in gray signify inhibition of adhesion under the given conditions.

the membrane surface increases sufficiently to induce crowding.[41]

We hypothesize that the introduction of crowding agents gradually increases the steric pressure within the membrane adhesion zone and hence might lead to a change in glycomacromolecular conformation from a coiled to an extended structure, concomitant with a decrease in lateral entropy and an increase in binding enthalpy, thus establishing more stable bonds with the ConA surfaces and consequently resulting in higher relative adhesion strengths. This effect is amplified when using 0.2 mol % pGC, which putatively possesses a higher steric demand compared to short GC crowders. When the concentration of pGC is further increased (i.e., doping with 2 mol % pGC), this effect may be counterbalanced by the simultaneous unfolding of the pGC crowders, resulting in no measurable change in relative adhesion strength overall. Presumably, this occurs because the ligands remain mobile within the heteromultivalent ensemble.

Similar effects have been previously described by Delaveris et al. Employing fluorescence interference contrast microscopy (FLIC) and dynamic light scattering (DLS), it was demonstrated that synthetic mucin mimetics in supported lipid bilayers unfold from the bilayer and extend beyond the membrane when the concentration of membrane-bound constituents is increased.[27]

In conclusion, when homomultivalent systems are doped with crowding agents, three general scenarios can be observed: (1) crowding decreases the adhesion of heteromultivalent systems, when the adhesion of the homomultivalent system was initially strong and when the molar amount of pGC is ≥ to the (p)MC amount, (2) crowding has no directly measurable effect on adhesion as long as GC or low molar amounts of pGC are used, and (3) crowding agents slightly increase the initial weak adhesion of vesicles.

Subsequently, we conducted inhibition studies on the heteromultivalent systems again using 5 mM MeMan as the antagonist and compared the resulting normalized relative adhesion strengths to those of the homomultivalent systems in the presence of 5 mM MeMan. Generally, the observed trends in the normalized relative adhesion strengths were consistent with those observed in the absence of the inhibitor. Specifically, higher concentrations and valences of crowding agents led to reduced adhesion in the presence of MeMan. A higher overall Man density resulted in increased relative adhesion strengths. At comparable Man densities of pMC and MC (e.g., 0.05 mol % pMC and 0.5 mol % MC) without a crowding agent, pMC ligands were more difficult to inhibit due to the higher local density of Man units (Figure 9).

It is noteworthy that the systems with the lowest ligand densities (0.5 mol % MC and 0.05 mol % pMC or less) were already inhibited in the presence of 5 mM MeMan when introduced homomultivalently. Adding crowding agents did not result in any significant changes. We believe that the low concentration of ligands is insufficient to compete with the MeMan antagonist, resulting in the inhibition of the adhesion of the vesicles to the ConA surfaces.

The addition of 2 mol % GC to vesicles that are decorated with 2 mol % MC does not seem to have any noticeable impact on adhesion. However, when vesicles are decorated with high concentrations of pMC (i.e., 0.2, 0.5, or 2 mol %) and are doped with 2 mol % GC, adhesion significantly decreases in a concentration-dependent manner (i.e., more ligand results in more adhesion).

Incorporating 0.2 mol % of the long crowding agent pGC into vesicles decorated with 0.5 mol % pMC results in

https://doi.org/10.1021/acs.biomac.4c00646
Biomacromolecules 2024, 25, 5979−5994

significantly reduced adhesion. For the other systems (i.e., 2 mol % MC, 0.2 mol % pMC, and 2 mol % pMC), no noticeable influence is observed.

The presence of 2 mol % pGC in homomultivalent systems overall leads to a significant reduction in adhesion in all cases. For the GUVs functionalized with either 2 mol % MC, 0.2 mol % pMC, or 0.5 mol % pMC, adhesion is nearly completely inhibited, while only vesicles decorated with 2 mol % pMC and 2 mol % pGC retain a certain level of adhesion.

Our findings provide evidence for our hypothesis that the presence of crowding agents restricts the movement and accessibility of the ligands, particularly in systems of high glycomacromolecular density, and makes it more challenging for the Man moieties to compete with the MeMan inhibitor for the ConA binding sites. The results also show that the short crowder GC has generally a negative impact on the relative adhesion strengths of the polymeric ligands pMC in a concentration-dependent manner, which was not observed in the absence of a competitor. While we would expect the longer polymer chains to extend beyond the short GC crowders and maintain their interaction with ConA, this does not seem to be the case. Then again, the short crowder has no significant impact on the adhesion of vesicles decorated with 2 mol % of the short ligand MC, which is rather astonishing.

Overall, our findings indicate that especially at higher ligand densities steric hindrance becomes a dominant factor governing the glyco-mediated GUV adhesion to the ConA surfaces, and the addition of crowding agents reduces binding. However, at sufficiently low ligand densities and moderate concentrations of crowding agents, the ligands can apparently still assume favorable positions, which facilitate strong binding. In this case, crowding may even enhance binding by elongating the carbohydrate chains, thereby increasing the sampling range for binding to receptors.

In conclusion, this comprehensive study demonstrates how crowding results in different effects on membrane adhesion depending on the contour length, conformation, and density of constituents. The concentration regime probed shows that all possible cases of (i) inhibited, (ii) unaltered, and (iii) promoted adhesion occur. Thus, this provides an important basis to further study the configuration as well as spatial and dynamic molecular organization in crowded glycocalyces.

CONCLUSIONS

A series of membrane-anchoring glycomacromolecules systematically varying the chain length and composition of the glycan mimetic headgroup was synthesized using previously established SPPoS in combination with TIRP. This strategy allows for a site-selective introduction of functional handles (e.g., fluorescent markers and membrane anchors), while the glycoheadgroup can be precisely tailored regarding glycosylation and valency. The thus prepared glycomacromolecules were successfully introduced into GUVs as model membrane systems and were analyzed in terms of their incorporation efficiency via FCS. The obtained incorporation efficiencies of our glycomacromolecules were found to be far below the expected values, implying that cholesterol as a membrane tether might not function as efficiently as previously assumed to tether membrane constituents. We then investigated homomultivalent systems in terms of their binding to ConA surfaces. Using RICM and fluorescence microscopy, we were able to characterize the relative strength of adhesion. Man-functionalized membranes specifically adhere to the substrate depending on the ligand density and valency. Interestingly, while Gal-decorated vesicles show no interaction, non-functionalized control vesicles showed nonspecific binding to the lectin substrate, suggesting that crowding agents in native cell membranes might additionally serve the purpose of suppressing nonspecific interactions associated with the glycocalyx.

The simultaneous incorporation of both binding and nonbinding glycomacromolecules, allowed us to mimic the complex and densely crowded architecture of native glycocalyces in a reductionist but highly controlled fashion. Investigating these systems with respect to their binding to ConA surfaces, we found that the presence of various crowding agents either does not affect the binding or diminishes it or, in some cases, even promotes it, depending on the constitution and density of the constituents used.

We attribute negative effects on binding to a restriction of the mobility and accessibility of the ligands by the crowding agents. Strikingly, several heteromultivalent mixtures of crowding agents and ligands at lower concentrations adhere equally well to or even better than the respective mixtures at higher ligand densities. We assume that in these scenarios, the steric demand of the crowding agents might trigger the segregation of the binding ligands into local clusters or change into more accessible conformations, which is reflected in an increase in the resulting adhesion. These fundamental findings show that crowding in heterogeneous, naïve glycocalyces can have very multifaceted effects and, accordingly, require further analytical investigation.

We envision that our synthetic platform for glycomacromolecular crowding in model membrane systems will provide a valuable tool for studying the impact of the glycocalyx environment on distinct mechanisms. Our ongoing research will be directed to further investigate the dynamics and spatial rearrangement of glycan mimetics within the crowded ensemble of glycocalyx mimetics. Also, with our modular toolbox in hand, we will focus on developing more complex mimetics of native glycans (e.g., mimetics of sulfated glycosaminoglycans or branched structures to mimic membrane-associated mucins) as well as studying more complex glycocalyces in terms of their lipid heterogeneity to account for the lipid-mediated formation of local clusters and patches in natural cell membranes.

ASSOCIATED CONTENT

Supporting Information

The Supporting Information is available free of charge at https://pubs.acs.org/doi/10.1021/acs.biomac.4c00646.

Information about used materials and analytical methods, as well as detailed analytical data for all compounds and additional data on performed experiments (PDF)

AUTHOR INFORMATION

Corresponding Author

Laura Hartmann − *Department for Organic Chemistry and Macromolecular Chemistry, Heinrich Heine University Duesseldorf, 40225 Düsseldorf, Germany; Department for Macromolecular Chemistry, University of Freiburg, 79104 Freiburg i.Br., Germany;* orcid.org/0000-0003-0115-6405; Phone: +49 761 203 6270; Email: laura.hartmann@makro.uni-freiburg.de

https://doi.org/10.1021/acs.biomac.4c00646
Biomacromolecules 2024, 25, 5979−5994

Authors

Luca-Cesare Blawitzki − *Department for Organic Chemistry and Macromolecular Chemistry, Heinrich Heine University Duesseldorf, 40225 Düsseldorf, Germany; Department for Macromolecular Chemistry, University of Freiburg, 79104 Freiburg i.Br., Germany*

Nina Bartels − *Department for Experimental Medical Physics, Heinrich Heine University Duesseldorf, 40225 Düsseldorf, Germany*

Lorand Bonda − *Department for Organic Chemistry and Macromolecular Chemistry, Heinrich Heine University Duesseldorf, 40225 Düsseldorf, Germany*

Stephan Schmidt − *Department for Organic Chemistry and Macromolecular Chemistry, Heinrich Heine University Duesseldorf, 40225 Düsseldorf, Germany; Department for Macromolecular Chemistry, University of Freiburg, 79104 Freiburg i.Br., Germany;* orcid.org/0000-0002-4357-304X

Cornelia Monzel − *Department for Experimental Medical Physics, Heinrich Heine University Duesseldorf, 40225 Düsseldorf, Germany;* orcid.org/0000-0003-0892-3427

Complete contact information is available at: https://pubs.acs.org/10.1021/acs.biomac.4c00646

Author Contributions

The manuscript was written through contributions of all authors. All authors have given approval to the final version of the manuscript. Author contributions are as follows: Conceptualization: L.H. Methodology: L.-C.B., N.B., and L.B. Investigation: L.-C.B. and N.B. Visualization: L.-C.B. Supervision: L.H., C.M., and S.S. Writing − original draft: L.-C.B., L.H., C.M., and S.S.

Funding

L.H., L.-C.B., N.B. and C.M. acknowledge financial support from the Deutsche Forschungsgemeinschaft (DFG, German Research Foundation) through CRC1208 'Identity and Dynamics of Membrane Systems' (A11 and A12, Project ID 267205415). C.M. further acknowledges financial support via the "Freigeist fellowship" of VolkswagenFoundation and of the Deutsche Forschungsgemeinschaft (DFG, German Research Foundation) through CRC1535 "Microbial Networks" (A09, Project ID 458090666).

Notes

The authors declare no competing financial interest.

■ ACKNOWLEDGMENTS

The authors thank the CeMSA@HHU (Center for Molecular and Structural Analytics @ Heinrich Heine University) for recording the mass-spectrometric and the NMR-spectroscopic data.

■ ABBREVIATIONS

ConA	concanavalin A
CuAAC	copper-mediated azide−alkyne cycloaddition
EDS	ethylene glycol diamine succinic acid
FCS	fluorescence correlation spectroscopy
Gal	β-D-galactose
GUV	giant unilamellar vesicle
LBB	lectin binding buffer
Man	α-D-mannose
MeMan	methyl α-D-mannopyranoside
RICM	reflection interference contrast microscopy
SPPoS	solid-phase polymer synthesis
TDS	triple bond diethylenetriamine succinic acid
TIRP	thiol-induced, light-activated controlled radical polymerization

■ REFERENCES

(1) Möckl, L. The Emerging Role of the Mammalian Glycocalyx in Functional Membrane Organization and Immune System Regulation. *Front. Cell Dev. Biol.* **2020**, *8*, 253.

(2) Zeng, Y.; Tang, F.; Shi, W.; Dong, Q.; Huang, W. Recent advances in synthetic glycoengineering for biological applications. *Curr. Opin. Biotechnol.* **2022**, *74*, 247−255.

(3) Varki, A.; Cummings, R. D.; Esko, J. D.; Stanley, P.; Hart, G. W.; Aebi, M.; Darvill, A. G.; Kinoshita, T.; Packer, N. H.; Prestegard, J. H. et al. *Essentials of Glycobiology*, 3rd ed.; Cold Spring Harbor: NY, 2015.

(4) Reitsma, S.; Slaaf, D. W.; Vink, H.; van Zandvoort, M. A. M. J.; oude Egbrink, M. G. A. The endothelial glycocalyx: composition, functions, and visualization. *Pfluegers Arch.* **2007**, *454*, 345−359.

(5) Wagner, C. E.; Wheeler, K. M.; Ribbeck, K. Mucins and Their Role in Shaping the Functions of Mucus Barriers. *Annu. Rev. Cell Dev. Biol.* **2018**, *34*, 189−215.

(6) Weinbaum, S.; Tarbell, J. M.; Damiano, E. R. The structure and function of the endothelial glycocalyx layer. *Annu. Rev. Biomed. Eng.* **2007**, *9*, 121−167.

(7) Cummings, R. D. Stuck on sugars—how carbohydrates regulate cell adhesion, recognition, and signaling. *Glycoconjugate J.* **2019**, *36*, 241−257.

(8) Purcell, S. C.; Godula, K. Synthetic glycoscapes: addressing the structural and functional complexity of the glycocalyx. *Interface Focus* **2019**, *9*, No. 20180080.

(9) Smith, B. A. H.; Bertozzi, C. R. The clinical impact of glycobiology: targeting selectins, Siglecs and mammalian glycans. *Nat. Rev. Drug Discovery* **2021**, *20*, 217−243.

(10) Chettri, D.; Boro, M.; Sarkar, L.; Verma, A. K. Lectins: Biological significance to biotechnological application. *Carbohydr. Res.* **2021**, *506*, No. 108367.

(11) Wittmann, V.; Pieters, R. J. Bridging lectin binding sites by multivalent carbohydrates. *Chem. Soc. Rev.* **2013**, *42*, 4492−4503.

(12) Cairo, C. W.; Gestwicki, J. E.; Kanai, M.; Kiessling, L. L. Control of multivalent interactions by binding epitope density. *J. Am. Chem. Soc.* **2002**, *124*, 1615−1619.

(13) Jiménez Blanco, J. L.; Ortiz Mellet, C.; García Fernández, J. M. Multivalency in heterogeneous glycoenvironments: hetero-glycoclusters, -glycopolymers and -glycoassemblies. *Chem. Soc. Rev.* **2013**, *42*, 4518−4531.

(14) Löwe, M.; Kalacheva, M.; Boersma, A. J.; Kedrov, A. The more the merrier: effects of macromolecular crowding on the structure and dynamics of biological membranes. *FEBS J.* **2020**, *287*, 5039−5067.

(15) Honigfort, D. J.; Altman, M. O.; Gagneux, P.; Godula, K. Glycocalyx crowding with synthetic mucin mimetics strengthens interactions between soluble and virus-associated lectins and cell surface glycan receptors. *Proc. Natl. Acad. Sci. U.S.A.* **2021**, *118*, No. e2107896118.

(16) Hlavacek, W. S.; Posner, R. G.; Perelson, A. S. Steric effects on multivalent ligand-receptor binding: exclusion of ligand sites by bound cell surface receptors. *Biophys. J.* **1999**, *76*, 3031−3043.

(17) Ellis, R. J. Macromolecular crowding: obvious but underappreciated. *Trends Biochem. Sci.* **2001**, *26*, 597−604.

(18) Löwe, M.; Hänsch, S.; Hachani, E.; Schmitt, L.; Weidtkamp-Peters, S.; Kedrov, A. Probing macromolecular crowding at the lipid membrane interface with genetically-encoded sensors. *Protein Sci.* **2023**, *32*, No. e4797.

(19) Li, Y.; Wang, M.; Hong, S. Live-Cell Glycocalyx Engineering. *ChemBioChem* **2023**, *24*, No. e202200707.

(20) Critcher, M.; O'Leary, T.; Huang, M. L. Glycoengineering: scratching the surface. *Biochem. J.* **2021**, *478*, 703−719.

(21) Okajima, T.; Reddy, B.; Matsuda, T.; Irvine, K. D. Contributions of chaperone and glycosyltransferase activities of O-fucosyltransferase 1 to Notch signaling. *BMC Biol.* **2008**, *6*, 1.
(22) Omidvar, R.; Römer, W. Glycan-decorated protocells: novel features for rebuilding cellular processes. *Interface Focus* **2019**, *9*, No. 20180084.
(23) Stuhr-Hansen, N.; Madl, J.; Villringer, S.; Aili, U.; Römer, W.; Blixt, O. Synthesis of Cholesterol-Substituted Glycopeptides for Tailor-Made Glycocalyxification of Artificial Membrane Systems. *ChemBioChem* **2016**, *17*, 1403−1406.
(24) Huang, M. L.; Tota, E. M.; Verespy, S.; Godula, K. Glycocalyx Scaffolding to Control Cell Surface Glycan Displays. *Curr. Protoc. Chem. Biol.* **2018**, *10*, No. e40.
(25) Paszek, M. J.; DuFort, C. C.; Rossier, O.; Bainer, R.; Mouw, J. K.; Godula, K.; Hudak, J. E.; Lakins, J. N.; Wijekoon, A. C.; Cassereau, L.; et al. The cancer glycocalyx mechanically primes integrin-mediated growth and survival. *Nature* **2014**, *511*, 319−325.
(26) Woods, E. C.; Yee, N. A.; Shen, J.; Bertozzi, C. R. Glycocalyx Engineering with a Recycling Glycopolymer that Increases Cell Survival In Vivo. *Angew. Chem., Int. Ed.* **2015**, *54*, 15782−15788.
(27) Delaveris, C. S.; Webster, E. R.; Banik, S. M.; Boxer, S. G.; Bertozzi, C. R. Membrane-tethered mucin-like polypeptides sterically inhibit binding and slow fusion kinetics of influenza A virus. *Proc. Natl. Acad. Sci. U.S.A.* **2020**, *117*, 12643−12650.
(28) Ponader, D.; Wojcik, F.; Beceren-Braun, F.; Dernedde, J.; Hartmann, L. Sequence-defined glycopolymer segments presenting mannose: synthesis and lectin binding affinity. *Biomacromolecules* **2012**, *13*, 1845−1852.
(29) Schröer, F.; Paul, T. J.; Wilms, D.; Saatkamp, T. H.; Jäck, N.; Müller, J.; Strzelczyk, A. K.; Schmidt, S. Lectin and *E. coli* Binding to Carbohydrate-Functionalized Oligo(ethylene glycol)-Based Microgels: Effect of Elastic Modulus, Crosslinker and Carbohydrate Density. *Molecules* **2021**, *26*, No. 263, DOI: 10.3390/molecules26020263.
(30) Boden, S.; Reise, F.; Kania, J.; Lindhorst, T. K.; Hartmann, L. Sequence-Defined Introduction of Hydrophobic Motifs and Effects in Lectin Binding of Precision Glycomacromolecules. *Macromol. Biosci.* **2019**, *19*, No. e1800425.
(31) Sun, Q.; Cai, S.; Peterson, B. R. Practical synthesis of 3beta-amino-5-cholestene and related 3beta-halides involving i-steroid and retro-i-steroid rearrangements. *Org. Lett.* **2009**, *11*, 567−570.
(32) Banger, A.; Pasch, P.; Blawitzki, L.-C.; Weber, S.; Otten, M.; Monzel, C.; Schmidt, S.; Voskuhl, J.; Hartmann, L. Detection of Lectin Clustering in Self-Assembled, Glycan-Functionalized Amphiphiles by Aggregation-Induced Emission Luminophores. *Macromol. Chem. Phys.* **2023**, *224*, No. 2200314.
(33) Fischer, L.; Steffens, R. C.; Paul, T. J.; Hartmann, L. Catechol-functionalized sequence-defined glycomacromolecules as covalent inhibitors of bacterial adhesion. *Polym. Chem.* **2020**, *11*, 6091−6096.
(34) Mueller, L. K.; Baumruck, A. C.; Zhdanova, H.; Tietze, A. A. Challenges and Perspectives in Chemical Synthesis of Highly Hydrophobic Peptides. *Front. Bioeng. Biotechnol.* **2020**, *8*, 162.
(35) Bonda, L.; Valles, D. J.; Wigger, T. L.; Meisner, J.; Braunschweig, A. B.; Hartmann, L. TIRP—Thiol-Induced, Light-Activated Controlled Radical Polymerization. *Macromolecules* **2023**, *56*, 5512−5523.
(36) Camaleño de la Calle, A.; Gerke, C.; Chang, X. J.; Grafmüller, A.; Hartmann, L.; Schmidt, S. Multivalent Interactions of Polyamide Based Sequence-Controlled Glycomacromolecules with Concanavalin A. *Macromol. Biosci.* **2019**, *19*, No. e1900033.
(37) Steinkühler, J.; Tillieux, P. de.; Knorr, R. L.; Lipowsky, R.; Dimova, R. Charged giant unilamellar vesicles prepared by electroformation exhibit nanotubes and transbilayer lipid asymmetry. *Sci. Rep.* **2018**, *8*, No. 11838.
(38) Yu, L.; Lei, Y.; Ma, Y.; Liu, M.; Zheng, J.; Dan, D.; Gao, P. A Comprehensive Review of Fluorescence Correlation Spectroscopy. *Front. Phys.* **2021**, *9*, No. 644450.
(39) Chiantia, S.; Schwille, P.; Klymchenko, A. S.; London, E. Asymmetric GUVs prepared by MβCD-mediated lipid exchange: an FCS study. *Biophys. J.* **2011**, *100*, L1−L3.
(40) Birtalan, E.; Rudat, B.; Kölmel, D. K.; Fritz, D.; Vollrath, S. B. L.; Schepers, U.; Bräse, S. Investigating rhodamine B-labeled peptoids: scopes and limitations of its applications. *Biopolymers* **2011**, *96*, 694−701.
(41) Bartels, N.; van der Voort, N. T. M.; Greife, A.; Bister, A.; Wiek, C.; Seidel, C. A. M.; Monzel, C. *A Minimal Model of CD95 Signal Initiation Revealed by Advanced Super-resolution and Multi-parametric Fluorescence Microscopy*; bioRxiv, 2022.
(42) Clayton, A. H. A.; Chattopadhyay, A. Taking care of bystander FRET in a crowded cell membrane environment. *Biophys. J.* **2014**, *106*, 1227−1228.
(43) Jan Akhunzada, M.; D'Autilia, F.; Chandramouli, B.; Bhattacharjee, N.; Catte, A.; Di Rienzo, R.; Cardarelli, F.; Brancato, G. Interplay between lipid lateral diffusion, dye concentration and membrane permeability unveiled by a combined spectroscopic and computational study of a model lipid bilayer. *Sci. Rep.* **2019**, *9*, No. 1508.
(44) Przybylo, M.; Sýkora, J.; Humpolíckova, J.; Benda, A.; Zan, A.; Hof, M. Lipid diffusion in giant unilamellar vesicles is more than 2 times faster than in supported phospholipid bilayers under identical conditions. *Langmuir* **2006**, *22*, 9096−9099.
(45) Thomas, F. A.; Visco, I.; Petrášek, Z.; Heinemann, F.; Schwille, P. Diffusion coefficients and dissociation constants of enhanced green fluorescent protein binding to free standing membranes. *Data Brief* **2015**, *5*, 537−541.
(46) Streicher, P.; Nassoy, P.; Bärmann, M.; Dif, A.; Marchi-Artzner, V.; Brochard-Wyart, F.; Spatz, J.; Bassereau, P. Integrin reconstituted in GUVs: a biomimetic system to study initial steps of cell spreading. *Biochim. Biophys. Acta, Biomembr.* **2009**, *1788*, 2291−2300.
(47) Bryce, R. A.; Hillier, I. H.; Naismith, J. H. Carbohydrate-protein recognition: molecular dynamics simulations and free energy analysis of oligosaccharide binding to concanavalin A. *Biophys. J.* **2001**, *81*, 1373−1388.
(48) Jacobi, F.; La Camaleño de Calle, A.; Boden, S.; Grafmüller, A.; Hartmann, L.; Schmidt, S. Multivalent Binding of Precision Glycooligomers on Soft Glycocalyx Mimicking Hydrogels. *Biomacromolecules* **2018**, *19*, 3479−3488.
(49) Schmidt, D.; Bihr, T.; Fenz, S.; Merkel, R.; Seifert, U.; Sengupta, K.; Smith, A.-S. Crowding of receptors induces ring-like adhesions in model membranes. *Biochim. Biophys. Acta, Mol. Cell Res.* **2015**, *1853*, 2984−2991.
(50) Lu, C.-H.; Pedram, K.; Tsai, C.-T.; Jones, T.; Li, X.; Nakamoto, M. L.; Bertozzi, C. R.; Cui, B. Membrane curvature regulates the spatial distribution of bulky glycoproteins. *Nat. Commun.* **2022**, *13*, No. 3093.
(51) Callan-Jones, A.; Sorre, B.; Bassereau, P. Curvature-driven lipid sorting in biomembranes. *Cold Spring Harbor Perspect. Biol.* **2011**, *3*, No. a004648.
(52) Fenz, S. F.; Smith, A.-S.; Merkel, R.; Sengupta, K. Intermembrane adhesion mediated by mobile linkers: Effect of receptor shortage. *Soft Matter* **2011**, *7*, 952−962.
(53) Bendix, P. M.; Pedersen, M. S.; Stamou, D. Quantification of nano-scale intermembrane contact areas by using fluorescence resonance energy transfer. *Proc. Natl. Acad. Sci. U.S.A.* **2009**, *106*, 12341−12346.
(54) Jain, A.; Liu, R.; Xiang, Y. K.; Ha, T. Single-molecule pull-down for studying protein interactions. *Nat. Protoc.* **2012**, *7*, 445−452.
(55) Sato, K.; Imoto, Y.; Sugama, J.; Seki, S.; Inoue, H.; Odagiri, T.; Hoshi, T.; Anzai, J. Sugar-induced disintegration of layer-by-layer assemblies composed of concanavalin A and glycogen. *Langmuir* **2005**, *21*, 797−799.
(56) Chervenak, M. C.; Toone, E. J. Calorimetric analysis of the binding of lectins with overlapping carbohydrate-binding ligand specificities. *Biochemistry* **1995**, *34*, 5685−5695.
(57) Igde, S.; Röblitz, S.; Müller, A.; Kolbe, K.; Boden, S.; Fessele, C.; Lindhorst, T. K.; Weber, M.; Hartmann, L. Linear Precision

Glycomacromolecules with Varying Interligand Spacing and Linker Functionalities Binding to Concanavalin A and the Bacterial Lectin FimH. *Macromol. Biosci.* **2017**, *17*, No. 1700198.
(58) Shi, J.; Yang, T.; Kataoka, S.; Zhang, Y.; Diaz, A. J.; Cremer, P. S. GM1 clustering inhibits cholera toxin binding in supported phospholipid membranes. *J. Am. Chem. Soc.* **2007**, *129*, 5954−5961.

https://doi.org/10.1021/acs.biomac.4c00646
Biomacromolecules 2024, 25, 5979−5994

Supplementary Information

Glycomacromolecules to Tailor Crowded and Heteromultivalent Glycocalyx Mimetics

Luca-Cesare Blawitzki[a,c], Lorand Bonda[a], Nina Bartels[b], Stephan Schmidt[a,c], Cornelia Monzel[b], Laura Hartmann[a,c*]

[a] Department for Organic Chemistry and Macromolecular Chemistry, Heinrich Heine University Duesseldorf, Universitätsstraße 1, 40225 Düsseldorf, Germany

[b] Department for Experimental Medical Physics, Heinrich Heine University Duesseldorf, Universitätsstraße 1, 40225 Düsseldorf, Germany

[c] Department for Macromolecular Chemistry, University of Freiburg, Stefan-Meier-Str. 31, 79104 Freiburg i.Br., Germany

* Correspondence to Tel: +49 761 203 6270; E-mail: laura.hartmann@makro.uni-freiburg.de

Materials

D-(+)-galactose, D-(+)-mannose, N,N-dimethylformamide, oxalyl chloride, piperidine and tosyl chloride were purchased from Acros Organics. Ethyl trifluoroacetate and PyBOP were purchased from Apollo Scientific. Acetonitrile and cholesterol were purchased from AppliChem. Fmoc-Cl and tris(2-phenylpyridine)-iridium(III) were purchased from bld pharm. succinic anhydride was purchased from Carbolution Chemicals. DIPEA and sodium chloride were purchased from Carl Roth. 1.4-dioxane, acetic anhydride, calcium chloride, ethyl acetate, HEPES, n-hexane, hydrochloric acid (37%), manganese dichloride, potassium carbonate, sodium azide, sodium bicarbonate, sodium hydroxide (1M), sodium methoxide and trimethylamine were purchased from Fisher Scientific. Fluorescein and triethylsilane were purchased from fluorochem. Fmoc-Cys(Trt)-OH, Fmoc-Lys(Boc)-OH and Fmoc-Lys(Dde)-OH were purchased from Iris Biotech. Concanavalin A was purchased from MP Biomedicals. 2,2′-(Ethylenedioxy)bis(ethylamine), 2-bromoethanol, 4-pentynoic acid, boron trifluoride diethyl etherate, Bovine Serum Albumin, dichloromethane, diethyl ether, diethylenetriamine, formic acid, methyl α-D-mannopyranoside, methanol, tetrahydrofuran, trifluoroacetic acid and triisopropylsilane were purchased from Sigma-Aldrich. Diphenyl-(2,4,6-trimethylbenzoyl)-phosphineoxide(>98%), N-hydroxyethylacrylamide, Rhodamine B, TCEP, trimethylsilyl azide and trityl chloride were purchased from TCI chemicals. NeutrAvidin and sodium diethyldithiocarbamate were purchased from Thermo Scientific.

All solvents and reagents used were purchased in the highest purity available and used without further purification.

TentaGel® S RAM resin (loading: 0.26 mmol/g) was purchased from RAPP Polymere GmbH.

DOPC, 18:1 PEG2000-PE, 16:0 Biotinyl Cap PE and 16:0 Liss Rhod PE were purchased from Avanti Polar Lipids.

Dialysis was performed via diafiltration in VIVASPIN 20 centrifugal concentrators (MWCO: 10 kDa; PES) from sartorius.

Experiments were conducted in 18-well glass bottom µ-slides from ibidi GmbH.

Instrumentation

Reversed Phase- High Pressure Liquid Chromatography- Mass Spectrometry (RP-HPLC-MS)/Electron Spray Ionization- Mass Spectrometry (ESI-MS)

RP-HPLC-MS was carried out on an Agilent 1260 Infinity instrument coupled to a variable wavelength detector (VWD) (set to 214 nm) and a 6120 Quadrupole LC/MS containing an Electrospray Ionization (ESI) source (operation mode positive, m/z range from 200 to 2000). An MZ-AquaPerfect C18 (3.0 × 50 mm, 3 µm) RP column from MZ-Analysentechnik was used. As eluent system water/acetonitrile containing 0.1 vol% formic acid was applied. The mobile phases A and B were: System A) water/acetonitrile (95/5, v/v); System B) water/acetonitrile (5/95, v/v). The samples were analyzed at a flow rate of 0.4 ml/min using a linear gradient, starting with 100% of system A) and reaching 100% system B) within 17 min. The temperature of the column room was set to 25 °C. All purities were determined using the OpenLab ChemStation software for LC/MS from Agilent Technologies.

Ultra High Resolution - Mass Spectrometry (UHR-MS)

UHR-MS measurements were performed with a Bruker UHR-QTOF maXis 4G instrument with a direct inlet via syringe pump, an ESI source and a quadrupole followed by a Time of Flight (QTOF) mass analyzer.

Nuclear Magnetic Resonance Spectroscopy (NMR)

The ^{1}H-NMR spectra were recorded on a Bruker Avanace III 600 (300 or 600 MHz). These spectra were evaluated according to the following scheme: (frequency in MHz, deuterated solvent), chemical shift in ppm (multiplicity, coupling constant, integral, signal assignment). The chemical shift is given in relation to the ^{1}H signals of the deuterated solvents used.

Size Exclusion Chromatography-Multi-Angle Light Scattering (H_2O-SEC-MALS)

SEC analysis was conducted with an Agilent 1200 series HPLC system and three aqueous SEC columns provided by Polymer Standards Service (PSS). The columns were two Suprema Lux analytical columns(8 mm diameter and 5µm particle size) and one precolumn (50 mm, 2×160 Å of 300 mm and 1000 Å of 300mm). The eluent was a buffer system consisting of MilliQ water and 30% acetonitrile with 50 mM NaH2PO4, 150 mM NaCl and 250 ppm NaN3 with a pH = 7.0 (via addition of 50 mL of 3 molar aqueous sodium hydroxide solution) filtered with an inline 0.1µm membrane filter and running at 0.8 mL per min. Multi-angle light scattering is

recorded via mini DAWNTREOS and differential refractive index spectra with Optilab rEX both supplied by Wyatt Technologies EU. Data analysis was committed with Astra 5 software and a dn/dc value of 0.156 for each polymer.

Lyophilization

The final glycomacromolecules were lyophilized with an Alpha 1-4 LD plus instrument from Martin Christ Freeze Dryers GmbH (-40 °C, 0.1 mbar).

Fluorescence Microscopy

Giant Unilamellar Vesicles were imaged on an inverted microscope (Olympus IX73, Japan) equipped with an Olympus 60x NA 1.35 oil-immersion objective (Olympus, Japan), and a CMOS camera (DMK 33UXI174L, The Imaging Source, Germany) was used for imaging.

Reflection Interference Contrast Microscopy (RICM)

RICM on an inverted microscope (Olympus IX73) was used to obtain the contact area between GUVs and Concanavalin A covered glass surfaces. For illumination a monochromatic (530 nm) collimated LED (Thorlabs, Germany, M530L2-C1) was used. An UPlanFL N 60x/0.90 dry objective (Olympus Corporation, Japan), additional polarizers and a quarter waveplate (Thorlabs, germany) to avoid internal reflections and a monochrome CMOS camera (DMK 33UX174, The Imaging Source Europe GmbH, Germany) were used to image the RICM patterns.

UV-Vis Spectroscopy

UV-Vis measurements were performed at 25 °C on a dual-trace spectrometer Specord® 210 Plus from Analytik Jena AG (Jena, Germany), using Win ASPECT PLUS software to operate the instrument.

Dynamic Light Scattering

The measurements were conducted with a Malvern Zetasizer Nano ZS (Malvern Panalytical, Kassel, Germany) equipped with a He-Ne-laser (wavelength of 633 nm) as a light source. The scattered light was detected with a scattering angle of 173°. The glycopolymer samples at a concentration of 1 mg/mL in LBB were prepared in a 1 cm polystyrene cuvette. The samples were measured at 25°C in triplicates. The hydrodynamic diameters were determined by the software provided by the manufacturer.

Fluorescence Correlation Spectroscopy

Sample preparation. GUVs and protein-passivated glass-measuring chambers were prepared as described in the experimental part. Imaging was performed using 8-well glass bottom slides (#80827, ibidi GmbH, Gräfelfing, Germany) coated with either a ConA substrate (40 µg/µl) , SigmaAldrich) or a NeutrAvidin substrate (40 µg/µl) (Thermo Scientific). The GUV solution was pipetted into the well >25 minutes before the measurements to ensure sufficient time for the GUVs to attach.

Setup. Measurements were performed on an Abberior Expert Line system (Abberior Instruments GmbH, Göttingen, Germany), as described previously.[1] Polarization control was achieved using λ/2 and λ/4 waveplates (Abberior Instruments) and a SK010PA-vis 450-800 nm polarization analyzer (Schäfter Kirchhoff GmbH, Hamburg, Germany). The instrument was operated using the customized Abberior microscope software Imspector (version 14.0.3060, Abberior Instruments GmbH).

Calibration. The calibration of the setup was performed before each measurement. Briefly, the optimal correction collar setting was found by minimizing the number of Rhodamine B (TCI Deutschland GmbH) molecules in the focus. For all our experiments the correction collar matched our coverslip thickness (170 µm). The instrument response function (IRF) was measured using Erythrosine in 5 M potassium iodide solution at 561nm excitation. Next, a Rhodamine B solution with 1-5 molecules in the focus was measured to obtain 1) a calibration for the confocal detection volume and 2) the ratio of the parallel and perpendicular detection efficiency by assuming a Rhodamine B diffusion constant of D = 370 µm²/s for recordings at lab room temperature of 19.6 °C.[2]

The 561nm laser power was measured at the sample using an immersion S170C power meter head (Thorlabs GmbH, Lübeck, Germany) attached to a PM400 power meter body (Thorlabs GmbH, Lübeck, Germany). As the power varied by ~10% when translating in x, y and z, we avoided a systematic error by varying the position until the maximum power was reached.

Recording procedure. the confocal microscope settings were used to bring GUVs in focus. Subsequently, the diffraction limited focus was placed in a stationary position at the middle of the GUV top and bottom. FCS curves were recorded for 2 minutes using between 3µW and 4 µW (depending on measurement day) 561 nm pulsed excitation beam, a 1.7 AU pinhole, a 60x water objective (UPLSAPO 1.2 NA objective, Olympus Europa SE & CO. KG, 1063 Hamburg, Germany) and polarization sensitized readout.

FCS curve fitting. FCS curves were created and fitted using the Triplet Extended (2D) fitting model of the SymPhoTime software (PicoQuant GmbH, Berlin, Germany).

General Methods

Solid Phase Polymer Synthesis

All structures were prepared on Tentagel® S RAM resin (batch size: 0.1 mmol). All washing steps were conducted with 4 mL solvent. Polypropylene reactors equipped with polyethylene frits and closed with Luer-stoppers were used. For the short glycomacromolecules, the backbone sequence was first assembled, followed by glycoconjugation via CuAAC (copper(I)-catalyzed alkyne-azide cycloaddition), Lys-side chain deprotection (Boc), fluorescent dye conjugation, terminal Fmoc-deprotection and capping with 4-pentynoic acid before conjugation of the cholesteryl tether via CuAAC.

General coupling protocol.

For all compounds, the resin was first swollen in 4 mL DCM for 30 min, subsequently washed ten times with DMF, Fmoc-deprotected by treating with 25% piperidine in DMF (three times for ten minutes) and again washed fifteen times with DMF. Employed building blocks were coupled to the *N*-terminus by adding the respective building block (5eq.), PyBOP (5 eq.) and DIPEA (20 eq.) in 4 mL DMF to the resin and shaking for 1h. Then, the resin was washed fifteen times with DMF and the *N*-terminus was again deprotected followed by the next coupling step.

Fmoc cleavage

The Fmoc-protecting group of the resin as well as from the coupled building blocks or amino acids was cleaved by means of 4 mL of a 25% solution of piperidine in DMF to release the primary amine. The deprotection was carried out twice for 10 min. Afterwards the resin was washed 10 times with DMF before coupling.

Boc cleavage

The resin was washed five times with THF before a solution of 4 M HCl in dioxane was drawn into the syringe reactor. The resin was rocked for 5 min before the solution was discarded. Fresh solution was drawn into the reactor and the resin was rocked for 30 min before the solution was again discarded. The resin was then washed ten times with DMF.

Dde cleavage

The Dde side chain protective group was cleaved via treatment with a freshly prepared solution of 2% hydrazine hydrate in DMF (v/v). After rocking for 5 min, the solution was discarded and the resin was washed three times with DMF. The cleavage procedure was repeated twice.

CuAAC protocol for glycosylation

To the oligomeric structure loaded on the resin 2.5 eq of acetyl protected 2-azidoethyl pyranoside (α-Mannose/ β-Galactose) per alkyne group dissolved in 4 mL DMF were added. Secondly 50 mol% sodium ascorbate per alkyne group and 50 mol% $CuSO_4$ per alkyne group were dissolved each in a small amount of water and also added to the resin. The syringe reactor was rocked for 18 h before the solution was discarded. The resin was washed three times with DMF and subsequently treated with a 23 mM solution of sodium diethyldithiocarbamate in DMF and water (50/50, v/v) and alternating with DMF and DCM until no further color change occured.

CuAAC protocol for conjugation of cholesteryl-anchor

To the oligomeric structure loaded on the resin 2.5 eq of 3-β-azidocholesterol in 4 mL THF were added. Then 50 mol% sodium ascorbate per alkyne group and 50 mol% CuSO4 per alkyne group were dissolved each in a small amount of water and also added to the resin. The syringe reactor was rocked for 18 h before the solution was discarded. The resin was washed three times with DMF and subsequently treated with a 23 mM solution of sodium diethyldithiocarbamate in DMF and water (50/50, v/v) and alternating with DMF and DCM until no further color change occured.

On-resin deacetylation

Glycooligomers MC and GC were deacetylated under Zemplén conditions. The resin was washed five times with methanol, before 5 mL of a 0.2 M solution of NaOMe in MeOH was drawn into the reactor. The resin was rocked for 30 min, before the solution was discarded. The resin was then washed twice with MeOH before another 5 mL of the methoxide solution were drawn into the reactor. After 30 min, the solution was again discarded and the resin was washed five times with MeOH.

Cleavage from the solid phase

The resin was washed five times with DCM before acidic cleavage from the resin with a cocktail consisting of TFA, TIPS and DCM (95/2.5/2.5, v/v/v) for 30 min.

The cleavage solution of MC and GC was precipitated in ether. The precipitate was collected via centrifugation, dried under a gentle stream of nitrogen and dialyzed via diafiltration against ultrapure water in five cycles (20 mL each, 5% triethylamine in water was used in the first cycle, 1 M HCl was used in the second cycle). The dialyzed compounds were dissolved in fresh ultrapure water and lyophilized.

Macroinitiators pMC and pGC were precipitated in a mixture of 25% ether in hexanes and collected via centrigugation at -5°C. The supernatant was decanted and the precipitate was dried under high vacuum. Stock solutions of the dried macroinitiators in DMSO were then prepared (c = 0.033 M).

Synthesis of Glycopolymers via TIRP

One equivalent of glyco monomer (100 mol%) and tris(2-phenylpyridine)iridium-(III) (Ir(ppy)3, 0.05 mol%) are dissolved in DMF [10 wt %], sealed in a 5mL glass flask and flushed with argon as inert gas for 10 min. In a second step, the macroinitiator (2.5 mol%) and equimolar amounts of diphenyl-(2,4,6-trimethylbenzoyl)-phosphineoxide (TPO, 2.5 mol%) are also dissolved in DMF [10 wt %] and sealed in a 5 mL microwave reaction vial. A spatula tip of TCEP is dissolved in a single drop of H_2O and added to the reaction solution to reduce possible disulfides. The thiol/TPO solution is flushed under an Ar-atmosphere for 10 min and irradiated with UV-light (405nm wavelength, 2% intensity) for 3 min. Subsequently, the monomer/$Ir(ppy)_3$ mixture is added to the TPO/ thiol solution under an inert atmosphere, and the polymerization solution is irradiated further at an unchanged light intensity. After an hour, the irradiation is stopped and the polymer solution precipitated in diethyl ether. The precipitated glycopolymer was dryed under a gentle stream of nitrogen, dissolved in ultrapure water, dialyzed via diafiltration against ultrapure water in five cycles (20 mL each, 1 M HCl was used in the first cycle). The dialyzed compounds were dissolved in fresh ultrapure water and lyophilized.

Chemical Structures of the Target Glycomacromolecules

Glycooligomer MC

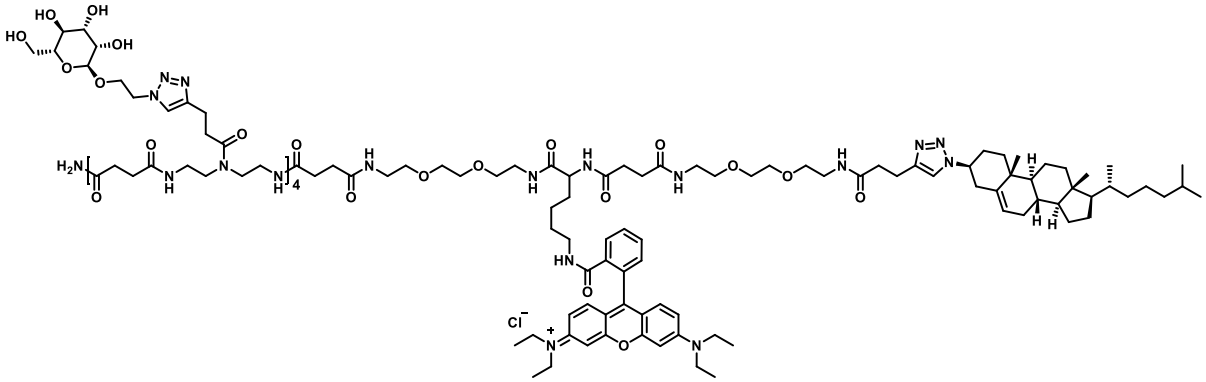

Figure S1. Chemical structure of glycooligomer MC.

Glycooligomer GC

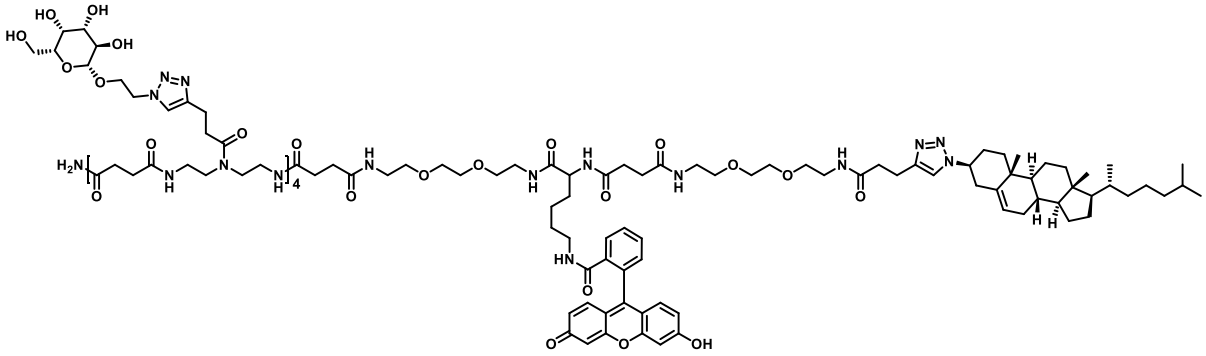

Figure S2. Chemical structure of glycooligomer GC.

Glycopolymer pMC

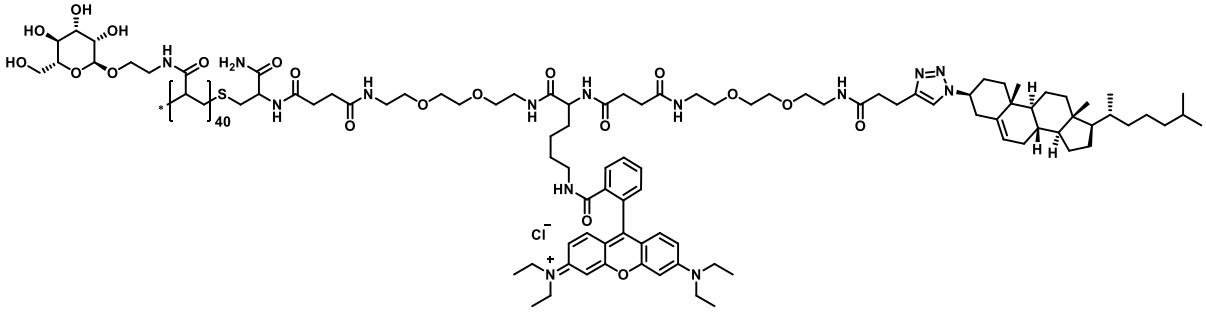

Figure S3. Chemical structure of glycopolymer pMC.

Glycopolymer pGC

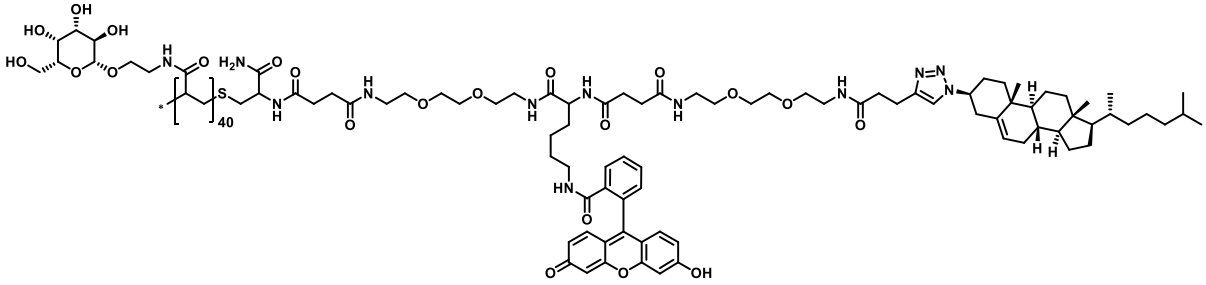

Figure S4. Chemical structure of glycopolymer pGC.

Analytical Data

Glycooligomer Backbone

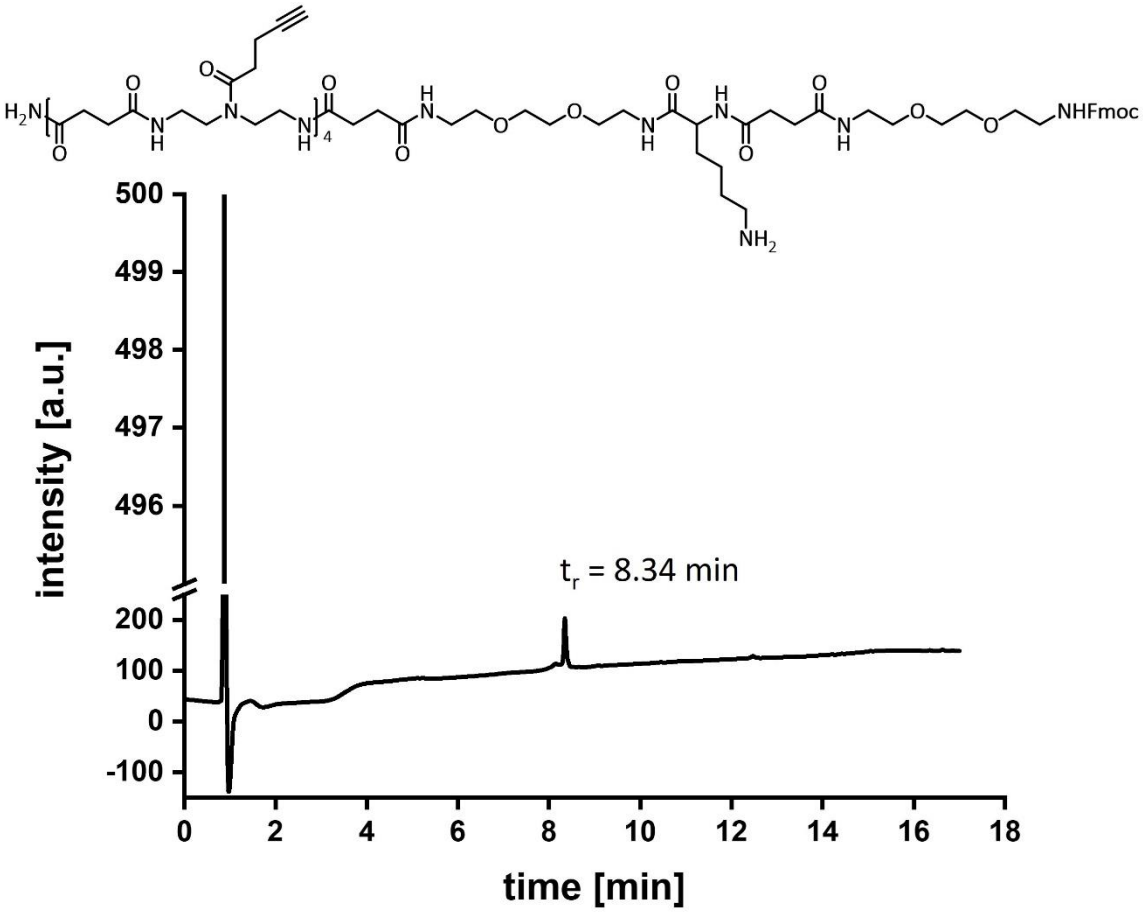

Figure S5. Oligomer backbone detected with relative purities >97% by RP-HPLC analysis (linear gradient from 5 – 95 vol% eluent H_2O/acetonitrile) in 17 min at 25 °C.

Glycooligomer MC

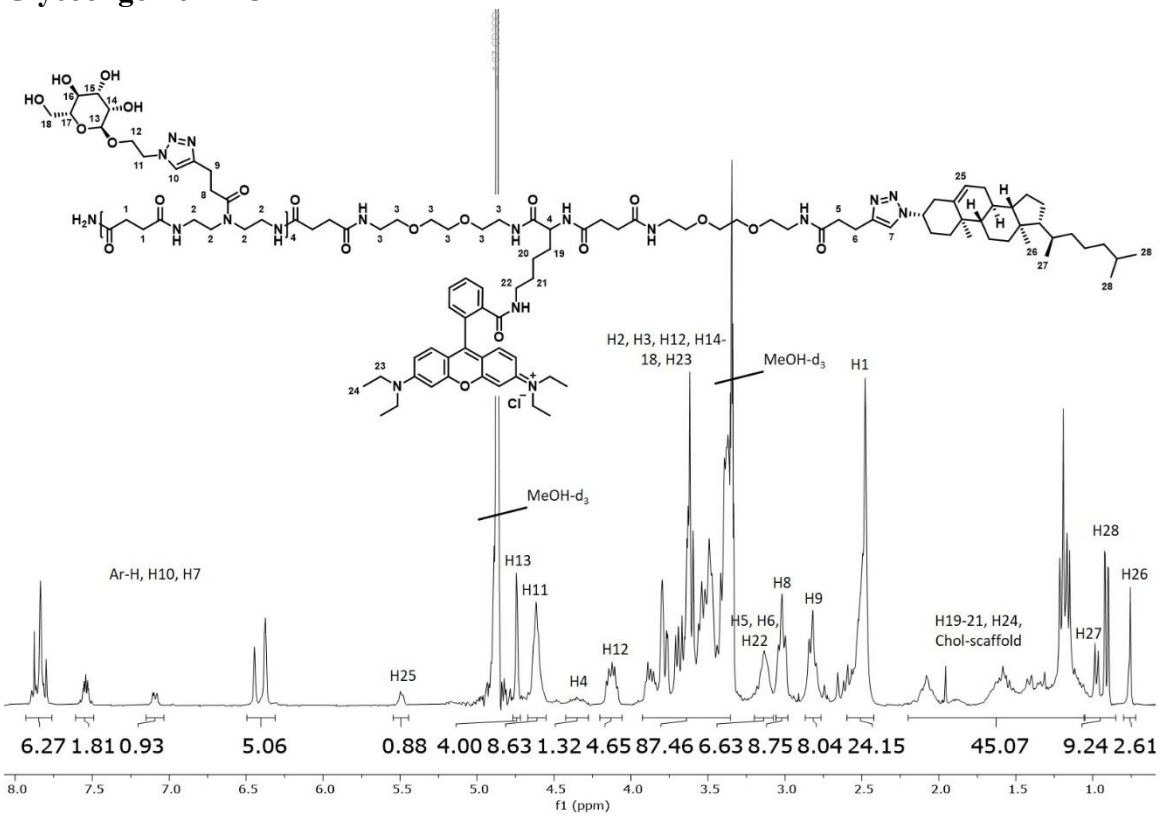

Figure S6. ^{1}H-NMR (300 MHz, MeOH-d_4) of MC.

^{1}H-NMR (300 MHz, MeOH-d_4): δ [ppm] = 7.93-7.76 (m, 6H, H7, H10, Ar-H), 7.60-7.49 (m, 2H, Ar-H), 7.15-7.03 (m, 1H, Ar-H), 6.49-6.31 (m, 5H, Ar-H), 5.54-5.44 (m, 1H, H25), 4.74 (d, 4H, H13, J = 1.6 Hz), 4.67-4.55 (m, 8H, H11), 4.42-4.27 (m, 1H, H4), 4.20-4.05 (m, 4H, H12), 3.92-3.35 (m, 88H, H2, H3, H12, H14-18, H23), 3.19-3.07 (m, 6H, H5, H6, H22), 3.01 (t, 8H, H8), 2.81 (t, 8H, H9), 2.59-2.42 (m, 24H, H1), 2.19-1.05 (m, 48H, H19-21, H24, Chol-scaffold), 0.97 (d, 3H, H27, J = 6.51 Hz), 0.91 (dd, 6H, H28, J = 6.61 Hz, J = 1.13 Hz), 0.75 (s, 3H, H26)

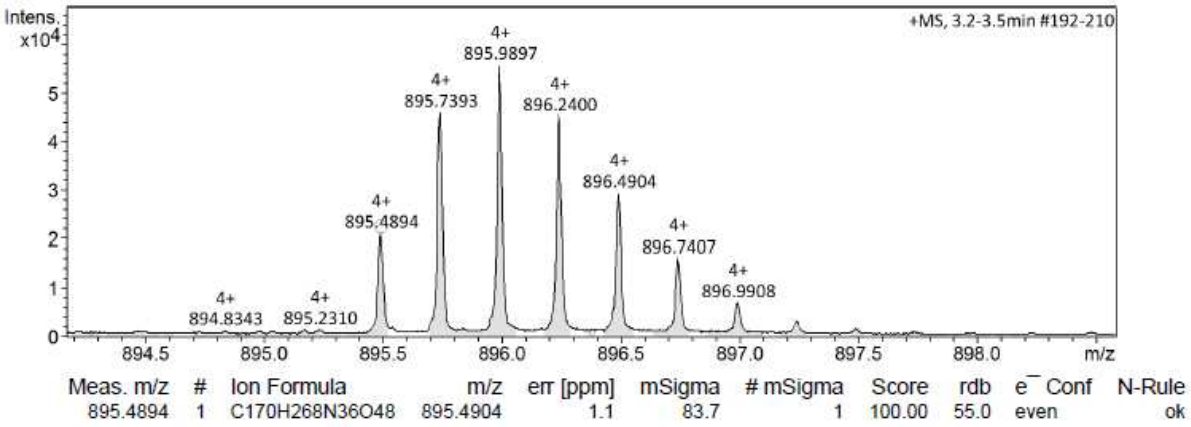

Figure S7. HR-ESI-MS of MC.

HR-ESI-MS: for $C_{170}H_{265}N_{36}O_{48}$+ m/z $[M+4H]^{4+}$ calcd.: 895.7430, found: 895.9897 mass error 275.413818 ppm.

Glycooligomer GC

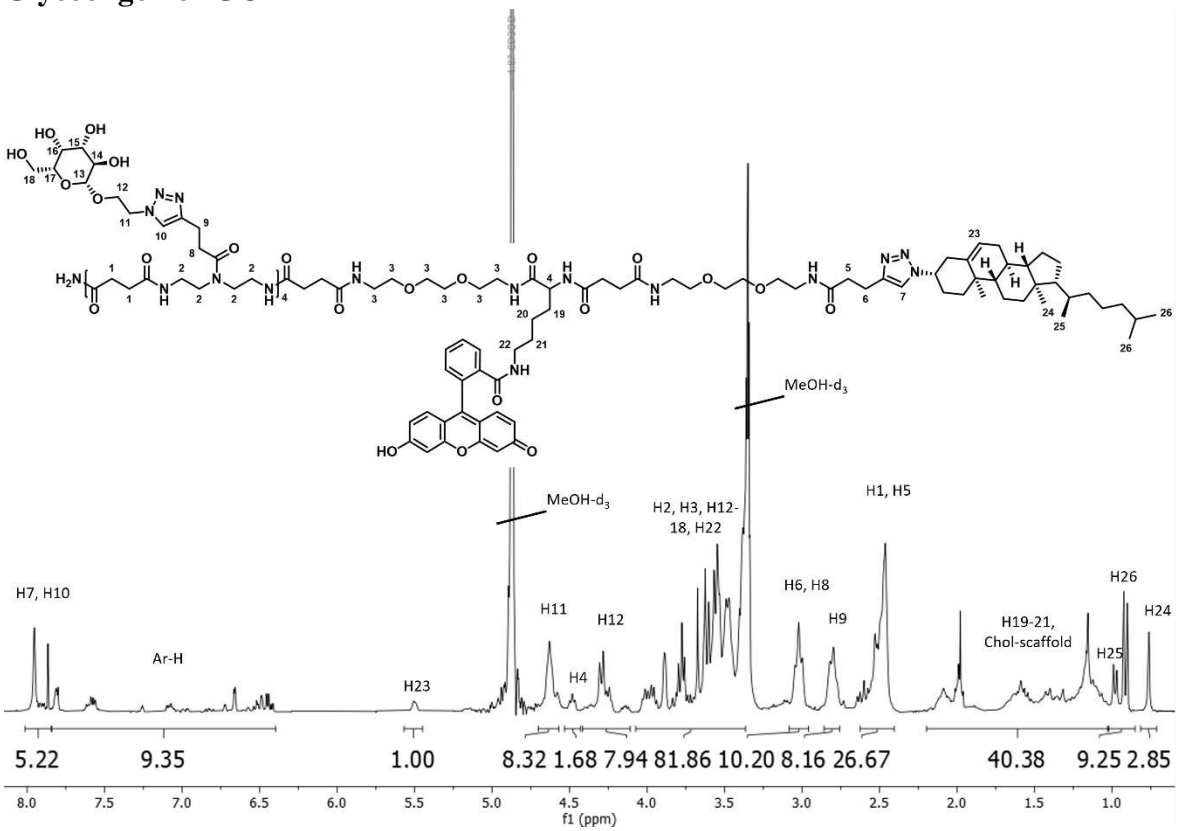

Figure S8. [1]H-NMR (300 MHz, MeOH-d_4) of GC.

[1]H-NMR (300 MHz, MeOH-d_4): δ [ppm] = 8.01-7.84 (m, 5H, H7, H10), 7.84-6.39 (10H, Ar-H), 5.56-5.44 (m, 1H, H23), 4.70-4.56 (m, 8H, H11), 4.48 (t, 1H, H4), 4.41-4.10 (m, 8H, H12), 4.07-3.36 (m, 80H, H2, H3, H12-18, H22), 3.08-2.95 (m, 10H, H6, H8), 2.85-2.75 (m, 8H, H9), 2.62-2.40 (m, 26H, H1, H5), 2.19-1.02 (m, 40H, H19-21, Chol-scaffold), 0.98 (d, 3H, H25, J = 6.70 Hz), 0.91 (dd, 6H, H26, J = 6.61 Hz, J = 1.23 Hz), 0.76 (s, 3H, H24)

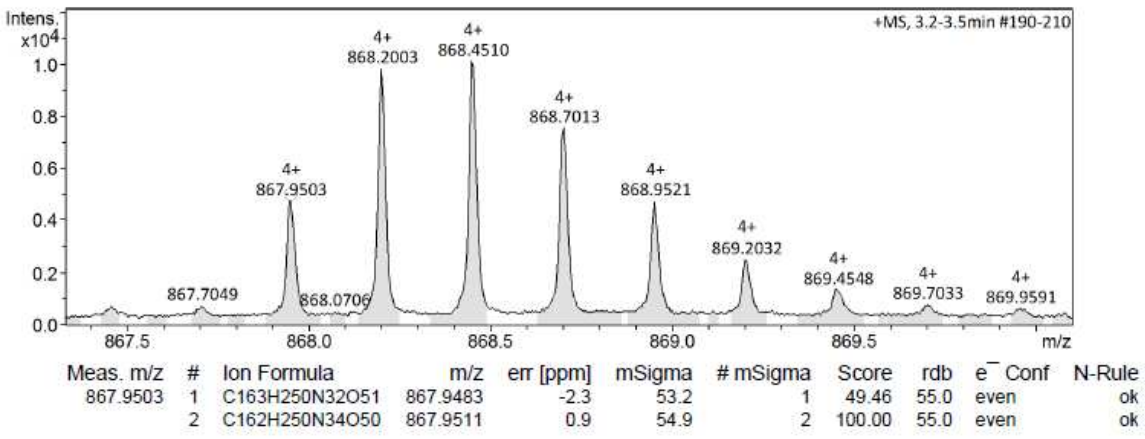

Meas. m/z	#	Ion Formula	m/z	err [ppm]	mSigma	# mSigma	Score	rdb	e⁻ Conf	N-Rule
867.9503	1	C163H250N32O51	867.9483	-2.3	53.2	1	49.46	55.0	even	ok
	2	C162H250N34O50	867.9511	0.9	54.9	2	100.00	55.0	even	ok

Figure S9. HR-ESI-MS of GC.

HR-ESI-MS: for $C_{162}H_{246}N_{34}O_{50}$ m/z $[M+4H]^{4+}$ calcd.: 867.9530, found: 868.2003 mass error 284.923262 ppm.

Macroinitiator Backbone

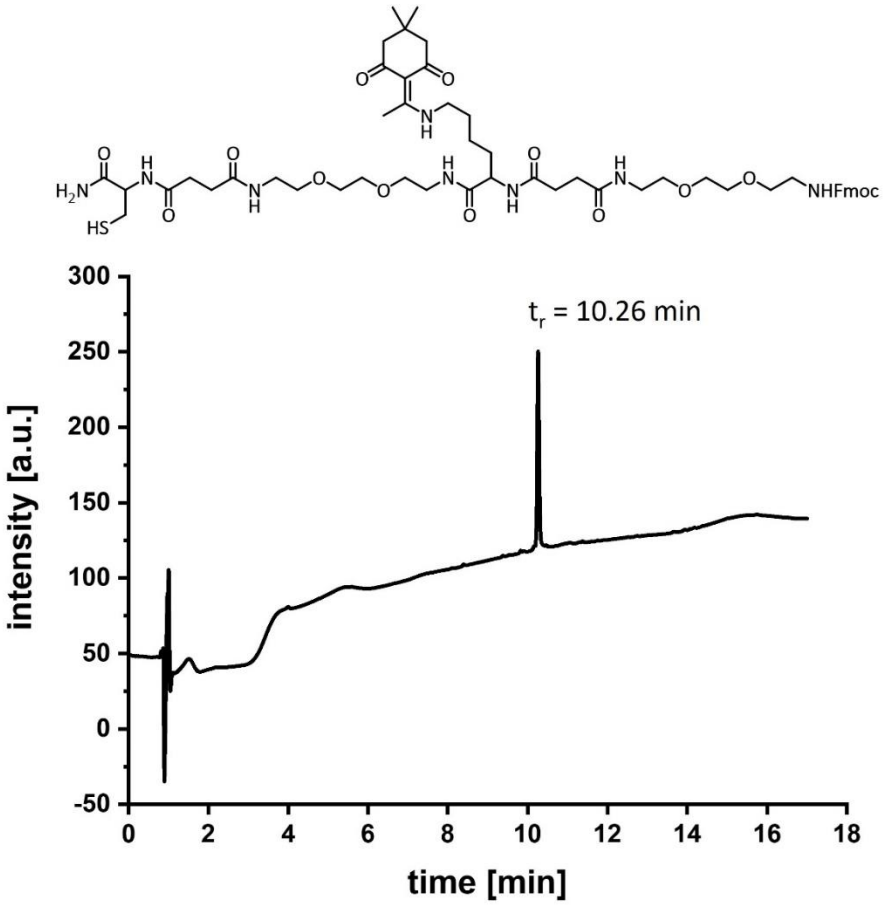

Figure S10. Macroinitiator backbone detected with relative purities >97% by RP-HPLC analysis (linear gradient from 5 – 95 vol% eluent H20/acetonitrile) in 17 min at 25 °C.

Macroinitiator pMC

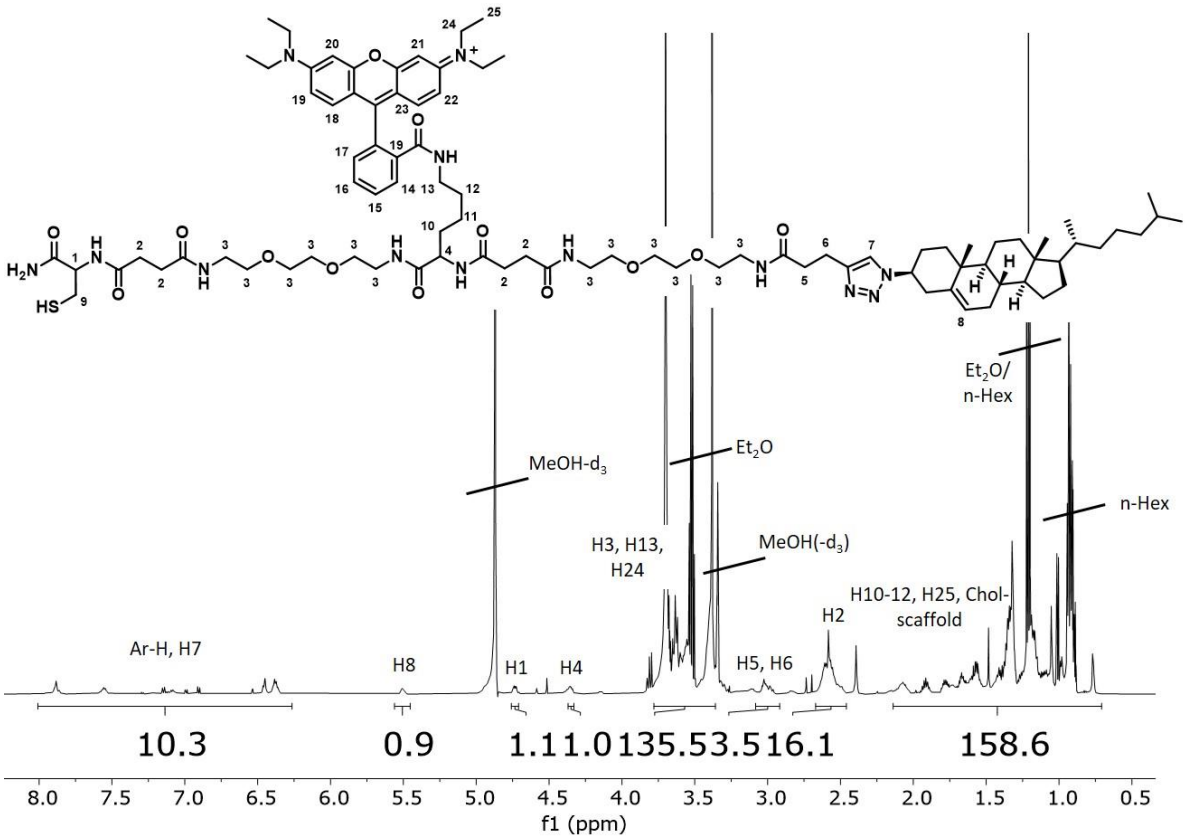

Figure S11. [1]H-NMR (600 MHz, MeOH-d_4) of macroinitiator pMC.

[1]H-NMR (600 MHz, MeOH-d_4): δ [ppm] = 8.00-6.26 (m, 11H, Ar-H, H7), 5.56-5.45 (m, 1H, H8), 4.75-4.71 (m, 1H, H1), 4.36-4.33 (m, 1H, H4), 3.78-3.35 (m, 34H, H3, H13, H24), 3.08-2.91 (m, 4H, H5, H6), 2.67-2.45 (m, 8H, H2), 2.13-0.70 (m, 62H, H10-12, H25, Chol-scaffold)

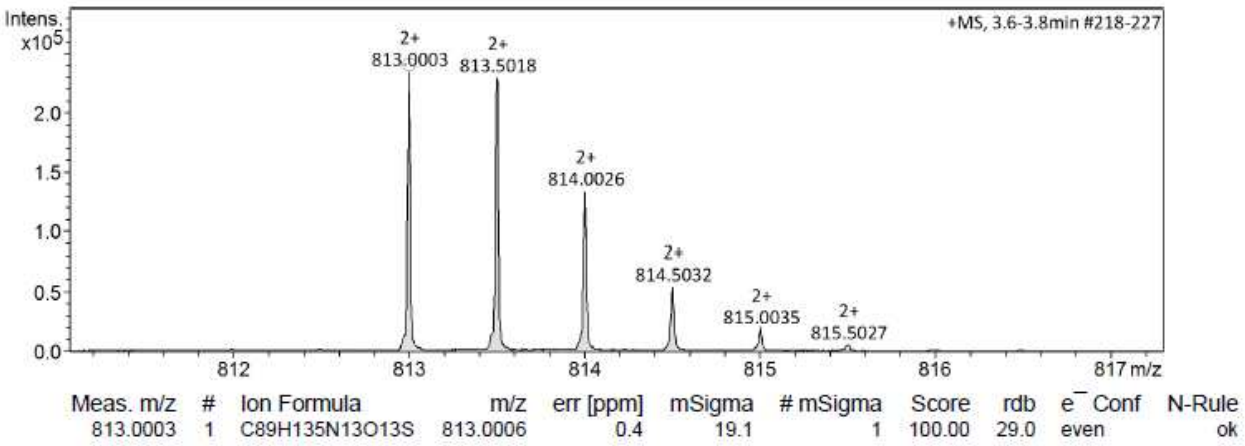

Figure S12. HR-ESI-MS of macroinitiator pMC.

HR-ESI-MS: for $C_{89}H_{134}N_{13}O_{13}S^+$ m/z $[M+2H]^{2+}$ calcd.: 813.5030, found: 813.5018 mass error - 1.475102 ppm.

Macroinitiator pGC

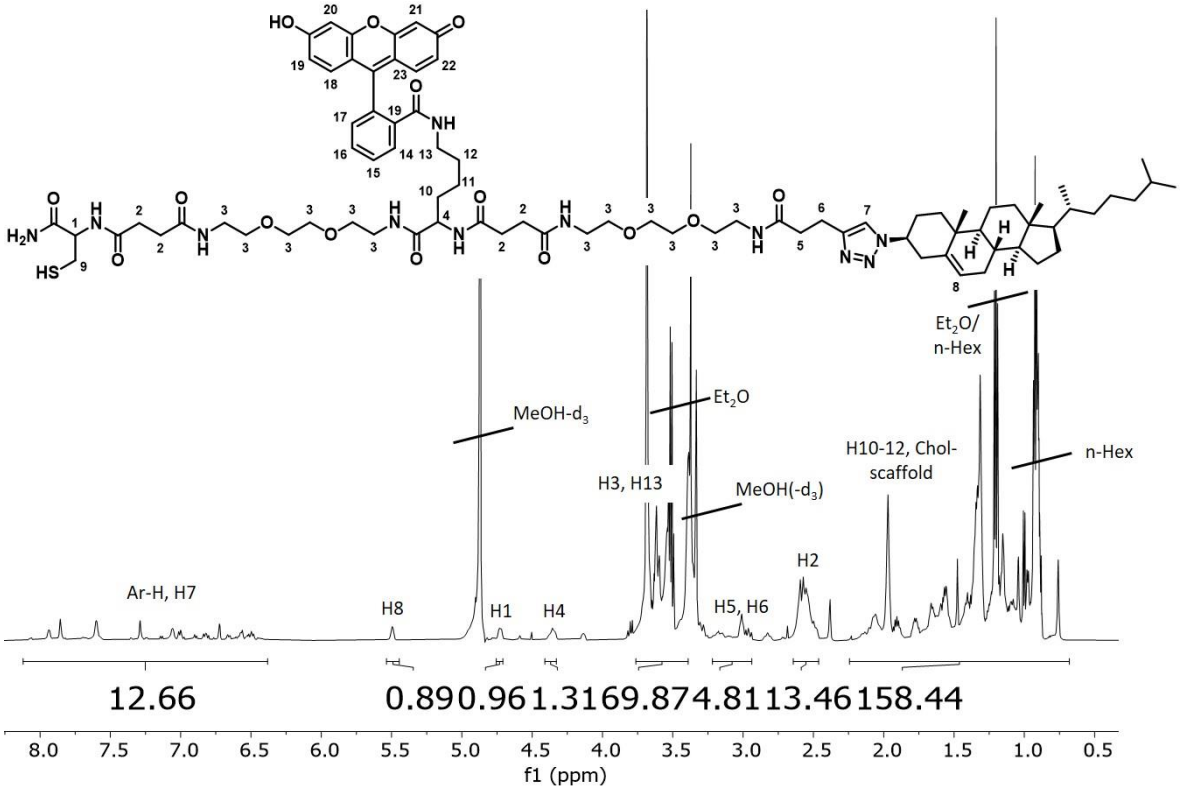

Figure S13. ^{1}H-NMR (600 MHz, MeOH-d_4) of macroinitiator pGC.

^{1}H-NMR (600 MHz, MeOH-d_4): δ [ppm] = 8.12-6.38 (3, 11H, Ar-H, H7), 5.49 (s, 1H, H8), 4.75-4.70 (m, 1H, H1), 4.41-4.32 (m, 1H, H4), 3.76-3.39 (m, 26H, H3, H13), 3.21-2.93 (m, 4H, H5, H6), 2.64-2.46 (m, 8H, H2), 2.24-0.68 (m, 50H, H10-H12, Chol-scaffold)

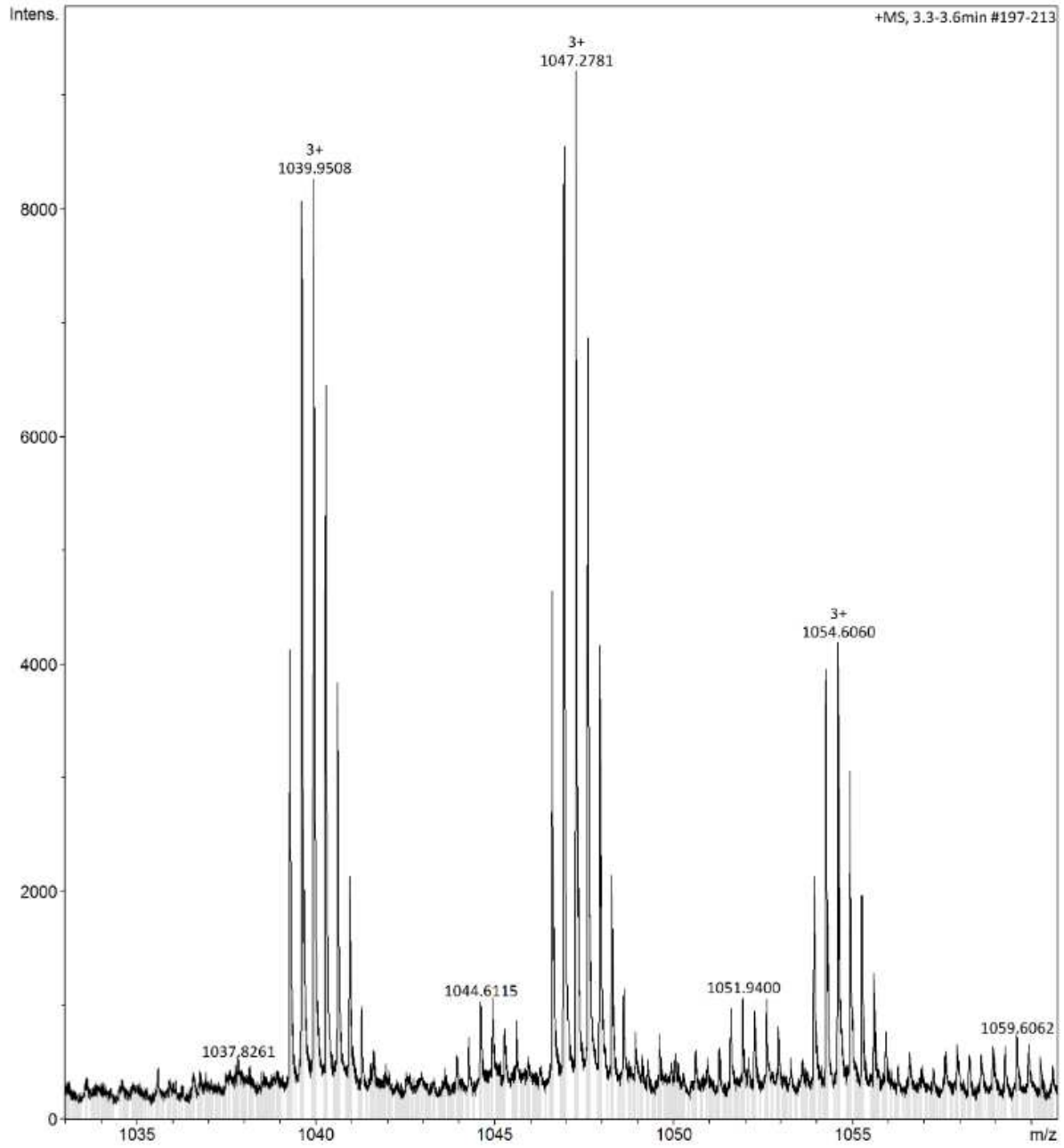

Figure S14. ESI-MS of macroinitiator pGC.

ESI-MS: for $C_{164}H_{236}N_{22}O_{32}S_2$ m/z $[2M+2H+Na+2MeOH]^{3+}$ calcd.: 1038.2350, found: 1039.9508 mass error 1652.612366 ppm.

for $C_{164}H_{236}N_{22}O_{32}S_2$ m/z $[2M+H+2Na+2MeOH]^{3+}$ calcd.: 1045.5630, found: 1047.2781 mass error 1640.360265 ppm.

for $C_{164}H_{236}N_{22}O_{32}S_2$ m/z $[2M+3Na+2MeOH]^{3+}$ calcd.: 1052.8900, found: 1054.6060 mass error 1629.799884 ppm.

Glycopolymer pMC

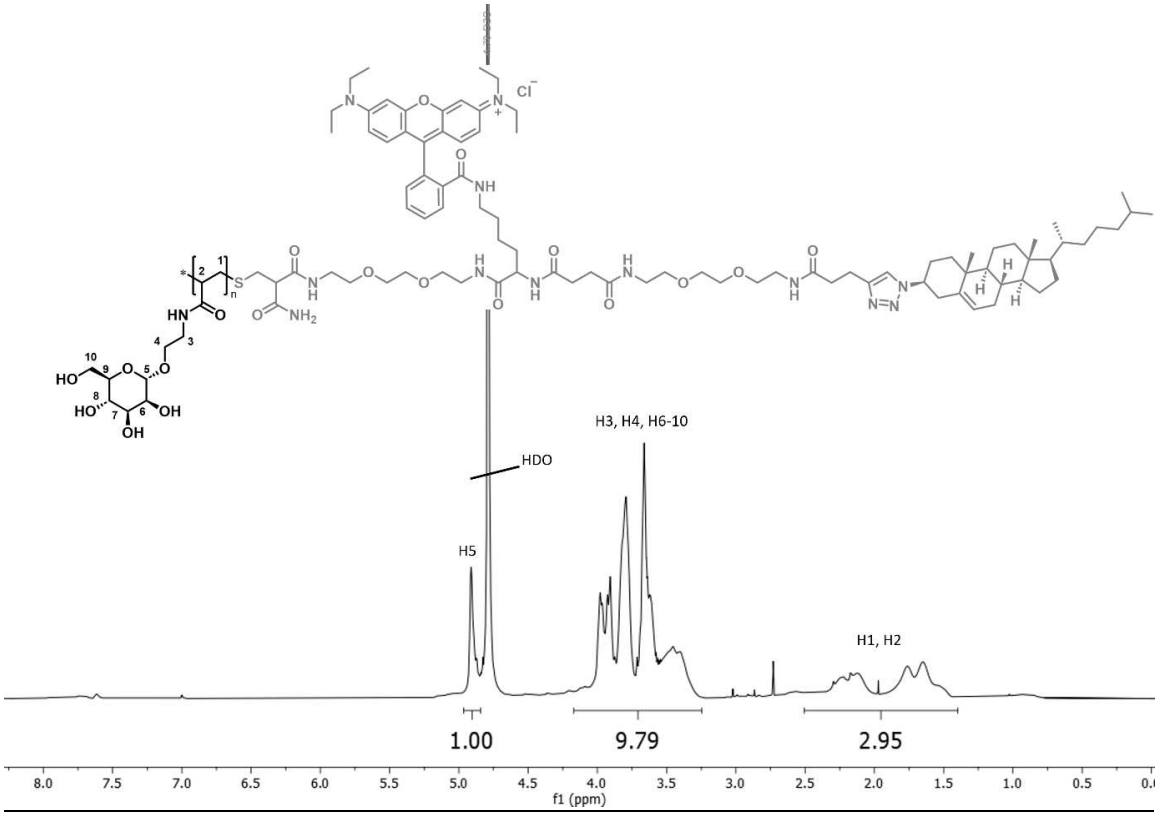

Figure S15. ^{1}H-NMR (600 MHz, D_2O) of pMC.

^{1}H-NMR (600 MHz, D_2O): δ [ppm] = 4.90 (s, H5), 4.17-3.24 (m, H3, H4, H6-10), 2.50-1.39 (m, H1, H2)

$Đ$ (via H_2O-SEC, MALS coupled RI-detector): 1.08

$\bar{M}_n$ [kDa] (via H_2O-SEC, MALS coupled RI-detector): 12.8

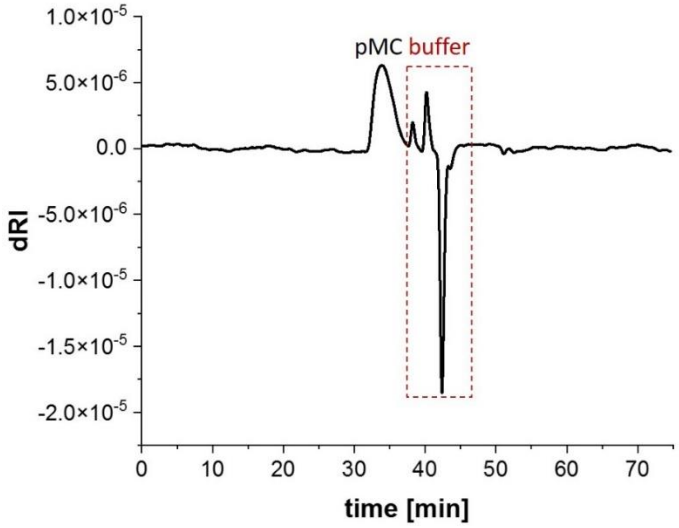

Figure S16. H_2O-SEC-MALS of pMC.

Glycopolymer pGC

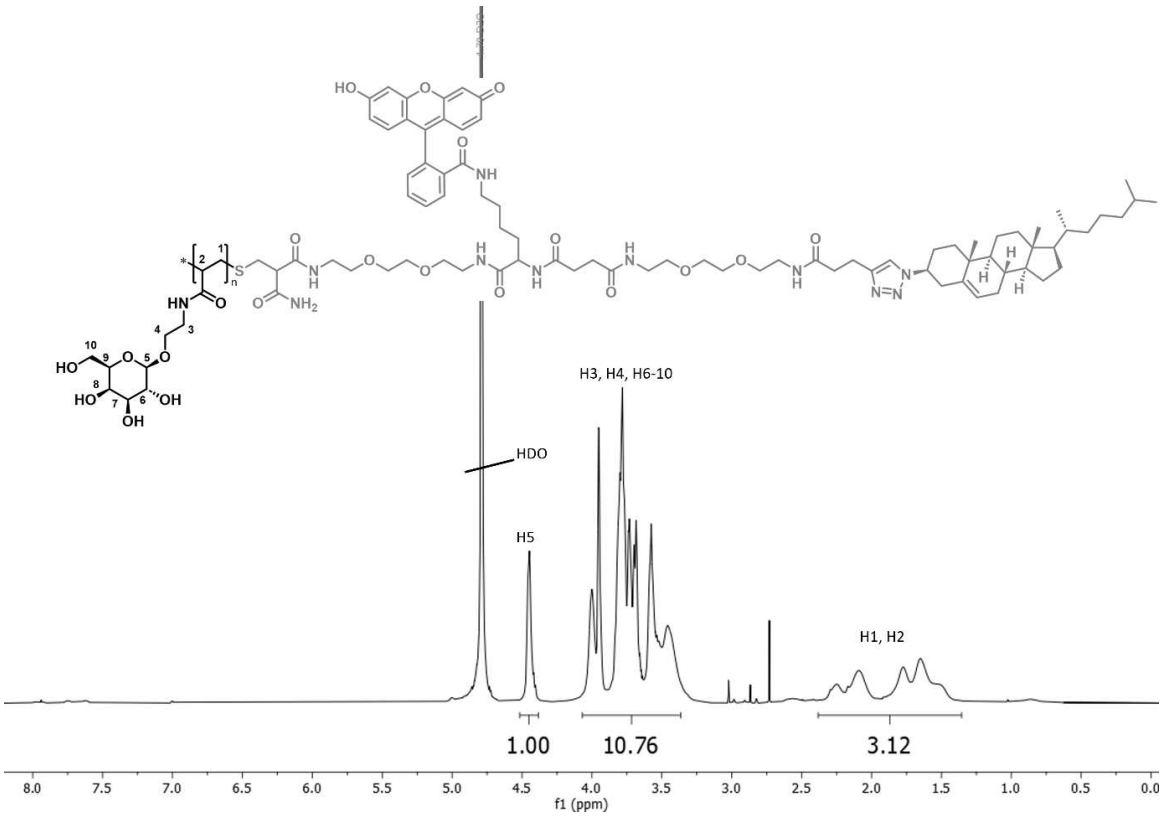

Figure S17. ^{1}H-NMR (600 MHz, D_2O) of pGC.

^{1}H-NMR (600 MHz, D_2O): δ [ppm] = 4.44 (s, H5), 4.06-3.36 (m, H3, H4, H6-10), 2.38-1.35 (m, H1, H2)

Đ (via H_2O-SEC, MALS coupled RI-detector): 1.38

$\overline{M}_n$ [kDa] (via H_2O-SEC, MALS coupled RI-detector): 13.4

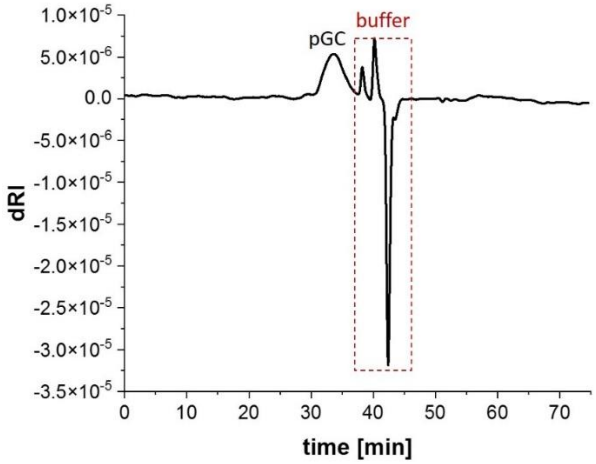

Figure S18. H_2O-SEC-MALS of pGC.

Experimental

Degree of Active Labelling

To determine the DoAL for **MC** and **pMC** a calibration curve of Rhodamine B in lectin binding buffer was determined. Absorption of Rhodamine B was determined at different concentrations and the respective maxima of the absorption curves (555 nm) were plotted against the concentration. The data points represent the respective mean value of three individual measurements.

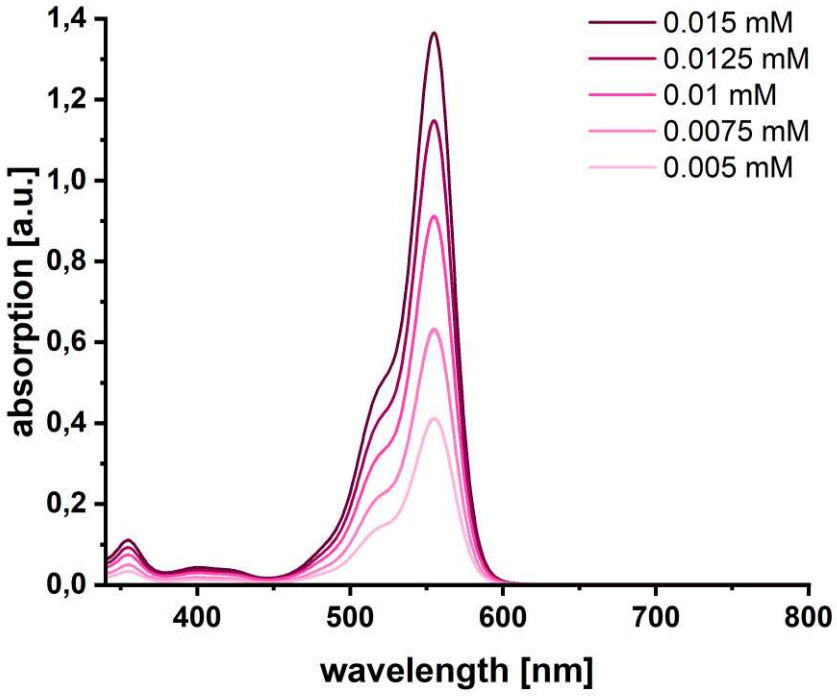

Figure S19. Absorption spectra of Rhodamine B in LBB at various concentrations.

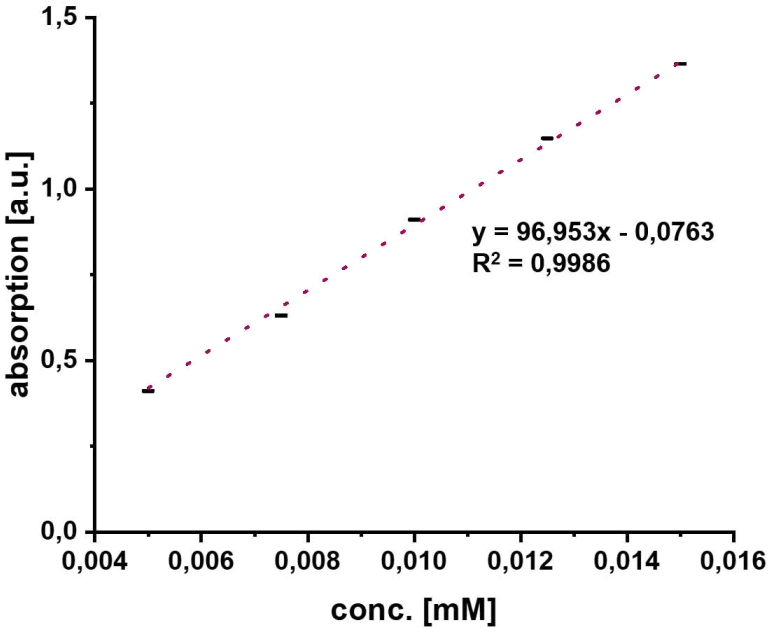

Figure S20. Regression line for the maximum absorption of Rhodamine B against the respective concentration in LBB.

The absorption of **MC** and **pMC**, respectively, was determined at a concentration of 0.1 mM. The presented graphs represent the mean value of three individual measurements.

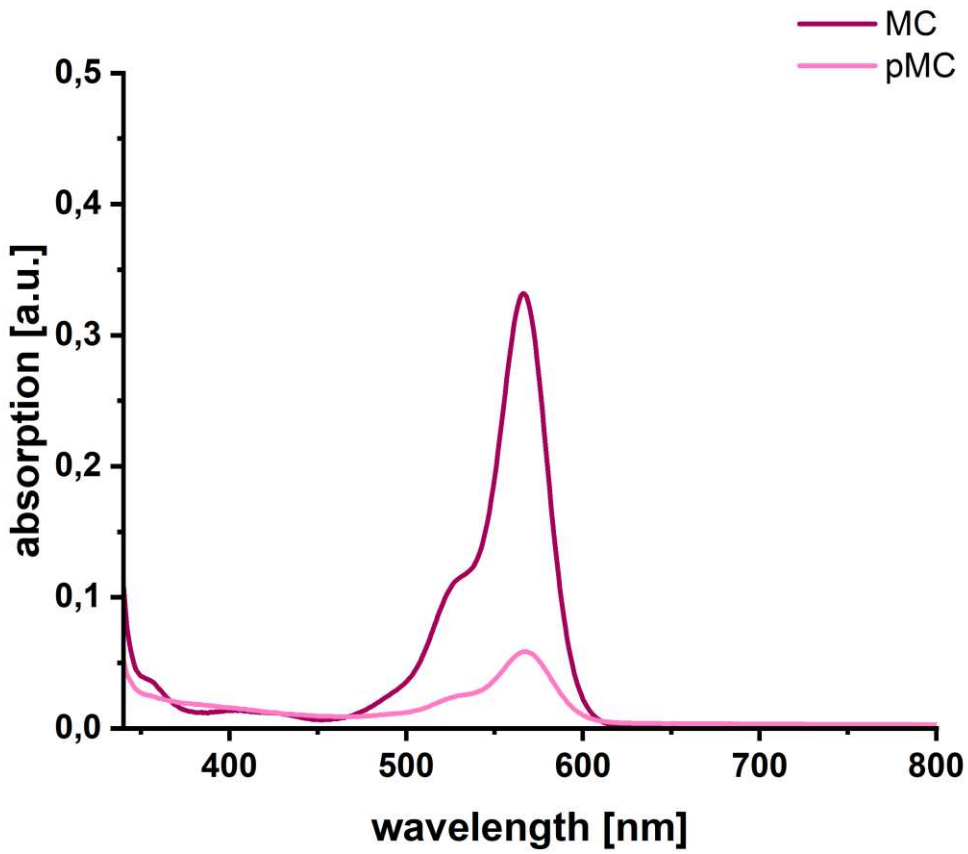

Figure S21. Absorption spectra for MC and pMC measured from 340 – 800 nm at a respective concentration of 0.1 mM in LBB.

The determined absorption maxima at 566 nm for MC (0,331829±0,000457754) and pMC (0,05861233±0,00010705) were substituted into the regression equation of the regression line determined for Rhodamine B to calculate a respective concentration.

MC: $0{,}331829 = 96{,}953\,x - 0{,}0763 \equiv x = 0{,}0042095551 \pm 0{,}000457754\,mM$

pMC: $0{,}05861233 = 96{,}953\,x - 0{,}0763 \equiv x = 0{,}001391523 \pm 0{,}00010705\,mM$

The calculated concentrations were related to the weighed concentrations (0.1 mM) to calculate the Degree of Active Labelling (DoAL):

DoAL(**MC**): $0{,}0042095551 \pm 0{,}000457754\,mM / 0.1\,mM \equiv 4.26\,\%$

DoAL(**pMC**): $0{,}001391523 \pm 0{,}00010705\,mM / 0.1\,mM \equiv 1.39\,\%$

Partitioning Studies

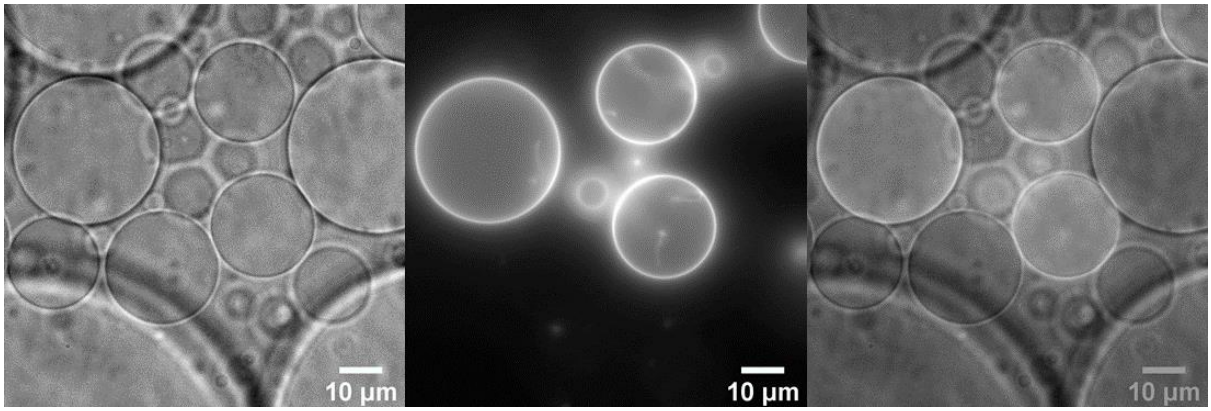

Figure S22. Partitioning experiment. (left) Transmission microscopy of MC- and PMC-functionalized GUVs and control GUVs. (middle) Rhodamine B fluorescence of glyco-decorated GUVs. (right) merge.

To evaluate the stability of glycomacromolecule tethering to the GUVs, vesicles containing either 2 mol% MC or pMC and non-functionalized vesicles were mixed and incubated for 18h at 4° C. Analysis of the vesicle mixture via fluorescence microscopy revealed no partitioning of Rhodamine B-functionalized glycomacromolecules into non-functionalized GUVs (i.e. non-fluorescent control vesicles remained non-fluorescent after incubation).

Exemplary Images of Vesicle Adhesion to ConA Surfaces (Homomultivalent)

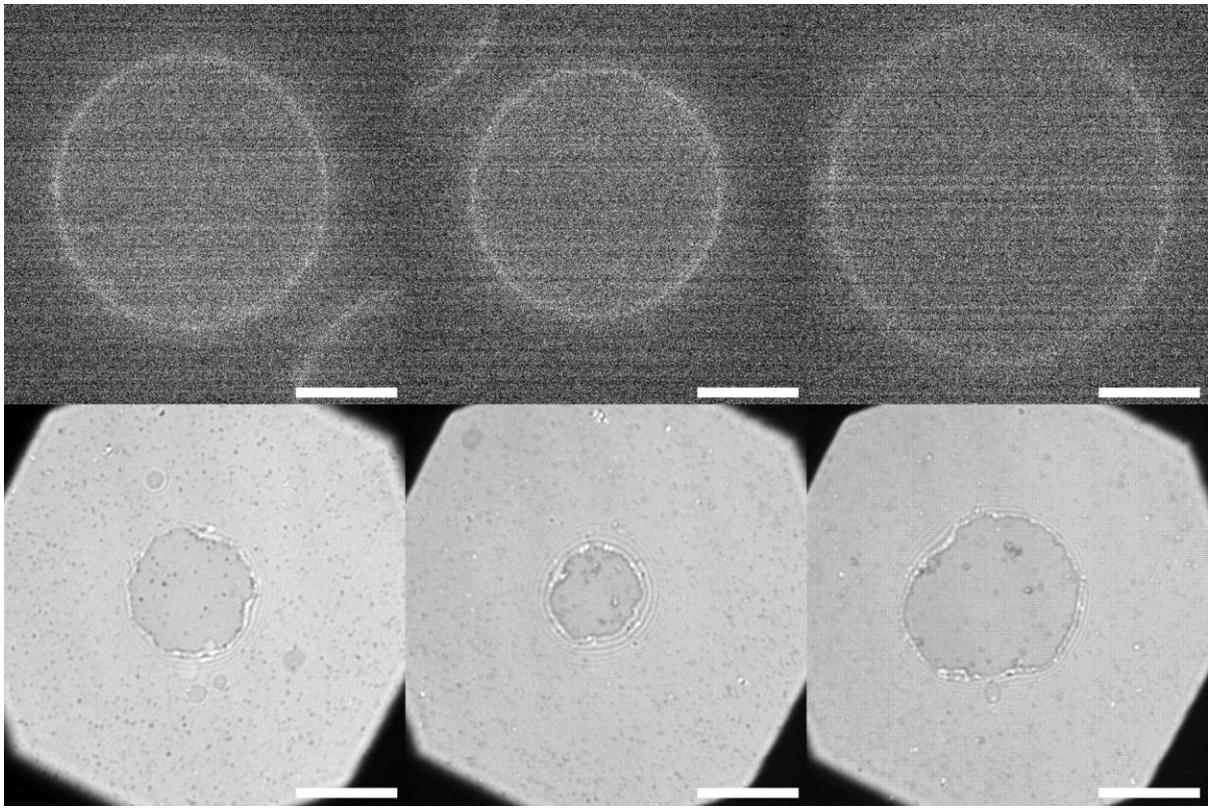

Figure S23. Fluorescence microscopy (top) and RICM images (bottom) of GUVs containing 0.5 mol% MC. Scale bar: 10 µm.

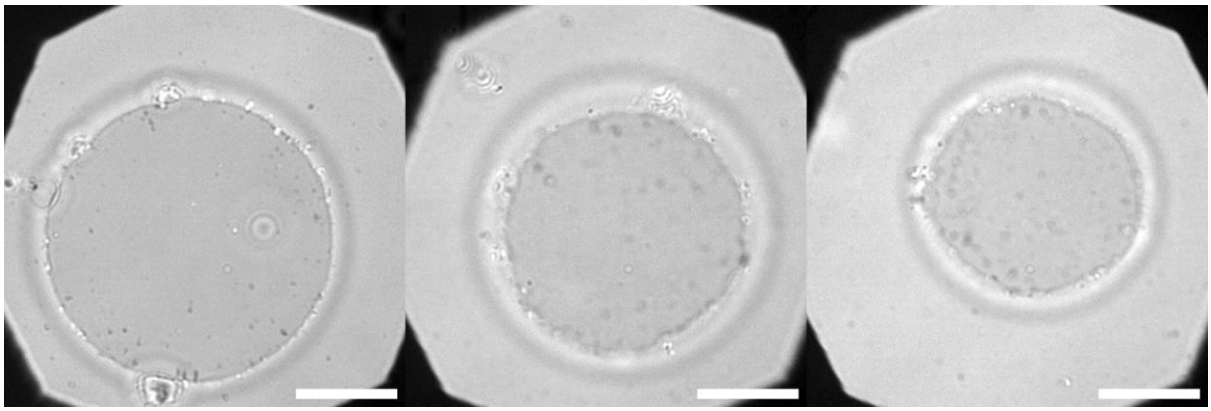

Figure S24. RICM images of GUVs containing 2 mol% MC. The outer vesicle projection is in line with the maximum vesicle circumference. Scale bar: 10 µm.

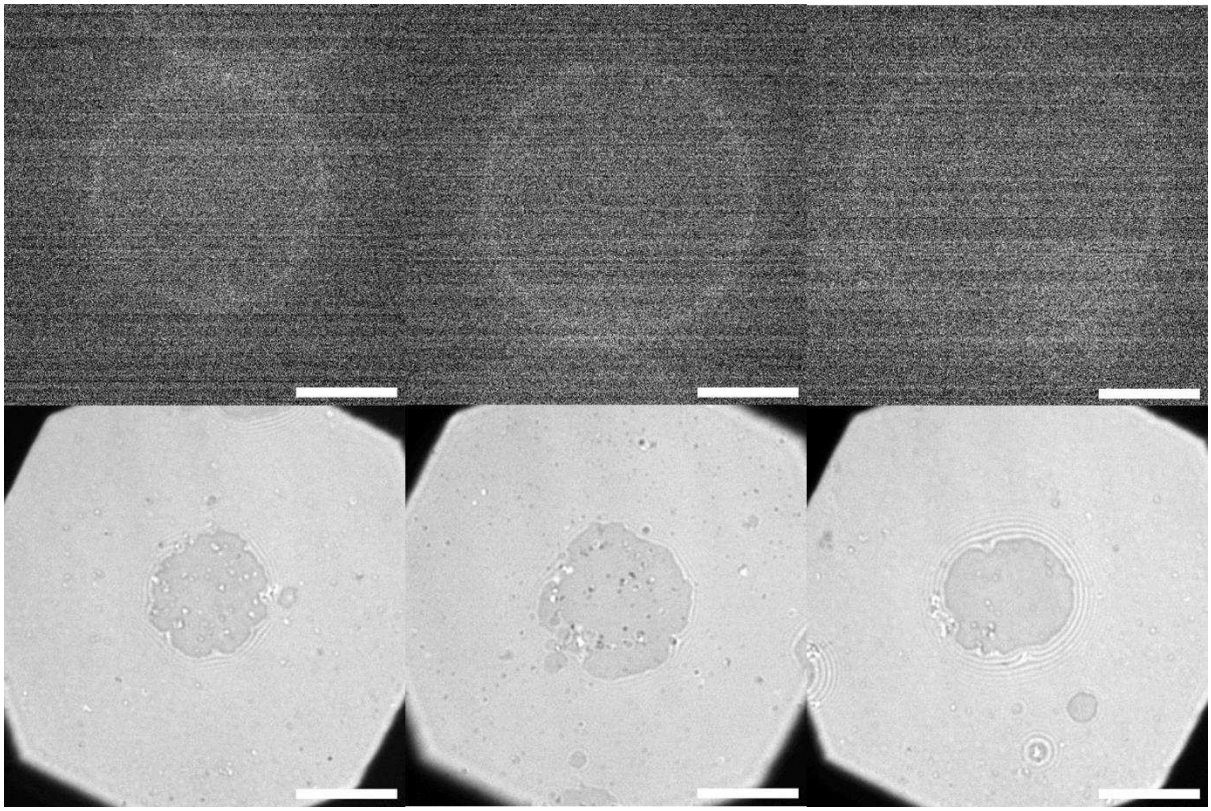

Figure S25. Fluorescence microscopy (top) and RICM images (bottom) of GUVs containing 0.05 mol% pMC. Scale bar: 10 µm.

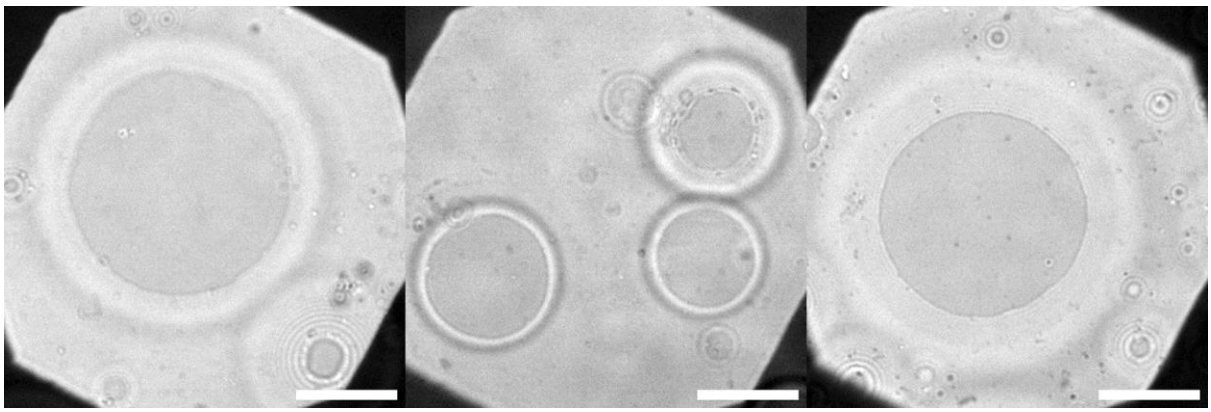

Figure S26. RICM images of GUVs containing 0.2 mol% pMC. The outer vesicle projection is in line with the maximum vesicle circumference. Scale bar: 10 µm.

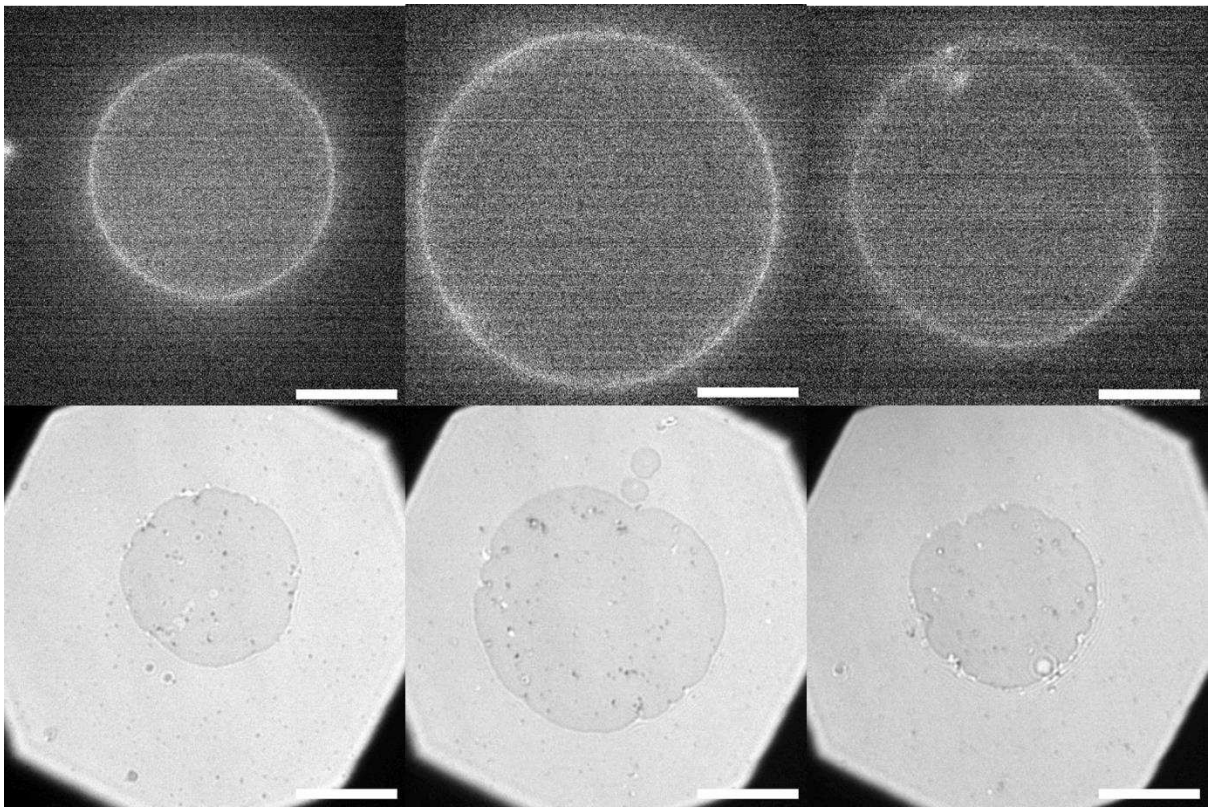

Figure S27. Fluorescence microscopy (top) and RICM images (bottom) of GUVs containing 0.5 mol% pMC. Scale bar: 10 µm.

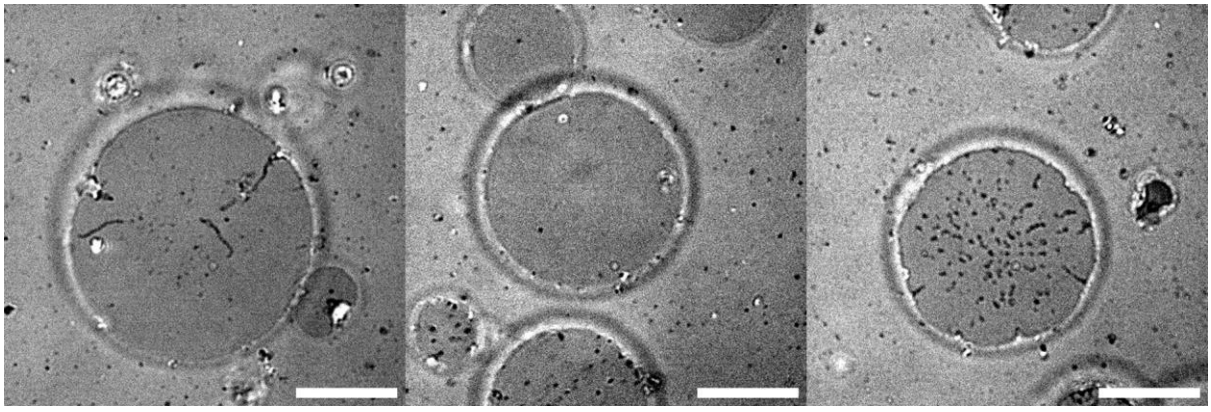

Figure S28. RICM images of GUVs containing 2 mol% pMC. The outer vesicle projection is in line with the maximum vesicle circumference. Scale bar: 10 µm.

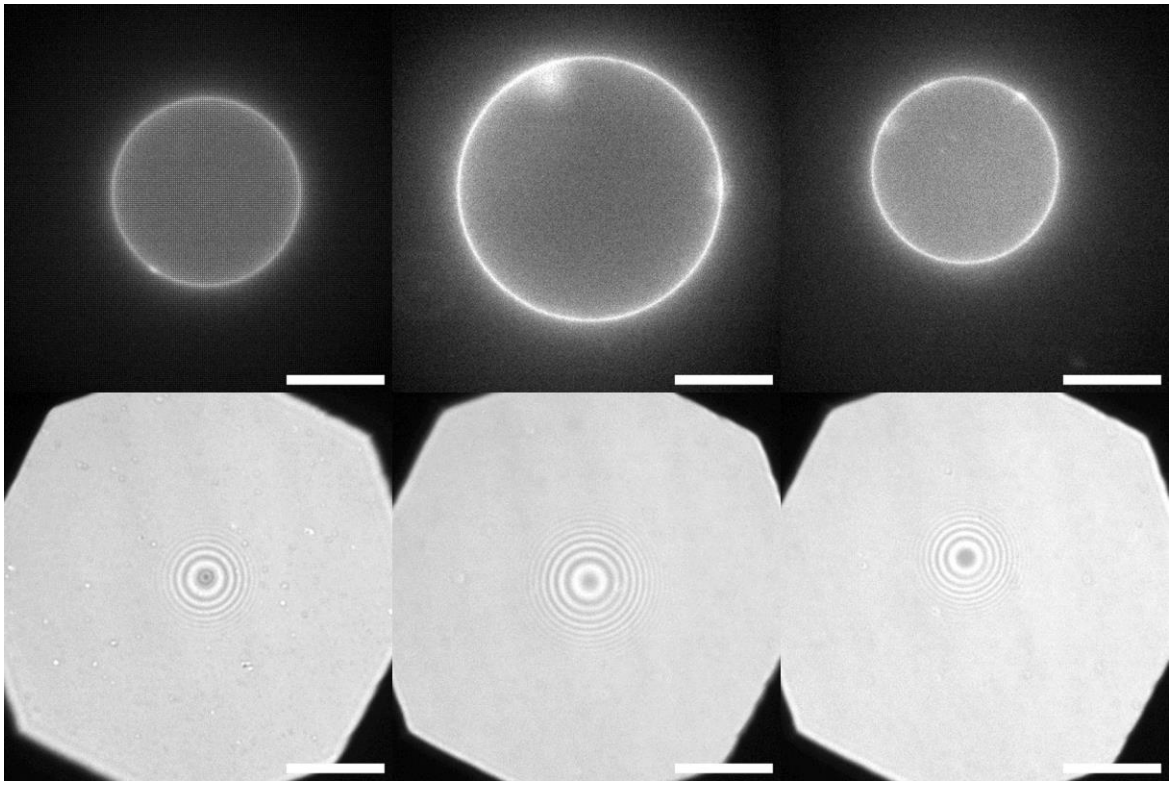

Figure S29. Fluorescence microscopy (top) and RICM images (bottom) of GUVs containing 2 mol% GC. Scale bar: 10 µm.

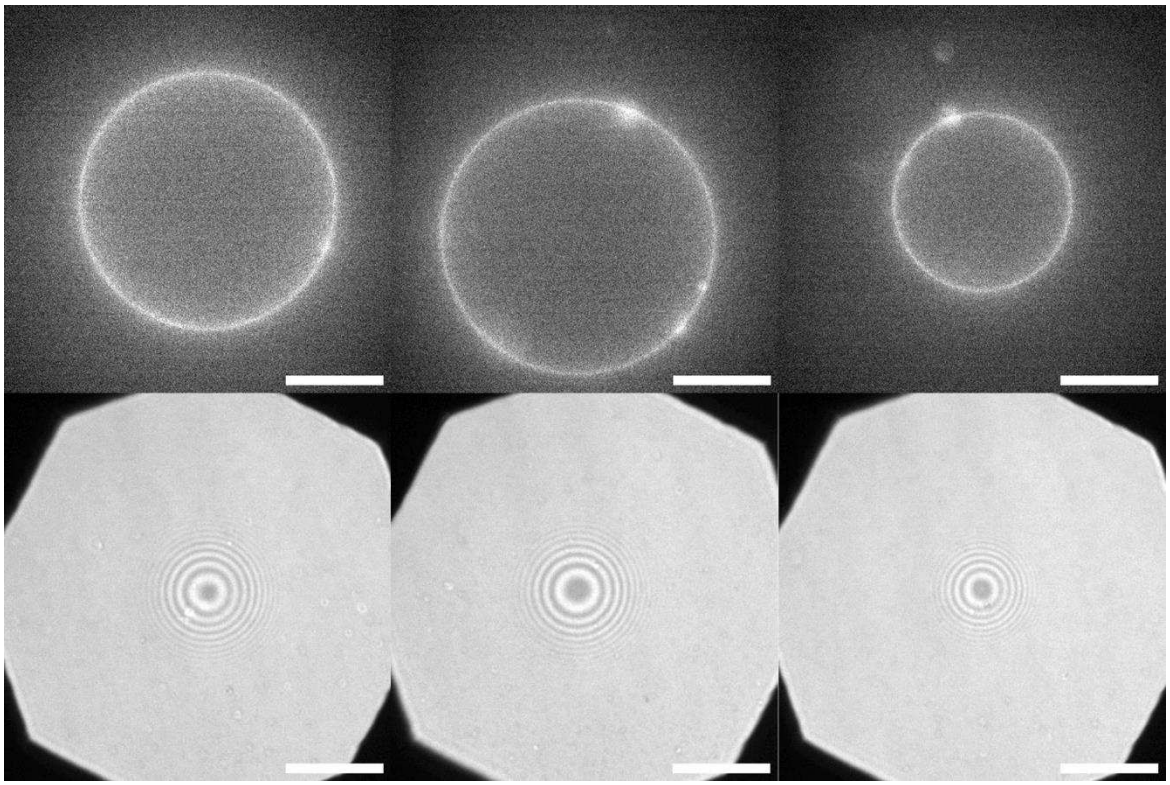

Figure S30. Fluorescence microscopy (top) and RICM images (bottom) of GUVs containing 0.2 mol% pGC. Scale bar: 10 µm.

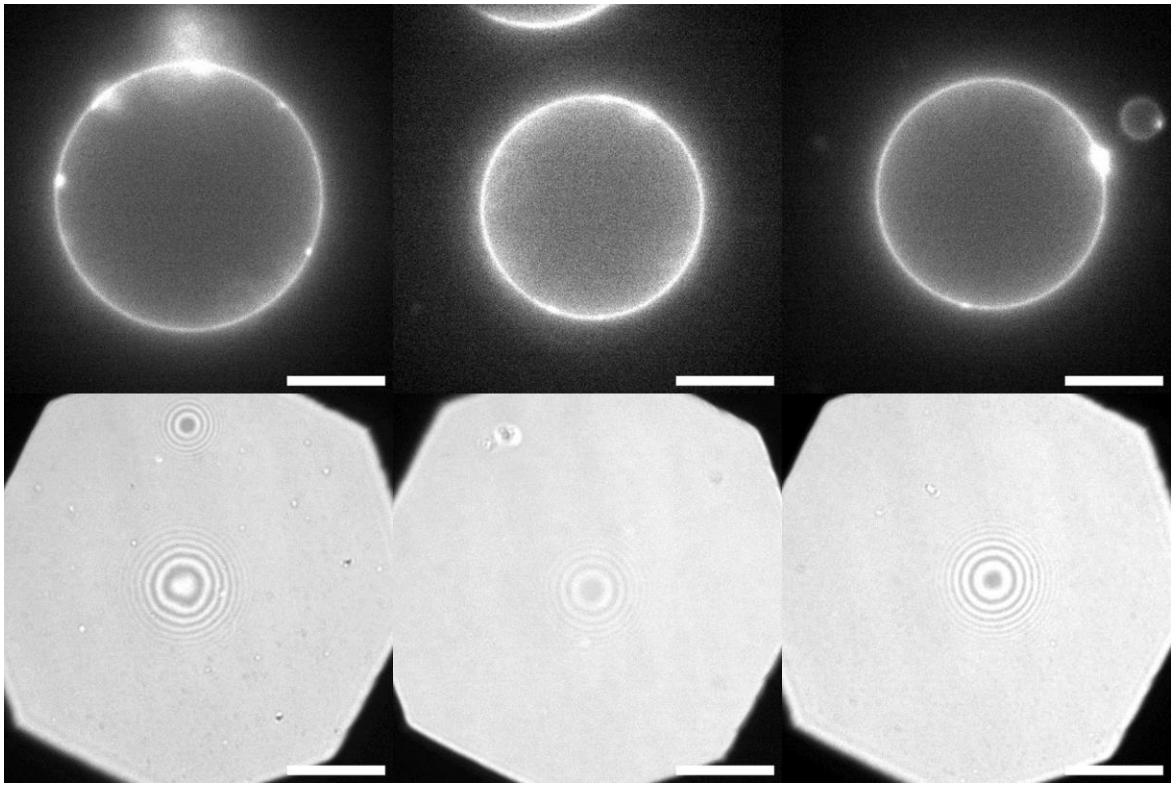

Figure S31. Fluorescence microscopy (top) and RICM images (bottom) of GUVs containing 2 mol% pGC. Scale bar: 10 µm.

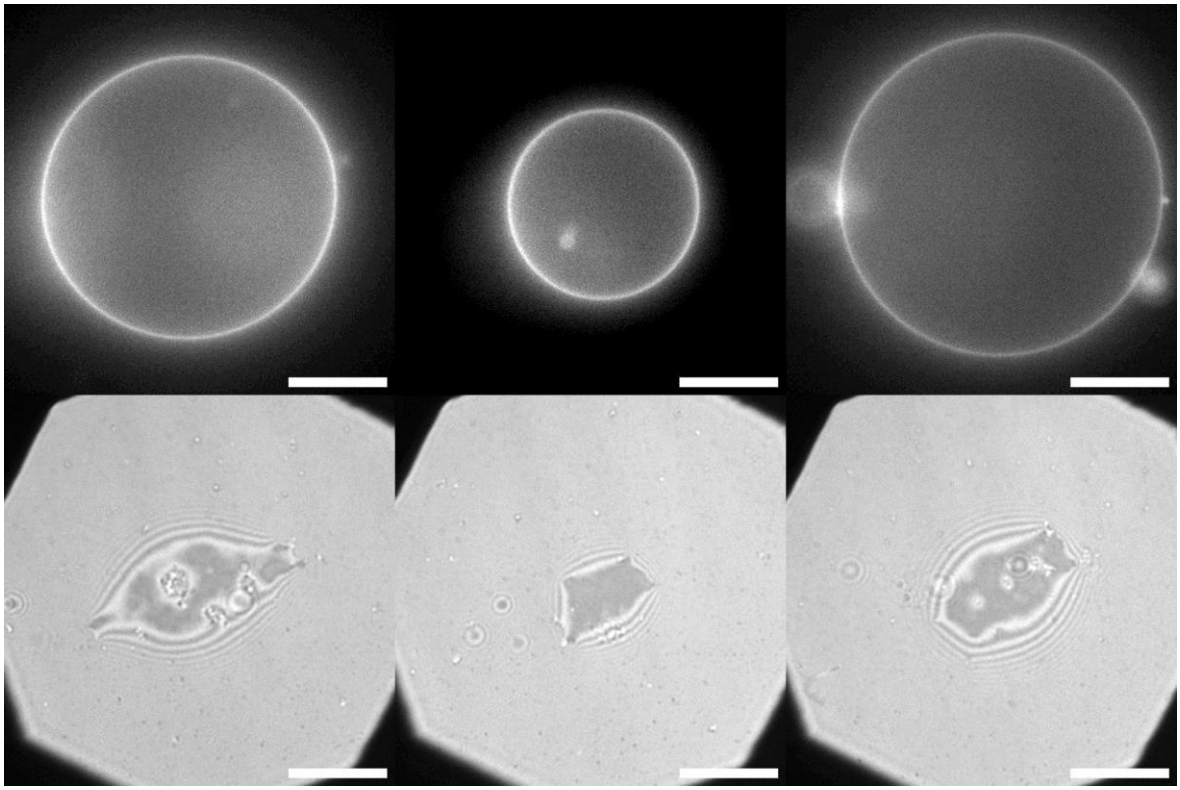

Figure S32. Fluorescence microscopy (top) and RICM images (bottom) of GUVs containing no added glycomacromolecules. Scale bar: 10 µm.

Exemplary Images of Vesicle Adhesion to ConA Surfaces (Homomultivalent) in the Presence of 5 mM MeMan.

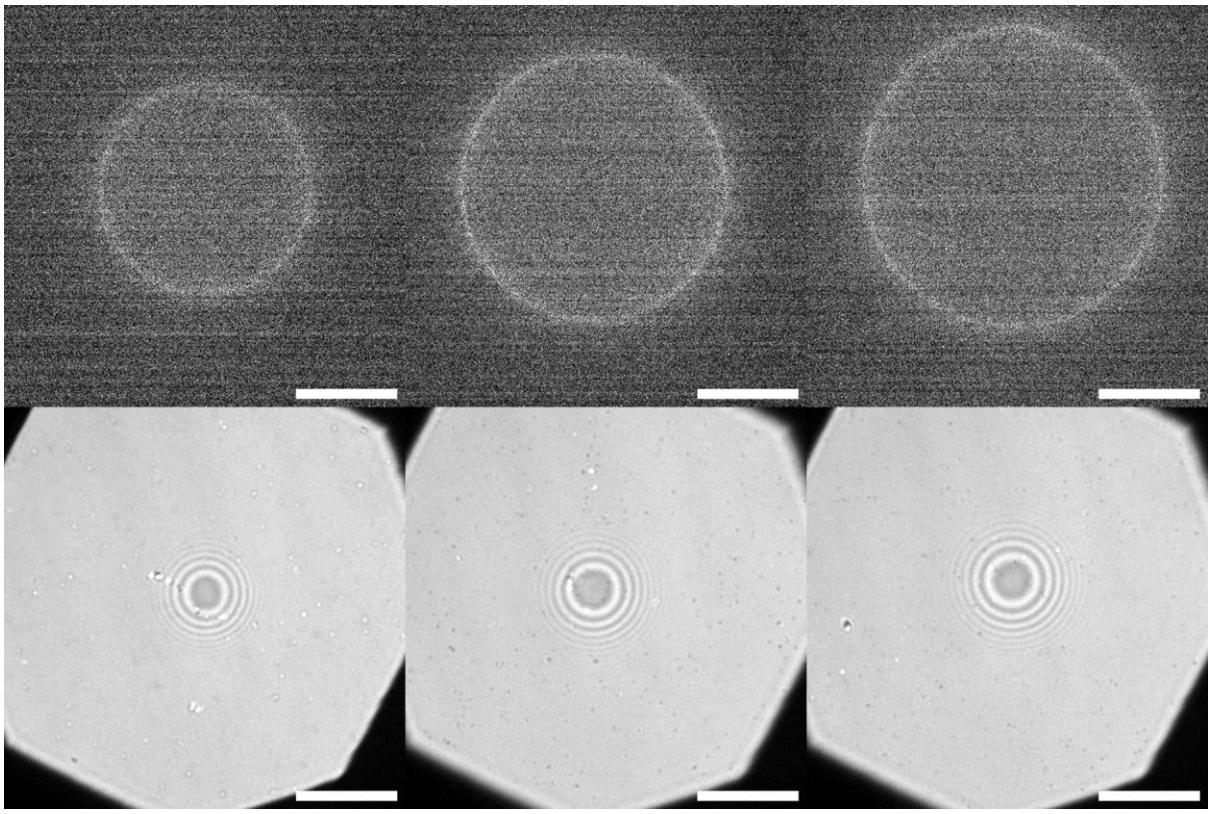

Figure S33. Fluorescence microscopy (top) and RICM images (bottom) of GUVs containing 0.5 mol% MC. Scale bar: 10 µm.

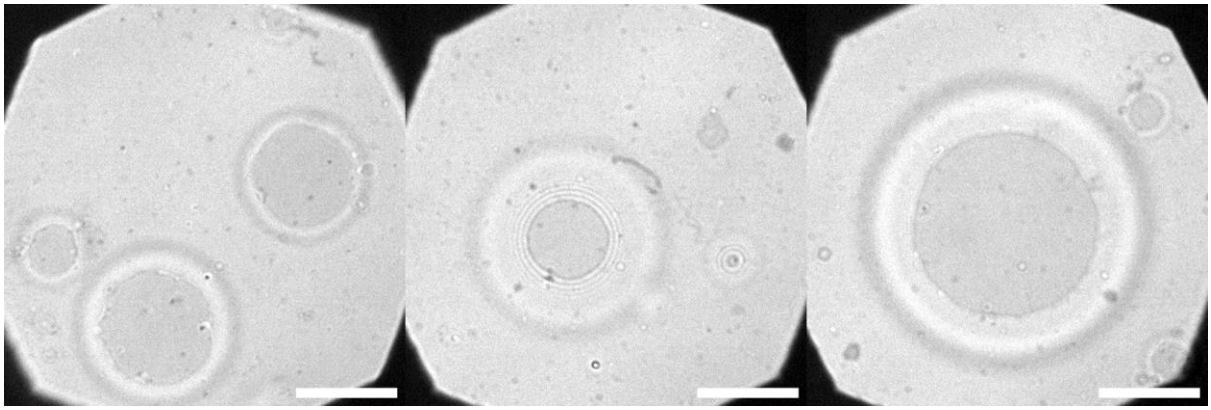

Figure S34. RICM images of GUVs containing 2 mol% MC. The outer vesicle projection is in line with the maximum vesicle circumference. Scale bar: 10 µm.

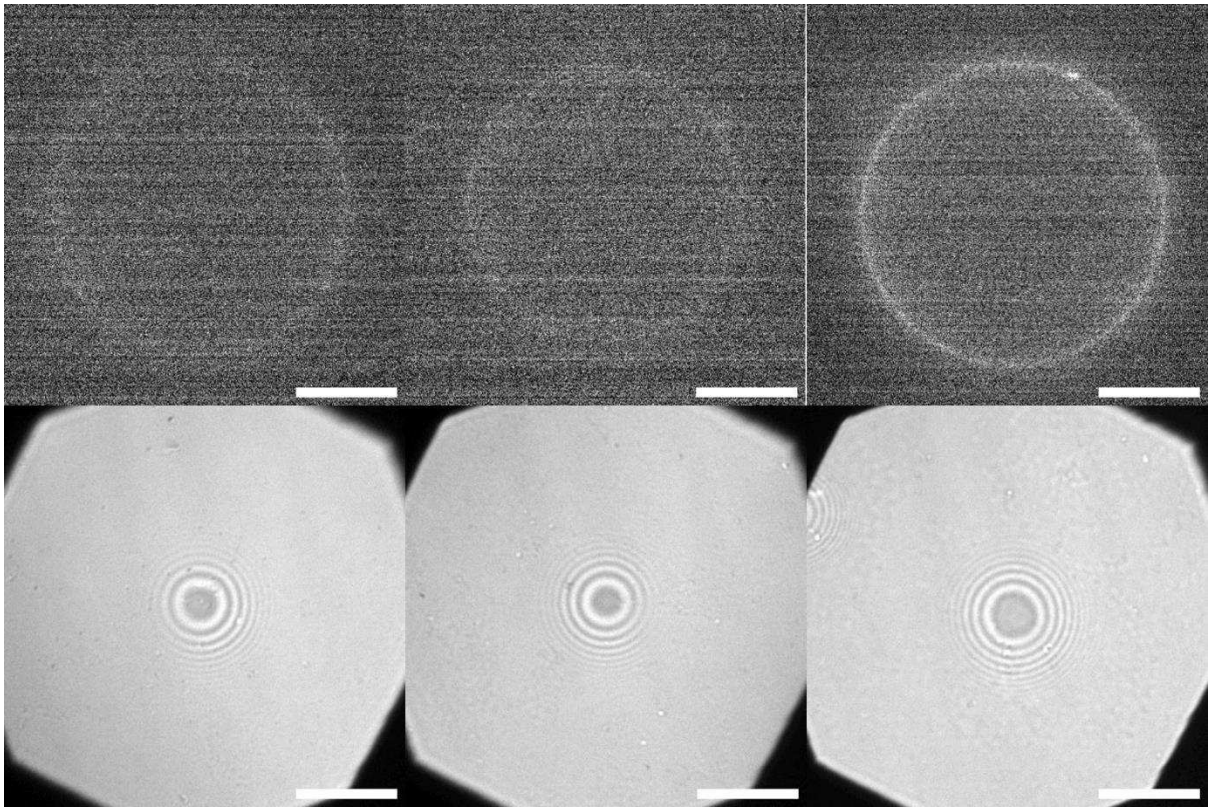

Figure S35. Fluorescence microscopy (top) and RICM images (bottom) of GUVs containing 0.05 mol% pMC. Scale bar: 10 µm.

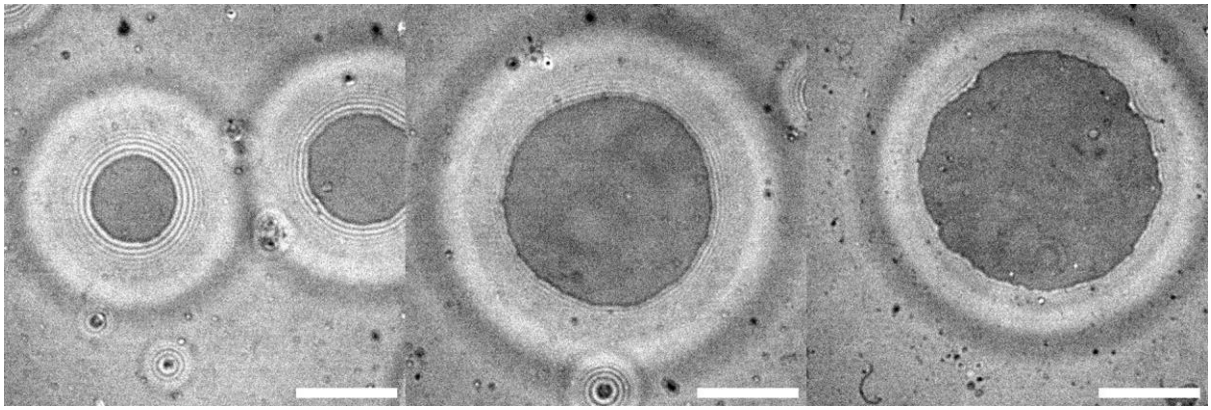

Figure S36. RICM images of GUVs containing 0.2 mol% pMC. The outer vesicle projection is in line with the maximum vesicle circumference. Scale bar: 10 µm.

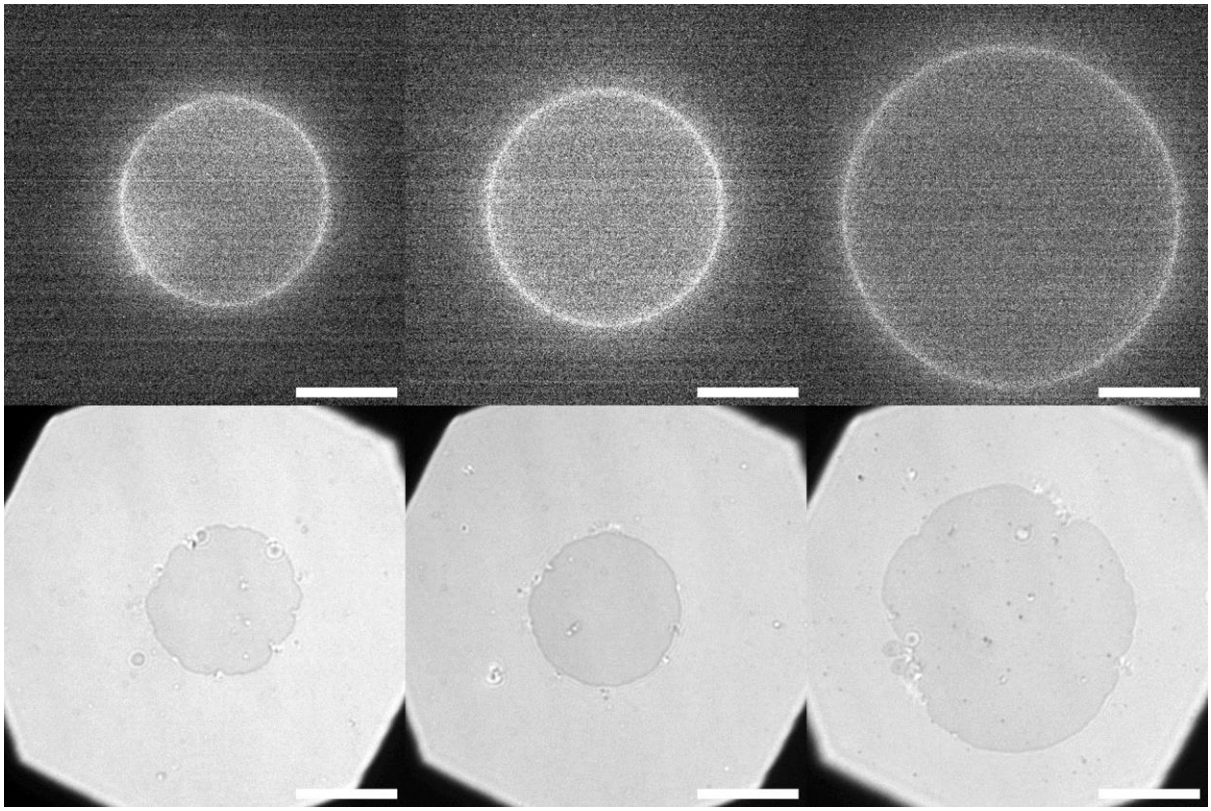

Figure S37. Fluorescence microscopy (top) and RICM images (bottom) of GUVs containing 0.5 mol% pMC. Scale bar: 10 µm.

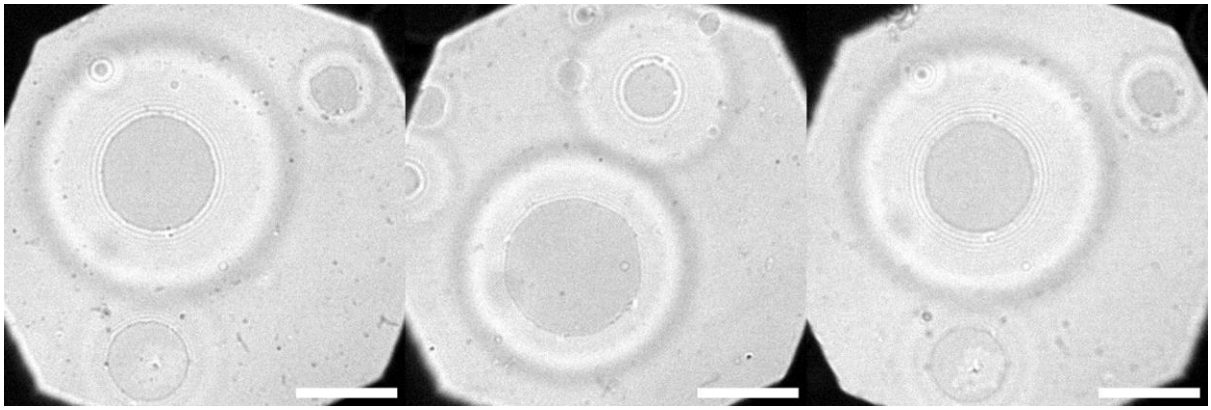

Figure S38. RICM images of GUVs containing 2 mol% pMC. The outer vesicle projection is in line with the maximum vesicle circumference. Scale bar: 10 µm.

Inhibition Studies on Homomultivalent Vesicles.

ConA surfaces were incubated with MeMan in different concentrations before the vesicles were added and let to settle on the surface. For 2 mol% MC a final concentration of 50 mM MeMan led to inhibition of adhesion. 2 mol% pMC were not inhibited at either concentration. We attribute the lacking inhibition to the high multivalent presentation of Man-moieties on the vesicles, which displace the monovalent MeMan antagonist.

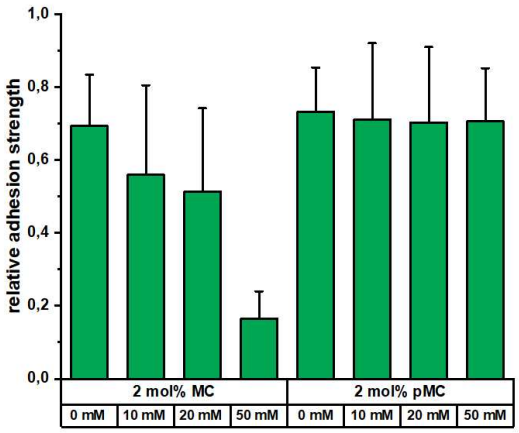

Figure S39. Adhesion profiles for MC and pMC decorated vesicles in the presence of various concentrations of MeMan.

Incubation of the ConA surfaces with a multivalent Man-polymer (i.e. Man_{300}) prior to vesicle adhesion lead to complete inhibition of vesicle adhesion.

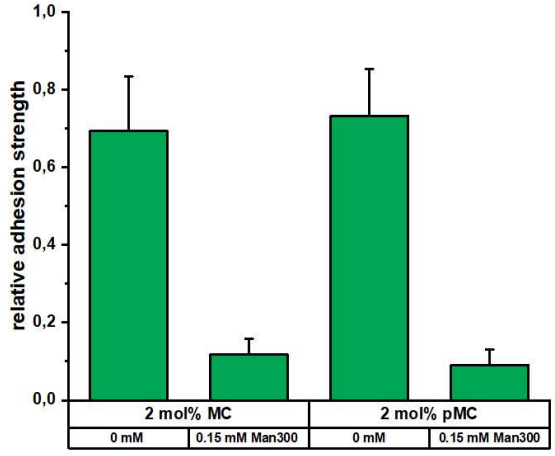

Figure S40. Adhesion profiles for MC and pMC decorated vesicles in the presence of multivalent Man-polymer inhibitor.

Vesicle Adhesion of Heteromultivalently Glyco-Decorated GUVs on ConA Surfaces.

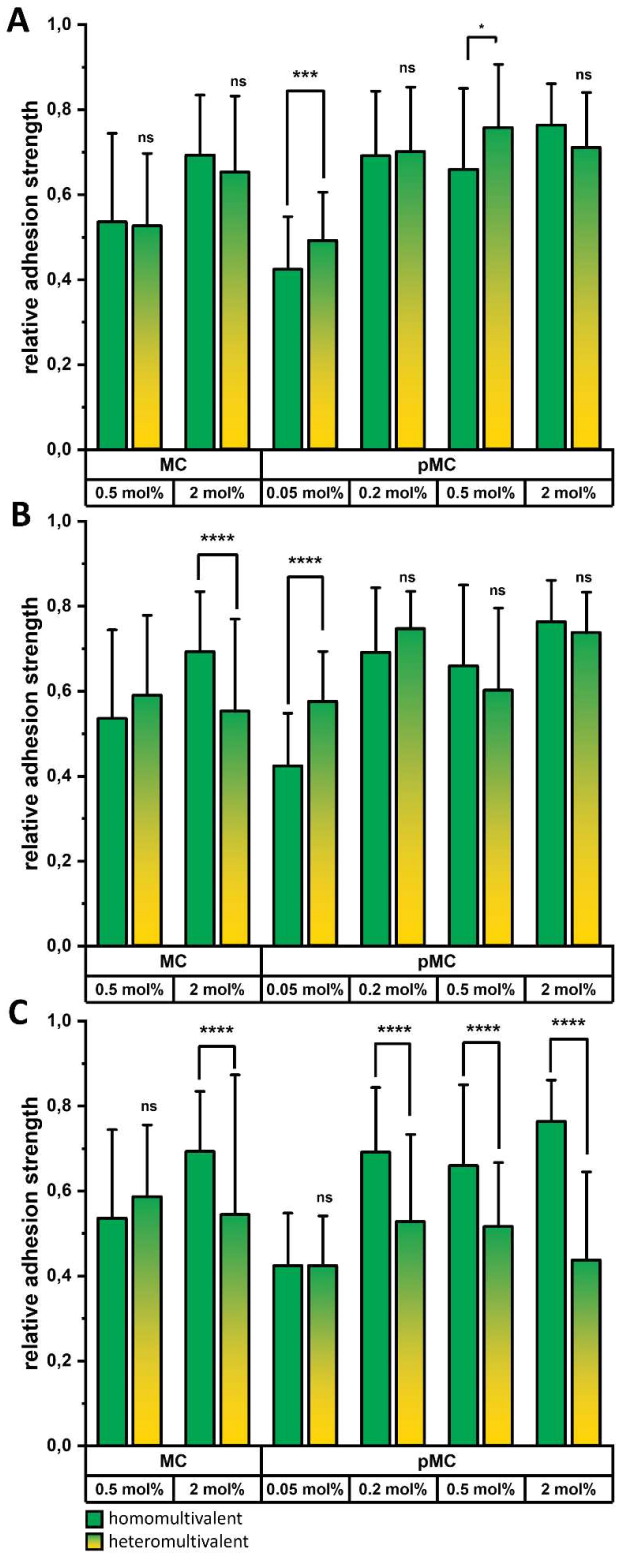

Figure S41. Relative Adhesion Strength of the heteromultivalent systems in comparison to the respective homomultivalent systems. Heteromultivalent vesicles are doped with 2 mol% GC (**A**), 0.2 mol% pGC (**B**) or 2 mol% pGC (**C**). Data are presented as mean + SEM and where evaluated using one-way ANOVA followed by Bonferroni correction (****: $p < 0.001$; ***: $p < 0.005$; **: $p < 0.01$; ***: $p < 0.05$; ns: not significant).

Exemplary Images of Vesicle Adhesion on ConA Surfaces (Heteromultivalent).

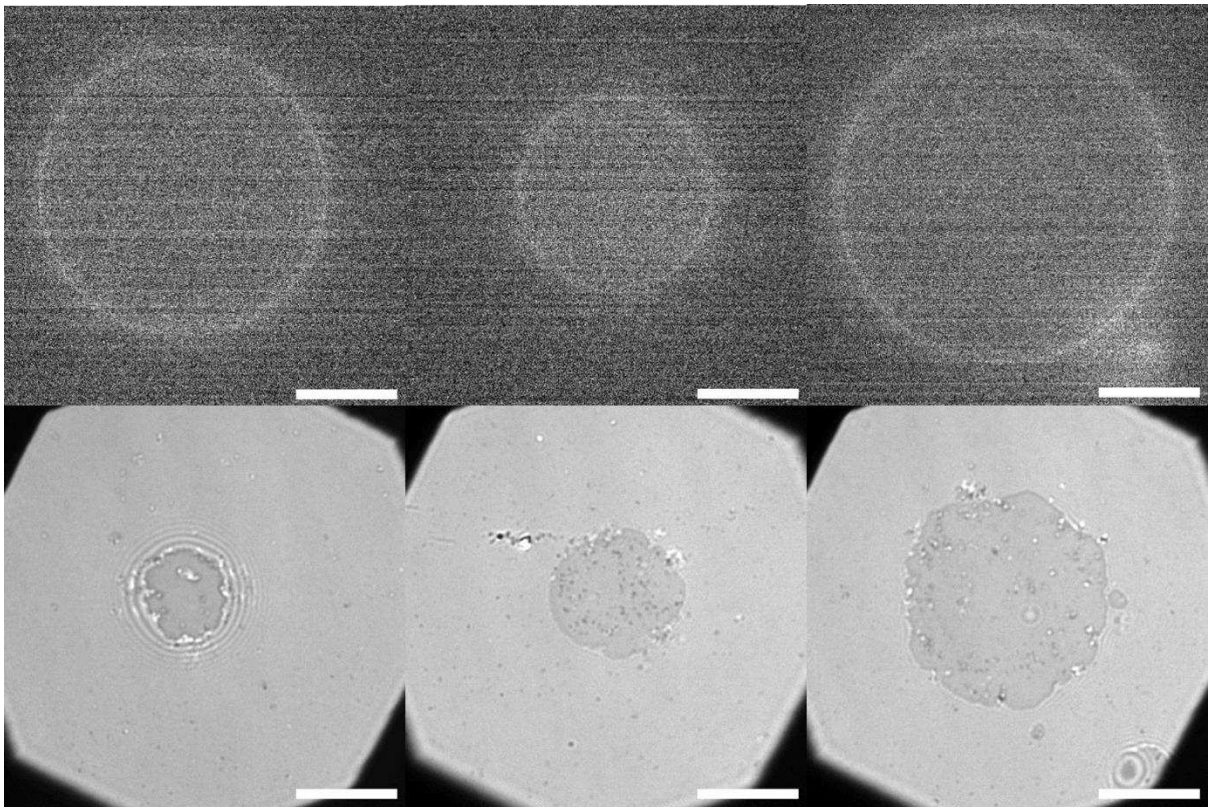

Figure S42. Fluorescence microscopy (top) and RICM images (bottom) of GUVs containing 0.5 mol% MC and 2 mol% GC. Scale bar: 10 µm.

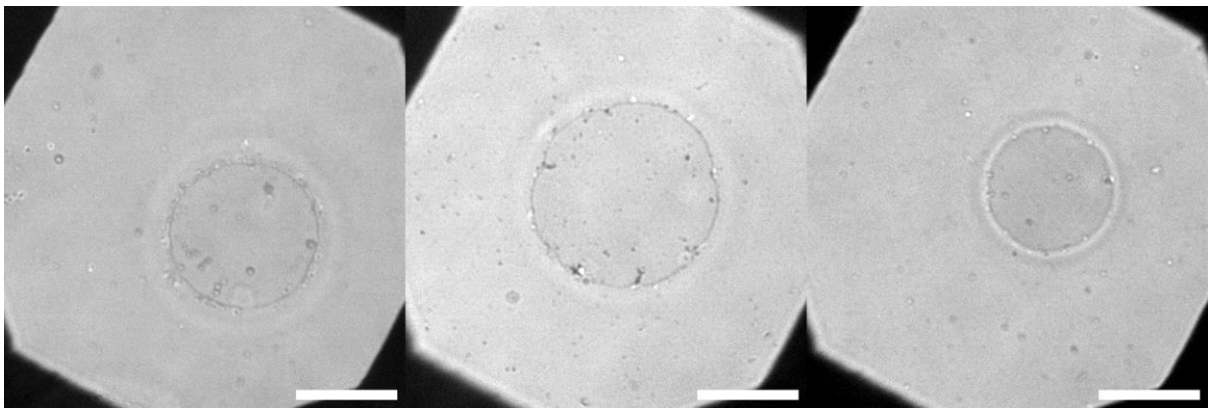

Figure S43. RICM images of GUVs containing 2 mol% MC and 2 mol% GC. The outer vesicle projection is in line with the maximum vesicle circumference. Scale bar: 10 µm.

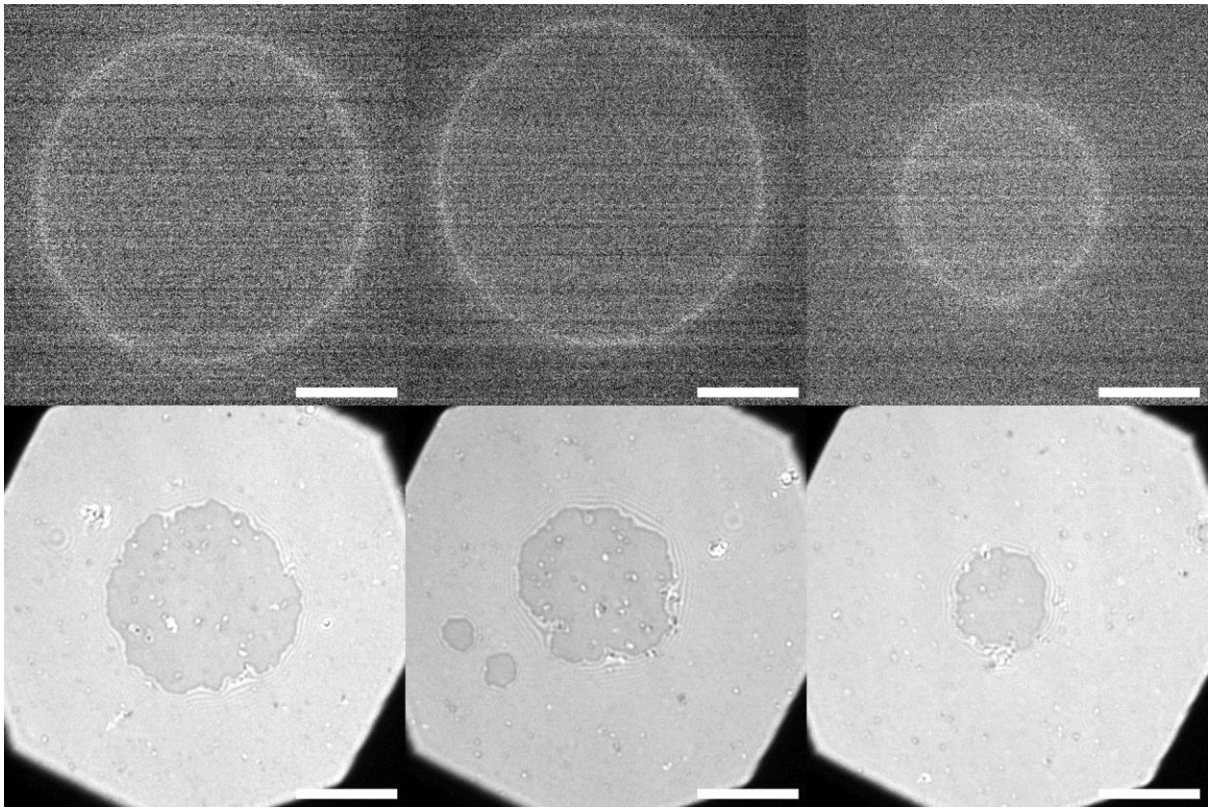

Figure S44. Fluorescence microscopy (top) and RICM images (bottom) of GUVs containing 0.05 mol% pMC and 2 mol% GC. Scale bar: 10 µm.

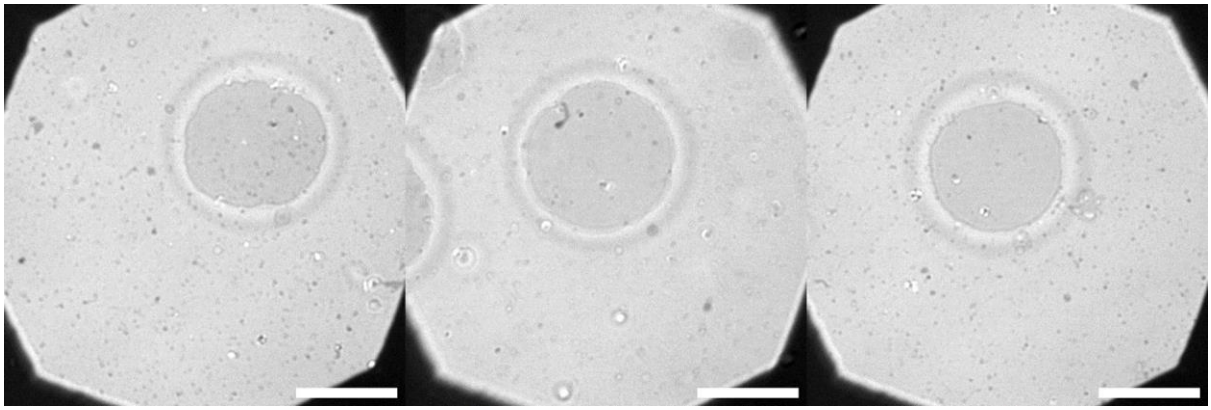

Figure S45. RICM images of GUVs containing 0.2 mol% pMC and 2 mol% GC. The outer vesicle projection is in line with the maximum vesicle circumference. Scale bar: 10 µm.

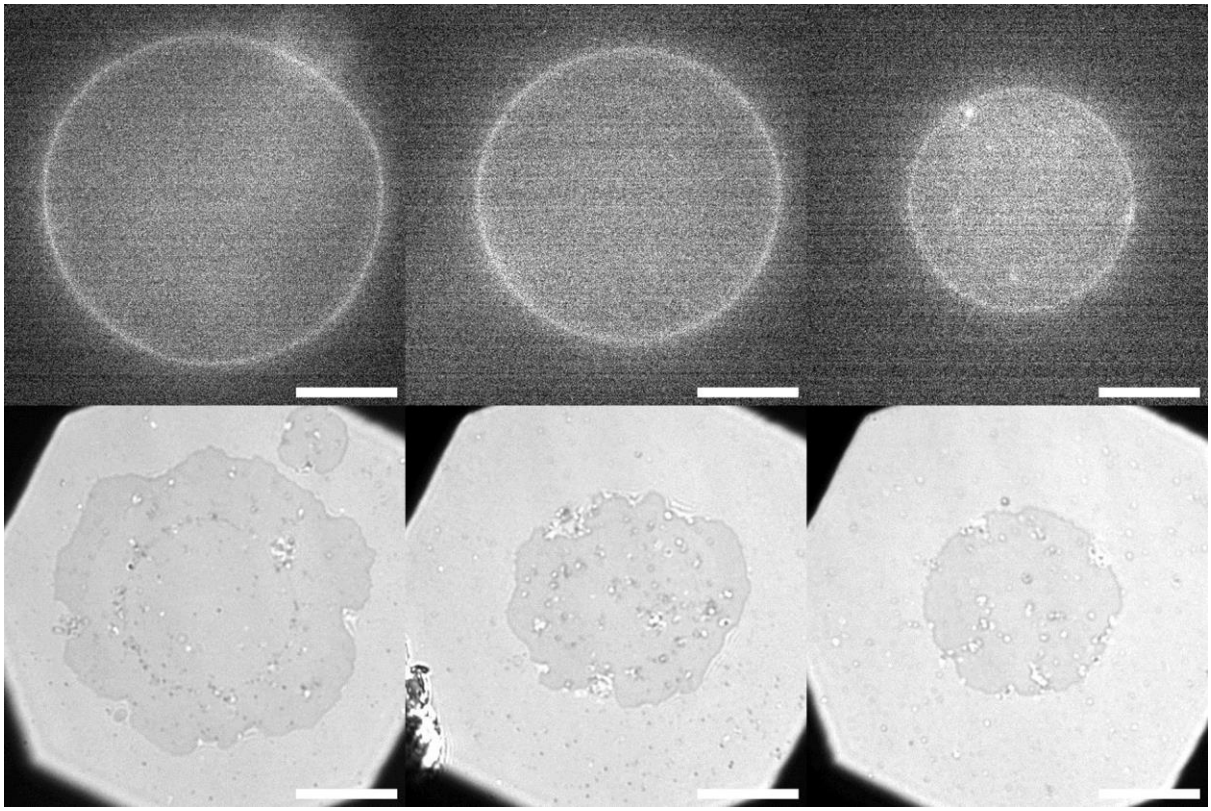

Figure S46. Fluorescence microscopy (top) and RICM images (bottom) of GUVs containing 0.5 mol% pMC and 2 mol% GC. Scale bar: 10 µm.

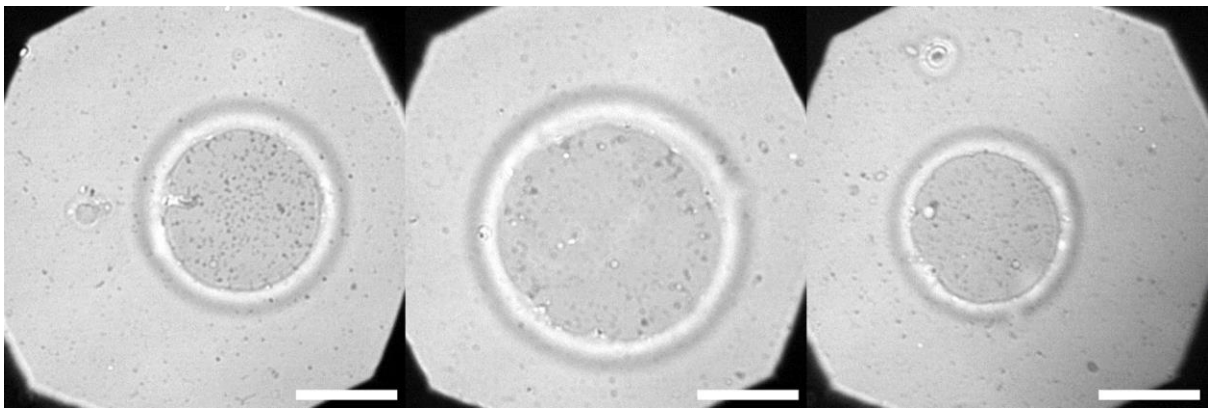

Figure S47. RICM images of GUVs containing 2 mol% pMC and 2 mol% GC. The outer vesicle projection is in line with the maximum vesicle circumference. Scale bar: 10 µm.

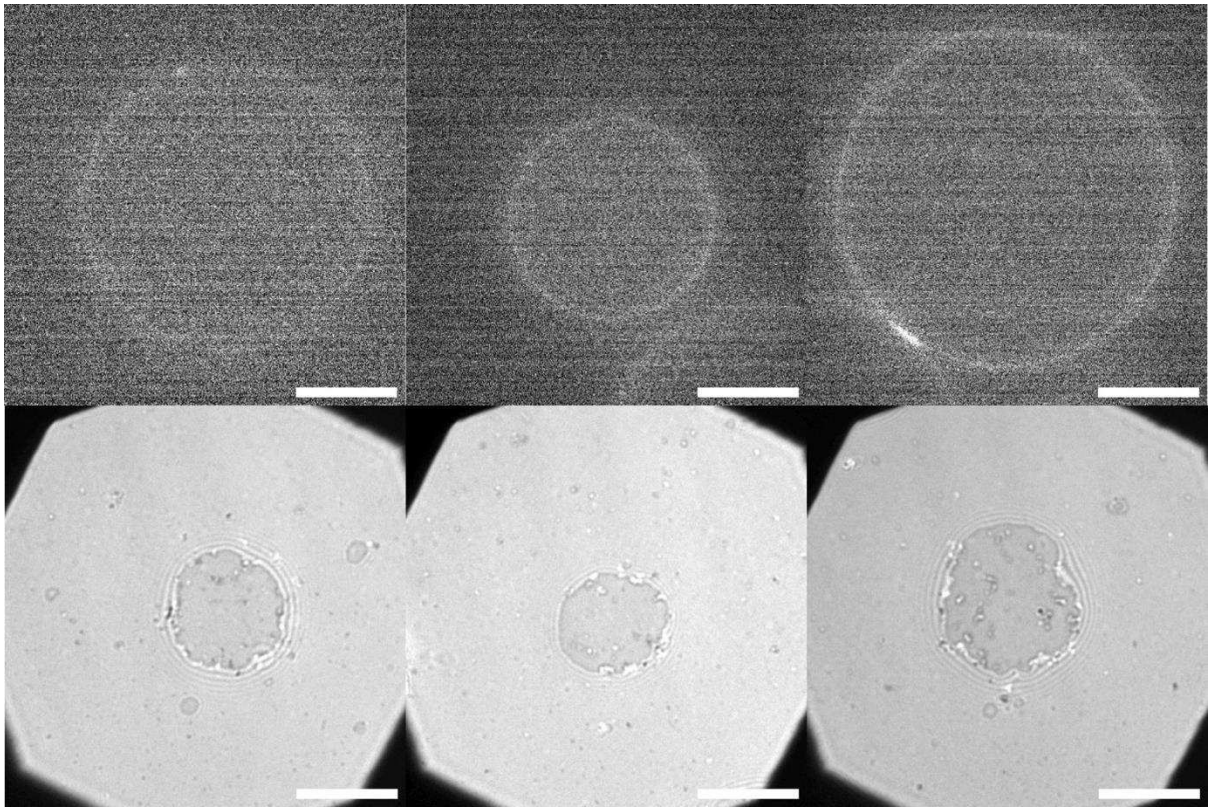

Figure S48. Fluorescence microscopy (top) and RICM images (bottom) of GUVs containing 0.5 mol% MC and 0.2 mol% pGC. Scale bar: 10 µm.

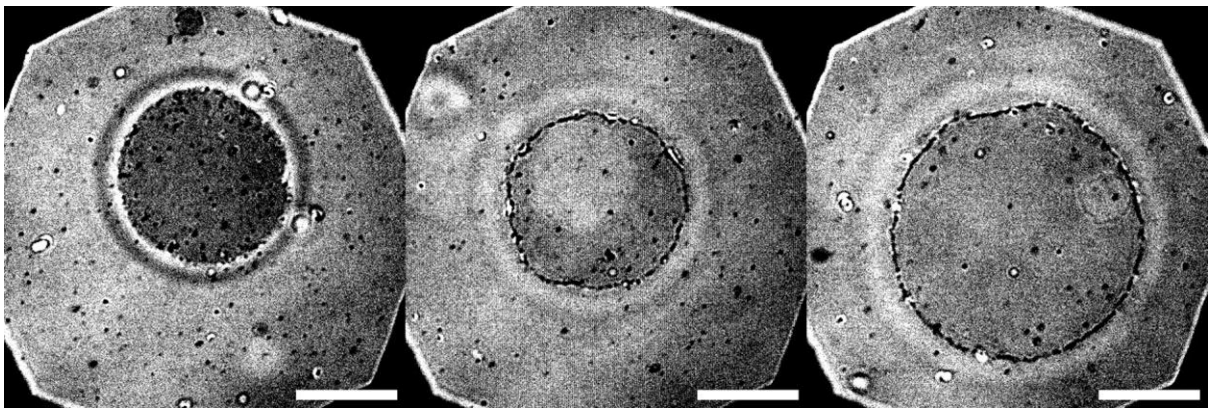

Figure S49. RICM images of GUVs containing 2 mol% MC and 0.2 mol% pGC. The outer vesicle projection is in line with the maximum vesicle circumference. Scale bar: 10 µm.

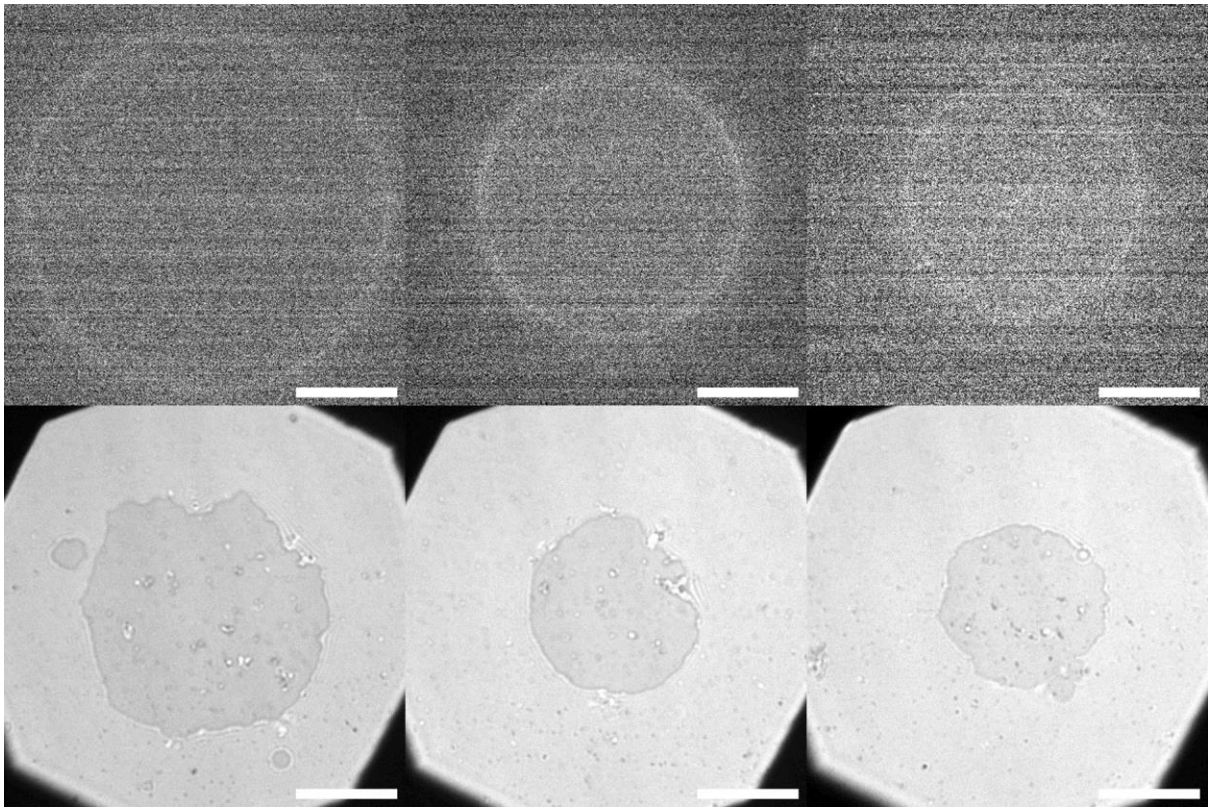

Figure S50. Fluorescence microscopy (top) and RICM images (bottom) of GUVs containing 0.05 mol% pMC and 0.2 mol% pGC. Scale bar: 10 µm.

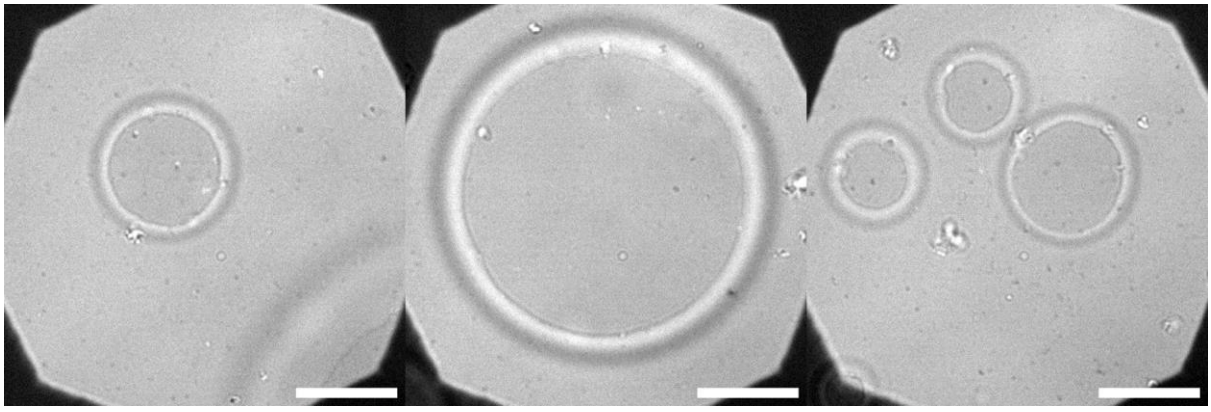

Figure S51. RICM images of GUVs containing 0.2 mol% pMC and 0.2 mol% pGC. The outer vesicle projection is in line with the maximum vesicle circumference. Scale bar: 10 µm.

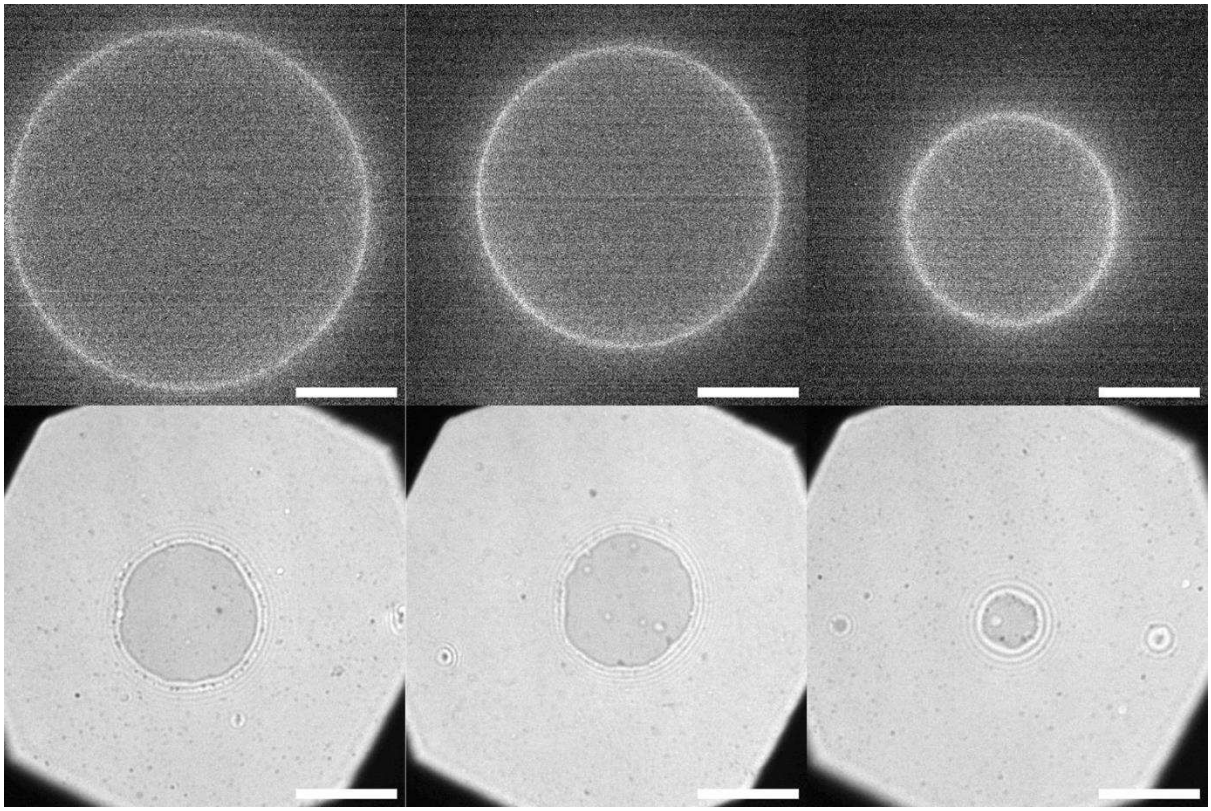

Figure S52. Fluorescence microscopy (top) and RICM images (bottom) of GUVs containing 0.5 mol% pMC and 0.2 mol% pGC. Scale bar: 10 µm.

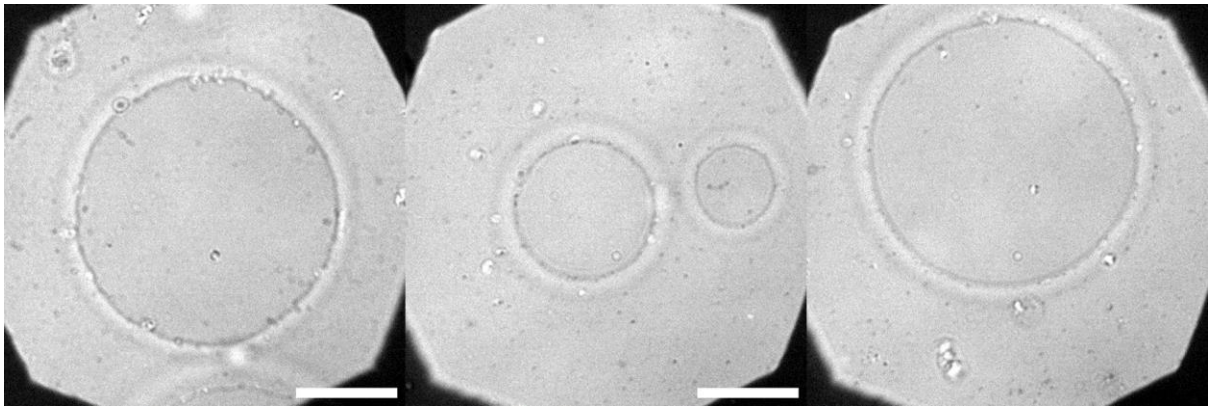

Figure S53. RICM images of GUVs containing 2 mol% pMC and 0.2 mol% pGC. The outer vesicle projection is in line with the maximum vesicle circumference. Scale bar: 10 µm.

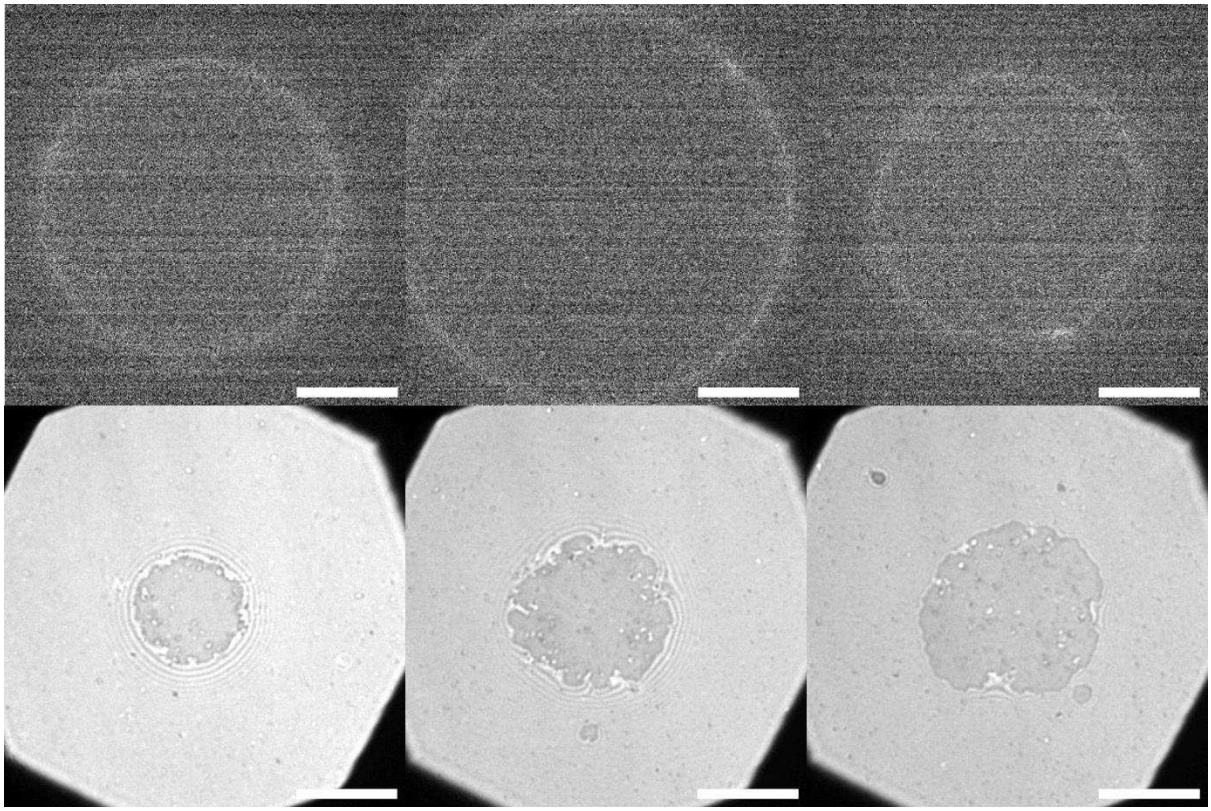

Figure S54. Fluorescence microscopy (top) and RICM images (bottom) of GUVs containing 0.5 mol% MC and 2 mol% pGC. Scale bar: 10 µm.

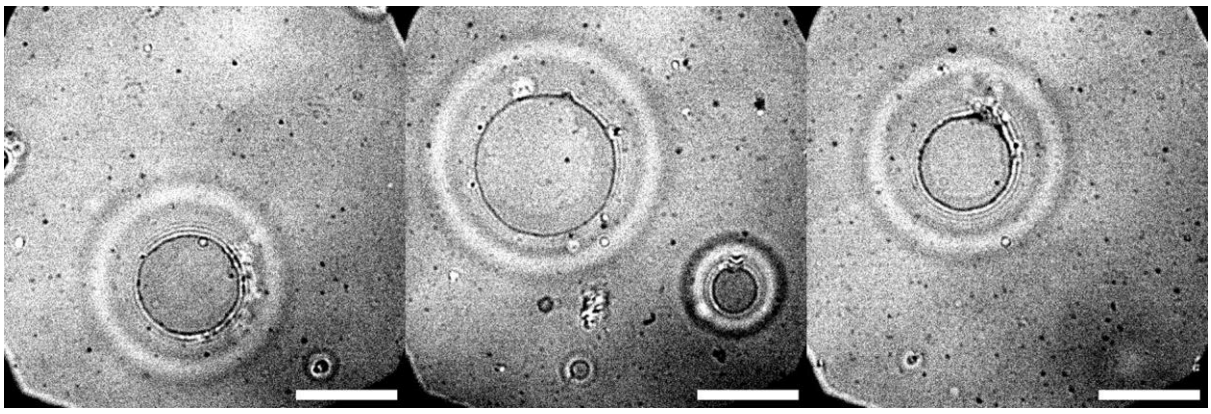

Figure S55. RICM images of GUVs containing 2 mol% MC and 2 mol% pGC. The outer vesicle projection is in line with the maximum vesicle circumference. Scale bar: 10 µm.

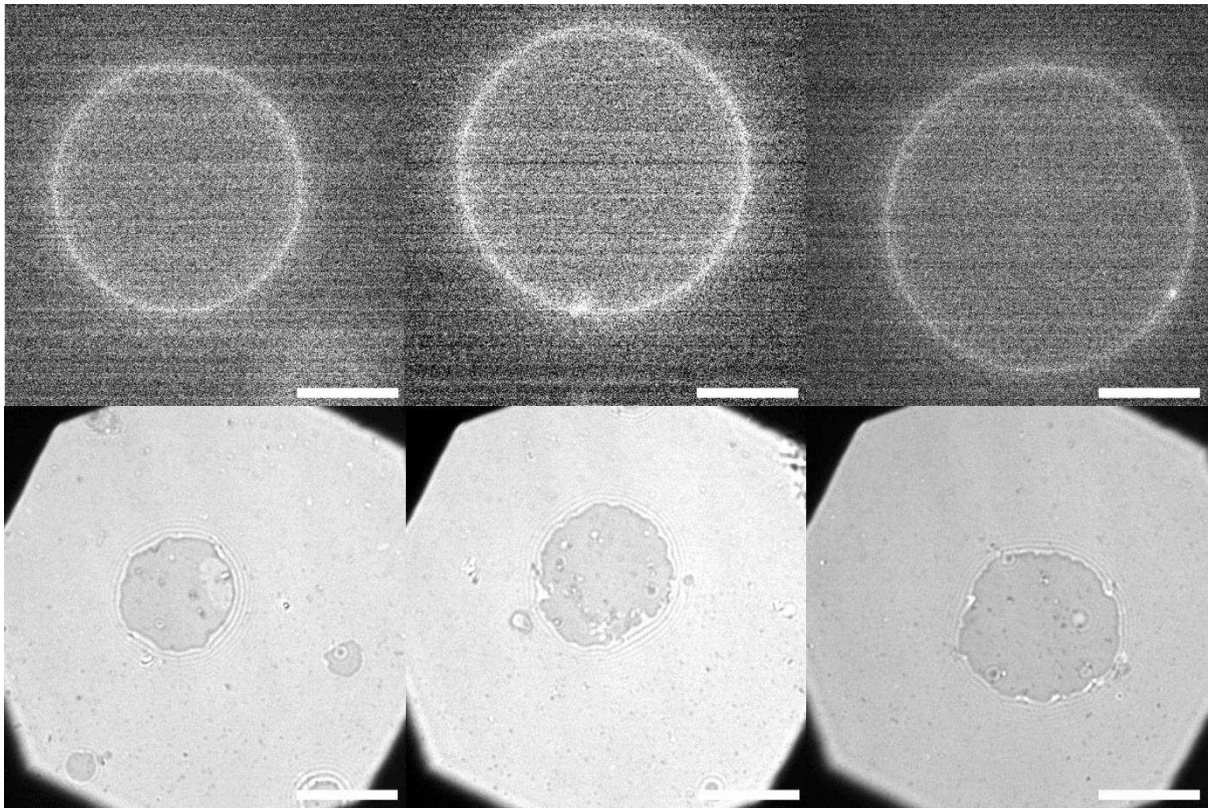

Figure S56. Fluorescence microscopy (top) and RICM images (bottom) of GUVs containing 0.05 mol% pMC and 2 mol% pGC. Scale bar: 10 µm.

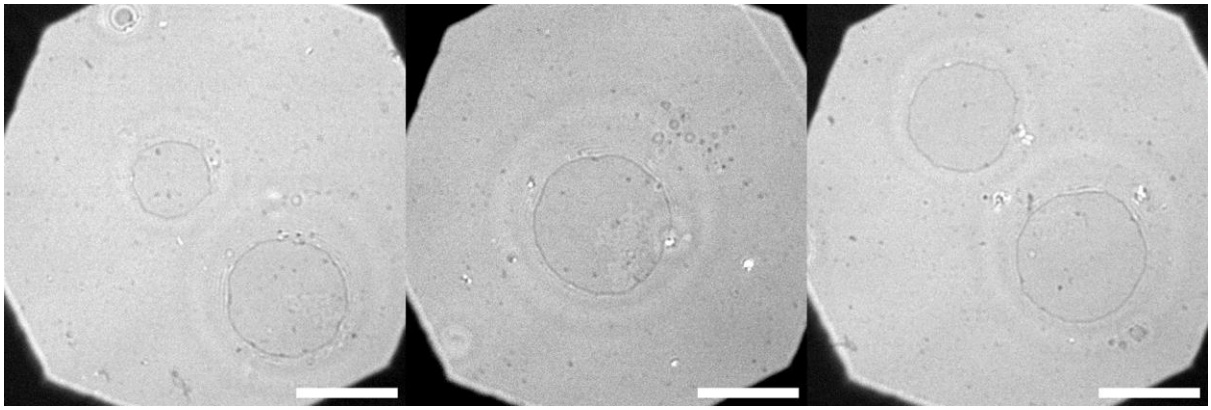

Figure S57. RICM images of GUVs containing 0.2 mol% pMC and 2 mol% pGC. The outer vesicle projection is in line with the maximum vesicle circumference. Scale bar: 10 µm.

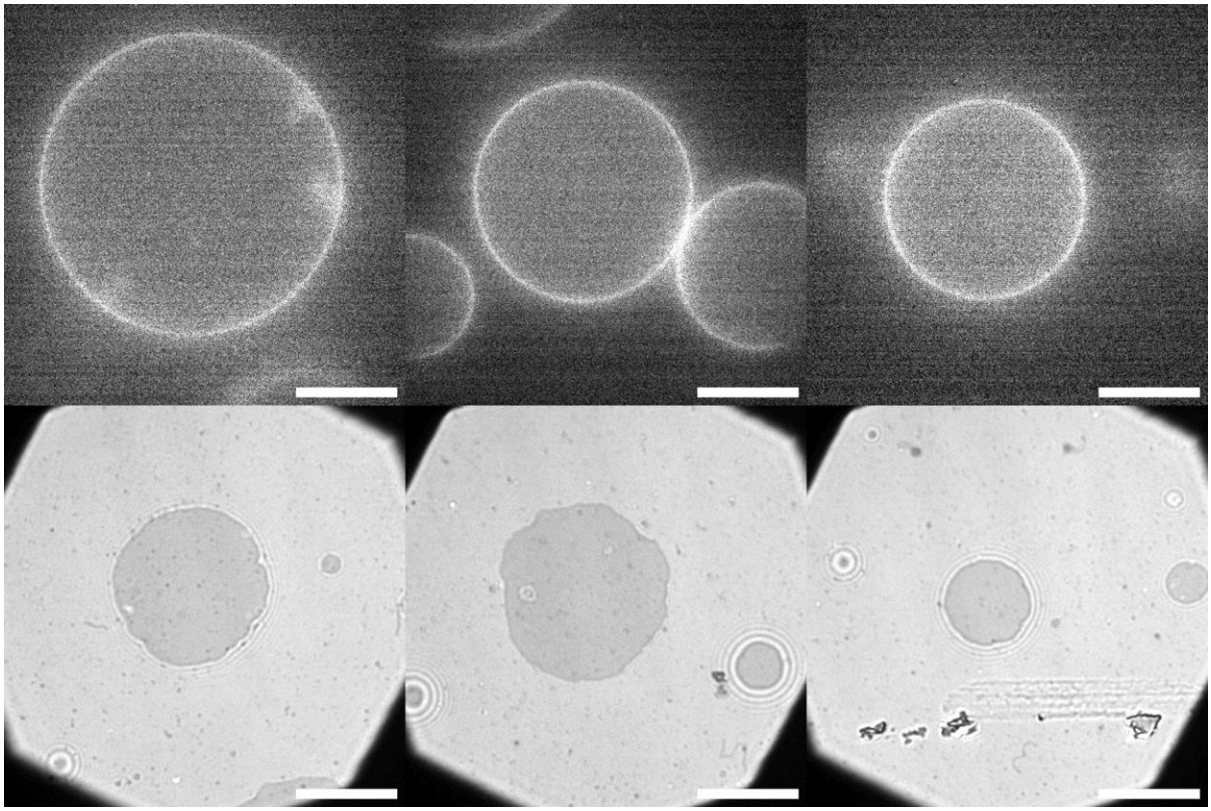

Figure S58. Fluorescence microscopy (top) and RICM images (bottom) of GUVs containing 0.5 mol% pMC and 2 mol% pGC. Scale bar: 10 µm.

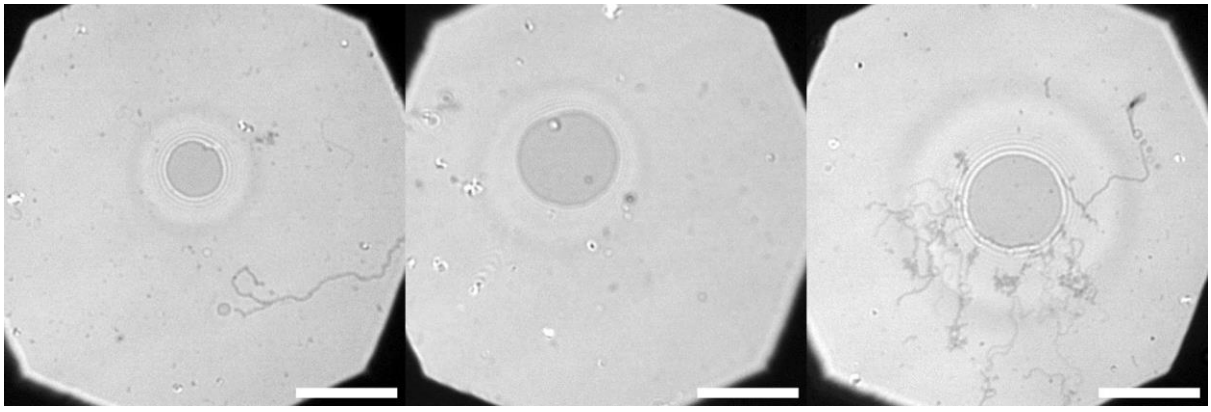

Figure S59. RICM images of GUVs containing 2 mol% pMC and 2 mol% pGC. The outer vesicle projection is in line with the maximum vesicle circumference. Scale bar: 10 µm.

Vesicle Adhesion of Heteromultivalently Glyco-Decorated GUVs on ConA Surfaces in the Presence of 5 mM MeMan.

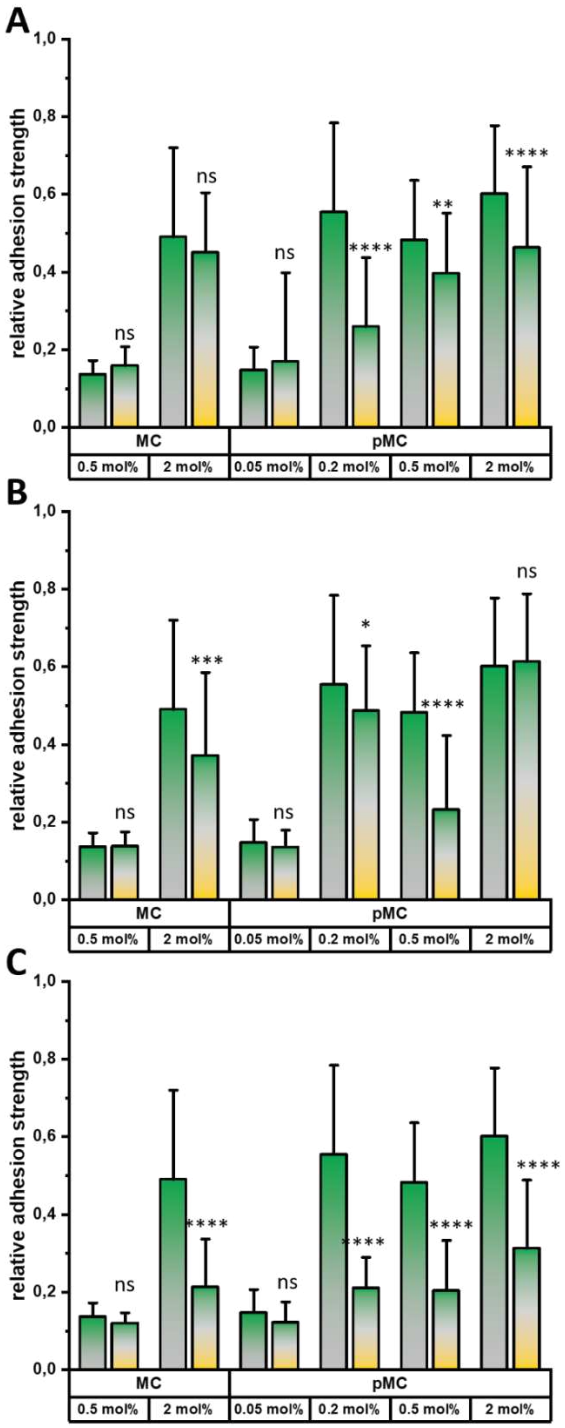

Figure S60. Relative Adhesion Strength of the heteromultivalent systems in the presence of 5 mM MeMan in comparison to the respective homomultivalent system. Heteromultivalent vesicles are doped with 2 mol% GC (**A**), 0.2 mol% pGC (**B**) or 2 mol% pGC (**C**). Data are presented as mean + SEM and where evaluated using one-way ANOVA followed by Bonferroni correction (****: $p < 0.001$; ***: $p < 0.005$; **: $p < 0.01$; ***: $p < 0.05$; ns: not significant).

Exemplary Images of Vesicle Adhesion to ConA Surfaces (Heteromultivalent) in the Presence of 5 mM MeMan.

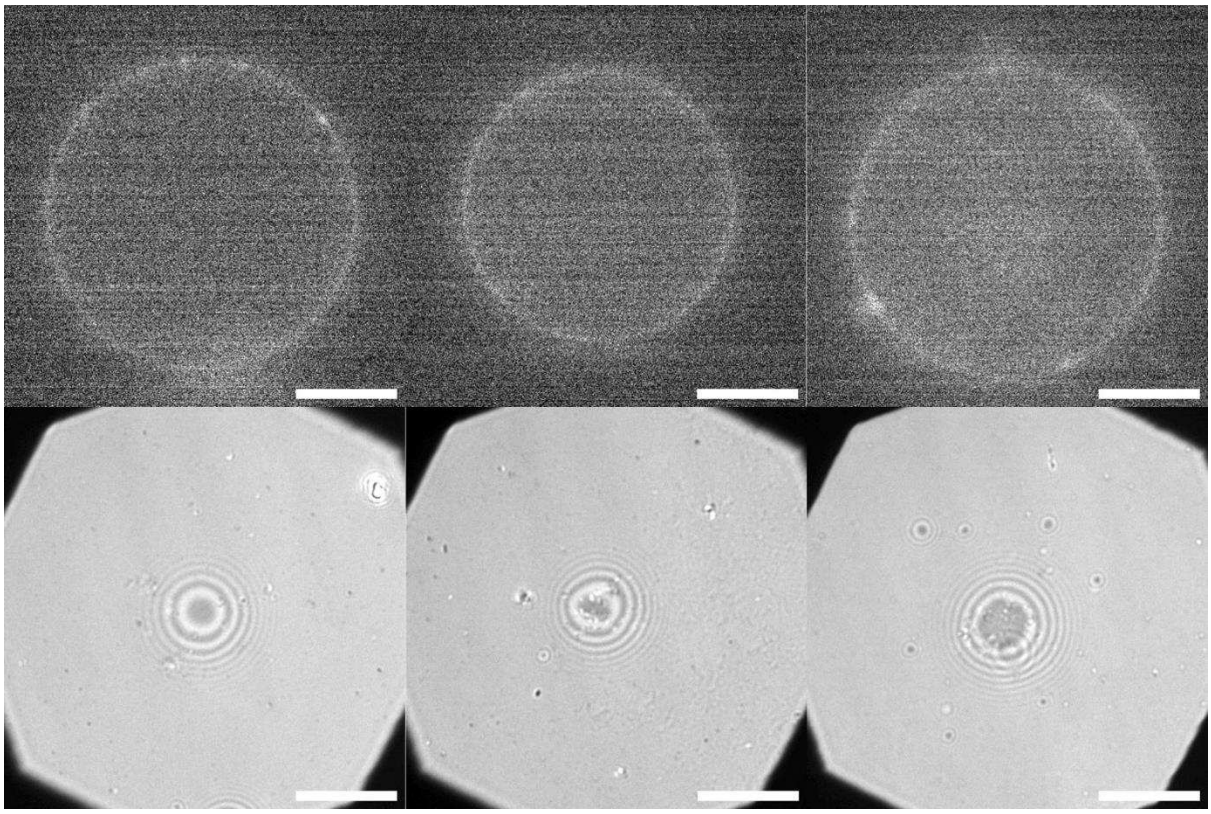

Figure S61. Fluorescence microscopy (top) and RICM images (bottom) of GUVs containing 0.5 mol% MC and 2 mol% GC. Scale bar: 10 µm.

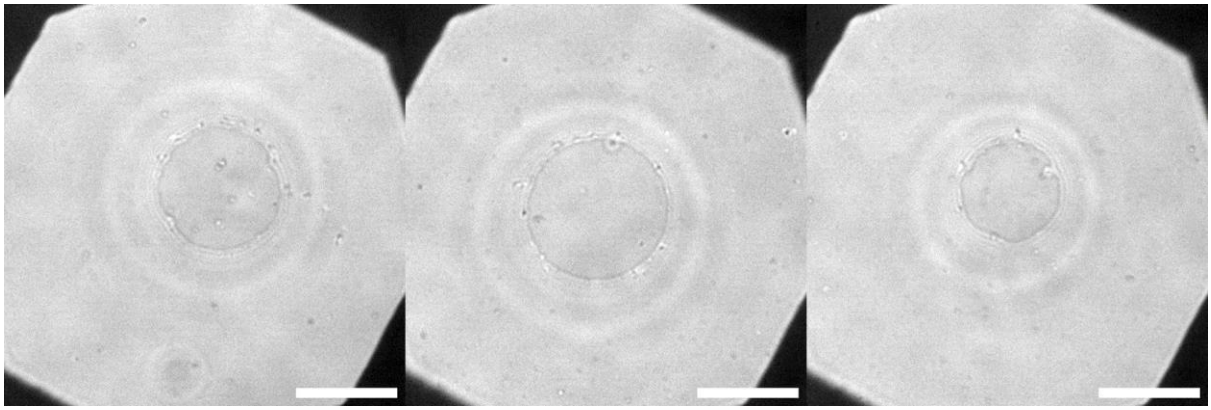

Figure S62. RICM images of GUVs containing 2 mol% MC and 2 mol% GC. The outer vesicle projection is in line with the maximum vesicle circumference. Scale bar: 10 µm.

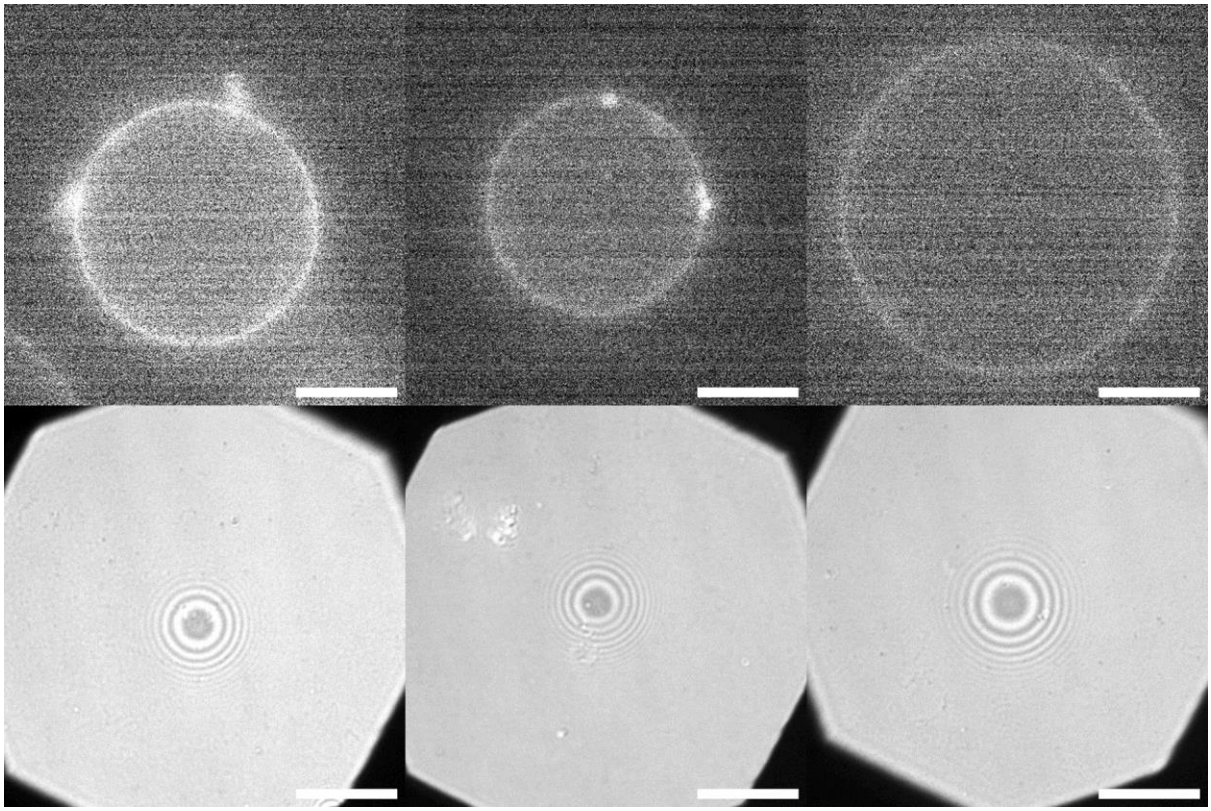

Figure S63. Fluorescence microscopy (top) and RICM images (bottom) of GUVs containing 0.05 mol% pMC and 2 mol% GC. Scale bar: 10 µm.

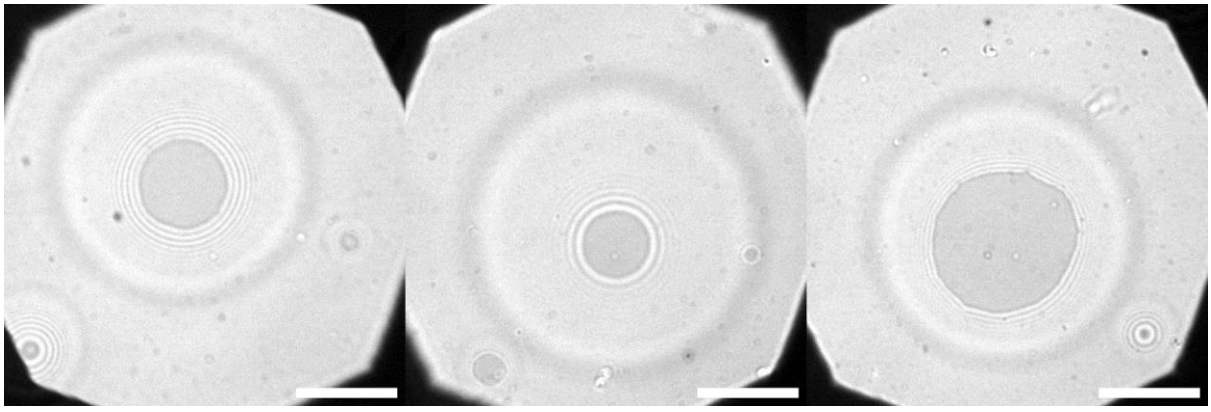

Figure S64. RICM images of GUVs containing 0.2 mol% pMC and 2 mol% GC. The outer vesicle projection is in line with the maximum vesicle circumference. Scale bar: 10 µm.

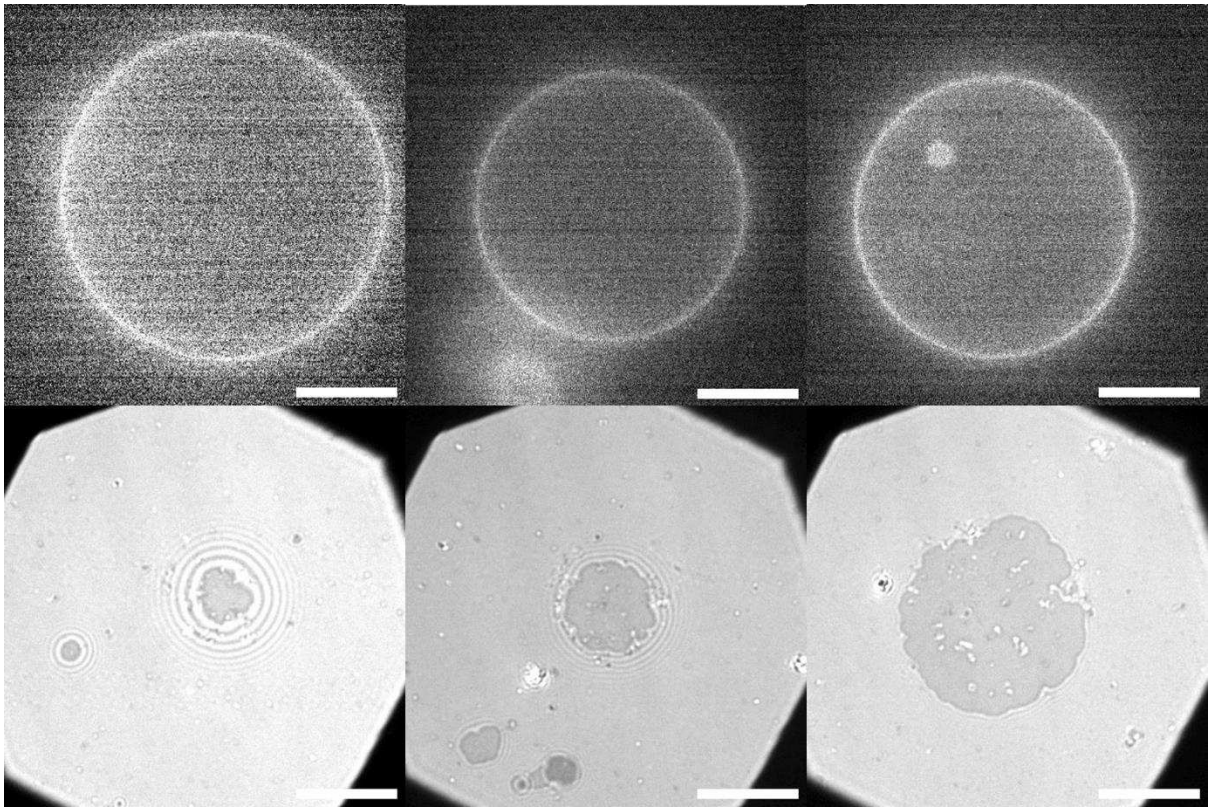

Figure S65. Fluorescence microscopy (top) and RICM images (bottom) of GUVs containing 0.5 mol% pMC and 2 mol% GC. Scale bar: 10 µm.

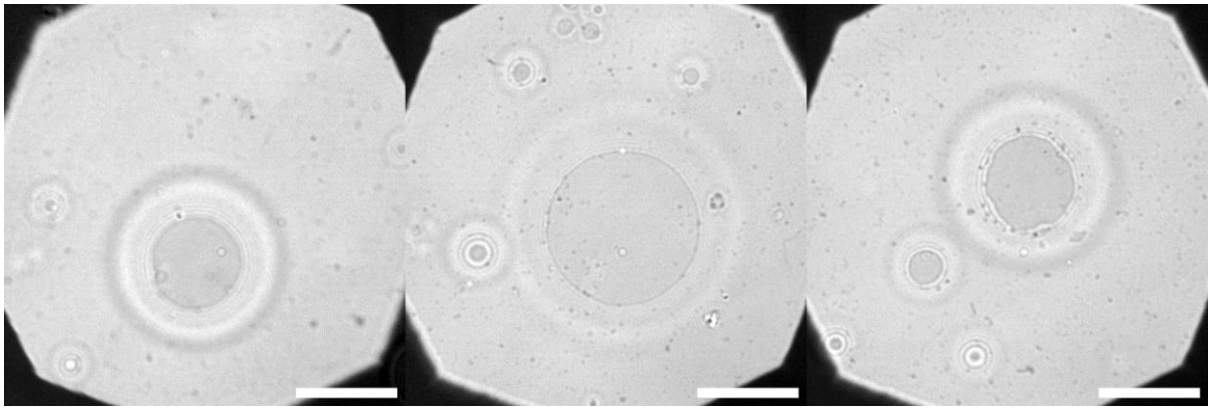

Figure S66. RICM images of GUVs containing 2 mol% pMC and 2 mol% GC. The outer vesicle projection is in line with the maximum vesicle circumference. Scale bar: 10 µm.

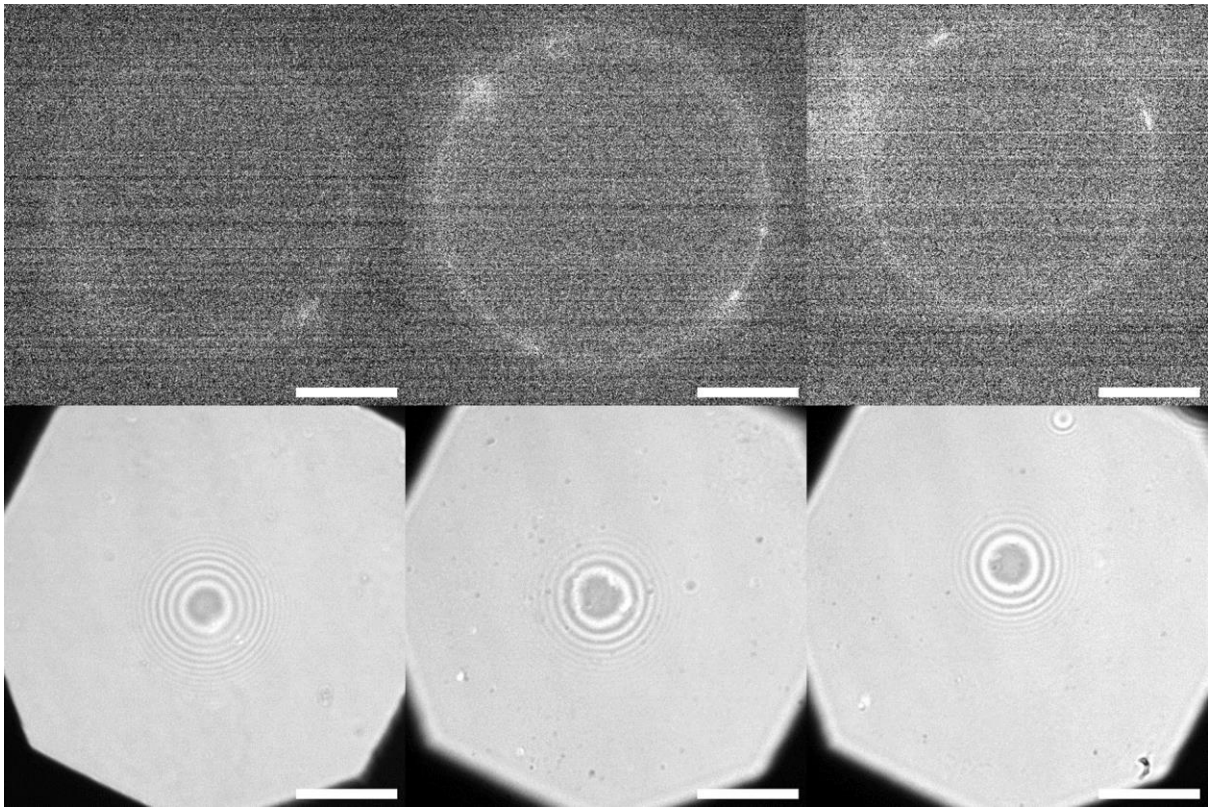

Figure S67. Fluorescence microscopy (top) and RICM images (bottom) of GUVs containing 0.5 mol% MC and 0.2 mol% pGC. Scale bar: 10 µm.

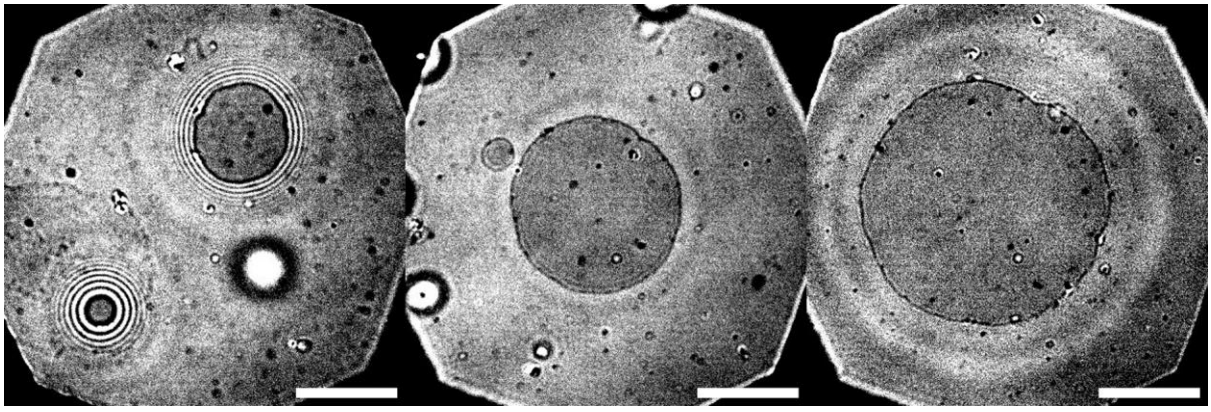

Figure S68. RICM images of GUVs containing 2 mol% MC and 0.2 mol% pGC. The outer vesicle projection is in line with the maximum vesicle circumference. Scale bar: 10 µm.

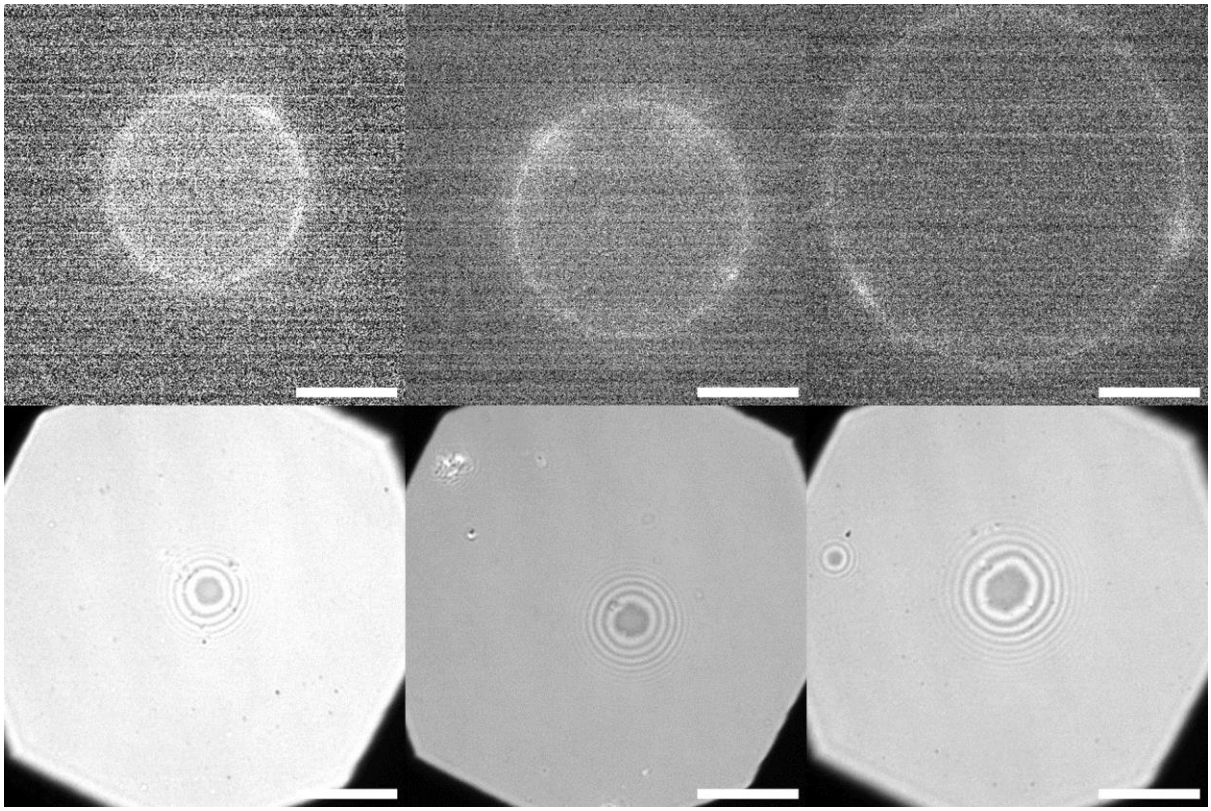

Figure S69. Fluorescence microscopy (top) and RICM images (bottom) of GUVs containing 0.05 mol% MC and 0.2 mol% pGC. Scale bar: 10 µm.

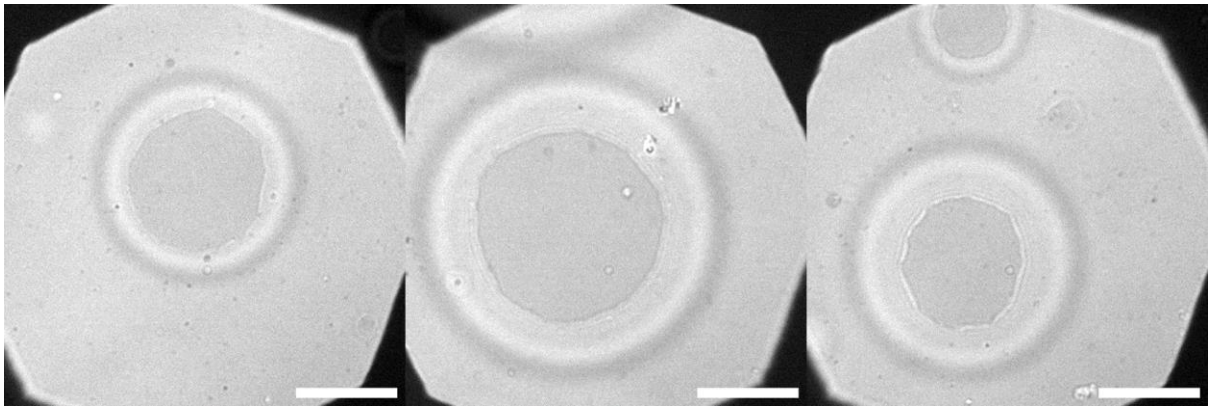

Figure S70. RICM images of GUVs containing 0.2 mol% pMC and 0.2 mol% pGC. The outer vesicle projection is in line with the maximum vesicle circumference. Scale bar: 10 µm.

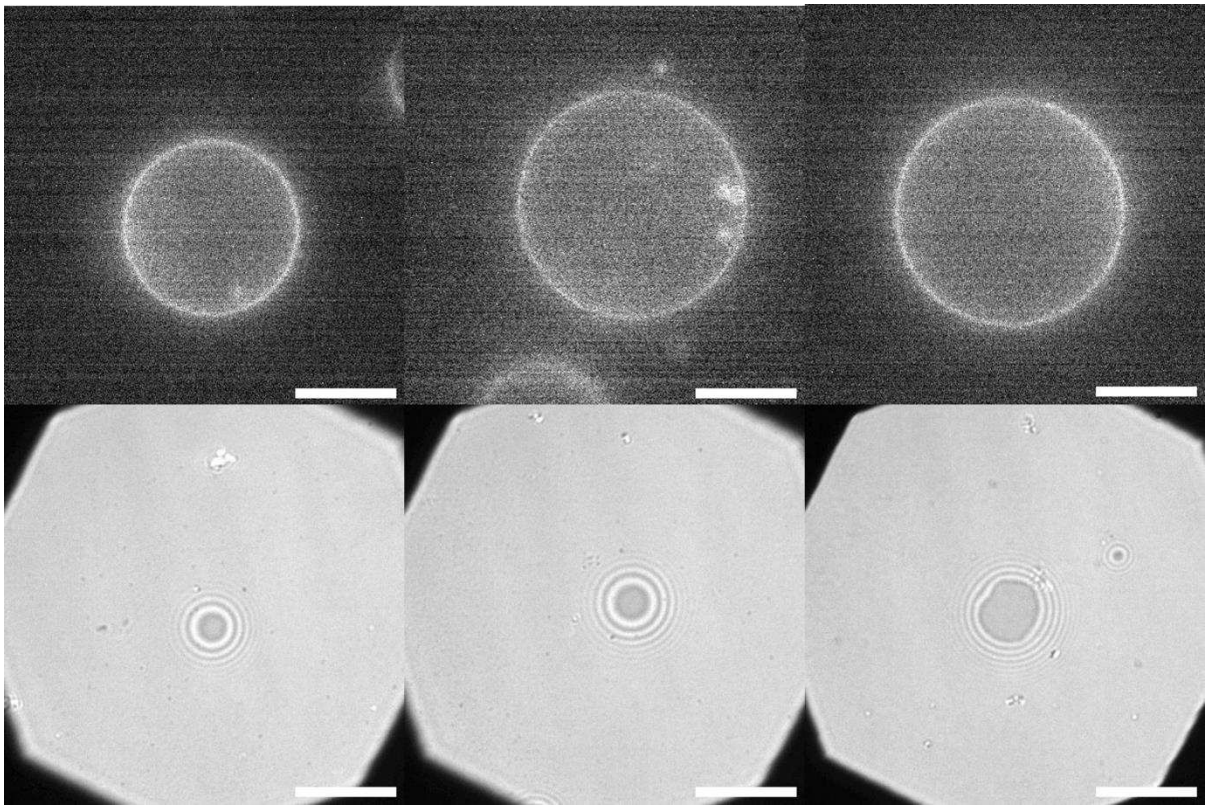

Figure S71. Fluorescence microscopy (top) and RICM images (bottom) of GUVs containing 0.5 mol% pMC and 0.2 mol% pGC. Scale bar: 10 µm.

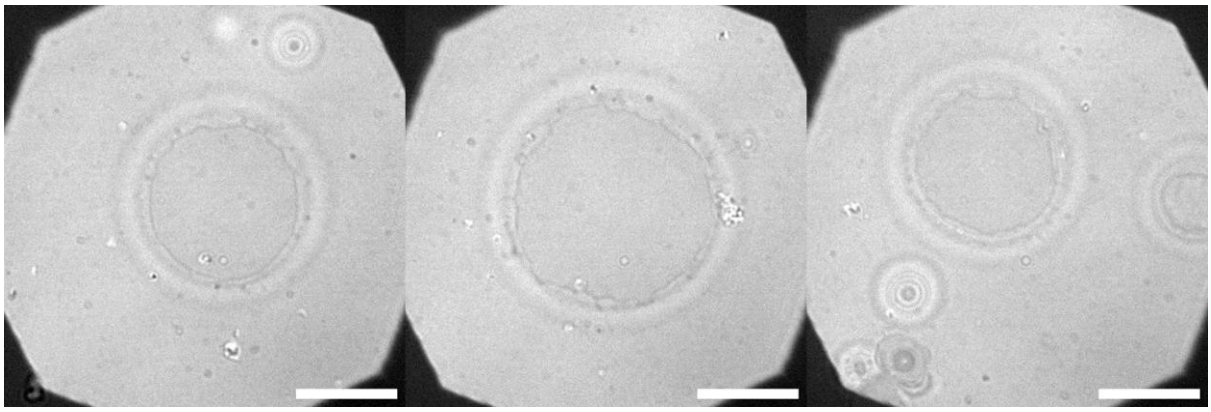

Figure S72. RICM images of GUVs containing 2 mol% pMC and 0.2 mol% pGC. The outer vesicle projection is in line with the maximum vesicle circumference. Scale bar: 10 µm.

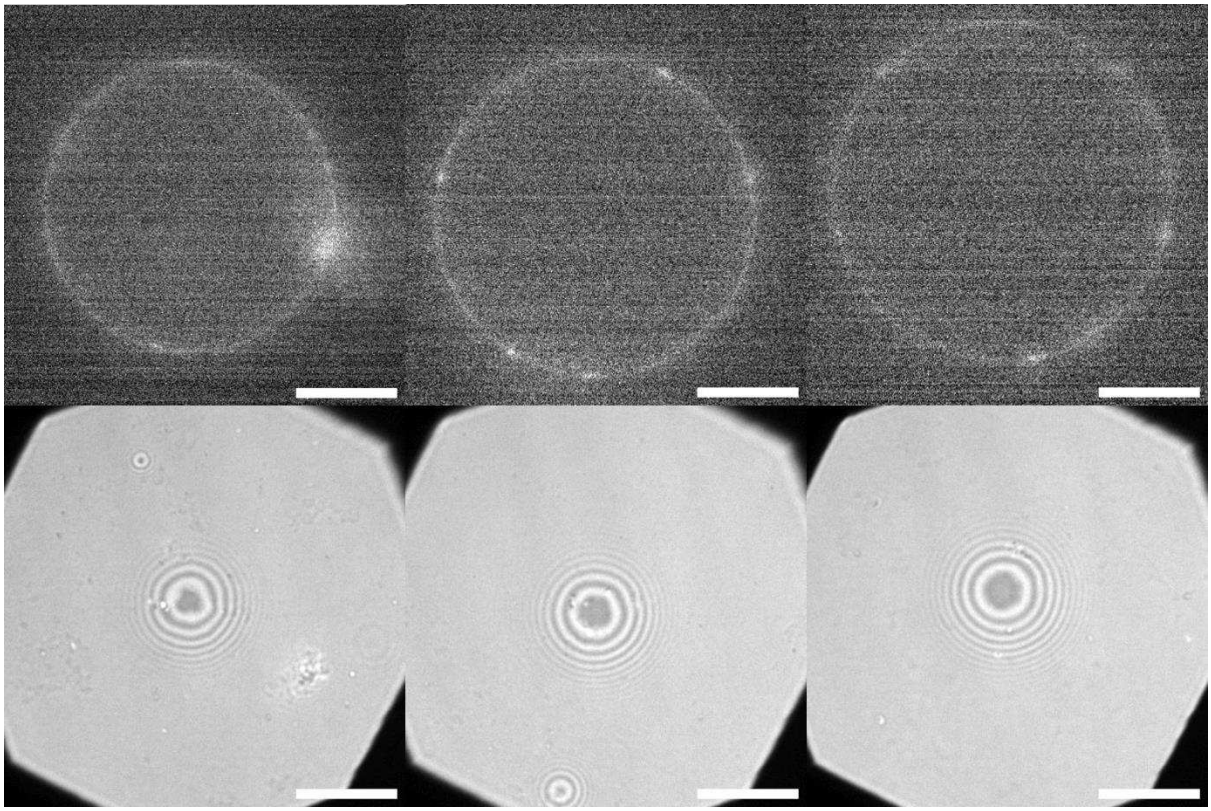

Figure S73. Fluorescence microscopy (top) and RICM images (bottom) of GUVs containing 0.5 mol% MC and 2 mol% pGC. Scale bar: 10 µm.

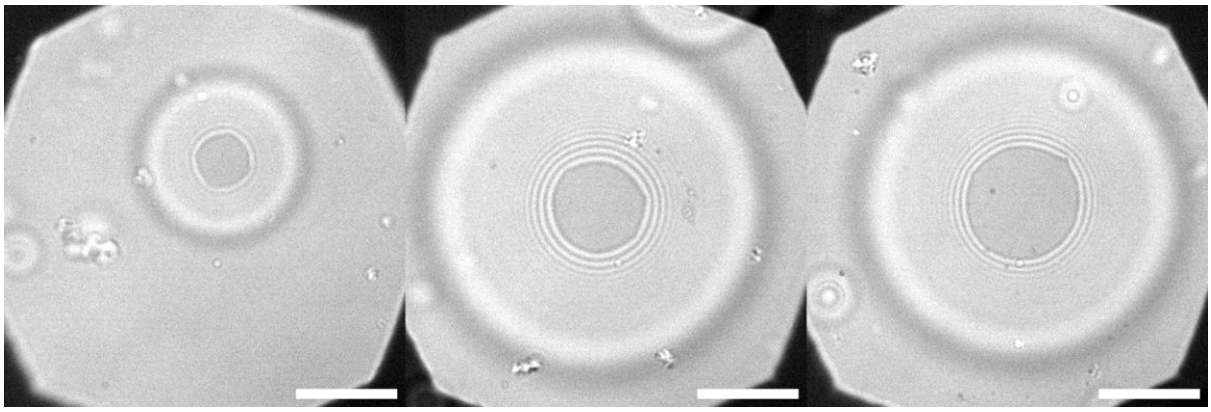

Figure S74. RICM images of GUVs containing 2 mol% MC and 2 mol% pGC. The outer vesicle projection is in line with the maximum vesicle circumference. Scale bar: 10 µm.

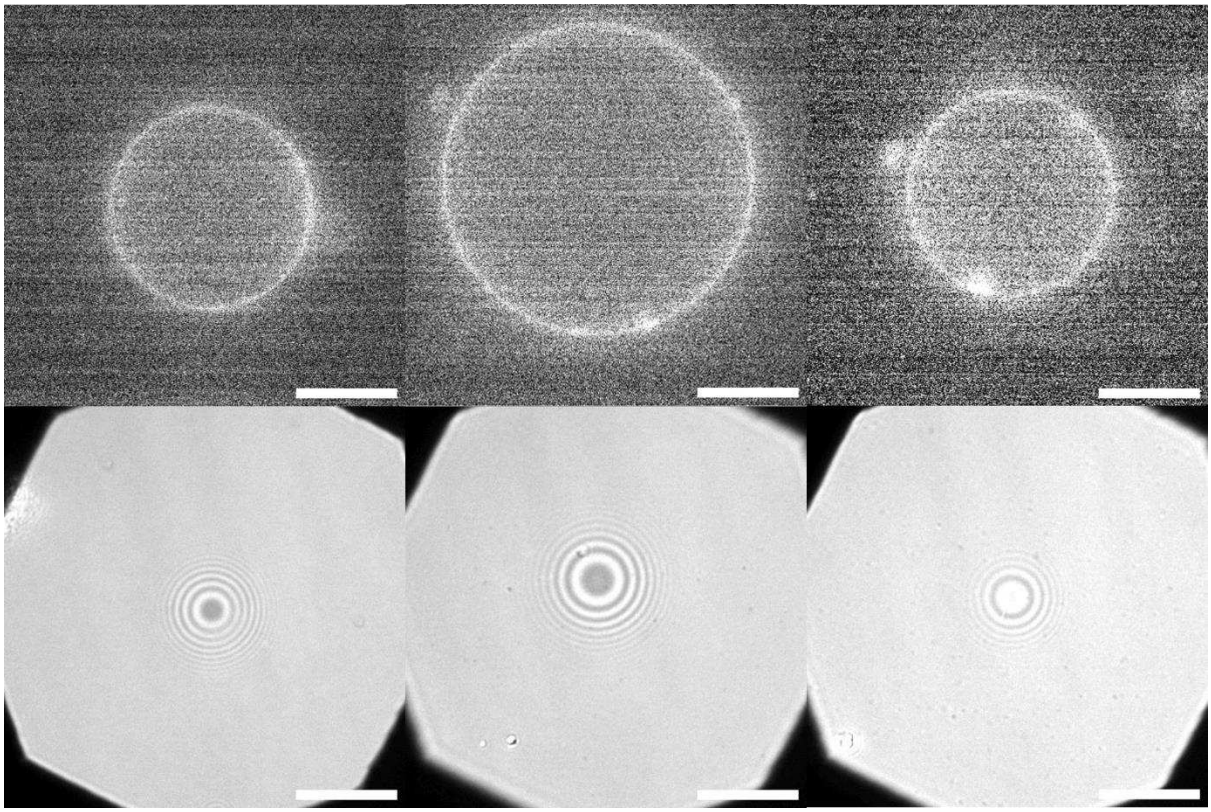

Figure S75. Fluorescence microscopy (top) and RICM images (bottom) of GUVs containing 0.05 mol% pMC and 2 mol% pGC. Scale bar: 10 µm.

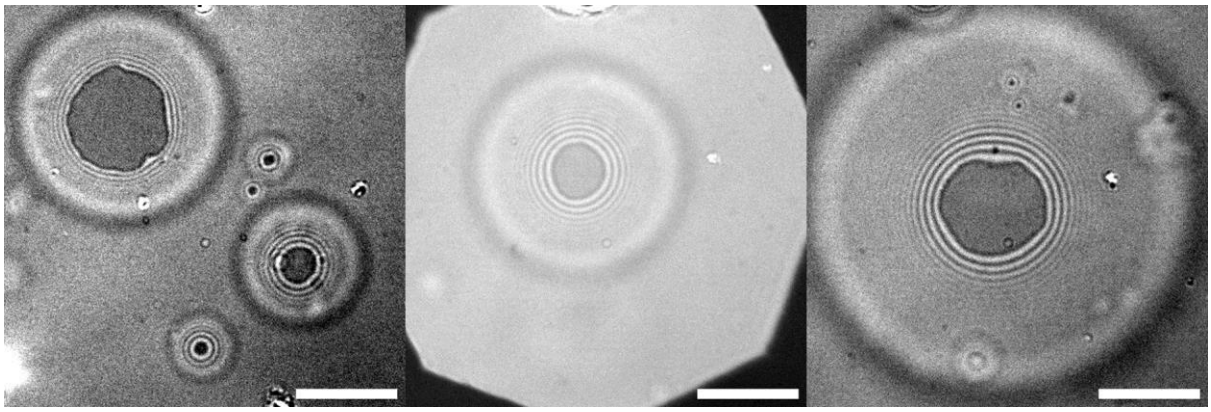

Figure S76. RICM images of GUVs containing 0.2 mol% pMC and 2 mol% pGC. The outer vesicle projection is in line with the maximum vesicle circumference. Scale bar: 10 µm.

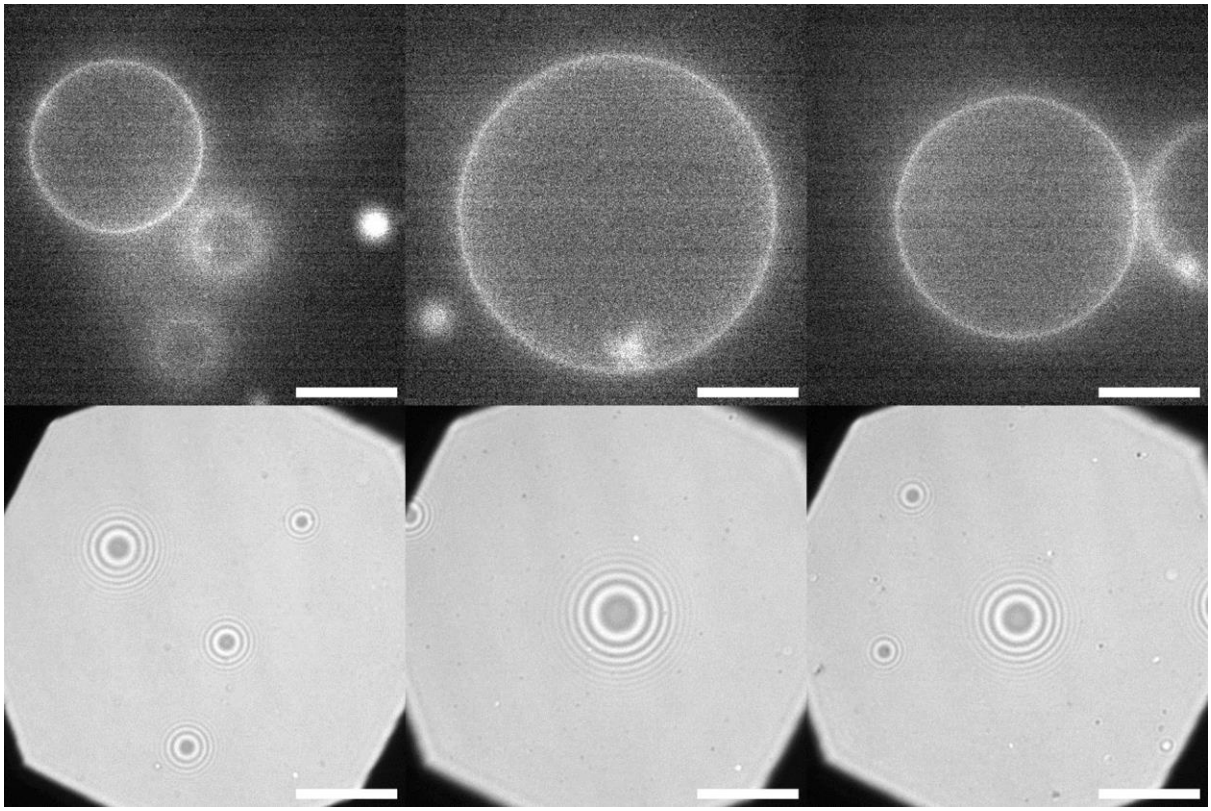

Figure S77. Fluorescence microscopy (top) and RICM images (bottom) of GUVs containing 0.5 mol% pMC and 2 mol% pGC. Scale bar: 10 µm.

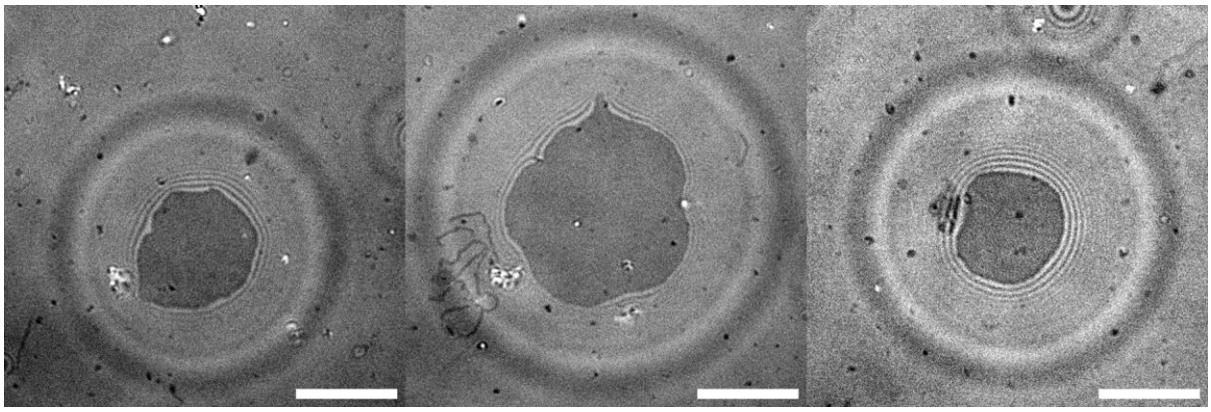

Figure S78. RICM images of GUVs containing 2 mol% pMC and 2 mol% pGC. The outer vesicle projection is in line with the maximum vesicle circumference. Scale bar: 10 µm.

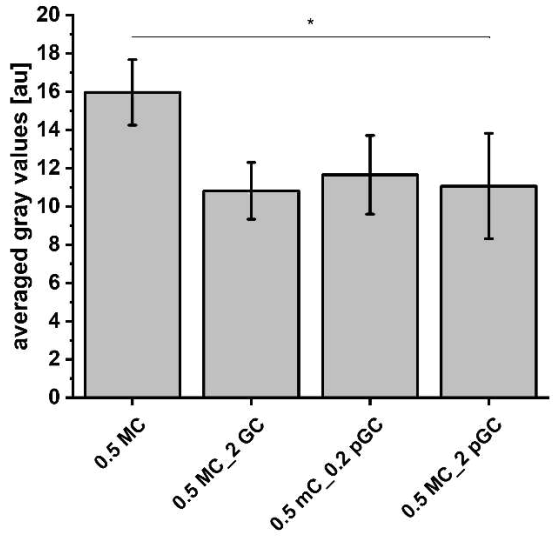

Figure S79. Averaged gray value intensities taken from the fluorescent vesicle membrane of homo- and heteromultivalently glycodecorated GUVs containing 0.5 mol% MC. Data are presented as mean ± SEM for at least 10 GUVs. Gray values do not differ significantly between the heteromultivalent systems, indicating a similar incorporation efficiency of the MC ligand.

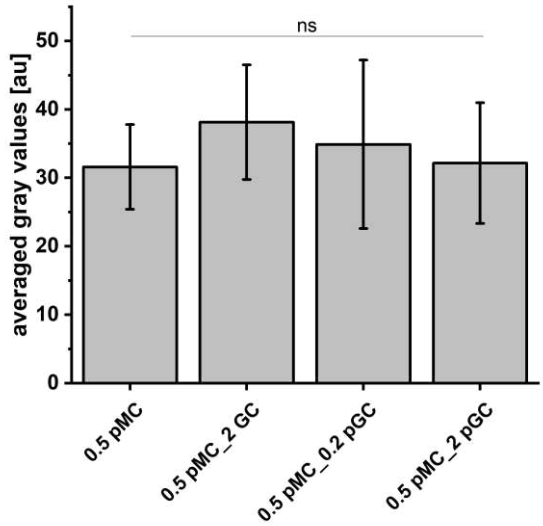

Figure S80. Averaged gray value intensities taken from the fluorescent vesicle membrane of homo- and heteromultivalently glycodecorated GUVs containing 0.5 mol% pMC. Data are presented as mean ± SEM for at least 10 GUVs. Gray values do not differ significantly between the systems, indicating a similar incorporation efficiency of the pMC ligand.

DLS analysis of pMC and pGC

Of note, only the first peak was considered, when averaging the hydrodynamic radius of single polymers in solution. The other peaks are likely aggregates or remaining dust in the sample.

			Size (r.nm):	% Intensity:	St Dev (r.nm...
Z-Average (r.nm):	13.43	Peak 1:	9.216	60.4	3.065
PdI:	0.601	Peak 2:	111.6	37.1	47.18
Intercept:	0.930	Peak 3:	2394	2.5	365.9
Result quality :	Good				

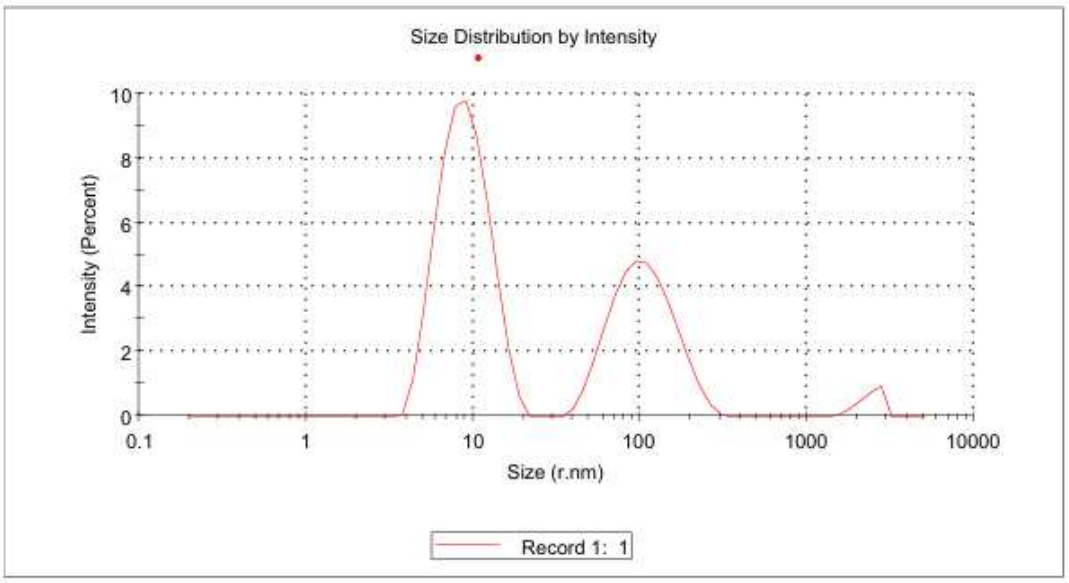

Figure S81. Size Distribution Report of pMC by Intensity (measurement 1).

			Size (r.nm):	% Intensity:	St Dev (r.nm...
Z-Average (r.nm):	13.39	Peak 1:	9.055	61.0	2.918
PdI:	0.599	Peak 2:	98.27	36.5	36.64
Intercept:	0.930	Peak 3:	2527	2.5	289.3
Result quality :	Good				

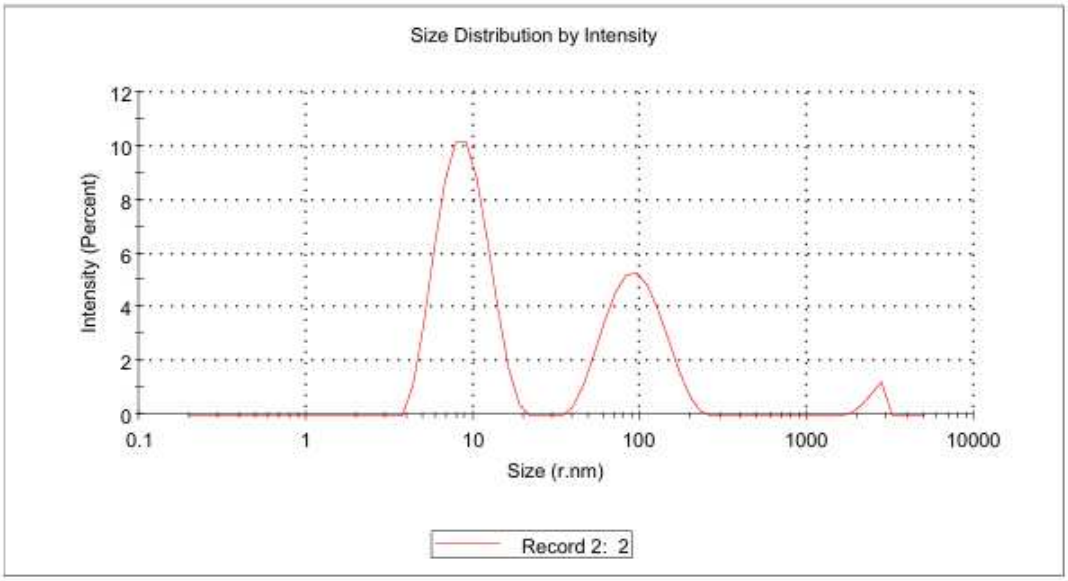

Figure S82. Size Distribution Report of pMC by Intensity (measurement 2).

		Size (r.nm):	% Intensity:	St Dev (r.nm...
Z-Average (r.nm): 13.72	Peak 1:	9.636	62.1	3.636
PdI: 0.633	Peak 2:	107.7	35.5	41.86
Intercept: 0.932	Peak 3:	2582	2.4	248.6
Result quality : Good				

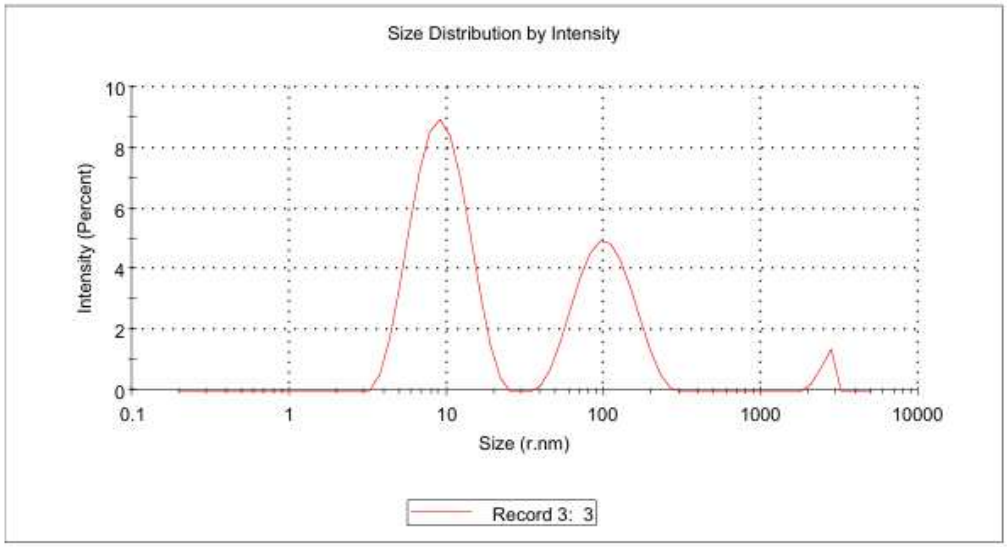

Figure S83. Size Distribution Report of pMC by Intensity (measurement 3).

		Size (r.nm):	% Intensity:	St Dev (r.nm...
Z-Average (r.nm): 12.85	Peak 1:	9.840	68.0	3.483
PdI: 0.421	Peak 2:	112.8	32.0	48.03
Intercept: 0.942	Peak 3:	0.000	0.0	0.000
Result quality : Good				

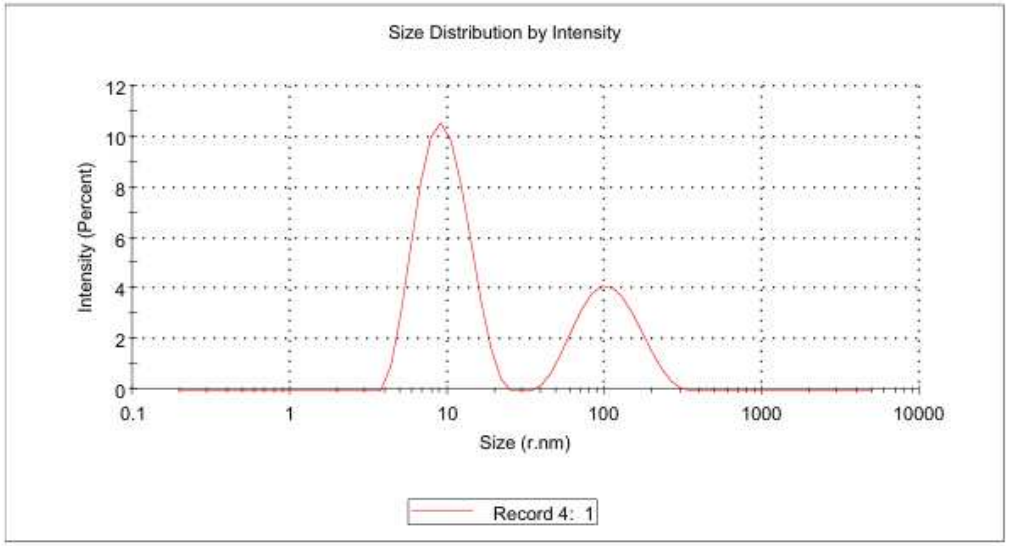

Figure S84. Size Distribution Report of pGC by Intensity (measurement 1).

		Size (r.nm):	% Intensity:	St Dev (r.nm...
Z-Average (r.nm): 12.65	Peak 1:	9.971	68.3	3.916
PdI: 0.418	Peak 2:	123.3	31.7	56.54
Intercept: 0.941	Peak 3:	0.000	0.0	0.000
Result quality : Good				

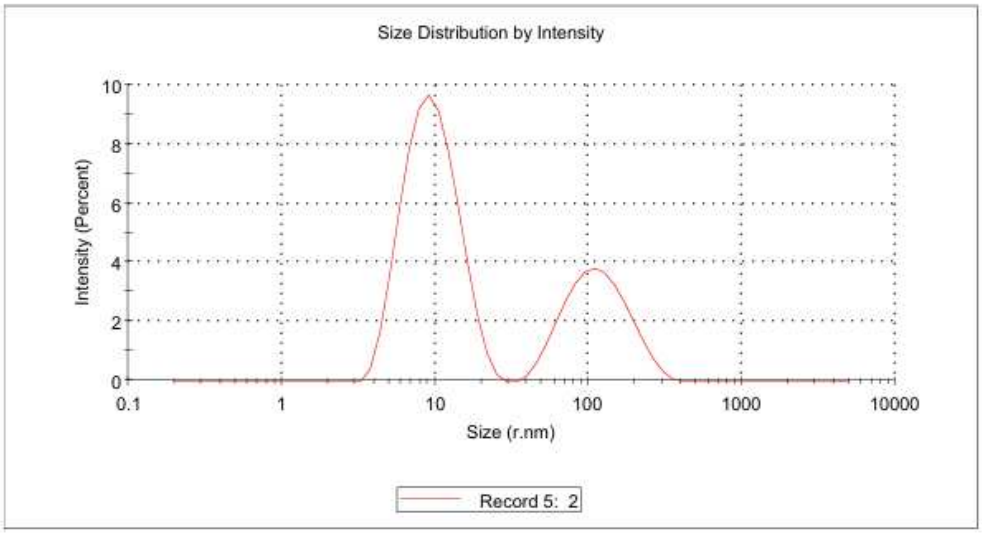

Figure S85. Size Distribution Report of pGC by Intensity (measurement 2).

		Size (r.nm):	% Intensity:	St Dev (r.nm...
Z-Average (r.nm): 12.54	Peak 1:	9.716	66.9	3.923
PdI: 0.416	Peak 2:	109.2	33.1	52.82
Intercept: 0.939	Peak 3:	0.000	0.0	0.000
Result quality : Good				

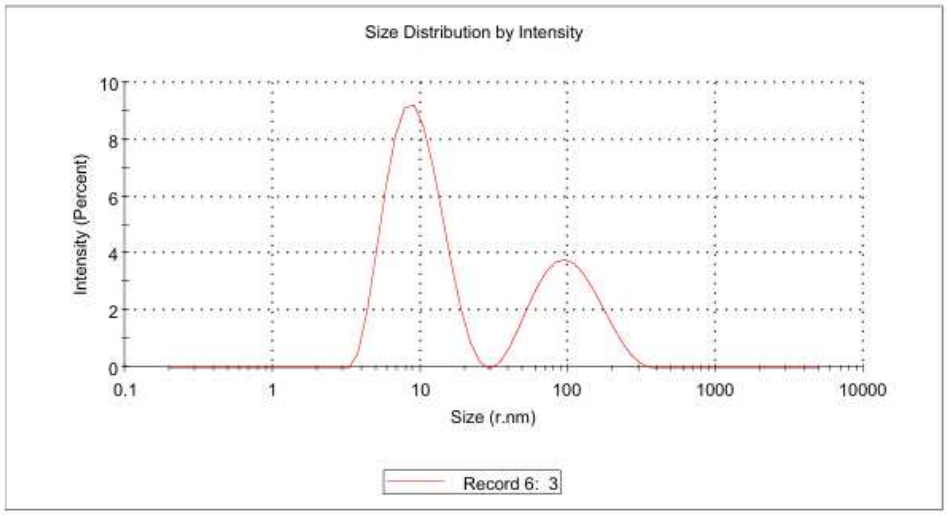

Figure S86. Size Distribution Report of pGC by Intensity (measurement 3).

Supporting Literature

(1) Budde, J.-H. et al. FRET nanoscopy enables seamless imaging of molecular assemblies with subnanometer resolution. *arXiv*, 2108.00024 (2021).

(2) P. O. Gendron, F. Avaltroni, K. J. Wilkinson, Diffusion Coefficients of Several Rhodamine Derivatives as Determined by Pulsed Field Gradient-Nuclear Magnetic Resonance and Fluorescence Correlation Spectroscopy. *Journal of Fluorescence* **18**, 1093-1101 (2008).

3.2 Lipidated Glycan Mimetics for Selective Presentation in Ordered or Disordered Membrane Phases and Complex Glycocalyx Models

Authors: Luca-Cesare Blawitzki, Cornelia Monzel, Stephan Schmidt and Laura Hartmann

Journal: Angewandte Chemie (Int. Ed.)

DOI: doi.org/10.1002/anie.202414847

Impact Factor: 16.6 (as of 2023)

Contribution: Collaborative conceptualization of the work. Establishment of a synthetic route to synthesize lipidated precision glycomacromolecules. Synthesis and purification of lipidated precision glycomacromolecules, as well as characterization of the derived compounds via RP-HPLC-MS, ^{1}H-NMR and HR-ESI-MS. Establishment of a protocol to formulate glyco-decorated phase separating GUVs. Determination of incorporation efficiency. Conduction of fluorescence microscopy experiments. Collaborative evaluation and interpretation of the gathered data as well as visualization of the results. Collaborative writing of the manuscript.

How to cite: *Angew. Chem. Int. Ed.* **2025**, *64*, e202414847
doi.org/10.1002/anie.202414847

Phase Separation **Hot Paper**

Selective Glycan Presentation in Liquid-Ordered or -Disordered Membrane Phases and its Effect on Lectin Binding

*Luca-Cesare Blawitzki, Cornelia Monzel, Stephan Schmidt, and Laura Hartmann**

Abstract: Glycan-protein interactions play a key role in various biological processes from fertilization to infections. Many of these interactions take place at the glycocalyx—a heavily glycosylated layer at the cell surface. Despite its significance, studying the glycocalyx remains challenging due to its complex, dynamic, and heterogeneous nature. This study introduces a glycocalyx model allowing for the first time to control spatial organization and heterogeneity of the glycan moieties. Glycan-mimetics with lipid-moieties that partition into either liquid-ordered (Lo, *lipid rafts*) or liquid-disordered (Ld) phases of giant unilamellar vesicles (GUVs), which serve as simplified cell membrane models mimicking lipid rafts, are developed. This phase-specific allocation allows controlled placement of glycan motifs in distinct membrane environments, creating heteromultivalent systems that replicate the natural glycocalyx's complexity. We show that phase localization of glycan mimetics significantly influences recruitment of protein receptors to the membrane. Glycan-conjugates in the ordered phase demonstrate enhanced lectin binding, supporting the idea that raft-like domains facilitate stronger receptor interactions. This study provides a platform for systematically investigating spatial and dynamic presentation of glycans in biological systems and presents the first experimental evidence that glycan accumulation in lipid rafts enhances receptor binding affinity, offering deeper insights into the glycocalyx's functional mechanisms.

[*] L.-C. Blawitzki, Prof. Dr. S. Schmidt, Prof. Dr. L. Hartmann
Department for Macromolecular Chemistry
University of Freiburg
Stefan-Meier-Straße 31, 79104 Freiburg i.Br., Germany
E-mail: laura.hartmann@makro.uni-freiburg.de

L.-C. Blawitzki
Department for Organic and Macromolecular Chemistry
Heinrich Heine University Duesseldorf
Universitätsstraße 1, 40225 Düsseldorf, Germany

Prof. Dr. C. Monzel
Department for Experimental Medical Physics
Heinrich Heine University Duesseldorf
Universitätsstraße 1, 40225 Düsseldorf, Germany

Introduction

The glycocalyx is a highly heterogeneous and dynamic layer of glycoproteins, proteoglycans, and glycolipids that densely covers the membrane surface of cells. It acts as a physiological barrier, regulating accessibility to adjacent entities, and plays a pivotal role in various cellular functions, including cell-cell-communication, adhesion, signaling and pathogen infection.[1,2] Glycan heteromultivalency plays a pivotal role in various membrane associated cellular processes, enhancing the binding affinity and specificity of protein receptors to the cell surface glycans.[3] Such enhancement in binding has been demonstrated to correlate with induced clustering, cooperative binding or entropic effects.[4–6] Additionally, the organization and dynamics of the glycocalyx are closely connected to the critically discussed existence of locally organized microdomains termed lipid rafts.[7] Lipid rafts are distinct microdomains within the cell membrane that are rich in cholesterol, sphingolipids and specific receptor proteins and are believed to organize and regulate the glycocalyx's structure and function by controlling the distribution of glycoproteins and glycolipids within the glycocalyx.[7–10] Accordingly, lipid rafts have been found to be involved in the recruitment of various receptors and signaling molecules and thus provide a platform for mediating various signaling and adhesion processes.[8,10,11] Recent studies have shown, that the interaction of glycans with sphingolipids in the plasma membrane favors the formation of patterned membrane structures by stabilizing ordered lipid phases through hydrogen bonding with the sphingolipid head groups, similar to the interaction of cholesterol with the lipid moieties of the sphingolipids.[12,13] Furthermore, studies have shown that pathogens, including viruses and bacteria, exploit these signaling mechanisms associated with lipid rafts to enter cells and evade the cell's immune response.[14]

Studying cellular processes related to the glycocalyx and the cellular membrane is challenging due to the high complexity and compositional heterogeneity of living cells and the active remodeling and interactions among cellular membrane components that potentially contribute to raft formation.[2,15] For this reason, libraries of artificial glycan mimetics with lipid membrane anchors have been developed, which are valuable tools for understanding glycocalyx interactions. Mucin-mimetics, for instance, have been used to model the native glycocalyx on erythrocytes to study their impact on sialic acid mediated lectin and virus adhesion.[5]

Although advanced glycocalyx editing in living cells has demonstrated the ability to reveal and observe the complex mechanisms by which the glycocalyx regulates biological processes, manipulating the architecture and glycosylation pattern of glycans with molecular precision in living cells remains a challenging task.[2] Also, the extent to which cellular microdomains are formed by the membrane constituents, membrane mechanics and thermodynamics, or actively modulated processes remains unclear and requires further investigation.[10]

To overcome this challenge, synthetic membrane systems are often used as biomimetic alternatives, providing a powerful tool for studying the glycocalyx in a defined environment. With precise control over the choice of membrane lipids, natural or synthetic glycans and other membrane components, this approach enables the study of carbohydrate-protein or protein-protein interactions and the impact of biophysical membrane properties on the glycosylated proteins and lipids, among others.[16,17] Commonly employed model membranes comprise GUVs, which are cellular sized, spherical lipid bilayers, or supported lipid bilayers (SLBs), which are flat lipid bilayers on a solid support.[18] By tuning the composition of lipids and glycans in these systems, researchers can mimic the cellular environment and investigate interactions between the artificial model glycocalyx and its surroundings.

Fundamental aspects resulting in lipid raft formation are well studied in such biomimetic membrane systems, which are often composed of only a few lipids and can be systematically tuned to alter membrane properties.[10] Phase separation in membranes and the formation of physically distinct microdomains were first detected in synthetic phospholipid membranes composed of a ternary mixture of lipids consisting of cholesterol, a saturated and an unsaturated lipid.[19,20] The saturated lipids and cholesterol segregate into a liquid-ordered phase (Lo), which is physically distinct from the disordered unsaturated lipids (Ld) and is believed to be the equivalent of naturally occurring lipid rafts.[7,21] Such lateral membrane segregation occurs under specific conditions involving a particular lipid composition and cholesterol content, but may also arise from external stimuli such as temperature changes or lipid oxidation through illumination.[10] These model systems allow for visualization and characterization of phase-separated lipid domains, offering valuable insights into the behavior of lipid rafts and their potential influence on the glycocalyx. Preferential partitioning of membrane components into specific phases within model membrane systems has also provided insights into the potential role of lipid rafts in organizing the glycocalyx and influencing its physiological functions. For instance, the recruitment of GPI-anchored proteins or signaling complexes into lipid rafts has been reported.[22] Similarly, *Ewers* et al. have shown, that the recruitment of GM1-ganglioside-binding *simian virus 40* (SV40) particles on phase separating model membranes relies on the interaction of the virus like particles with the glycan headgroup of the ganglioside, but the allocation of the ganglioside into either Lo or Ld is strongly dictated by the type of the acyl moiety employed for membrane anchoring.[23]

However, to the best of our knowledge, little to no effort has yet been dedicated to depicting the natural inhomogeneity regarding local accumulations of glycan mimetics in either ordered or disordered phases in glycocalyx mimetics.[16] To resemble more closely natural cellular membranes, we present here a modular platform to construct artificial phospholipid membranes with distinct local domains that present different glyco-motifs.

To tackle the lack of organizational diversity in biomimetic membrane systems, we applied previously established solid-phase polymer synthesis (SPPoS) to derive four different membrane-anchoring glycan mimetics that differ in their respective glycosylation pattern (mannose (Man) or galactose (Gal) head group) and their membrane tether (saturated or unsaturated fatty acid chains). The different physico-chemical behavior of these glycan mimetics then allows for a favorable partitioning into either liquid-ordered (Lo) or liquid-disordered (Ld) domains in phase separated GUVs. Thereby we aim at creating glycosylation patterns, mirroring the organization of lipid rafts in native cellular membranes, that enable also the partitioning of carbohydrate recoginizing protein receptors into the Ld or Lo domain. In this manner, we provide a simplistic biomimetic platform for investigating the organization and function of the glycocalyx more realistically in terms of microdomain formation and spatial glycan accumulation.

Results and Discussion

Synthesis of Lipid-Tethered Glycan-Mimetics

To initiate our studies, four different lipid-tethered glycan mimetics were synthesized, presenting either Man or Gal moieties, which were functionalized with either a stearyl- or an oleyl-tether for later intercalation into phospholipid membranes. Recently, we established a synthetic strategy, based on previously established protocols and building blocks, to derive synthetic, cholesteryl-anchored precision glycan mimetics via Fmoc-compatible SPPoS.[4,24] The use of tailor-made functional building blocks allows for an iterative assembly of the scaffold, thereby allowing precise control over positioning, density and valency of glycan motifs as well as other functional handles, such as fluorophores for fluorescence imaging. The *N*-terminal introduction of a lipid moiety then enables the subsequent incorporation of the glycan mimetics into phospholipid bilayers.

Unlike our previous studies, we omitted the use of a cholesteryl-moiety as a membrane tether, despite its essential role in native lipid rafts and its widespread acceptance as a convenient membrane anchor for glycan-mimetics.[5,25] *Stuhr-Hansen* et al. demonstrated that cholesteryl-functionalized glycopeptides are excluded from liquid-ordered domains in phase-separating vesicles because the free hydroxyl group of cholesterol needs to

interact with adjacent amides or esters to be efficiently incorporated into highly ordered lipid domains.[16] Instead, we opted to use synthetic analogues of dioleoylphosphatidylcholine (DOPC) and distearylphosphatidylcholine (DSPC), which are commonly employed lipids to prepare model membranes mimicking native cellular membranes and should allow to tune the glycan-mimetics localization to the Ld and Lo phase, respectively.[10,26] Most natural glycolipids, tend to preferentially localize to lipid rafts due to their saturated ceramide backbone.[27] However, to study the influence of presenting glycan-mimetics in both phases (Ld and Lo), we prepared two different anchor moieties. Specifically, stearic and oleic acid, both C_{18}-fatty acids, were employed as hydrophobic lipid-tethers. Stearic acid, with its saturated alkane-chain, promotes a more rigid packing of glycan mimetics in phospholipid membranes and is hence prone to localize to the Lo phase. Conversely, oleic acid is a monounsaturated omega-9 fatty acid with a cis-double bond geometry likely disrupting the tight packing of the glycan-conjugates and lipids, making the membrane more fluid and less prone to spatial organization. Hence, oleic acids are more likely to localize to the Ld phase. 2,3-Diaminopropionic acid (Dap) was selected as the lipid junction due to its (i) resemblance to the composition of native phosphoglycerolipids and (ii) its ability to introduce fatty acids via amide bond formation, thus eliminating the use of labile ester moieties. Furthermore, it resembles naturally occurring glycosphingolipids, which are highly accumulated in natural lipid rafts due to their ability to engage in hydrogen bonding, facilitating tight packing of these molecules.[12,28]

Though fluorescent dyes facilitate the visualization and localization of phospholipid membrane constituents, we omitted fluorescent labels in our glycan mimetics. The hydrophobic nature of fluorophores can strongly affect the physical behavior of membrane tethering molecules.[29] Instead, we relied on fluorescently labeled lectins *Concanavalin A* (ConA, with high specificity towards α-Man-residues) and *Ricinus Communis Agglutinin* (RCA, with high specificity towards β-Gal-moieties) to bind specifically to the carbohydrate moieties in our glycan mimetic structures, thus visualizing their localization within the lipid membrane.

The assembly of the backbone started from commercially available TentaGel S RAM resin, employing iterative assembly of building blocks bearing a free carboxylic acid and an Fmoc-protected primary amine via stepwise Fmoc-deprotection and coupling procedures. Four triple bond diethylenetriamine succinyl (TDS) building blocks, carrying an alkyne functionality in their side chain for later glycosylation via copper(I)-catalyzed alkyne-azide cycloaddition (CuAAC) were installed followed by introducing three ethylene glycol diamine succinyl (EDS) units as hydrophilic spacer. After assembly of the scaffold, CuAAC was employed to functionalize the backbone with either Man or Gal via their respective acetylated and azido-functionalized derivatives. Finally, the solid-supported glycan-head group was *N*-terminally functionalized with either two stearyl- or oleyl-moieties via amide bond formation, joined by an Fmoc-Dap-(Fmoc)–OH residue (Figure 1). After the complete assembly of the amphiphilic glycan mimetics, the carbohydrate moieties were deprotected under Zemplén conditions, cleaved off the resin, collected via precipitation, and further purified by diafiltration.

In total, four different lipidated glycan mimetics were synthesized, each comprising a tetravalent glyco-head group (Man or Gal) and either a saturated (DSDap) or unsaturated (DODap) lipid moiety for subsequent membrane anchoring (Figure 1B). All structures were confirmed by RP-HPLC-MS, ^{1}H NMR and HR-ESI-MS (see Supporting Information).

Preparation of Phase Separating GUVs and Incorporation of Glycan Mimetics

After the successful synthesis of the first set of glycan mimetics, we sought to test their functionality in phase-separated phospholipid membranes. Phase separation in biomimetic membranes can be triggered by temperature changes, illumination, or osmotic pressure gradients.[10,30] Mimicking natural lipid-raft-like domains in synthetic membrane systems can be achieved by applying ternary mixtures of cholesterol, a saturated (high melting point) lipid and an unsaturated (low melting point) lipid.[10,31] Under suitable conditions, the membrane segregates into physically distinct microdomains, i.e., cholesterol and the saturated lipids form a tightly packed and more viscous liquid ordered phase (Lo), resembling lipid rafts in native phospholipid membranes, while unsaturated lipids separate into a more fluid, disordered phase (Ld).[10,31,32]

We prepared our GUVs via electroformation from a ternary lipid mixture consisting of DOPC, an unsaturated lipid, DSPC, a saturated lipid, and cholesterol in a molar ratio of 2:1:1. This mixture results in well-studied model membrane systems for investigating putative raft formation.[19,33] 16:0 Liss Rho PE was used as Ld-domain marker to visualize raft formation via fluorescence microscopy.

The GUVs were in the range of 10–50 μm in diameter and displayed selective areas of lipid membrane staining, indicating successful phase separation. As expected, the lipid composition of our GUVs led to segregation into a major DOPC-rich Ld domain (Figure 2A, blue arrows) and a minor DSPC- and cholesterol-rich Lo domain (Figure 2A, red arrows). Cholesterol interacts more thermodynamically favorably with the saturated DSPC than with the unsaturated DOPC, counteracting the entropic tendency of random mixing of the lipids throughout the membrane.[34] Eventually, the thermodynamic interaction energy between cholesterol and saturated lipids outweighs the entropically favorable random mixing of lipids, resulting in the formation of stable lateral domains within the membrane.[35] Phase assignment was verified using the membrane dye 16:0 Liss Rho PE, which preferentially partitions out of Lo phases into Ld phases.[36]

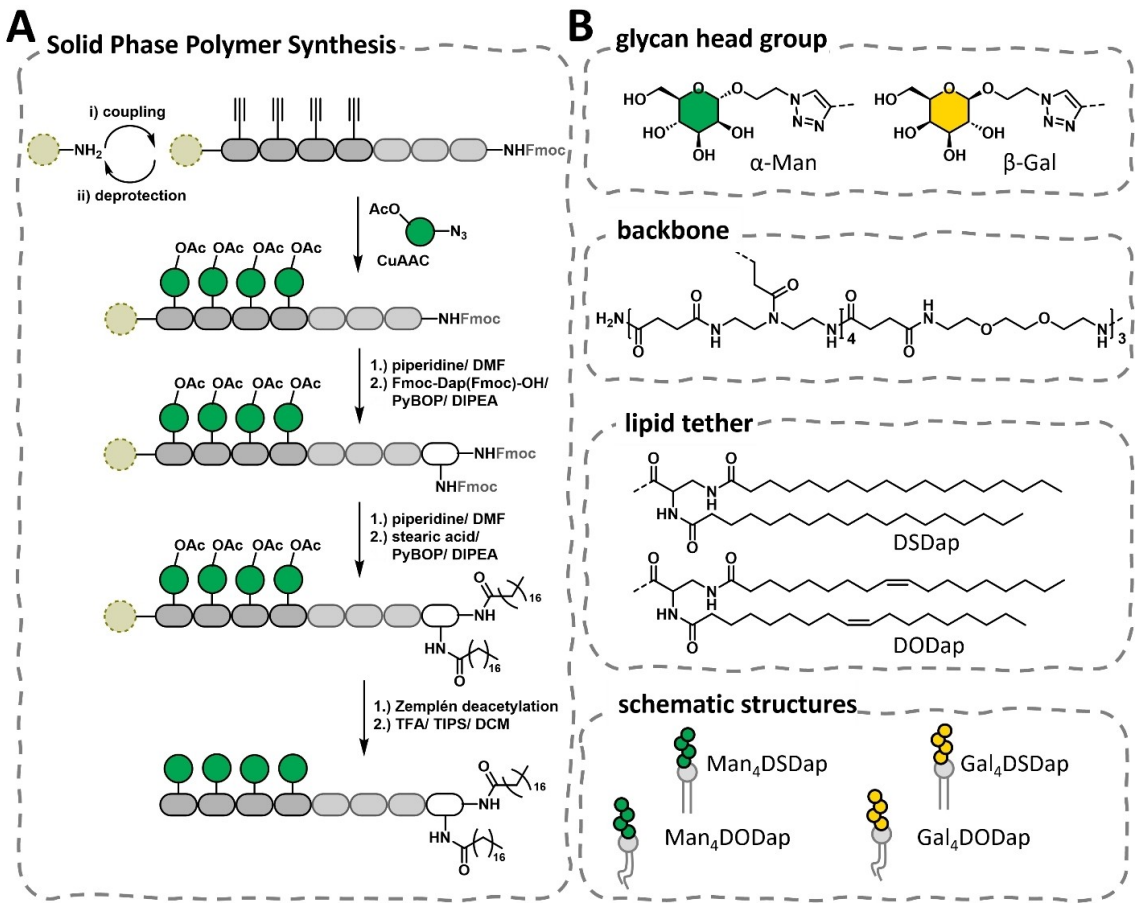

Figure 1. **A**: Schematic presentation of the Solid Phase Polymer Synthesis (SPPoS) of Man_4DSDap. **B**: Chemical structures and schematic structures of the synthesized lipid-tethered glycan-mimetics.

In order to introduce glycan mimetics into the phase-separated GUVs, 1 mol % of Man_4DSDap or Gal_4DSDap and 4 mol % (to account for the extent of the Ld phase) of Man_4DODap or Gal_4DODap were mixed with the matrix lipid composition before preparing the GUVs as described. After cooling to ambient temperature, the vesicles were incubated with 200 nM ConA-AF647 (for Man-decorated vesicles) or 200 nM RCA-FITC (for Gal-decorated vesicles) for 1 hour before imaging. The homomultivalently glyco-decorated vesicles displayed a phase separation topology comparable to the control GUVs without added glycan mimetics, with non-fluorescent Lo domains and homogeneously fluorescent Ld domains.

For the saturated ligands Man_4DSDap (Figure 2B) and Gal_4DSDap (Figure 2D), the fluorescence of membrane-recruited lectins ConA-AF647 or RCA-FITC does not colocalize with the fluorescence of the Ld marker 16:0 Liss Rho PE, which indicates that the glycan mimetics functionalized with the saturated lipid-tether partition into the highly ordered Lo domain of the vesicles. Conversely, the ligands functionalized with the unsaturated lipid-anchor, i.e., Man_4DODap (Figure 2C) and Gal_4DODap (Figure 2E), partition preferentially into the Ld domains of the vesicle membrane, as the respective fluorescence of the membrane-bound lectin colocalizes with the fluorescence of 16:0 Liss Rho PE.

Heteromultivalent Spatially Resolved Presentation of Glycan Mimetics in GUVs

To mimic local inhomogeneities in constituent distribution of the glycocalyx, we then sought to construct heteromultivalent membrane mimetics where both domains, i.e., Lo and Ld, are decorated with distinct glycan mimetics. We prepared lipid mixtures containing both, the saturated Man_4DSDap (1 mol %), and the unsaturated Gal_4DODap (4 mol %), to incorporate both ligands into the GUVs and formulated the vesicles as described previously. The GUVs were then incubated with 200 nM ConA-AF647 or 200 nM RCA-FITC.

The formed GUVs again displayed a well-defined phase separated topology. Vesicles incubated with RCA-FITC showed recruitment of the Gal-binding lectin on the Ld phase (Figure 3A), while incubation with ConA-AF647 displayed lectin fluorescence exclusively colocalizing with the Lo domain (Figure 3B). Simultaneous incubation with RCA-FITC and ConA-AF647 showed homogeneous membrane staining in either channel (FITC or

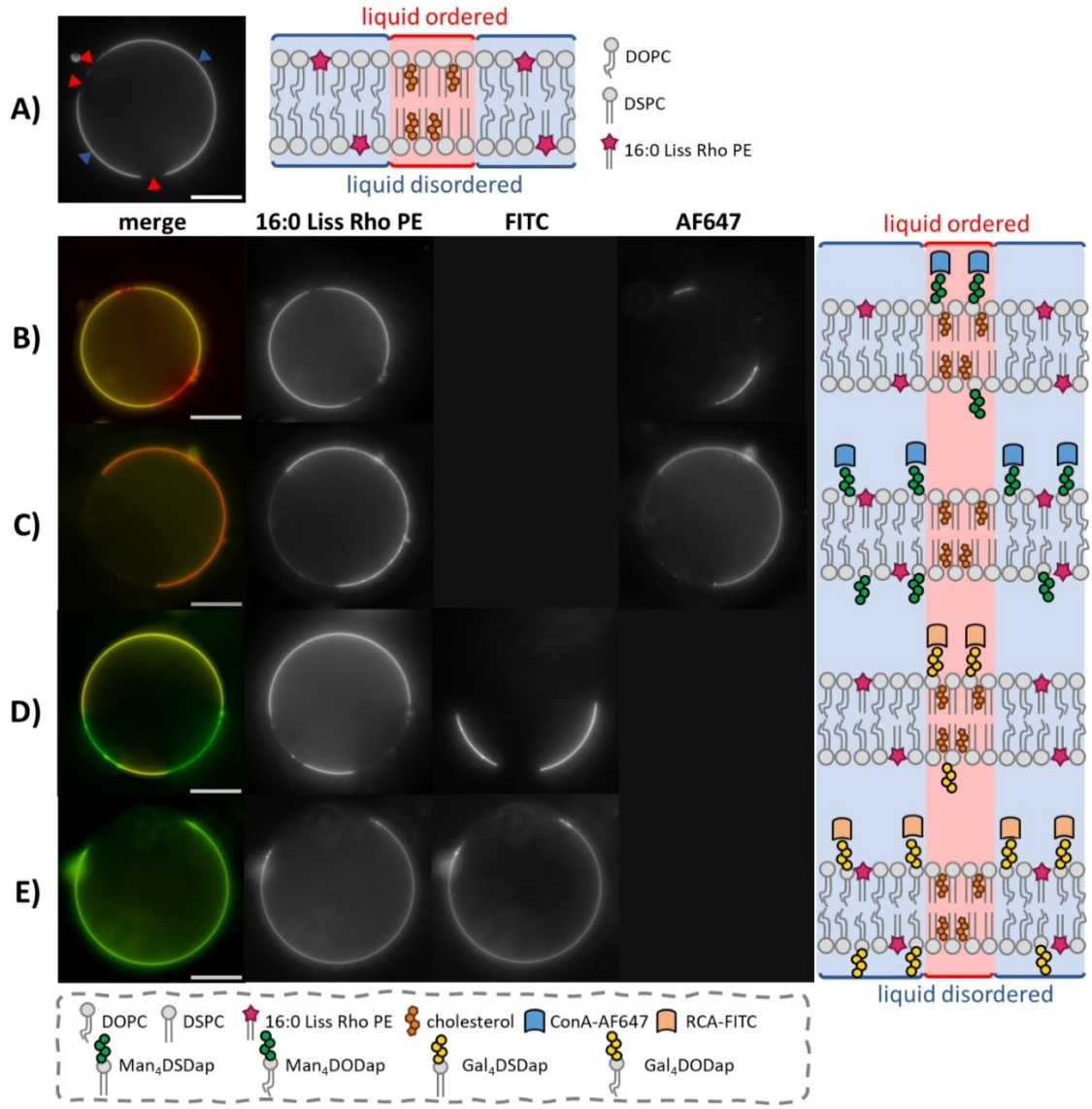

Figure 2. **A)**: Control GUVs prepared from DOPC:DSPC:cholesterol (2:1:1) display phase separation into Ld (blue arrows) and Lo (red arrows) domains as evidenced by the partitioning of the Ld marker Liss Rho PE into selective areas. **B)**: Phase separating GUVs functionalized with 1 mol% Man_4DSDap after incubation with ConA-AF647. Lectin fluorescence (red) does not colocalize with the fluorescence of the Ld marker (yellow), indicating the localization of ligands in the Lo domain of the GUVs. **C)**: Phase separating GUVs functionalized with 4 mol% Man_4DODap after incubation with ConA-AF647. Lectin fluorescence (red) colocalizes with the fluorescence of the Ld marker (yellow), indicating localization of the ligands in the Ld domain of the GUVs. **D)**: Phase separating GUVs functionalized with 1 mol% Gal_4DSDap after incubation with RCA-FITC. Lectin fluorescence (green) does not colocalize with the fluorescence of the Ld marker (yellow), indicating localization of the ligands in the Lo domain of the GUVs. **E)**: Phase separating GUVs functionalized with 4 mol% Gal_4DODap after incubation with RCA-FITC. Lectin fluorescence (green) colocalizes with the fluorescence of the Ld marker (yellow), indicating localization of the ligands in the Ld domain of the GUVs. Scale bars: 10 μm.

AF647) (see Figure S15C). Since the individual staining with either ConA or RCA clearly shows partitioning of Man_4DSDap into the Lo phase and Gal_4DODap into the Ld phase, we attribute this to non-specific interactions between the ConA and the RCA.

As a proof of concept, we also prepared phase separating GUVs displaying respectively 0.5 mol% Man_4DSDap and 0.5 mol% Gal_4DSDap in the Lo phase and 4 mol% Man_4DODap in the Ld phase. Incubation with ConA-AF647 showed homogeneous lectin fluorescence along the vesicle membrane (see Figure S16), corresponding to Man-ligands being present in both, the Ld and the Lo phase, while fluorescence of RCA-FITC strictly colocalized only with the Lo domain of the GUVs (see Figure S17), as was shown before. This demonstrates the general feasibility of our approach, enabling the formation of spatially separated heteromultivalent glycocalyx models but also the formation of locally resolved heteromultivalent domains.

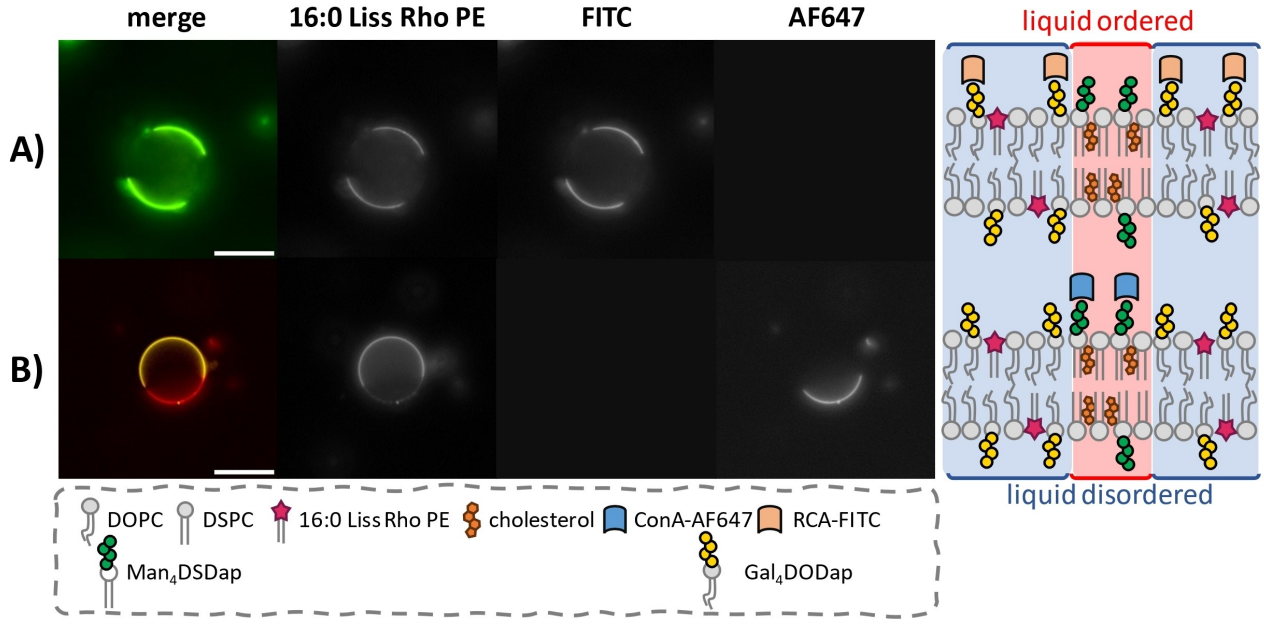

Figure 3. Heteromultivalent glycan-decoration of phase-separated GUVs and lectin binding. **A)**: RCA-FITC (green) binds to the unsaturated Gal_4DODap ligands, colocalizing with the Ld marker 16:0 Liss Rho PE (yellow). **B)**: ConA-AF647 fluorescence (red) does not colocalize with the Ld marker (yellow), indicating partitioning of the saturated Man_4DSDap ligands into the Lo domain. Scale bars: 10 μm.

Phase-Dependent Lectin Binding in GUVs

Next, we quantitatively analyzed the effect of phase separation on ligand-receptor mediated protein binding to the vesicle membrane. We prepared phase separating vesicles comprising either 1 mol % of the saturated Man_4DSDap or 1 mol % of the monounsaturated Man_4DODap.

To assess the impact of ligands on protein recruitment, it was essential to first quantify the number of ligands incorporated into the GUV membrane. To evaluate the incorporation efficiency of Man_4DSDap and Man_4DODap, respectively, phenol sulfuric acid (PSA) method was employed (see Supporting Information for details). The concentration of ligands in solution before vesicle formation and in the supernatant after formation were measured to determine the incorporation efficiency. Post-formation, about 19 % of Man_4DSDap and 2 % of Man_4DODap remained in the supernatant, showing that the unsaturated ligands integrate more efficiently into the GUV membrane than the saturated ligands (Figure 4C). While no explicit information on different incorporation efficiencies of membrane constituents regarding their respective lipid anchor are reported, we hypothesize, that the lower incorporation of the saturated DSDap ligand might be due to a potential saturation of the highly ordered Lo phase, excluding further ligands from incorporating into the vesicle membrane.

The glyco-decorated vesicles were incubated with 200 nM ConA-AF647 for one hour before imaging. As observed previously, the ConA-fluorescence on the Man_4DSDap vesicles colocalized with the Lo (i.e. non-fluorescent) domain of the vesicle membrane, while on the Man_4DODap vesicles, ConA colocalized with the Ld marker 16:0 Liss Rho PE.

The ConA fluorescence on the Man_4DSDap vesicles was noticeably more pronounced than on the Man_4DODap vesicles. Also, while the ConA fluorescence was rather homogeneously distributed along the Lo phases of the vesicles functionalized with Man_4DSDap, it only occurred scarcely and in local clusters on vesicles functionalized with Man_4DODap (Figure 4A). To quantify the differences in lectin binding efficiency, we plotted averaged intensity profiles of confocal images of the glyco-decorated GUVs over the angle of the respective membrane domains (Ld or Lo) as shown in the inset in Figure 4A (Figure 4B).

Based on the mean maximum fluorescence intensities, ligands accumulated in the Lo phase of the vesicles (though displaying roughly 20 % less ligand overall) led to an increase in lectin binding by 65 % on average compared to the ligands partitioning into the Ld phase (Figure 4B).

Multivalent binding is favorable when the overall free energy of the system ($\triangle G$) is reduced, which is particularly true for membrane constituents that can be organized in a spatial arrangement.[37] The involvement of the membrane bound glyco-ligands in lectin-binding generally results in a loss of translational freedom, thus a decrease in entropy ($\triangle S$). This decrease in entropy is especially high for ligands that are localized in the liquid disordered phase and can diffuse relatively freely. For ligands in the Lo phase, this cost in entropy has already been paid through the accumulation in a thermodynamically favored ordered state, hence their dynamic behavior does not change significantly upon binding and, consequently, the entropic cost for multivalent

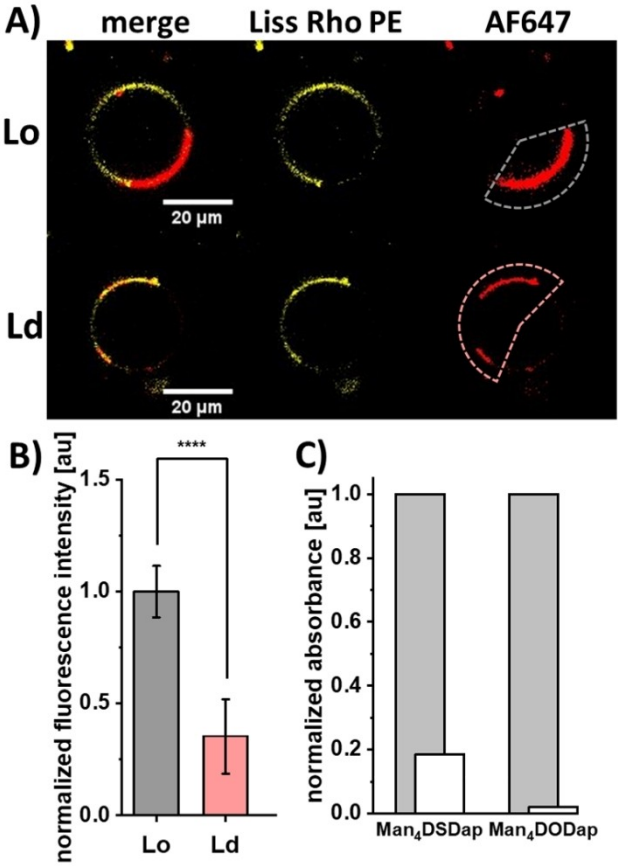

Figure 4. **A)**: Confocal images of phase separated GUVs containing either 1 mol% Man_4DSDap (accumulating in the Lo domain) or 1 mol% Man_4DODap (accumulating in the Ld domain along with 16:0 Liss Rho PE (yellow fluorescence)) after incubation with 200 nM ConA-AF647 (red fluorescence). Contrast adjusted for better visibility. **B)**: Mean radial fluorescence intensity values averaged over the respective membrane domain angle (as shown in the inset in **A)**). Normalized data are presented as mean ± SEM for $n = 14$ experimental replicates and were evaluated using one-way ANOVA followed by Bonferroni correction (****: $p < 0.001$). **C)**: Normalized absorption values of the employed ligands determined via sulfuric acid-phenol assay. The grey bars correspond to the respective absorption of ligands before vesicle formation, while the white bars correspond to non-incorporated ligands after vesicle formation. Measurements were conducted in triplicates and are presented as means.

complexation is effectively lower.[38] Moreover, the high local density of ligands in the Lo phase increases the association constant (k_{on}) of the lectin-carbohydrate binding and at the same time, the dissociation constant (k_{off}) decreases, since rebinding of the multivalent lectin is facilitated through the high density of accessible annual ligands, which shifts the resulting binding equilibrium to lower K_d values ($K_d = k_{off}/k_{on}$).[39]

To substantiate this hypothesis, we also performed inhibition studies on the GUVs containing 1 mol% Man_4DSDap or Man_4DODap, respectively. We incubated the vesicles with 200 nM ConA-AF647 in the presence of increasing concentrations of MeMan as inhibitor and measured the radial fluorescence intensity of the lectin along the respective membrane phase (Figure 4). Indeed, we found that lectin binding associated with the Ld phase was completely inhibited at a concentration of 3 mM MeMan (see Figure S33), while for lectin binding associated with the Lo phase it required 5 mM MeMan to completely inhibit lectin binding (see Figure S26).

These findings are consistent with the well-accepted function of lipid rafts, which selectively concentrate and recruit distinct membrane constituents (e.g. proteins or gangliosides) and facilitate multivalent ligand-receptor mediated interactions (e.g. signaling or adhesion).[40]

Conclusions

Using SPPoS of sequence-defined glycomacromolecules we developed lipid-tethered glycan mimetics reconstructing membrane anchoring moieties of glycosphingolipids. The choice of lipid tether allowed for specific introduction of glycan mimetics into either ordered or non-ordered phases of synthetic membranes, such as GUVs. This advancement allowed us to control the spatial organization of glycan mimetics in membranes. By combining glycan mimetics presenting different carbohydrate moieties, we could create heteromultivalent, spatially controlled glycocalyx models. To the best of our knowledge, this is the first example of such complex yet controlled glycocalyx model systems. Furthermore, we demonstrated that the localization of glycan mimetics also affects lectin binding. Quantitative studies on protein binding to ligands in either the liquid-ordered or -disordered phase revealed that the local accumulation of ligands into ordered membrane domains increased receptor recruitment by on average 65%. This highlights the importance of naturally occurring lipid rafts regarding glycan mediated interactions, such as signaling and pathogen infection, and will now be further explored to address specific questions in the role of glycan localization in lipid rafts in viral attachment and uptake.

We believe that the predictable partitioning behavior of our synthetic glycan mimetic lipid conjugates is a valuable property for constructing even more complex biomimetic membranes including other membrane constituents such as proteins. We envision that this strategy has the potential to incorporate other synthetic glycans and bioligands as well as non-natural structures into phospholipid membranes. This will facilitate the study of distribution, organization, and accessibility effects of membrane-associated ligand-receptor binding, in both synthetic and potentially also biological membranes.

Supporting Information

The authors have cited additional references within the Supporting Information.[41,42]

Acknowledgements

The authors thank the CeMSA@HHU (Center for Molecular and Structural Analytics @ Heinrich Heine University) for recording the mass-spectrometric and the NMR-spectroscopic data. LH, LCB and CM acknowledge partial financial support of the Deutsche Forschungsgemeinschaft (DFG, German Research Foundation) through CRC1208 'Identity and Dynamics of Membrane Systems' (A11 and A12, Project ID 267205415). CM further acknowledges financial support via the 'Freigeist fellowship' of Volkswagen Foundation and of the Deutsche Forschungsgemeinschaft (DFG, German Research Foundation) through CRC1535 'Microbial Networks' (A09, Project ID 458090666). This work is supported partially by ERC grant (GLYMCE, 101088228). Funded by the European Union. Views and opinions expressed are however those of the author(s) only and do not necessarily reflect those of the European Union or the European Research Council Executive Agency. Neither the European Union nor the granting authority can be held responsible for them. Open Access funding enabled and organized by Projekt DEAL.

Conflict of Interest

The authors declare no conflict of interest.

Data Availability Statement

The data that support the findings of this study are available in the supplementary material of this article.

Keywords: glycocalyx · glycoconjugates · solid-phase synthesis · phase separation · vesicles

[1] a) S. Reitsma, D. W. Slaaf, H. Vink, M. A. M. J. van Zandvoort, M. G. A. oude Egbrink, *Pfluegers Arch.* **2007**, *454*, 345; b) C. A. Foote, R. N. Soares, F. I. Ramirez-Perez, T. Ghiarone, A. Aroor, C. Manrique-Acevedo, J. Padilla, L. Martinez-Lemus, *Comprehensive Physiology* **2022**, *12*, 3781.
[2] S. C. Purcell, K. Godula, *Interface Focus* **2019**, *9*, 20180080.
[3] a) J. L. Jiménez Blanco, C. Ortiz Mellet, J. M. García Fernández, *Chem. Soc. Rev.* **2013**, *42*, 4518; b) A. Bernardi, J. Jiménez-Barbero, A. Casnati, C. de Castro, T. Darbre, F. Fieschi, J. Finne, H. Funken, K.-E. Jaeger, M. Lahmann, et al., *Chem. Soc. Rev.* **2013**, *42*, 4709; c) H.-K. Choi, D. Lee, A. Singla, J. S.-I. Kwon, H.-J. Wu, *Glycobiology* **2019**, *29*, 397; d) M. González-Cuesta, C. Ortiz Mellet, J. M. García Fernández, *Chem. Commun.* **2020**, *56*, 5207.
[4] L.-C. Blawitzki, N. Bartels, L. Bonda, S. Schmidt, C. Monzel, L. Hartmann, *Biomacromolecules* **2024**, *25*, 5979.
[5] D. J. Honigfort, M. O. Altman, P. Gagneux, K. Godula, *Proc. Natl. Acad. Sci. USA* **2021**, *118*.
[6] P. J. Coombs, R. Harrison, S. Pemberton, A. Quintero-Martinez, S. Parry, S. M. Haslam, A. Dell, M. E. Taylor, K. Drickamer, *J. Mol. Biol.* **2010**, *396*, 685.
[7] H.-M. Wu, Y.-H. Lin, T.-C. Yen, C.-L. Hsieh, *Sci. Rep.* **2016**, *6*, 20542.
[8] M. L. Kraft, *Mol. Biol. Cell* **2013**, *24*, 2765.
[9] D. Lingwood, H.-J. Kaiser, I. Levental, K. Simons, *Biochem. Soc. Trans.* **2009**, *37*, 955.
[10] V. Rathe, D. Kuckla, C. Monzel, in *Adv. Biomembr. Lipid Self-Assem.* **2021**, pp. 31–66.
[11] D. A. Zacharias, J. D. Violin, A. C. Newton, R. Y. Tsien, *Science* **2002**, *296*, 913.
[12] P. M. Winkler, F. Campelo, M. I. Giannotti, M. F. Garcia-Parajo, *J. Phys. Chem. Lett.* **2021**, *12*, 1175.
[13] A. B. Subramaniam, G. Guidotti, V. N. Manoharan, H. A. Stone, *Nat. Mater.* **2013**, *12*, 128.
[14] a) R. Kulkarni, E. A. C. Wiemer, W. Chang, *Front. Immunol.* **2021**, *12*, 815020; b) S. Aigal, J. Claudinon, W. Römer, *Biochim. Biophys. Acta* **2015**, *1853*, 858; c) D. W. Zaas, M. Duncan, J. Rae Wright, S. N. Abraham, *Biochim. Biophys. Acta* **2005**, *1746*, 305.
[15] Y. Zeng, J. M. Tarbell, *PLoS One* **2014**, *9*, e86249.
[16] N. Stuhr-Hansen, J. Madl, S. Villringer, U. Aili, W. Römer, O. Blixt, *ChemBioChem* **2016**, *17*, 1403.
[17] S. Majeed, A. B. Ahmad, U. Sehar, E. R. Georgieva, *Membranes* **2021**, *11*.
[18] a) R. Dimova, *Annu. Rev. Biophys.* **2019**, *48*, 93; b) L. Coen, D. A. Kuckla, A. Neusch, C. Monzel, *Colloids Interfaces* **2024**, *8*, 54; c) C. Monzel, K. Sengupta, *J. Phys. D* **2016**, *49*, 243002.
[19] S. L. Veatch, S. L. Keller, *Biophys. J.* **2003**, *85*, 3074.
[20] T. Baumgart, S. T. Hess, W. W. Webb, *Nature* **2003**, *425*, 821.
[21] A. C. Brown, S. P. Wrenn, *Langmuir* **2013**, *29*, 9832.
[22] a) R. Dong, Y. Tan, A. Fan, Z. Liao, H. Liu, P. Wei, *J. Phys. Chem. B* **2020**, *124*, 504; b) W. Zhang, S. Zhou, G. Liu, F. Kong, S. Chen, H. Yan, *Purinergic Signalling* **2018**, *14*, 443.
[23] H. Ewers, W. Römer, A. E. Smith, K. Bacia, S. Dmitrieff, W. Chai, R. Mancini, J. Kartenbeck, V. Chambon, L. Berland, et al., *Nat. Cell Biol.* **2010**, *12*(11–8), sup pp 1–12.
[24] A. Banger, P. Pasch, L.-C. Blawitzki, S. Weber, M. Otten, C. Monzel, S. Schmidt, J. Voskuhl, L. Hartmann, *Macromol. Chem. Phys.* **2023**, *224*.
[25] a) N. Stuhr-Hansen, C.-D. Vagianou, O. Blixt, *Chemistry* **2017**, *23*, 9472; b) E. C. Woods, N. A. Yee, J. Shen, C. R. Bertozzi, *Angew. Chem. Int. Ed. Engl.* **2015**, *54*, 15782.
[26] D. G. Ackerman, G. W. Feigenson, *Essays Biochem.* **2015**, *57*, 33.
[27] a) P. Arora, S. S. Kharkwal, T. W. Ng, S. Kunnath-Velayudhan, N. K. Saini, C. T. Johndrow, Y.-T. Chang, G. S. Besra, S. A. Porcelli, *Chem. Phys. Lipids* **2015**, *191*, 75; b) K. Hanafusa, T. Hotta, K. Iwabuchi, *Front. Cell Dev. Biol.* **2020**, *8*, 589799.
[28] a) B. P. Atshaves, J. R. Jefferson, A. L. McIntosh, A. Gallegos, B. M. McCann, K. K. Landrock, A. B. Kier, F. Schroeder, *Lipids* **2007**, *42*, 871; b) R. Y. Patel, P. V. Balaji, *Int. J. Carbohydr. Chem.* **2011**, *2011*, 1; c) A. Hall, T. Róg, M. Karttunen, I. Vattulainen, *J. Phys. Chem. B* **2010**, *114*, 7797.
[29] S. Rissanen, M. Grzybek, A. Orłowski, T. Róg, O. Cramariuc, I. Levental, C. Eggeling, E. Sezgin, I. Vattulainen, *Front. Membr. Physiol. Membr. Biophys.* **2017**, *8*, 252.
[30] a) E. Sparr, H. Wennerström, *Biophys. J.* **2001**, *81*, 1014; b) K. Oglęcka, J. Sanborn, A. N. Parikh, R. S. Kraut, *Front. Membr. Physiol. Membr. Biophys.* **2012**, *3*, 120.
[31] H. Himeno, H. Ito, Y. Higuchi, T. Hamada, N. Shimokawa, M. Takagi, *Phys. Rev. E* **2015**, *92*, 62713.
[32] K. Bacia, P. Schwille, T. Kurzchalia, *Proc. Natl. Acad. Sci. USA* **2005**, *102*, 3272.
[33] P. Husen, L. R. Arriaga, F. Monroy, J. H. Ipsen, L. A. Bagatolli, *Biophys. J.* **2012**, *103*, 2304.
[34] a) M. R. Ali, K. H. Cheng, J. Huang, *Proc. Natl. Acad. Sci. USA* **2007**, *104*, 5372; b) W. F. D. Bennett, J. L. MacCallum, D. P. Tieleman, *J. Am. Chem. Soc.* **2009**, *131*, 1972.
[35] N. Shimokawa, T. Hamada, *Life* **2023**, *13*.

[36] T. Baumgart, G. Hunt, E. R. Farkas, W. W. Webb, G. W. Feigenson, *Biochim. Biophys. Acta* **2007**, *1768*, 2182.
[37] M. Schvartzman, M. Palma, J. Sable, J. Abramson, X. Hu, M. P. Sheetz, S. J. Wind, *Nano Lett.* **2011**, *11*, 1306.
[38] D. Morzy, M. Bastings, *Angew. Chem. Int. Ed. Engl.* **2022**, *61*, e202114167.
[39] a) B. R. Caré, H. A. Soula, *BMC Syst. Biol.* **2011**, *5*, 48; b) M. Gopalakrishnan, K. Forsten-Williams, M. A. Nugent, U. C. Täuber, *Biophys. J.* **2005**, *89*, 3686.
[40] a) H.-R. Lee, S. Q. Choi, *Adv. Sci.* **2021**, *8*, e2101766; b) L. Li, J. Hu, B. Różycki, J. Ji, F. Song, *Front. Mol. Biosci.* **2022**, *9*, 1019477.
[41] a) S. Boden, F. Reise, J. Kania, T. K. Lindhorst, L. Hartmann, *Macromol. Biosci.* **2019**, *19*, e1800425; b) D. Ponader, F. Wojcik, F. Beceren-Braun, J. Dernedde, L. Hartmann, *Biomacromolecules* **2012**, *13*, 1845.
[42] M. Ionescu, Z. Petrovic, *J. Serb. Chem. Soc.* **2011**, *76*, 591.

Manuscript received: August 5, 2024
Accepted manuscript online: October 16, 2024
Version of record online: November 13, 2024

Supplementary Information

Selective Glycan Presentation in Liquid-Ordered or -Disordered Membrane Phases and its Effect on Lectin Binding

Luca-Cesare Blawitzki[a,b], Cornelia Monzel[c], Stephan Schmidt[a], Laura Hartmann*[a]

[a] Department for Macromolecular Chemistry, University of Freiburg, Stefan-Meier-Str. 31, 79104 Freiburg i.Br., Germany

[b] Department for Organic Chemistry and Macromolecular Chemistry, Heinrich Heine University Duesseldorf, Universitätsstraße 1, 40225 Düsseldorf, Germany

[c] Department for Experimental Medical Physics, Heinrich Heine University Duesseldorf, Universitätsstraße 1, 40225 Düsseldorf, Germany

* Correspondence to Tel: +49 761 203 6270; E-mail: laura.hartmann@makro.uni-freiburg.de

Table of Contents

Materials

D-(+)-galactose, D-(+)-mannose, N,N-dimethylformamide, oxalyl chloride, piperidine and sulfuric acid were purchased from Acros Organics. Ethyl trifluoroacetate and PyBOP were purchased from Apollo Scientific. Acetonitrile and oleic acid (65.0-88.0%) were purchased from AppliChem. Fmoc-Cl and stearic acid were purchased from bld pharm. Succinic anhydride was purchased from Carbolution Chemicals. DIPEA and sodium chloride were purchased from Carl Roth. 1.4-dioxane, acetic anhydride, calcium chloride, ethyl acetate, HEPES, n-hexane, hydrochloric acid (37%), manganese dichloride, potassium carbonate, sodium azide, sodium bicarbonate, sodium hydroxide (1M), sodium methoxide, Concanavalin A-AF647 and trimethylamine were purchased from Fisher Scientific. Triethylsilane was purchased from fluorochem. 2,2'-(Ethylenedioxy)bis(ethylamine), 2-bromoethanol, 4-pentynoic acid, boron trifluoride diethyl etherate, Bovine Serum Albumin, dichloromethane, diethyl ether, diethylenetriamine, formic acid, methanol, phenol, tetrahydrofuran, trifluoroacetic acid and triisopropylsilane were purchased from Sigma-Aldrich. Trityl chloride was purchased from TCI chemicals. Sodium diethyldithiocarbamate was purchased from Thermo Scientific. RCA-FITC was purchased from vector laboratories.

All solvents and reagents used were purchased in the highest purity available and used without further purification.

TentaGel® S RAM resin (loading: 0.26 mmol/g) was purchased from RAPP Polymere GmbH.

DOPC, DSPC, cholesterol and 16:0 Liss Rhod PE were purchased from Avanti Polar Lipids.

Dialysis was performed via diafiltration in VIVASPIN 20 centrifugal concentrators (MWCO: 10 kDa; PES) from sartorius.

Experiments were conducted in 18-well glass bottom µ-slides from ibidi GmbH.

Instrumentation

Reversed Phase- High Pressure Liquid Chromatography- Mass Spectrometry (RP- HPLC-MS)/Electron Spray Ionization- Mass Spectrometry (ESI-MS)

RP-HPLC-MS was carried out on an Agilent 1260 Infinity instrument coupled to a variable wavelength detector (VWD) (set to 214 nm) and a 6120 Quadrupole LC/MS containing an Electrospray Ionization (ESI) source (operation mode positive, m/z range from 200 to 2000). An MZ-AquaPerfect C18 (3.0 × 50 mm, 3 µm) RP column from MZ-Analysentechnik was used. As eluent system water/acetonitrile containing 0.1 vol% formic acid was applied. The mobile phases A and B were: System A) water/acetonitrile (95/5, v/v); System B) water/acetonitrile (5/95, v/v). The samples were analyzed at a flow rate of 0.4 ml/min using a linear gradient, starting with 100% of system A) and reaching 100% system B) within 17 min. The temperature of the column room was set to 25 °C. All purities were determined using the OpenLab ChemStation software for LC/MS from Agilent Technologies.

Ultra High Resolution - Mass Spectrometry (UHR-MS)

UHR-MS measurements were performed with a Bruker UHR-QTOF maXis 4G instrument with a direct inlet via syringe pump, an ESI source and a quadrupole followed by a Time of Flight (QTOF) mass analyzer.

Nuclear Magnetic Resonance Spectroscopy (NMR)

The ^{1}H-NMR spectra were recorded on a Bruker Avanace III 600 (600 MHz). These spectra were evaluated according to the following scheme: (frequency in MHz, deuterated solvent), chemical shift in ppm (multiplicity, coupling constant, integral, signal assignment). The chemical shift is given in relation to the ^{1}H signals of the deuterated solvents used.

Lyophilization

The final glycomacromolecules were lyophilized with an Alpha 1-4 LD plus instrument from Martin Christ Freeze Dryers GmbH (-40 °C, 0.1 mbar).

Fluorescence Microscopy

Giant Unilamellar Vesicles were imaged on an inverted epi-fluorescence microscope (Olympus IX83, Shinjuku, Tokyo, Japan), equipped with a 60× oil-objective with (NA 1.25), with the CellSense Dimensions Software (Olympus) by sequential imaging of the yellow, green and red channel.

Confocal Images were acquired on a Leica DMi8 inverted microscope (Leica Microsystems CMS GmbH, Wetzlar, Germany), equipped with a 63x oil-objective and a Leica DFC9000 GT camera, operating the LAS X software.

Images were evaluated via ImageJ 1.54g.

UV-Vis Spectroscopy

UV-Vis measurements were performed on a dual-trace spectrometer Specord® 210Plus from Analytik Jena AG (Jena, Germany),using Win ASPECT PLUS softwareto operatethe instrument.

General Methods

Synthesis of Building Blocks

The building blocks EDS and TDS, as well as tetra-*O*-Acetyl-azidoethyl-α-D-mannopyranoside and tetra-*O*-acetyl-azidoethyl-β-D-galactopyranoside were synthesized as reported earlier.[41]

Solid Phase Polymer Synthesis

All structures were prepared on Tentagel® S RAM resin (batch size: 0.1 mmol). All washing steps were conducted with 4 mL solvent. Polypropylene reactors equipped with polyethylene frits and closed with Luer-stoppers were used. The backbone sequence was first assembled ($[TDS]_4$-$[EDS]_3$-Fmoc), followed by glycoconjugation via CuAAC (copper(I)-catalyzed alkyne-azide cycloaddition), Fmoc-Dap-(Fmoc)-OH conjugation and *N*-terminal conjugation of fatty acids. Before cleavage from the resin, carbohydrates were deacetylated under Zemplén conditions.

General coupling protocol.

For all compounds, the resin was first swollen in 4 mL DCM for 30 min, subsequently washed ten times with DMF, Fmoc-deprotected by treating with 25% piperidine in DMF (two times for ten minutes) and again washed fifteen times with DMF. Employed building blocks were coupled to the *N*-terminus by adding the respective building block (5eq.), PyBOP (5 eq.) and DIPEA (20 eq.) in 4 mL DMF to the resin and shaking for 1h. Then, the resin was washed fifteen times with DMF and the *N*-terminus was again deprotected followed by the next coupling step.

Fmoc cleavage

The Fmoc-protecting group of the resin as well as from the coupled building blocks or amino acids was cleaved by means of 4 mL of a 25% solution of piperidine in DMF to release the primary amine. The deprotection was carried out twice for 10 min. Afterwards the resin was washed 10 times with DMF before coupling.

CuAAC protocol for glycosylation

To the oligomeric structure loaded on the resin 2.5 eq of acetyl protected 2-azidoethyl pyranoside (α-Mannose/ β-Galactose) per alkyne group dissolved in 4 mL DMF were added. Secondly 50 mol% sodium ascorbate per alkyne group and 50 mol% $CuSO_4$ per alkyne group were dissolved each in a small amount of water and also added to the resin. The syringe reactor was rocked for 18 h before the solution was discarded. The resin was washed three times with DMF and subsequently treated with a 23 mM solution of sodium diethyldithiocarbamate in DMF and water (50/50, v/v) and alternating with DMF and DCM until no further color change occured.

Coupling of fatty acids

After Fmoc-deprotection of the *N*-terminal Dap-moiety, the resin was washed five times with DCM. 10 eq of either oleic acid or stearic acid, along with 10 eq PyBOP and 40 eq DIPEA were dissolved in 5 mL DCM and drawn in the syringe reactor. The reaction was left to proceed overnight. Afterwards, the solution was discarded and the resin was washed excessively with DCM.

On-resin deacetylation

Glycooligomers MC and GC were deacetylated under Zemplén conditions. The resin was washed five times with methanol, before 5 mL of a 0.2 M solution of NaOMe in MeOH was drawn into the reactor. The resin was rocked for 30 min, before the solution was discarded. The resin was then washed twice with MeOH before another 5 mL of the methoxide solution were drawn into the reactor. After 30 min, the solution was again discarded and the resin was washed five times with MeOH.

Cleavage from the solid phase

The resin was washed five times with DCM before acidic cleavage from the resin with a cocktail consisting of TFA, TIPS and DCM (95/2.5/2.5, v/v/v) for 30 min.

The cleaved product was precipitated in ether/ hexanes (1:1, v/v), collected via centrifugation, dried under a gentle stream of nitrogen and dialyzed via diafiltration against ultrapure water in five cycles (20 mL each, 5% triethylamine in water was used in the first cycle). The dialyzed compounds were dissolved in fresh ultrapure water and lyophilized.

Preparation of Giant Unilamellar Vesicles (GUVs)

A stock solution of DOPC, DSPC and cholesterol (2 mg/mL, molar ratio 2:1:1) with 0.5 mol% of the Ld-domain marker 16:0 Liss Rho PE was prepared in chloroform. Aliquots of 25 uL of this stock solution were mixed with a respective amount of glycan mimetics dissolved in methanol (1 mg/mL). GUVs were prepared via electroformation using a custom-built swelling chamber. Briefly, the lipid mixture was deposited on cleaned ITO glasses (pgo GmbH, Iserlohn, Germany) with clean glass capillary tubes (cp. **Figure S1A)** and the organic solvent was removed under reduced pressure for 1 h in a vacuum oven. The swelling chamber was assembled, filled with 1000 µL of a 115 mM sorbitol solution (to match the osmolarity of the measuring buffer (lectin binding buffer (LBB) (10 mM HEPES, 50 mM NaCl, 1 mM $MnCl_2$, 1 mM $CaCl_2$, pH 7.4))), and an AC field was applied to the ITO slides (divided by a Teflon spacer) using a function generator with an amplitude of 2.4 V and a frequency of 89 Hz (cp. **Figure S1B**). Electroformation was carried out for 75 min at 65°C in a vacuum oven at ambient pressure to exceed the transition temperature of all employed lipids and enable homogenous lipid mixing (cp. **Figure S1C**). Subsequently, the GUV chamber was cooled to ambient temperature in a time span of approximately 3 h before subjecting the vesicles to microscopy.

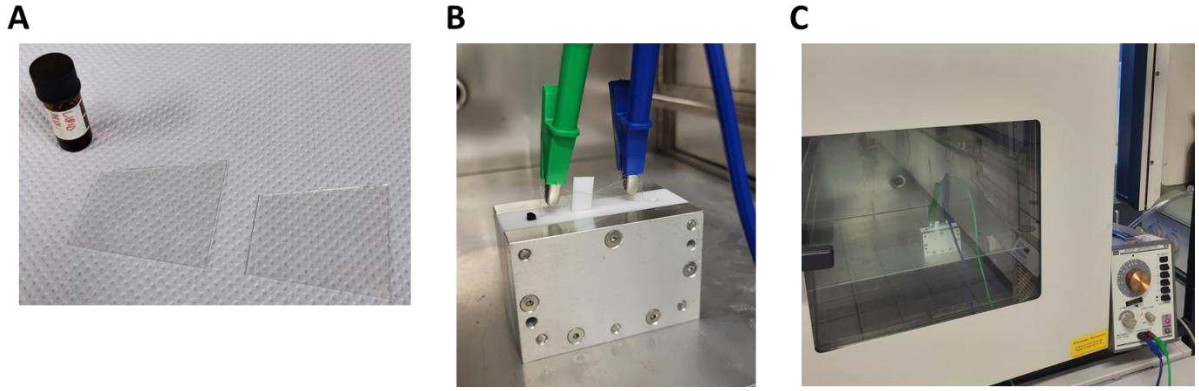

Figure S1. Preparation of phase separating GUVs via electroformation at elevated temperatures. **A**: The lipid mixture is evenly spread on cleaned and dryed ITO-coated glasses. **B**: The swelling chamber is assembled and the lipid-coated ITO-glasses are connected to a function generator. **C**: The swelling chamber is equilibrated at 70°C before applying an AC field to electroswell the GUVs.

Preparation of Measuring Chambers.

18-well slides (ibidi GmbH, Martinsried, Germany) were cleaned and activated by UV ozone treatment (UV Ozone Cleaner UVC-1014 from, NanoBioAnalytics) for 30 min. Then the activated chambers were filled with 150 µL of a solution of BSA in ultrapure water (5 mg/mL) and rocked for 30 min. The chambers were rinsed 5 times with LBB and filled with fresh LBB.

Lectin Binding Experiments

20 µL phase separating GUVs were suspended in a solution of ConA-AF647 or RCA-FITC in LBB to reach a final concentration of 200 nM lectin. The vesicles were incubated for 60 min before imaging.

Phenol Sulfuric Acid (PSA) Method

The concentration of ligands before and after vesicle formation was determined via the PSA method.

Briefly, 100 µL of analyte solution were mixed with 100 µL of a 5 wt% solution of phenol in dH_2O and 500 µL conc. sulfuric acid. The solution was thoroughly mixed and left at ambient temperature for 30 minutes for the color to develop.

Absorption was measured at 490 nm against dH_2O as blank at 25°C in disposable polystyrene cuvettes. All measurements were performed in triplicates and the obtained values were corrected by a blank sample (100 µL dH_2O, 100 µL of a 5 wt% solution of phenol in dH_2O and 500 µL conc. sulfuric acid). The ratio of absorption after and before vesicle formulation was taken as a direct measure of incorporation efficiency. Of note, absorption of the DODap-functionalized ligands was considerably higher than of the saturated DSDap-functionalized ligands. This is likely due to the formation of colored, phenolated products of the oleyl chains, as was reported earlier.[42]

To determine the amount of free ligand before vesicle formation, the respective amount of ligand (dissolved in MeOH at a concentration of 1 mg/mL) (1 mol% of the employed matrix lipid mixture for vesicle formulation) was placed in an Eppendorf tube and dried under a gentle stream of nitrogen, before dissolving the ligand in 1000 µL dH_2O.

To determine the amount of free ligand after vesicle formation in the supernatant, GUVs were formed as described but in 1000 µL dH_2O instead of the 115 mOsM sorbitol solution (sorbitol,

too, reacts with phenol and sulfuric acid to give a colored product!). After electroswelling, the vesicle solution was transferred to an Eppendorf tube and centrifugated for 60 minutes at 1°C (15000 rpm) to pellet the GUVs.

Inhibition Experiments

20 µL phase separating GUVs were suspended in a solution of ConA-AF647 and MeMan in LBB to reach a final concentration of 200 nM ConA and MeMan in the given concentrations. The vesicles were incubated for 60 min before imaging.

Analytical Data

Glycooligomer Backbone

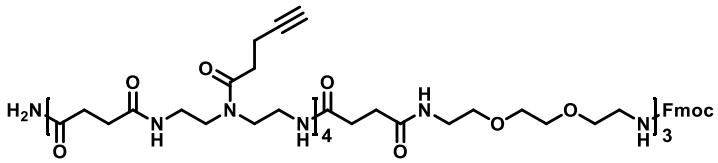

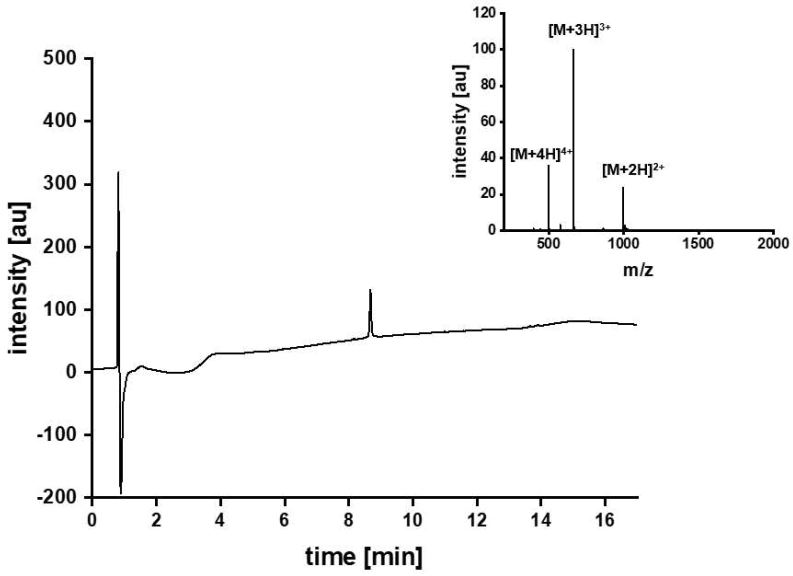

Figure S2. Oligomer backbone detected with relative purities >97% by RP-HPLC-MS analysis (linear gradient from 5 – 95 vol% eluent H_2O/acetonitrile) in 17 min at 25 °C with t_r = 8.67 min.

ESI-MS for $C_{97}H_{143}N_{19}O_{26}$ m/z $[M+2H]^{2+}$ calcd.: 996.0, found 996.4 (mass error 401.6 ppm)

ESI-MS for $C_{97}H_{143}N_{19}O_{26}$ m/z $[M+3H]^{3+}$ calcd.: 664.4, found 664.6 (mass error 301.0 ppm)

ESI-MS for $C_{97}H_{143}N_{19}O_{26}$ m/z $[M+4H]^{4+}$ calcd.: 498.5, found 498.6 (mass error 200.6 ppm)

Glycooligomer Man$_4$DSDap

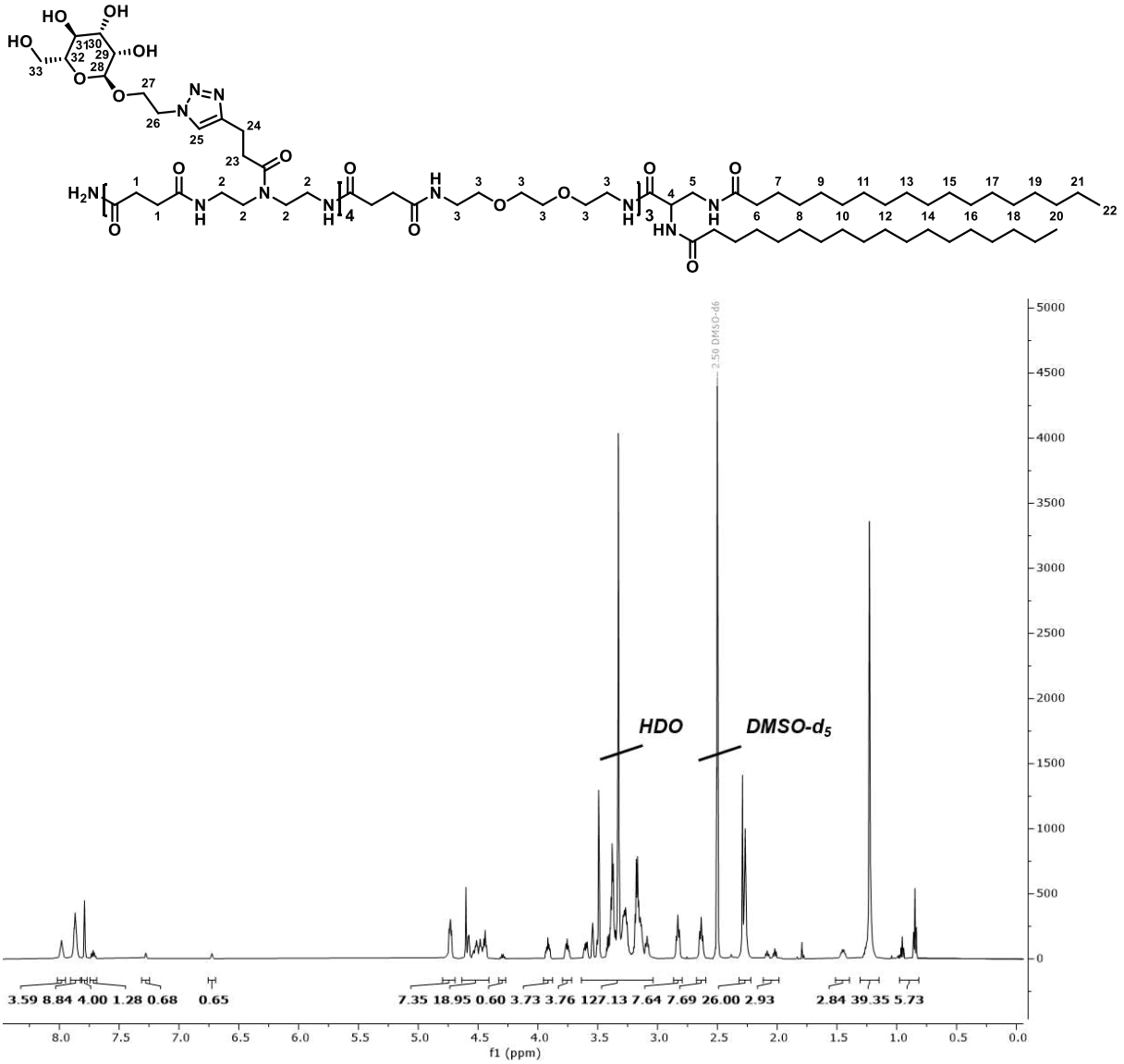

Figure S3. ^{1}H-NMR (600 MHz, DMSO-d$_6$, ambient temperature) of Man$_4$DSDap.

^{1}H-NMR (600 MHz, DMSO-d$_6$): δ [ppm] = 8.01-7.94 (m, 4H, -N*H*C(O)-), 7.90-7.82 (m, 9H, -N*H*C(O)-), 7.79 (s, 4H, H25), 7.74-7.68 (m, 1H, -N*H*C(O)-), 7.27 (s, 1H, -N*H*C(O)-), 6.72 (s, 1H, -N*H*C(O)-), 4.79-4.69 (m, 8H, H26), 4.63-4.40 (m, 20H, H28, -O*H*), 4.29 (q, 1H, H4, J = 7.99 Hz), 3.95-3.87 (m, 4H, H27), 3.79-3.71 (m, 4H, H27'), 3.63-3.03 (m, 94H, H2, H3, H5, H29-33), 2.83 (t, 8H, H24, J = 7.6 Hz), 2.63 (t, 8H, H23, J = 7.7 Hz), 2.31-2.22 (m, 28H, H1), 2.11-1.98 (m, 4H, H6), 1.51-1.39 (m, 4H, H7), 1.30-1.14 (m, 56H, H8-H21), 0.97-0.81 (m, 6H, H22)

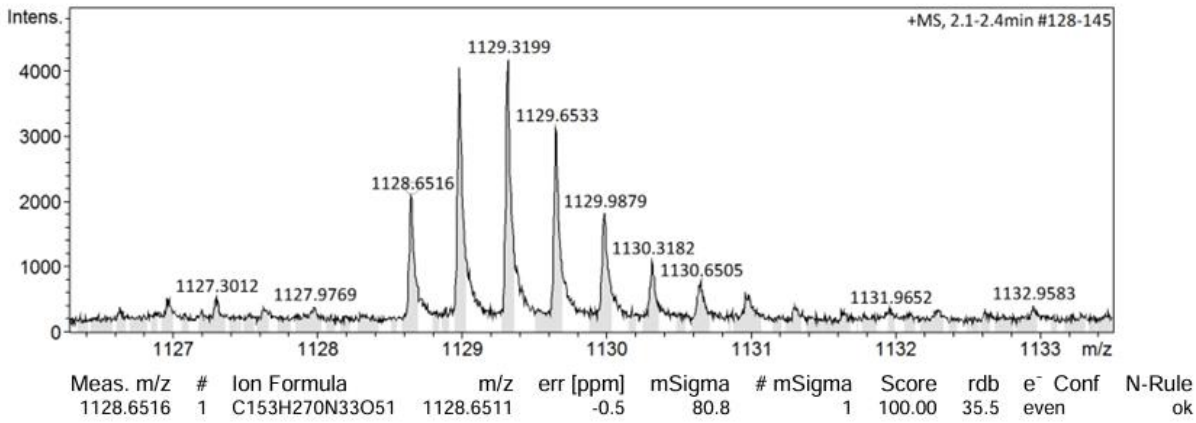

Figure S4. HR-ESI-MS of Man_4DSDap

HR-ESI-MS for $C_{153}H_{267}N_{33}O_{51}$ m/z $[M+3H]^{3+}$ calcd.: 1128.6513, found 1128.6516

mass error 0.265804 ppm

Glycooligomer Man$_4$DODap

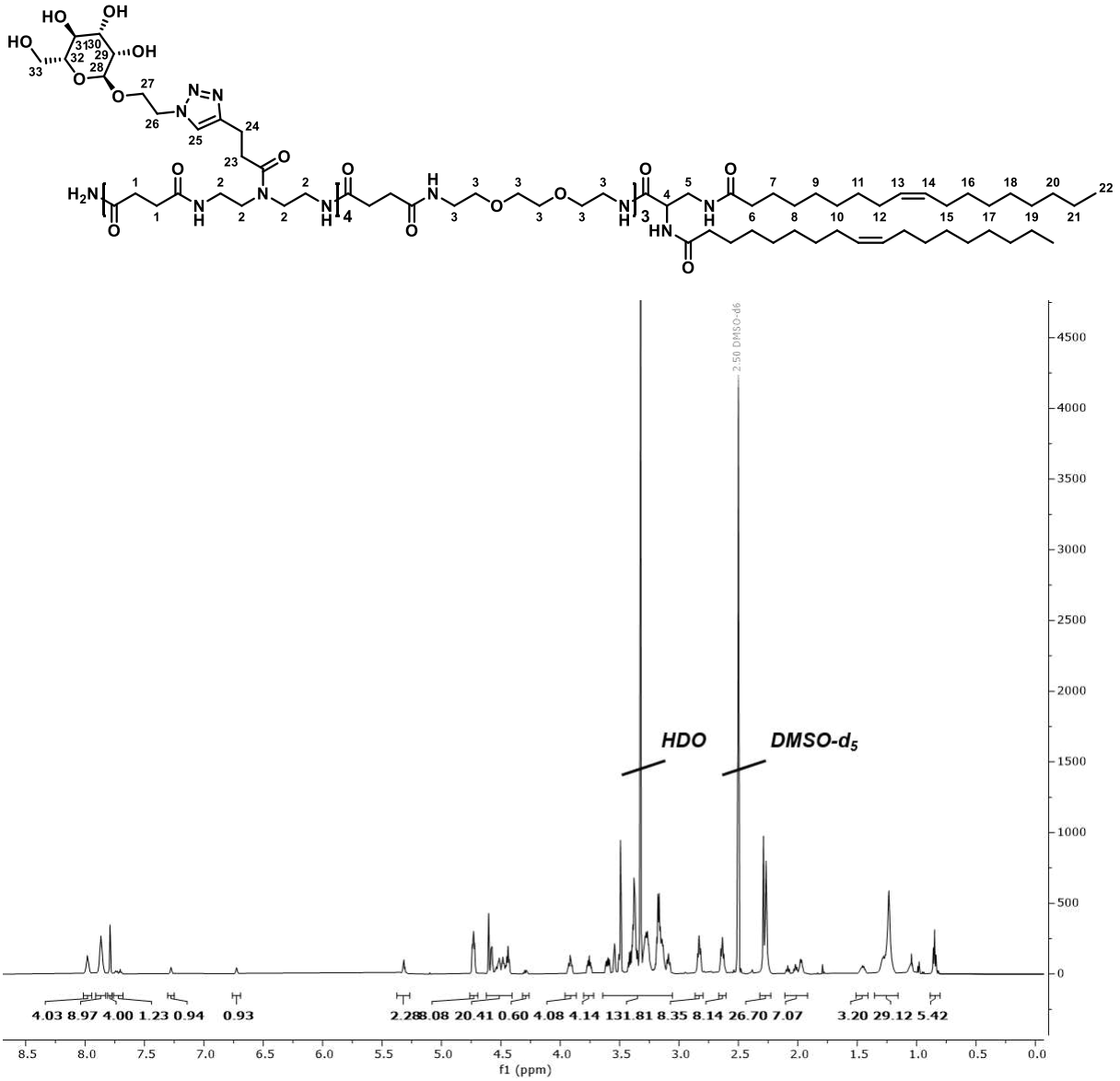

Figure S5. ^{1}H-NMR (600 MHz, DMSO-d$_6$, ambient temperature) of Man$_4$DODap.

^{1}H-NMR (600 MHz, DMSO-d$_6$): δ [ppm] = 8.01-7.94 (m, 4H, -N*H*C(O)-), 7.91-7.82 (m, 9H, -N*H*C(O)-), 7.80-7.77 (m, 4H, H25), 7.76-7.68 (m, 1H, -N*H*C(O)-), 7.27 (s, 1H, -N*H*C(O)-), 6.72 (s, 1H, -N*H*C(O)-), 5.37-5.27 (m, 4H, H13, H14) 4.76-4.69 (m, 8H, H26), 4.62-4.40 (m, 20H, H28, -O*H*), 4.29 (q, 1H, H4, J = 7.99 Hz), 3.95-3.86 (m, 4H, H27), 3.80-3.71 (m, 4H, H27'), 3.64-3.05 (m, 94H, H2, H3, H5, H29-33), 2.83 (t, 8H, H24, J = 7.5 Hz), 2.63 (t, 8H, H23, J = 7.7 Hz), 2.32-2.22 (m, 28H, H1), 2.10-1.91 (m, 12H, H6, H12, H15), 1.51-1.41 (m, 4H, H7), 1.35-1.15 (m, 40H, H8-11, H16-21), 0.88-0.80 (m, 6H, H22)

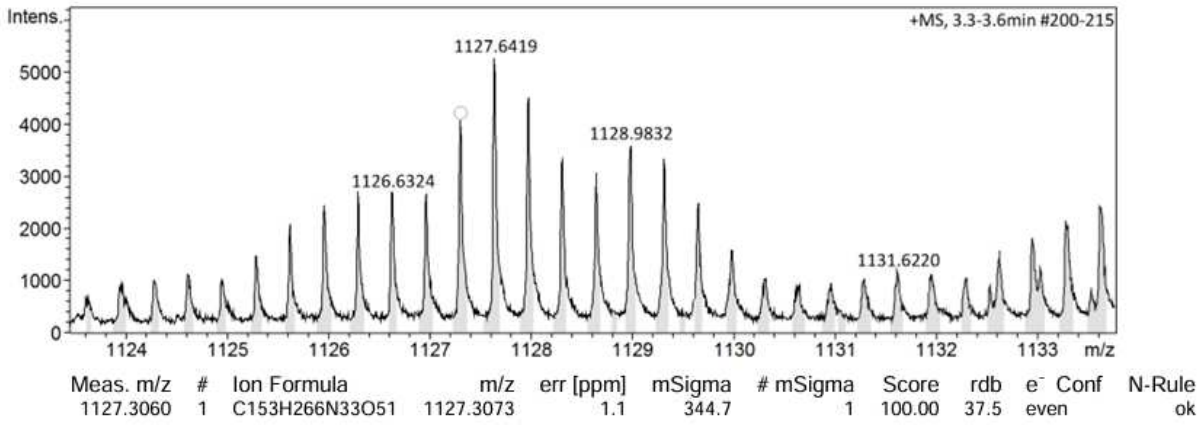

Figure S6. HR-ESI-MS of Man_4DODap

HR-ESI-MS for $C_{153}H_{263}N_{33}O_{51}$ m/z $[M+3H]^{3+}$ calcd.: 1127.3079, found 1127.3060

mass error -1.685431 ppm

Glycooligomer Gal$_4$DSDap

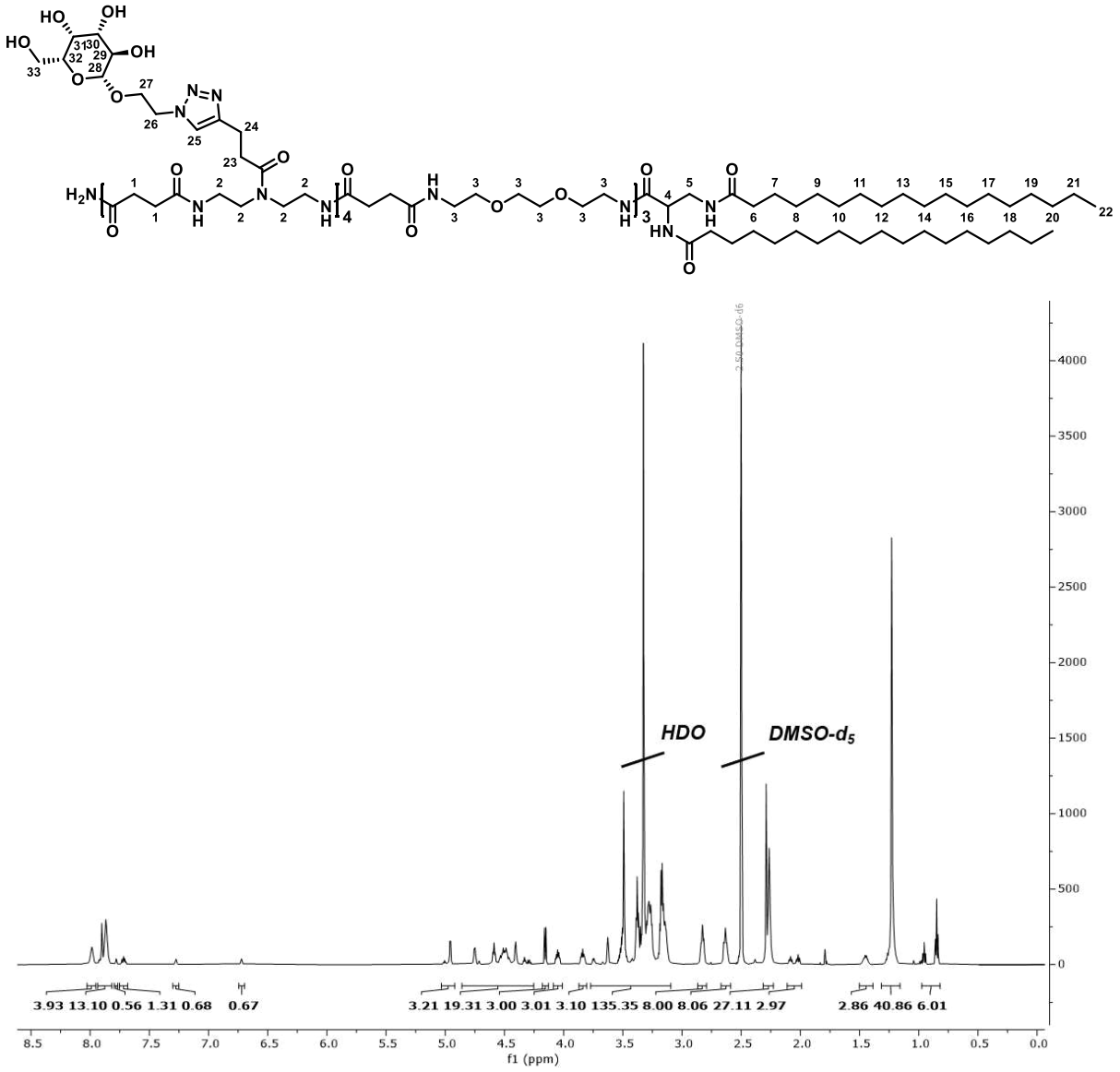

Figure S7. ^{1}H-NMR (600 MHz, DMSO-d$_6$, ambient temperature) of Gal$_4$DSDap.

^{1}H-NMR (600 MHz, DMSO-d$_6$): δ [ppm] = 8.01-7.90 (m, 4H, -N*H*C(O)-), 7.93-7.81 (m, 13H, -N*H*C(O)-, H25), 7.79-7.76 (s, 1H, -N*H*C(O)-), 7.75-7.68 (m, 1H, -N*H*C(O)-), 7.27 (s, 1H, -N*H*C(O)-), 6.72 (s, 1H, -N*H*C(O)-), 5.03-4.92 (m, 4H, H26), 4.85-4.26 (m, 21H, H4, H26', -O*H*), 4.15 (d, 4H, H28, J = 7.3 Hz), 4.08-4.01 (m, 4H, H27), 3.87-3.80 (m, 4H, H27'), 3.77-3.09 (m, 94H, H2, H3, H5, H29-33), 2.82 (t, 8H, H24, J = 7.7 Hz), 2.63 (t, 8H, H23, J = 7.6 Hz), 2.31-2.22 (m, 28H, H1), 2.11-1.99 (m, 4H, H6), 1.50-1.38 (m, 4H, H7), 1.31-1.15 (m, 56H, H8-H21), 0.97-0.81 (m, 6H, H22)

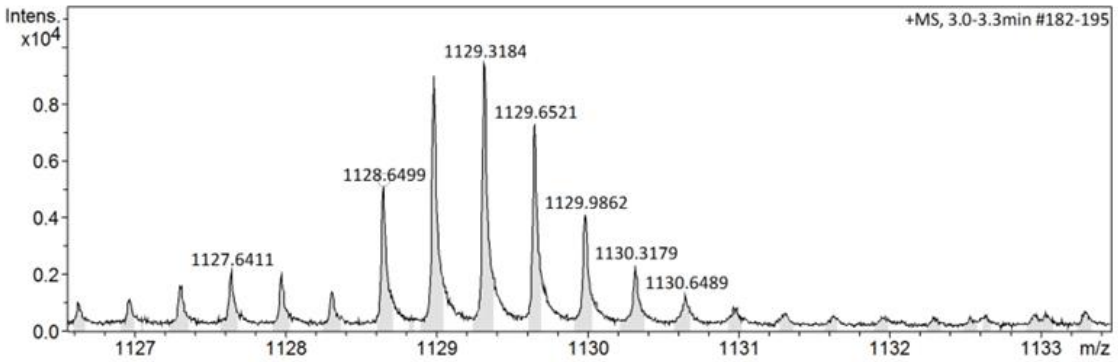

Meas. m/z	#	Ion Formula	m/z	err [ppm]	mSigma	# mSigma	Score	rdb	e⁻ Conf	N-Rule
1128.6499	1	C153H270N33O51	1128.6511	1.0	73.5	1	100.00	35.5	even	ok

Figure S8. HR-ESI-MS of Gal_4DSDap

HR-ESI-MS for $C_{153}H_{267}N_{33}O_{51}$ m/z $[M+3H]^{3+}$ calcd.: 1128.6513, found 1128.6499

mass error -1.240419 ppm

Glycooligomer Gal$_4$DODap

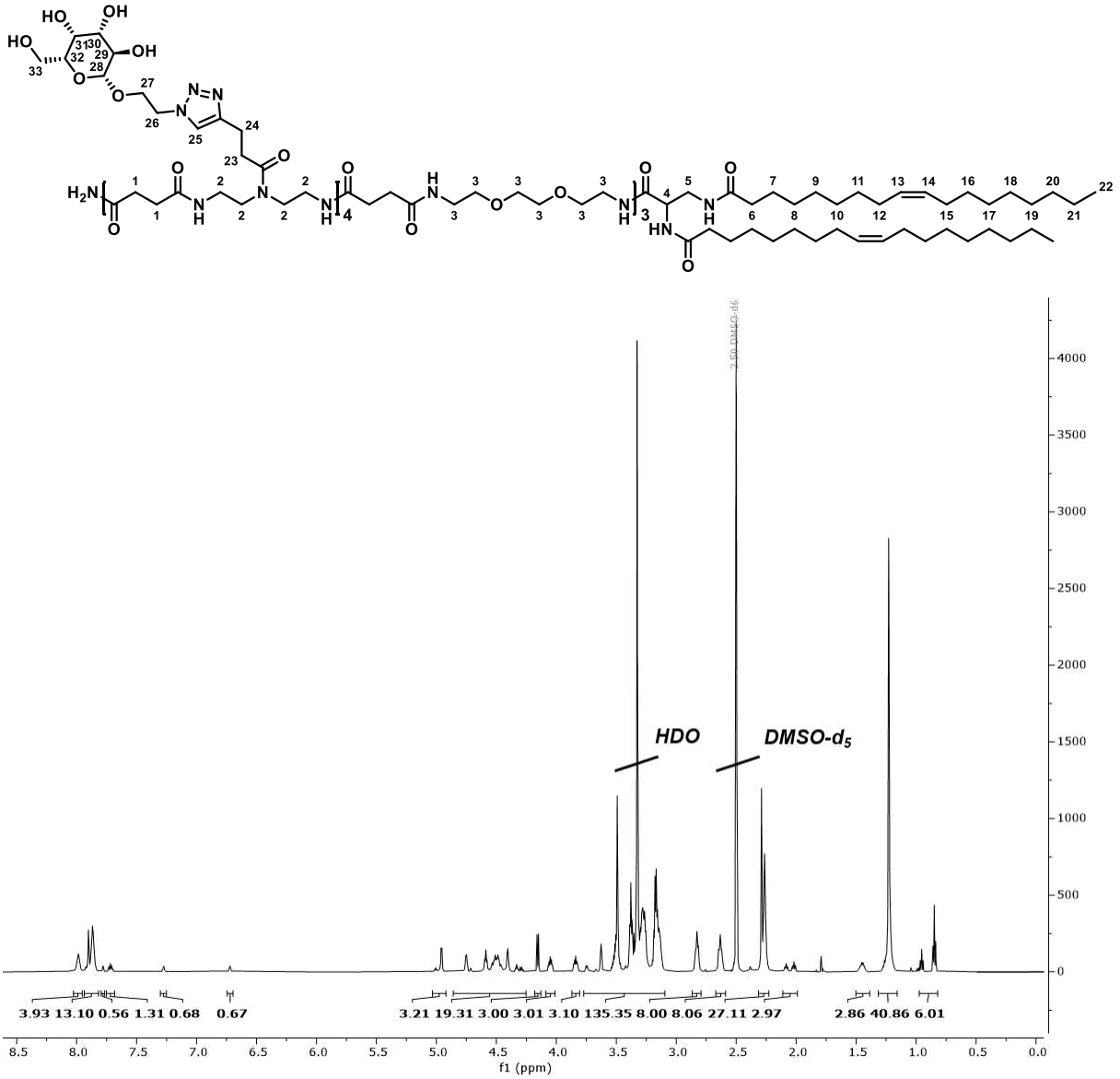

Figure S9. ^{1}H-NMR (600 MHz, DMSO-d$_6$, ambient temperature) of Gal$_4$DODap.

^{1}H-NMR (600 MHz, DMSO-d$_6$): δ [ppm] = 8.08-7.65 (m, 19H, -N*H*C(O)-, H25), 7.27 (s, 1H, -N*H*C(O)-), 6.72 (s, 1H, -N*H*C(O)-), 5.37-5.26 (m, 4H, H13, H14), 5.03-4.91 (m, 4H, H26), 4.81-4.26 (m, 21H, H4, H26', -O*H*), 4.15 (d, 4H, H28, J = 7.3 Hz), 4.09-4.01 (m, 4H, H27), 3.87-3.80 (m, 4H, H27'), 3.77-3.05 (m, 94H, H2, H3, H5, H29-33), 2.82 (t, 8H, H24, J = 7.1 Hz), 2.63 (t, 8H, H23, J = 4.6 Hz), 2.33-2.20 (m, 28H, H1), 2.11-1.92 (m, 12H, H6, H12, H15), 1.50-1.41 (m, 4H, H7), 1.34-1.13 (m, 40H, H8-11, H16-21), 1.00-0.81 (m, 6H, H22)

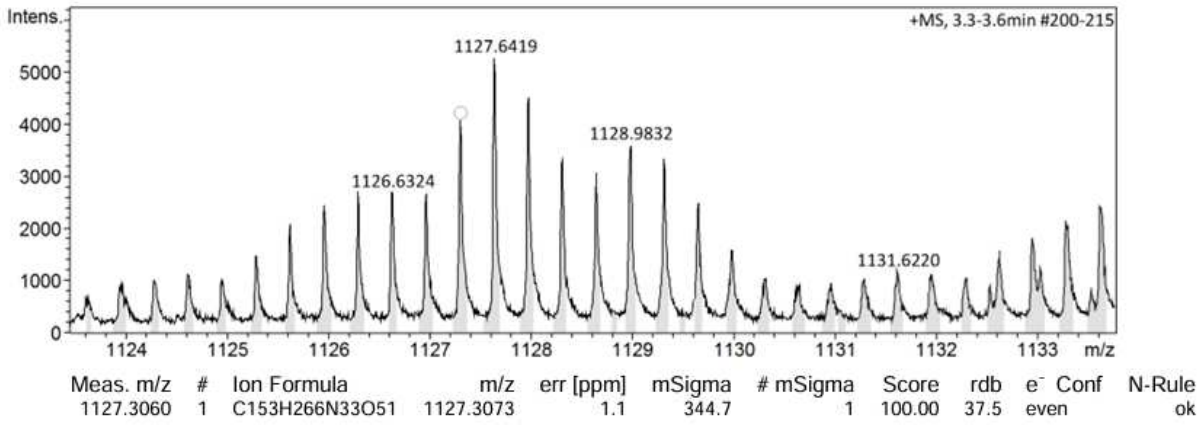

Figure S10. HR-ESI-MS of Gal_4DODap

HR-ESI-MS for $C_{153}H_{263}N_{33}O_{51}$ m/z $[M+3H]^{3+}$ calcd.: 1127.3079, found 1127.3060

mass error -1.685431 ppm

Microscopy Images and Additional Data

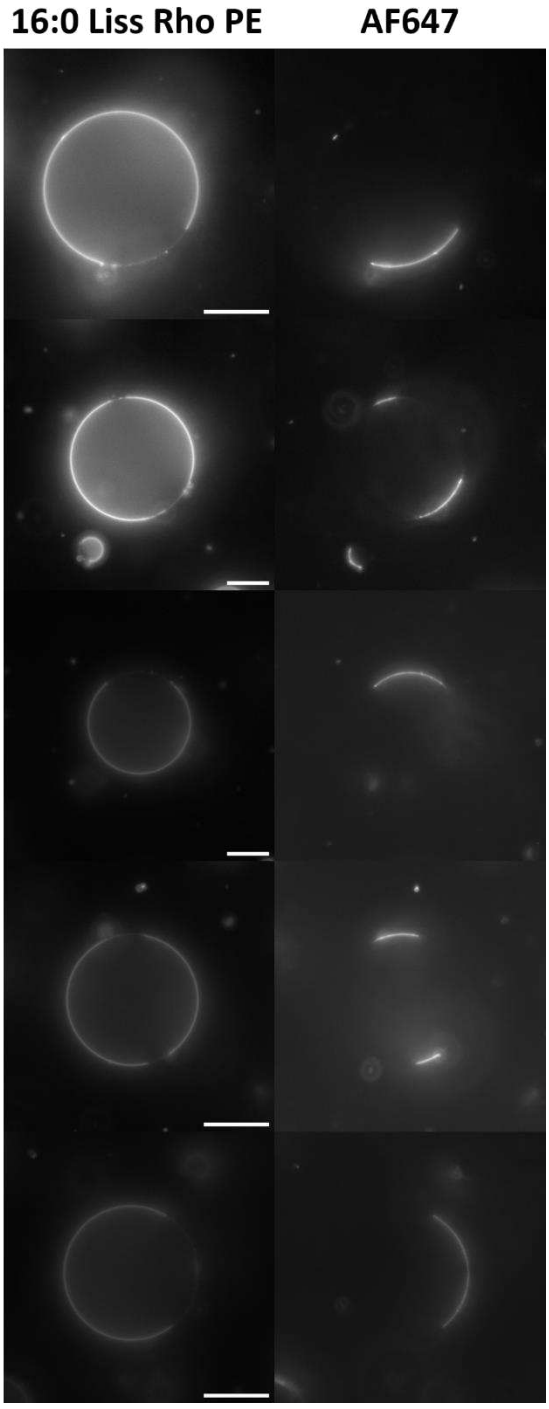

Figure S11. Exemplary images of phase separating GUVs containing 0.5 mol% of the Ld-domain marker 16:0 Liss Rho PE and 1 mol% Man_4DSDap after incubation with 200 nM ConA-AF647. The lectin fluorescence colocalizes with the Lo domain of the vesicles. Scale bar: 10 µm.

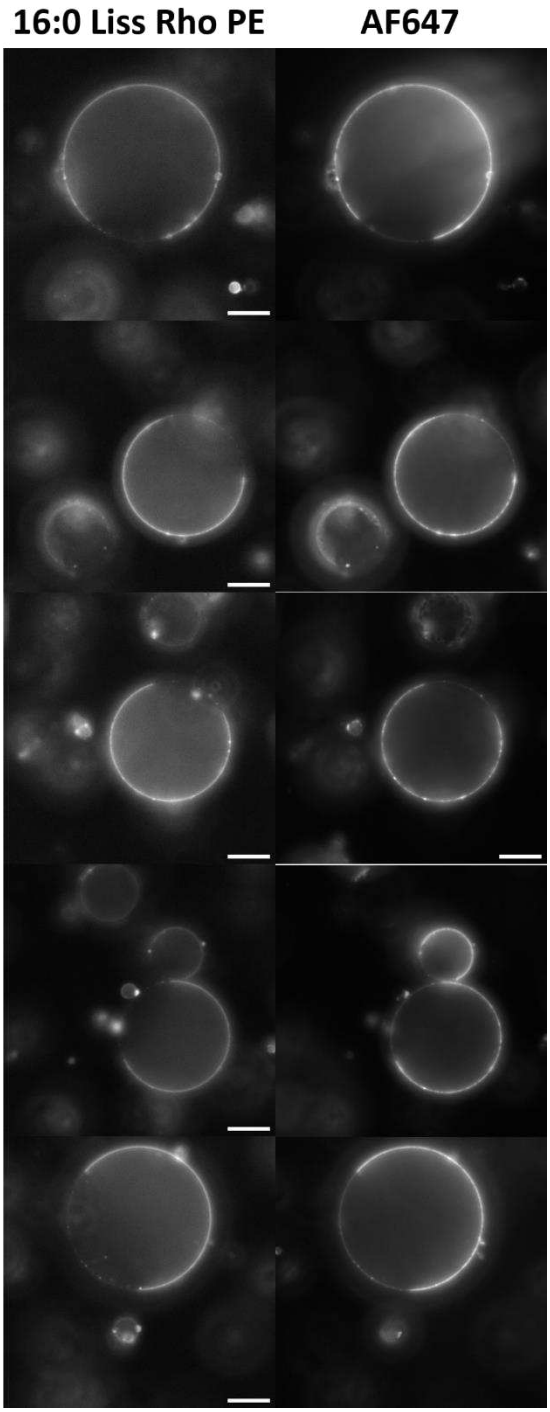

Figure S12. Exemplary images of phase separating GUVs containing 0.5 mol% of the Ld-domain marker 16:0 Liss Rho PE and 4 mol% Man_4DODap after incubation with 200 nM ConA-AF647. The lectin fluorescence colocalizes with the Ld domain of the vesicles. Scale bar: 10 µm.

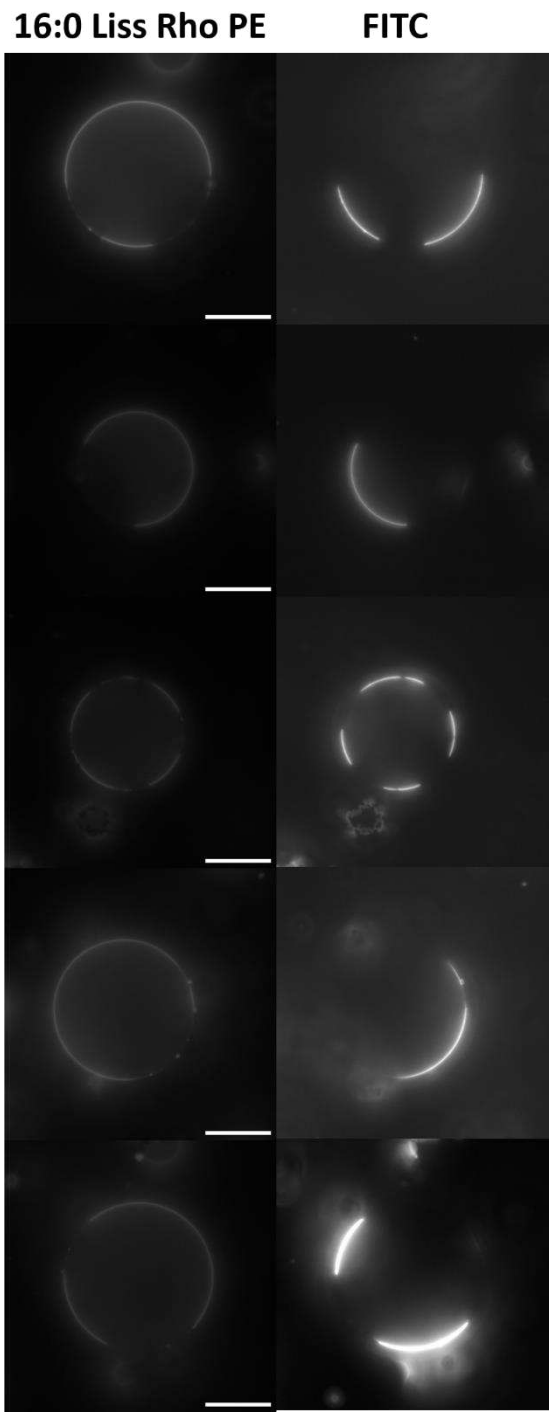

Figure S13. Exemplary images of phase separating GUVs containing 0.5 mol% of the Ld-domain marker 16:0 Liss Rho PE and 1 mol% Gal_4DSDap after incubation with 200 nM RCA-FITC. The lectin fluorescence colocalizes with the Lo domain of the vesicles. Scale bar: 10 µm.

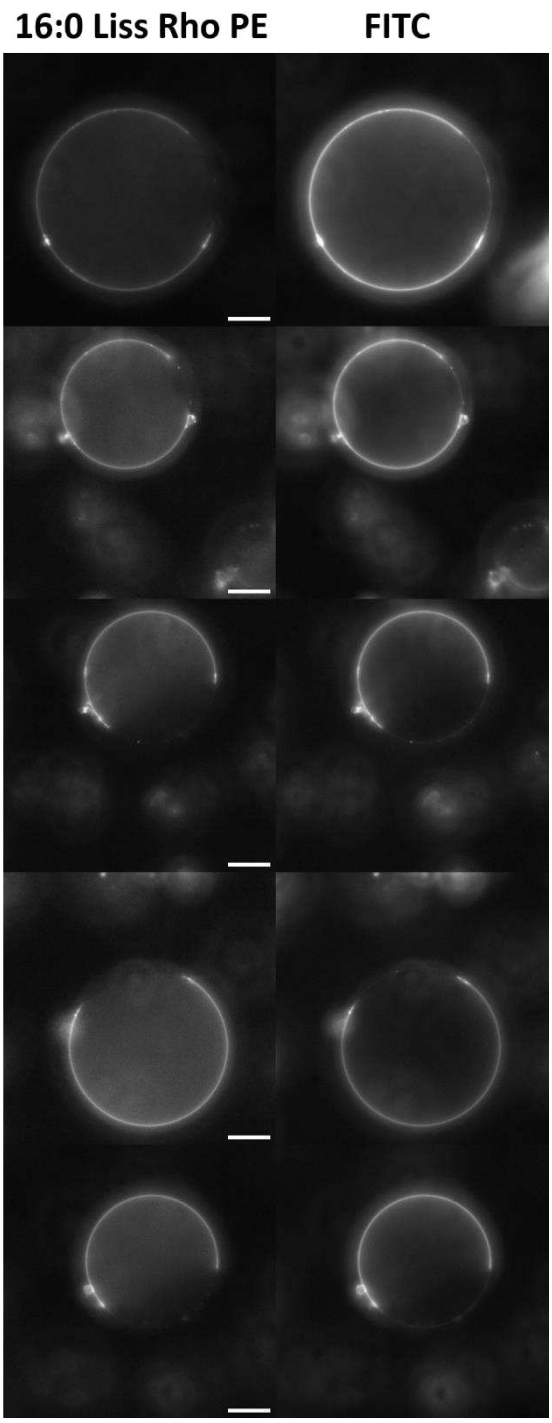

Figure S14. Exemplary images of phase separating GUVs containing 0.5 mol% of the Ld-domain marker 16:0 Liss Rho PE and 1 mol% Gal_4DODap after incubation with 200 nM RCA-FITC. The lectin fluorescence colocalizes with the Ld domain of the vesicles. Scale bar: 10 µm.

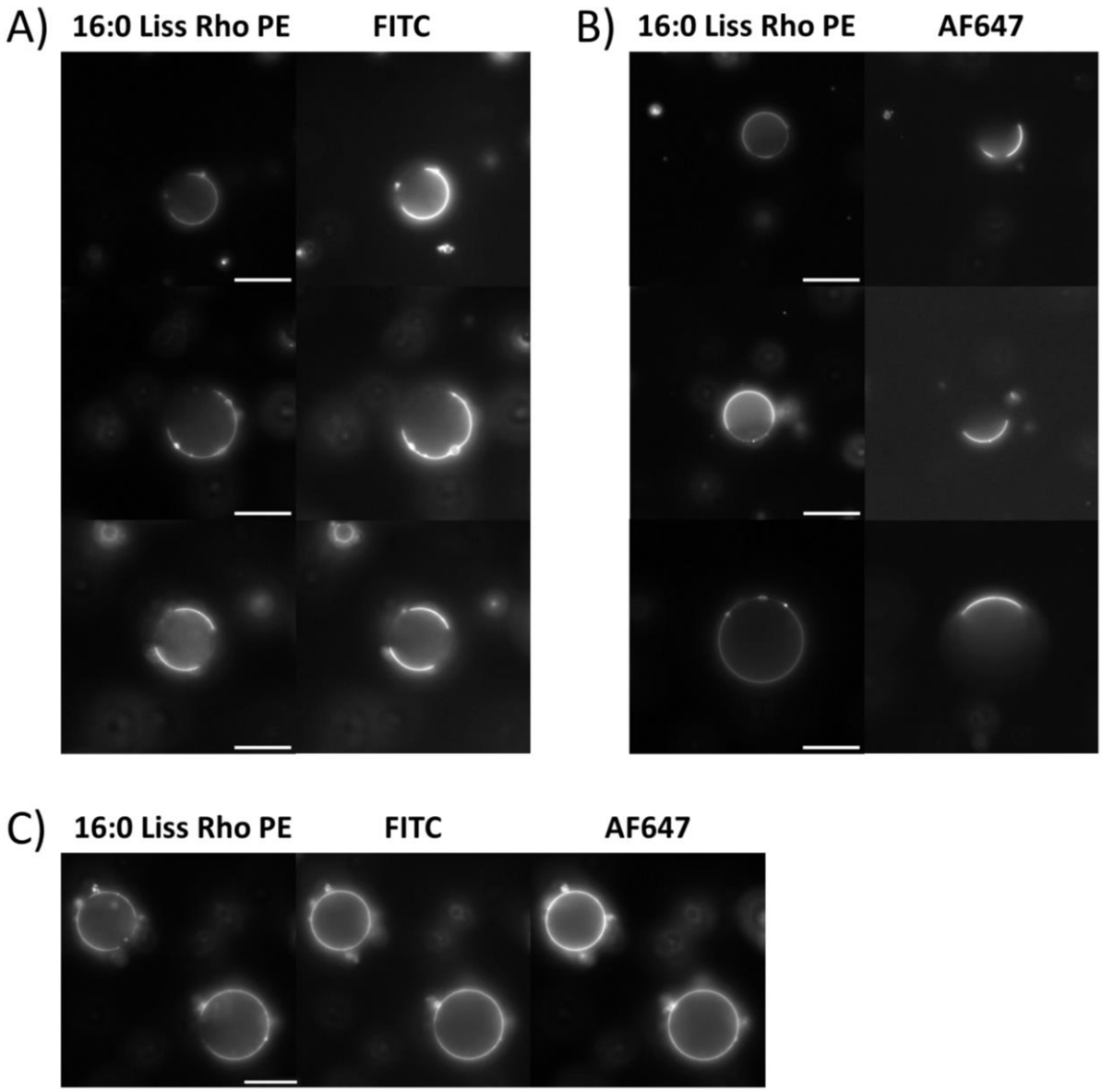

Figure S15. Exemplary images of phase separating GUVs containing 0.5 mol% of the Ld-domain marker 16:0 Liss Rho PE, 1 mol% of Man_4DSDap and 4 mol% Gal_4DODap. **A):** Vesicles incubated with 200 nM RCA-FITC; the lectin fluorescence colocalizes with the Ld domain of the vesicles. **B):** Vesicles incubated with 200 nM ConA-AF647; the lectin fluorescence colocalizes with the Lo domain of the vesicles. **C):** Vesicles incubated simultaneously with 200 nM ConA-AF647 and 200 nM RCA-FITC; lectin fluorescence is homogenously distributed along the membrane in either channel, putatively due to unspecific interactions between ConA and RCA. Scale bars: 10 µm.

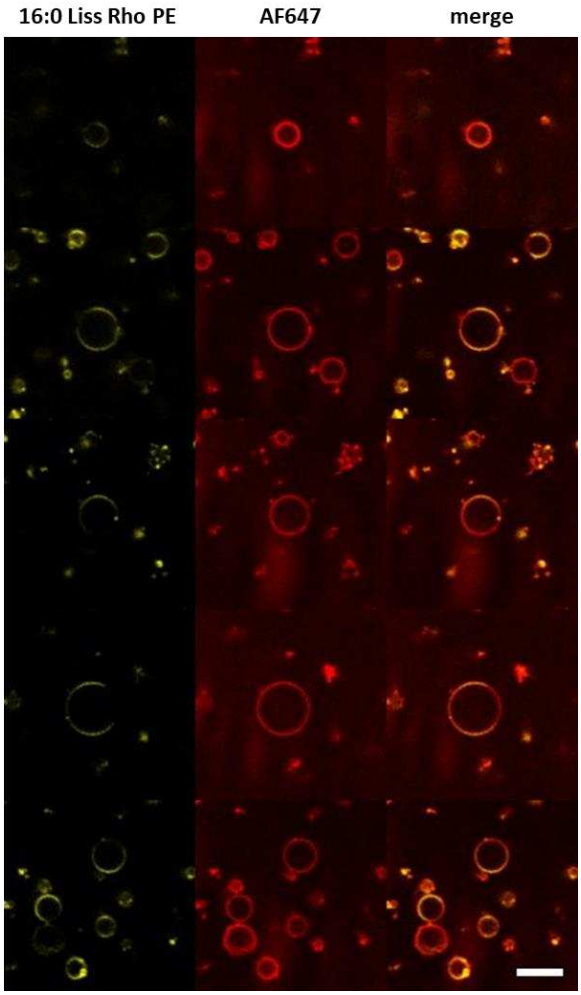

Figure S16. Confocal images of phase separating GUVs containing 0.1 mol% of the Ld-domain marker 16:0 Liss Rho PE (left), 4 mol% Man_4DODap, 0.5 mol% Man_4DSDap and 0.5 mol% Gal_4DSDap after incubation with 200 nM ConA-AF647 (middle). Lectin fluorescence is distributed homogenously across the whole vesicle membrane, since Man-ligands are distributed in the Lo as well as in the Ld domains. Scale bar: 10 µm.

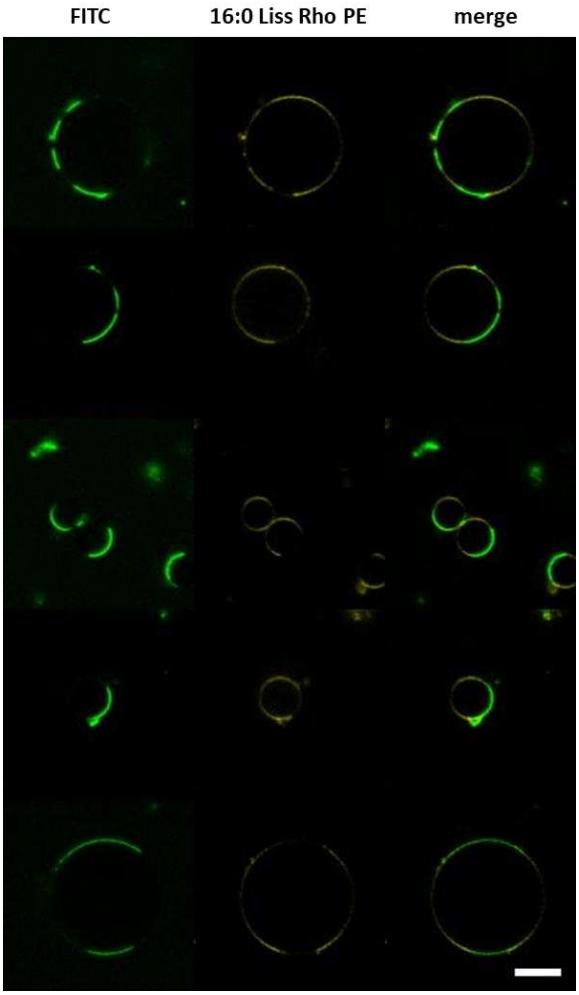

Figure S17. Confocal images of phase separating GUVs containing 0.1 mol% of the Ld-domain marker 16:0 Liss Rho PE (middle), 4 mol% Man_4DODap, 0.5 mol% Man_4DSDap and 0.5 mol% Gal_4DSDap after incubation with 200 nM RCA-FITC (left). Lectin fluorescence colocalized with the Lo phases of the vesicles, since Gal-ligands are located only in the Lo domains. Scale bar: 10 µm.

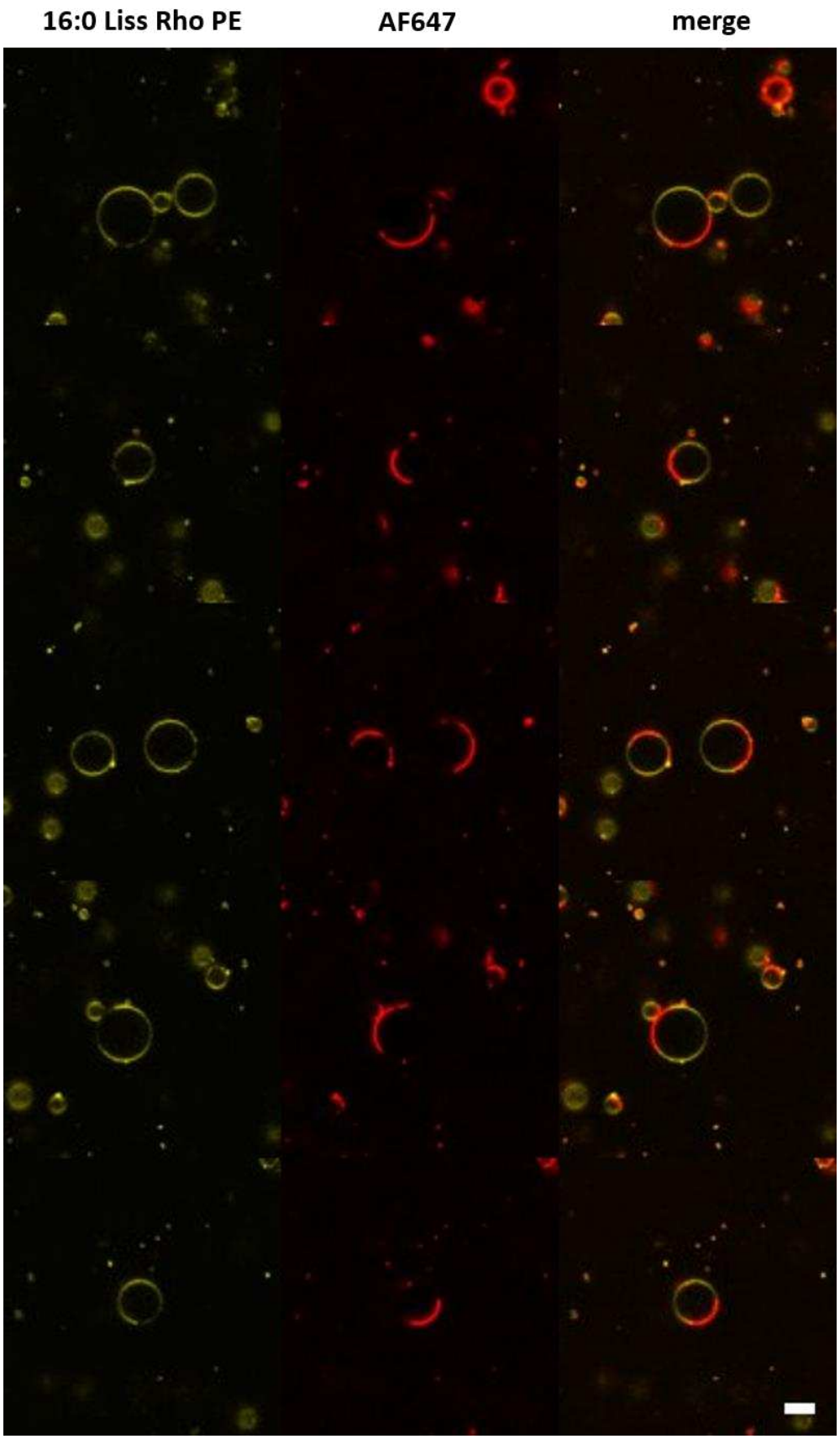

Figure S18. Confocal images of phase separating GUVs containing 0.5 mol% of the Ld-domain marker 16:0 Liss Rho PE and 1 mol% Man_4DSDap after incubation with 200 nM ConA-AF647. Scale bar: 10 µm.

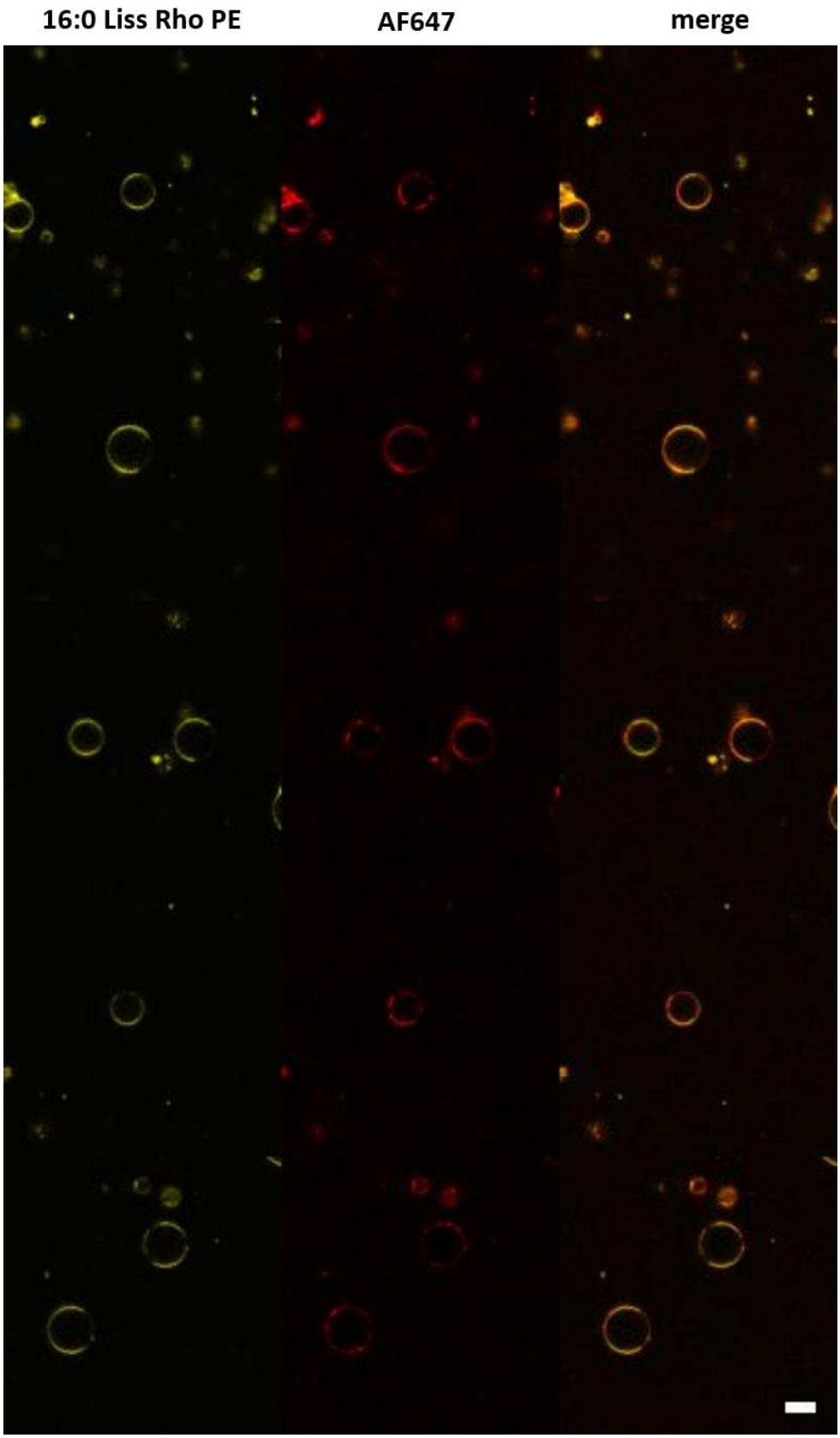

Figure S19. Confocal images of phase separating GUVs containing 0.5 mol% of the Ld-domain marker 16:0 Liss Rho PE and 1 mol% Man_4DODap after incubation with 200 nM ConA-AF647. Scale bars: 20 µm.

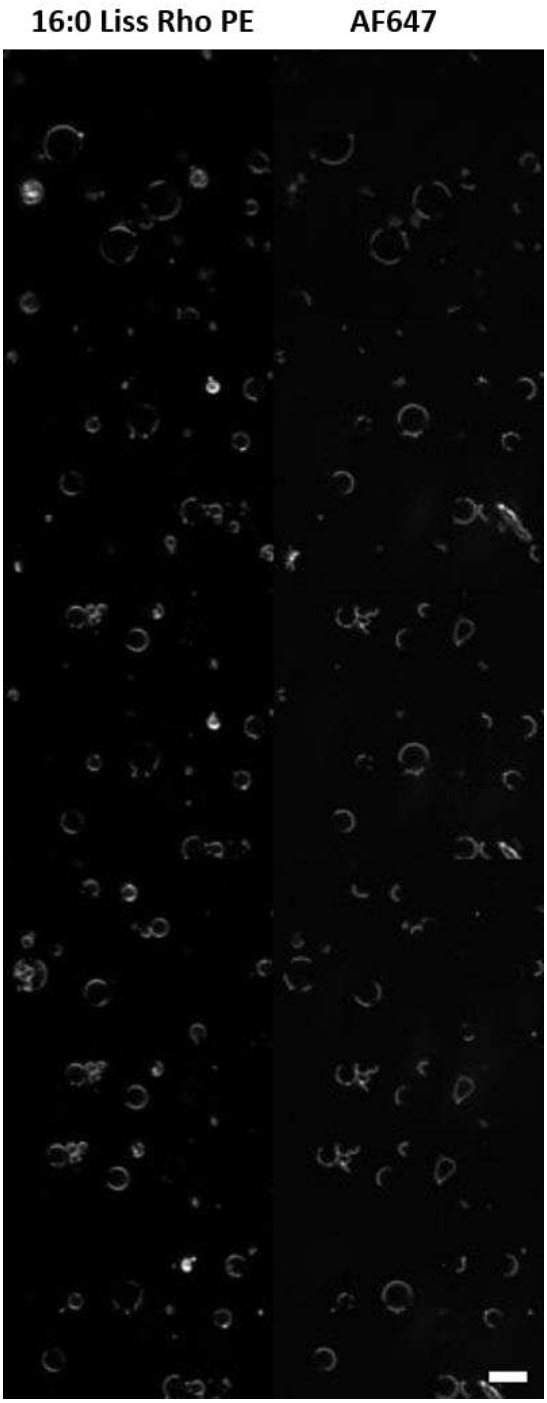

Figure S20. Confocal images of phase separating GUVs containing 0.1 mol% of the Ld-domain marker 16:0 Liss Rho PE (left) and 1 mol% Man_4DSDap after incubation with 200 nM ConA-AF647 without added inhibitor. Scale bar: 10 µm.

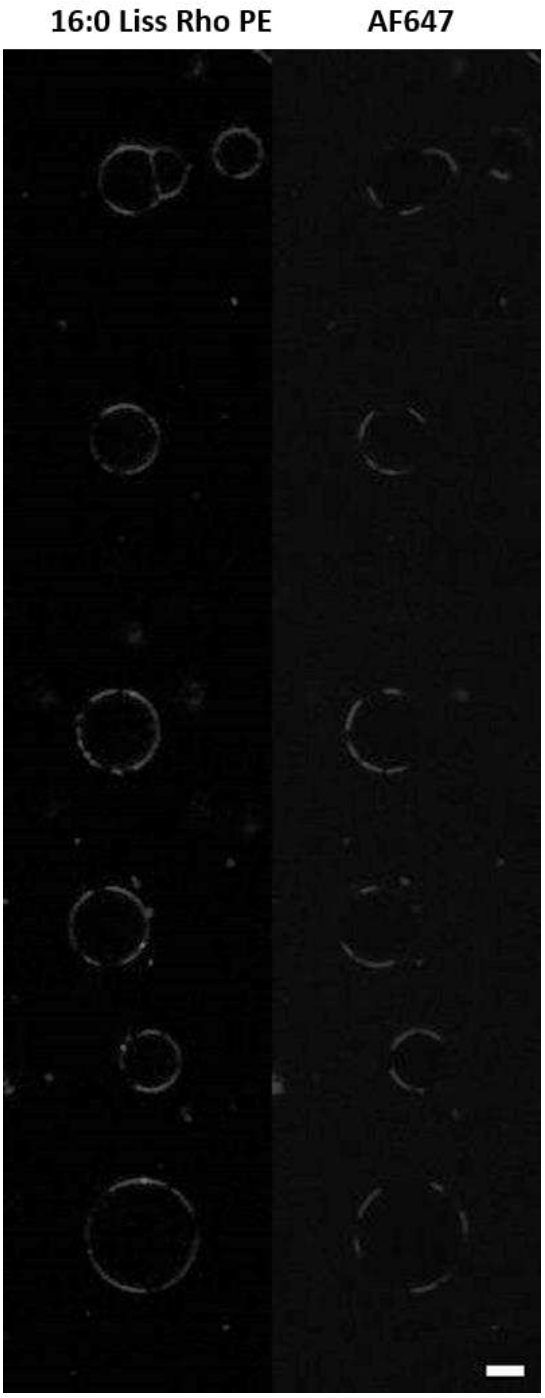

Figure S21. Confocal images of phase separating GUVs containing 0.1 mol% of the Ld-domain marker 16:0 Liss Rho PE (left) and 1 mol% Man_4DSDap after incubation with 200 nM ConA-AF647 with 0.5 mM MeMan inhibitor. Scale bar: 10 µm. Brightness adjusted for better visibility.

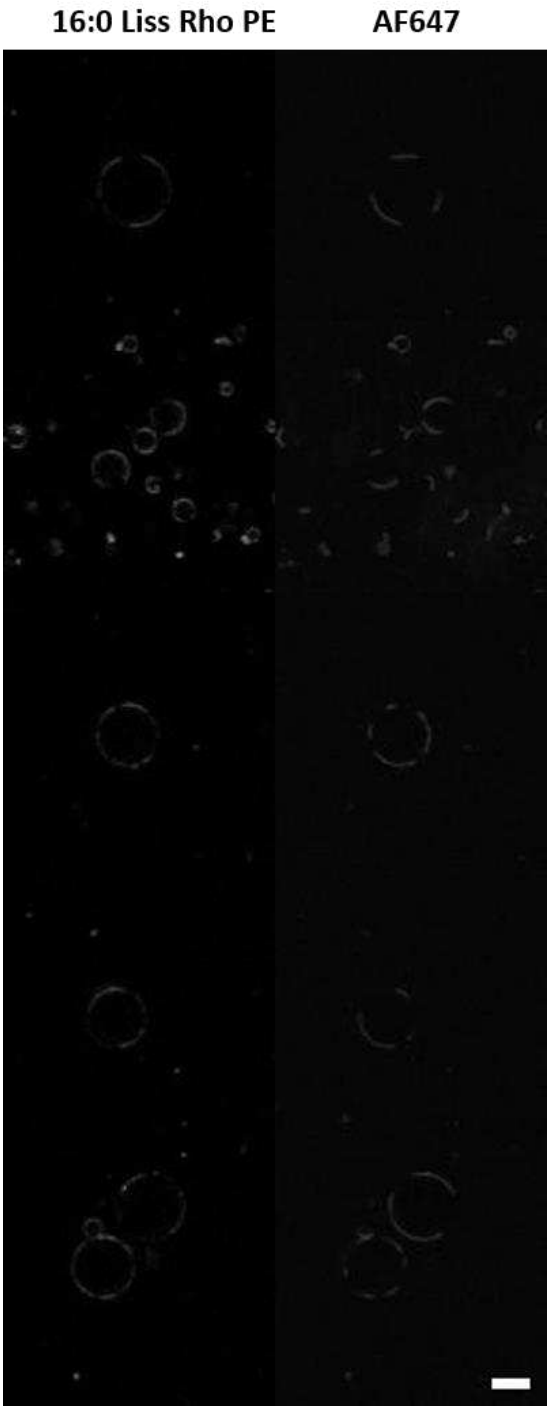

Figure S22. Confocal images of phase separating GUVs containing 0.1 mol% of the Ld-domain marker 16:0 Liss Rho PE (left) and 1 mol% Man_4DSDap after incubation with 200 nM ConA-AF647 with 1 mM MeMan inhibitor. Scale bar: 10 µm. Brightness adjusted for better visibility.

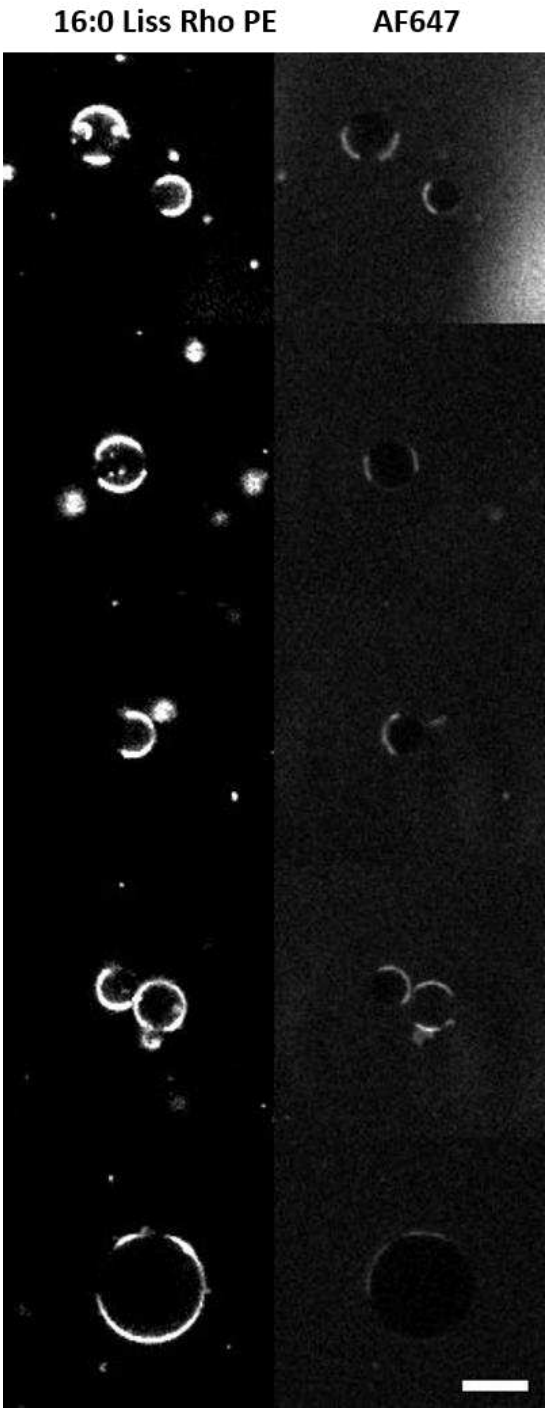

Figure S23. Confocal images of phase separating GUVs containing 0.1 mol% of the Ld-domain marker 16:0 Liss Rho PE (left) and 1 mol% Man_4DSDap after incubation with 200 nM ConA-AF647 with 3 mM MeMan inhibitor. Scale bar: 10 µm. Contrast adjusted for better visibility.

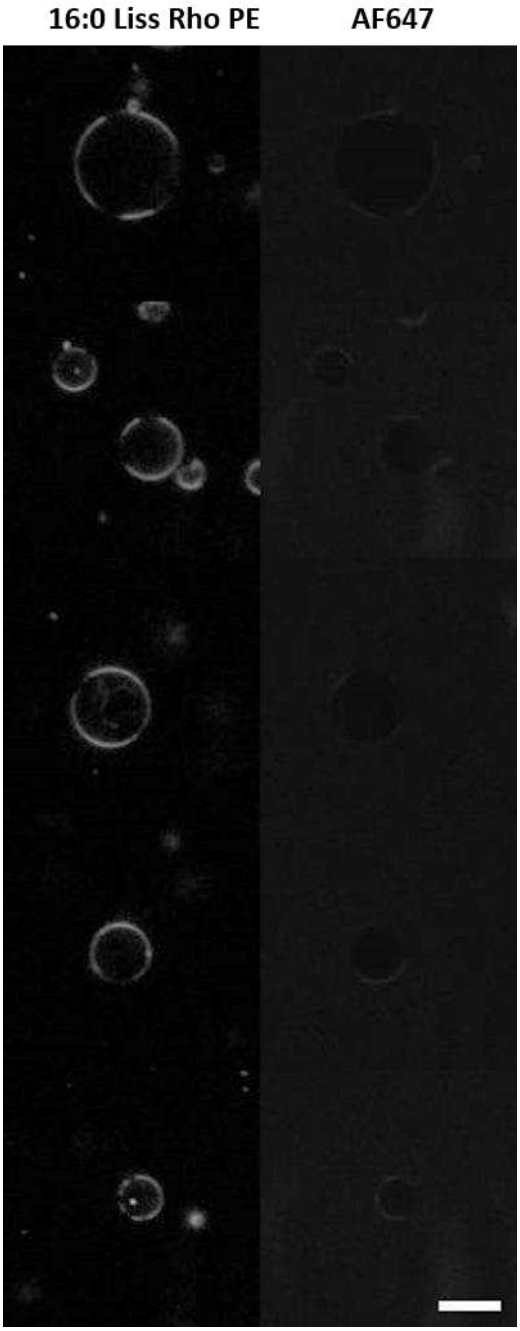

Figure S24. Confocal images of phase separating GUVs containing 0.1 mol% of the Ld-domain marker 16:0 Liss Rho PE (left) and 1 mol% Man_4DSDap after incubation with 200 nM ConA-AF647 with 4 mM MeMan inhibitor. Scale bar: 10 µm. Brightness adjusted for better visibility.

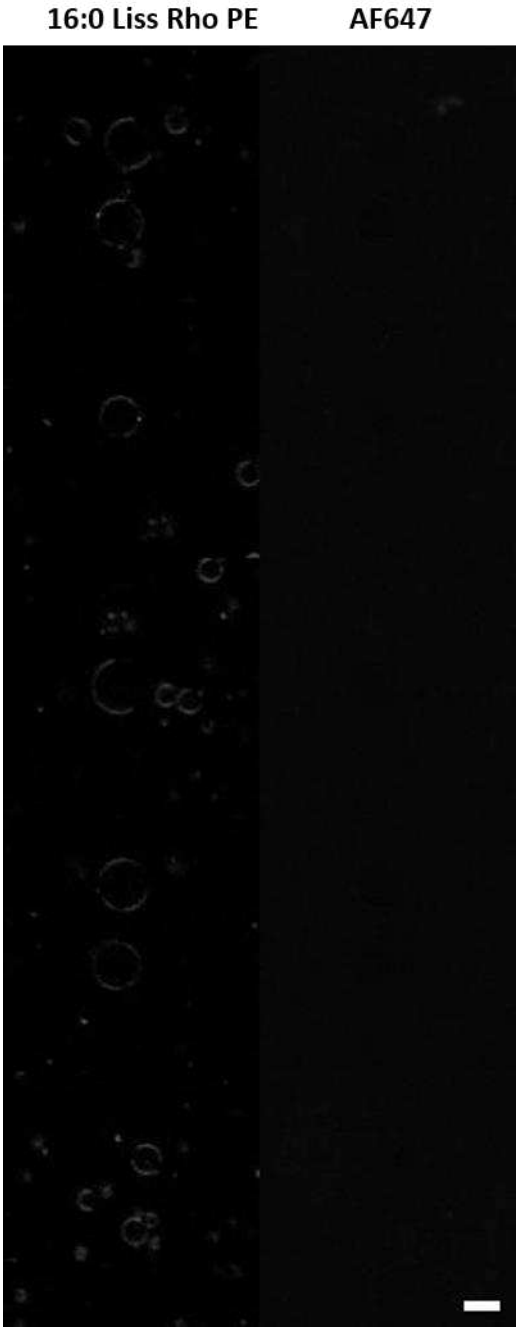

Figure S25. Confocal images of phase separating GUVs containing 0.1 mol% of the Ld-domain marker 16:0 Liss Rho PE (left) and 1 mol% Man_4DSDap after incubation with 200 nM ConA-AF647 with 5 mM MeMan inhibitor. Scale bar: 10 µm. Contrast adjusted for better visibility.

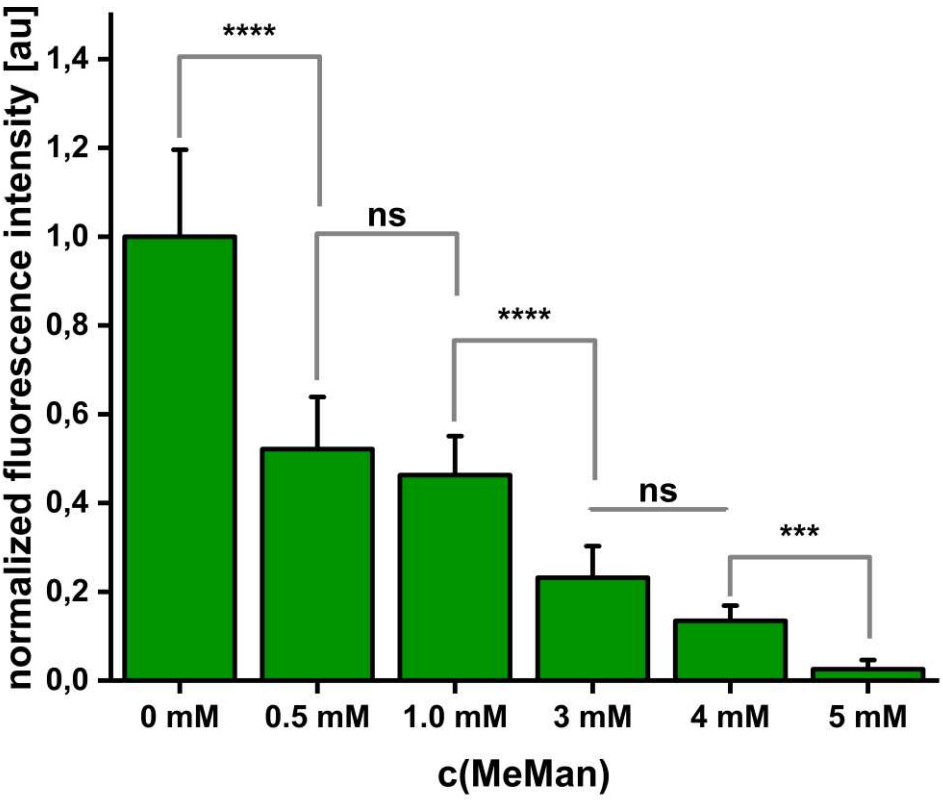

Figure S26. Normalized mean radial relative fluorescence intensity values averaged over the respective membrane domain angle of phase separating GUVs containing 1 mol% Man4DSDap ligand after incubation with 200 nM ConA-AF647 against various concentrations of MeMan as inhibitor. Data are presented as mean + SEM for n = 10 experimental replicates and were evaluated using one-way ANOVA followed by Bonferroni correction (****: $p < 0.001$; ***: $p < 0.005$; ns: not significant). Ligand association with the Lo phase of the GUVs requires 5 mM MeMan to completely inhibit lectin binding.

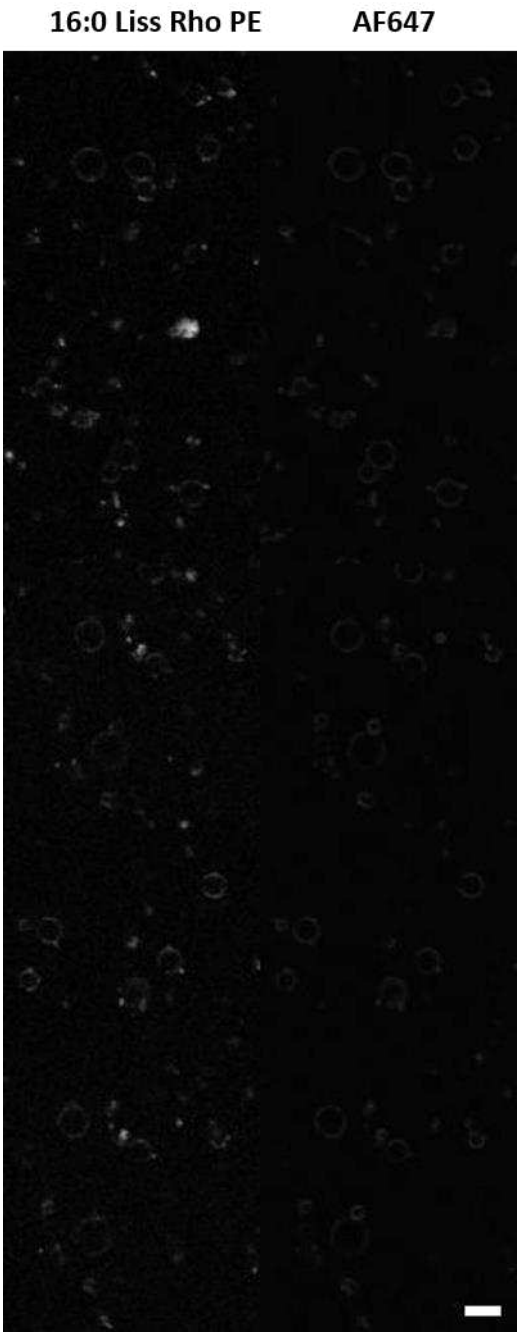

Figure S27. Confocal images of phase separating GUVs containing 0.1 mol% of the Ld-domain marker 16:0 Liss Rho PE (left) and 1 mol% Man_4DODap after incubation with 200 nM ConA-AF647 without added inhibitor. Scale bar: 10 µm. Brightness adjusted for better visibility.

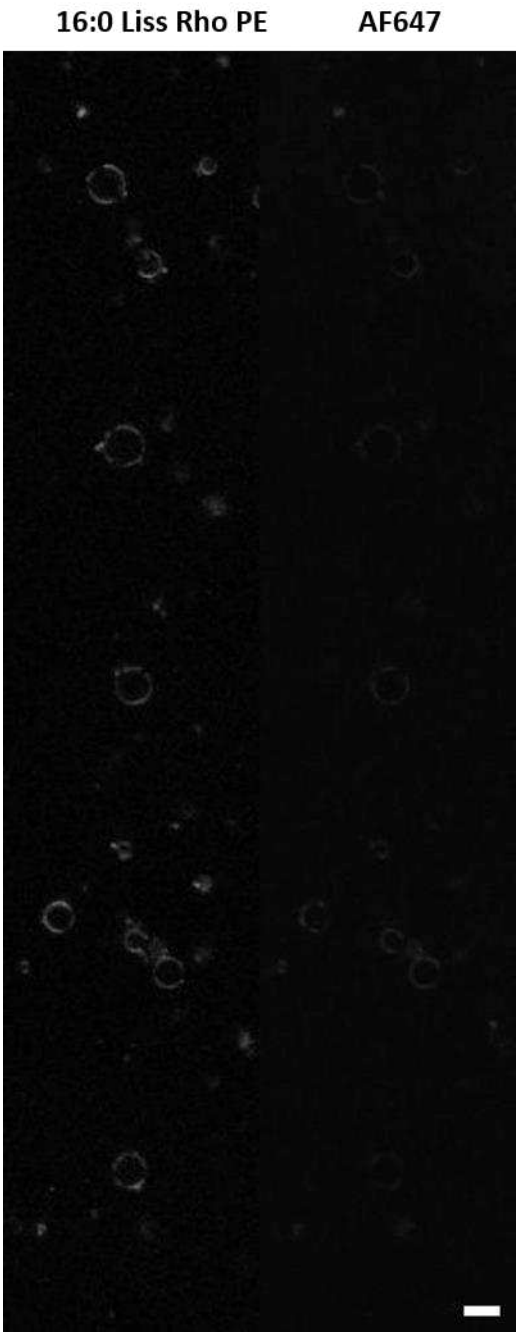

Figure S28. Confocal images of phase separating GUVs containing 0.1 mol% of the Ld-domain marker 16:0 Liss Rho PE (left) and 1 mol% Man_4DODap after incubation with 200 nM ConA-AF647 with 0.5 mM MeMan inhibitor. Scale bar: 10 µm. Brightness adjusted for better visibility.

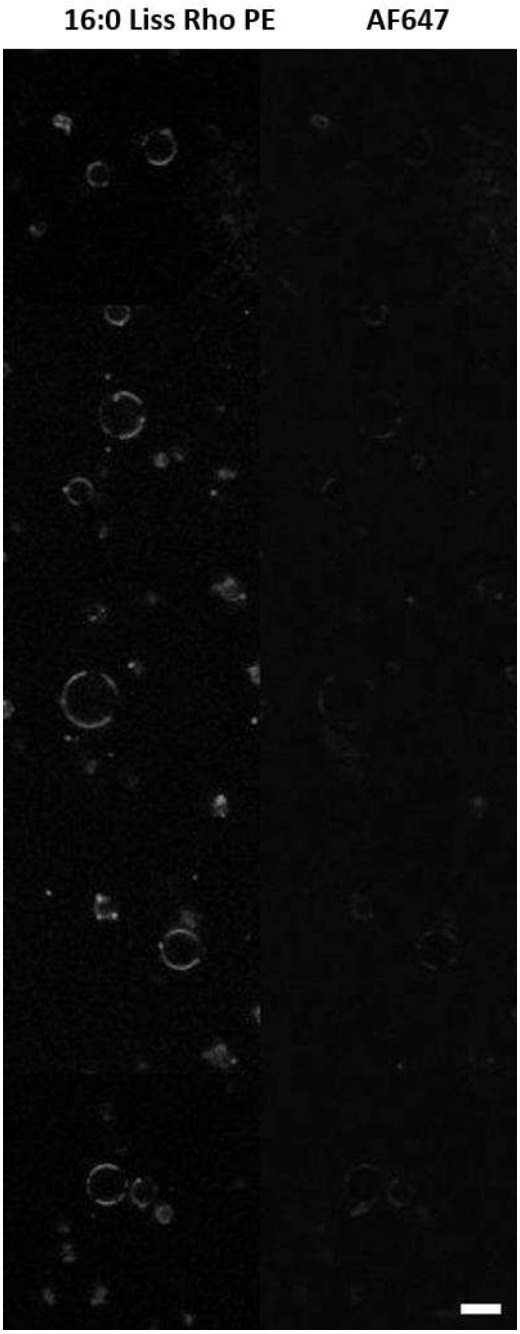

Figure S29. Confocal images of phase separating GUVs containing 0.1 mol% of the Ld-domain marker 16:0 Liss Rho PE (left) and 1 mol% Man_4DODap after incubation with 200 nM ConA-AF647 with 1 mM MeMan inhibitor. Scale bar: 10 µm. Brightness adjusted for better visibility.

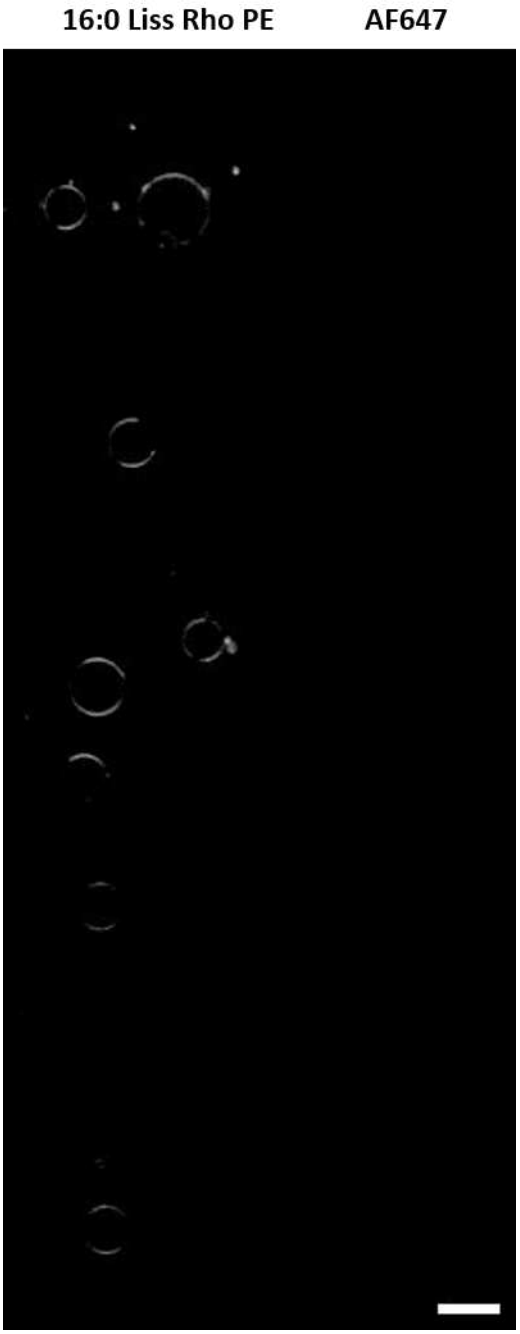

Figure S30. Confocal images of phase separating GUVs containing 0.1 mol% of the Ld-domain marker 16:0 Liss Rho PE (left) and 1 mol% Man_4DODap after incubation with 200 nM ConA-AF647 with 3 mM MeMan inhibitor. Scale bar: 10 µm. Contrast adjusted for better visibility.

Figure S31. Confocal images of phase separating GUVs containing 0.1 mol% of the Ld-domain marker 16:0 Liss Rho PE (left) and 1 mol% Man_4DODap after incubation with 200 nM ConA-AF647 with 4 mM MeMan inhibitor. Scale bar: 10 µm. Contrast adjusted for better visibility.

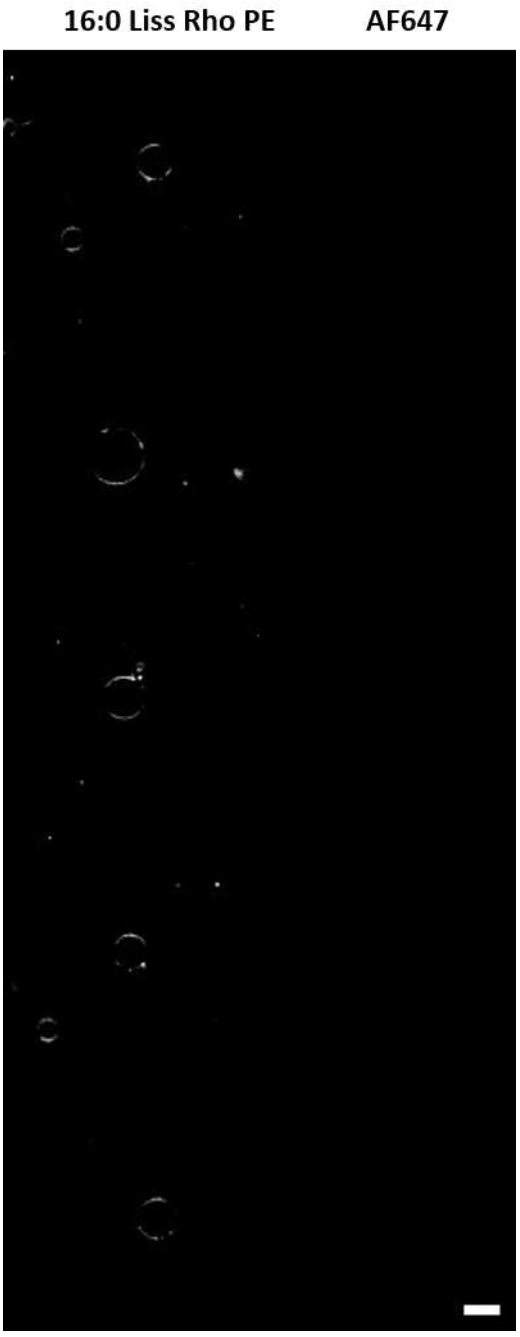

Figure S32. Confocal images of phase separating GUVs containing 0.1 mol% of the Ld-domain marker 16:0 Liss Rho PE (left) and 1 mol% Man_4DODap after incubation with 200 nM ConA-AF647 with 5 mM MeMan inhibitor. Scale bar: 10 µm. Contrast adjusted for better visibility.

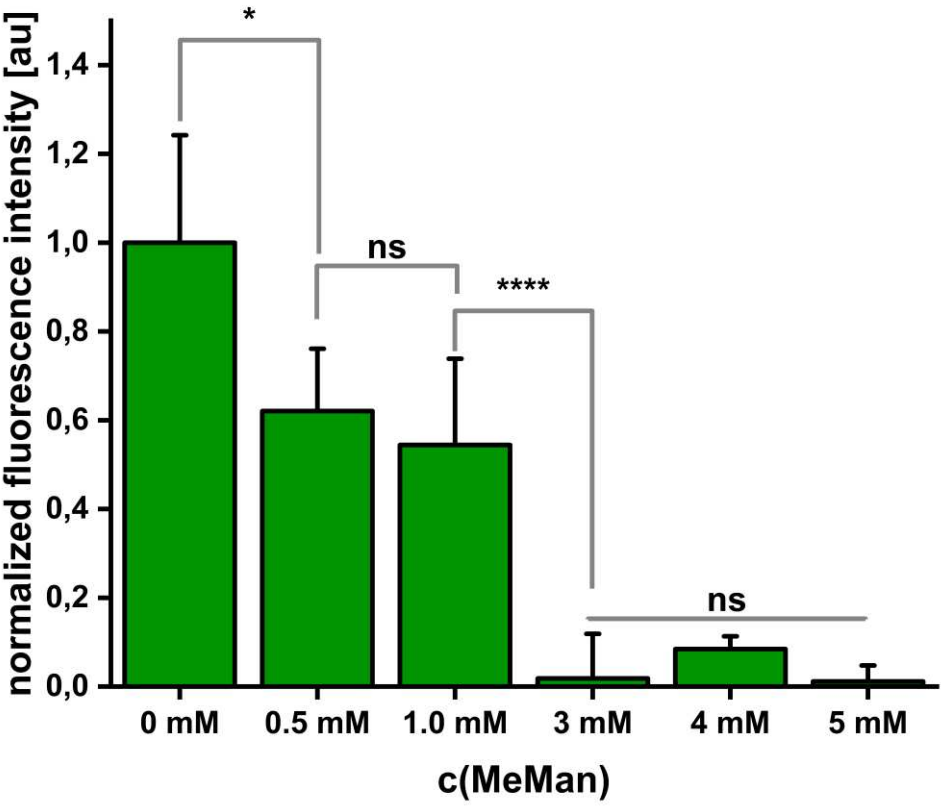

Figure S33. Normalized mean radial relative fluorescence intensity values averaged over the respective membrane domain angle of phase separating GUVs containing 1 mol% Man_4DODap ligand after incubation with 200 nM ConA-AF647 against various concentrations of MeMan as inhibitor. Data are presented as mean + SEM for n = 10 experimental replicates and were evaluated using one-way ANOVA followed by Bonferroni correction (****: $p < 0.001$; ***: $p < 0.005$; ns: not significant). Ligand association with the Ld phase of the GUVs requires 3 mM MeMan to completely inhibit lectin binding.

Supporting Literature

[41] a) S. Boden, F. Reise, J. Kania, T. K. Lindhorst, L. Hartmann, *Macromolecular bioscience* **2019**, *19*, e1800425; b) D. Ponader, F. Wojcik, F. Beceren-Braun, J. Dernedde, L. Hartmann, *Biomacromolecules* **2012**, *13*, 1845.

[42] M. Ionescu, Z. Petrovic, *J Serb Chem Soc* **2011**, *76*, 591.

3.3 Synthesis of Membrane-Tethering sGAG Mimetics and First Studies on Virus-Membrane-Interactions

Many viruses exploit sulfated GAGs (sGAGs) on cell surfaces to bind to and infect their target cells.[187–189] sGAGs act as their first point of contact and facilitate virus binding through unspecific ionic interactions with viral proteins. This binding is often the first step in the infection process that allows viruses to enter cells.[59] sGAGs are difficult to access and study due to their structural complexity and variability, making them difficult to analyze and understand their interactions with viruses.[190,191] Nevertheless, it is of great interest to study these interactions on cell membranes, as this may lead to new insights into the mechanisms of viral infection and potentially to the development of new antiviral therapies. The study of virus-sGAG interactions could thus enable decisive advances in virology and infection biology.

Based on the established synthetic procedures to derive lipid-functionalized precision glycomacromolecules and their introduction into GUVs as model membrane systems (chapter 3.1 and 3.2), these protocols shall now be further developed to access highly defined mimetics of natural sulfated GAGs to develop a convenient platform that enables a systematic study of virus-membrane interactions.

Of note, the rational design, synthesis and characterization of the short sGAG mimetics was jointly executed with M. Hoffmann. The rational design and synthesis of the long sGAG mimetics was executed in collaboration with L. Bonda (own contribution: synthesis and characterization of the macroinitiators).

In brief, a total of eight short and long sGAG mimetics was synthesized. All of the derived structures display a set of key functionalities, i.e. a glyco-head group, a membrane anchor and a fluorescent dye (Rhodamine B) for probing via fluorescence microscopy. The short sGAG mimetics thereby display five glyco-moieties, while for the longer sGAG mimetics 70 glyco-moieties in their headgroup were targeted. The target structures are summarized in **Figure 11**.

Class A sGAG mimetics display a cholesteryl moiety as membrane anchor, as well as a Rhodamine B fluorophore. In class B, the membrane anchor was switched for a bisalkyl moiety, to analyze the effect of the different lipid moiety on membrane incorporation and mobility. In class C, the employment of Rhodamine B was omitted, to study the potential contribution of the dye on membrane and virus interaction. In class D, the employment of the *N*-terminal lipid moiety was omitted, to derive structures that serve as potential viral inhibitors in later assays.

Of note, even though Man is not abundant in natural sGAGs, previous studies by *Soría et al.* have shown that sulfated Man-glycopolymers serve as suitable viral inhibitors in cellular assays, hence Man was employed as glyco-motive in all structures.[190]

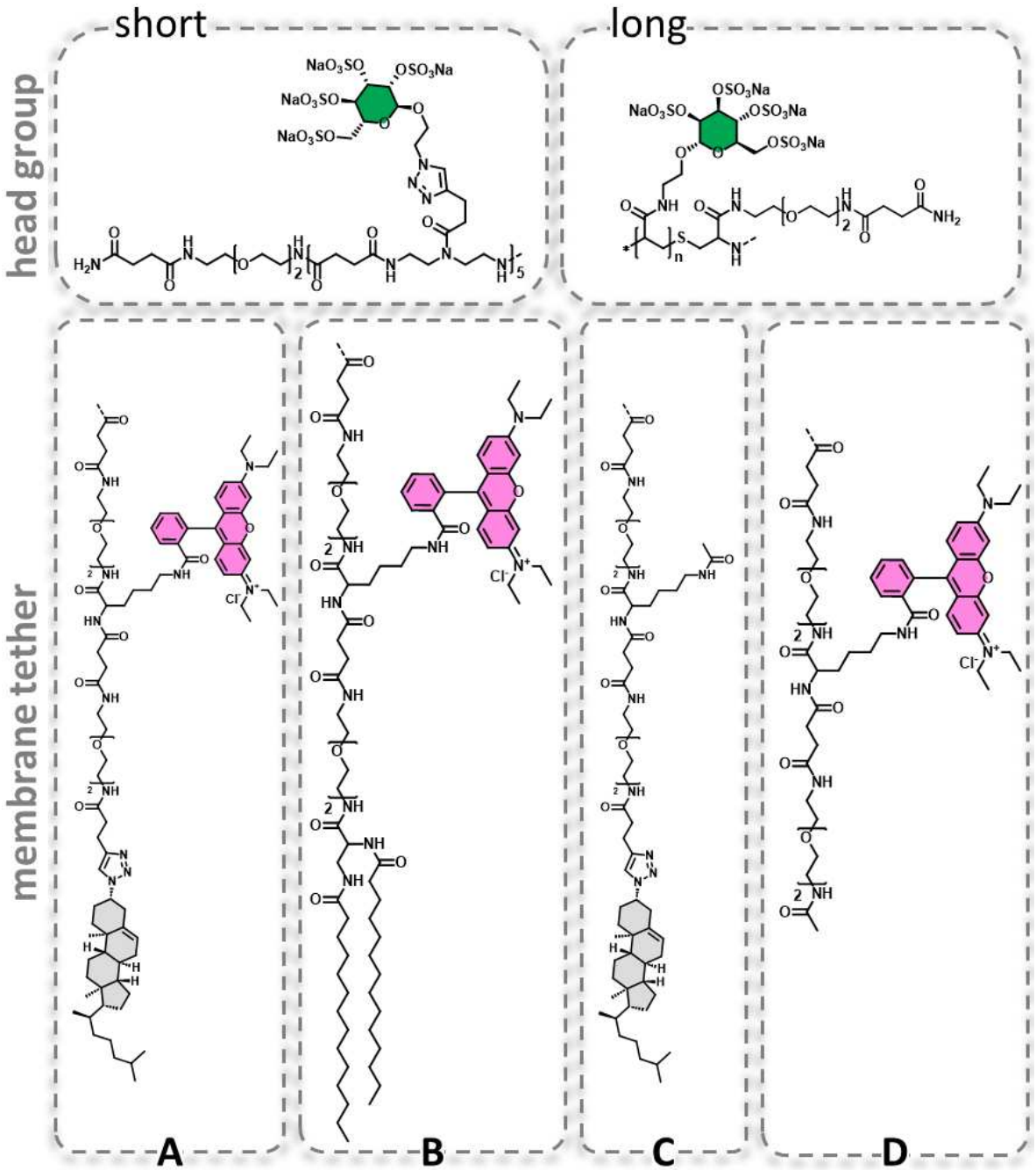

Figure 11. Overview of the synthesized long and short sGAG mimetics.

3.3.1 Synthesis of Short sGAG Mimetics

For the establishment of a synthetic route to derive sequence-defined and sulfated glycan mimetics, SPPoS was employed. As was written in chapter 1.3.1, the type of linker chosen to attach the backbone to the carrier resin dictates the cleavage conditions of the solid phase derived structure. Sulfation of hydroxyl-moieties on the solid phase has earlier been reported to not withstand the harsh cleavage conditions of the rink amide linker (95% TFA), which results in the cleavage of sulfate moieties.[192] To prevent this, the commercially available Fmoc-Photolinker was employed on a TentaGel® S NH_2 resin. The photolinker is completely orthogonal to the reaction conditions employed to assemble the glycooligomer on the backbone and is cleaved via irradiation with 360 nm. In the doctoral thesis by M. Hoffman, an optimized protocol was established, to generate sequence defined and sulfated glycooligomers, hence the figured conditions were transferred to the synthesis of this next generation of membrane anchoring sGAG mimetics.[193,194]

For all structures the same backbone was employed and later further functionalized. The sequence [EDS]-[TDS]5-[EDS]-[Lys(Boc)]-[EDS]-Fmoc was assembled on the resin, employing previously established coupling protocols. The exemplary synthesis of $_{short}$A is schematically shown in **Figure 12**.

After assembly of the backbone, the alkyne moieties were functionalized with azidoethyl functionalized peracetylated mannose via CuAAC. Subsequently, the batch was splitted into four.

For $_{short}$A, the *N*-terminus was subsequently deprotected and functionalized with 4-pentynoic acid, before introducing the cholesteryl moiety via CuAAC employing 3-β-azidocholesterol. Then, the Lys side chain was Boc-deprotected via treatment with 4M HCl in dioxane, before the Rhodamine dye was conjugated to the free amine. For $_{short}$B, the *N*-terminus was deprotected and conjugated with Fmoc-Dap(Fmoc)-OH. After again deprotecting the Fmoc-protected terminal amines, myristic acid was conjugated to the backbone. Myristic acid, a saturated C_{14}-fatty acid was chosen, because previous studies by et al have demonstrated, that a C_{14}-alkyl moiety is best suited to incorporate glycan mimetics into phospholipid membranes and to ensure a stable insertion with low partitioning coefficients.[170] After *N*-terminal acylation, the Lys side chain was again deprotected and Rhodamine B was conjugated to the backbone. For $_{short}$C, the synthesis proceeded analogous to the synthesis of $_{short}$A, omitting conjugation of the Rhodamine B but therefore acetylating the Lys-side chain with acetic anhydride. For $_{short}$D, after glycosylation via CuAAC, the *N*-terminus was Fmoc-deprotected and subsequently acetylated, before deprotecting the Lys side chain and conjugating the Rhodamine B dye.

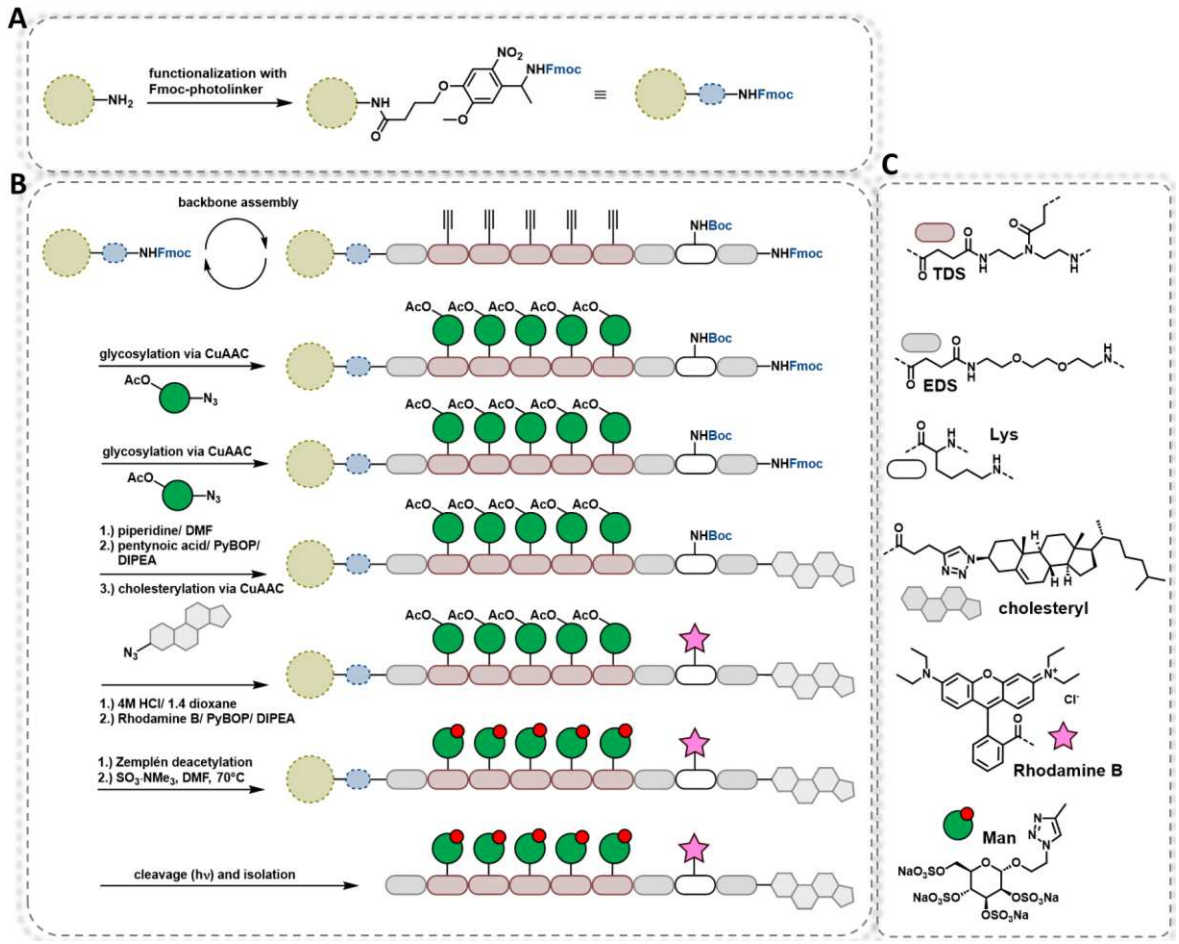

Figure 12. A: Conjugation of the commercially available Fmoc-Photolinker to a TentaGel NH_2 resin. **B:** Schematic presentation of the solid phase polymer synthesis of short sGAG mimetics. **C:** Library of employed building blocks.

After assembly of the glycooligomers on the backbone, the Man-moieties were deacetylated employing Zemplén conditions (0.2 M NaOMe in MeOH). On-resin sulfation of the carbohydrate moieties was conducted according to the optimized conditions explored by *M. Hoffmann*.[193,194] In brief, the resin-bound glycooligomers were treated with 50 eq SO3·NMe3 per hydroxyl group in DMF at 70°C for 16h. Subsequently, the solution was discarded and the reaction was quenched with a 10% solution of NaOAc in water. The resin was washed several times with this solution, with water and DMF to remove any excess reagent. Afterwards, the target structures were cleaved off the resin via irradiation with 365 nm. The cleaved structures were purified via diafiltration and characterized via ^{1}H-NMR, elemental analysis, RP-HPLC-MS and HR-ESI-MS. Key characteristics of the short target structures are summarized in **Table 1**.

Table 1: Overwiev of the molecular weights and the determined degrees of sulfation for the short sGAG mimetics.

sample	M_w [g/mol][a]	DS [%][b]
$_{short}A^S$	6366.77	98
$_{short}B^S$	6381.82	99
$_{short}C^S$	5983.25	94
$_{short}D^S$	5917.04	94

[a]assuming a DS of 100%, [b]determined via elemental analysis

Sulfation of the glycan mimetics was confirmed via ^{1}H-NMR spectroscopy. Sulfation of the pyranose hydroxyl moieties induces a downfield shift of the pyranose protons, which is caused by the deductive effect of the sulfate moieties (**Figure 13**).

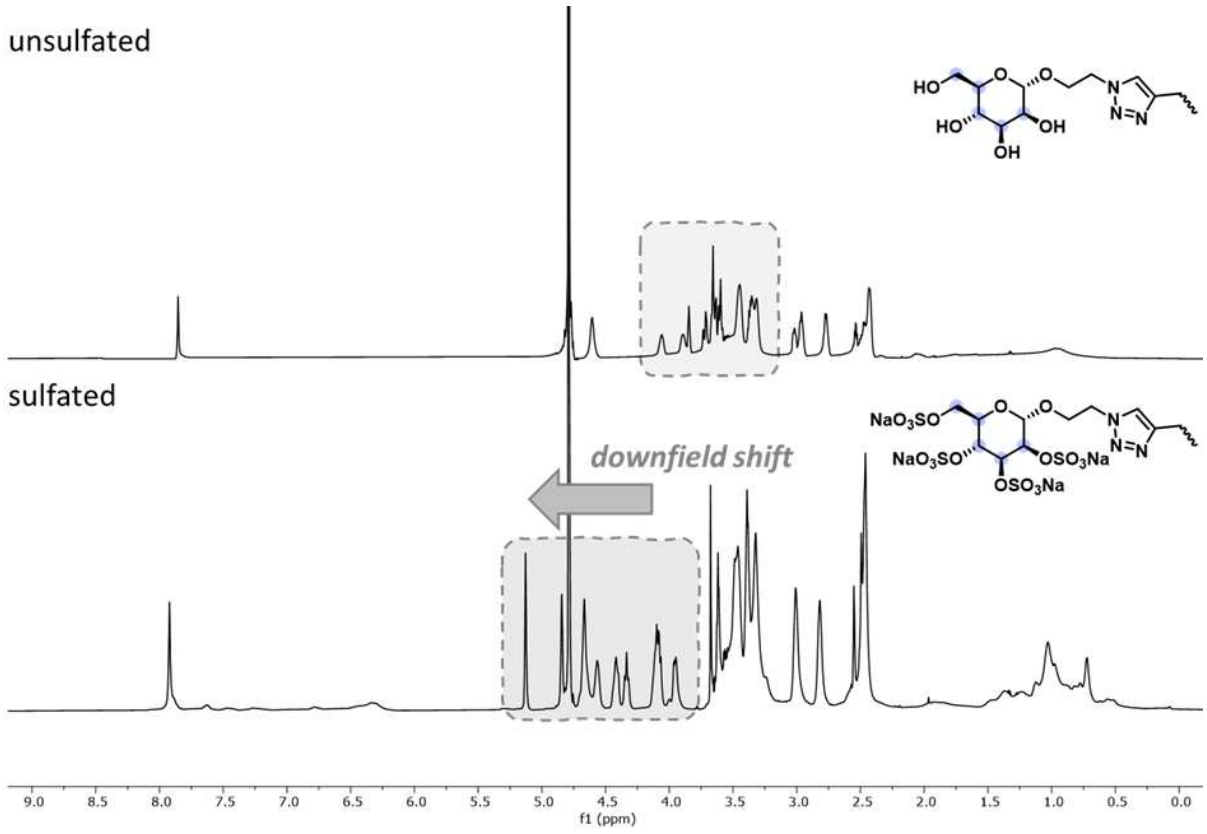

Figure 13. Stacked proton NMR spectra of $_{short}A^{OH}$ (unsulfated) and $_{short}A^S$ (sulfated) (600 MHz, D_2O, ambient temperature). Sulfation of the hydroxyl moieties results in a downfield shift of the pyranose protons (highlighted in dashed boxes). For the fully analyzed spectrum see *Experimental Section*.

As a negative control, $_{short}$A and $_{short}$B were also prepared without sulfation of the glyco-moieties, termed as $_{short}A^{OH}$ and $_{short}B^{OH}$, purified via diafiltration and characterized via ^{1}H-NMR and HR-ESI-MS (see *Experimental Section*).

3.3.2 Synthesis of Long sGAG Mimetics

To derive the longer derivatives of the scheduled target structures, the macroinitiator approach that was proposed in chapter 3.1 was employed.

First, the macroinitiator backbone was assembled on the TentaGel S RAM resin ([EDS]-[Cys(Trt)]-[EDS]-[Lys(Dde)]-[EDS]-Fmoc)(**Figure 14A**). Of note, the TDS moieties were substituted for a trityl protected Cys-moiety serving as later grafting point for TIRP and the Boc-protected Lys was switched for a the respective Dde-protected derivative to ensure orthogonality between the Cys- and the Lys-protecting group. After assembly of the backbone, the batch was again split in four. The further functionalization occurred analogous to the synthesis of the short glycooligomers with the exception that the Lys-side chain was now deprotected via treatment with 2% hydrazine hydrate in DMF to remove the Dde protecting group.

After assembly of the four macroinitiators, they were cleaved off the resin employing 95% TFA/ 2.5 % TIPS/ 2.5 % DCM and precipitated twice in 25% diethyl ether in hexanes. The derived macroinitiators were dried and characterized via ^{1}H-NMR, HR-ESI-MS and RP-HPLC-MS (see *Experimental Section*).

Of note, the preparation of the polymers via the macroinitiators, as well as the subsequent sulfation and characterization, was carried out by Lóránd Bonda. To obtain the glycopolymers, the macroinitiators were polymerized via TIRP employing peracetylated Man-hydroxyethylacrylamide monomers (**Figure 14B**). After finishing the polymerization, the solution was poured into 0.2 M NaOMe in MeOH for Zemplén deacetylation. Hereafter, the polymers were precipitated in diethyl ether and dried. After purification via diafiltration, the polymers were characterized via ^{1}H-NMR and SEC. Key characteristics of the polymers are summarized in **Table 2**.

Table 2. Overwiev of the molecular weights, degrees of polymerization, dispersities and the determined degrees of sulfation for the long sGAG mimetics

sample	Mn [kDa][a]	Pn[b]	Đ[b]	Degree of Sulfation [%][c]
$_{long}A^{S}$	54.0	76	1.4	99
$_{long}B^{S}$	56.0	79	1.1	87
$_{long}C^{S}$	53.0	75	1.1	97
$_{long}D^{S}$	49.0	70	1.3	97

[a]number average molar mass assuming 100% sulfation, [b]determined via *H_2O-SEC-MALS*, [c]determined via elemental analysis

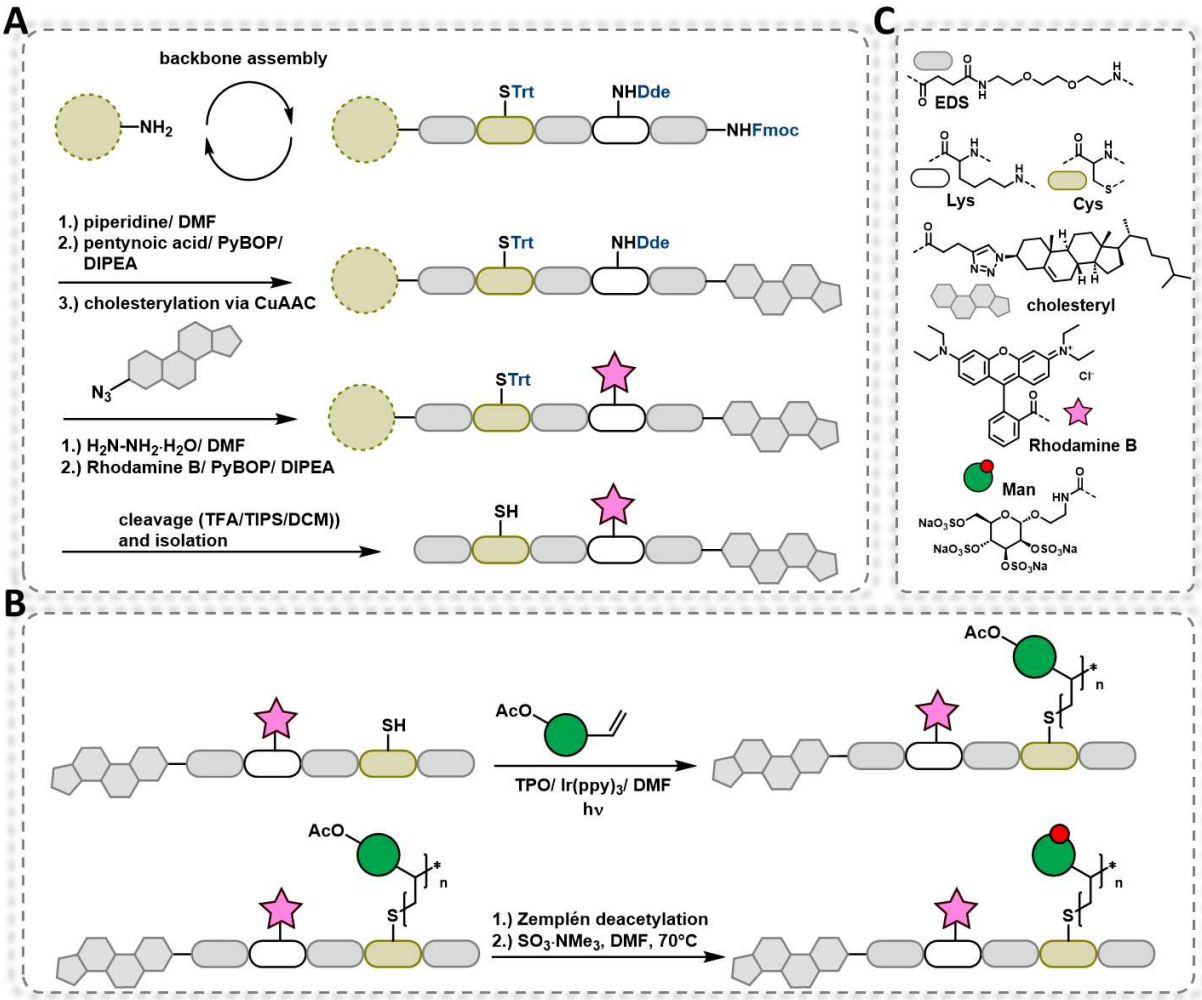

Figure 14. A: Schematic presentation of the solid phase polymer synthesis of functional macroinitiators. **B:** Schematic presentation of the synthesis of long sGAG mimetics employing TIRP. **C:** Library of employed building blocks.

In the next step, the polymers were sulfated as described above. Briefly, the polymers were dissolved in a mixture of 50 eq SO3·NMe3 per hydroxyl group in DMF and reacted at 70°C for 16h. Afterwards, the reaction mixture was quenched with a 10% solution of NaOAc in water. The solvent was evaporated and the remaining mixture of sulfated polymers and salt was again purified via diafiltration.

The sulfated polymers were characterized via ^{1}H-NMR and elemental analysis. Again, sulfation of the mannosylated polymers was confirmed by the downfield shift of the pyranose protons via ^{1}H-NMR (see **Figure 15**).

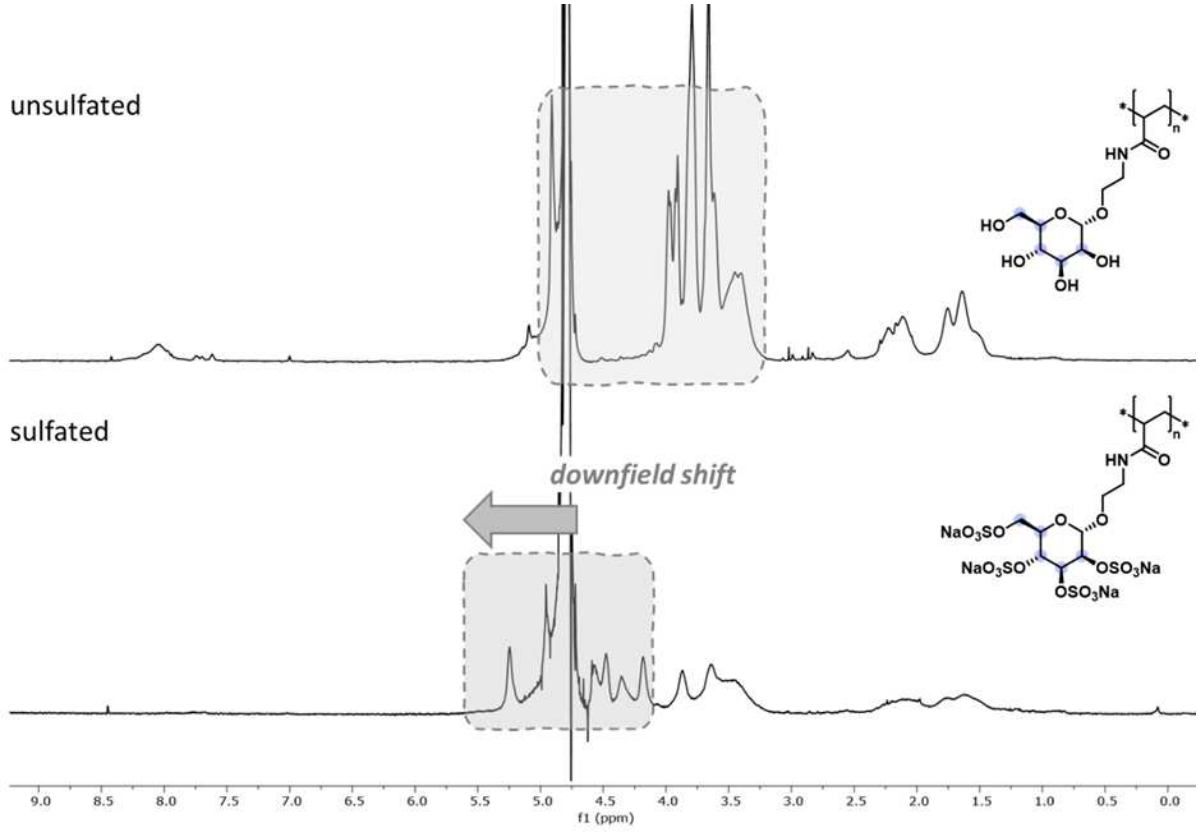

Figure 15. Stacked proton NMR spectra of $_{long}A^{OH}$ (unsulfated) and $_{long}A^{S}$ (sulfated) (600 MHz, D_2O, ambient temperature). Sulfation of the hydroxyl moieties results in a downfield shift of the pyranose protons (highlighted in dashed boxes). For the fully analyzed spectrum see *Experimental Section*.

3.3.3 First studies on Virus-Membrane Interactions

To assess the applicability of the synthesized sGAG mimetics to study virus-membrane interactions, first experiments were performed in cooperation with Dr. R. Groza, K. Schmidt, and Prof. Dr. H. Ewers.[1] Therefore, the cholesteryl-functionalized, sulfated glycopolymer $_{long}A^{S}$ was introduced into GUVs as simple glycocalyx mimetics and cells by means of *de novo glycocalyx engineering*. As viral equivalents, virus like particles derived from three different viruses (simian virus 40 (SV40), merkel cell polyomavirus (MCPyV) and human papillomavirus type 16 (HPV16)) were employed, each functionalized with AF647 as fluorescent probe for fluorescence microscopy.

SV40 and MCPyV are both polyomaviruses, a class of small, non-enveloped DNA viruses. Specifically MCPyV is highly associated with cancer, predominantly merkel cell carcinoma (MCC), an aggressive type of skin cancer.[195] While SV40 is known to infect cells through specifically binding sialylated

[1] *Freie Universität Berlin, Department for Chemistry and Biochemistry*; own contribution: collaborative development of a protocol to formulate GUVs with incorporated sGAG mimetics, first studies on the interaction of VLPs with sGAG-decorated GUVs via fluorescence microscopy

gangliosides,[196,197] MCPyV requires an initial binding to sGAGs present on the cell surface before progressing to a ganglioside receptor and initiating infection.[198]

HPV16 is a small, non-enveloped DNA virus that is highly associated with several cancers, most predominantly cervical cancer.[199] It has been shown to initially bind to heparin sulfate proteoglycans (HSPGs) on epithelial cells, which mediates its progression to the cell surface and the initiation of infection.[200]

To construct the glycocalyx mimetics with the polymeric GAG mimetic, GUVs were prepared from DOPC (97%), Bodipy-FL-C12-HPC (1%, as membrane dye) and 2% of $_{long}A^{S}$ via electroformation. The assembled GUVs were then incubated with HPV16 or MCPyV VLPs, respectively. As was evidenced by the colocalizing fluorescence of Rhodamine B, conjugated to the sGAG mimetic, and VLP-AF647, both VLPs bind to the sGAG mimetic decorated surfaces (**Figure 16**).

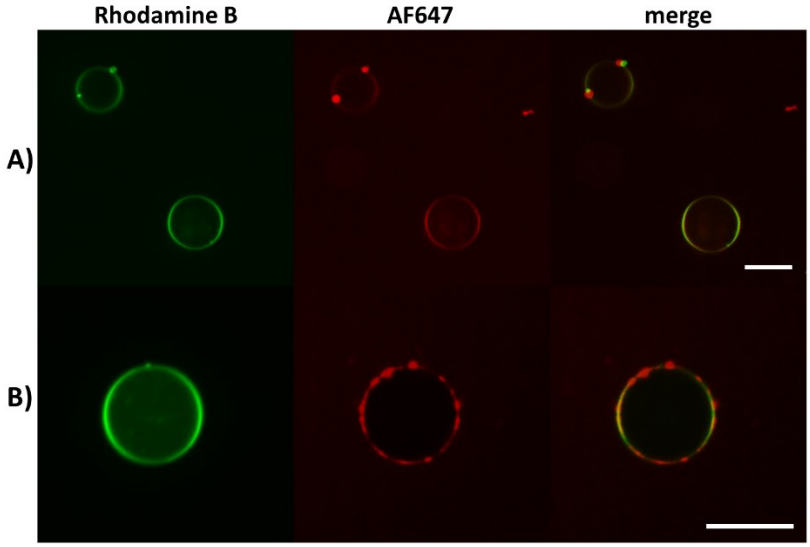

Figure 16. AF647-labelled VLPs HPV16 (**A**) and MCPyV (**B**) bind to GUVs decorated with the sulfated GAG mimetic $_{long}A^{S}$. Scale bars: 10 microns.

After performing the first binding studies on GUVs, next GM95 cells were incubated with the $_{long}A^{S}$ glycopolymer. GM95 is a cancerous cell line derived from mice with no ceramide glucosyltransferase activity.[201] The glucosylation of ceramide is an essential first step in the biosynthesis of glycolipids and consequently, enzymatic inactivity leads to a deficiency of native glycolipids, such as the GT1b trisialoganglioside, which are required for MCPyV and SV40 to initiate infection of a host cell.[202]

The cultured cells were treated with the sGAG mimetic in serum-free medium for 16 hours before washing with PBS and incubating on ice to hold up active endocytosis. Then, the cells were incubated

with VLPs of MCPyV and SV40 for 20 minutes, before washing with PBS. As a control, GM95 cells that were not treated with the sGAG mimetic were also incubated with the VLPs (**Figure 17**).

Evidenced by the colocalizing fluorescence of the Rhodamine B labelled sGAG mimetic, the polymers incorporated well into the cell membrane of the GM95 cells. As was demonstrated before in the GUV experiments, MCPyV-VLPs strongly bind to the sGAG mimetic-decorated cell surfaces. By comparing the mean fluorescence intensities of the GAG mimetic-decorated cells and non-functionalized cells, it is shown that the binding of MCPyV is increased through the employed sGAG mimetic (see **Figure 58**, *Appendix*).

As was expected, SV40-VLPs did not adhere significantly to the cells. As was stated above, SV40 requires the GT1b-ganglioside to bind to the cell surface and does not interact with sGAGs-functionalized proteoglycans on the cell surface.[198] Incubation with the SV40-VLPs rules out unspecific binding and serves as a negative control.

The presented sGAG mimetics offer the potential to study viral interactions with sGAGs on native cellular membranes. To further refine the set-up, deglycosylation of the native cell membrane (i.e. sequestering native sGAGs from the cell surface) should yield more insights into the interaction, since VLP binding can then be specifically deduced to the presence of the sGAG mimetics.

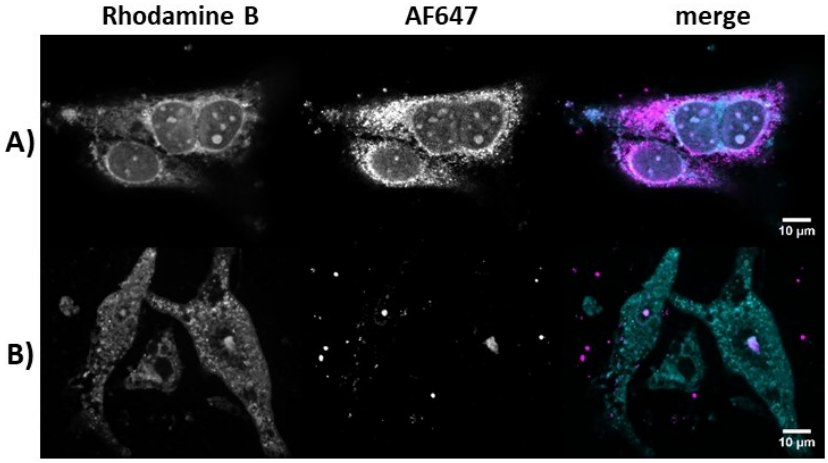

Figure 17. GM95 cells were incubated with the sulfated GAG mimetic $_{long}\mathbf{A}^{S}$. While MCPyV-VLPs strongly accumulate on the cells (**A)**), SV40-VLPs show no interaction with the cell surface (**B)**).

In summary, the synthetic toolbox, that was already introduced in chapters 3.1 and 3.2 to derive high precision, lipidated glycan mimetics has been extended to access now also highly sulfated derivatives to serve as mimetics of naturally occurring sGAGs. The presented first set of experiments demonstrates the applicability and feasibility of sulfated GAG mimetics to study viral interactions on glycocalyx mimetics and cellular glycocalyces by means of *de novo glycocalyx engineering*. For further

studies a rational design of the set-up, employing the short and long GAG mimetics, bears the potential to examine the fundamental mechanisms that are associated with viral adhesion on eukaryotic membranes. Systematic variations in ligand valency and density, as well as ligand mobility in the membrane could shed light on the prerequisites that need to be met in order for viruses to initially attach to a cell surface, before eventually infecting the host cell.

3.4 Diacetylene-Functionalized Glycan Mimetics for Receptor-Mediated Cluster Imprinting in Model Membranes

Authors: Luca-Cesare Blawitzki, Nicholas Jäck, Lina Charlotte Assenmacher, Cornelia Monzel, Stephan Schmidt and Laura Hartmann

Journal: *manuscript in preparation (paper draft)*

Contribution: Collaborative conceptualization of the work. Establishment of a synthetic route to synthesize a polymerizable diacetylene building block for SPPoS. Establishment of building block conjugation on the solid phase. Collaborative synthesis and purification of polymerizable and lipid-functionalized precision glycomacromolecules, as well as characterization of the derived compounds via RP-HPLC-MS, ^{1}H-NMR and HR-ESI-MS. Establishment of a protocol to incorporate the diacetylene-functionalized glycan mimetics into GUVs. Conduction of fluorescence microscopy experiments. Collaborative evaluation and interpretation of the gathered data as well as visualization of the results. Collaborative writing of the manuscript.

Diacetylene-Functionalized Glycan Mimetics for Receptor-Mediated Cluster Imprinting in Model Membranes

*Luca-Cesare Blawitzki[a,c], Nicholas Jäck[a,c], Lina Charlotte Assenmacher[a], Cornelia Monzel[b] and Laura Hartmann[c]**

[a] Department for Organic and Macromolecular Chemistry, Heinrich Heine University Duesseldorf, Universitätsstraße 1, 40225 Düsseldorf, Germany

[b] Department for Experimental Medical Physics, Heinrich Heine University Duesseldorf, Universitätsstraße 1, 40225 Düsseldorf, Germany

[c] Department for Macromolecular Chemistry, University of Freiburg, Stefan-Meier-Str. 31, 79104 Freiburg i.Br., Germany

*Email: laura.hartmann@makro.uni-freiburg.de

ABSTRACT

The glycocalyx, a dense layer of glycoproteins and glycolipids on eukaryotic cells, is crucial for cellular functions, such as communication, signaling, and pathogen interactions. Certain components are spontaneously organized into lipid rafts - membrane microdomains that enhance glycan-lectin interactions by clustering membrane glycoproteins and -lipids. However, studying these dynamic systems in native membranes is challenging due to their immense heterogeneity. To address this, synthetic glycocalyx mimetics have emerged as valuable tools for replicating these complex interactions.

In this study, we aim to refine these mimetic systems by using diacetylene-containing ligands that polymerize upon irradiation to form stable glycan clusters, mimicking the dynamic clustering of glycans in lipid rafts. We synthesized a novel type of cholesteryl-tethered glycan mimetics, now featuring a polymerizable diacetylene belt. These ligands self-assemble in aqueous environments and can be incorporated into giant unilamellar vesicles (GUVs). Upon irradiation, the diacetylene units polymerize, forming fluorescent polydiacetylene clusters that replicate receptor-mediated glycan clustering in cell membranes.

This approach allows for precise control over glycan cluster formation, enabling the study of multivalent glycan-lectin interactions in membrane microdomains. By minimizing nonspecific crosslinking and enhancing the stability of glycan clusters, this system provides a more accurate platform for studying glycocalyx-mediated cellular processes. This novel method offers significant potential for advancing our understanding of membrane-associated glycan interactions and their role in cellular signaling.

Key words: glycocalyx, clustering, polydiacetylenes, GUV, solid phase synthesis

INTRODUCTION

Eukaryotic cells are covered by a dense layer of glycoproteins and glycolipids, which is commonly referred to as the glycocalyx and is involved in a myriad of biological processes such as cellular communication, signaling and pathogen infection. [1,2] Membrane-associated glycans and proteins are organized hierarchically into local microdomains, termed *lipid rafts*, which cluster membrane proteins and glycoproteins to enhance functional interactions and help cells adapt to changing environments. [3,4] In fact, this *glycoside cluster effect* increases the affinity and selectivity of glycan-lectin interactions and can amplify signaling pathways by bringing together receptors and their ligands. [5,6] Furthermore, the spatial arrangement of glycans can create zones that exclude certain molecules, thereby directing cellular behavior and responses. [7,8]

Due to the heterogenous and dynamic nature of native glycocalyces, glycocalyx mimetics have emerged as a valuable tool to recreate simple cell membrane models. [9,10] To fully mimic the complexity of biological membranes, it's essential to enhance these synthetic systems by adjusting composition, dynamics, and local carbohydrate heterogeneities. We recently introduced phase-separating glycocalyx mimetics that replicate lipid raft formation in native cells. Employing solid phase polymer synthesis (SPPoS), we created lipid-tethered glycan mimetics, which localize liquid disordered (Ld) or highly ordered (Lo) membrane domains in GUVs, depending on their respective lipid tether. We observed that lectin binding to ligands in Lo vesicle domains significantly increased compared to Ld domains, emphasizing the role of lipid rafts in enhancing multivalent lectin-glycan interactions. While this method gives rise to a convenient platform to study raft-associated processes, these model raft domains are microns in size, whereas native lipid rafts are much smaller, ranging from nanodomains (5-20 nm) to larger aggregates (200 nm) and form spontaneously in response to stimuli like receptor activation. [11,12] Thus, a covalent fixation of receptor-mediated glycan clusters may further refine glycocalyx mimetics to better reflect dynamic responses and local microheterogeneity.

Photo crosslinkers, such as diazirines, aryl azides, and benzophenone-derivatives, are increasingly being employed in the study of glycan clusters and in identifying binding interactions in native glycocalyces. [13–15] *Yarravarapu et al.*, for instance, enzymatically functionalized cell-surface glycans with diazirine-modified sialic acid to enable the photo

crosslinking of glycoproteins. [16] However, photo crosslinkers form covalent bonds with adjacent molecules upon UV irradiation, hence nonspecific crosslinking may obscure the specific binding events of interest. [15,17] Also, they can mask core glycan structures, hindering selective lectin recognition and complicating glycan interaction analysis. [18,19]

Earlier, *Morigaki et al.*, employed a diacetylene-containing phospholipid (1,2-bis(10,12-tricosadiynoyl)-sn-glycero-3-phosphocholine, DiynePC) to generate covalently fixed lipid patterns on supported lipid bilayers. [20] The diacetylene moiety is a conjugated 1.3-diyne that can polymerize upon irradiation with UV light (254 nm) under suitable conditions to give polydiacetylenes exhibiting alternating double and triple bonds, concomitant with an intense coloration due to the extended π-system. [21,22] This trigger-responsive chromism of polydiacetylene makes it ideal as a colorimetric probe, with many studies using head-group modified diacetylenes as colorimetric sensors for specific metal ions or biomolecules. [23–25] The polymerization of the diacetylene moieties requires a certain spatial arrangement of the monomers to one another and is therefore termed as a topochemical polymerization. [26,27] Secondary interactions, such as hydrophobic interactions, hydrogen bonding or π-stacking can muchly facilitate the appropriate alignment of the diacetylene monomers. [28–30] Additionally, diacetylenes preferably react with adjacent diacetylenes under optimal packing conditions, hence minimizing unspecific crosslinking with adjacent entities. [31]

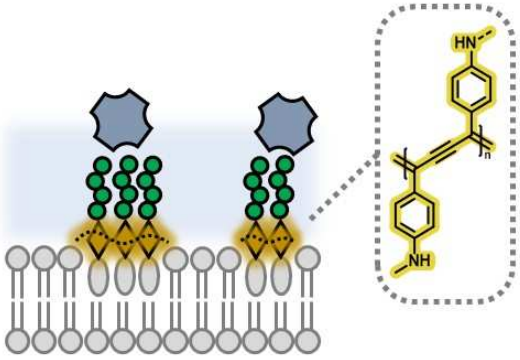

TOC. Diacetylene-functionalized glycan-mimetics cluster upon receptor binding. Irradiation of the cluster covalently crosslinks the ligands, imprinting the receptor-mediated glycan-cluster into the membrane.

To generate the patterned lipid membranes, *Morigaki et al.* prepared supported lipid bilayers of DiynePC via the Langmuir-Blodgett/ Langmuir-Schäfer technique and

subsequently polymerized the aligned diacetylene monomers, employing a mask, via UV-irradiation. After removal of the non-polymerized lipids followed by filling the gaps between polymerized regions with native phospholipids, they obtained patterned phospholipid bilayers featuring immobilized polydiacetylene areas interspersed with fluid phospholipid regions. [20]

In this study, we want to employ the methodology proposed by *Morigaki et al.* to create patterned glycocalyx mimetics, driven by the selective recruitment of glycan-ligands into clusters by multivalent ligands. Therefore, we derived a solid phase synthesis-compatible diacetylene moiety and synthesized cholesteryl-tethered glycan mimetics, containing a site-specific polymerizable diacetylene-belt. These amphiphilic ligands were characterized regarding their capacity to self-assemble in aqueous solution and polymerize upon irradiation. Subsequently, we incorporated our ligands into GUVs to create a simplistic glycocalyx model and incubated the vesicles with a suitable lectin to promote ligand-receptor-mediated glycan-clustering. Following this, irradiation led to the formation of fluorescent polydiacetylene-clusters, mimicking the dynamic receptor-mediated clustering of glycans into lipid rafts in native cellular membranes.

RESULTS AND DISCUSSION

Synthesis of the Polymerizable Building Block Fragments and Establishment of the On-Resin Cadiot-Chodkiewicz Coupling

One major limitation of commercially available diacetylenes is the requirement for harsh irradiation conditions to initiate polymerization. Specifically, the diacetylene group necessitates exposure to 254 nm UV light, which risks damaging biological molecules. [32,33] Moreover, the use of readily available diacetylene-containing fatty acids and lipids restricts the choice of lipid moieties, a factor that significantly influences the physico-chemical properties of the ligands in phospholipid membranes. [34]

Zhu et al. recently reported on a diacetylene motif, 4,4'-(buta-1,3-diyne-1,4-diyl)dianiline, that exhibits a bathochromically shifted absorption profile for polymerization, due to the adjacent aryl moieties, allowing for telechelic functionalization. [35] The diacetylene precursor was synthesized via Eglinton coupling from p-ethynylaniline and subsequently underwent asymmetric functionalization.

During the development of a synthetic strategy for a diacetylene-containing building block, we anticipated several issues that required careful consideration. The use of an aromatic diamine precursor poses challenges due to the reduced reactivity of the aromatic amine groups, which could lead to lower yields and decreased coupling efficiency during SPPoS. [36,37] Additionally, the diacetylene group's susceptibility to polymerization in the solid state further raised concerns about the shelf life of the desired building block.

To address these issues, we decided to divide the target diacetylene containing building block (termed DADS, **D**i**A**cetylene **D**iamine **S**uccinic acid) into two distinct fragments – DADS(I) bearing the carboxylic acid, and DADS(II) bearing an Fmoc-protected aliphatic amine. The full DADS structure can then be formed on-resin by first coupling DADS(I) utilizing standard SPPoS coupling protocols, followed by alkyne heterodimerization with DADS(II). This approach preserves the option for further elongation on the solid phase due to the terminal Fmoc-protected amine group of DADS(II). Conventionally, conjugated diacetylenes are synthesized through Glaser couplings or similar reactions, which work efficiently for symmetric diacetylenes but produce a mixture of coupling products when applied to asymmetric ones. [38] Therefore, we employed the Cadiot-Chodkiewicz coupling

for selective heterocoupling, which uses a terminal haloalkyne and a terminal alkyne, thus minimizing homodimerization as the haloalkyne cannot undergo homocoupling. [39] Accordingly, DADS(I) will be converted into a haloalkyne to enable efficient coupling with DADS(II) via this method on the solid phase.

The synthesis of both fragments originated from commercially available p-ethynylaniline **(1)**. For DADS(I), the aromatic amine was converted into intermediate **(2)** with methyl succinyl chloride and catalytic amounts of 4-dimethylaminopyridine (DMAP). Next, **(2)** was terminally brominated with *N*-bromosuccinimide (NBS) and AgNO3 in acetone to give the respective haloalkyne **(3)**. Finally, **(3)** was hydrolyzed under alkaline conditions to give the target building block fragment DADS(I).

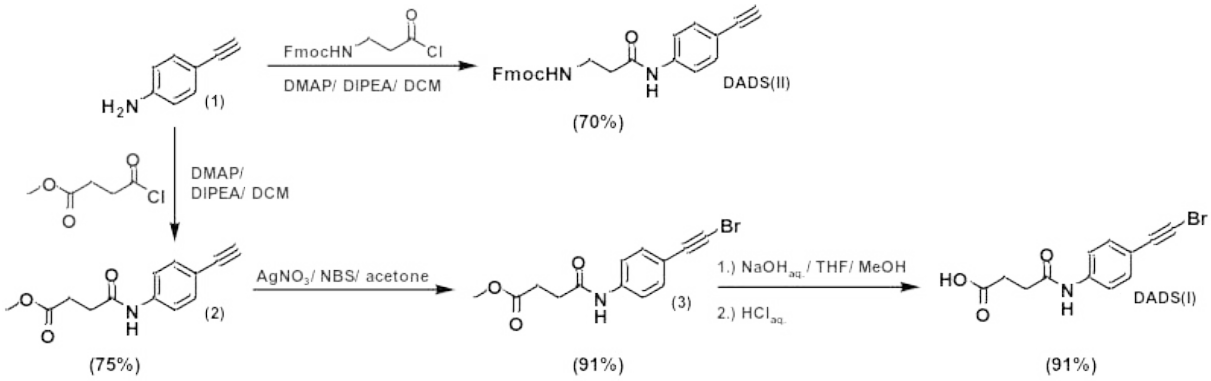

Figure 1. Schematic procedure for the synthesis of **DADS** building block fragments.

For the synthesis of DADS(II), **(1)** was incubated with Fmoc-β-Ala-Cl and catalytic amounts of DMAP to give the target building block fragment in good yield. The introduction of the β-alanine introduces an aliphatic and, hence, more nucleophilic *N*-terminus for a more efficient elongation. In this manner, both fragments were synthesized in acceptable yields (DADS(I): 62% over three synthetic steps, DADS(II): 70%) and characterized via ^{1}H-NMR, ^{13}C-NMR and RP-HPLC-MS.

To demonstrate the applicability of our building block fragment approach, a test sequence was prepared utilizing TentaGel S RAM as the solid phase. After sequentially coupling one ethylene glycol diamine succinyl (EDS) as a hydrophilic spacer and DADS(I) to the resin, a small fraction was incubated with a mixture containing trifluoroacetic acid (TFA), dichloromethane (DCM), and the scavenger triisopropyl silane (TIPS) (95:2.5:2.5, v:v:v) cleaving the oligomer from the resin and enabling RP-HPLC-MS analysis. The analysis

confirmed the desired product EDS-DADS(I) with a relative purity of 52 % and the formation of an unknown byproduct (see Supporting Information). However, we decided to proceed with the Cadiot-Chodkiewicz coupling of the DADS fragments on solid support. As this is, to the best of our knowledge, the first reporting of this reaction on solid phase the reaction conditions were adopted from established in solution procedures and modified accordingly: DADS(II) (3 eq) was dissolved in a mixture of MeOH and DMF (1:1, v:v) and drawn into the syringe reactor. Meanwhile, 0.1 eq CuI was suspended in DMF and complexed with 0.1 eq tetramethylethylenediamine (TEMED). The blue solution was also drawn into the syringe reactor and incubated on an automated shaker for 16h. Afterward, the solution was discarded, the resin was washed five times with DMF and residual copper was removed employing sodium diethyl dithiocarbamate with subsequent washing steps including water, DMF and DCM. RP-HPLC-MS analysis indicated complete conversion to give the fully assembled DADS construct with a relative purity of 90 %. The other products formed were identified as the Fmoc-deprotected product (i.e. not a side product per se) and a small amount of homodimer product (see Supporting Information). However, the absence of a significant byproduct after DADS(II) conjugation supports our abovementioned assumption regarding the side reaction observed of the preceding structure terminated with DADS(I) resulting from either the cleavage process. Subsequent Fmoc-deprotection and further conjugation with another EDS unit proceeded quantitatively, only giving the target product, demonstrating the feasibility of our fragment approach.

As our main goal was to synthesize diacetylene-functionalized, lipidated glycan-mimetics, we had to test the orthogonality of the DADS towards copper(I)-catalyzed alkyne-azide cycloaddition (CuAAC), a method utilized in our group for the coupling of azido functionalized sugars to alkynes via SPPoS. Accordingly, the test sequence was subsequently elongated with 4-pentynoic acid before glycosylation with azido functionalized Man (see Supporting Information for synthetic procedure). RP-HPLC-MS analysis indicated the predominant formation of the target product. However, we also observed the formation of a side product, corresponding to the cleavage of the diacetylene bond and subsequent triazole formation of the *N*-terminal alkyne (See Supporting Information).

While this study demonstrates the general applicability of the fragment approach to incorporate diacetylene moieties in a sequence defined matter into a synthetic scaffold via

SPPoS, it is noteworthy that the diacetylene moiety is not stable under our employed CuAAC conditions and, consequently, for the synthesis of the desired structures has to be installed after glycosylation reactions with CuAAC.

Synthesis of Diacetylene-Functionalized, Lipidated Glycan-Mimetics

For the synthesis of the desired lipidated and diacetylene-bearing glycan mimetics, we employed our established SPPoS protocols. [9,40] The use of tailor-made functional building blocks allows for an iterative assembly of the scaffold, thereby enabling precise control over positioning, density and valency of the glycan motifs as well as other functional handles, such as the diacetylene moiety and the membrane tether.

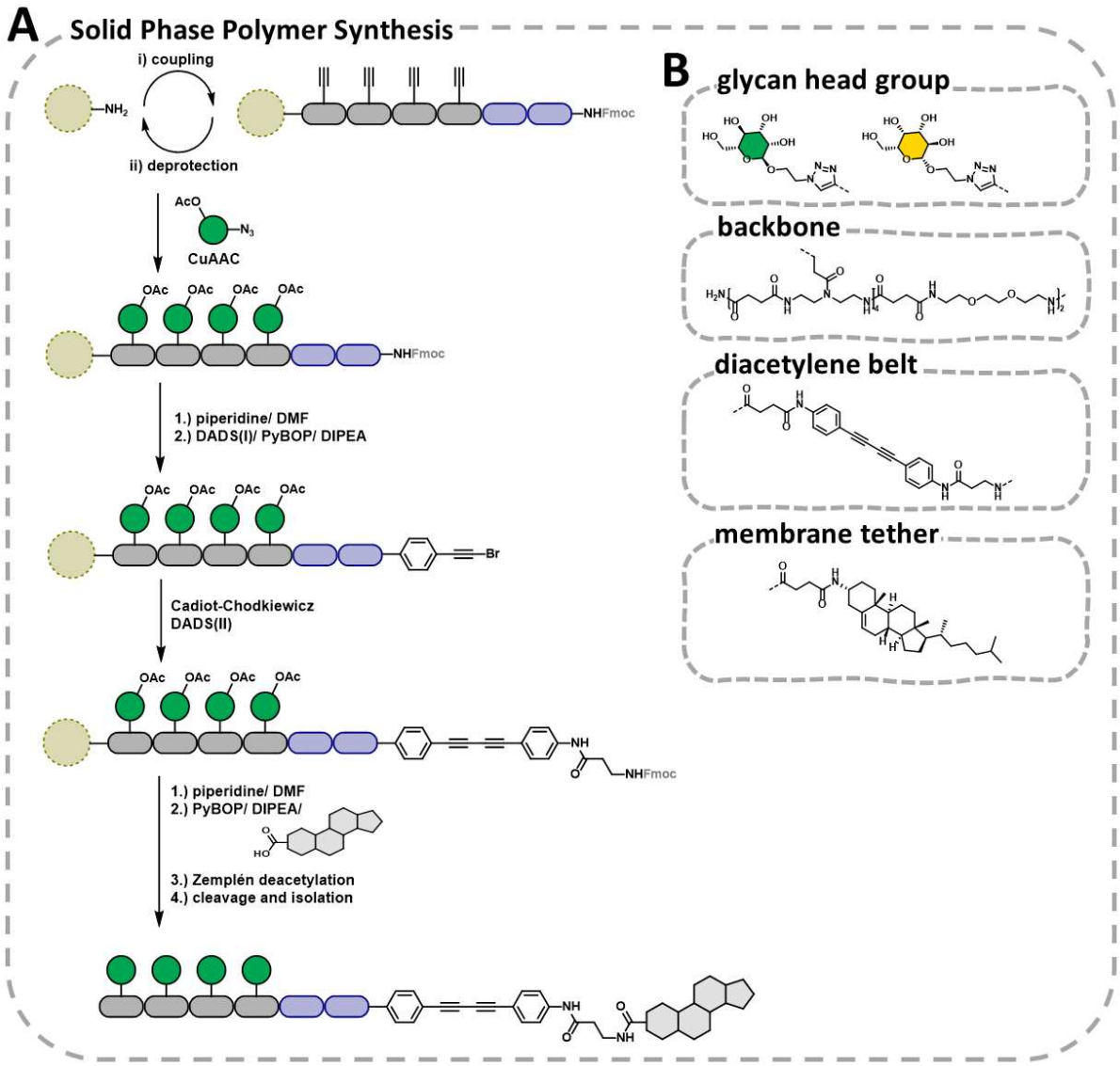

Figure 2. A: Schematic SPPoS of ManDAChol. **B**: Chemical structures of the synthesized ligands ManDAChol and GalDAChol.

The synthesis of the ligands is depicted in **Figure 2A.** The assembly of the backbone started from commercially available TentaGel S RAM resin, employing iterative assembly of

building blocks bearing a free carboxylic acid and an Fmoc-protected primary amine via stepwise Fmoc-deprotection and coupling procedures. Four triple bond diethylenetriamine succinyl (TDS) building blocks, carrying an alkyne functionality in their side chain for later glycosylation via CuAAC were installed followed by introducing two EDS units as hydrophilic spacer. After assembly of the scaffold, CuAAC was employed to functionalize the backbone with either Man or Gal via their respective acetylated and azido-functionalized derivatives. Subsequently, the *N*-terminus was deprotected and functionalized with the DADS(I) fragment, before conjugating the DADS(II) fragment via on-resin Cadiot-Chodkiewicz coupling. Finally, the solid-supported macromolecule was *N*-terminally functionalized with *N*-Suc-3-β-aminocholesterol. Unlike in our previous studies, we omitted the use of 3-β-azidocholesterol, since the required CuAAC for conjugation leads to partial cleavage of the diacetylene moiety, as described above. [9] After the complete assembly of the polymerizable glycan mimetic, the carbohydrate moieties were deprotected under Zemplén conditions, the structure was cleaved off the resin, collected via precipitation, and further purified by diafiltration.

In this manner, two different glycan mimetics were synthesized, each comprising a tetravalent glyco-head group (Man or Gal), a polymerizable diacetylene-moiety and a cholesteryl-moiety for subsequent membrane anchoring (**Figure 2B**). Both structures were confirmed by RP-HPLC-MS, ^{1}H-NMR and HR-ESI-MS (see Supporting Information).

Self-Assembly and Polymerization Behavior of Diacetylene-Containing Glycan Mimetics

After the successful synthesis of the diacetylene-functionalized glycan mimetics, we aimed to characterize our ligands regarding their capacity to polymerize upon irradiation and their self-assembly behavior.

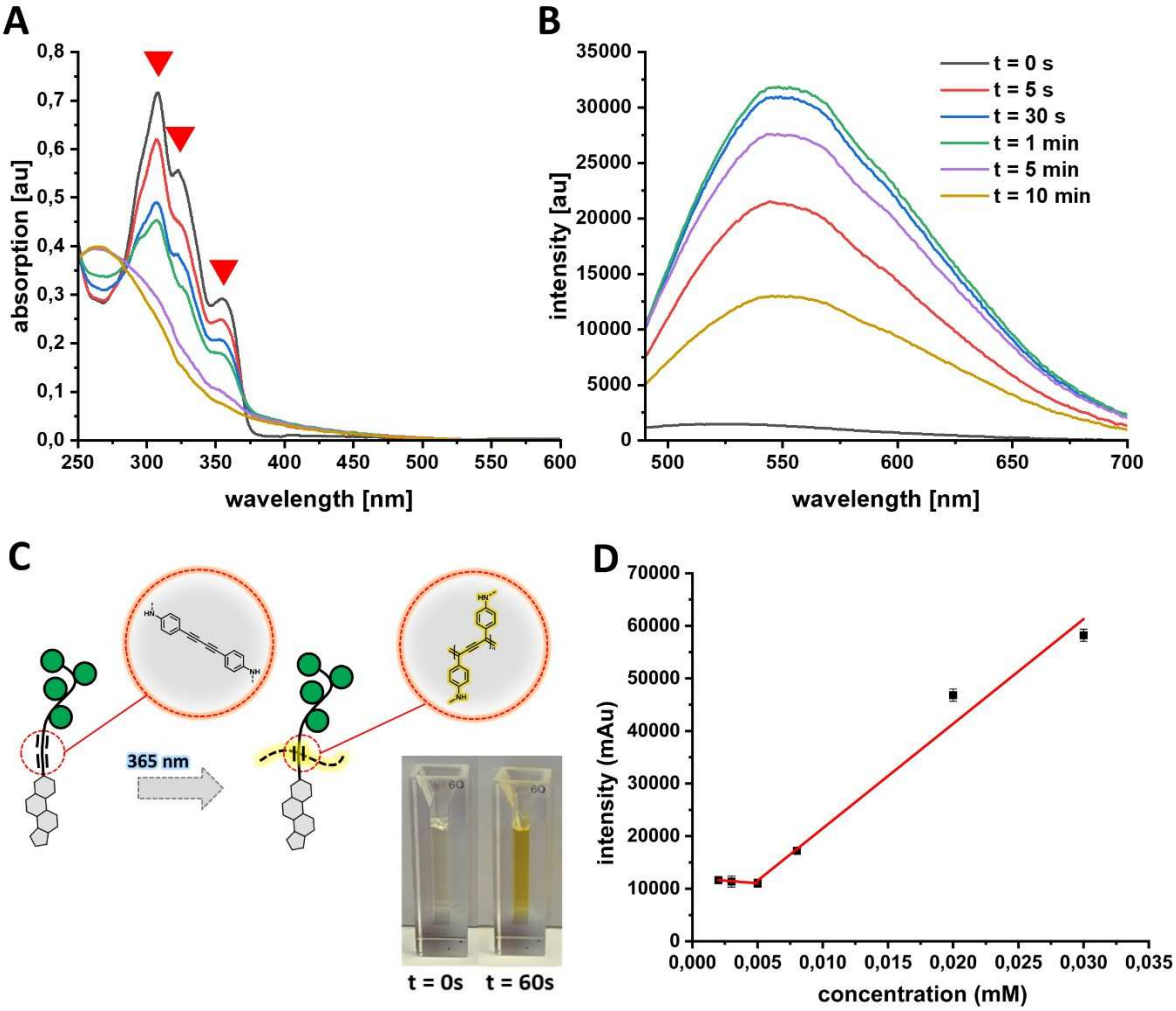

Figure 3. A: The absorption spectrum of the diacetylene moiety shows three absorption maxima at 305 nm, 320 nm and 355 nm (red arrows). Upon irradiation with an LED spotlight (365 nm, approximately 285 mW/cm^2) the absorption intensity decreases due to the formation of a polymer network. **B**: Upon irradiation, the emission intensity of the diacetylene moiety increases gradually up to 1 min and decreases afterwards, putatively due to photobleaching. **C**: Schematic depiction of the crosslinking mechanism upon irradiation, concomitant with an amberish coloration due to an elongated π-system. **D**: Determination of the CMC for ManDAChol via Nile Red method. Measurements were performed in triplicates and data points are presented as mean + SEM.

We chose ManDAChol as model compound, since both ligands only differ in their respective glycan head group and, hence, the physico-chemical properties of the two ligands should be very similar. First, we wanted to analyze the polymerization properties of our ligand upon irradiation. Therefore, we prepared a 0.2 mM solution of the ligand in deionized water and measured its absorption profile (λ = 250 – 600 nm), as well as its emission profile (λ_{ex} = 450 nm). The non-polymerized diacetylene macromolecules exhibit a pronounced absorption profile in the range of 275 – 375 nm with three absorption maxima at λ = 305 nm, 320 nm and 355 nm (cp. **Figure 3A**), which is in accordance with the findings of *Zhu et al*. [35] Upon irradiation with 365 nm, the absorption profile decreases over time. Similarly, the emission profile increases gradually with a maximum fluorescence after 1 min of irradiation and a maximum emission wavelength of λ = 550 nm (cp. **Figure 3B**). Upon prolonged irradiation, the emission profile begins to decrease, putatively due to photochemical damage to the π-backbone of the polydiacetylene. In addition, the color change of the solution from clear to bright yellow upon UV exposure further indicates successful polymerization and the formation of an extended conjugated structure, allowing for visible light absorption (cp. **Figure 3C**).

In addition, we analyzed the polymerization behavior of the ligand via size exclusion chromatography. While a non-irradiated sample yielded no measurable result, an irradiated sample gave a significant peak in the chromatogram, corresponding to a molecular weight of approximately 354 kDa, with a dispersity of 1.02 (see **Figure S30**).

Next, we determined the critical micellar concentration (CMC) of our ligand employing Nile red as fluorescence read-out, as was described before. [41,42] Therefore, a concentration series in deionized water was prepared and the fluorescence intensity was measured. The gathered fluorescence intensity values were then plotted against the concentration of the ligand. The CMC was then determined as the cross section of the two linear fits before and after the steep fluorescence increase, yielding a CMC of approximately 5 µM (cp. **Figure 3D**). In a recent study, we characterized similar amphiphilic structures containing identical sugar head groups and an aromatic moiety in the backbone, though lacking the diacetylene unit and featuring a different apolar tail group. The CMC values for those structures were found to be in a comparable range to the CMC measured in this study. [42]

Self-Assembly and Polymerization Behavior of Diacetylene-Functionalized Glycan Mimetics

To further investigate the self-assembling properties of our ligands, we performed TEM imaging, focusing on the micelle morphology in aqueous solutions and their stability in organic solvents, both before and after polymerization. As shown in **Figure 4A** (before polymerization) and **Figure 4C** (after polymerization), spherical micelles are formed in ultra-pure water at a concentration of 1 mM (c > CMC) with a homogenous size distribution, consistent with the previously determined low dispersity via SEC.

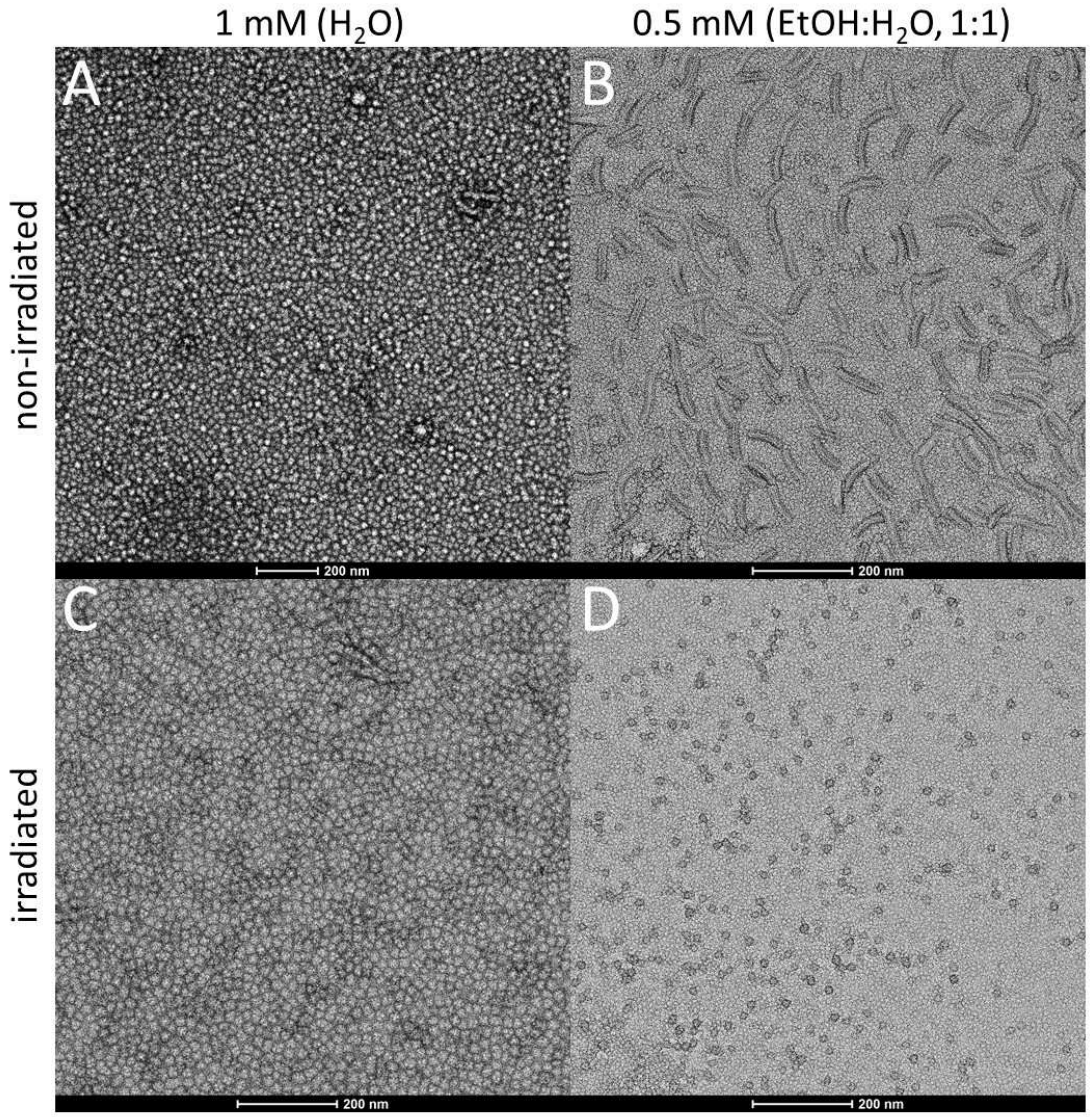

Figure 4. TEM images of the irradiated and non-irradiated micellar assemblies. At c = 1 mM the ligands form spherical micelles in water (**A** and **C**). Upon dilution with EtOH, the crosslinked micelles remain spherical (**D**), while the non-crosslinked micelles rearrange into worm-like micelles (**B**).

To assess the stability of these micelles, we diluted both samples with ethanol (1:1, v/v), a solvent known to disrupt micelle formation in similar amphiphilic ligands. [41] Notably, the irradiated micelles retained their spherical morphology even after ethanol dilution (**Figure 4D**), indicating enhanced stability through polymerization. Interestingly, the non-irradiated sample also formed micellar aggregates after dilution. However, the morphology shifted markedly from spherical aggregates to larger, worm-like micelles, suggesting a molecular rearrangement induced by ethanol dilution (**Figure 4B**). This can be attributed, at least in part, to the TEM preparation and drying process. During sample drying, ethanol tends to evaporate first, which at low ethanol concentrations can promote aggregation. This likely drives the formation of larger, worm-like structures as a result of molecular rearrangement to limit solvent exposure. Without polymerization, the micelles remain dynamic and prone to reorganization, resulting in the observed change in morphology during the drying phase. In contrast, the irradiated (i.e. polymerized) sample retains its spherical structure, suggesting increased stability and resistance to ethanol-induced rearrangement.

Lectin-Mediated Microdomain Formation in GUVs as Membrane Mimetics

Building on the general applicability of our crosslinkable glycan mimetics, we next explored their use in giant unilamellar vesicles (GUVs) as model membranes to study glycan clustering through lectin-mediated ligand recruitment. Therefore, we incorporated our crosslinkable glycan mimetic (ManDAChol) into GUVs prepared by electroformation using DOPC (2 mg/mL) as matrix lipid and 0.5 mol% of ManDAChol. Confocal fluorescence microscopy of the GUVs revealed a slight and homogenous fluorescence along the membrane upon excitation (405 nm)(caused by autofluorescence of the phospholipids) and a diameter range of 10 – 50 µm (**Figure 5A**). To initiate glycan-clustering, the GUVs were first incubated with 20 nM non-labelled Concanavalin A for 30 min at ambient temperature, followed by 30 min at 4°C to equilibrate the glycan-lectin binding and slow down ligand diffusion within the phospholipid membrane. After Con A incubation, the vesicles were irradiated with 365 nm for 60 s to induce diacetylene polymerization, capturing the glycan clusters in place before imaging. Confocal fluorescence microscopy showed the formation of distinct fluorescent patches along the vesicle surface, indicative of multivalent clustering and subsequent crosslinking via photo-induced diacetylene polymerization (**Figure 5B**).

To assess the stability of these clusters, we then incubated the GUVs with 0.2 mM of a polyvalent Man-polymer (Pn = 175) as inhibitor to compete for the Con A binding sites. Following incubation for 30 minutes, we observed that the fluorescence patches remained intact, demonstrating that the glycan clusters were stabilized through covalent crosslinking of the diacetylenes. This stability, even in the absence of Con A-mediated interactions, highlights the potential of our glycan mimetics to form stable, receptor-induced microdomain clusters in phospholipid membranes, mimicking the dynamic formation and persistence of lipid rafts in native cellular membranes.

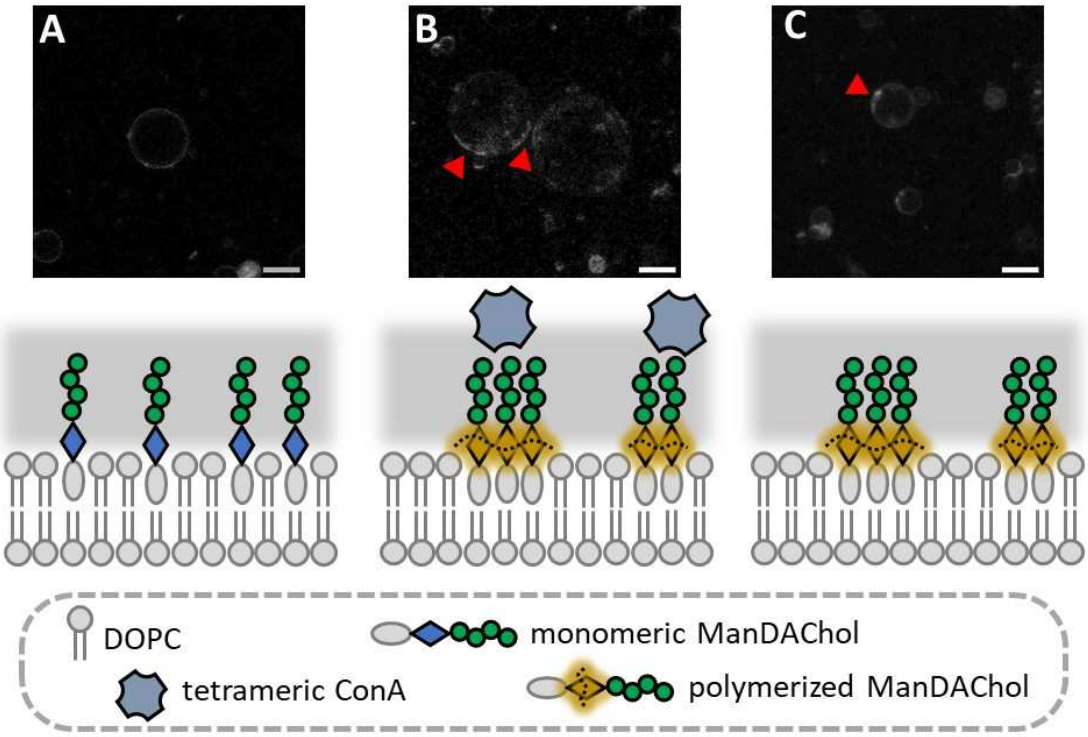

Figure 5. Confocal microscope z-stack projections (excitation wavelength 405 nm) and schematic representations. **A**: GUVs decorated with 0.5 mol% ligand exhibit a slight fluorescence upon excitation due to autofluorescence of the phospholipids. **B**: Incubation with Con A (20 nM) leads to the formation of multivalent Con A-Man-clusters that are cured upon irradiation with 365 nm (red arrows). **C**: Crosslinked ligand-patches remain intact after inhibiting membrane-bound Con A with 0.2 mM Man-polymer (red arrow). Scale bars: 25 µm. Contrast adjusted for better visibility.

CONCLUSION

In this study we developed a method to site-selectively introduce of a diacetylene moiety into the backbone of lipidated glycan mimetics via solid phase polymer synthesis. The diacetylene unit is introduced through an on-resin Cadiot-Chodkiewicz coupling between two novel building block fragments. This reaction proceeds efficiently, achieving high conversion rates with no detectable side-product formation and is compatible with standard coupling protocols for SPPoS. In this manner, two exemplary diacetylene-containing lipidated glycan-mimetics were prepared, displaying a tetravalent Man or Gal head group and a cholesteryl moiety for later membrane anchoring. The self-assembly behavior of the Man-ligand and its capability to polymerize upon irradiation in aqueous solution was evaluated.

Subsequently, the polymerizable Man-ligand was incorporated into GUVs to derive simple glycocalyx mimetics. Incubation with native Con A has been demonstrated to induce multivalent ligand clustering within the membrane. Subsequent irradiation with 365 nm led to the crosslinking of these ligand domains, to give fluorescent microdomains within the vesicle membrane, which persisted after the removal of the membrane bound Con A with a multivalent Man-inhibitot.

In conclusion, we have developed a novel type of glycan mimetics that now allows us to mimic the dynamic formation and fixation of ligand clusters in phospholipid membranes. This now enables to mirror more properly the dynamic formation of local glycan-clusters in cell membranes and should allow for the constructions of more realistic models of the glycocalyx in ongoing studies.

ACKNOWLEDGEMENTS

The authors thank Lóránd Bonda for perfoming the SEC measurements, as well as Negin Mohammadalipourshirmahalle for supporting CMC determination. The authors further thank the CeMSA@HHU (Center for Molecular and Structural Analytics @ Heinrich Heine University) for recording mass-spectrometric and NMR-spectroscopic data. LH, LCB and CM acknowledge partial financial support of the Deutsche Forschungsgemeinschaft (DFG, German ResearchFoundation) through CRC1208 'Identity and Dynamics of Membrane Systems' (A11 and A12, Project ID 267205415). CM further acknowledges financial support via the 'Freigeist fellowship' of Volkswagen Foundation and of the Deutsche Forschungsgemeinschaft (DFG, German Research Foundation) through CRC1535 'Microbial Networks' (A09, Project ID458090666). This work is supported by ERC grant (GLYMCE, 101088228). Funded by the European Union. Views and opinions expressed are however those of the author(s) only and do not necessarily reflect those of the European Union or the European Research Council Executive Agency. Neither the European Union nor the granting authority can be held responsible for them.

REFERENCES

(1) Möckl, L. The Emerging Role of the Mammalian Glycocalyx in Functional Membrane Organization and Immune System Regulation. *Frontiers in cell and developmental biology* **2020**, 8, 253.

(2) Huang, M. L.; Fisher, C. J.; Godula, K. Glycomaterials for probing host–pathogen interactions and the immune response. *Exp Biol Med (Maywood)* **2016**, 241, 1042–1053.

(3) McGuinn, K. P.; Mahoney, M. G. Lipid rafts and detergent-resistant membranes in epithelial keratinocytes. *Methods in molecular biology (Clifton, N.J.)* **2014**, 1195, 133–144.

(4) George, K. S.; Wu, S. Lipid raft: A floating island of death or survival. *Toxicology and applied pharmacology* **2012**, 259, 311–319.

(5) Ieong, N. S.; Biggs, C. I.; Walker, M.; Gibson, M. I. Comparison of RAFT derived Poly(vinylpyrolidone) verses Poly(oligoethyleneglycol methacrylate) for the Stabilization of Glycosylated Gold Nanoparticles. *Journal of polymer science. Part A, Polymer chemistry* **2017**, 55, 1200–1208.

(6) Richards, S.-J.; Jones, M. W.; Hunaban, M.; Haddleton, D. M.; Gibson, M. I. Probing bacterial-toxin inhibition with synthetic glycopolymers prepared by tandem post-polymerization modification: role of linker length and carbohydrate density. *Angewandte Chemie (International ed. in English)* **2012**, 51, 7812–7816.

(7) Dennis, J. W.; Brewer, C. F. Density-dependent lectin-glycan interactions as a paradigm for conditional regulation by posttranslational modifications. *Molecular & cellular proteomics : MCP* **2013**, 12, 913–920.

(8) Nolan, W.; McHale-Owen, H.; Bate, C. Sialylated glycosylphosphatidylinositols suppress the production of toxic amyloid-β oligomers. *The Biochemical journal* **2017**, 474, 3045–3058.

(9) Blawitzki, L.-C.; Bartels, N.; Bonda, L.; Schmidt, S.; Monzel, C.; Hartmann, L. Glycomacromolecules to Tailor Crowded and Heteromultivalent Glycocalyx Mimetics. *Biomacromolecules* **2024**, 25, 5979–5994.

(10) Honigfort, D. J.; Altman, M. O.; Gagneux, P.; Godula, K. Glycocalyx crowding with synthetic mucin mimetics strengthens interactions between soluble and virus-associated lectins and cell surface glycan receptors, **2021**.

(11) Zhong, T.; Chen, Y.; Yan, X.; Li, Y.; Wang, H.; Zhong, Y.; Li, K.; Xie, R.; Dong, H.; Ding, L.; et al. A Patching and Coding Lipid Raft-Localized Universal Imaging Platform. *Chemical & Biomedical Imaging* [Online early access]. DOI: 10.1021/cbmi.3c00109.

(12) Kennedy, C.; Nelson, M. D.; Bamezai, A. K. Analysis of detergent-free lipid rafts isolated from CD4+ T cell line: interaction with antigen presenting cells promotes coalescing of lipid rafts. *Cell communication and signaling : CCS* **2011**, 9, 31.

(13) Mishra, P. K.; Yoo, C.-M.; Hong, E.; Rhee, H. W. Photo-crosslinking: An Emerging Chemical Tool for Investigating Molecular Networks in Live Cells. *Chembiochem : a European journal of chemical biology* **2020**, 21, 924–932.

(14) Lougee, M. G.; Pagar, V. V.; Kim, H. J.; Pancoe, S. X.; Mach, R. H.; Garcia, B. A.; Petersson, E. J. Harnessing the Intrinsic Photochemistry of Isoxazoles for the Development of Chemoproteomic Crosslinking Methods, **2021**.

(15) Capota, E.; Wu, H.; Kohler, J. J. Photocrosslinking O-GlcNAcylated Proteins to Neighboring Biomolecules. *Current protocols* **2021**, 1, e201.

(16) Yarravarapu, N.; Reddy Konada, R. S.; Darabedian, N.; Pedowitz, N. J.; Krishnamurthy, S. N.; Pratt, M. R.; Kohler, J. J. Exo-enzymatic addition of diazirine-modified sialic acid to cell surfaces enables photocrosslinking of glycoproteins, **2021**.

(17) Pham, N. D.; Parker, R. B.; Kohler, J. J. Photocrosslinking approaches to interactome mapping. *Current opinion in chemical biology* **2013**, 17, 90–101.

(18) McCombs, J. E.; Zou, C.; Parker, R. B.; Cairo, C. W.; Kohler, J. J. Enhanced Cross-Linking of Diazirine-Modified Sialylated Glycoproteins Enabled through Profiling of Sialidase Specificities. *ACS Chem. Biol.* **2016**, 11, 185–192.

(19) Bond, M. R.; Zhang, H.; Kim, J.; Yu, S.-H.; Yang, F.; Patrie, S. M.; Kohler, J. J. Metabolism of diazirine-modified N-acetylmannosamine analogues to photo-cross-linking sialosides. *Bioconjugate chemistry* **2011**, 22, 1811–1823.

(20) Morigaki, K.; Kiyosue, K.; Taguchi, T. Micropatterned composite membranes of polymerized and fluid lipid bilayers. *Langmuir : the ACS journal of surfaces and colloids* **2004**, 20, 7729–7735.

(21) Jelinek, R.; Ritenberg, M. Polydiacetylenes – recent molecular advances and applications. *RSC Adv.* **2013**, 3, 21192.

(22) Qian, X.; Städler, B. Recent Developments in Polydiacetylene-Based Sensors. *Chem. Mater*. **2019**, 31, 1196–1222.

(23) Wu, J.; Zawistowski, A.; Ehrmann, M.; Yi, T.; Schmuck, C. Peptide functionalized polydiacetylene liposomes act as a fluorescent turn-on sensor for bacterial lipopolysaccharide. *Journal of the American Chemical Society* **2011**, 133, 9720–9723.

(24) Wang, M.; Wang, F.; Wang, Y.; Zhang, W.; Chen, X. Polydiacetylene-based sensor for highly sensitive and selective Pb2+ detection. *Dyes and Pigments* **2015**, 120, 307–313.

(25) Ma, G.; Cheng, Q. Vesicular polydiacetylene sensor for colorimetric signaling of bacterial pore-forming toxin. *Langmuir : the ACS journal of surfaces and colloids* **2005**, 21, 6123–6126.

(26) van den Heuvel, M.; Löwik, D. W. P. M.; van Hest, J. C. M. Self-assembly and polymerization of diacetylene-containing peptide amphiphiles in aqueous solution. *Biomacromolecules* **2008**, 9, 2727–2734.

(27) Vellutini, L.; Errien, N.; Froyer, G.; Lacoudre, N.; Boileau, S.; Tran-Van, F.; Chevrot, C. Polymerization of Supramolecular Diacetylenic Monomer Embedded in Porous Silicon Matrix. *Chem. Mater*. **2007**, 19, 497–502.

(28) Lee, J.; Yarimaga, O.; Lee, C. H.; Choi, Y.-K.; Kim, J.-M. Network Polydiacetylene Films: Preparation, Patterning, and Sensor Applications. *Adv Funct Materials* **2011**, 21, 1032–1039.

(29) Nyayachavadi, A.; Mason, G. T.; Nazir Tahir, M.; Ocheje, M. U.; Rondeau-Gagné, S. Covalent Cross-Linking of Diketopyrrolopyrrole-Based Organogels with Polydiacetylenes. *Langmuir : the ACS journal of surfaces and colloids* **2018**, 34, 12126–12136.

(30) Tahir, M. N.; Harati, M.; Nyayachavadi, A.; Rezapour, M.; Eichhorn, S. H.; Rondeau-Gagné, S. Intrinsically Porous Polydiacetylene from a Functionalized Bowl-Shaped Hexaphenoxycyclotriphosphazene Derivative. *ACS Appl. Polym. Mater.* **2021**, 3, 191–199.

(31) George, M.; Weiss, R. G. Low Molecular-Mass Gelators with Diyne Functional Groups and Their Unpolymerized and Polymerized Gel Assemblies. *Chem. Mater.* **2003**, 15, 2879–2888.

(32) Zhang, X.; Borda, M. J.; Schoonen, M. A. A.; Strongin, D. R. Pyrite oxidation inhibition by a cross-linked lipid coating. *Geochem. Trans.* **2003**, 4, 8.

(33) Kim, H. J.; Ishii, T.; Zheng, M.; Watanabe, S.; Toh, K.; Matsumoto, Y.; Nishiyama, N.; Miyata, K.; Kataoka, K. Multifunctional polyion complex micelle featuring enhanced stability, targetability, and

endosome escapability for systemic siRNA delivery to subcutaneous model of lung cancer. *Drug delivery and translational research* **2014**, 4, 50–60.

(34) Levental, K. R.; Malmberg, E.; Symons, J. L.; Fan, Y.-Y.; Chapkin, R. S.; Ernst, R.; Levental, I. Lipidomic and biophysical homeostasis of mammalian membranes counteracts dietary lipid perturbations to maintain cellular fitness. *Nature communications* **2020**, 11, 1339.

(35) Zhu, M.; Zhu, L. Rational Design of Diphenyldiacetylene-Based Fluorescent Materials Enabling a 365-nm Light-Initiated Topochemical Polymerization. *Chemistry, an Asian journal* **2021**, 16, 2048–2054.

(36) Ponader, D.; Wojcik, F.; Beceren-Braun, F.; Dernedde, J.; Hartmann, L. Sequence-Defined Glycopolymer Segments Presenting Mannose: Synthesis and Lectin Binding Affinity. *Biomacromolecules* **2012**, 13, 1845–1852.

(37) Pujala, B.; Rana, S.; Chakraborti, A. K. Zinc tetrafluoroborate hydrate as a mild catalyst for epoxide ring opening with amines: scope and limitations of metal tetrafluoroborates and applications in the synthesis of antihypertensive drugs (RS)/(R)/(S)-metoprolols. *The Journal of organic chemistry* **2011**, 76, 8768–8780.

(38) Tripp, V. T.; Lampkowski, J. S.; Tyler, R.; Young, D. D. Development of Solid-Supported Glaser–Hay Couplings. *ACS Comb. Sci.* **2014**, 16, 164–167.

(39) Danilkina, N. A.; Kulyashova, A. E.; Khlebnikov, A. F.; Bräse, S.; Balova, I. A. Electrophilic Cyclization of Aryldiacetylenes in the Synthesis of Functionalized Enediynes Fused to a Heterocyclic Core. *J. Org. Chem*. **2014**, 79, 9018–9045.

(40) Banger, A.; Pasch, P.; Blawitzki, L.-C.; Weber, S.; Otten, M.; Monzel, C.; Schmidt, S.; Voskuhl, J.; Hartmann, L. Detection of Lectin Clustering in Self-Assembled, Glycan-Functionalized Amphiphiles by Aggregation-Induced Emission Luminophores. *Macro Chemistry & Physics* **2023**, 224.

(41) Banger, A.; Sindram, J.; Otten, M.; Kania, J.; Wilms, D.; Strzelczyk, A.; Miletic, S.; Marlovits, T. C.; Karg, M.; Hartmann, L. Synthesis and self-assembly of amphiphilic precision glycomacromolecules. *Polym. Chem.* **2021**, 12, 4795–4802.

(42) Jäck, N.; Hemming, A.; Hartmann, L. Synthesis of Dual-Responsive Amphiphilic Glycomacromolecules: Controlled Release of Glycan Ligands via pH and UV Stimuli. *Macromolecular rapid communications* **2024**, e2400439.

(43) Pu, K.-Y.; Shi, J.; Wang, L.; Cai, L.; Wang, G.; Liu, B. Mannose-Substituted Conjugated Polyelectrolyte and Oligomer as an Intelligent Energy Transfer Pair for Label-Free Visual Detection of Concanavalin A. *Macromolecules* **2010**, 43, 9690–9697.

(44) Villringer, S.; Madl, J.; Sych, T.; Manner, C.; Imberty, A.; Römer, W. Lectin-mediated protocell crosslinking to mimic cell-cell junctions and adhesion. *Scientific reports* **2018**, 8, 1932.

Supplementary Information

Diacetylene-Functionalized Glycan Mimetics for Receptor-Mediated Cluster Imprinting in Model Membranes

Luca-Cesare Blawitzki[a,c], Nicholas Jäck[a,c], Lina Charlotte Assenmacher[a], Cornelia Monzel[b] and Laura Hartmann[c]*

[a] Department for Organic and Macromolecular Chemistry, Heinrich Heine University Duesseldorf, Universitätsstraße 1, 40225 Düsseldorf, Germany

[b] Department for Experimental Medical Physics, Heinrich Heine University Duesseldorf, Universitätsstraße 1, 40225 Düsseldorf, Germany

[c] Department for Macromolecular Chemistry, University of Freiburg, Stefan-Meier-Str. 31, 79104 Freiburg i.Br., Germany

*Email: laura.hartmann@makro.uni-freiburg.de

Table of Contents

Materials

D-(+)-galactose, D-(+)-mannose, N,N-dimethylformamide, oxalyl chloride, piperidine and tosyl chloride were purchased from Acros Organics. Ethyl trifluoroacetate and PyBOP were purchased from Apollo Scientific. Acetonitrile and cholesterol were purchased from AppliChem. Fmoc-Cl and p-ethynylaniline were purchased from bld pharm. Succinic anhydride was purchased from Carbolution Chemicals. DIPEA and sodium chloride were purchased from Carl Roth. 1.4-dioxane, acetic anhydride, calcium chloride, ethyl acetate, HEPES, n-hexane, hydrochloric acid (37%), manganese dichloride, potassium carbonate, sodium azide, sodium bicarbonate, sodium hydroxide, sodium methoxide and trimethylamine were purchased from Fisher Scientific. Triethylsilane was purchased from fluorochem. Fmoc-β-Ala-OH was purchased from Iris Biotech. Concanavalin A was purchased from MP Biomedicals. 2,2'-(Ethylenedioxy)bis(ethylamine), 2-bromoethanol, 4-pentynoic acid, boron trifluoride diethyl etherate, Bovine Serum Albumin, dichloromethane, diethyl ether, diethylenetriamine, formic acid, methanol, tetrahydrofuran, trifluoroacetic acid, NBS, silver nitrate and triisopropylsilane were purchased from Sigma-Aldrich. Trimethylsilyl azide and trityl chloride were purchased from TCI chemicals. Methyl succinyl chloride and sodium diethyldithiocarbamate were purchased from Thermo Scientific.

All solvents and reagents used were purchased in the highest purity available and used without further purification.

TentaGel® S RAM resin (loading: 0.26 mmol/g) was purchased from RAPP Polymere GmbH.

DOPC was purchased from Avanti Polar Lipids.

Dialysis was performed via diafiltration in VIVASPIN 20 centrifugal concentrators (MWCO: 10 kDa; PES) from sartorius.

Experiments were conducted in 18-well glass bottom µ-slides from ibidi GmbH.

Instrumentation

Reversed Phase- High Pressure Liquid Chromatography- Mass Spectrometry (RP- HPLC-MS)/Electron Spray Ionization- Mass Spectrometry (ESI-MS)

RP-HPLC-MS was carried out on an Agilent 1260 Infinity instrument coupled to a variable wavelength detector (VWD) (set to 214 nm) and a 6120 Quadrupole LC/MS containing an Electrospray Ionization (ESI) source (operation mode positive, m/z range from 200 to 2000). An MZ-AquaPerfect C18 (3.0 × 50 mm, 3 µm) RP column from MZ-Analysentechnik was used. As eluent system water/acetonitrile containing 0.1 vol% formic acid was applied. The mobile phases A and B were: System A) water/acetonitrile (95/5, v/v); System B) water/acetonitrile (5/95, v/v). The samples were analyzed at a flow rate of 0.4 ml/min using a linear gradient, starting with 100% of system A) and reaching 100% system B) within 17 min. The temperature of the column room was set to 25 °C. All purities were determined using the OpenLab ChemStation software for LC/MS from Agilent Technologies.

Ultra High Resolution - Mass Spectrometry (UHR-MS)

UHR-MS measurements were performed with a Bruker UHR-QTOF maXis 4G instrument with a direct inlet via syringe pump, an ESI source and a quadrupole followed by a Time of Flight (QTOF) mass analyzer.

Nuclear Magnetic Resonance Spectroscopy (NMR)

The 1H-NMR spectra were recorded on a Bruker Avanace III 600 (300 or 600 MHz). These spectra were evaluated according to the following scheme: (frequency in MHz, deuterated solvent), chemical shift in ppm (multiplicity, coupling constant, integral, signal assignment). The chemical shift is given in relation to the 1H signals of the deuterated solvents used.

Lyophilization

The final glycomacromolecules were lyophilized with an Alpha 1-4 LD plus instrument from Martin Christ Freeze Dryers GmbH (-40 °C, 0.1 mbar).

Fluorescence Microscopy

Giant Unilamellar Vesicles were imaged confocally on a Leica DMi8 inverted microscope (Leica Microsystems CMS GmbH, Wetzlar, Germany), equipped with a 63x oil-objective and a Leica DFC9000 GT camera, operating the LAS X software.

Emission with a 405 nm UV laser (power 40%); emission width 430-468 nm. Pinhole 5.18 Airy.

Images were evaluated via ImageJ 1.54g.

UV-Vis Spectroscopy

UV-Vis measurements were performed at 25 °C on a dual-trace spectrometer Specord® 210 Plus from Analytik Jena AG (Jena, Germany), using Win ASPECT PLUS software to operate the instrument.

Size Exclusion Chromatography-Multi-Angle Light Scattering (H_2O-SEC-MALS)

SEC analysis was conducted with an Agilent 1200 series HPLC system and three aqueous SEC columns provided by Polymer Standards Service (PSS). The columns were two Suprema Lux analytical columns(8 mm diameter and 5µm particle size) and one precolumn (50 mm, 2×160 Å of 300 mm and 1000 Å of 300mm). The eluent was a buffer system consisting of MilliQ water and 30% acetonitrile with 50 mM NaH2PO4, 150 mM NaCl and 250 ppm NaN3 with a pH = 7.0 (via addition of 50 mL of 3 molar aqueous sodium hydroxide solution) filtered with an inline 0.1µm membrane filter and running at 0.8 mL per min. Multi-angle light scattering is S3 recorded via mini DAWNTREOS and differential refractive index spectra with Optilab rEX both supplied by Wyatt Technologies EU. Data analysis was committed with Astra 5 software and a dn/dc value of 0.156 for each polymer.

General Methods

Solid Phase Polymer Synthesis

All structures were prepared on Tentagel® S RAM resin (batch size: 0.1 mmol). All washing steps were conducted with 4 mL solvent. Polypropylene reactors equipped with polyethylene frits and closed with Luer-stoppers were used. For the glycomacromolecules, the head-group sequence was first assembled, followed by glycoconjugation via CuAAC (copper(I)-catalyzed alkyne-azide cycloaddition), DADS(I) conjugation, DADS(II) conjugation via Cadiot-Chodkiewicz coupling, terminal Fmoc-deprotection and capping with *N*-Suc-3-β-aminocholesterol.

General coupling protocol.

For all compounds, the resin was first swollen in 4 mL DCM for 30 min, subsequently washed ten times with DMF, Fmoc-deprotected by treating with 25% piperidine in DMF (three times for ten minutes) and again washed fifteen times with DMF. Employed building blocks were coupled to the N-terminus by adding the respective building block (5eq.), PyBOP (5 eq.) and DIPEA (20 eq.) in 4 mL DMF to the resin and shaking for 1h. Then, the resin was washed fifteen times with DMF and the N-terminus was again deprotected followed by the next coupling step.

Fmoc cleavage

The Fmoc-protecting group of the resin as well as from the coupled building blocks or amino acids was cleaved by means of 4 mL of a 25% solution of piperidine in DMF to release the primary amine. The deprotection was carried out twice for 10 min. Afterwards the resin was washed 10 times with DMF before coupling.

CuAAC protocol for glycosylation

To the oligomeric structure loaded on the resin 2.5 eq of acetyl protected 2-azidoethyl pyranoside (α-Mannose/ β-Galactose) per alkyne group dissolved in 4 mL DMF were added. Secondly 50 mol% sodium ascorbate per alkyne group and 50 mol% CuSO4 per alkyne group were dissolved each in a small amount of water and also added to the resin. The syringe reactor was rocked for 18 h before the solution was discarded. The resin was washed three times with DMF and subsequently treated with a 23 mM solution of sodium

diethyldithiocarbamate in DMF and water (50/50, v/v) and alternating with DMF and DCM until no further color change occured.

On-resin Cadiot-Chodkiewicz Coupling

3 eq of DADS(II) and 20 eq of DIPEA were dissolved in a mixture of MeOH and DMF (1:1, v:v). 0.1 eq CuI was suspended in little DMF and complexated with 0.1 eq TEMED. The copper and the DADS(II) solution were drawn into the syringe reactor and rocked for 16h. The solution was discarded and remaining copper was removed via treatment with a 23 mM solution of sodium diethyldithiocarbamate in DMF and water (50/50, v/v) and alternating washing steps with DMF and DCM until no further color change occured.

On-resin deacetylation

Glycooligomers were deacetylated under Zemplén conditions. The resin was washed five times with methanol, before 5 mL of a 0.2 M solution of NaOMe in MeOH was drawn into the reactor. The resin was rocked for 30 min, before the solution was discarded. The resin was then washed twice with MeOH before another 5 mL of the methoxide solution were drawn into the reactor. After 30 min, the solution was again discarded and the resin was washed five times with MeOH.

Cleavage from the solid phase

The resin was washed five times with DCM before acidic cleavage from the resin with a cocktail consisting of TFA, TIPS and DCM (95/2.5/2.5, v/v/v) for 30 min.

The cleavage solution was precipitated in ether. The precipitate was collected via centrifugation, dried under a gentle stream of nitrogen and dialyzed via diafiltration against ultrapure water in five cycles (20 mL each). The dialyzed compounds were dissolved in fresh ultrapure water and lyophilized.

Preparation of Giant Unilamellar Vesicles (GUVs)

25 µL of DOPC (2 mg/mL) in chloroform were dried in a glass vial under a gentle stream of nitrogen. 500 µL ultrapure water were added, along with 0.5 mol% ManDAChol (1 mg/mL in ultrapure water). The heterogenous mixture was repeatedly sonicated and vortexed to yield a clear solution. The resulting liposome mixture was deposited dropwise on cleaned ITO

glasses (pgo GmbH, Iserlohn, Germany) and dried under reduced pressure for 1 h in a vacuum oven at 40°C. The swelling chamber was assembled, filled with 1000 µL of a 115 mM sorbitol solution (to match the osmolarity of the measuring buffer (lectin binding buffer (LBB) (10 mM HEPES, 50 mM NaCl, 1 mM MnCl2, 1 mM CaCl2, pH 7.4))), and an AC field was applied to the ITO slides (divided by a Teflon spacer) using a function generator with an amplitude of 2.4 V and a frequency of 89 Hz. Electroformation was carried out for 75 min at ambient temperature.

Preparation of Measuring Chambers

18-well ibidi glass slides were passivated with BSA (5 mg/ml in ultrapure water) for 20 min. The chambers were rinsed thrice with lectin binding buffer and filled with fresh lectin binding buffer.

Lectin Binding Buffer

Lectin Binding Buffer (LBB) 50 mM NaCl, 1 mM $MnCl_2$, 1 mM $CaCl_2$, 10 mM HEPES, pH = 7.4) was degassed under high vacuum and flushed with nitrogen prior to use to remove dissolved oxygen.

Con A Reconstitution

Concanavalin A was dissolved at a concentration of 0.1 mg/mL in LBB containing 10 mM MeMan and 0.2 mg/mL casein to minimize condensation and compaction of protein aggregates.[1]

Experimental Section

Synthesis of Building Blocks and Monomers

The building blocks ethylene glycol diamine succinic acid (EDS) and triple bond diethylenetriamine succinic acid (TDS) were prepared as reported earlier.[2] Tetra-O-acetyl-azidoethyl-α-d-mannopyranoside and tetra-O-acetyl-azidoethyl-β-d-galactopyranoside were synthesized according to the literature protocols.[3] N-Suc3-β-aminocholesterol was synthesized according to a protocol by *Kim et al*.[4] Fmoc-β-Ala-Cl was synthesized according to a protocol by *Song et al*.[5]

Synthesis of methyl 4-((4-ethynylphenyl)amino)-4-oxobutanoate (2)

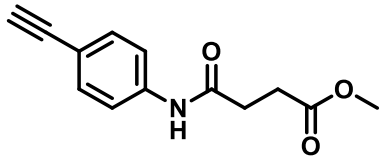

0.5 g 4-Ethinylaniline (4.2 mmol), 5 eq DIPEA and 0.1 eq DMAP were dissolved in 15 mL of DCM and cooled in an ice bath. 1.3 eq monomethylsuccinyl chloride were dissolved in 10 mL of DCM and added dropwise to the solution. The mixture was left to stir for 16 h, thereby allowed to reach ambient temperature. The solution was then washed thrice with 20% citric acid in water, the organic phase was dried over sodium sulfate, filtered and the solvent was removed under reduced pressure.

The crude product was purified via column chromatography (hexanes: ethyl acetate, 1:1, v:v).

r_f = 0.61

yield: 0.73 g of a crystalline, brownish solid (75%)

^{1}H-NMR (400 MHz, $CDCl_3$) δ [ppm] = 7.87 (s, 1H*,* Ar-N*H*), 7.47 (d, *J* = 8.3 Hz, 2H, Ar-*H*), 7.43 – 7.39 (m, 2H, Ar-*H*), 3.70 (s, 1H, -C*H*$_3$), 3.03 (s, 1H, alkyne-*H*), 2.74 (dd, *J* = 7.2, 5.7 Hz, 2H, Ar-NHC(O)C*H*$_2$CH$_2$C(O)), 2.66 (dd, *J* = 7.5, 5.9 Hz, 2H, Ar-NHC(O)CH$_2$C*H*$_2$C(O))

Synthesis of methyl 4-((4-(bromoethynyl)phenyl)amino)-4-oxobutanoate (3)

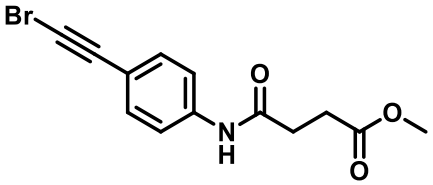

0.5 g **(2)** (2.2 mmol) and 1.1 eq freshly recrystallized NBS were dissolved in 20 mL acetone. The flask was covered in aluminum foil to minimize exposure to light and 0.1 eq AgNO3 was added. The mixture was stirred for 16 h before quenching with 50 mL of a saturated solution of sodium thiosulfate. The aqueous solution was extracted thrice with ethyl acetate, the pooled organic fractions were washed with brine, dried over magnesium sulfate and the solvent was removed under reduced pressure.

The crude product was directly used for the subsequent reaction.

Yield: 0.61 g of a crystalline, amberish solid (91%)

Synthesis of DADS (I)

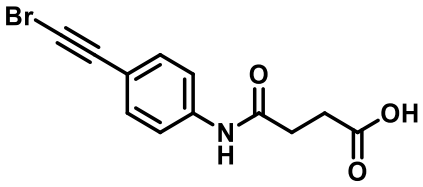

The crude **(3)** (0.61 g, 2.0 mmol) was dissolved in 15 mL of a mixture of methanol, THF and 2 M $NaOH_{aq.}$ (4:4:2, v:v) and stirred for 16 h. The organic solvents were evaporated under reduced pressure, the remaining solution was diluted with 10 mL of water and acidified with cold 0.5 M hydrochloric acid (pH = 3). The aqueous solution was extracted thrice with ethyl acetate, the pooled organic fractions were dried over magnesium sulfate, filtered and the solvent was removed under reduced pressure.

Yield: 0.54 g of a crystalline, sand-colored solid (91%)

^{1}H-NMR (400 MHz, DMSO-d6) δ [ppm] = 12.13 (s, 1H, -COO*H*), 10.15 (s, 1H, Ar-N*H*-), 7.62 – 7.54 (m, 2H, Ar-*H*), 7.43 – 7.35 (m, 2H, Ar-*H*), 2.61 – 2.45 (m, 4H, C(O)CH_2CH_2C(O))

^{13}C-NMR (400 MHz, DMSO-d6) δ [ppm] = 173.79 (C*4*), 170.43 (C*1*), 139.96 (C*5*), 132.49 (C*7*), 118.74 (C*6*), 115.89 (C*8*), 79.86 (C*9*), 51.29 (C*10*), 31.15 (C*2*), 28.71 (C*3*)

ESI-MS calc. for C12H10BrNO3: $[M+1H]^{1+}$ 296.0; found 296.0 $[M+1H]^{1+}$

RP-HPLC: t_R = 9.84 min, >98% relative purity (UV), from 95/5 to 5/95 Vol. % Water/acetonitrile with 0,1% formic acid in 20 min at 25 °C.

Synthesis of DADS(II)

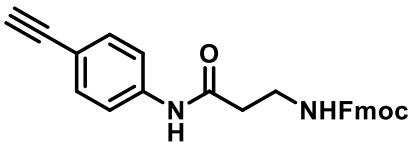

0.5 g p-Ethynylaniline (4.2 mmol), 5 eq DIPEA and 0.1 eq DMAP were dissolved in 20 mL DCM and cooled in an ice bath. 1.2 eq Fmoc-β-Ala-Cl was dissolved in 10 mL DCM and added dropwise to the solution. The mixture was left to stir for 16 h. The solution was then washed with a 20% citric acid solution, twice with brine, dried over magnesium sulfate and evaporated to dryness. The crude product was recrystallized from a solution of 2% MeOH in chloroform.

Yield: 1.2 g of an amorphous, sand-colored solid (70%)

^{1}H-NMR (400 MHz, DMSO-d6) δ [ppm] = 10.10 (s, 1H, Ar-N*H*-), 7.86 (d, *J* = 1.0 Hz, 2H, Ar-*H*), 7.69 – 7.56 (m, 4H, Ar-*H*), 7.48 – 7.22 (m, 7H, N*H*C(O)O, Ar-*H*), 4.33 – 4.13 (m, 3H, N*H*C(O)OC*H*$_2$C*H*-), 4.05 (s, 1H, alkyne-*H*), 3.27 (t, *J* = 6.4 Hz, 2H, Ar-NHC(O)CH$_2$C*H*$_2$NH), 2.54 – 2.48 (m, 2H, Ar-NHC(O)C*H*$_2$CH$_2$NH)

^{13}C-NMR (400 MHz, DMSO-d6) δ [ppm] = 169.52 (C*7*), 156.05 (C*10*), 143.89 (C*13*), 140.72 (C*18*), 139.63 (C*6*), 132.33 (C*4*), 127.59 (C*16*), 127.04 (C*17*), 125.16 (C*15*), 120.09 (C*5*), 118.83 (C*14*), 115.96 (C*3*), 83.61 (C*2*), 79.73 (C*1*), 65.37 (C*11*), 46.69 (C*12*), 36.75 (C*8*), 36.63 (C*9*)

ESI-MS calc. for C12H10BrNO3: $[M+1H]^{1+}$ 411.2; found 411.2 $[M+1H]^{1+}$

RP-HPLC: t_R = 13.23 min, >98% relative purity (UV), from 95/5 to 5/95 Vol. % Water/acetonitrile with 0,1% formic acid in 20 min at 25 °C.

Analytical Data

N-Suc-4-ethynylaniline methyl ester **(2)**

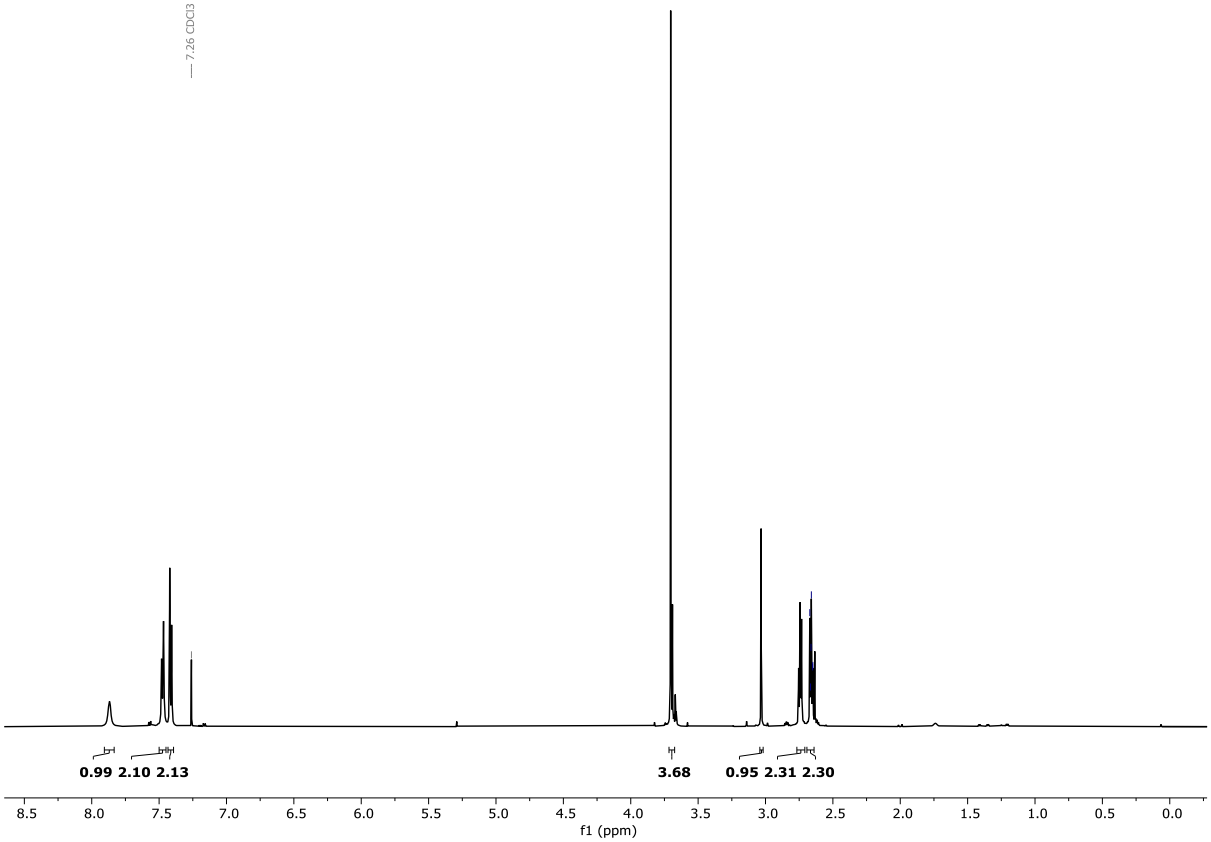

Figure S1. ^{1}H-NMR (400 MHz, $CDCl_3$) of **(2)**.

DADS(I)

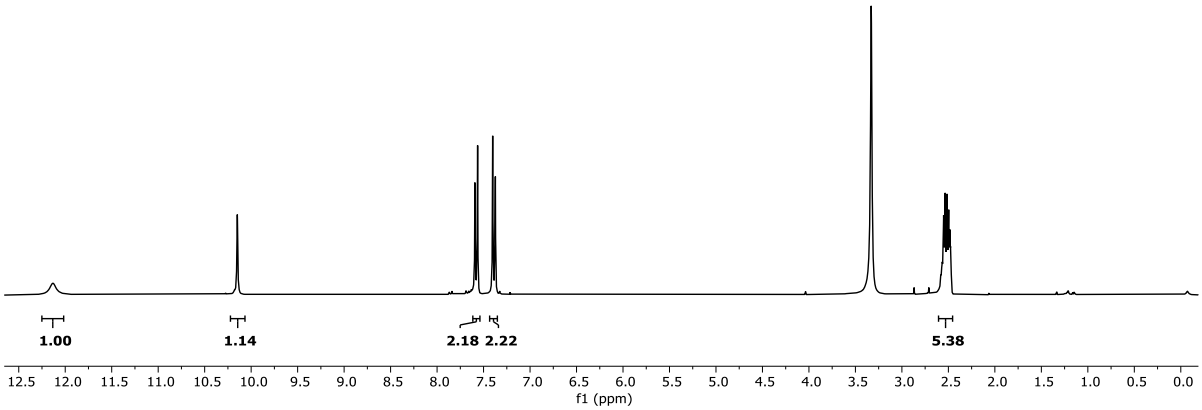

Figure S2. ^{1}H-NMR (400 MHz, DMSO-d6) of DADS(I).

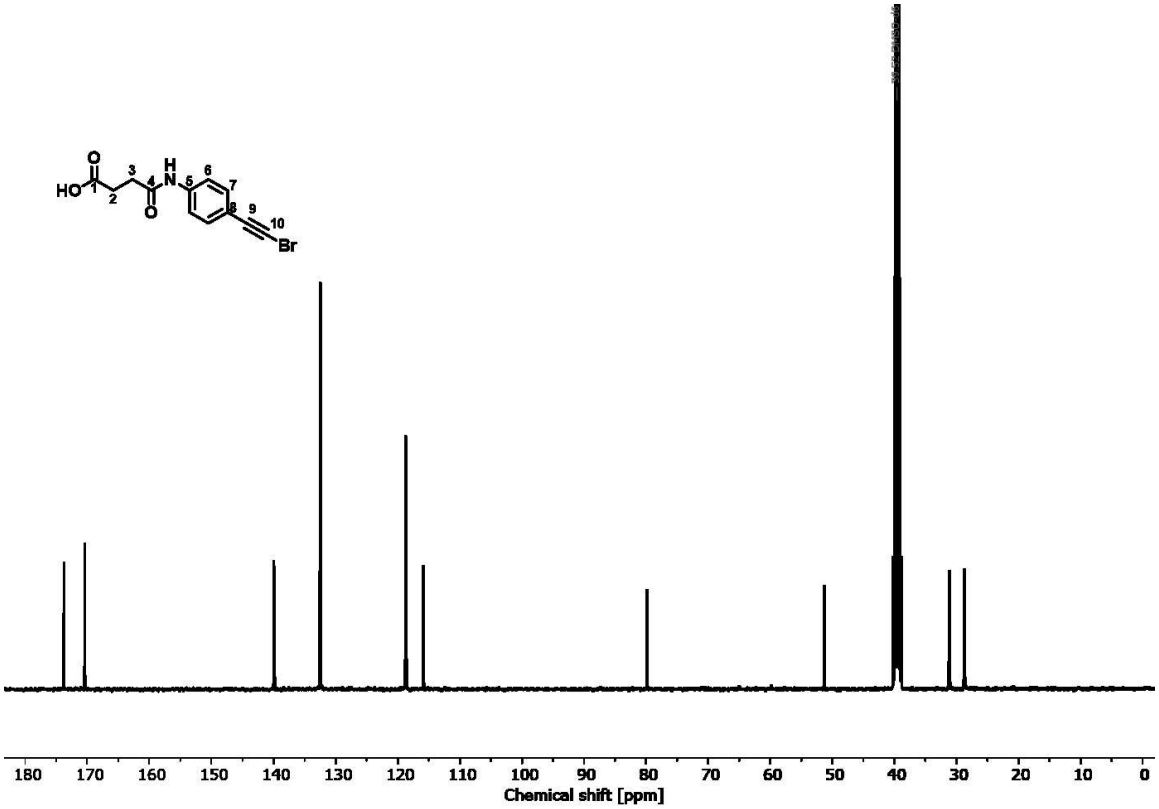

Figure S3. ^{13}C-NMR (400 MHz, DMSO-d6) of DADS(I).

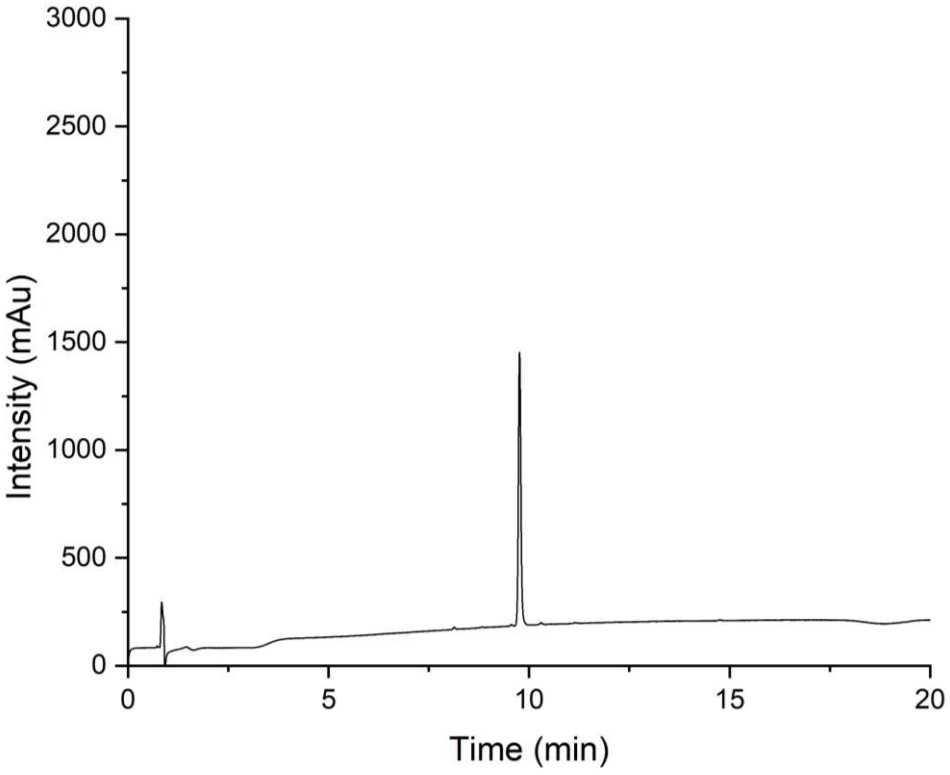

Figure S4. RP-HPLC chromatogram (from 95/5 to 5/95 Vol. % Water/acetonitrile with 0,1% formic acid in 20 min at 25 °C) of DADS(I).

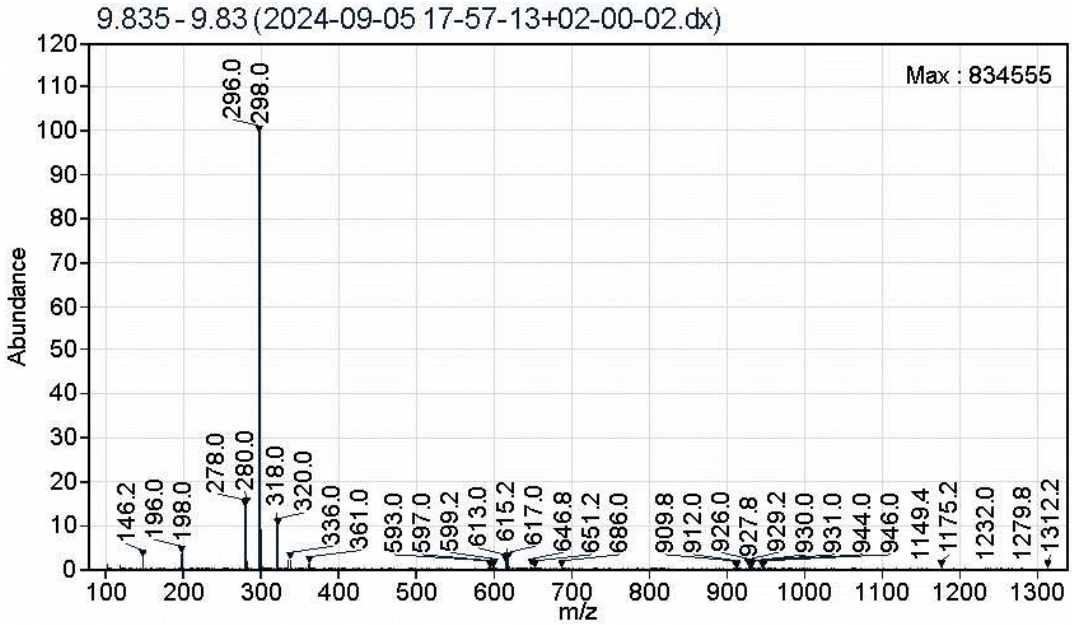

Figure S5. ESI-MS Spectrum of DADS(I).

DADS(II)

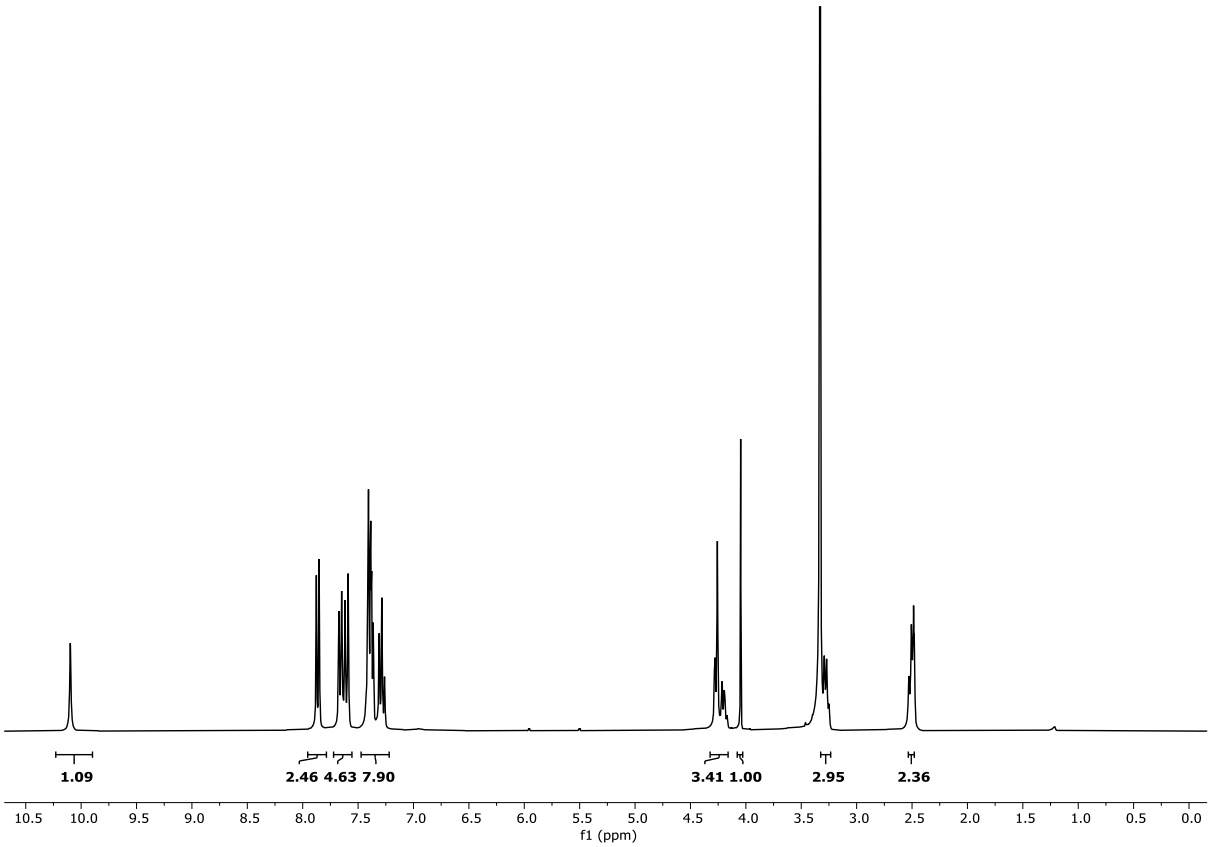

Figure S6. ^{1}H-NMR (400 MHz, DMSO-d6) of DADS(II).

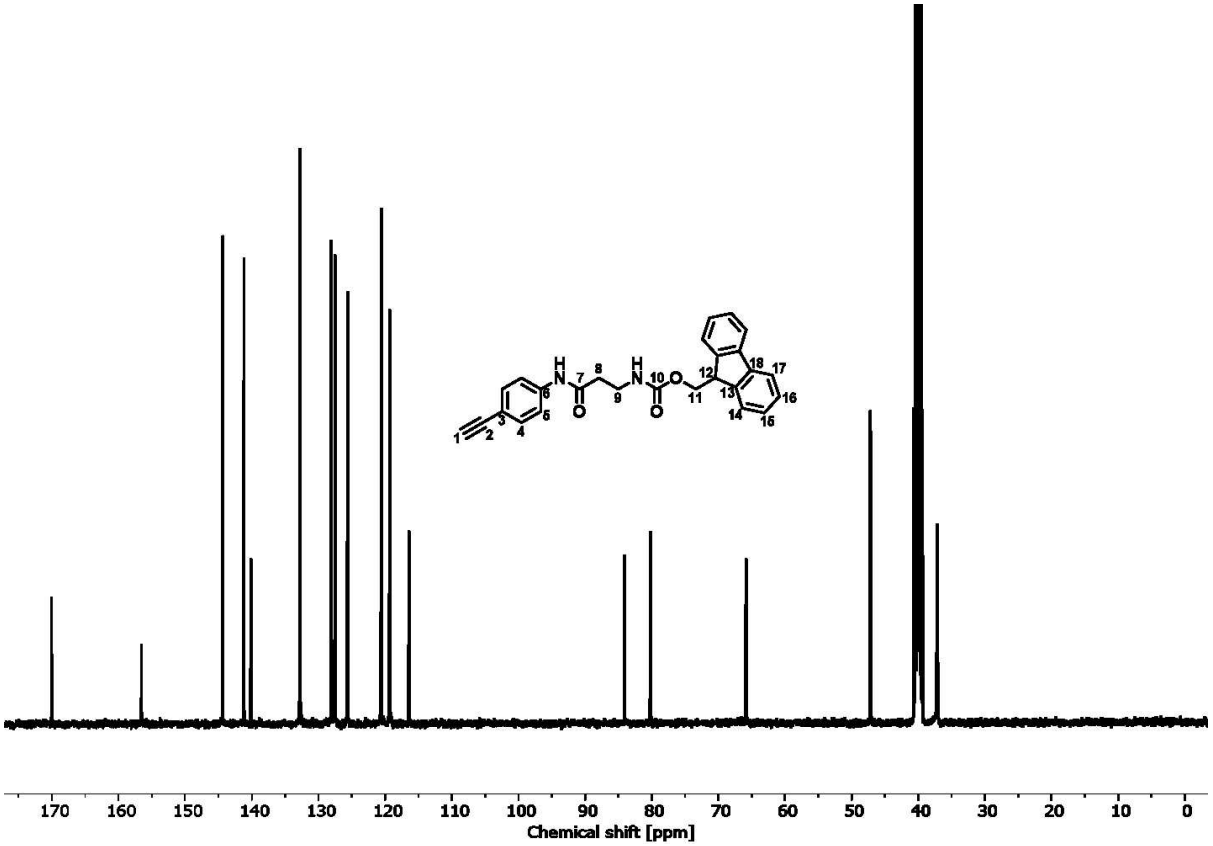

Figure S7. ^{13}C-NMR (400 MHz, DMSO-d6) of DADS(II).

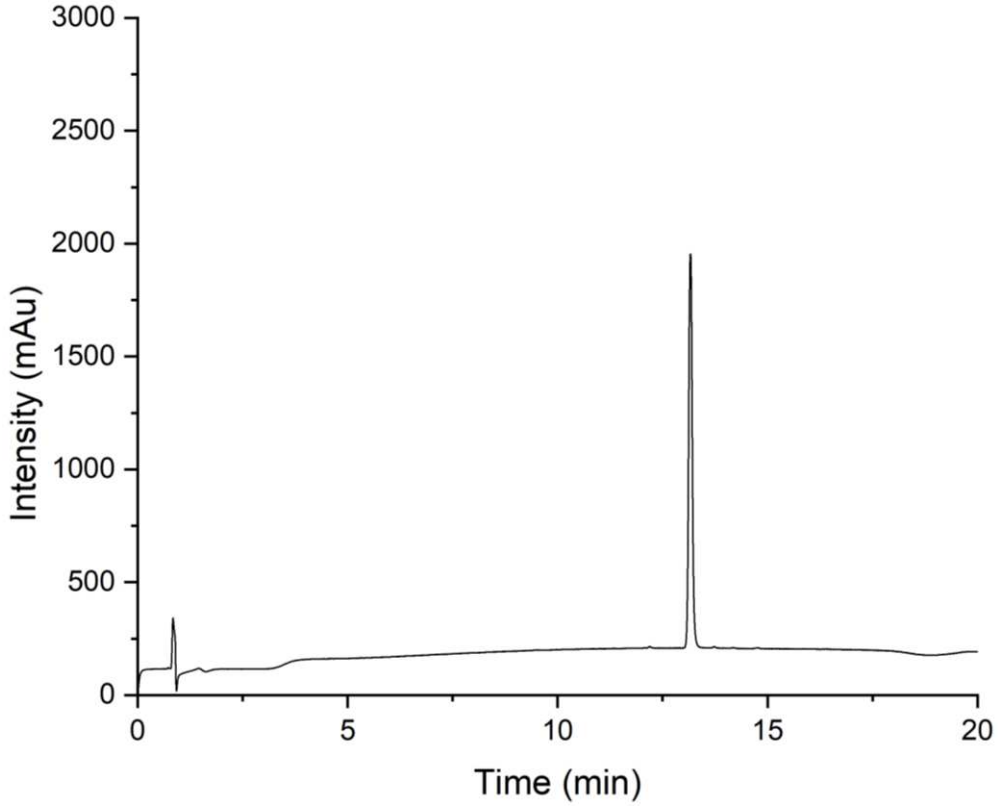

Figure S8. RP-HPLC chromatogram (from 95/5 to 5/95 Vol. % Water/acetonitrile with 0,1% formic acid in 20 min at 25 °C) of DADS(II).

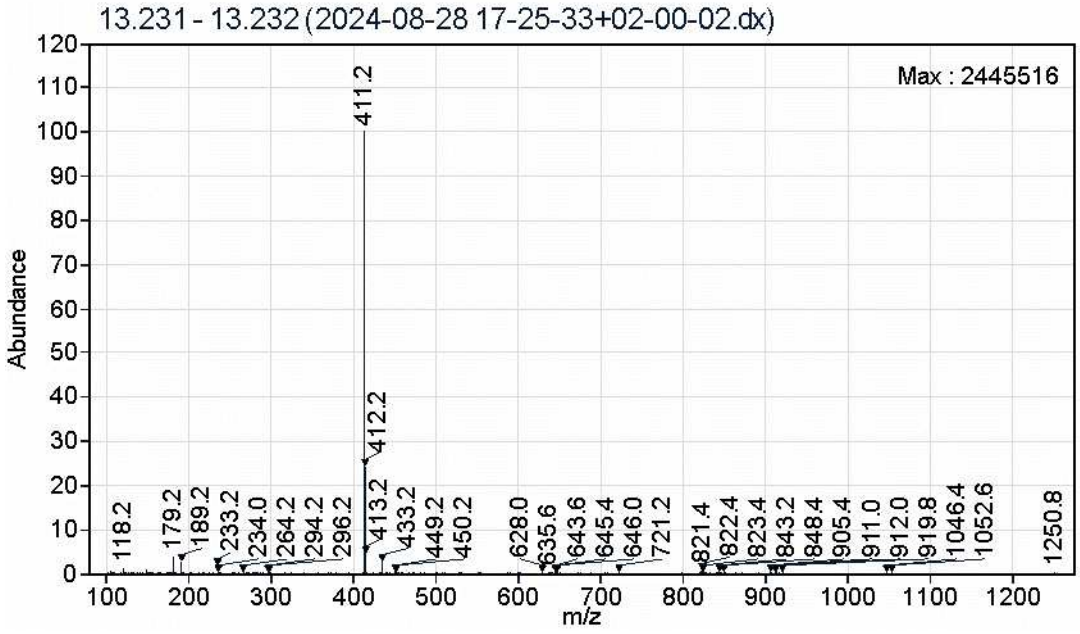

Figure S9. ESI-MS Spectrum of DADS(II).

Test sequences for on-resin DADS synthesis and compatibility with SPPoS.

1) **EDS-DADS(I)**

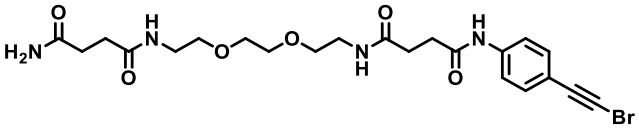

RP-HPLC: t_R = 8.66 min, 52 % relative purity (UV), from 95/5 to 5/95 Vol. % Water/acetonitrile with 0,1% formic acid in 20 min at 25 °C.

ESI-MS calc. for C12H10BrNO3: $[M+1H]^{1+}$ 525.1; found 525.2 $[M+1H]^{1+}$.

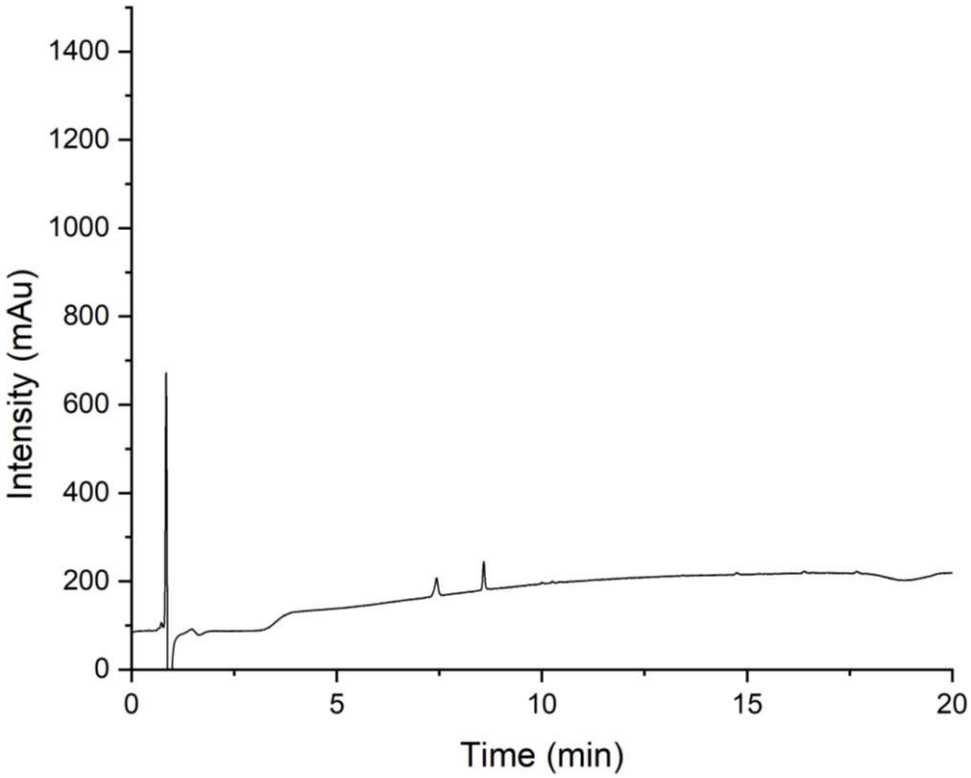

Figure S10. RP-HPLC chromatogram (from 95/5 to 5/95 Vol. % Water/acetonitrile with 0,1% formic acid in 20 min at 25 °C) of EDS-DADS(I) (t_R = 8.66) and an unknown side product (t_R = 7.50).

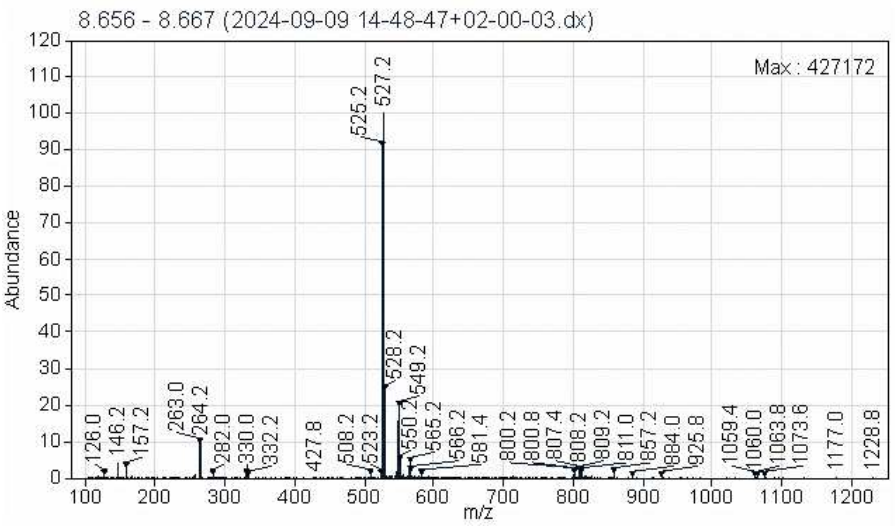

Figure S11. ESI-MS Spectrum of EDS-DADS(I) (t_R = 8.66).

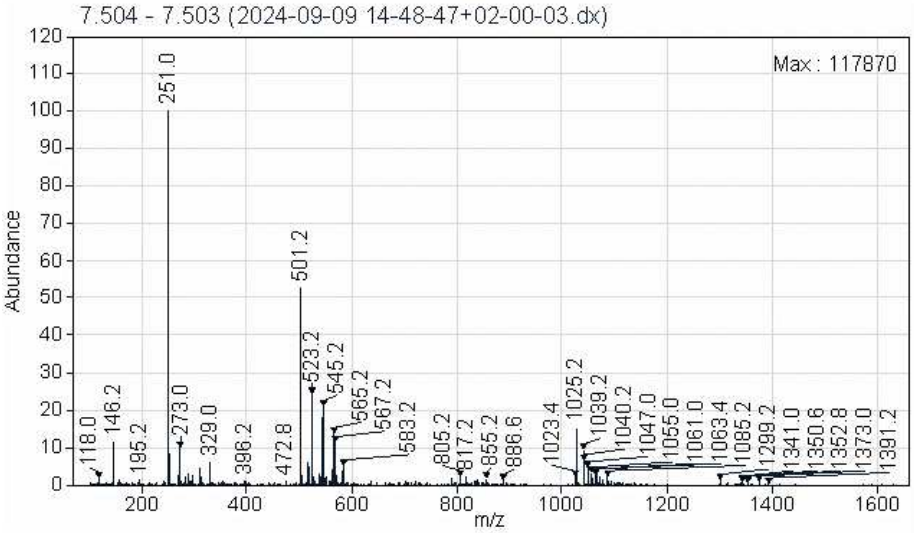

Figure S12. ESI-MS Spectrum of the unknown side product (t_R = 7.50).

2) EDS-DADS-Fmoc

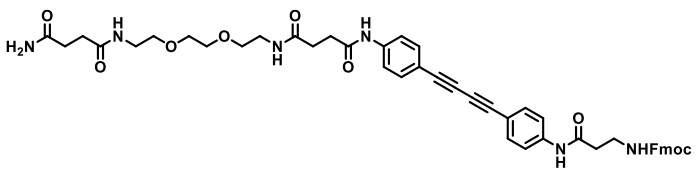

RP-HPLC: t_R = 12.17 min, 90 % relative purity (UV), from 95/5 to 5/95 Vol. % Water/acetonitrile with 0,1% formic acid in 20 min at 25 °C.

ESI-MS calc. for C48H50N6O9: $[M+1H]^{1+}$ 855.4, $[M+2H]^{2+}$ 428.2; found 855.6 $[M+1H]^{1+}$, 428.4 $[M+2H]^{2+}$.

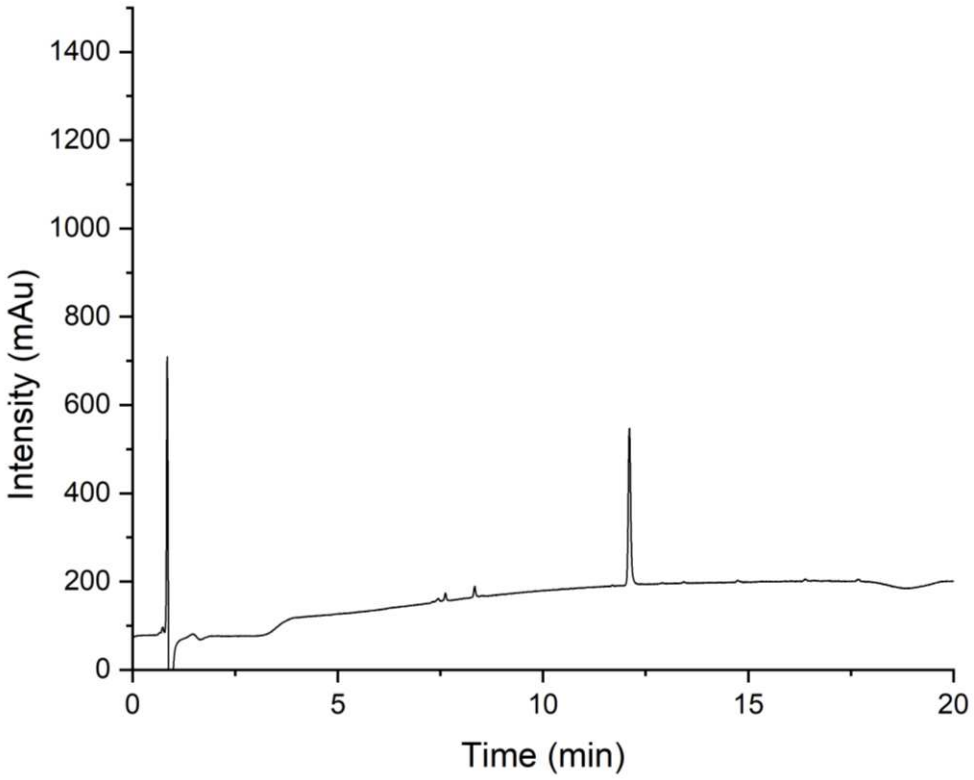

Figure S13. RP-HPLC chromatogram (from 95/5 to 5/95 Vol. % Water/acetonitrile with 0,1% formic acid in 20 min at 25 °C) of EDS-DADS-Fmoc.

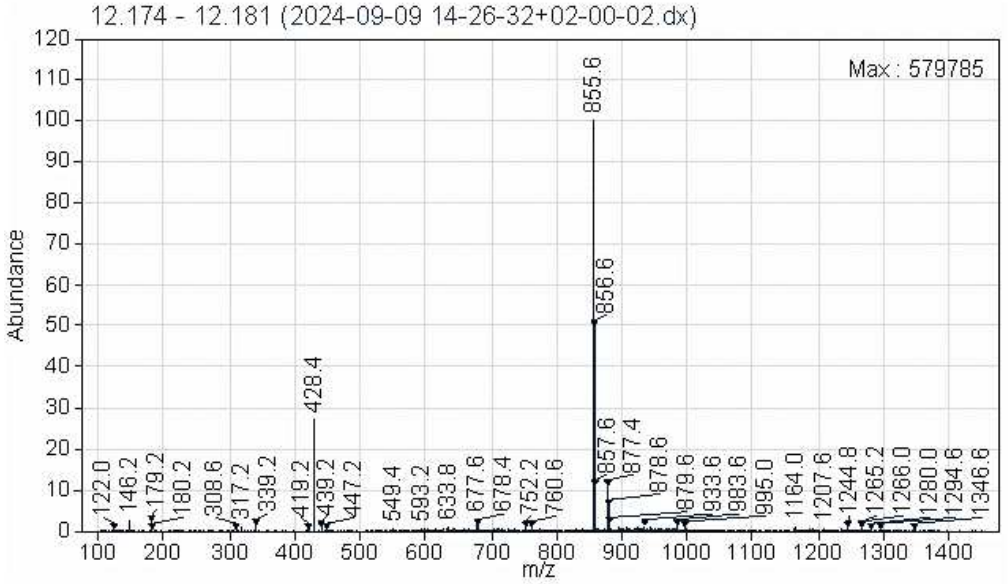

Figure S14. ESI-MS Spectrum of EDS-DADS-Fmoc (t_R = 12.17).

Side product (1):

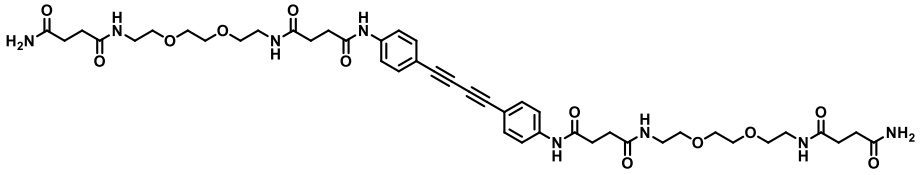

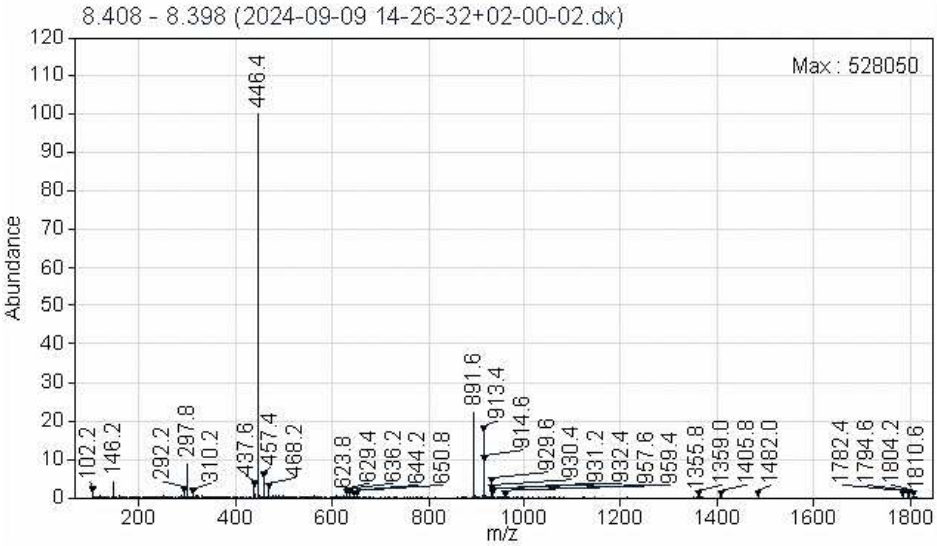

Figure S15. ESI-MS Spectrum of side product (1) (t_R = 8.41).

Side product (2):

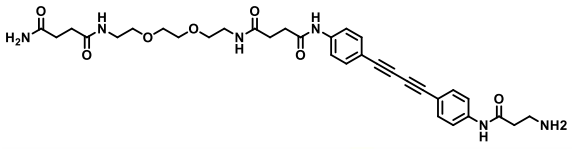

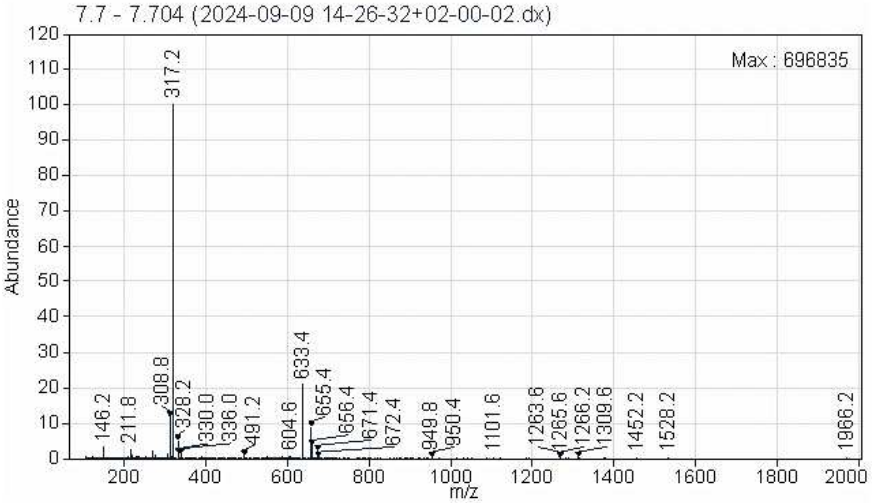

Figure S16. ESI-MS Spectrum of side product (2) (t_R = 7.70).

3) EDS-DADS-EDS-Fmoc

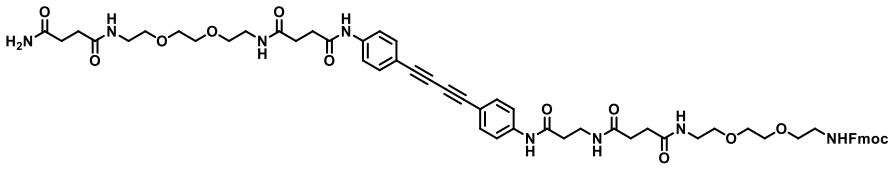

RP-HPLC: t_R = 10.89 min, 98 % relative purity (UV), from 95/5 to 5/95 Vol. % Water/acetonitrile with 0,1% formic acid in 20 min at 25 °C.

ESI-MS calc. for C58H68N8O13: $[M+1H]^{1+}$ 1085.5, $[M+2H]^{2+}$ 543.3; found 1085.6 $[M+1H]^{1+}$, 543.6 $[M+2H]^{2+}$.

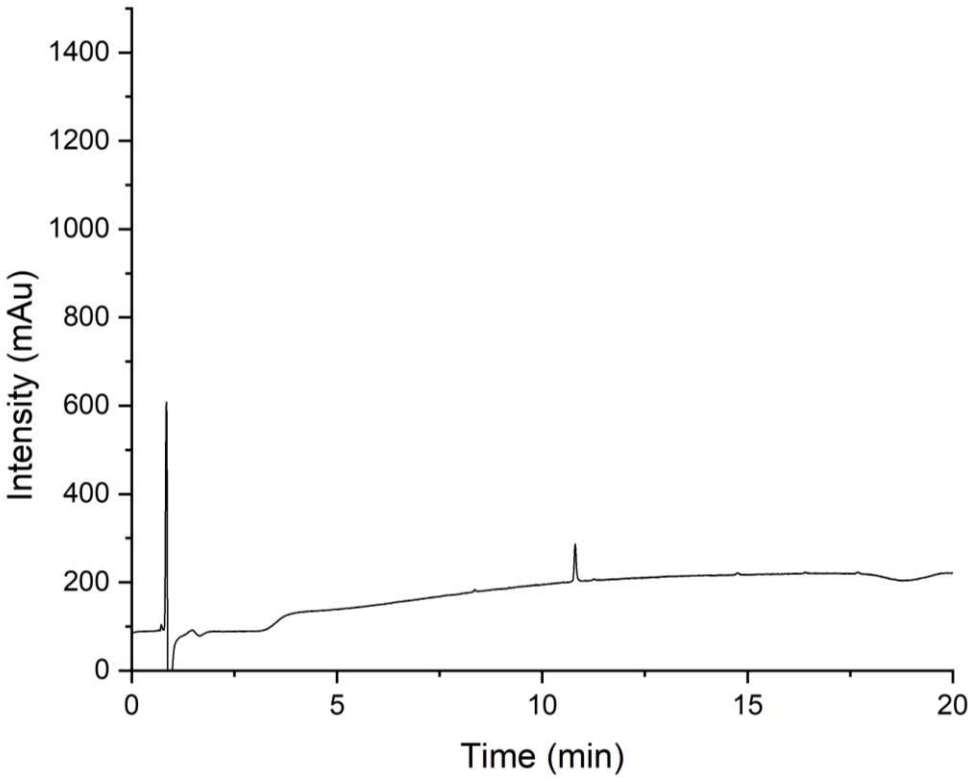

Figure S17. RP-HPLC chromatogram (from 95/5 to 5/95 Vol. % Water/acetonitrile with 0,1% formic acid in 20 min at 25 °C) of EDS-DADS-EDS-Fmoc.

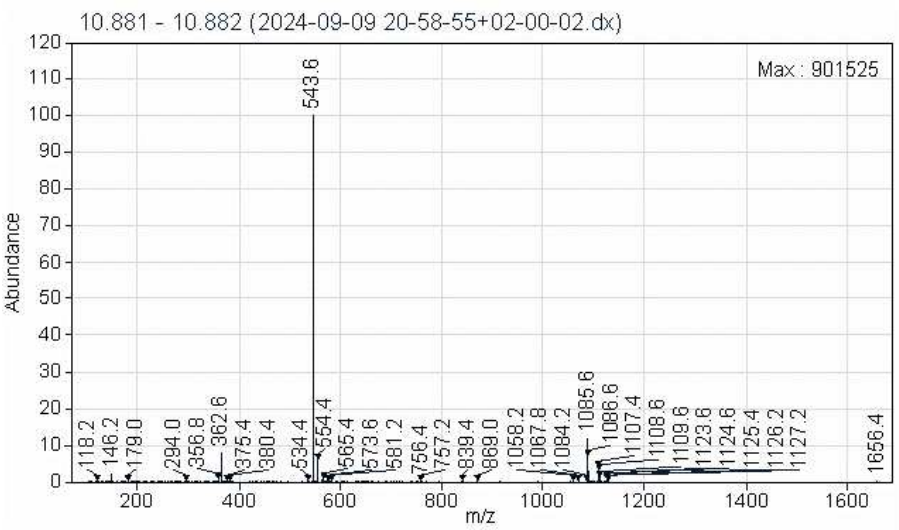

Figure S18. ESI-MS spectrum of EDS-DADS-EDS-Fmoc.

4) EDS-DADS-EDS-PA

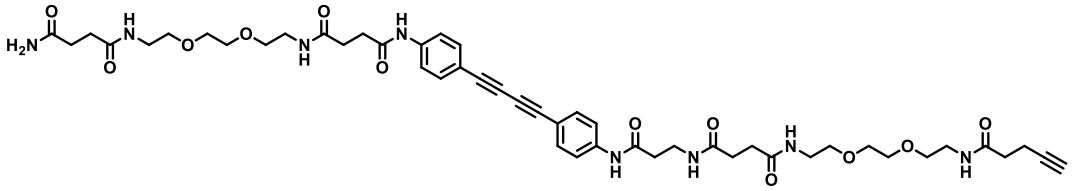

RP-HPLC: t_R = 8.85 min, 95 % relative purity (UV), from 95/5 to 5/95 Vol. % Water/acetonitrile with 0,1% formic acid in 20 min at 25 °C.

ESI-MS calc. for C48H62N8O12: $[M+1H]^{1+}$ 943.5, $[M+2H]^{2+}$ 472.3; found 943.6 $[M+1H]^{1+}$, 472.4 $[M+2H]^{2+}$.

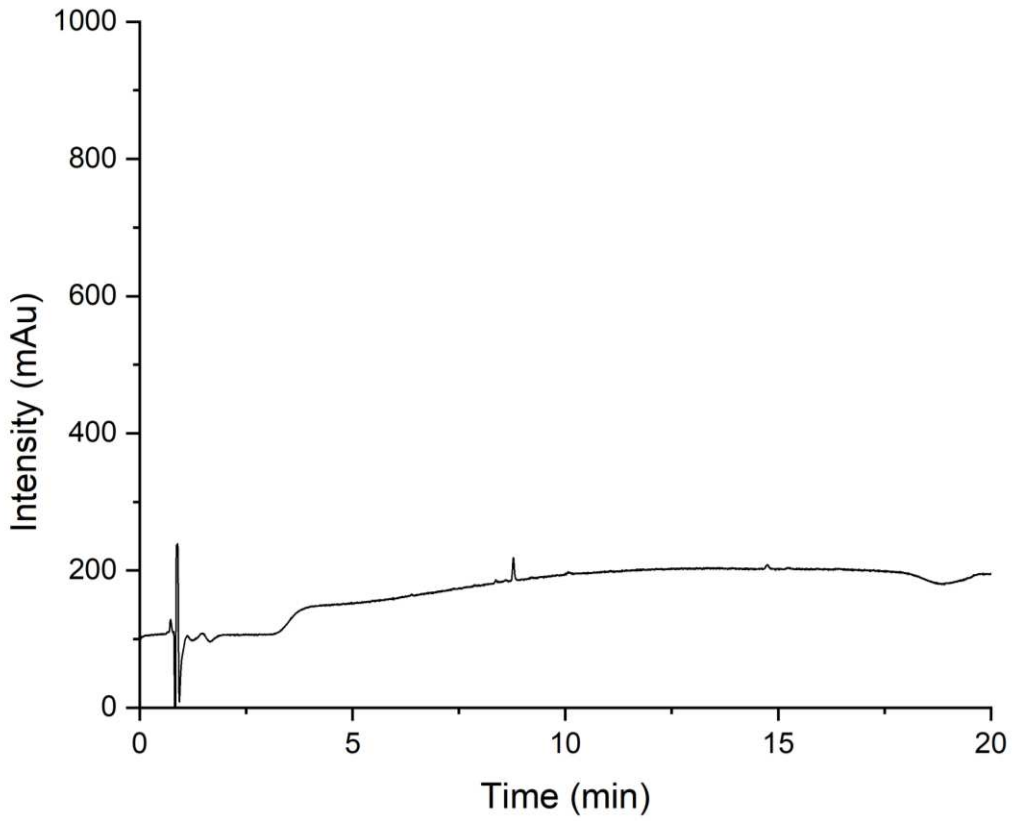

Figure S19. RP-HPLC chromatogram (from 95/5 to 5/95 Vol. % Water/acetonitrile with 0,1% formic acid in 20 min at 25 °C) of EDS-DADS-EDS-PA.

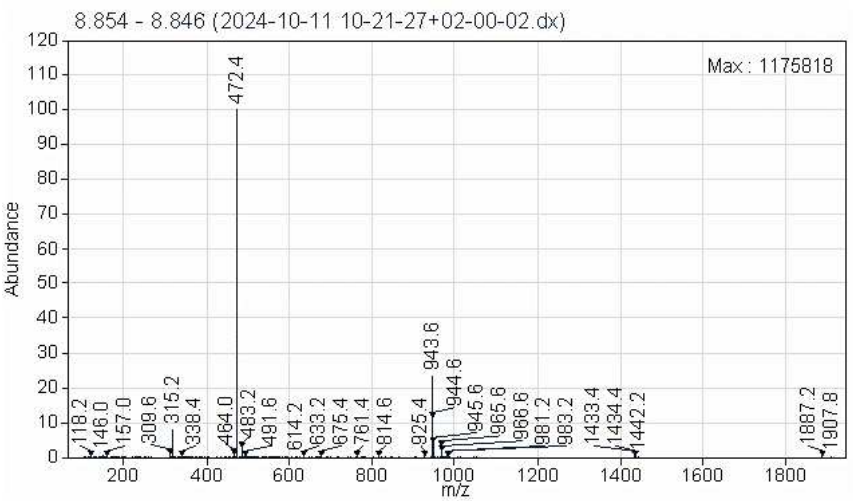

Figure S20. ESI-MS spectrum of EDS-DADS-EDS-PA.

5) EDS-DADS-EDS-PA-Man

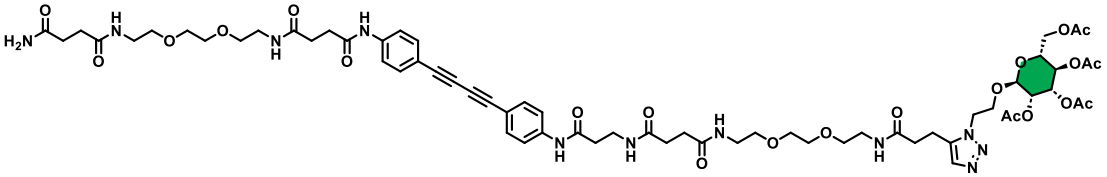

RP-HPLC: t_R = 9.33 min, 90 % relative purity (UV), from 95/5 to 5/95 Vol. % Water/acetonitrile with 0,1% formic acid in 20 min at 25 °C.

ESI-MS calc. for C48H62N8O12: $[M+2H]^{2+}$ 680.8, $[M+3H]^{3+}$ 454.2; found 681.0 $[M+2H]^{2+}$, $[M+3H]^{3+}$454.4.

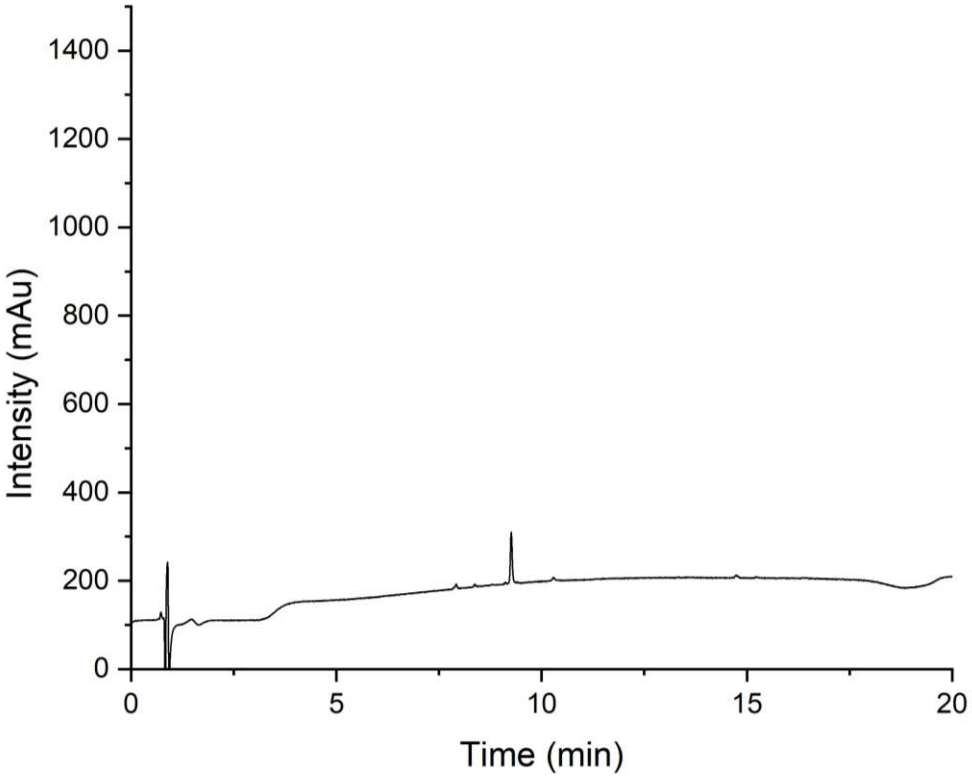

Figure S21. RP-HPLC chromatogram (from 95/5 to 5/95 Vol. % Water/acetonitrile with 0,1% formic acid in 20 min at 25 °C) of EDS-DADS-EDS-PA-Man.

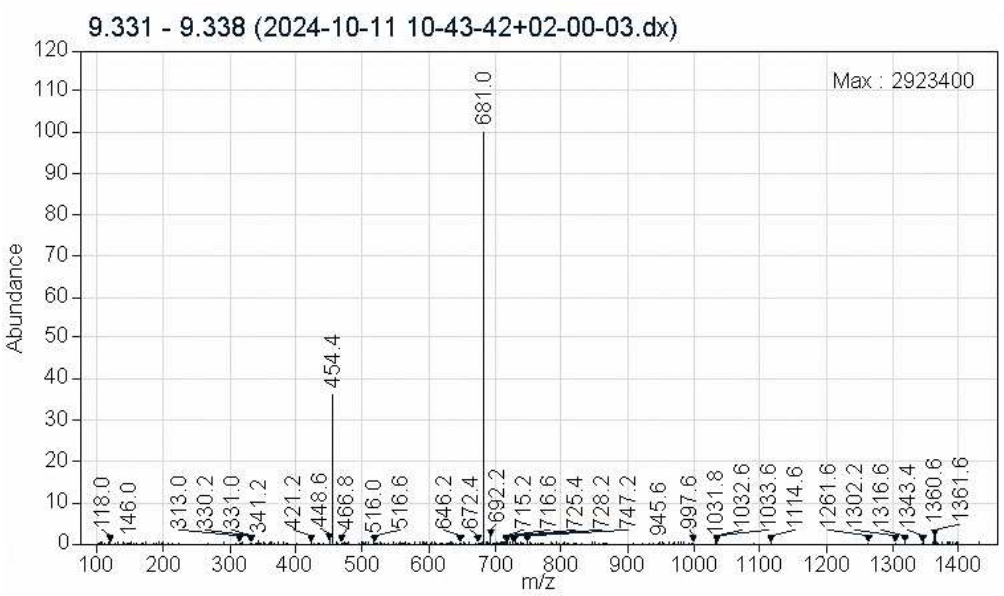

Figure S22. ESI-MS spectrum of EDS-DADS-EDS-PA-Man (t_R = 9.33).

Side product

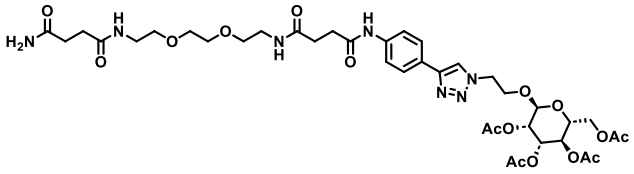

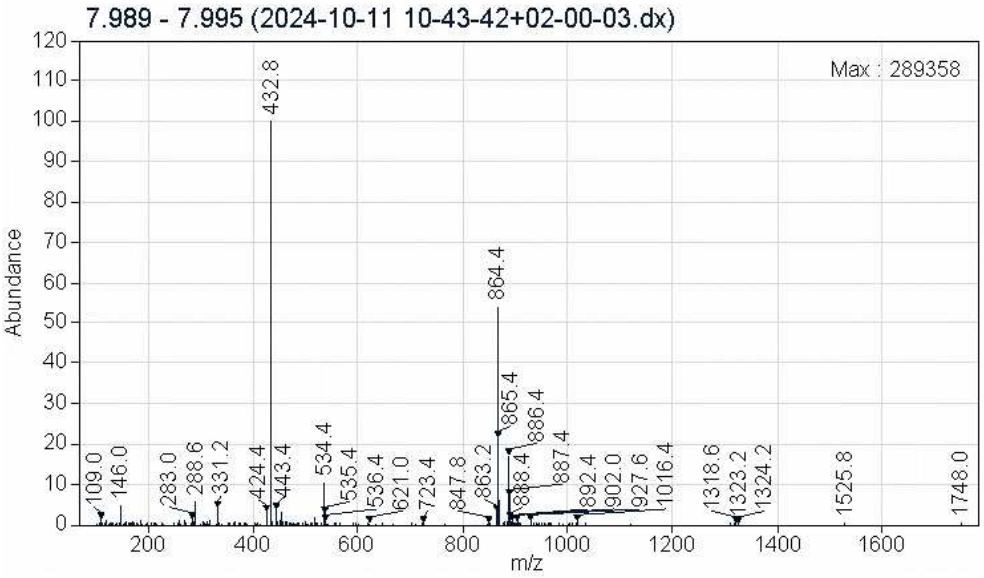

Figure S23. ESI-MS spectrum of the Side product (t_R = 7.99).

Glycooligomer ManDAChol

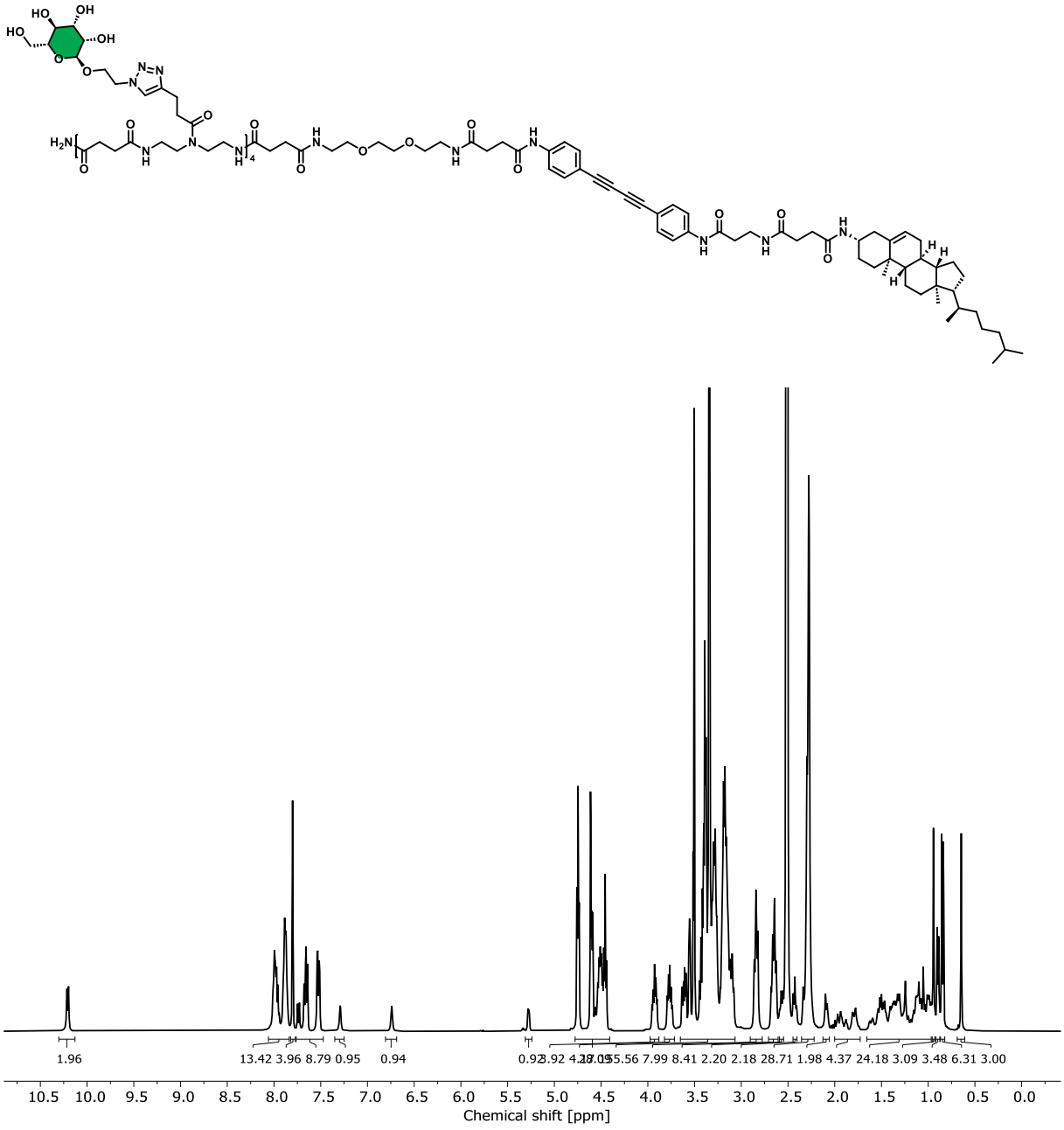

Figure S24. ^{1}H-NMR (400 MHz, DMSO-d6) of Man_4DA-Chol.

^{1}H-NMR (400 MHz, DMSO-d6) δ [ppm] = 10.21 (d, *J* = 6.8 Hz, 2H, Ar-N*H*), 8.04 – 7.84 (m, 11H, Amide-N*H*), 7.82 – 7.78 (m, 4H, Triazole-C*H*), 7.76 – 7.49 (m, 9H, Chol-N*H*, Ar-C*H*), 7.29 (s, 1H, C(O)NH_2), 6.74 (s, 1H, C(O)NH_2), 5.29 – 5.26 (m, 1H, Chol-C=C*H*), 4.78 – 4.43 (m, 28H, Man-O*H*, Anom.-C*H*, Triazole-NCH_2), 3.98 – 3.88 (m, 4H, Man-C*H*OH), 3.82 – 3.72 (m, 4H, Man-C*H*OH), 3.65 – 3.06 (m, 83H, Chol-NHC*H*, β-Ala-CH_2NH, DADS-NHC(O)CH$_2$CH_2NH, EDS-CH_2, TDS-CH_2NCH_2, TDS-CH_2NHC(O), Man-C*H*OH, Man-C*H*CH_2OH, Triazole-NCH$_2$CH_2O), 2.84 (m, 8H TDS-NC(O)CH$_2$CH_2C), 2.71 – 2.61 (m, 8H,TDS-NC(O)CH_2CH$_2$C), 2.57 (t, J = 7.1 Hz, 2H, DADS-

NHC(O)CH_2CH$_2$C(O)NH), 2.43 (t, *J* = 7.1 Hz, 2H, DADS-NHC(O)CH_2CH$_2$NH), 2.37 – 2.22 (m, 28H, C(O)CH_2CH_2C(O)), 2.12-2.05 (m, 2H, Chol-NHC(O)CH_2), 2.00 – 1.73 (m, 4H, Chol-C=CHCH_2, Chol-C=CCH_2), 1.66 – 0.97 (m, 24H, Chol-C*H*, Chol-CH_2), 0.96 – 0.82 (m, 12H, Chol-CH_3), 0.65 (s, 3H, Chol-CH_3).

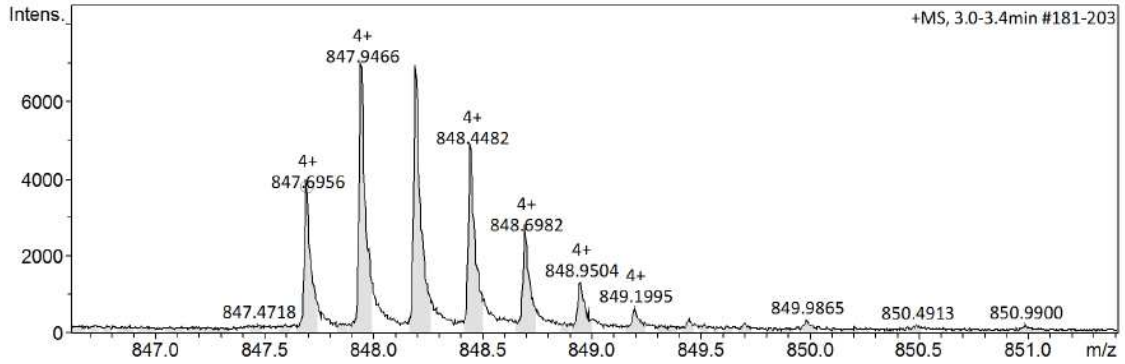

Meas. m/z	#	Ion Formula	m/z	err [ppm]	mSigma	# mSigma	Score	rdb	e¯ Conf	N-Rule
847.6956	1	C158H247N33O49	847.6957	0.2	22.9	1	100.00	52.0	even	ok
	2	C153H247N35O51	847.6947	-1.0	27.8	2	63.97	48.0	even	ok

Figure S25. HR-ESI-MS of Man$_4$DA-Chol.

HR-ESI-MS: for $C_{158}H_{243}N_{33}O_{49}$ m/z $[M+4H]^{4+}$ calcd.: 847.6954, found: 847.6956
mass error 0.235934 ppm.

Glycooligomer GalDAChol

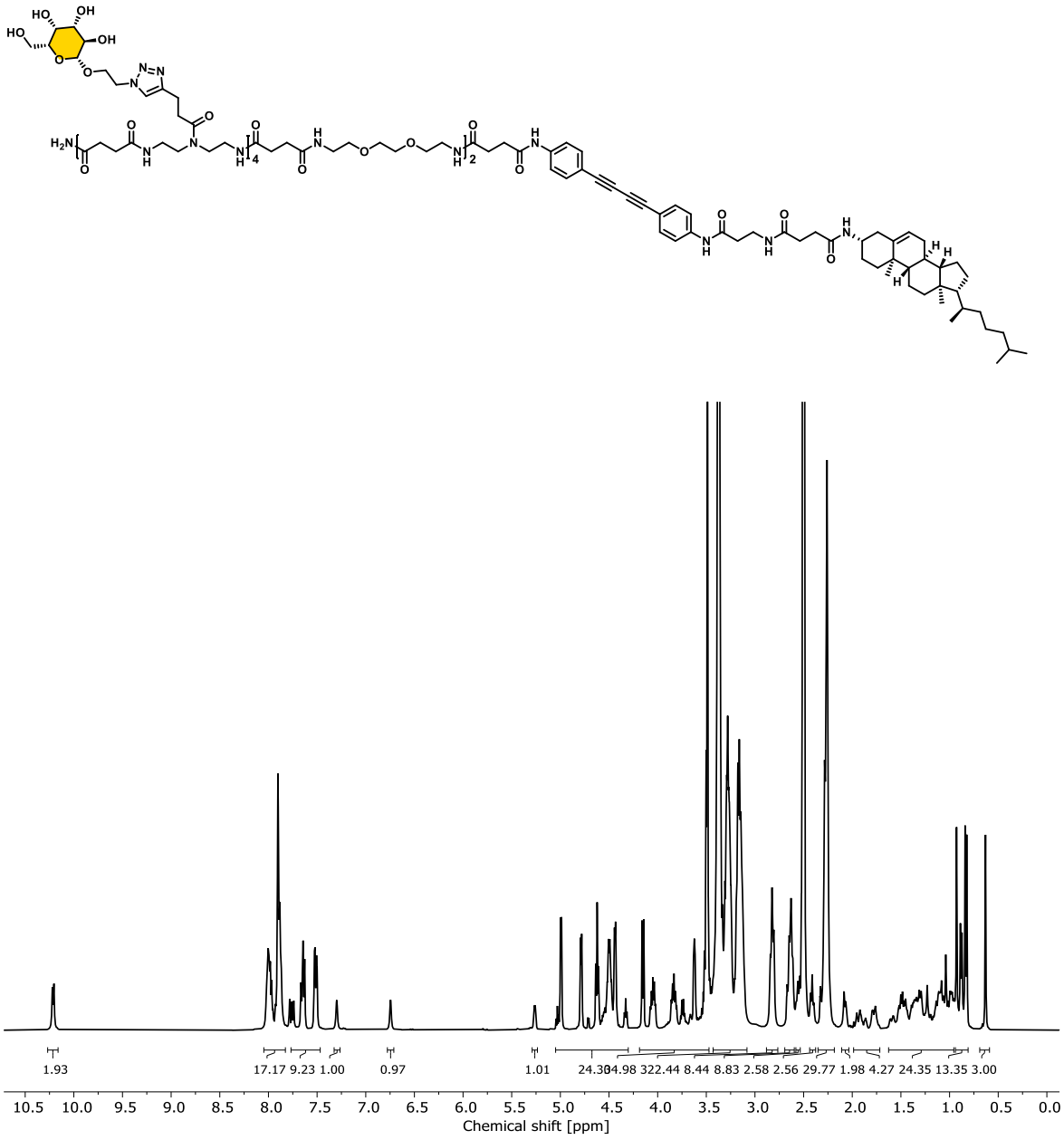

Figure S28. ^{1}H-NMR (400 MHz, DMSO-d6) of Gal$_4$DA-Chol.

^{1}H-NMR (400 MHz, DMSO-d6) δ [ppm] = 10.21 (d, J = 6.4 Hz, 2H, Ar-N*H*), 8.05 – 7.81 (m, 15H, Amide-N*H,* Triazole-C*H*), 7.77 – 7.46 (m, 9H, Chol-N*H*, Ar-C*H*), 7.30 (s, 1H, C(O)N*H*$_2$), 6.75 (s, 1H, C(O)N*H*$_2$), 5.26 (d, J = 4.8 Hz, 1H, Chol-C=C*H*), 5.05 – 4.30 (m, 24H, Gal-O*H*, Triazole-NC*H*$_2$), 4.18 – 3.47 (m, 34H, Anom.-C*H,* Gal-C*H*OH, Gal-C*H*C*H*$_2$OH), 3.43 – 3.08 (m, 61H, Chol-NHC*H*, β-Ala-C*H*$_2$NH, DADS-NHC(O)CH$_2$*CH*$_2$NH, EDS-C*H*$_2$, TDS-C*H*$_2$NC*H*$_2$, TDS-C*H*$_2$NHC(O), Gal-C*H*OH, Triazole-NCH$_2$C*H*$_2$O), 2.88 – 2.76 (m, 8H, TDS-NC(O)CH$_2$C*H*$_2$*C*), 2.69 – 2.59 (m, 8H, TDS-NC(O)C*H*$_2$CH$_2$*C*), 2.57-2.53 (m, 2H, DADS-NHC(O)C*H*$_2$CH$_2$C(O)NH), 2.41 (t, J = 7.0 Hz, 2H, DADS-

NHC(O)CH_2CH_2NH), 2.35 – 2.18 (m, 28H, C(O)CH_2CH_2C(O)), 2.12-2.05 (m, 2H, Chol-NHC(O)CH_2), 1.98 – 1.72 (m, 4H, Chol-C=CHCH_2, Chol-C=CCH_2), 1.62 – 0.96 (m, 24H, Chol-CH, Chol-CH_2), 0.94 – 0.81 (m, 12H, Chol-CH_3), 0.63 (s, 3H, Chol-CH_3).

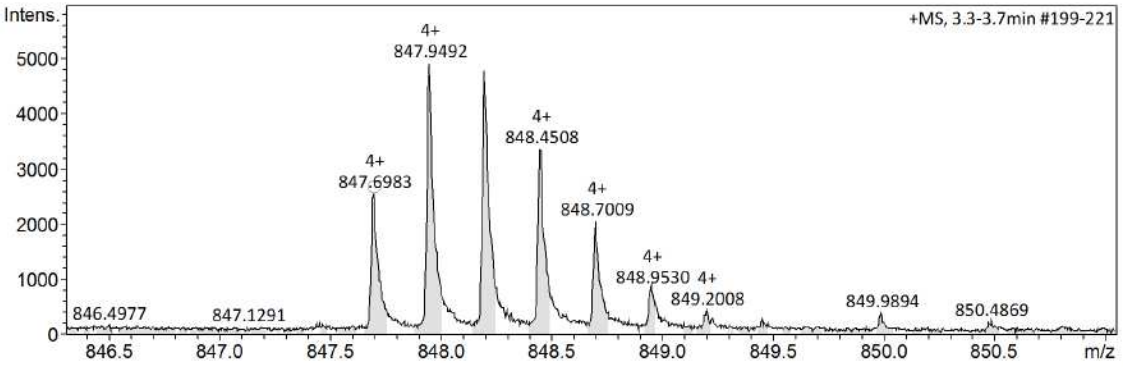

Meas. m/z	#	Ion Formula	m/z	err [ppm]	mSigma	# mSigma	Score	rdb	e¯ Conf	N-Rule
847.6983	1	C158H247N33O49	847.6957	-3.1	25.1	1	21.88	52.0	even	ok
	2	C157H247N35O48	847.6985	0.3	26.5	2	99.40	52.0	even	ok
	3	C156H251N31O52	847.6982	-0.1	28.0	3	100.00	47.0	even	ok
	4	C155H251N33O51	847.7010	3.2	29.8	4	17.99	47.0	even	ok

Figure S29. HR-ESI-MS of Gal_4DA-Chol.

HR-ESI-MS: for $C_{158}H_{243}N_{33}O_{49}$ m/z $[M+4H]^{4+}$ calcd.: 847.6954, found: 847.6983 mass error 3.421040 ppm.

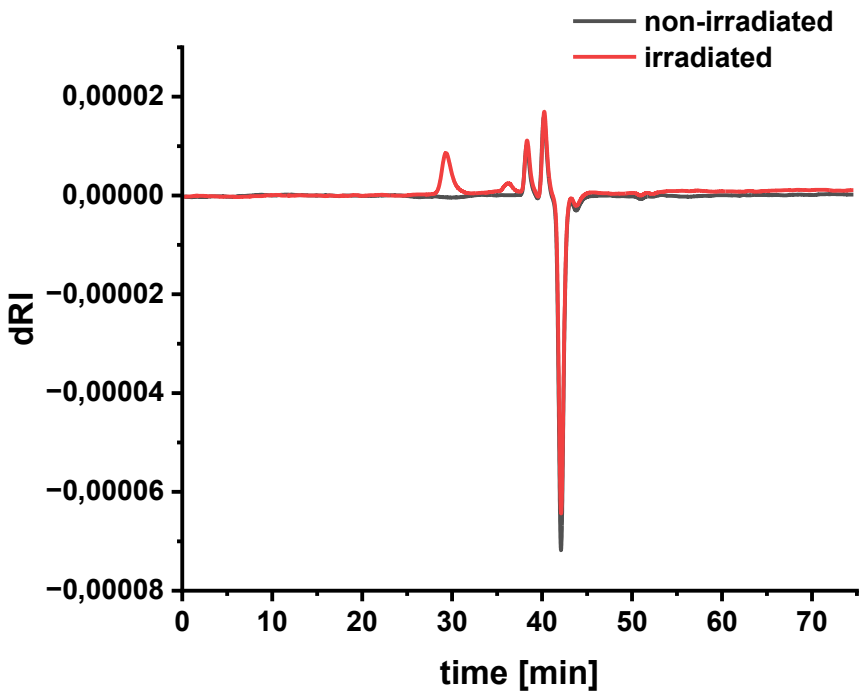

Figure S30. H_2O-SEC-MALS of ManDAChol (non-irradiated, grey) and ManDAChol (irradiated, red).

Đ (via H_2O-SEC, MALS coupled RI-detector): 1.02

M_n [kDa] (via H_2O-SEC, MALS coupled RI-detector): 354

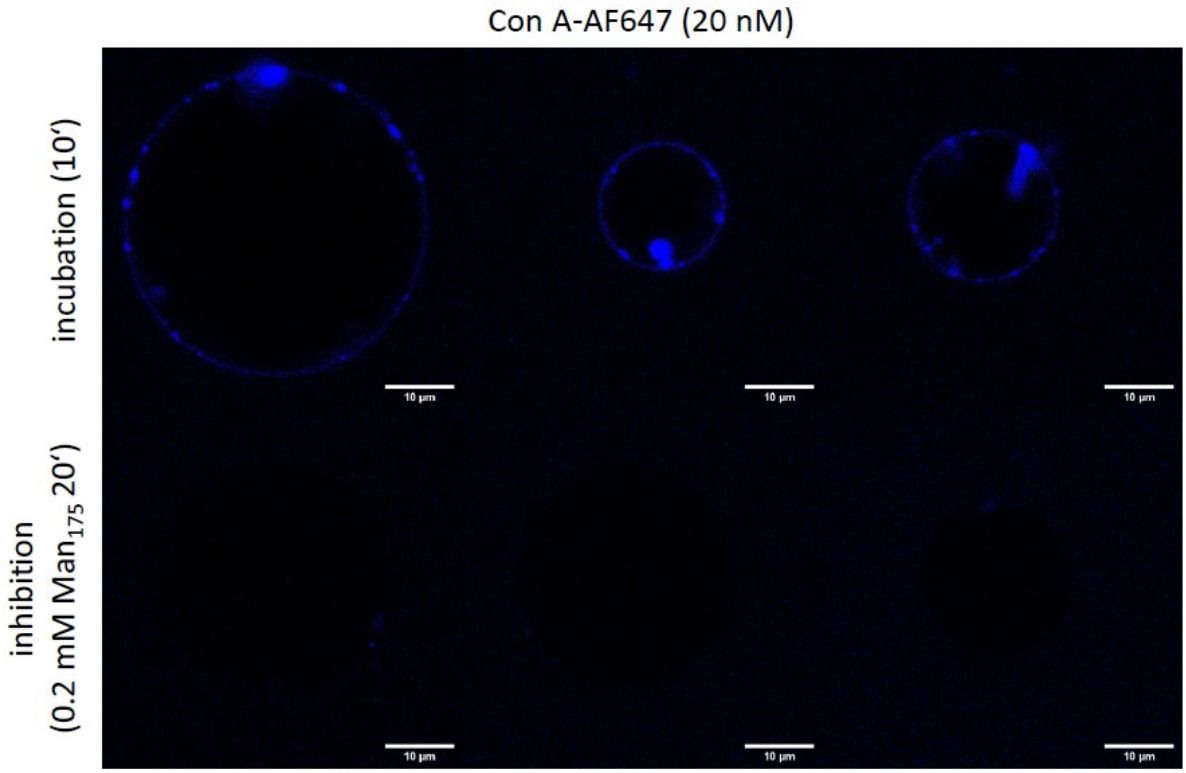

Figure S31. Confocal fluorescence microscopy images of GUVs containing 0.5 mol% Man_4DAChol incubated with Con A-AF647 before (top) and after incubation (bottom) with a polyvalent Man-polymer inhibitor.

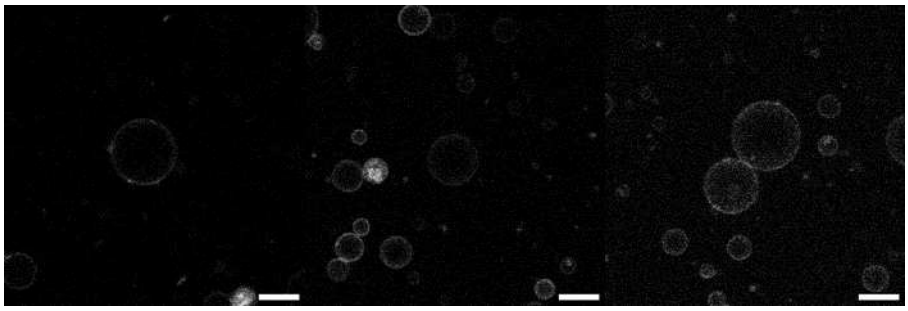

Figure S32. Additional confocal images of ManDAChol decorated GUVs. Contrast adjusted for better visibility. Scale bars: 25 µm.

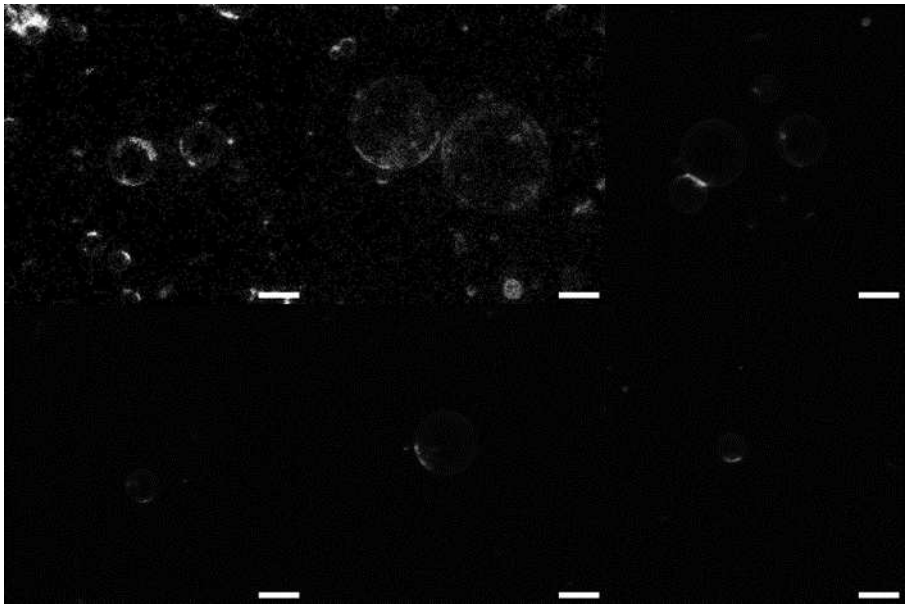

Figure S33. Additional confocal images of ManDAChol decorated GUVs incubated with 20 nM ConA after irradiation with 365 nm. Contrast adjusted for better visibility. Scale bars: 25 µm.

References

(1) Carrotta, R.; Vilasi, S.; Librizzi, F.; Martorana, V.; Bulone, D.; San Biagio, P. L. α-Casein inhibition mechanism in concanavalin A aggregation process. *The journal of physical chemistry. B* **2012**, 116, 14700–14707.

(2) Ponader, D.; Wojcik, F.; Beceren-Braun, F.; Dernedde, J.; Hartmann, L. Sequence-Defined Glycopolymer Segments Presenting Mannose: Synthesis and Lectin Binding Affinity. *Biomacromolecules* **2012**, 13, 1845–1852.

(3) Boden, S.; Reise, F.; Kania, J.; Lindhorst, T. K.; Hartmann, L. Sequence-Defined Introduction of Hydrophobic Motifs and Effects in Lectin Binding of Precision Glycomacromolecules. *Macromolecular bioscience* **2019**, 19, e1800425.

(4) Kim, H. J.; Ishii, T.; Zheng, M.; Watanabe, S.; Toh, K.; Matsumoto, Y.; Nishiyama, N.; Miyata, K.; Kataoka, K. Multifunctional polyion complex micelle featuring enhanced stability, targetability, and endosome escapability for systemic siRNA delivery to subcutaneous model of lung cancer. *Drug delivery and translational research* **2014**, 4, 50–60.

(5) Song, Z.-J.; Meng, S.-Y.; Wang, Q.-R. Total Synthesis of Marine Alkaloids Motuporamines A and B via Ring Expansion of Cyclic β-Keto Esters. *ACS Omega* **2021**, 6, 881–888.

4. Conclusions and Outlook

The aim of this thesis was the establishment of a synthetic platform to derive highly tailorable precision mimetics of naturally occurring cell-surface glycans that are suitable to be incorporated into phospholipid membranes and to create more advanced models of native cellular glycocalyces. Important key structural parameters that drastically influence glycocalyx interactions, e.g. in terms of lectin binding or interaction with pathogens, are the type of glycosylation, glycan valency, as well as the physico-chemical properties of the employed lipid moiety for membrane tethering. Additionally, incorporation of functional handles, such as fluorophores or crosslinkable moieties, into the glycan mimetics facilitates their localization in phospholipid membranes and enables a systematic analysis of their interaction with adjacent entities.

The approach presented in this thesis to synthesize highly tailorable glycan mimetics combines previously established SPPoS with TIRP and thus enables precise control over these above-mentioned key structural parameters: via SPPoS a functional backbone can be constructed that can then be further functionalized site-specifically with glycan moieties, lipids, as well as further functionalities, such as fluorophores. While SPPoS is limited with regard to accessible chain lengths, meaning that only short glycan mimetics can be synthesized in a sequence-defined manner, it allows for the site selective introduction such as Cys moieties to serve as later grafting points for TIRP. These thusly derived structures can then be employed as macroinitiators to derive polymeric glycan mimetics with narrow dispersities, while retaining a sequence defined functional backbone. Post-synthesis modifications, such as global sulfation of the glycan moieties, allows to prepare even more advanced glycan mimetics that resemble naturally occurring sGAGs, for instance.

In this manner a highly tailorable library of lapidated glycan mimetics was synthesized in the course of this thesis that allowed the subsequent construction of different glycocalyx models to mimic key structural parameters of native glycocalyces: 1.) their highly crowded nature, 2.) local constituent inhomogeneities due to the existence of lipid rafts, 3.) the abundance of highly sulfated glycosaminoglycans covalently attached to proteoglycan cores and 4.) the dynamic formation of glycan clusters in the cell membrane upon receptor-interactions.

In the first part of this thesis, an initial series of precision lipidated glycomacromolecules was successfully synthesized and employed to construct a glycocalyx model to mimic the high density of glycans on native cellular membranes. Employing SPPoS, two sequence defined, tetravalent, cholesteryl-functionalized glycan mimetics, bearing a fluorescent probe were synthesized, presenting either a Man or a Gal head group. By combining SPPoS and TIRP, also polyvalent derivatives were

successfully synthesized. Therefore, the same functional backbone, that was employed for the glycooligomers, was equipped with a Cys-moiety, omitting the carbohydrate presenting part. In this manner, for the first time, solid-phase derived macroinitiators were synthesized that were subsequently polymerized employing TIRP with Man- or Gal-acrylamide monomers to give the respective polyvalent Man or Gal functionalized glycan mimetics.

In total, four different glycan mimetics were prepared, each bearing a short (four carbohydrate moieties) or long (approximately forty carbohydrates) glyco-head group (Man or Gal), a cholesteryl moiety for membrane anchoring and a fluorophore (Rhodamine B for Man or Fluorescein for Gal functionalized glycomacromolecules) for visualization via fluorescence microscopy techniques.

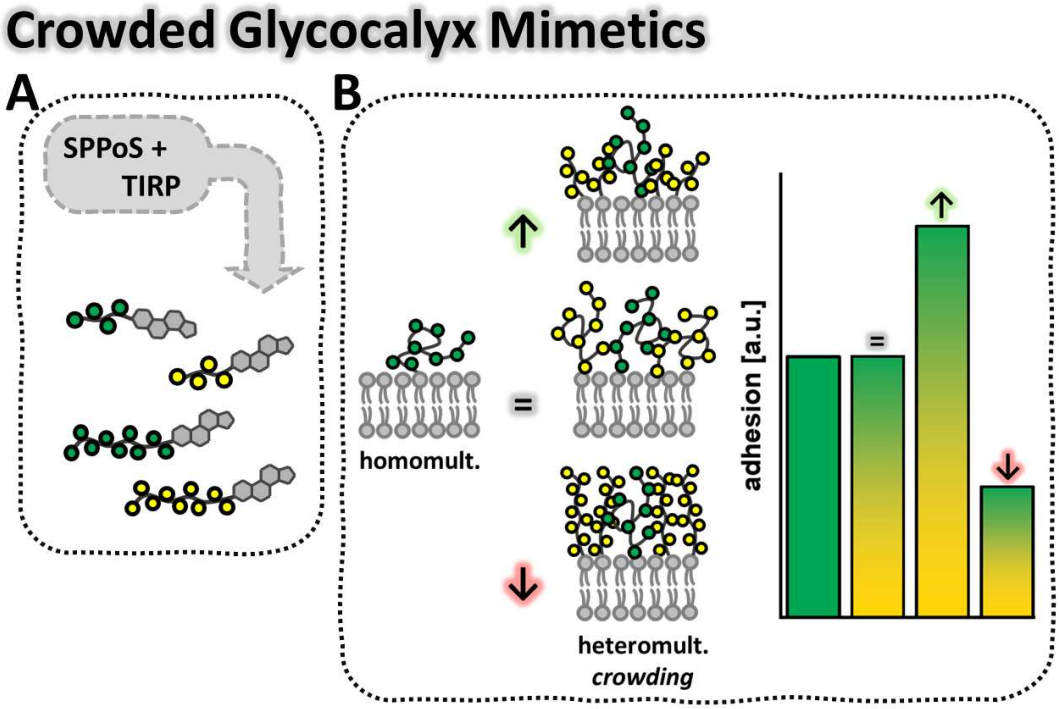

Figure 18. Summary of the results of the first part of the thesis. **A**: A combination of SPPoS and TIRP yields short and long glycan mimetics featuring site-selective functionalities, such as an oligovalent or polyvalent glycan head group, a fluorophore for fluorescence microscopy, as well as a cholesteryl-tether for subsequent intercalation into lipid membranes. **B**: Incorporation of short and long Man-ligands yields simplistic homomultivalent glycocalyx mimetics with different adhesion strength on Con A-covered surfaces, depending on valency and concentration of the employed ligands. Doping of the homomultivalent systems with short and long crowding agents (non-binding ligands, crowders) either leaves the adhesion unaffected, increases or decreases the adhesion, depending on the valency of the crowders and the overall constituent density in the glycocalyx mimetics.

Subsequently, the incorporation of the glycan mimetics into GUVs as membrane mimetics was established. Employing electroformation, giant unilamellar vesicles could be generated that incorporate the derived glycan mimetics homogenously into the inner and outer membrane leaflet to

yield naïve mimetics of natural glycocalyces. Next, the incorporation efficiency and the molecular dynamics of the glycan mimetics in the phospholipid membranes was examined employing FCS. It was found that the glycomacromolecules, equipped with a cholesteryl moiety, only incorporate by about 20% of the initially employed ligand concentration with a linear correlation at different concentrations. This indicates that the incorporation of ligands quickly reaches an equilibrium between membrane-inserted and dissolved ligands, rendering the cholesteryl-moiety a rather loose membrane anchor. The diffusion constants of all analyzed structures were found to be close to the diffusion constant of native DOPC in similar lipid mixtures, which substantiates a sufficient and adequate mobility of the ligands in the membrane.

To mimic cellular adhesion processes, the adhesion of homomultivalent glycan mimetic-decorated GUVs onto lectin-covered surfaces was qualitatively studied via RICM and fluorescence microscopy. Employing Con A as well-studied model lectin, Man-functionalized vesicles thereby served as binders, leading to adhesion of the vesicles on the substrate, whereas Gal-functionalized vesicles served as non-binders that did not interact with the Con A surface. Interestingly, GUVs without glycan mimetics incorporated adhered rather unspecifically on the Con A surfaces, suggesting that cell-surface glycans not only mediate certain binding events, but likely also block unspecific interactions between receptors and the phospholipid membrane. Different compositions of Man-decorated vesicles regarding glycan valency and ligand concentration revealed different affinities of the simplistic Man-decorated glycocalyx models to the Con A substrate, whereby the polyvalent structures generally displayed higher binding avidities towards the Con A surfaces than the respective tetravalent glycomacromolecules in a concentration-dependent manner. This is likely due to the higher multivalent and local concentration presentation of binding motifs, resulting in higher avid binding with the lectin.

Next, mixtures of the long and short, binding and non-binding glycomacromolecules were incorporated into GUVs to create for the first time heteromultivalent crowded glycocalyx mimetics that resemble more closely the heterogeneity and highly crowded nature of native cellular glycocalyces in a very controlled setting. Employing the same binding assay, now the impact of the Gal-functionalized glycan mimetics as non-binders (or crowding agents) on the selective Man-mediated vesicle adhesion was studied and compared to the respective homomultivalent systems. It was found that based on the composition of long and short, binding and non-binding ligands in the GUVs, vesicle adhesion is either unaltered, decreased or in some cases even increased, highly depending on the valency and overall concentration of the employed binders and non-binders. Generally, high concentrations of the long, non-binding ligands significantly reduced adhesion, while the short, non-binding ligands had no negative effect on the Man-Con A-mediated adhesion. However, the long, non-binding crowding agents did not impact GUV adhesion when the vesicles contained low concentrations of the binding

ligands. Notably, GUVs with low concentrations of the long, binding ligands adhered more strongly when doped with high concentrations of the short, non-binding ligands and low concentrations of the long, non-binding ligands, suggesting a certain level of cooperativity that mediates glycocalyx-associated binding events in a density- and valency-dependent manner. These first results demonstrated for the first time the applicability and feasibility of glycan mimetics to create highly tunable glycocalyx mimetics, that resemble more closely the natural glycocalyx, which enables the systematic examination of glycocalyx mediated adhesion and, thus, a convenient toolbox was created to construct mimics of native glycocalyces with precise alterations in constitution, regarding glycosylation, macromolecular density and heteromultivalency.

In the second part of the thesis, a second series of lipidated glycan mimetics was introduced to systematically study the impact of glycan allocation in different membrane phases, mirroring the recruitment of native glycan constituents into cellular lipid rafts. Lipid rafts in cellular membranes are spatially resolved, highly ordered and dynamic microdomains within the surrounding fluid membrane, that are enriched in cholesterol and sphingolipids. The function and occurrence of these highly ordered nanodomains is highly discussed in the literature; common belief is that the local enrichment of glyco-sphingolipids and certain proteins, that are recruited into these lipid rafts, is a crucial cellular feature that mediates, e.g. signal cascading or pathogen infection in native cells. For this purpose, SPPoS was again employed to obtain sequence-defined, tetravalent glycan mimetics bearing either a Man- or Gal-head group. As membrane anchors, *N*-terminally conjugated C_{18}-fatty acids, joint via a 2.3-diaminopropionic acid moiety were employed, to yield lipid motives that resemble ceramides, a class of lipids that are highly associated with naturally occurring lipid rafts.

In this manner, a total of four different glycan mimetics was synthesized, each differing in their tetravalent glyco-head group (Man or Gal) and their respective lipid motif (bis(stearyl) or bis(oleyl)). Stearic acid and oleic acid were selected as membrane anchors, due to their abundance in natural membranes and their highly different physico-chemical behaviors regarding membrane fluidity. While stearic acid is a saturated fatty acid with high affinity for highly ordered membrane domains, oleic acid is a monounsaturated cis fatty acid, rendering the resulting lipid moiety inherently more fluid and space-consuming. These different physico-chemical behaviors were then evaluated regarding the preferential incorporation of the ligands into ordered and disordered membrane phases.

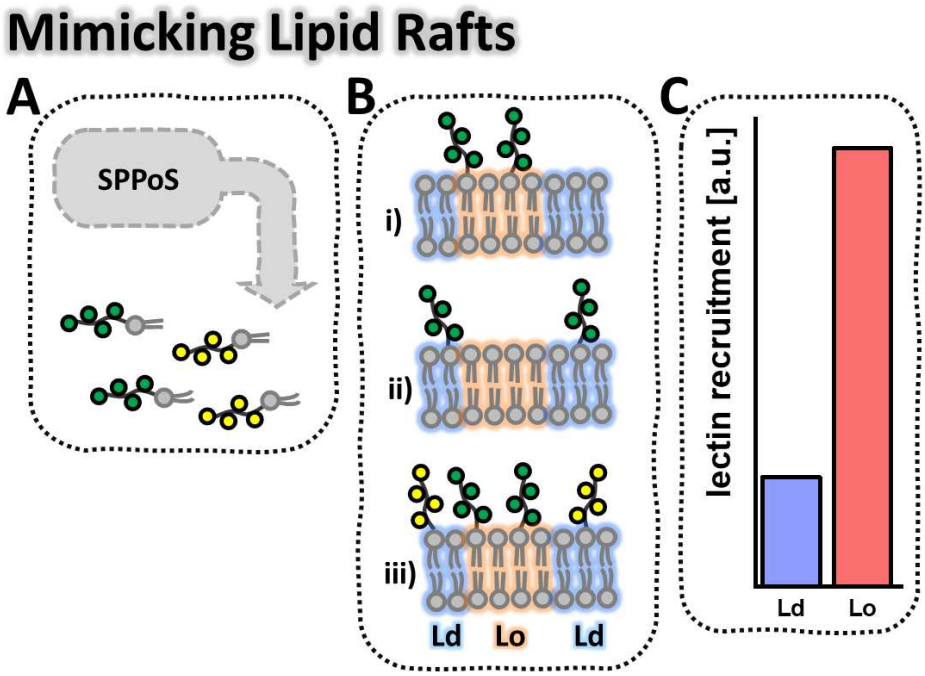

Figure 19. Summary of the results of the second part of the thesis. **A**: SPPoS yields glycan mimetics with different membrane tethers (bis(stearyl) or bis(oleyl)), varying significantly in their respective physico-chemical properties. **B**: Incorporation of the glycan mimetics into phase separating GUVs enables precise allocation of the ligands into either Lo (**i)**) or Ld (**ii)**) domains of the GUVs, governed by their respectively employed lipid tether. Similarly, heteromultivalent glycocalyx mimetics can be produced that present spatially resolved glycosylation patterns, differing between Ld and Lo (**iii)**). **C**: Lectin recruitment associated with ligands in Lo was found to be approximately 65% more efficient than with ligands associated in Ld, supporting the importance of lipid rafts in native cellular membranes.

The derived ligands were employed to construct glyco-decorated, phase separating GUVs as spatially heterogenous glycocalyx mimetics. Phase separation in model membranes is a sufficiently studied field that reflects the abundance of lipid rafts in native cellular plasma membranes. In GUVs this phenomenon can be modeled by employing ternary lipid mixtures that can segregate into distinct membrane domains under suitable conditions, where unsaturated lipids form a fluid, liquid disordered phase (Ld) and saturated lipids and cholesterol form a tightly packed and highly ordered Lo phase.

Since the Ld phase of the derived GUVs was stained with a suitable fluorescent membrane marker, it was possible to show, employing fluorescently labeled derivatives of Con A and RCA, that the derived ligands allocate into either the Ld or the Lo phase, dictated by their respective membrane tether (oleyl-moieties dictated preferential ligand accumulation in Ld phases, while stearyl-moieties mediated the incorporation of ligands into the Lo domains of the GUVs). For the first time, phase allocation of glycan mimetics in spatially distinct model membranes was shown.

In the next step, mixtures of Man and Gal ligands with different membrane anchors were employed, to generate heteromultivalent glycocalyx mimetics that present distinct glycosylation patterns on the vesicle membrane, governed by the phase allocation of the employed ligands into either Ld or Lo.

Finally, the impact of phase allocation of the glycan mimetics in either Ld or Lo on protein recruitment was analyzed quantitatively. Therefore, Man-ligands bearing either the stearyl- or the oleyl-lipid tail were incorporated in equal concentrations into either the Ld or the Lo phase of GUVs and subsequently incubated with fluorescently labelled Con A. Via analysis of the radial fluorescence intensity profiles of the membrane bound lectin in either Ld or Lo, it was shown, that protein recruitment in Ld resulted in the formation of small local clusters of ligands and receptors, while ligands in Lo demonstrated a homogenous adhesion of the protein on the membrane. In this manner, lectin binding was increased by 65%, which mirrors the putative function of lipid rafts, to serve as local amplifiers, e.g. facilitating signaling pathways through the ordered and concentrated presentation of ligands in ordered membrane domains.

The results demonstrated that the established synthetic toolbox to derive highly tunable glycan mimetics was complemented by the introduction of distinct lipid moieties, which allows for the first time to control the physico-chemical behavior of the derived ligands in heterogenous phospholipid membranes and, hence, to construct glycocalyx mimetics that resemble more closely the spatially heteromultivalent nature of native glycocalyces. The experimental evidence supports the hypothesis that lipid rafts serve as active platforms for organizing and enhancing molecular interactions on cellular membranes - such as cell signaling and pathogen entry -, by actively enhancing glycan-mediated interactions.

In the third part of the thesis, the previously established synthesis of long and short glycan mimetics was further developed to now also access globally sulfated glycan mimetics. Previous work by *Soria-Martinez et al.* has shown that soluble and globally sulfated glycooligomers and glycopolymers, mimicking naturally abundant glycosaminoglycans with high degrees of sulfation, can act as inhibitors for several viral infections. While these results give rise to hope that such glycomimetic inhibitors could potentially be progressed as potent therapeutics for viral infections, they also indicate that such precision glycan mimetics are suitable for systematically studying viral interactions (or more general pathogen interactions) with cellular glycocalyces.

In this manner, a first library of sGAG mimetics was prepared and characterized in close collaboration with M. Hoffmann and L. Bonda, thereby varying key functional parameters, such as the valency of the glycan-head group, the functionalization with a fluorophore and the type of membrane anchor to systematically study the effect of the sGAG mimetics' constitution on pathogen interactions.

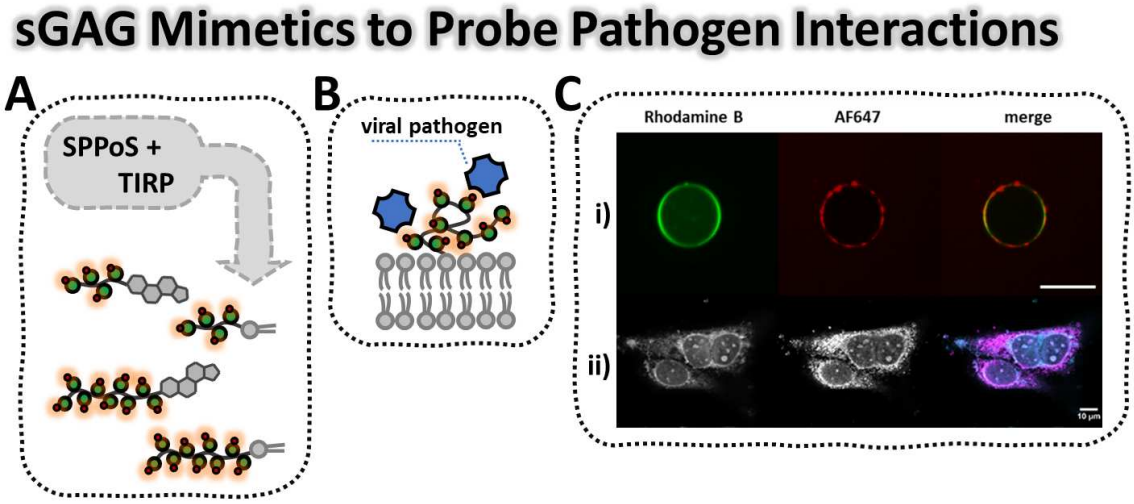

Figure 20. Summary of the results of the third part of the thesis. **A**: A combination of SPPoS and TIRP yields globally sulfated, short and long glycan mimetics (sGAG mimetics) featuring site-selective functionalities, such as an oligovalent or polyvalent glycan head group, a fluorophore for fluorescence microscopy, as well as a lipid-tether for subsequent intercalation into phospholipid membranes. **B**: Schematic presentation of the interaction between viral pathogens and a membrane-associated sGAG mimetic. **C**: First studies on the interaction of viral pathogens with membrane-associated sGAG mimetics. VLPs derived from MCPyV interact with sGAG mimetics displayed on GUVs (**i)**) or on the plasma membrane of GM95 cells (**ii)**). Scale bars: 10 microns.

Polymeric sGAG mimetics were prepared as described before – via TIRP of solid-phase derived macroinitiators and subsequent sulfation following previously established protocols. To access the respective glycooligomers, a protocol established by M. Hoffmann was used, which employs a photocleavable linker on the solid support. While the sulfate groups have been previously shown to not withstand the harsh acidic cleavage conditions of conventionally employed support resins, the photolinker enables cleavage of on-resin sulfated glycooligomers under mild conditions via photolysis.

To demonstrate the applicability of the thusly derived sGAG mimetics, first studies on GUVs as glycocalyx mimetics and cellular membranes by means of *de novo* glycocalyx engineering were conducted in collaboration with the team of Prof. H. Ewers. Therefore, virus-like particles derived from HPV16, MCPyV and SV40 were employed as viral receptor mimetics, to study interactions with a membrane-associated, polymeric sGAG mimetic in GUVs and in native cellular membranes of GM95 cells. As HPV16 and MCPyV are known to exploit naturally abundant sGAGs on cells to initiate infection of a host cell, it could be shown that the synthetic sGAGs indeed show interaction with the VLPs and, consequently, offer the potential to study these interactions in a highly controlled setting. These first results indicate that the presented toolbox to derive precision sGAG mimetics, can potentially enable a systematic study on the effect of structural sGAG-mimetic parameters, such as valency, degree and patterning of sulfation, as well as sGAG density in membranes, on the mechanisms involved in viral (or pathogen) infection.

Finally, the last part of this thesis focused on the dynamic formation and fixation of receptor-mediated glycan clustering in glycocalyx mimetics. Clustering of glycans upon interaction with receptors, such as lectins, is an important mechanism that is involved in many biological mechanisms unfolding on the cell membrane, such as adhesion, signaling and pathogen infection. The local assembly of nanoscale clusters upon an external stimulus is highly dynamic and promotes multivalent ligand-receptor interactions to mediate a subsequent event. The physically driven formation of multidomain lipid vesicles, as described in chapter 3.2, cannot accurately reflect this local dynamic clustering, so a different approach was chosen to investigate this phenomenon. For this purpose, an SPPoS-compatible functional diacetylene building block was rationally designed and synthesized. Diacetylenes are a special class of monomers that can be polymerized under topochemical conditions by irradiation, producing a fluorescent polydiacetylene backbone. This appears to be suitable to follow the above-described cluster formation dynamically *in vitro*, since the corresponding diacetylene-functionalized ligands can only be polymerized upon clustering (i.e. an appropriate spatial proximity and orientation to each other is given) and thereby directly generate a fluorescence read-out to visualize the clusters via fluorescence microscopy.

The diacetylene moiety (in accordance with the previously established building blocks by *Hartman et al.* termed DADS, DiAcetylene Diamine Succinic acid) was introduced into the glycomacromolecular backbone using two building block fragments, DADS(I) (functionalized with a carboxylic acid and a terminal bromoalkyne) and DADS(II) (functionalized with an *N*-Fmoc-protected primary amine and an alkyne), which were assembled on the solid phase employing a Cadiot-Chodkiewicz coupling to give the intact diacetylene building block in quantitative yield. It was shown that the DADS building block is orthogonal to the other reaction conditions involved in the preparation of SPPoS-derived glycan mimetics (i.e. Fmoc-cleavage with piperidine, Zemplén deacetylation, acidic cleavage with 95% TFA) and, hence, suitable for the preparation of diacetylene-functionalized glycan mimetics.

Subsequently, two glycan mimetics were synthesized and characterized, site selectively bearing the diacetylene moiety, an N-terminal cholesteryl-tether, as well as a tetravalent glycan-head group (either Man or Gal). The resulting amphiphilic Man-ligand was then investigated for its ability to polymerize upon irradiation in aqueous solution via UV-VIS spectrophotometry and transmission electron microscopy (TEM). Upon irradiation, the initial absorption band, corresponding to the diacetylene moiety, decreased over time concomitant with an increasing bathochromically shifted new absorption band, putatively corresponding to the expanding polydiacetylene network. Similarly, micellar assemblies of the diacetylene-containing glycan mimetics were analyzed via TEM. Irradiated and non-irradiated micelle samples were measured before and after dilution with EtOH to disrupt the micellar assemblies. Before dilution with EtOH, both the irradiated and the non-irradiated samples showed

homogenous, spherical assemblies, whereas after dilution, the non-irradiated samples underwent a change in morphology from spherical to worm-like micelles, while the irradiated sample remained spherical, indicating that the irradiation successfully crosslinked the spherical micelles.

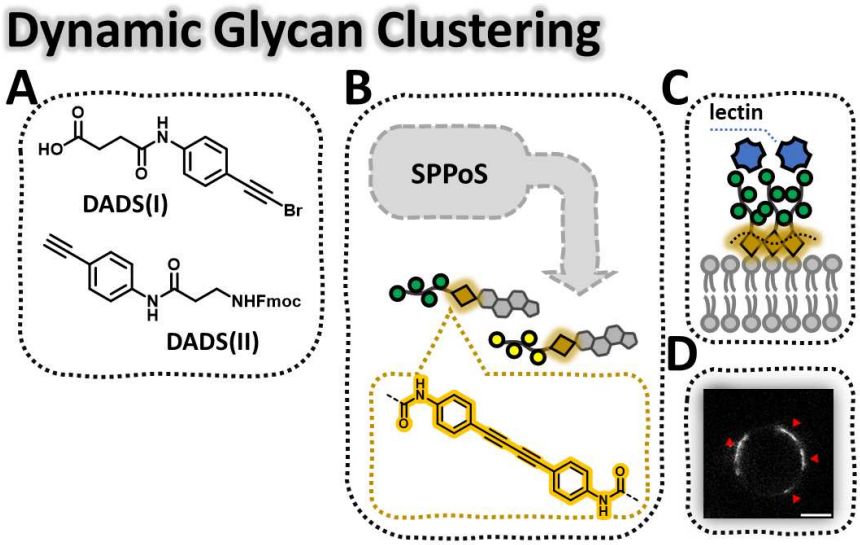

Figure 21. Summary of the results of the fourth part of the thesis. **A**: A novel SPPoS-compatible building block (DADS) was developed, enabling the site-selective incorporation of a diacetylene moiety into the macromolecular backbone via on-resin Cadiot-Chodkiewicz coupling. **B**: SPPoS yields sequence-defined glycan mimetics, featuring a polymerizable diacetylene moiety, as well as a cholesteryl tether for subsequent membrane-anchoring. **C**: Schematic presentation of the lectin-mediated glycan-cluster imprinting: Membrane-associated diacetylene ligands cluster upon interaction with multivalent lectins. Irradiation leads to topochemical polymerization of the glycan-clusters, concomitant with a fluorescent read out (**D**, red arrows). Scale bar: 10 microns.

Subsequently, initial experiments were performed in GUVs to demonstrate the applicability of dynamic cluster formation and following fixation via photochemical polymerization. Therefore, the diacetylene-functionalized Man-ligand was incorporated into GUVs and incubated with Con A to induce ligand-lectin clusters on the membrane and subsequently irradiated, giving a weak fluorescent read-out upon excitation, colocalizing with the preformed clusters.

Based on these preliminary results, this additional class of crosslinkable or polymerizable glycan mimetics could potentially offer the possibility to study dynamic cluster formation in glycocalyx mimetics. This, in turn, could enable a controlled analysis of transient or 'locked in' glycan assemblies in glycocalyx mimetics to systematically study how such clustering events affect membrane organization and provide insights into, for example, how pathogens exploit glycan assemblies for infection.

Overall, this work has contributed substantially to the existing portfolio of synthetic glycocalyx mimetics. The presented glycan mimetics and resulting glycocalyx models in this thesis now enable for

the first time (i) controlled synthesis of long and short multivalent glycan mimetics, which can be used to construct heteromultivalent and crowded glycocalyces, (ii) control over spatial localization of glycan mimetics in heterogeneous membrane systems (strongly governed by the choice of membrane anchor), (iii) presentation of highly controlled sGAG mimetics in model glycocalyces to probe pathogen interactions, as well as (iv) fixation and visualization of dynamic ligand-receptor-induced clusters in model membranes (**Figure 22**).

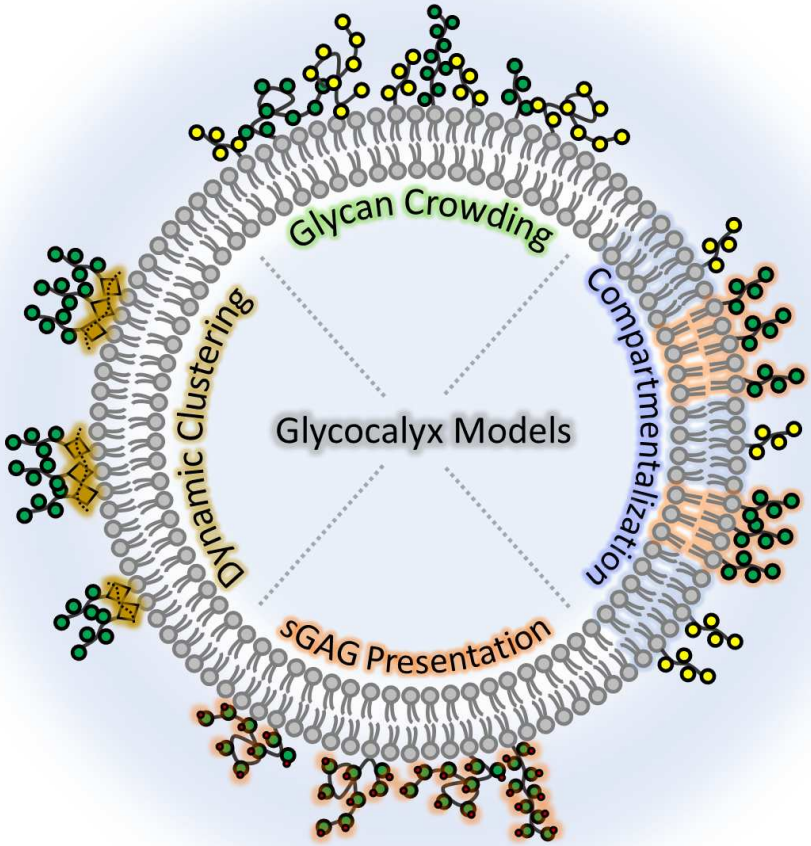

Figure 22. Overview of the glycocalyx mimetics presented in this thesis. A delicate combination of the introduced models bears the potential to create encompassing glycocalyx mimetics that mirror key features of native glycocalyces: crowded surfaces, dynamic clustering of constituents, spatially resolved inhomogeneities and the presentation of sGAG mimetics to probe pathogen interactions.

The presented features of the glycan mimetics and the resulting models bear the potential to mimic key parameters of native glycocalyces, i.e. constitutional heterogeneity, locally resolved constituent inhomogeneities and a highly crowded nature, to an extent that has not been possible before. The model systems can be precisely adjusted through targeted modifications of the highly

tailorable glycan mimetics and delicate constituent compositions, which enables a systematic investigation of glycocalyx-associated processes. Combinations of glycan mimetics and models could, for instance, be employed to systematically study pathogen interactions with locally accumulated, suitable ligands in highly crowded, sGAG mimetic presenting systems, to model the infection process of certain viruses from initial contact with the glycocalyx to infection of the host cell.

Although the models still lack the inherently complex heterogeneity and constitutional dynamics of native eukaryotic glycocalyces, this shortcoming could be compensated, for instance, by reconstituting native membrane proteins into the model membrane systems or employing more complex lipid compositions.

In summary, this work presents simple, tunable and predictable glycocalyx-mimetic models that can potentially be employed to systematically investigate fundamental questions in glycobiology and membrane biophysics in the future.

5. Experimental Section

5.1 Materials

D-(+)-galactose, D-(+)-mannose, N,N-dimethylformamide, oxalyl chloride, piperidine and tosyl chloride were purchased from Acros Organics. Ethyl trifluoroacetate and PyBOP were purchased from Apollo Scientific. Acetonitrile and cholesterol were purchased from AppliChem. Fmoc-Cl and tris(2-phenylpyridine)-iridium(III) were purchased from bld pharm. Succinic anhydride was purchased from Carbolution Chemicals. DIPEA and sodium chloride were purchased from Carl Roth. 1.4-Dioxane, acetic anhydride, calcium chloride, ethyl acetate, HEPES, n-hexane, hydrochloric acid (37%), manganese dichloride, potassium carbonate, sodium azide, sodium bicarbonate, sodium hydroxide (1M), sodium methoxide and trimethylamine were purchased from Fisher Scientific. Fluorescein and triethylsilane were purchased from fluorochem. Fmoc-Cys(Trt)-OH, Fmoc-Lys(Boc)-OH and Fmoc-Lys(Dde)-OH were purchased from Iris Biotech. Concanavalin A was purchased from MP Biomedicals. 2,2'-(Ethylenedioxy)bis(ethylamine), 2-bromoethanol, 4-pentynoic acid, boron trifluoride diethyl etherate, Bovine Serum Albumin, dichloromethane, diethyl ether, diethylenetriamine, formic acid, methyl α-D-mannopyranoside, methanol, tetrahydrofuran, trifluoroacetic acid and triisopropylsilane were purchased from Sigma-Aldrich. Diphenyl-(2,4,6-trimethylbenzoyl)-phosphineoxide(>98%), N-hydroxyethylacrylamide, Rhodamine B, TCEP, trimethylsilyl azide and trityl chloride were purchased from TCI chemicals. NeutrAvidin and sodium diethyldithiocarbamate were purchased from Thermo Scientific.

All solvents and reagents used were purchased in the highest purity available and used without further purification.

TentaGel® S RAM resin (loading: 0.26 mmol/g) was purchased from RAPP Polymere GmbH.

DOPC, 18:1 PEG2000-PE, 16:0 Biotinyl Cap PE and 16:0 Liss Rhod PE were purchased from Avanti Polar Lipids.

Dialysis was performed via diafiltration in VIVASPIN 20 centrifugal concentrators (MWCO: 10 kDa; PES) from sartorius.

Experiments were conducted in 18-well glass bottom µ-slides from ibidi GmbH.

5.2 Instrumentation

Reversed Phase- High Pressure Liquid Chromatography- Mass Spectrometry (RP- HPLC-MS)/Electron Spray Ionization- Mass Spectrometry (ESI-MS)

RP-HPLC-MS was carried out on an Agilent 1260 Infinity instrument coupled to a variable wavelength detector (VWD) (set to 214 nm) and a 6120 Quadrupole LC/MS containing an Electrospray Ionization (ESI) source (operation mode positive, m/z range from 200 to 2000). An MZ-AquaPerfect C18 (3.0 × 50 mm, 3 µm) RP column from MZ-Analysentechnik was used. As eluent system water/acetonitrile containing 0.1 vol% formic acid was applied. The mobile phases A and B were: System A) water/acetonitrile (95/5, v/v); System B) water/acetonitrile (5/95, v/v). The samples were analyzed at a flow rate of 0.4 ml/min using a linear gradient, starting with 100% of system A) and reaching 100% system B) within 17 min. The temperature of the column room was set to 25 °C. All purities were determined using the OpenLab ChemStation software for LC/MS from Agilent Technologies.

Ultra High Resolution - Mass Spectrometry (UHR-MS)

UHR-MS measurements were performed with a Bruker UHR-QTOF maXis 4G instrument with a direct inlet via syringe pump, an ESI source and a quadrupole followed by a Time of Flight (QTOF) mass analyzer.

Nuclear Magnetic Resonance Spectroscopy (NMR)

The ^{1}H-NMR spectra were recorded on a Bruker Avanace III 600 (300 or 600 MHz). These spectra were evaluated according to the following scheme: (frequency in MHz, deuterated solvent), chemical shift in ppm (multiplicity, coupling constant, integral, signal assignment). The chemical shift is given in relation to the ^{1}H signals of the deuterated solvents used.

Size Exclusion Chromatography-Multi-Angle Light Scattering (H_2O-SEC-MALS)

SEC analysis was conducted with an Agilent 1200 series HPLC system and three aqueous SEC columns provided by Polymer Standards Service (PSS). The columns were two Suprema Lux analytical columns(8 mm diameter and 5µm particle size) and one precolumn (50 mm, 2×160 Å of 300 mm and 1000 Å of 300mm). The eluent was a buffer system consisting of MilliQ water and 30% acetonitrile with 50 mM NaH2PO4, 150 mM NaCl and 250 ppm NaN3 with a pH = 7.0 (via addition of 50 mL of 3 molar aqueous sodium hydroxide solution) filtered with an inline 0.1µm membrane filter and running at 0.8 mL per min. Multi-angle light scattering is recorded via mini DAWNTREOS and differential refractive index spectra with Optilab rEX both supplied by Wyatt Technologies EU. Data analysis was committed with Astra 5 software and a dn/dc value of 0.156 for each polymer.

Lyophilization

The final glycomacromolecules were lyophilized with an Alpha 1-4 LD plus instrument from Martin Christ Freeze Dryers GmbH (-40 °C, 0.1 mbar).

Fluorescence Microscopy

Giant Unilamellar Vesicles were imaged on an inverted microscope (Olympus IX83, Japan) equipped with an Olympus 60x NA 1.35 oil-immersion objective (Olympus, Japan), and a CMOS camera (DMK 33UXI174L, The Imaging Source, Germany) was used for imaging. The system was operated with the Olympus software.

Elemental Analysis

The ratio of carbon, hydrogen, oxygen, nitrogfen and sulfur was determined on a Vario Micro Cube (Analysensysteme GmbH).

UV-Irradiation

UV-irradiation of the samples was carried out using a UV LED spot with a wavelength of 365 nm and a maximum irradiance of 950 mW/cm^2, operated with an LEDControl, both from Opsytec Dr. Gröbel.

5.3 General Methods

Solid Phase Polymer Synthesis

All structures were prepared on Tentagel® S RAM resin (batch size: 0.1 mmol). All washing steps were conducted with 4 mL solvent. Polypropylene reactors equipped with polyethylene frits and closed with Luer-stoppers were used. For the short glycomacromolecules, the backbone sequence was first assembled, followed by glycoconjugation via CuAAC (copper(I)-catalyzed alkyne-azide cycloaddition), Lys-side chain deprotection (Boc), fluorescent dye conjugation, terminal Fmoc-deprotection and capping with 4-pentynoic acid before conjugation of the cholesteryl tether via CuAAC.

General coupling protocol.

For all compounds, the resin was first swollen in 4 mL DCM for 30 min, subsequently washed ten times with DMF, Fmoc-deprotected by treating with 25% piperidine in DMF (three times for ten minutes) and again washed fifteen times with DMF. Employed building blocks were coupled to the *N*-terminus by adding the respective building block (5eq.), PyBOP (5 eq.) and DIPEA (20 eq.) in 4 mL DMF to the resin and shaking for 1h. Then, the resin was washed fifteen times with DMF and the *N*-terminus was again deprotected followed by the next coupling step.

Fmoc cleavage

The Fmoc-protecting group of the resin as well as from the coupled building blocks or amino acids was cleaved by means of 4 mL of a 25% solution of piperidine in DMF to release the primary amine. The deprotection was carried out twice for 10 min. Afterwards the resin was washed 10 times with DMF before coupling.

Boc cleavage

The resin was washed five times with THF before a solution of 4 M HCl in dioxane was drawn into the syringe reactor. The resin was rocked for 5 min before the solution was discarded. Fresh solution was drawn into the reactor and the resin was rocked for 30 min before the solution was again discarded. The resin was then washed ten times with DMF.

Dde cleavage

The Dde side chain protective group was cleaved via treatment with a freshly prepared solution of 2% hydrazine hydrate in DMF (v/v). After rocking for 5 min, the solution was discarded and the resin was washed three times with DMF. The cleavage procedure was repeated twice.

CuAAC protocol for glycosylation

To the oligomeric structure loaded on the resin 2.5 eq of acetyl protected 2-azidoethyl pyranoside (α-Mannose/ β-Galactose) per alkyne group dissolved in 4 mL DMF were added. Secondly 50 mol% sodium ascorbate per alkyne group and 50 mol% $CuSO_4$ per alkyne group were dissolved each in a small amount of water and also added to the resin. The syringe reactor was rocked for 18 h before the solution was discarded. The resin was washed three times with DMF and subsequently treated with a 23 mM solution of sodium diethyldithiocarbamate in DMF and water (50/50, v/v) and alternating with DMF and DCM until no further color change occured.

CuAAC protocol for conjugation of cholesteryl-anchor

To the oligomeric structure loaded on the resin 2.5 eq of 3-β-azidocholesterol in 4 mL THF were added. Then 50 mol% sodium ascorbate per alkyne group and 50 mol% CuSO4 per alkyne group were dissolved each in a small amount of water and also added to the resin. The syringe reactor was rocked for 18 h before the solution was discarded. The resin was washed three times with DMF and subsequently treated with a 23 mM solution of sodium diethyldithiocarbamate in DMF and water (50/50, v/v) and alternating with DMF and DCM until no further color change occured.

On-resin deacetylation

Glycooligomers MC and GC were deacetylated under Zemplén conditions. The resin was washed five times with methanol, before 5 mL of a 0.2 M solution of NaOMe in MeOH was drawn into the reactor. The resin was rocked for 30 min, before the solution was discarded. The resin was then washed twice with MeOH before another 5 mL of the methoxide solution were drawn into the reactor. After 30 min, the solution was again discarded and the resin was washed five times with MeOH.

Macroinitiator Cleavage from the Solid Phase

The resin was washed five times with DCM before acidic cleavage from the resin with a cocktail consisting of TFA, TIPS and DCM (95/2.5/2.5, v/v/v) for 30 min. The macroinitiators were precipitated in a mixture of 25% ether in hexanes and collected via centrigugation at -5°C. The supernatant was decanted, and the precipitate was dried under high vacuum. Stock solutions of the dried macroinitiators in DMSO were then prepared (c = 0.033 M).

Synthesis of Glycopolymers via TIRP

One equivalent of glyco monomer (100 mol%) and tris(2-phenylpyridine)iridium-(III) ($Ir(ppy)_3$, 0.05 mol%) are dissolved in DMF [10 wt %], sealed in a 5mL glass flask and flushed with argon as inert gas for 10 min. In a second step, the macroinitiator (2.5 mol%) and equimolar amounts of diphenyl-(2,4,6-

trimethylbenzoyl)-phosphineoxide (TPO, 2.5 mol%) are also dissolved in DMF [10 wt %] and sealed in a 5 mL microwave reaction vial. A spatula tip of TCEP is dissolved in a single drop of H_2O and added to the reaction solution to reduce possible disulfides. The thiol/TPO solution is flushed under an Ar-atmosphere for 10 min and irradiated with UV-light (405nm wavelength, 2% intensity) for 3 min. Subsequently, the monomer/$Ir(ppy)_3$ mixture is added to the TPO/ thiol solution under an inert atmosphere, and the polymerization solution is irradiated further at an unchanged light intensity. After an hour, the irradiation is stopped and the polymer solution precipitated in diethyl ether. The precipitated glycopolymer was dryed under a gentle stream of nitrogen, dissolved in ultrapure water, dialyzed via diafiltration against ultrapure water in five cycles (20 mL each, 1 M HCl was used in the first cycle). The dialyzed compounds were dissolved in fresh ultrapure water and lyophilized.

Sulfation of sGAG mimetics

On-resin sulfation of the short sGAG mimetics was carried out in 50 ml solid-phase synthesis glass reactors, equipped with a PTFE stopcock with a T-bore and a glass frit of medium porosity.

The resin was washed ten times with dry DMF and then a solution of TMA*SO3 (50 eq. per hydroxyl group) in DMF (8.65 ml/g) was added. The mixture was kept at 70°C for 16h. Afterwards, the resin was treated with a 10% sodium acetate solution in water (10 eq. based on TMA*SO3) and washed fifteen times with water, fifteen times with warm DMF (70 °C), thirty times with DMF (RT) and fifteen times with DCM.

To sulfate the long sGAG mimetics, the respective glycopolymers were dissolved in a solution of TMA*SO3 (50 eq. per hydroxyl group) in DMF (8.65 ml/g) and stirred at 70°C for 16h. Subsequently, the reaction was quenched by the addition of a 10% sodium acetate solution in water (10 eq. based on TMA*SO3). The solvent was evaporated to dryness and the crude product mixtre was redissolved in ultrapure water and purified via diafiltration.

Short sGAG-Cleavage from the Solid Phase (Fmoc-Photo-Linker)

After sulfation, the resin was swollen in DCM for 30 min and then washed with ACN and transferred to a glass vessel. The resin was suspended in a mixture of ACN and water (1/1) and placed under an LED spot (365 nm). The resin was then shaken for a total of 24 h at a power of 15 % of the maximum lamp power and at a distance of 3 cm from the lamp, resulting in an approximate irradiance of 285 mW/cm^2. The irradiation process was interrupted regularly, already separated product from the resin by washing with ACN and water and re-swelling the resin in DCM. The collected fractions were subsequently dried under reduced pressure.

Determination of the Degree of Sulfation (DS)

The DS was determined by calculating ratios for the experimental and theoretical values. Briefly, the S/C ratio was calculated for the experimentally measured values and for the theoretical values for a molecule with a degree of sulfation of 100 %. The values obtained were then expressed as ratios of experimental to theoretical S/C. The same was done for the S/N ratios. Both values obtained were averaged to obtain the degree of sulfation This method was used because the samples were very hygroscopic, which led to decreased values for C/N/S and increased values for H/O.

5.4 Analytical Data

5.4.1 Sequence-Defined Short sGAG Mimetics

Glycooligomer Backbone

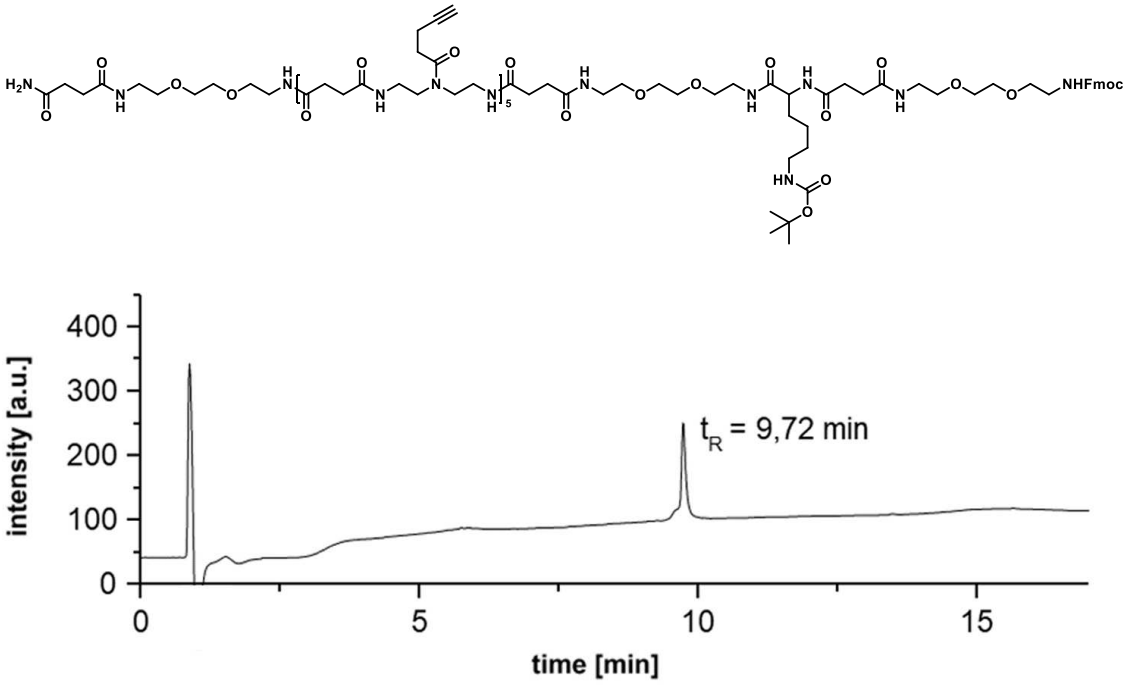

Figure 23. Oligomer backbone detected with relative purities >97% by RP-HPLC analysis (linear gradient from 5 – 95 vol% eluent H2O/acetonitrile) in 17 min at 25 °C.

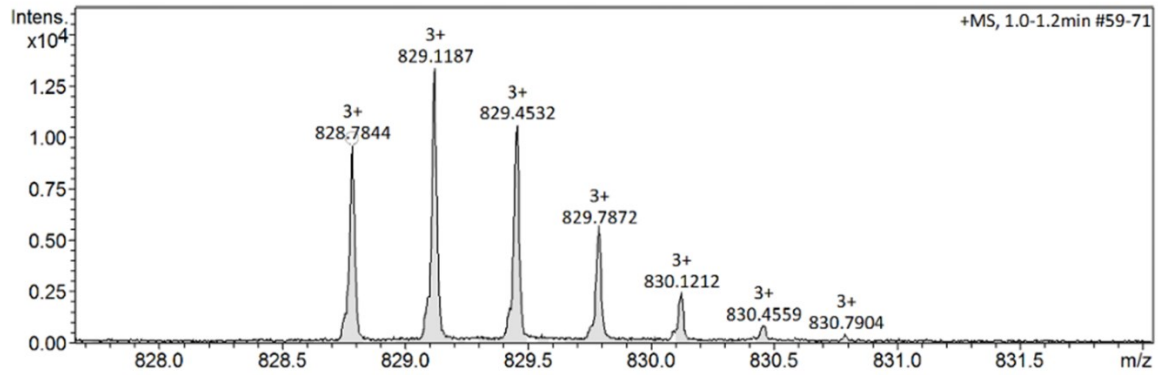

Figure 24. HR-ESI-MS of the glycooligomer backbone. Mass calcd. for $C_{121}H_{185}N_{24}O_{32}[M+3H]^{3+}$: 828.8; found: 828.8.

Glycooligomer $_{short}A^{OH}$

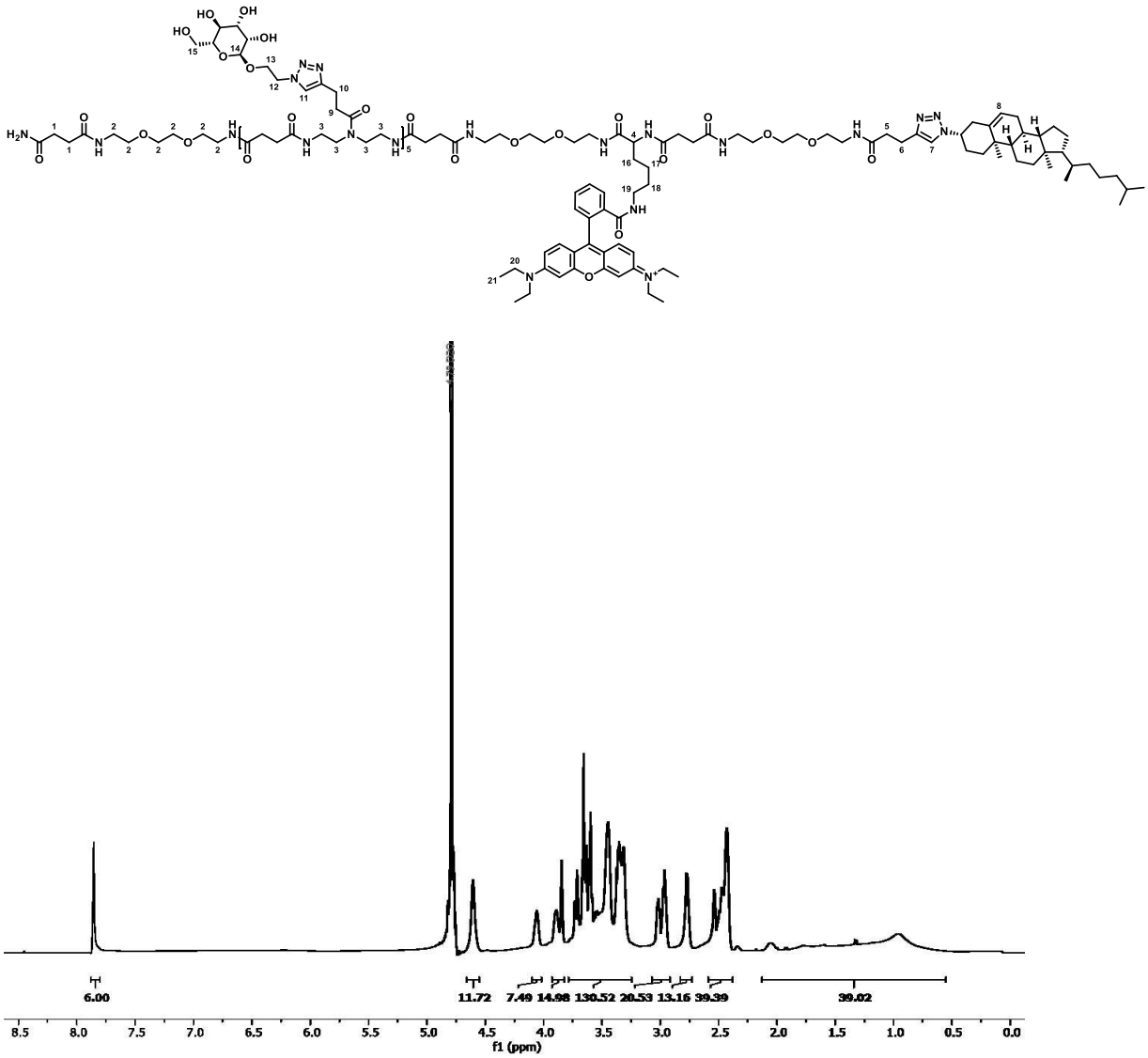

Figure 25. ^{1}H-NMR (600 MHz, D_2O, ambient temperature) of $_{short}A^{OH}$.

^{1}H-NMR (600 MHz, D_2O) δ [ppm] = 7.87-7.80 (m, 6H, H7, H11), 4.65-4.55 (m, 10H, H12), 4.16-3.22 (m, xH, $CH_{Pyranose}$, H2, H3, H4, H13, H20), 3.07-2.91 (m, 20H, $CH_{Pyranose}$, H6, H10), 2.82-2.72 (m, 12H, H5, H9), 2.58-2.37 (m, 32H, H1), 2.12-0.55 (m, 60H, H16-H18, H21, Chol).

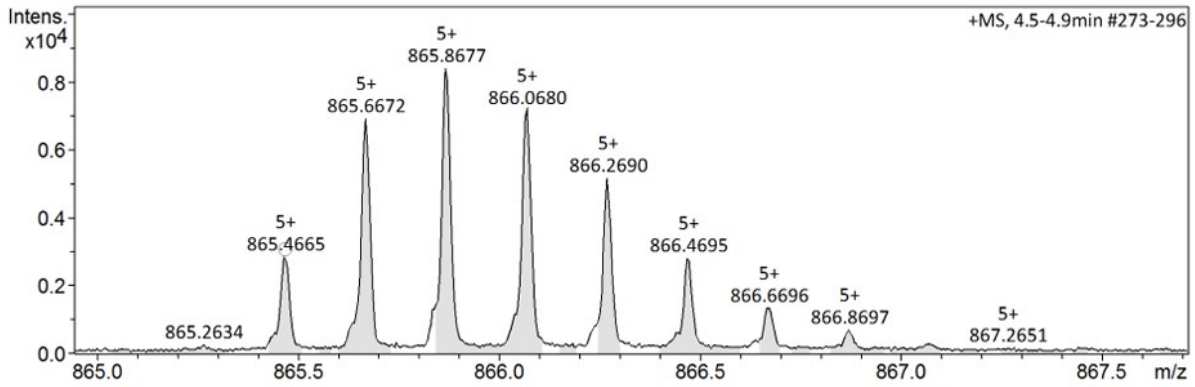

Figure 26. HR-ESI-MS of $_{short}A^{OH}$.

HR-ESI-MS for $C_{201}H_{317}N_{44}O_{61}^{+}$: $[M^{+}+4H]^{5+}$ calcd.: 865.7; found: 865.8.

Glycooligomer $_{short}A^{S}$

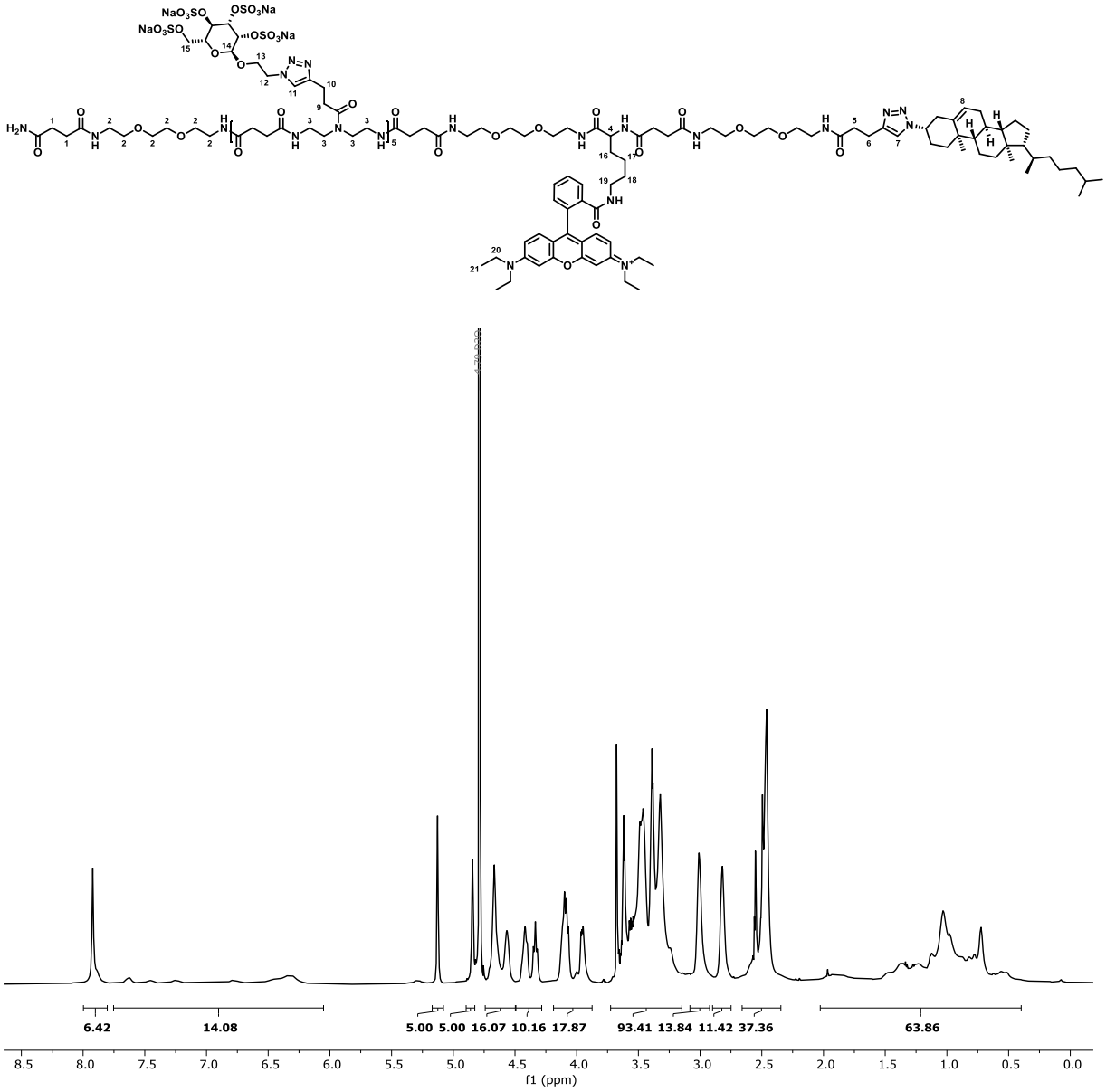

Figure 27. ^{1}H-NMR (600 MHz, D_2O, ambient temperature) of $_{short}A^{S}$.

^{1}H-NMR (600 MHz, D2O) δ [ppm] = 7.99-7.80 (m, 6H, H8, H11), 7.75-6.05 (m, 10H, Ar-H), 5.35-5.22 (m, 1H, H8), 5,13 (s, 5H, H14), 4.84 (m, 5H, $CH_{Pyranose}$), 4.74-4.49 (m, 15H, $CH_{Pyranose}$, H12), 4.49-4.28 (m, 10H, $CH_{Pyranose}$), 4.18-3.87 (m, 16H, $CH_{Pyranose}$, H4, H13), 3.72-3.14 (m, 89H, $CH_{Pyranose}$, H2, H3, H20), 3.08-2.92 (m, 14H, H6, H9, H16), 2.89-2.74 (m, 12H, H5, H9), 2.66-2.34 (m, 32H, H1), 2.02-0.39 (m, 60H, H16-H18, H21, Chol).

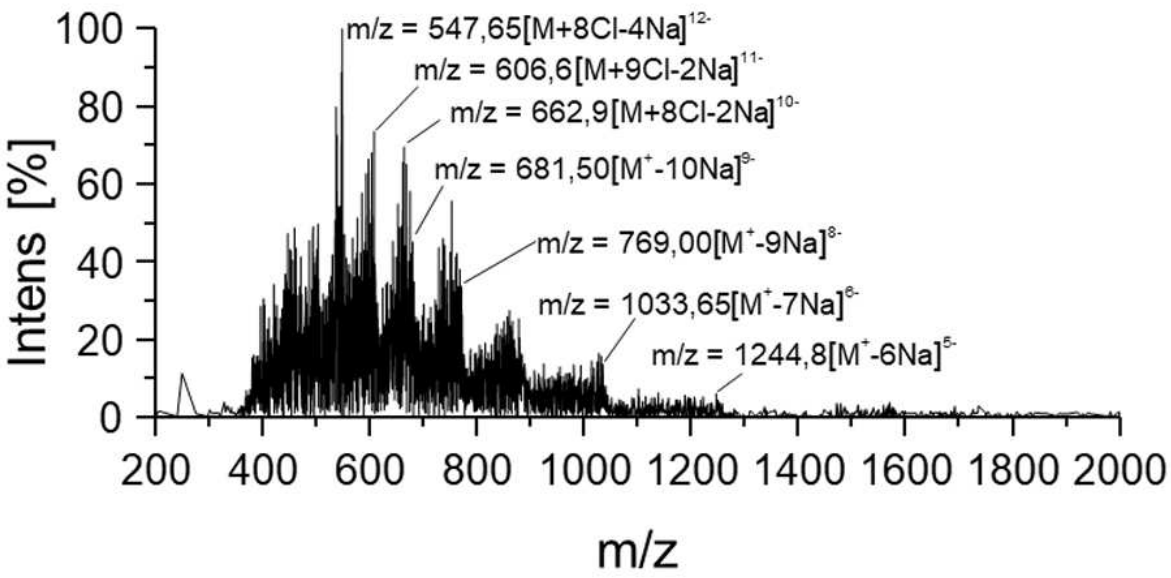

Figure 28. ESI-MS (neg. mode) of $_{short}A^{S}$.

ESI-MS for $C_{201}H_{297}N_{44}Na_{20}O_{121}S_{20}^{+}$: $[M^{+}\text{-}10Na^{+}]^{9-}$ calcd.: 681.4; found: 681.5.

DS determined via EA: 98%.

Glycooligomer $_{short}B^{OH}$

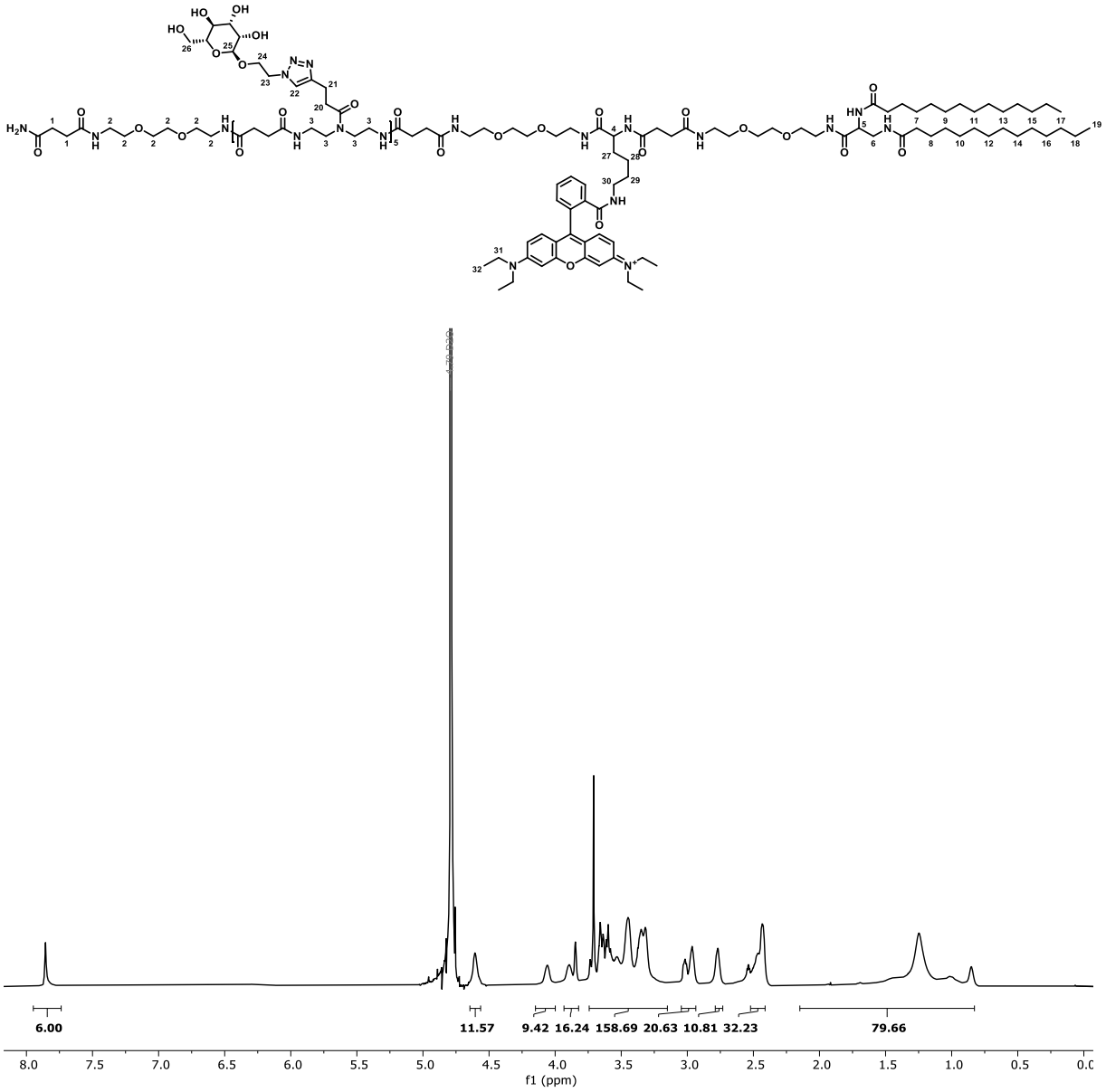

Figure 29. ^{1}H-NMR (600 MHz, D_2O, ambient temperature) of $_{short}B^{OH}$.

^{1}H-NMR (600 MHz, D2O) δ [ppm] = 7.94-7.73 (s, 6H, Ar-H, H22), 4.94-4.71 (m, 6H, $CH_{Pyranose}$, H5), 4.64-4.56 (m, 10H, H23), 4.14-3.99 (m, 10H, H24), 3.93-3.82 (m, 10H, $CH_{Pyranose}$), 3.74-3.15 (m, 104H, H2, H3, H4, H6, H30, H31, $CH_{Pyranose}$), 3.04-2.93 (m, 15H, $CH_{Pyranose}$, H20), 2.78-2.73 (m, 10H H21), 2.52-2.41 (m, 32H, H1), 2.14-0.73 (m, 72H, H7-19, H27-29, H32).

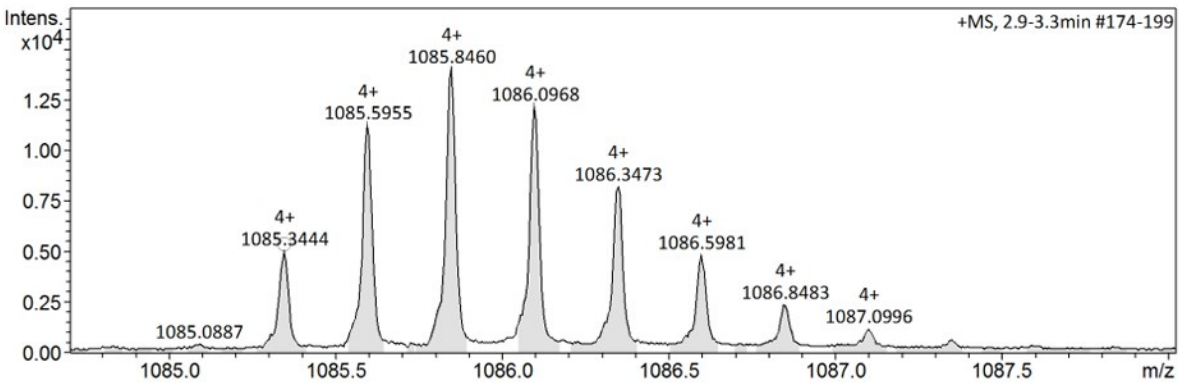

Figure 30. HR-ESI-MS of $_{short}B^{OH}$.

HR-ESI-MS for $C_{200}H_{326}N_{43}O_{63}^{+}$: $[M^{+}+3H]^{4+}$ calcd.: 1085.1; found 1085.3.

Glycooligomer $_{short}B^{S}$

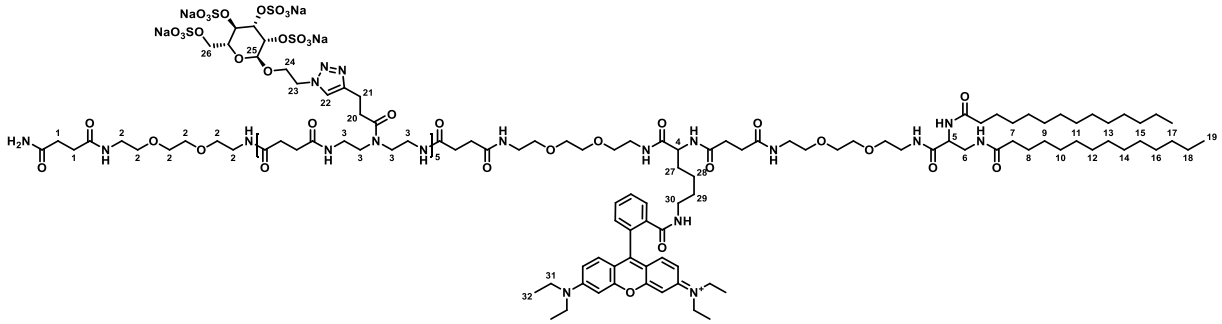

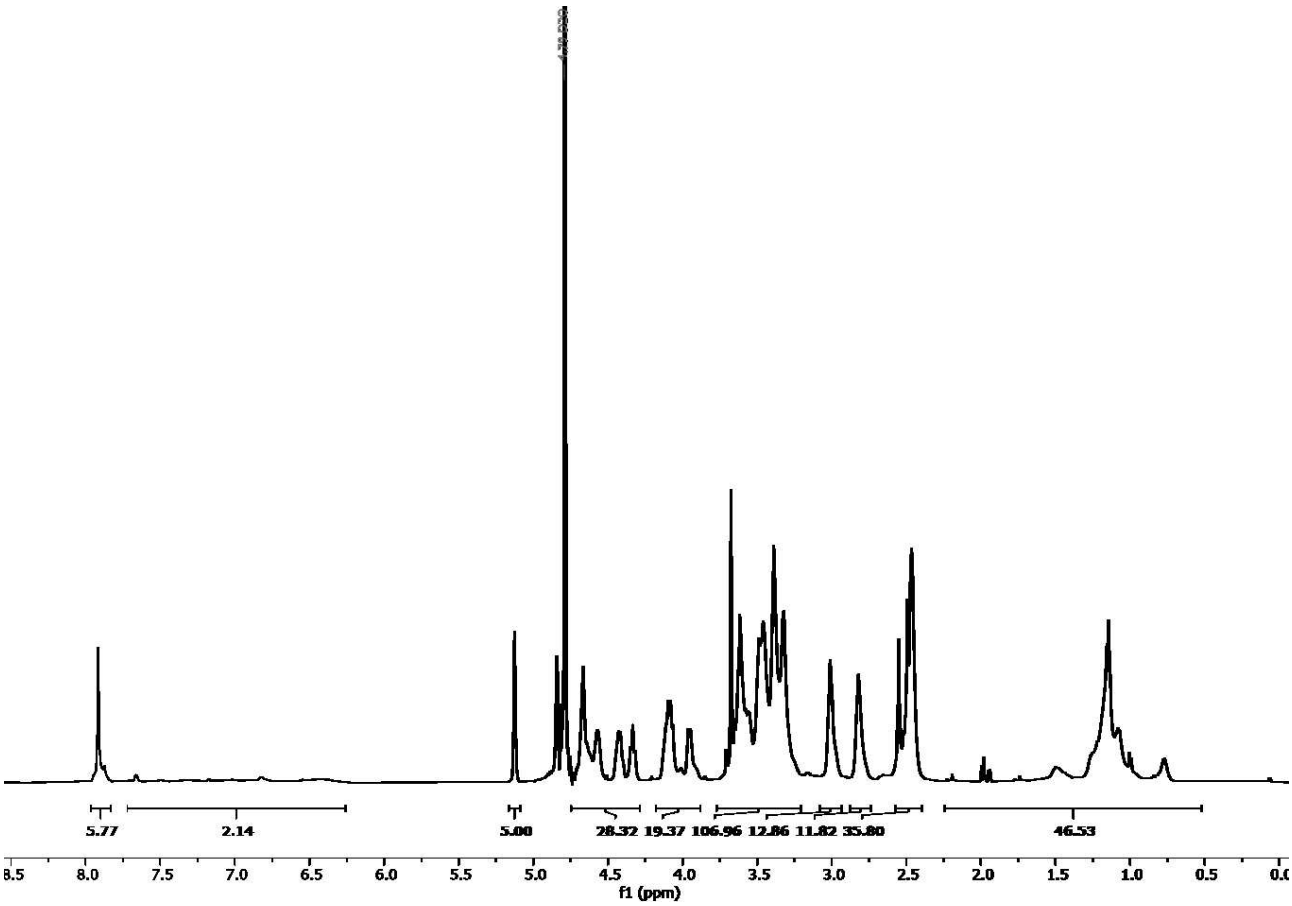

Figure 31. ^{1}H-NMR (600 MHz, D_2O, ambient temperature) of $_{short}B^{S}$.

^{1}H-NMR (600 MHz, D2O) δ [ppm] = 7.96-7.83 (m, 6H, Ar–H, H22), 7.72-6.25 (m, 9H, Ar-H), 5.13 (s, 5H, H25), 4.74-4.28 (25H, $CH_{Pyranose}$, H23), 4.17-3,88 (m, 16H, $CH_{Pyranose}$, H4, H24), 3.77-3.20 (m, 91H, $CH_{Pyranose}$, H2, H3, H6), 3.08-2.93 (m, 12H, H21), 2.87-2.73 (m, 12H, H20), 2.57-2.39 (m, 32H, H1), 2.24-0.51 (m, 72H, H7-19, H27-29, H32).

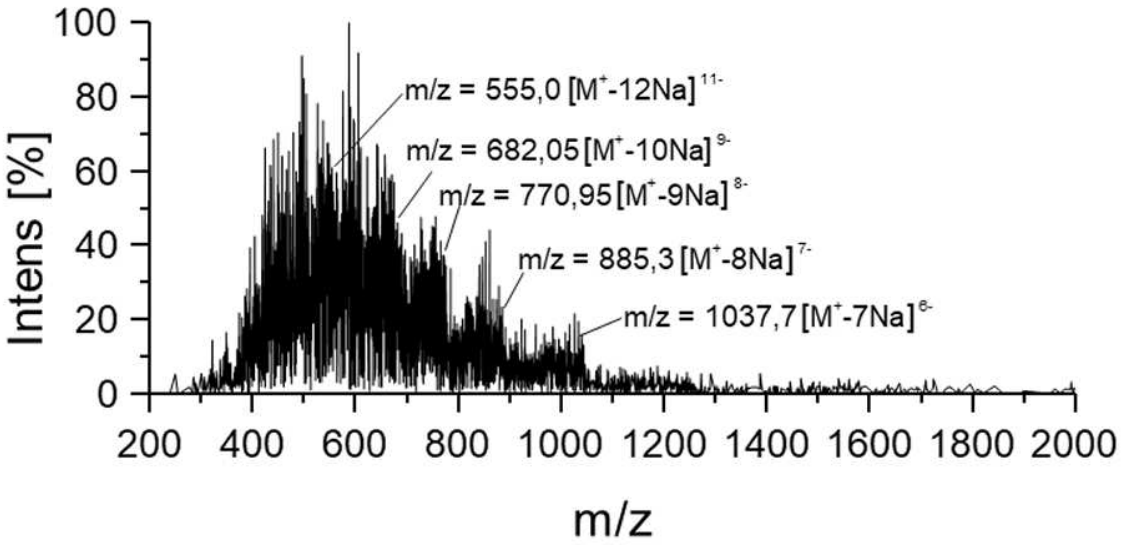

Figure 32. ESI-MS (neg. mode) of $_{short}B^{S}$.

ESI-MS for $C_{200}H_{306}N_{43}Na_{20}O_{123}S_{20}^{+}$: $[M^{+}\text{-}9Na^{+}]^{8-}$ calcd.: 771.3; found: 771.0.

DS determined via EA: 99%.

Glycooligomer $_{short}C^{S}$

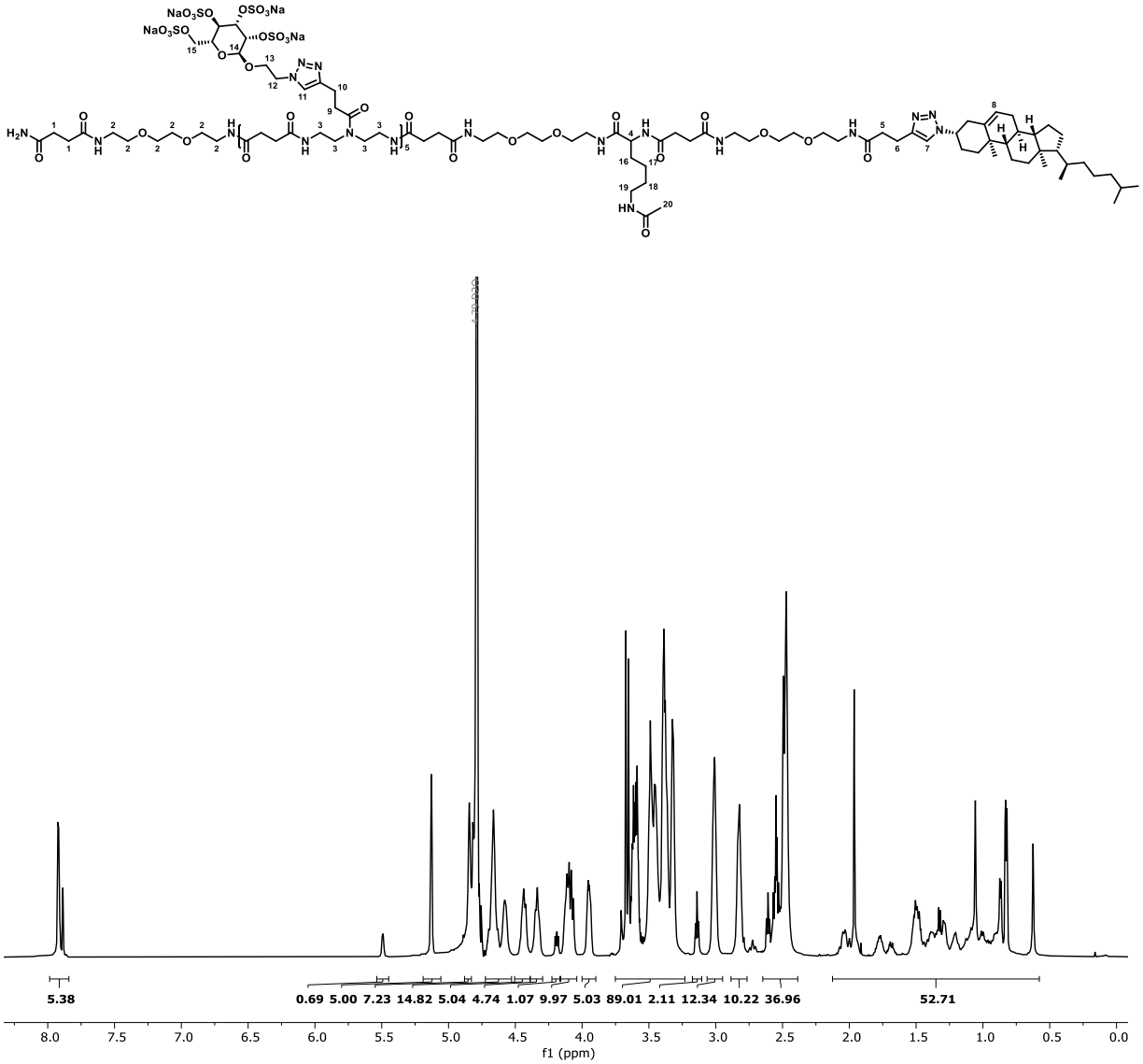

Figure 33. ^{1}H-NMR (600 MHz, D_2O, ambient temperature) of $_{short}C^{S}$.

^{1}H-NMR (600 MHz, D2O) δ [ppm] = 7.98-7.84 (m, 6H, H7, H11), 5.53-5.44 (m, 1H, H8), 5.12 (m, 5H, H14), 4.84 (s, 5H, $CH_{Pyranose}$), 4.72-4.52 (m, 15H, H12, $CH_{Pyranose}$), 4.50-4.38 (m, 5H, $CH_{Pyranose}$), 4.38-4.29 (m, 5H, $CH_{Pyranose}$), 4.22-4.16 (m, 1H, H4), 4.16-4.04 (m, 10H, H13), 4.00-3.89 (m, 5H, –NCH2CH2O– Seitenkette), 3.75-3.23 (m, 89H, H2, H3, $CH_{Pyranose}$), 3.13 (t, 2H, H19), 3.06-2.94 (m, 12H, H5, H9), 2.88-2.69 (m, 12H, H6, H10), 2.64-2.38 (m, 37H, H1) 2.12-0.57 (m, 53H, H16-18, H20, Chol).

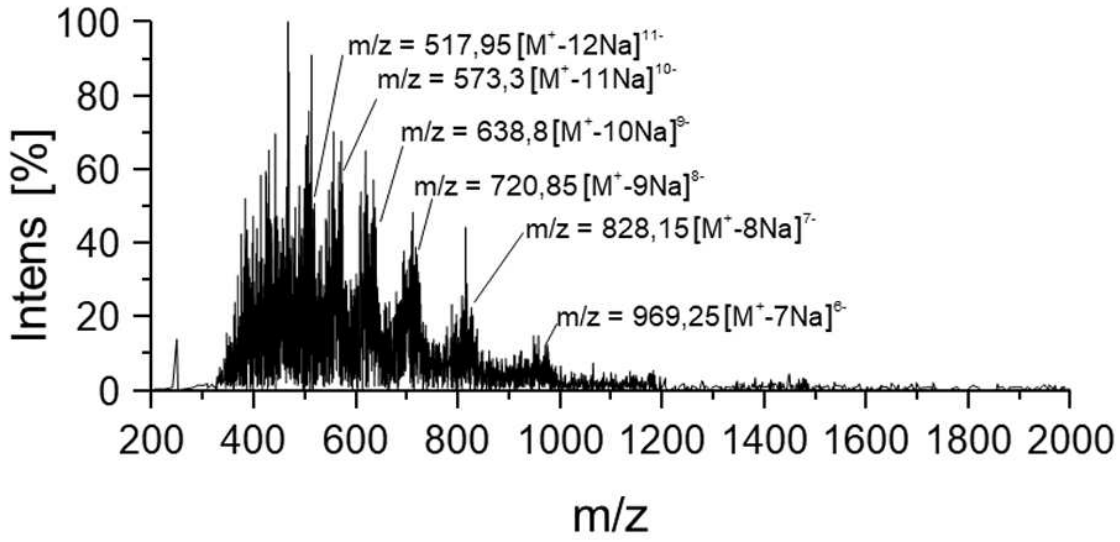

Figure 34. ESI-MS (neg- mode) of $_{short}C^{S}$.

ESI-MS for $C_{175}H_{270}N_{42}Na_{20}O_{120}S_{20}$: $[M\text{-}10Na^{+}]^{9-}$ calcd.: 638.8; found 638.8.

DS determined via EA: 94%.

Glycooligomer $_{short}D^{S}$

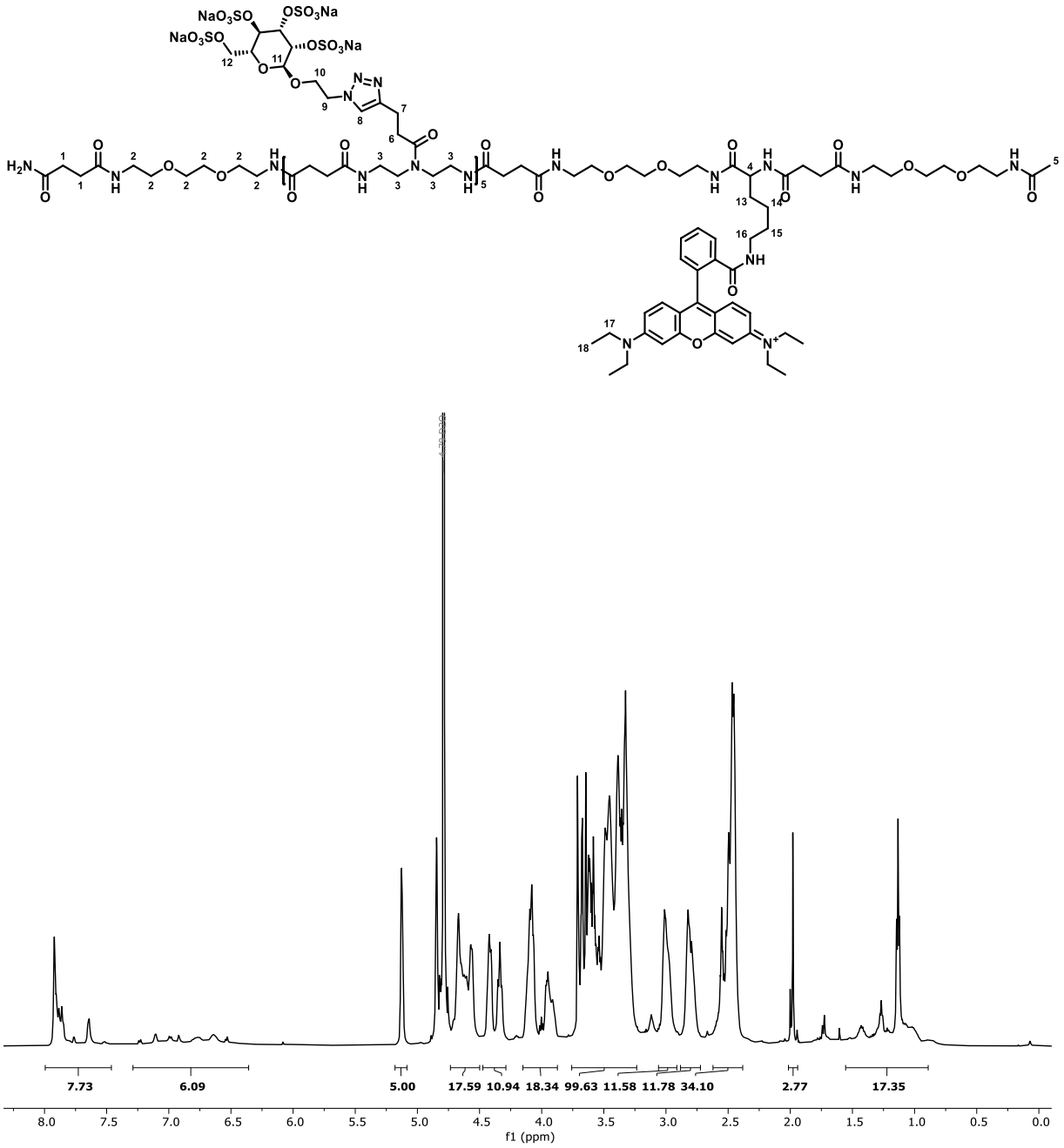

Figure 35. ^{1}H-NMR (600 MHz, D_2O, ambient temperature) of $_{short}D^{S}$.

^{1}H-NMR (600 MHz, D2O) δ [ppm] = 7.99-7.46 (m, 8H, Ar–H, H8), 7.28-6.35 (m, 7H, Ar-H), 5.12 (s, 5H, H11), 4.84 (m, 5H, $CH_{Pyranose}$), 4.73-4.49 (m, 19H, $CH_{Pyranose}$, H9), 4.47-4.28 (m, 10H, $CH_{Pyranose}$), 4.15-3.87 (m, 18H, $CH_{Pyranose}$, H4, H10), 3.75-3.23 (m, xH, $CH_{Pyranose}$, H2, H3, H17), 3.06-2.91 (m, 10H, H7), 2.88-2.72 (m, 10H, H6), 2.62-2.38 (m, 32H, H1), 2.01-1.94 (m, 3H, H5), 1.55-0.89 (m, 18H, H13-15, H18).

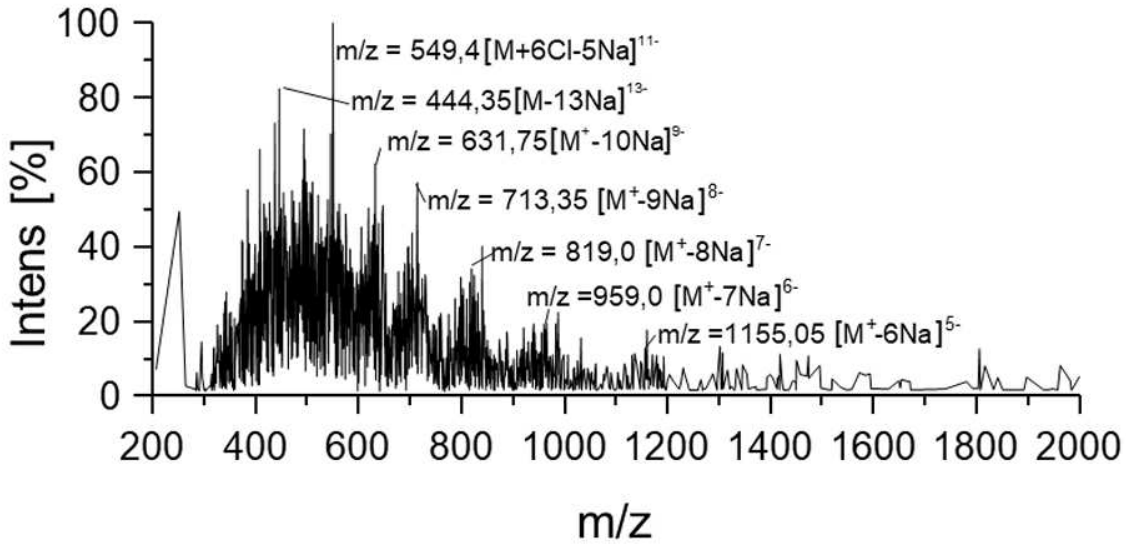

Figure 36. ESI-MS (neg. mode) of $_{short}D^{S}$.

ESI-MS for $C_{171}H_{250}N_{41}Na_{20}O_{121}S_{20}^{+}$: $[M^{+}\text{-}10Na^{+}]^{9-}$ calcd.: 631.4; found: 631.8.

DS determined via EA: 94%.

5.4.2 Macroinitiators

Macroinitiator Backbone

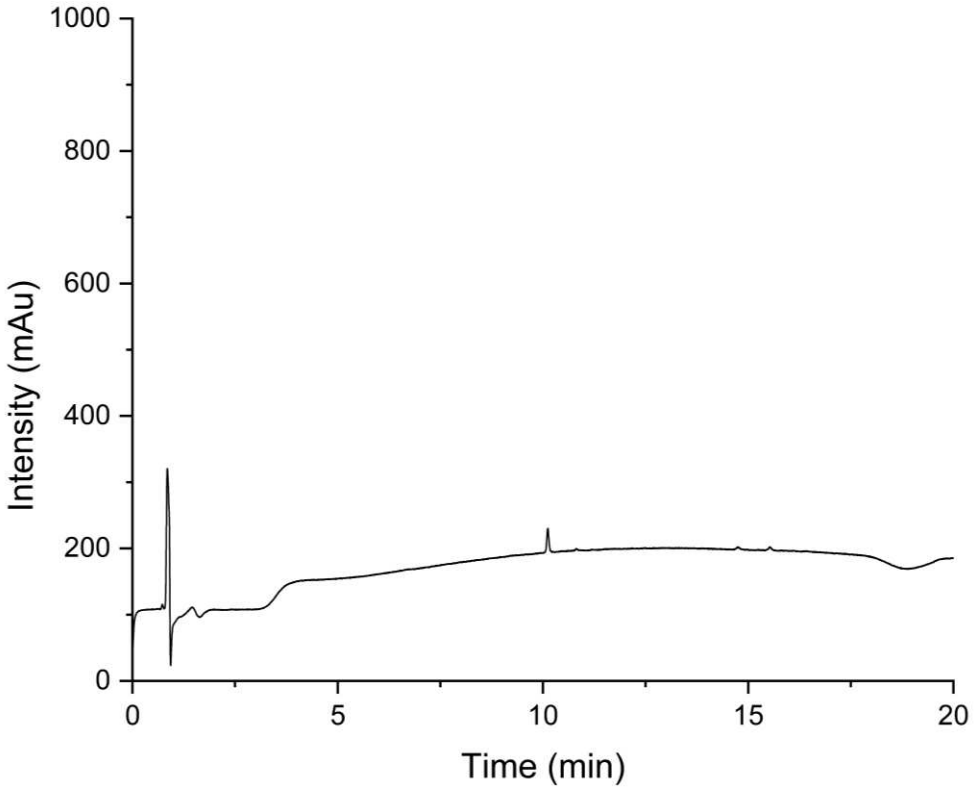

Figure 37. Oligomer backbone detected with relative purities >97% by RP-HPLC analysis (linear gradient from 5 – 95 vol% eluent H2O/acetonitrile) in 20 min at 25 °C.

Macroinitiator $_{long}$A

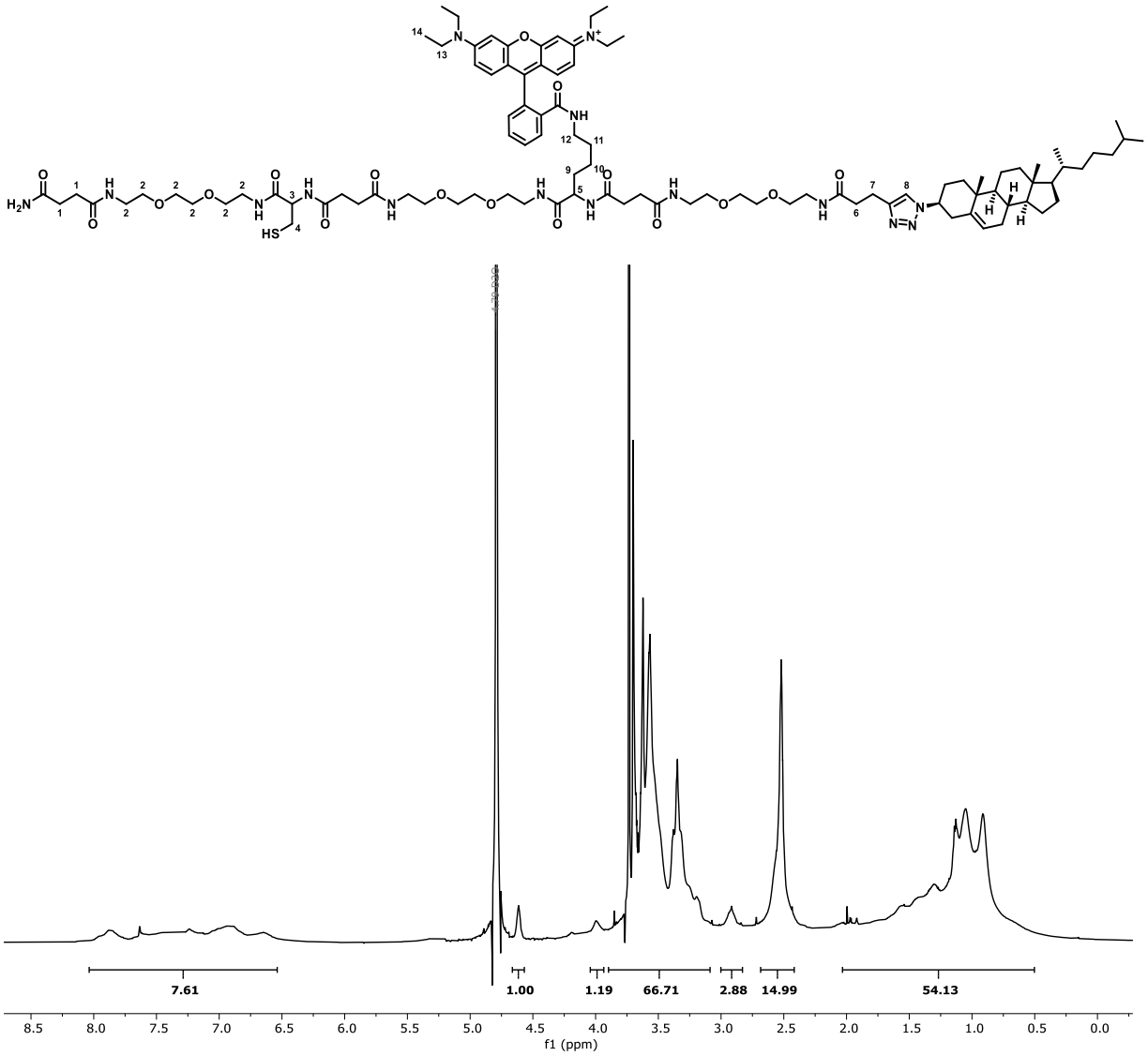

Figure 38. ^{1}H-NMR (600 MHz, D_2O, ambient temperature) of macroinitiator $_{long}$A.

^{1}H-NMR (600 MHz, D_2O) δ [ppm] = 8.03-6.53 (m, 11H, H8, Ar-H), 4.66-4.56 (m, 1H, H3), 4.04-3.93 (m, 1H, H5), 3.89-3.08 (m, 50H, H2, H4, H6, H7, H12, H13), 2.68-2.41 (m, 12H, H1), 2.03-0.50 (m, 50H, H9-11, Chol)

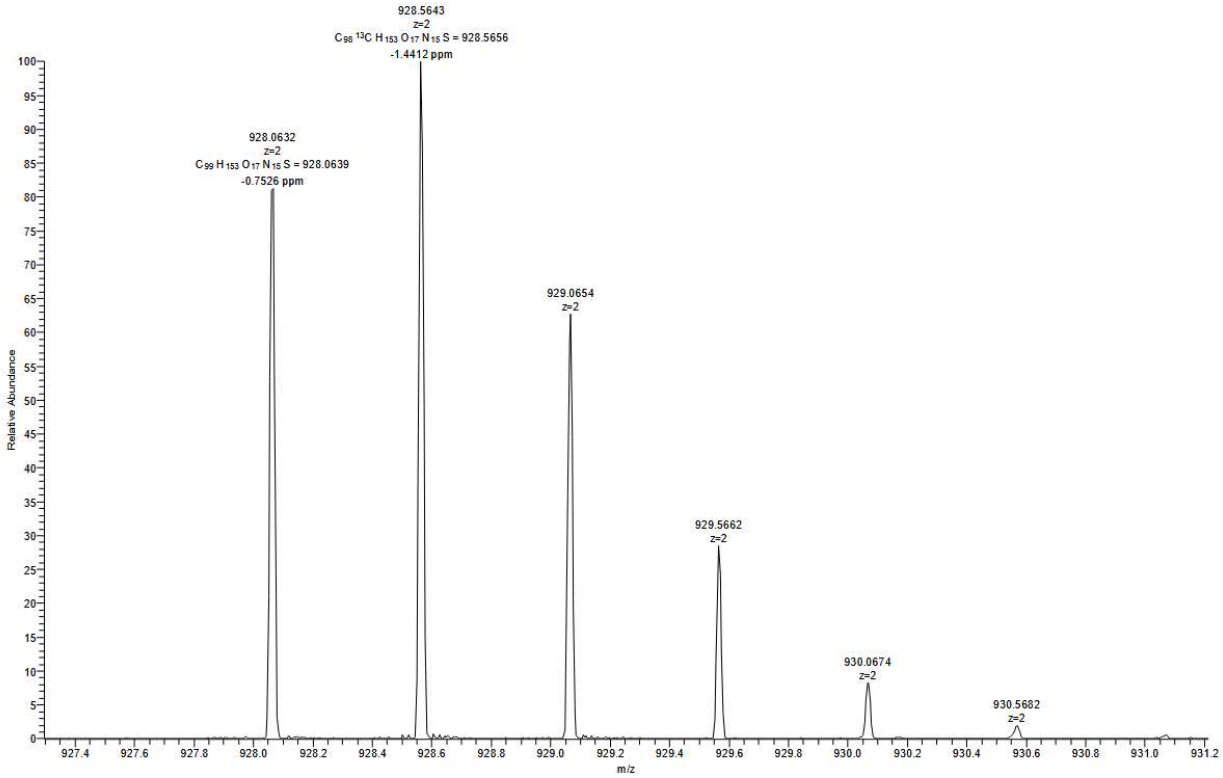

Figure 39. HR-ESI-MS of macroinitiator $_{long}$A.

HR-ESI-MS for $C_{99}H_{152}N_{15}O_{17}S^{+}$: $[M^{+}+2H]^{2+}$ calcd.: 928.57; found 928.56.

Macroinitiator $_{long}$B

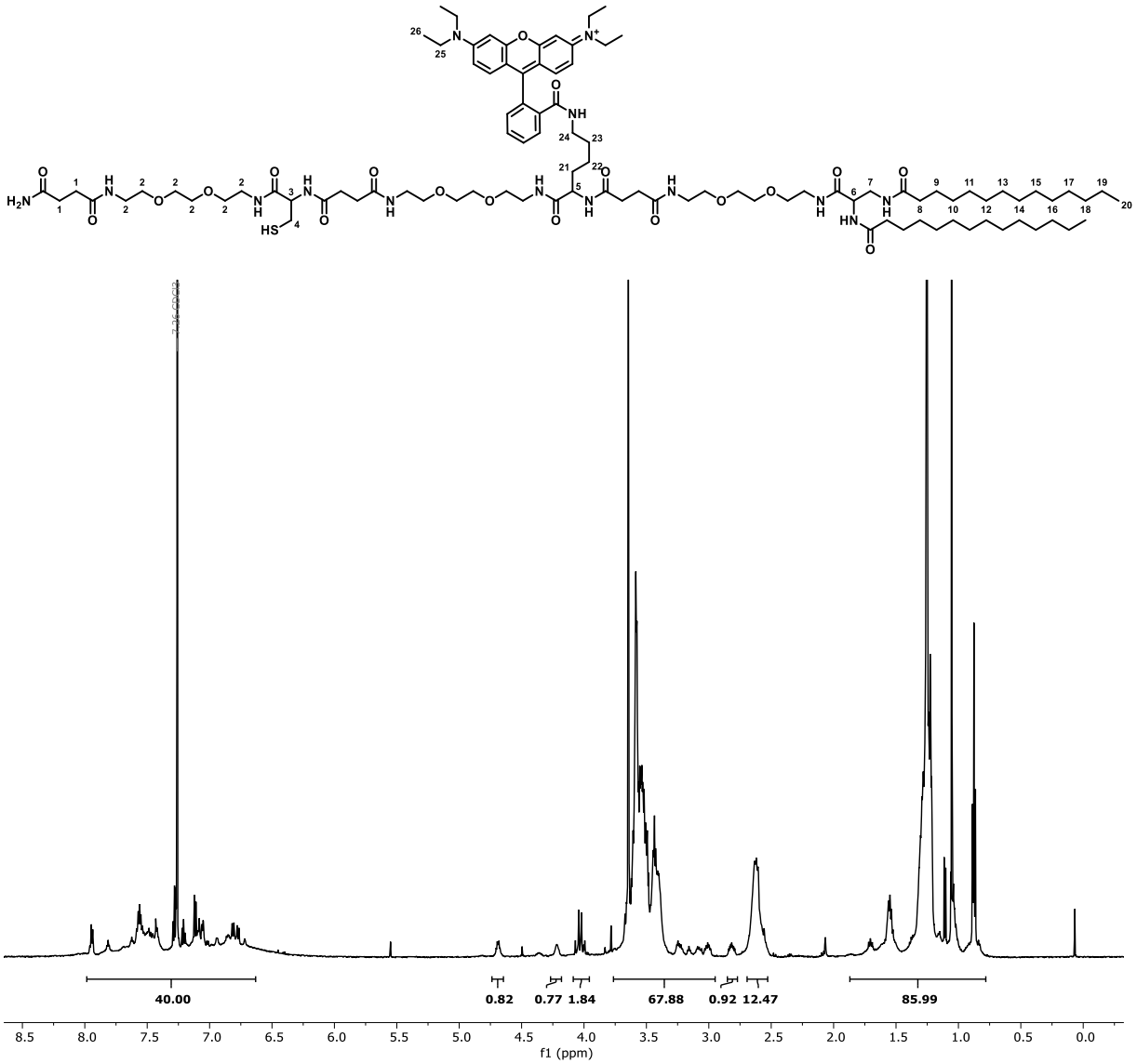

Figure 40. ^{1}H-NMR (600 MHz, $CDCl_3$, ambient temperature) of macroinitiator $_{long}$B.

^{1}H-NMR (600 MHz, $CDCl_3$) δ [ppm] = 7.98-6.63 (m, 10H, Ar-H), 4.73-4.64 (m, 1H, H3), 4.26-4.18 (m, 1H, H5), 4.08-3.95 (m, 2H, H7), 3.76-2.94 (m, 48H, H2, H4, H24, H25), 2.85-2.77 (m, 1H, H6), 2.69-2.52 (m, 12H, H1), 1.87-0.78 (m, 72 H, H8-20, H21-23, H26)

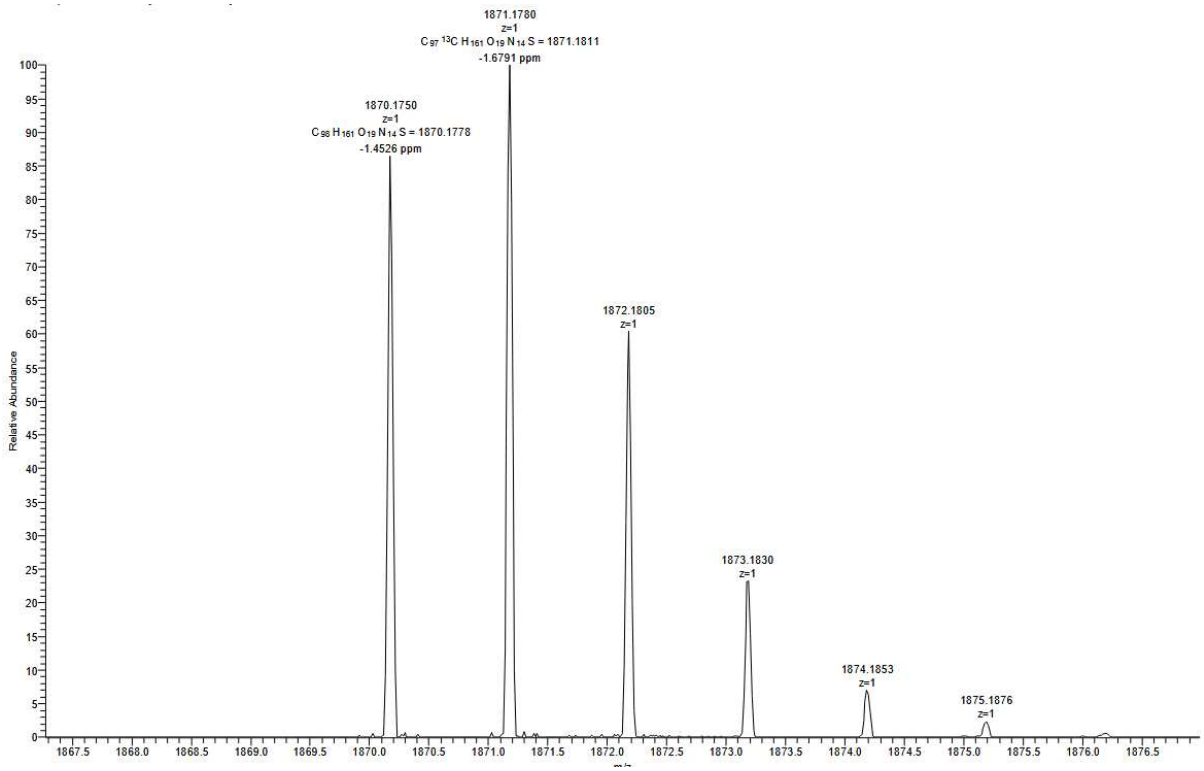

Figure 41. HR-ESI-MS of macroinitiator $_{long}$B.

HR-ESI-MS for $C_{98}H_{161}N_{14}O_{19}S^+$: $[M^+ + H]^+$ calcd.: 1871.18; found 1871.18.

Macroinitiator $_{long}$C

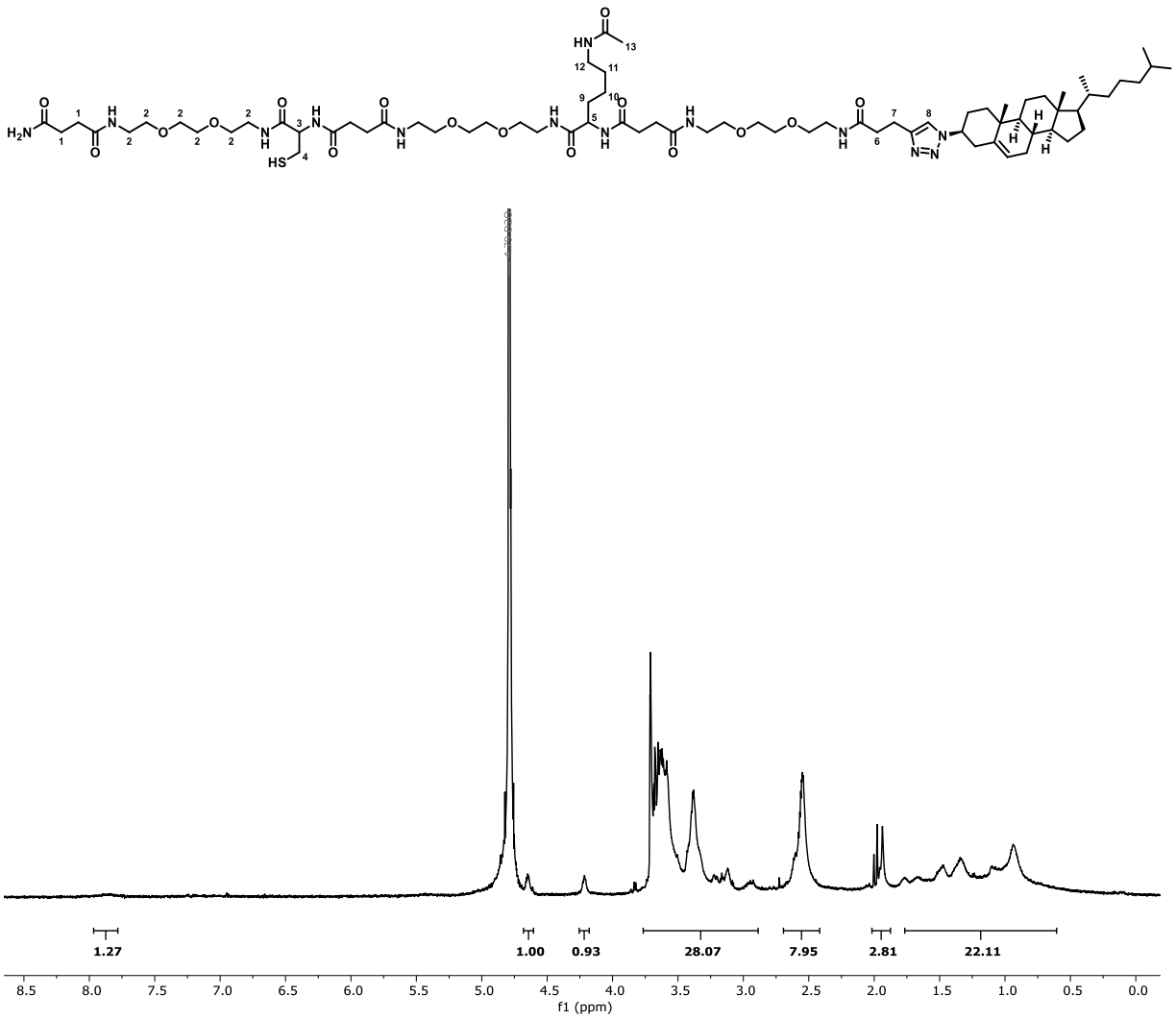

Figure 42. ^{1}H-NMR (600 MHz, D_2O, ambient temperature) of $_{long}$C.

^{1}H-NMR (600 MHz, D_2O) δ [ppm] = 7.88 (s, 1H, H8), 4.46-4.60 (m, 1H, H3), 4.25-4.17 (m, 1H, H5), 3.76-2.87 (m, 44H, H2, H4, H6, H7, H12), 2.69-2.41 (m, 12H, H1), 2.01-1.87 (m, 3H, H13), 1.76-0.60 (m, 50H, H9-11, Chol)

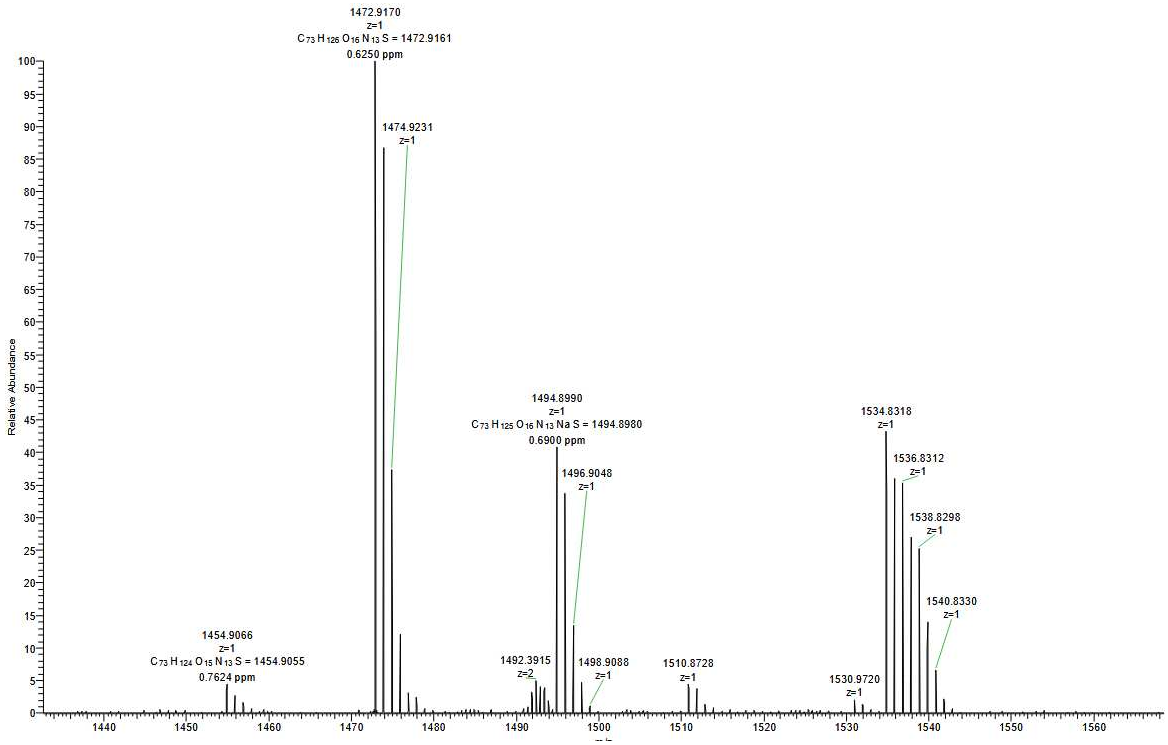

Figure 43. ESI-MS of macroinitiator $_{long}$C.

HR-ESI-MS for $C_{73}H_{125}N_{13}O_{16}S$: $[M+H]^+$ calcd.: 1472.91; found 1472.91.

Macroinitiator $_{long}$D

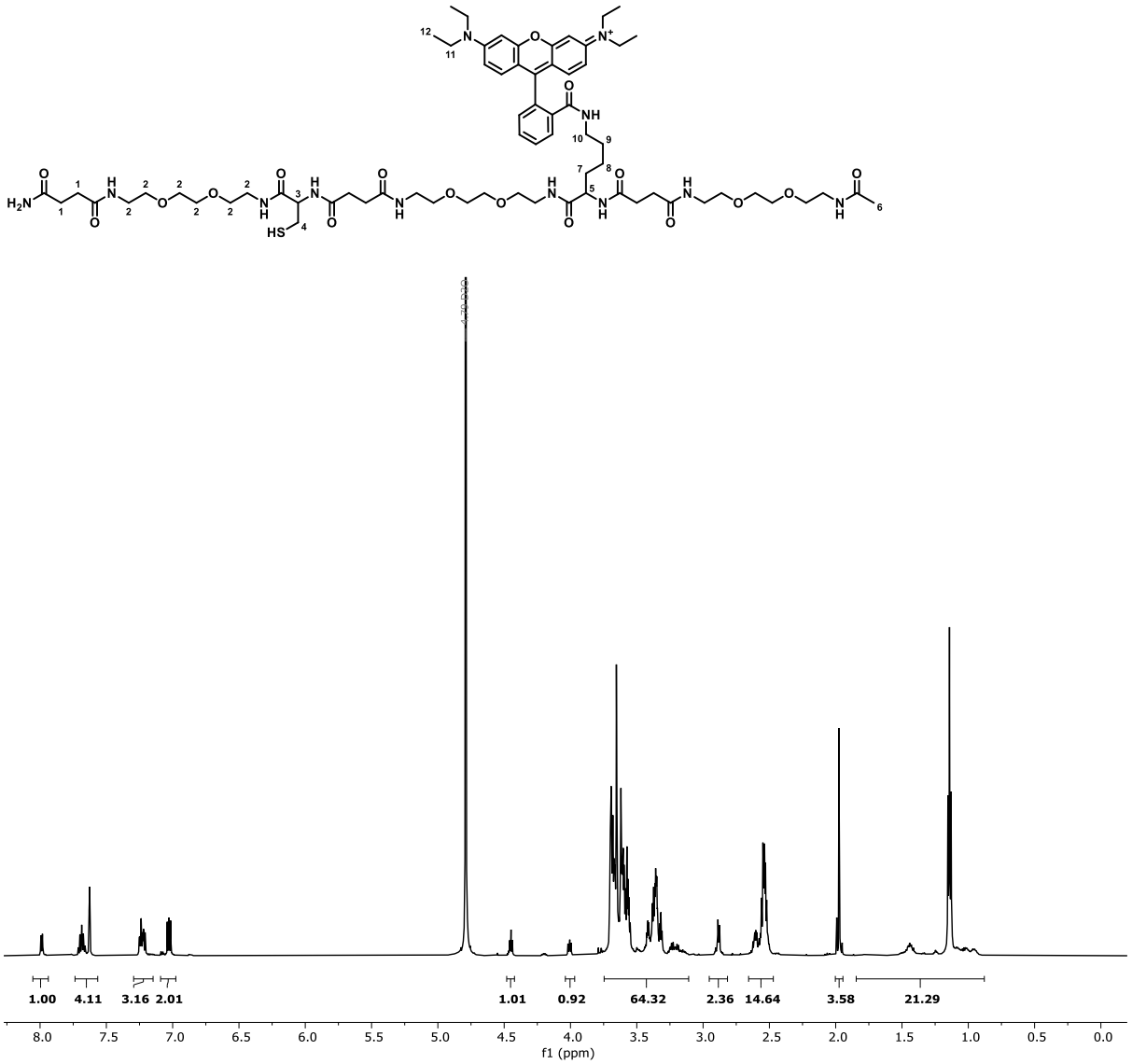

Figure 44. ^{1}H-NMR (600 MHz, D_2O, ambient temperature) of macroinitiator $_{long}$D.

^{1}H-NMR (600 MHz, D_2O) δ [ppm] = 8.05-7.93 (m, 1H, Ar-H), 7.73-7.56 (m, 4H, Ar-H), 7.29-7.14 (m, 3H, Ar-H), 7.09-6.97 (m, 2H, Ar-H), 4.48-4.42 (m, 1H, H3), 4.03-3.96 (m, 1H, H5), 3.74-3.10 (m, 46H, H2, H10, H11), 2.96-2.84 (m, 2H, H4), 2.65-2.47 (m, 12H, H1), 2.00-1.94 (m, 3H, H6), 1.84-0.87 (m, 18H, H7-9, H12)

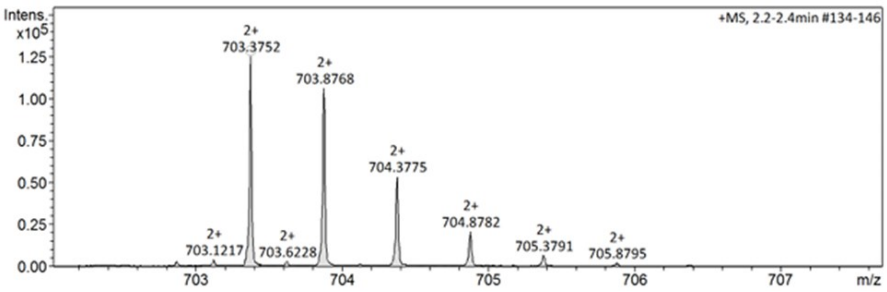

Figure 45. HR-ESI-MS of macroinitiator $_{long}$D.

HR-ESI-MS for $C_{69}H_{105}N_{12}O_{17}S^{+}$: $[M^{+}+2H]^{2+}$ calcd.: 703.87; found 703.87.

5.4.3 Long sGAG Mimetics

Glycopolymer $_{long}A^{OH}$

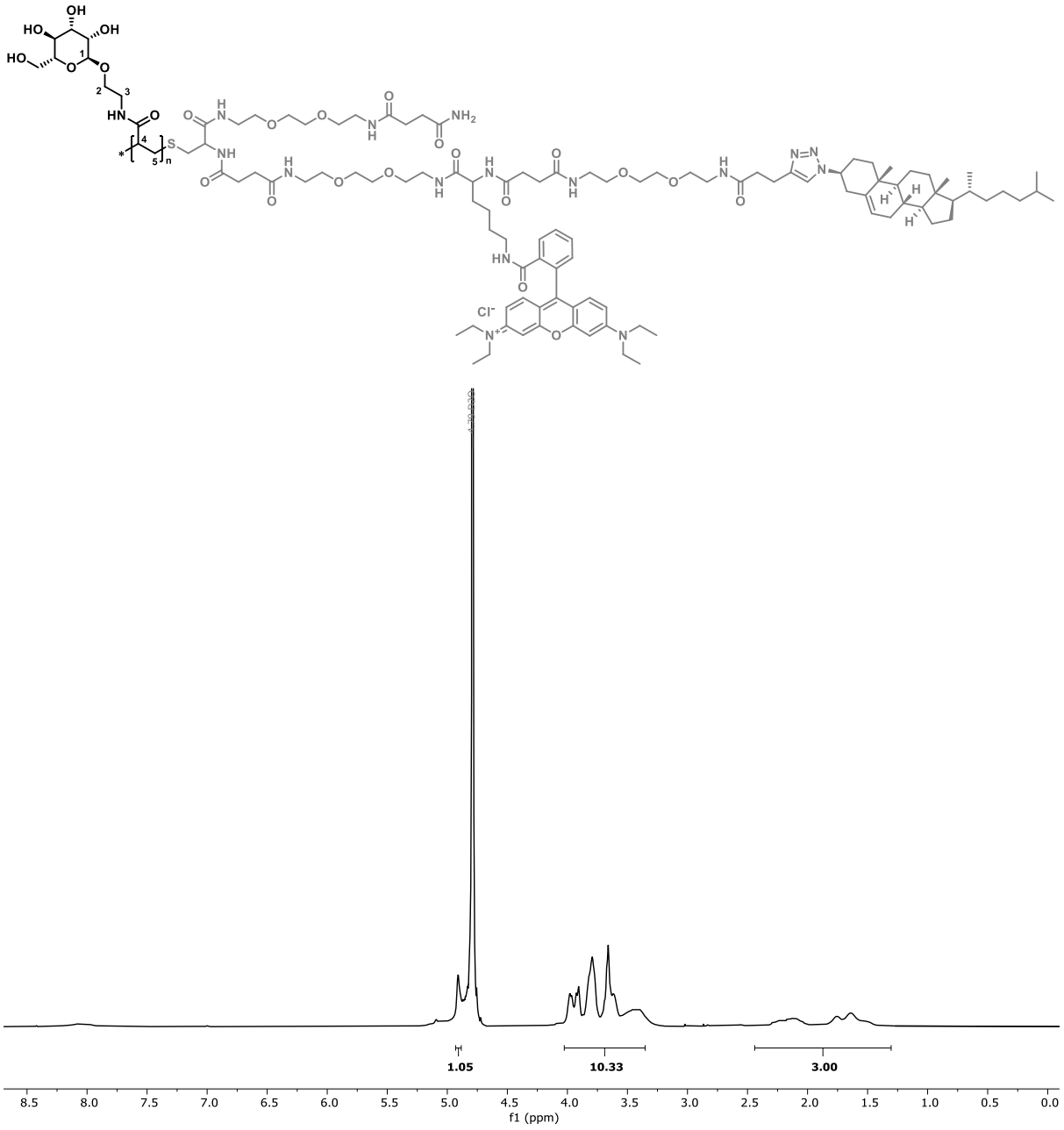

Figure 46. ^{1}H-NMR (600 MHz, D_2O, ambient temperature) of glycopolymer $_{long}A^{OH}$.

^{1}H-NMR (600 MHz, D_2O) δ [ppm] = 4.90 (s, 1H, H*1*), 4.02-3.35 (m, 10H, $CH_{Pyranose}$, H*2*, H*3*), 2.44-1.30 (m, 3H, H*4*, H*5*)

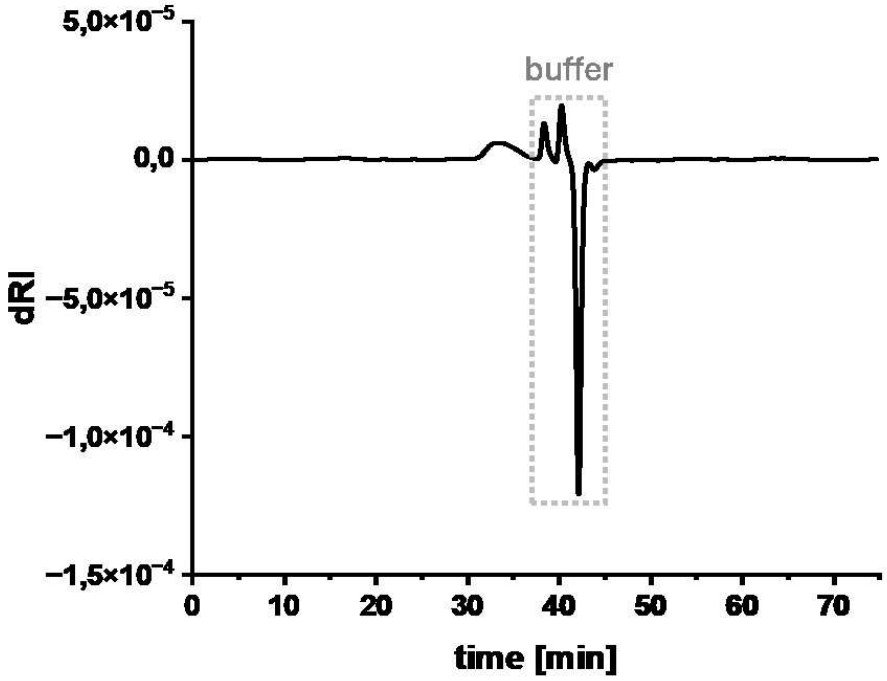

Figure 47. H_2O-SEC-MALS of $_{long}A^{OH}$.

Đ (via H2O-SEC, MALS coupled RI-detector): 1.4

Pn = 76

Mn [kDa] (via H2O-SEC, MALS coupled RI-detector): 23.0

Glycopolymer $_{long}A^{S}$

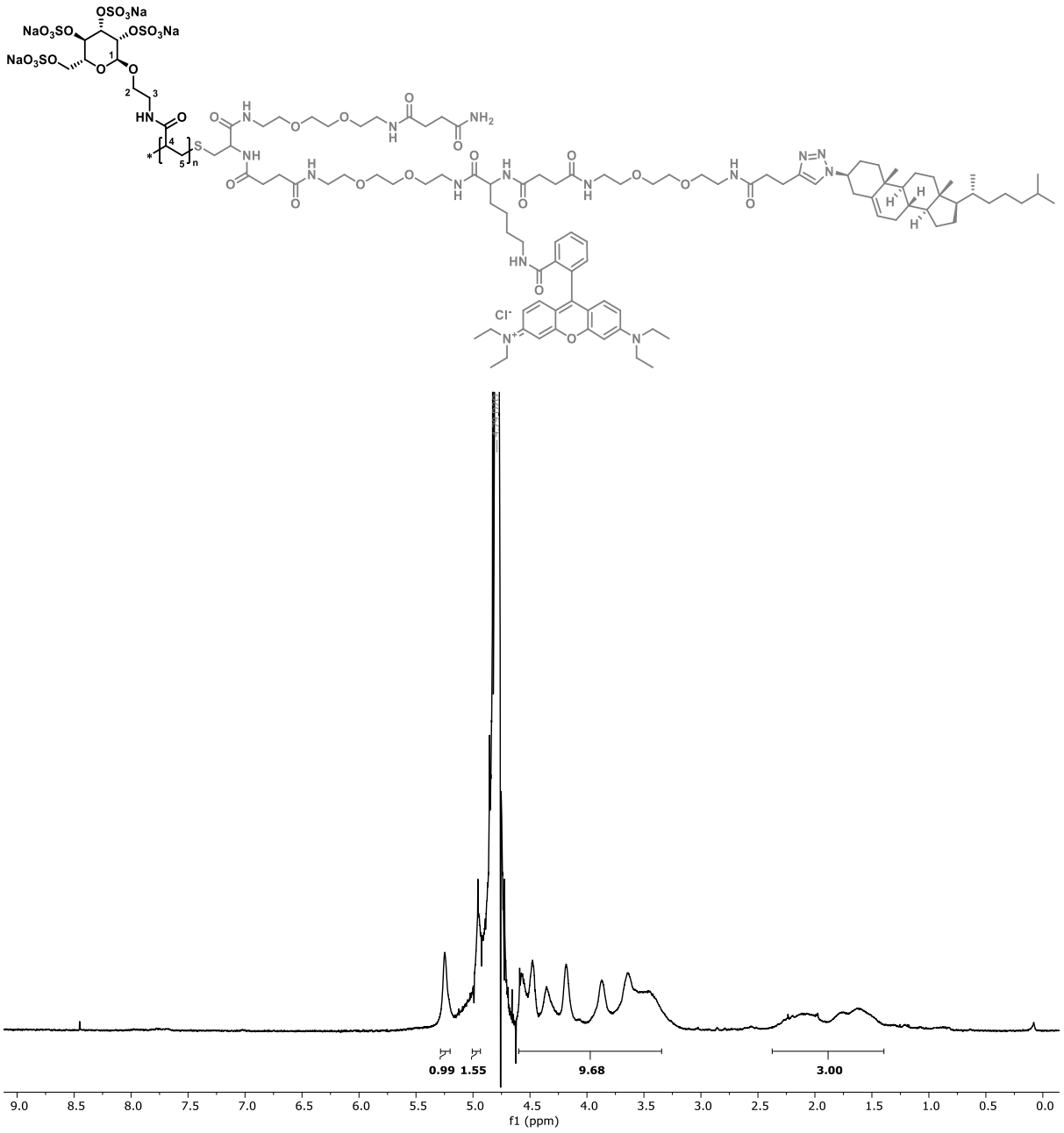

Figure 48. ^{1}H-NMR (600 MHz, D_2O, ambient temperature) of glycopolymer $_{long}A^{S}$.

^{1}H-NMR (600 MHz, D_2O) δ [ppm] = 5.24 (s, 1H, H*1*), 4.95 (s, 1H, $CH_{Pyranose}$), 4.59-3.34 (m, 9H, $CH_{Pyranose}$, H*2*, H*3*), 2.37-1.39 (m, 3H, H*4*, H*5*)

Mn [kDa] (assuming 100% DS): 53.7

DS determined via EA: 99%

Glycopolymer $_{long}B^{OH}$

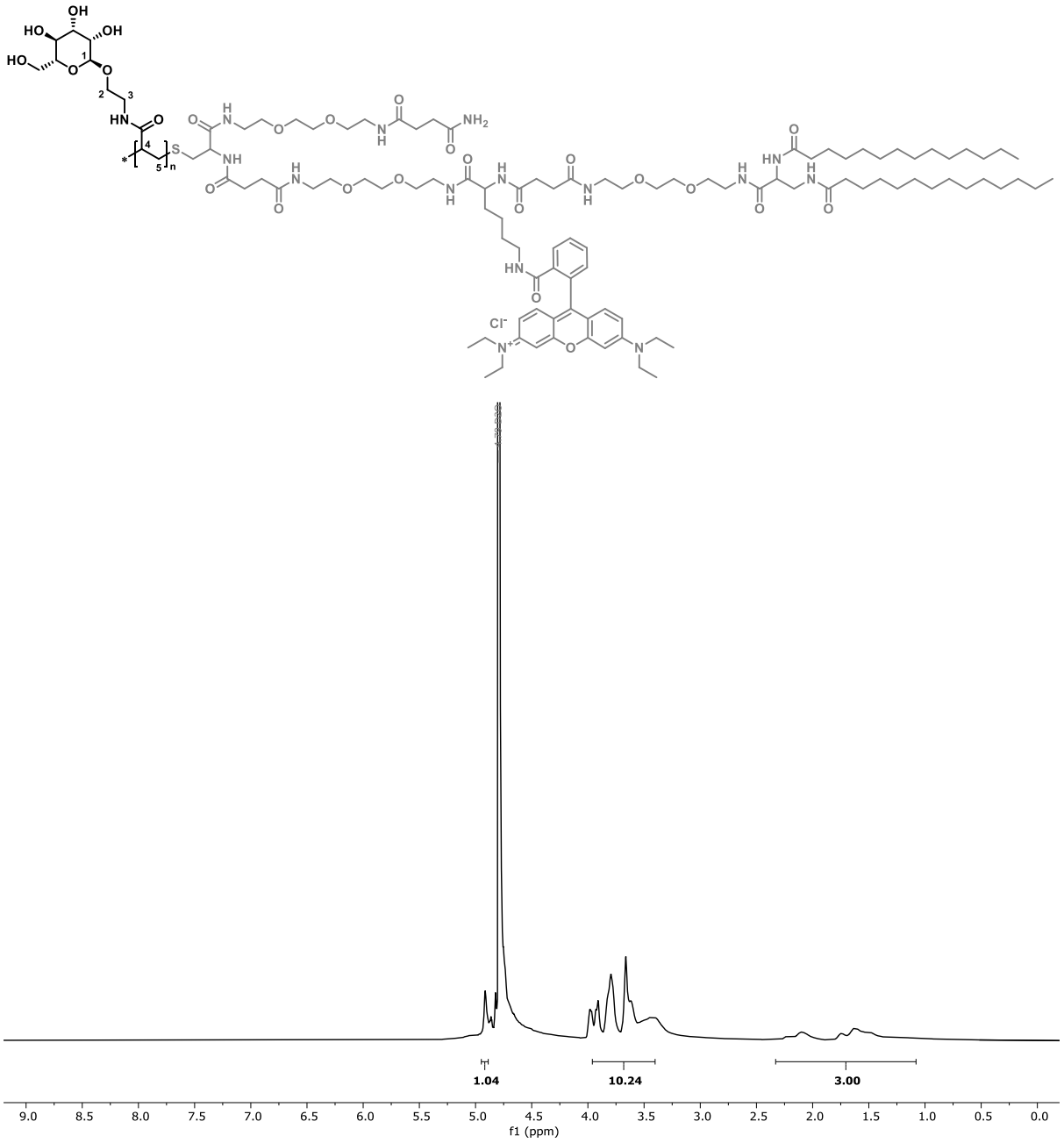

Figure 49. ^{1}H-NMR (600 MHz, D_2O, ambient temperature) of glycopolymer $_{long}B^{OH}$.

^{1}H-NMR (600 MHz, D_2O) δ [ppm] = 4.92 (s, 1H, H*1*), 4.05-3.25 (m, 10H, $CH_{Pyranose}$, H*2*, H*3*), 2.35-1.35 (m, 3H, H*4*, H*5*)

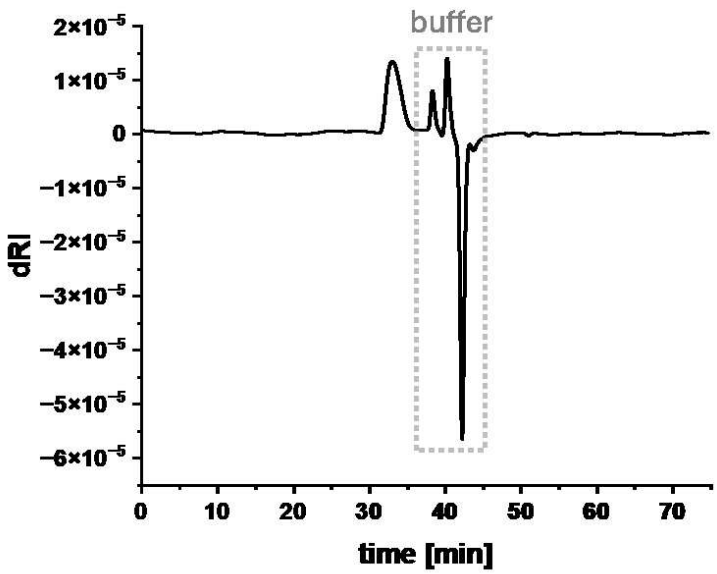

Figure 50. H_2O-SEC-MALS of $_{long}B^{OH}$.

Đ (via H_2O-SEC, MALS coupled RI-detector): 1.1

Pn = 79

Mn [kDa] (via H_2O-SEC, MALS coupled RI-detector): 24.0

Glycopolymer $_{long}B^{S}$

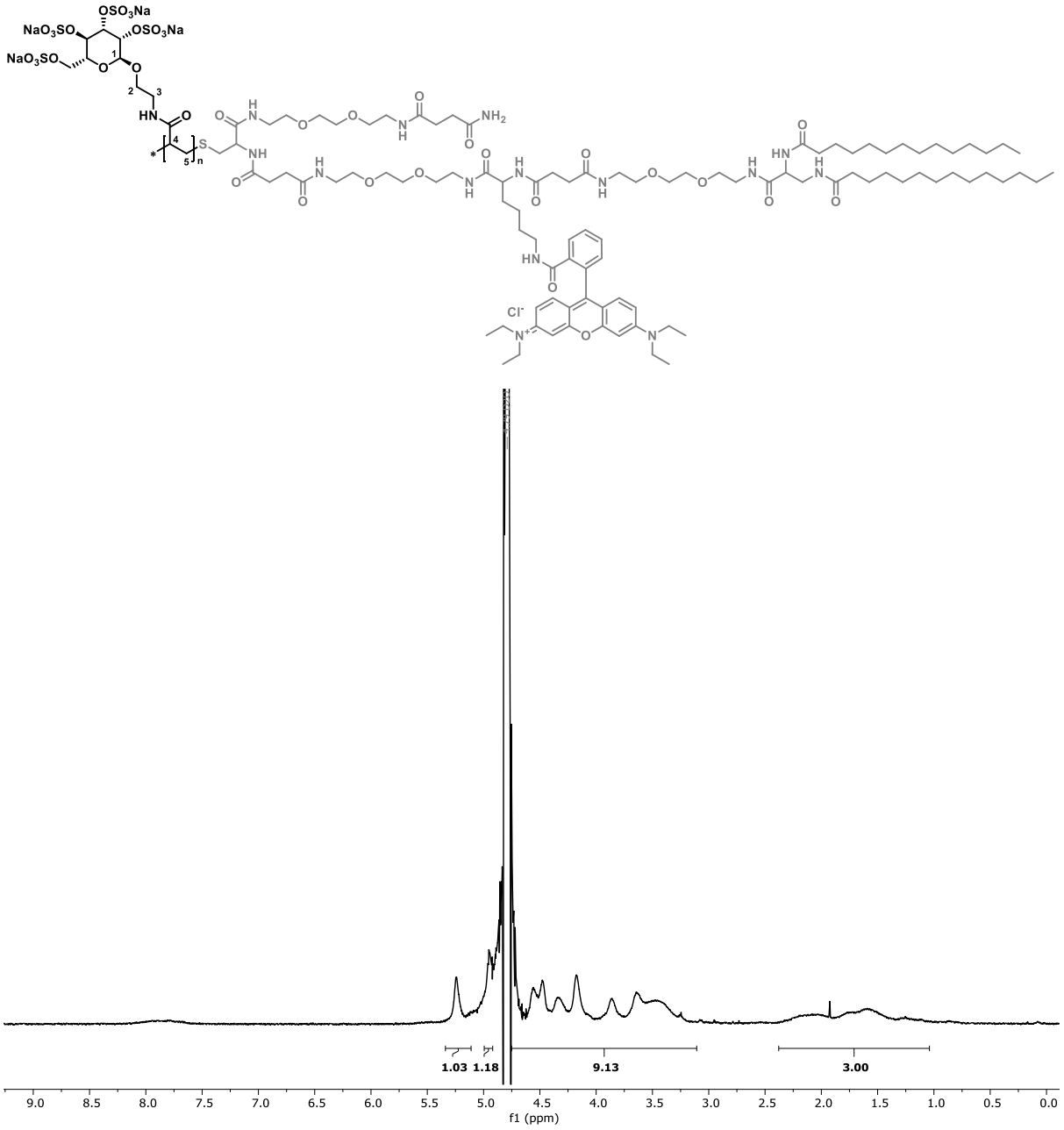

Figure 51. ^{1}H-NMR (600 MHz, D_2O, ambient temperature) of glycopolymer $_{long}B^{S}$.

^{1}H-NMR (600 MHz, D_2O) δ [ppm] = 5.24 (s, 1H, H*1*), 4.94 (s, 1H, $CH_{Pyranose}$), 4.75-3.10 (m, 9H, $CH_{Pyranose}$, H*2*, H*3*), 2.37-1.04 (m, 3H, H*4*, H*5*)

Mn [kDa] (assuming 100% DS): 56.0

DS determined via EA: 87%

Glycopolymer $_{long}C^{OH}$

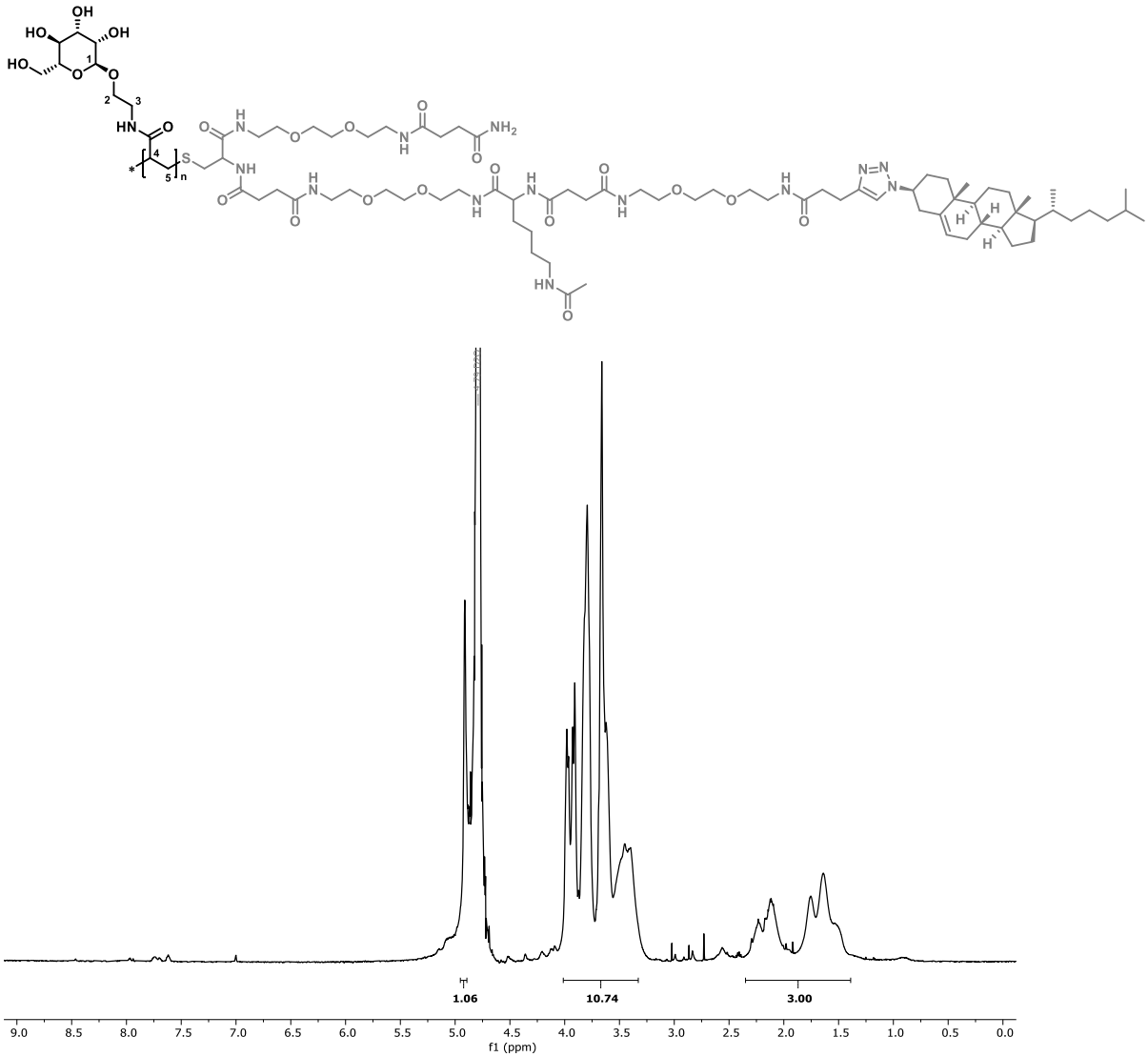

Figure 52. ^{1}H-NMR (600 MHz, D_2O, ambient temperature) of glycopolymer $_{long}C^{OH}$.

^{1}H-NMR (600 MHz, D_2O) δ [ppm] = 4.91 (s, 1H, H*1*), 4.01-3.32 (m, 10H, $CH_{Pyranose}$, H*2*, H*3*), 2.35-1.39 (m, 3H, H*4*, H*5*)

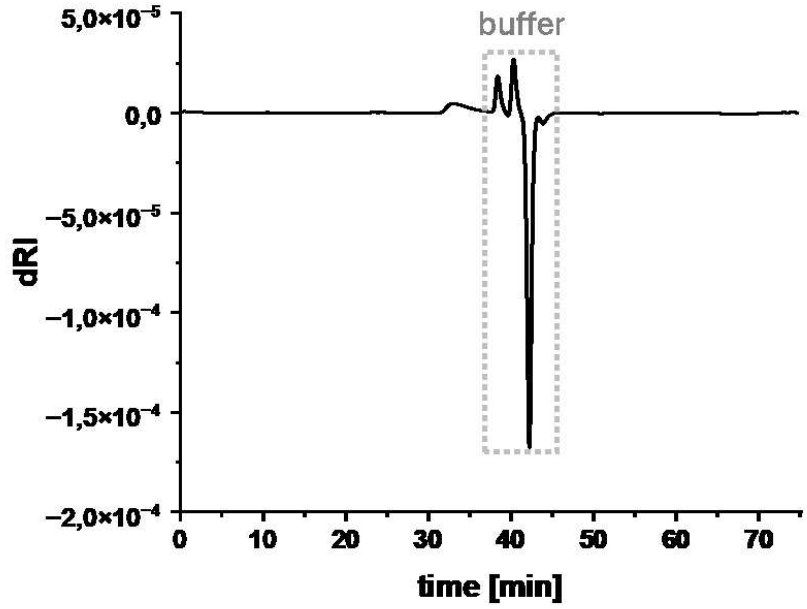

Figure 53. H_2O-SEC-MALS of $_{long}C^{OH}$.

Đ (via H_2O-SEC, MALS coupled RI-detector): 1.1

Pn = 75

Mn [kDa] (via H_2O-SEC, MALS coupled RI-detector): 22.3

Glycopolymer $_{long}C^{S}$

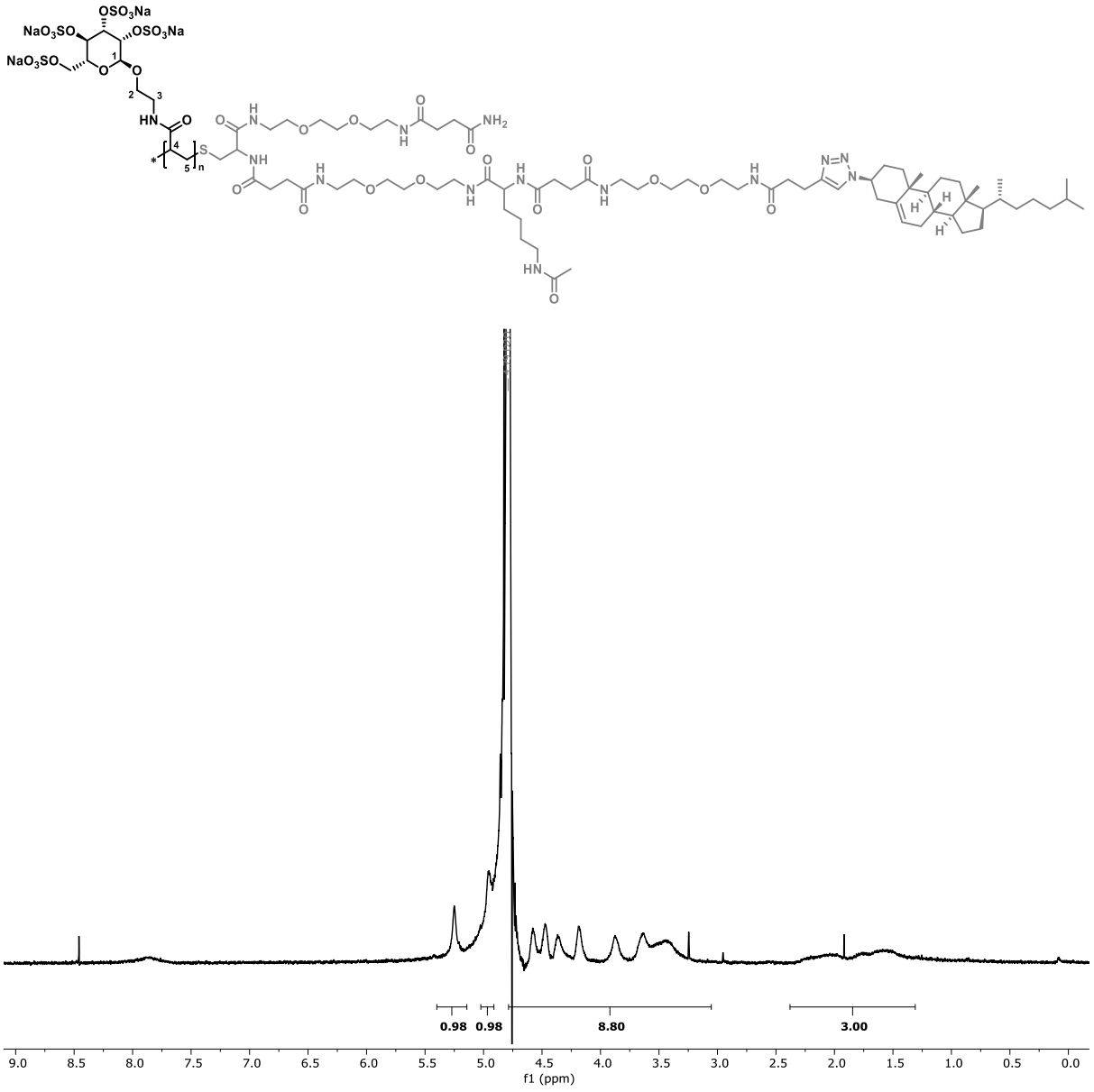

Figure 54. ^{1}H-NMR (600 MHz, D_2O, ambient temperature) of glycopolymer $_{long}C^{S}$.

^{1}H-NMR (600 MHz, D_2O) δ [ppm] = 5.25 (s, 1H, H*1*), 4.94 (s, 1H, $CH_{Pyranose}$), 4.78-3.05 (m, 9H, $CH_{Pyranose}$, H*2*, H*3*), 2.38-1.30 (m, 3H, H*4*, H*5*)

Mn [kDa] (assuming 100% DS): 53.0

DS determined via EA: 97%

Glycopolymer $_{long}D^{OH}$

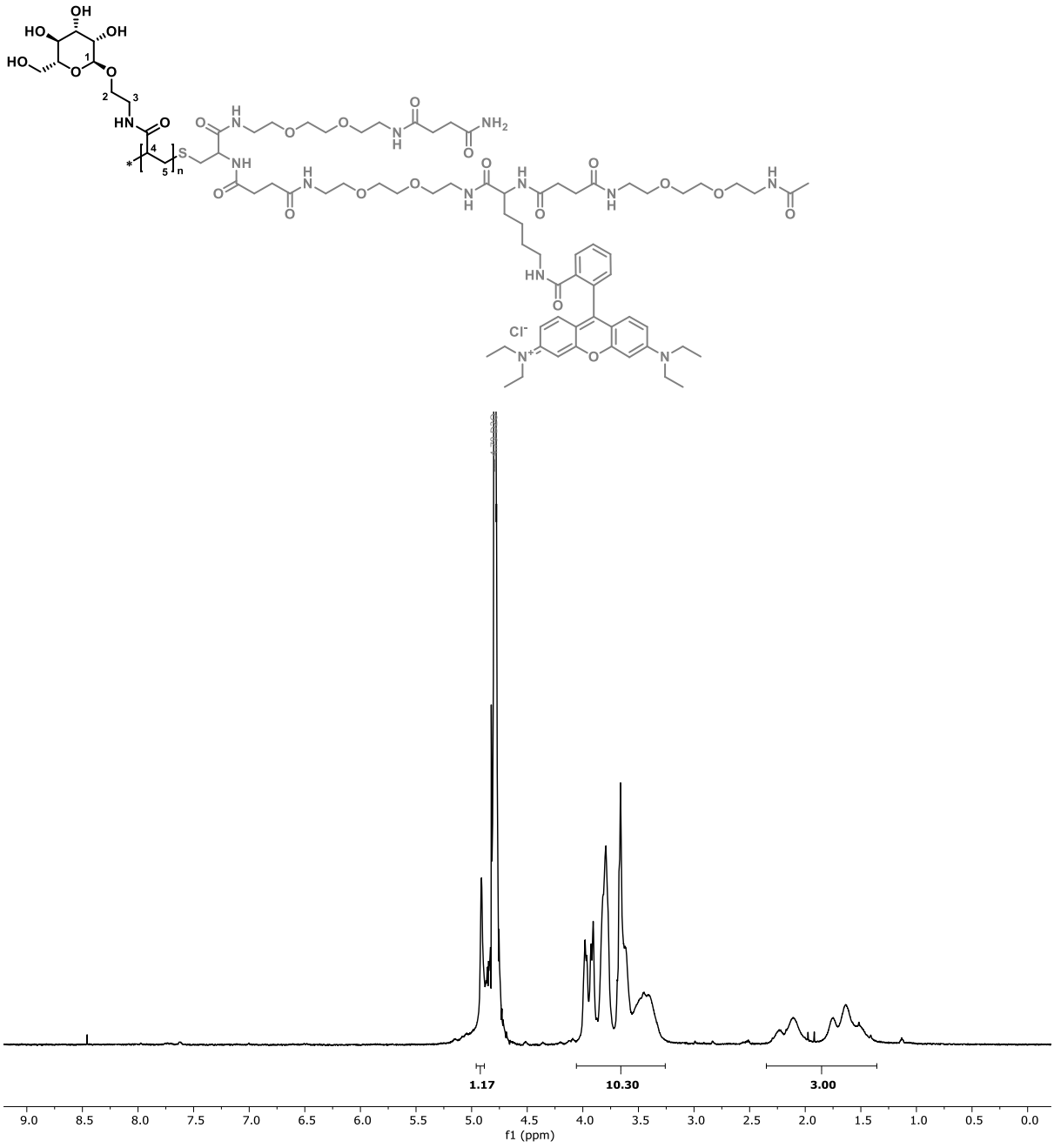

Figure 55. ^{1}H-NMR (600 MHz, D_2O, ambient temperature) of glycopolymer $_{long}D^{OH}$.

^{1}H-NMR (600 MHz, D_2O) δ [ppm] = 4.92 (s, 1H, H*1*), 4.05-3.25 (m, 10H, $CH_{Pyranose}$, H*2*, H*3*), 2.35-1.35 (m, 3H, H*4*, H*5*)

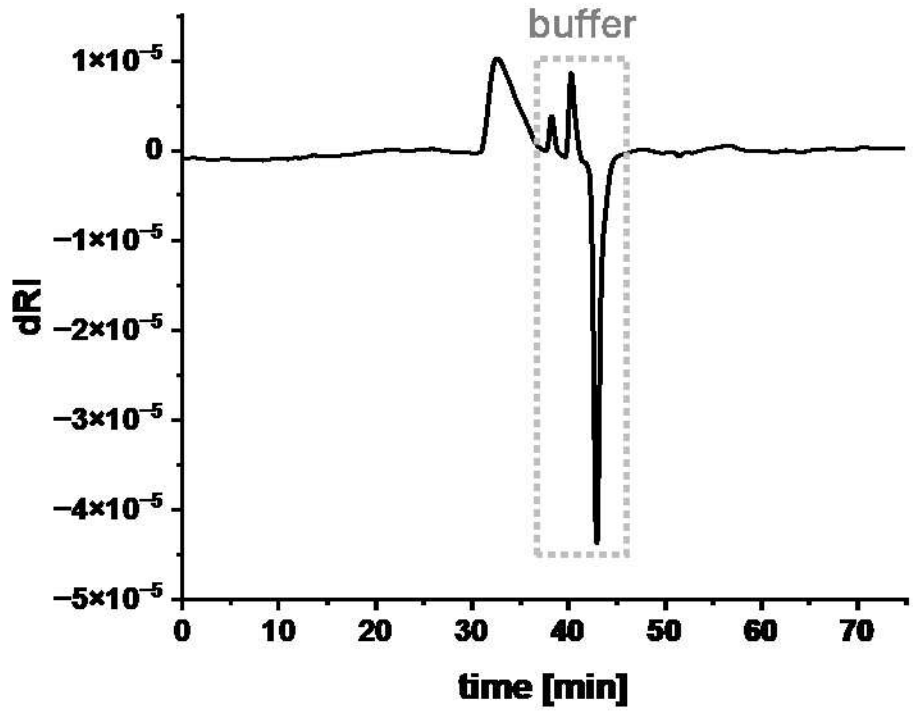

Figure 56. H_2O-SEC-MALS of $_{long}D^{OH}$.

Đ (via H_2O-SEC, MALS coupled RI-detector): 1.3

Pn = 70

Mn [kDa] (via H_2O-SEC, MALS coupled RI-detector): 20.8

Glycopolymer $_{long}D^{S}$

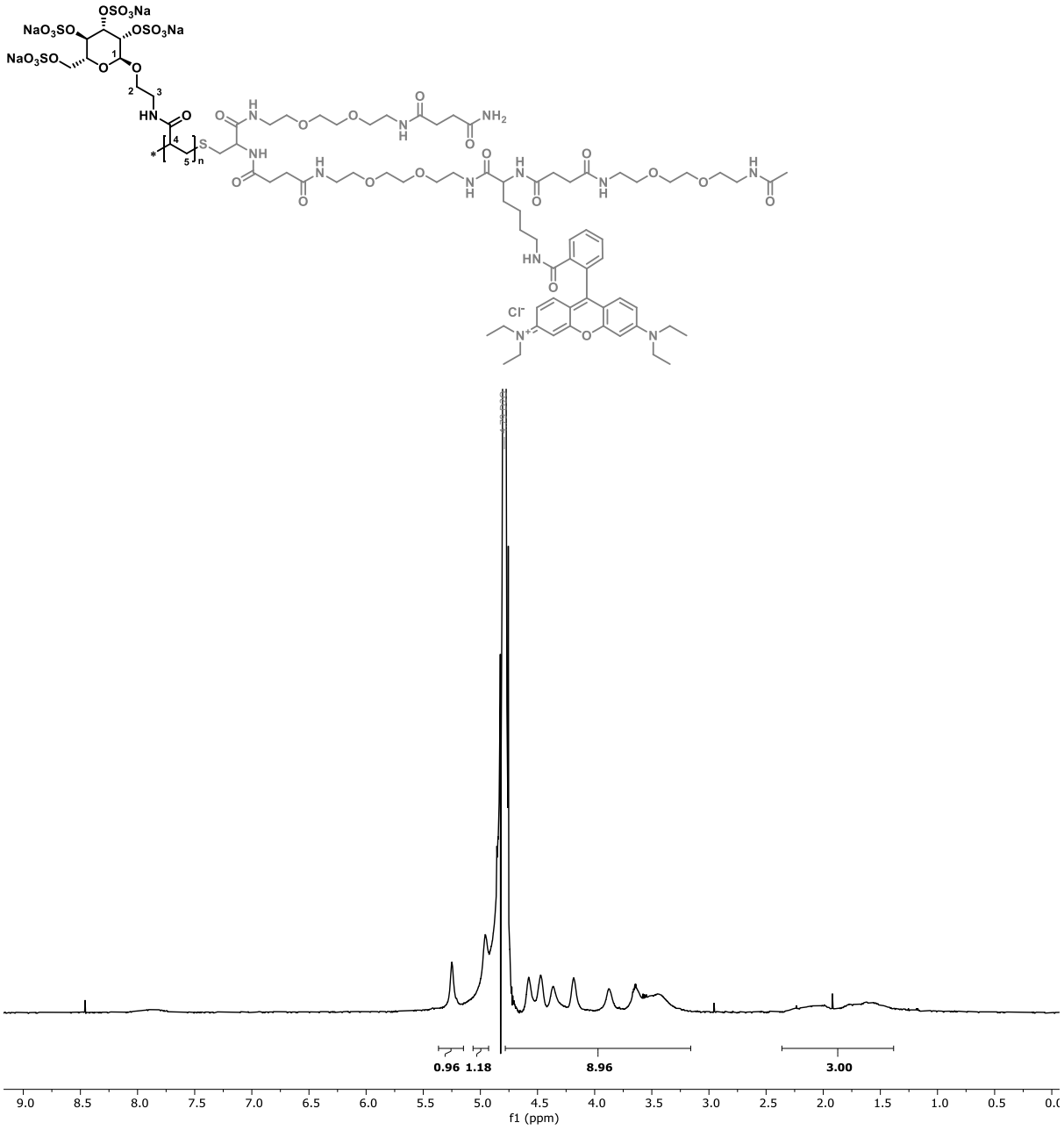

Figure 57. ^{1}H-NMR (600 MHz, D_2O, ambient temperature) of glycopolymer $_{long}D^{S}$.

^{1}H-NMR (600 MHz, D_2O) δ [ppm] = 5.25 (s, 1H, H*1*), 4.95 (s, 1H, $CH_{Pyranose}$), 4.78-3.16 (m, 9H, $CH_{Pyranose}$, H*2*, H*3*), 2.36-1.38 (m, 3H, H*4*, H*5*)

Mn [kDa] (assuming 100% DS): 49.0

DS determined via EA: 97 %

6. Appendix

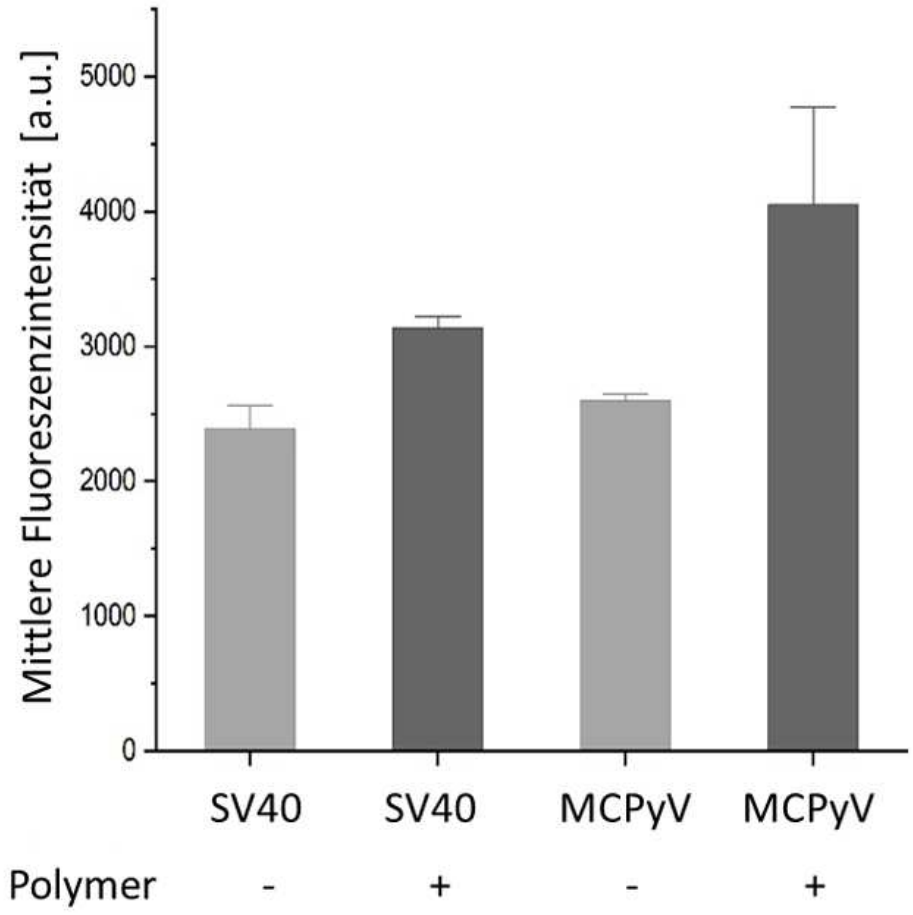

Figure 58. Quantification of measured mean fluorescence of GM95 cells after incubation with SV40 or MCPyV-VLPs before (-) and after (+) incubation with $_{long}A^{S}$.

6.1 List of Figures

6.2 List of Abbreviations

a.u.	arbitrary unit
AF647	Alexa Fluor 647 dye
ATRP	atom transfer radical polymerization
Boc	tert-butyloxycarbonyl protecting group
Con A	Concanavalin A
CRD	carbohydrate recognition domain
CuAAC	copper(I)-catalyzed azide-alkyne cycloaddition
Cys	cysteine
DADS	diacetylene diamine succinic acid
Dap	2.3-diaminopropanoic acid
DCM	dichloromethane
Dde	1-(4,4-dimethyl-2,6- dioxocyclohexylidene)ethyl protecting group
DIPEA	N-ethyl-N-(propan-2-yl)propan-2-amine
DLS	dynamic light scattering
DMF	dimethylformamide
DOPC	1.2-dioleylphosphatidylcholine
DPPE	1.2-dipalmitoylphosphatidylethanolamine
DSPC	1.2-distearylphosphatidylcholine
e.g.	exempli gratia
EDS	ethylene glycol diamine succinic acid
eq	equivalents
ESI	electrospray ionization
et al.	et alii
FCS	fluorescence correlation spectroscopy
Fmoc	fluorenylmethoxycarbonyl protecting group
Gal	galactose
GBPs	glycan binding proteins
GPI	glycophosphatidylinositol
GUVs	giant unilamellar vesicles

HPV16	human papillomavirus type 16
HR-ESI-MS	high resolution-electrospray ionization coupled to mass spectrometry
i.e.	id est
ITO	indium-tin oxide
(k)Da	(kilo) Dalton
K_d	dissociation constant
Ld	liquid disordered
Lo	liquid ordered
Lys	lysine
m/z	mass per charge ratio
MALDI	matrix-assisted laser desorption/ionization
Man	mannose
MCPyV	merkel cell polyomavirus
NMR	nuclear magnetic resonance
PBS	phosphate buffered saline
PyBOP	benzotriazol-1-yloxytripyrrolidinophosphonium hexafluorophosphate
RAFT	reversible-addition-fragmentation chain-transfer polymerization
RCA	Ricinus Communis Agglutinin
RICM	reflection interference contrast microscopy
ROMP	ring-opening metathesis polymerization
RP-HPLC-MS	reverse phase-high pressure liquid chromatography coupled to mass spectrometry
(s)GAGs	(sulfated) glycosaminoglycans
SEC	size exclusion chromatography
SLB	supported lipid bilayer
SPPoS	solid phase polymer synthesis
SPPS	solid phase peptide synthesis
SV40	simian virus 40
TDS	triple bond diamine succinic acid
TEM	transmission electron microscopy
TFA	trifluoroacetic acid
TIPS	triisopropyl silane

TIRP	thiol-induced, light activated controlled radical polymerization
UV-Vis	ultraviolet–visible
VLPs	virus-like particles

7. References

(1) La Bernardino de Serna, J.; Schütz, G. J.; Eggeling, C.; Cebecauer, M. There Is No Simple Model of the Plasma Membrane Organization. *Frontiers in cell and developmental biology* 2016, *4*, 106.

(2) Ozansoy, M.; Denizhan, Y. The Endomembrane System: A Representation of the Extracellular Medium? *Biosemiotics* 2009, *2*, 255–267.

(3) Simons, K.; Sampaio, J. L. Membrane organization and lipid rafts. *Cold Spring Harbor perspectives in biology* 2011, *3*, a004697.

(4) Bhattacharya, S.; Biswas, J. Understanding membranes through the molecular design of lipids. *Langmuir : the ACS journal of surfaces and colloids* 2010, *26*, 4642–4654.

(5) Dinter, F.; Thiehle, T.; Schedler, U.; Lehmann, W.; Schierack, P.; Rödiger, S. *Immobilisation of Lipophilic and Amphiphilic Biomarker on Hydrophobic Microbeads*, 2023.

(6) Singer, S. J.; Nicolson, G. L. The fluid mosaic model of the structure of cell membranes. *Science (New York, N.Y.)* 1972, *175*, 720–731.

(7) Bell, R. M.; Ballas, L. M.; Coleman, R. A. Lipid topogenesis. *Journal of Lipid Research* 1981, *22*, 391–403.

(8) Escribá, P. V.; Busquets, X.; Inokuchi, J.; Balogh, G.; Török, Z.; Horváth, I.; Harwood, J. L.; Vígh, L. Membrane lipid therapy: Modulation of the cell membrane composition and structure as a molecular base for drug discovery and new disease treatment. *Progress in lipid research* 2015, *59*, 38–53.

(9) Fujimoto, T.; Parmryd, I. Interleaflet Coupling, Pinning, and Leaflet Asymmetry-Major Players in Plasma Membrane Nanodomain Formation. *Frontiers in cell and developmental biology* 2016, *4*, 155.

(10) Rush, J. S. Role of Flippases in Protein Glycosylation in the Endoplasmic Reticulum. *Lipid insights* 2015, *8*, 45–53.

(11) van Meer, G.; Voelker, D. R.; Feigenson, G. W. Membrane lipids: where they are and how they behave. *Nature reviews. Molecular cell biology* 2008, *9*, 112–124.

(12) Casares, D.; Escribá, P. V.; Rosselló, C. A. Membrane Lipid Composition: Effect on Membrane and Organelle Structure, Function and Compartmentalization and Therapeutic Avenues. *International journal of molecular sciences* 2019, *20*.

(13) Barman, H.; Walch, M.; Latinovic-Golic, S.; Dumrese, C.; Dolder, M.; Groscurth, P.; Ziegler, U. Cholesterol in negatively charged lipid bilayers modulates the effect of the antimicrobial protein granulysin. *The Journal of membrane biology* 2006, *212*, 29–39.

(14) Li, X.; Adi, D.; Aizezi, A.; Wang, Y.; Liu, F.; Li, Y.; Li, Y.; Wei, X.; Kerem, M.; Ma, X.*; et al. A Unique Glycerophospholipid Metabolism Profile of Dilated Cardiomyopathy with Predictive value*, 2023.

(15) Ibrahim, H.; Caudron, E.; Kasselouri, A.; Prognon, P. Interest of fluorescence derivatization and fluorescence probe assisted post-column detection of phospholipids: a short review. *Molecules (Basel, Switzerland)* 2010, *15*, 352–373.

(16) Li, J.; Wang, X.; Zhang, T.; Wang, C.; Huang, Z.; Luo, X.; Deng, Y. A review on phospholipids and their main applications in drug delivery systems. *Asian Journal of Pharmaceutical Sciences* 2015, *10*, 81–98.

(17) Bou Khalil, M.; Hou, W.; Zhou, H.; Elisma, F.; Swayne, L. A.; Blanchard, A. P.; Yao, Z.; Bennett, S. A. L.; Figeys, D. Lipidomics era: accomplishments and challenges. *Mass spectrometry reviews* 2010, *29*, 877–929.

(18) Rivas-Marin, E.; Stettner, S.; Gottshall, E. Y.; Santana-Molina, C.; Helling, M.; Basile, F.; Ward, N. L.; Devos, D. P. Essentiality of sterol synthesis genes in the planctomycete bacterium Gemmata obscuriglobus. *Nature communications* 2019, *10*, 2916.

(19) Schneider, J.; Klein, T.; Mielich-Süss, B.; Koch, G.; Franke, C.; Kuipers, O. P.; Kovács, Á. T.; Sauer, M.; Lopez, D. Spatio-temporal remodeling of functional membrane microdomains organizes the signaling networks of a bacterium. *PLoS genetics* 2015, *11*, e1005140.

(20) TANAKA, M.; MORIYA, Y.; GOTO, S.; KANEHISA, M. ANALYSIS OF A LIPID BIOSYNTHESIS PROTEIN FAMILY AND PHOSPHOLIPID STRUCTURAL VARIATIONS. In *Genome Informatics 2009*; DeLisi, C., KANEHISA, M., Klipp, E., Miyano, S., Mohr, S., Wallach, I., Eds.; IMPERIAL COLLEGE PRESS, 2010; pp 191–201.

(21) Nickels, J. D.; Smith, M. D.; Alsop, R. J.; Himbert, S.; Yahya, A.; Cordner, D.; Zolnierczuk, P.; Stanley, C. B.; Katsaras, J.; Cheng, X.*; et al.* Lipid Rafts: Buffers of Cell Membrane Physical Properties. *The journal of physical chemistry. B* 2019, *123*, 2050–2056.

(22) Dupuy, A. D.; Engelman, D. M. Protein area occupancy at the center of the red blood cell membrane. *Proceedings of the National Academy of Sciences of the United States of America* 2008, *105*, 2848–2852.

(23) Goddard, A.; Román Lara, M. M.; Depping, P.; Oates, J.; Watts, A. Membrane Protein Function. In *Encyclopedia of Biophysics*; Roberts, G., Watts, A., Eds.; Springer Berlin Heidelberg: Berlin, Heidelberg, 2020; pp 1–7.

(24) Boes, D. M.; Godoy-Hernandez, A.; McMillan, D. G. G. Peripheral Membrane Proteins: Promising Therapeutic Targets across Domains of Life. *Membranes* 2021, *11*.

(25) Butler, T. J.; Smith, S. M. Strategies for the Purification of Membrane Proteins. *Methods in molecular biology (Clifton, N.J.)* 2023, *2699*, 477–491.

(26) Nastou, K. C.; Tsaousis, G. N.; Kremizas, K. E.; Litou, Z. I.; Hamodrakas, S. J. The human plasma membrane peripherome: visualization and analysis of interactions. *BioMed research international* 2014, *2014*, 397145.

(27) Vance, D. E.; Vance, J. E., Eds. *Biochemistry of lipids, lipoproteins and membranes*, 4. ed.; New comprehensive biochemistry v. 36; Elsevier: Amsterdam, 2002.

(28) Fuster, M. M.; Esko, J. D. The sweet and sour of cancer: glycans as novel therapeutic targets. *Nature reviews. Cancer* 2005, *5*, 526–542.

(29) Wang, Z.-X.; Deng, R.-P.; Jiang, H.-W.; Guo, S.-J.; Le, H.-Y.; Zhao, X.-D.; Chen, C.-S.; Zhang, J.-B.; Tao, S.-C. Global identification of prokaryotic glycoproteins based on an Escherichia coli proteome microarray. *PloS one* 2012, *7*, e49080.

(30) Schäffer, C.; Messner, P. Emerging facets of prokaryotic glycosylation. *FEMS microbiology reviews* 2017, *41*, 49–91.

(31) Möckl, L. The Emerging Role of the Mammalian Glycocalyx in Functional Membrane Organization and Immune System Regulation. *Frontiers in cell and developmental biology* 2020, *8*, 253.

(32) Zeng, Y.; Tang, F.; Shi, W.; Dong, Q.; Huang, W. Recent advances in synthetic glycoengineering for biological applications. *Current opinion in biotechnology* 2022, *74*, 247–255.

(33) Reitsma, S.; Slaaf, D. W.; Vink, H.; van Zandvoort, M. A. M. J.; oude Egbrink, M. G. A. The endothelial glycocalyx: composition, functions, and visualization. *Pflugers Archiv : European journal of physiology* 2007, *454*, 345–359.

(34) Foote, C. A.; Soares, R. N.; Ramirez-Perez, F. I.; Ghiarone, T.; Aroor, A.; Manrique-Acevedo, C.; Padilla, J.; Martinez-Lemus, L. Endothelial Glycocalyx. *Comprehensive Physiology* 2022, *12*, 3781–3811.

(35) Purcell, S. C.; Godula, K. Synthetic glycoscapes: addressing the structural and functional complexity of the glycocalyx. *Interface focus* 2019, *9*, 20180080.

(36) Delbianco, M.; Ogawa, Y. Visualizing the structural diversity of glycoconjugates. *Nature chemical biology* 2024, *20*, 11–12.

(37) Li, Y.; Wang, H.; Chen, Y.; Ding, L.; Ju, H. In Situ Glycan Analysis and Editing in Living Systems. *JACS Au* 2024, *4*, 384–401.

(38) Xu, D.; Prestegard, J. H.; Linhardt, R. J.; Esko, J. D. *Essentials of Glycobiology: Proteins That Bind Sulfated Glycosaminoglycans*, 4th; Cold Spring Harbor (NY), 2022.

(39) Taylor, M. E.; Drickamer, K.; Imberty, A.; et al., Eds. *Essentials of Glycobiology: Chapter 28: Discovery and Classification of Glycan-Binding Proteins*, 4th edition; NY, 2022.

(40) Aretz, J.; Wamhoff, E.-C.; Hanske, J.; Heymann, D.; Rademacher, C. Computational and experimental prediction of human C-type lectin receptor druggability. *Front. Immunol.* 2014, *5*, 323.

(41) Ting, S. R. S.; Chen, G.; Stenzel, M. H. Synthesis of glycopolymers and their multivalent recognitions with lectins. *Polym. Chem.* 2010, *1*, 1392.

(42) Lee, R. T.; Lee, Y. C. Affinity enhancement by multivalent lectin-carbohydrate interaction. *Glycoconjugate journal* 2000, *17*, 543–551.

(43) Liese, S.; Netz, R. R. Quantitative Prediction of Multivalent Ligand-Receptor Binding Affinities for Influenza, Cholera, and Anthrax Inhibition. *ACS nano* 2018, *12*, 4140–4147.

(44) Pieters, R. J. Maximising multivalency effects in protein-carbohydrate interactions. *Organic & biomolecular chemistry* 2009, *7*, 2013–2025.

(45) Lundquist, J. J.; Toone, E. J. The cluster glycoside effect. *Chem. Rev.* 2002, *102*, 555–578.

(46) Kiessling, L. L.; Gestwicki, J. E.; Strong, L. E. Synthetic multivalent ligands as probes of signal transduction. *Angewandte Chemie (International ed. in English)* 2006, *45*, 2348–2368.

(47) Jiménez Blanco, J. L.; Ortiz Mellet, C.; García Fernández, J. M. Multivalency in heterogeneous glycoenvironments: hetero-glycoclusters, -glycopolymers and -glycoassemblies. *Chemical Society Reviews* 2013, *42*, 4518–4531.

(48) Li, Y.; Zhang, S.; Dai, H.; Hong, Z.; Lin, Y. An enzyme-free photoelectrochemical sensing of concanavalin A based on graphene-supported TiO2 mesocrystal. *Sensors and Actuators B: Chemical* 2016, *232*, 226–233.

(49) Liu, B.; Zhang, B.; Chen, G.; Yang, H.; Tang, D. Proximity ligation assay with three-way junction-induced rolling circle amplification for ultrasensitive electronic monitoring of concanavalin A. *Analytical chemistry* 2014, *86*, 7773–7781.

(50) Rees, K.; Tran, M. V.; Massey, M.; Kim, H.; Krause, K. D.; Algar, W. R. Dextran-Functionalized Semiconductor Quantum Dot Bioconjugates for Bioanalysis and Imaging. *Bioconjugate chemistry* 2020, *31*, 861–874.

(51) Dam, T. K.; Roy, R.; Das, S. K.; Oscarson, S.; Brewer, C. F. Binding of multivalent carbohydrates to concanavalin A and Dioclea grandiflora lectin. Thermodynamic analysis of the "multivalency effect". *The Journal of biological chemistry* 2000, *275*, 14223–14230.

(52) Dohi, H.; Kanazawa, T.; Saito, A.; Sato, K.; Uzawa, H.; Seto, Y.; Nishida, Y. Bis(β-lactosyl)-60fullerene as novel class of glycolipids useful for the detection and the decontamination of biological toxins of the Ricinus communis family. *Beilstein journal of organic chemistry* 2014, *10*, 1504–1512.

(53) Cummings, R. D.; Schnaar, R. L.; Ozeki, Y. *Essentials of glycobiology: R-Type Lectins*, Fourth edition; Cold Spring Harbor Laboratory Press: Cold Spring Harbor, 2022.

(54) Wang, Y.; Yu, G.; Han, Z.; Yang, B.; Hu, Y.; Zhao, X.; Wu, J.; Lv, Y.; Chai, W. Specificities of Ricinus communis agglutinin 120 interaction with sulfated galactose. *FEBS letters* 2011, *585*, 3927–3934.

(55) Laughlin, S. T.; Bertozzi, C. R. Imaging the glycome. *Proceedings of the National Academy of Sciences of the United States of America* 2009, *106*, 12–17.

(56) Tozawa-Ono, A.; Kubota, M.; Honma, C.; Nakagawa, Y.; Yokomichi, N.; Yoshioka, N.; Tsuda, C.; Ohara, T.; Koizumi, H.; Suzuki, N. Glycan profiling using formalin-fixed, paraffin-embedded tissues: Hippeastrum hybrid lectin is a sensitive biomarker for squamous cell carcinoma of the uterine cervix. *The journal of obstetrics and gynaecology research* 2017, *43*, 1326–1334.

(57) Patwa, T. H.; Zhao, J.; Anderson, M. A.; Simeone, D. M.; Lubman, D. M. Screening of glycosylation patterns in serum using natural glycoprotein microarrays and multi-lectin fluorescence detection. *Analytical chemistry* 2006, *78*, 6411–6421.

(58) Meneghetti, M. C. Z.; Hughes, A. J.; Rudd, T. R.; Nader, H. B.; Powell, A. K.; Yates, E. A.; Lima, M. A. Heparan sulfate and heparin interactions with proteins. *Journal of the Royal Society, Interface* 2015, *12*, 589.

(59) Clausen, T. M.; Sandoval, D. R.; Spliid, C. B.; Pihl, J.; Perrett, H. R.; Painter, C. D.; Narayanan, A.; Majowicz, S. A.; Kwong, E. M.; McVicar, R. N.*; et al.* SARS-CoV-2 Infection Depends on Cellular Heparan Sulfate and ACE2. *Cell* 2020, *183*, 1043-1057.e15.

(60) Krasnova, L.; Wong, C.-H. Understanding the Chemistry and Biology of Glycosylation with Glycan Synthesis. *Annual review of biochemistry* 2016, *85*, 599–630.

(61) Schnaar, R. L.; Kinoshita, T. *Essentials of Glycobiology: Glycosphingolipids*, 3rd; Cold Spring Harbor (NY), 2015.

(62) Thompson, T. E.; Tillack, T. W. Organization of glycosphingolipids in bilayers and plasma membranes of mammalian cells. *Annual review of biophysics and biophysical chemistry* 1985, *14*, 361–386.

(63) Komatsuya, K.; Kikuchi, N.; Hirabayashi, T.; Kasahara, K. The Regulatory Roles of Cerebellar Glycosphingolipid Microdomains/Lipid Rafts. *International journal of molecular sciences* 2023, *24*.

(64) Kasahara, K.; Watanabe, K.; Takeuchi, K.; Kaneko, H.; Oohira, A.; Yamamoto, T.; Sanai, Y. Involvement of gangliosides in glycosylphosphatidylinositol-anchored neuronal cell adhesion molecule TAG-1 signaling in lipid rafts. *The Journal of biological chemistry* 2000, *275*, 34701–34709.

(65) Maalouf, K.; Jia, J.; Rizk, S.; Brogden, G.; Keiser, M.; Das, A.; Naim, H. Y. A modified lipid composition in Fabry disease leads to an intracellular block of the detergent-resistant membrane-associated dipeptidyl peptidase IV. *Journal of inherited metabolic disease* 2010, *33*, 445–449.

(66) You, J.; O'Hara, S. D.; Velupillai, P.; Castle, S.; Levery, S.; Garcea, R. L.; Benjamin, T. Ganglioside and Non-ganglioside Mediated Host Responses to the Mouse Polyomavirus. *PLoS pathogens* 2015, *11*, e1005175.

(67) Negi, G.; Sharma, A.; Chaudhary, M.; Gupta, D.; Harshan, K. H.; Parveen, N. SARS-CoV-2 Binding to Terminal Sialic Acid of Gangliosides Embedded in Lipid Membranes. *ACS infectious diseases* 2023, *9*, 1346–1361.

(68) Ferguson, M. A.; Williams, A. F. Cell-surface anchoring of proteins via glycosyl-phosphatidylinositol structures. *Annual review of biochemistry* 1988, *57*, 285–320.

(69) Ferguson, M. A.; Hart, G. W.; Kinoshita, T. *Essentials of Glycobiology: Glycosylphosphatidylinositol Anchors*, 3rd; Cold Spring Harbor (NY), 2015.

(70) Hiscox, S.; Hallett, M. B.; Morgan, B. P.; van den Berg, C. W. GPI-anchored GFP signals Ca2+ but is homogeneously distributed on the cell surface. *Biochemical and biophysical research communications* 2002, *293*, 714–721.

(71) Nicholson, T. B.; Stanners, C. P. Specific inhibition of GPI-anchored protein function by homing and self-association of specific GPI anchors. *The Journal of cell biology* 2006, *175*, 647–659.

(72) Brödel, A. K.; Sonnabend, A.; Roberts, L. O.; Stech, M.; Wüstenhagen, D. A.; Kubick, S. IRES-mediated translation of membrane proteins and glycoproteins in eukaryotic cell-free systems. *PloS one* 2013, *8*, e82234.

(73) Roch, G. J.; Sherwood, N. M. Glycoprotein hormones and their receptors emerged at the origin of metazoans. *Genome biology and evolution* 2014, *6*, 1466–1479.

(74) Irvine, E. B.; Alter, G. Understanding the role of antibody glycosylation through the lens of severe viral and bacterial diseases. *Glycobiology* 2020, *30*, 241–253.

(75) Bartold, P. M.; Wiebkin, O. W.; Thonard, J. C. Proteoglycans of human gingival epithelium and connective tissue. *The Biochemical journal* 1983, *211*, 119–127.

(76) Shi, D.; Sheng, A.; Chi, L. Glycosaminoglycan-Protein Interactions and Their Roles in Human Disease. *Frontiers in molecular biosciences* 2021, *8*, 639666.

(77) Bagdonaite, I.; Malaker, S. A.; Polasky, D. A.; Riley, N. M.; Schjoldager, K.; Vakhrushev, S. Y.; Halim, A.; Aoki-Kinoshita, K. F.; Nesvizhskii, A. I.; Bertozzi, C. R.*; et al.* Glycoproteomics. *Nat Rev Methods Primers* 2022, *2*.

(78) Davis, S. J.; Crispin, M. Solutions to the Glycosylation Problem for Low- and High-Throughput Structural Glycoproteomics. In *Functional and Structural Proteomics of Glycoproteins*; Owens, R., Nettleship, J., Eds.; Scholars Portal: Dordrecht, 2011; pp 127–158.

(79) Tan, N. Y.; Bailey, U.-M.; Jamaluddin, M. F.; Mahmud, S. H. B.; Raman, S. C.; Schulz, B. L. Sequence-based protein stabilization in the absence of glycosylation. *Nature communications* 2014, *5*, 3099.

(80) Zacchi, L. F.; Schulz, B. L. SWATH-MS Glycoproteomics Reveals Consequences of Defects in the Glycosylation Machinery. *Molecular & cellular proteomics : MCP* 2016, *15*, 2435–2447.

(81) Climer, L. K.; Dobretsov, M.; Lupashin, V. Defects in the COG complex and COG-related trafficking regulators affect neuronal Golgi function. *Frontiers in neuroscience* 2015, *9*, 405.

(82) Spiro, R. G. Protein glycosylation: nature, distribution, enzymatic formation, and disease implications of glycopeptide bonds. *Glycobiology* 2002, *12*, 43R-56R.

(83) van Kooyk, Y.; Rabinovich, G. A. Protein-glycan interactions in the control of innate and adaptive immune responses. *Nature immunology* 2008, *9*, 593–601.

(84) Lin, B.; Qing, X.; Liao, J.; Zhuo, K. Role of Protein Glycosylation in Host-Pathogen Interaction. *Cells* 2020, *9*.

(85) Corfield, A. P. Mucins: a biologically relevant glycan barrier in mucosal protection. *Biochimica et biophysica acta* 2015, *1850*, 236–252.

(86) Grondin, J. A.; Kwon, Y. H.; Far, P. M.; Haq, S.; Khan, W. I. Mucins in Intestinal Mucosal Defense and Inflammation: Learning From Clinical and Experimental Studies. *Front. Immunol.* 2020, *11*, 2054.

(87) Mauris, J.; Mantelli, F.; Woodward, A. M.; Cao, Z.; Bertozzi, C. R.; Panjwani, N.; Godula, K.; Argüeso, P. Modulation of ocular surface glycocalyx barrier function by a galectin-3 N-terminal deletion mutant and membrane-anchored synthetic glycopolymers. *PloS one* 2013, *8*, e72304.

(88) Cobo, E. R.; Kissoon-Singh, V.; Moreau, F.; Chadee, K. Colonic MUC2 mucin regulates the expression and antimicrobial activity of β-defensin 2. *Mucosal immunology* 2015, *8*, 1360–1372.

(89) Dymarska, M. Hyaluronic acid. Structure, properties and uses Kwas hialuronowy. Budowa, właściwości i zastosowanie. *CHEMICAL REVIEW* 2016, *1*, 136–138.

(90) Shriver, Z.; Capila, I.; Venkataraman, G.; Sasisekharan, R. Heparin and heparan sulfate: analyzing structure and microheterogeneity. *Handbook of experimental pharmacology* 2012, 159–176.

(91) Purushothaman, A.; Sugahara, K.; Faissner, A. Chondroitin sulfate "wobble motifs" modulate maintenance and differentiation of neural stem cells and their progeny. *The Journal of biological chemistry* 2012, *287*, 2935–2942.

(92) Yamada, S.; Sugahara, K. Potential therapeutic application of chondroitin sulfate/dermatan sulfate. *Current drug discovery technologies* 2008, *5*, 289–301.

(93) Pomin, V. H. Keratan sulfate: an up-to-date review. *International journal of biological macromolecules* 2015, *72*, 282–289.

(94) Vallet, S. D.; Clerc, O.; Ricard-Blum, S. Glycosaminoglycan-Protein Interactions: The First Draft of the Glycosaminoglycan Interactome. *The journal of histochemistry and cytochemistry : official journal of the Histochemistry Society* 2021, *69*, 93–104.

(95) Ihrcke, N. S.; Wrenshall, L. E.; Lindman, B. J.; Platt, J. L. Role of heparan sulfate in immune system-blood vessel interactions. *Immunology today* 1993, *14*, 500–505.

(96) Liao, Y.-E.; Liu, J.; Arnold, K. Heparan sulfates and heparan sulfate binding proteins in sepsis. *Frontiers in molecular biosciences* 2023, *10*, 1146685.

(97) John L Magnani; Beat Ernst. Glycomimetic Drugs - A New Source of Therapeutic Opportunities. *Discovery Medicine* 2009, *8*, 247–252.

(98) Stenzel, M. H. Glycopolymers for Drug Delivery: Opportunities and Challenges. *Macromolecules* 2022, *55*, 4867–4890.

(99) Aoi, K.; Tsutsumiuchi, K.; Aoki, E.; Okada, M. First Synthesis of Glycopeptide Macromonomers and Graft-Type Sugar-Containing Polymers with Glycopeptide Side Chains. *Macromolecules* 1996, *29*, 4456–4458.

(100) Muthukrishnan, S.; Jutz, G.; André, X.; Mori, H.; Müller, A. H. E. Synthesis of Hyperbranched Glycopolymers via Self-Condensing Atom Transfer Radical Copolymerization of a Sugar-Carrying Acrylate. *Macromolecules* 2005, *38*, 9–18.

(101) Loykulnant, S.; Hirao, A. Protection and Polymerization of Functional Monomers. 30. Anionic Living Polymerization of 4-Alkylstyrenes Containing Acetal-Protected Monosaccharide Residues. *Macromolecules* 2000, *33*, 4757–4764.

(102) Nagahori, N.; Nishimura, S. Tailored glycopolymers: controlling the carbohydrate-protein interaction based on template effect. *Biomacromolecules* 2001, *2*, 22–24.

(103) Gerke, C.; Ebbesen, M. F.; Jansen, D.; Boden, S.; Freichel, T.; Hartmann, L. Sequence-Controlled Glycopolymers via Step-Growth Polymerization of Precision Glycomacromolecules for Lectin Receptor Clustering. *Biomacromolecules* 2017, *18*, 787–796.

(104) Ghirardello, M.; Öberg, K.; Staderini, S.; Renaudet, O.; Berthet, N.; Dumy, P.; Hed, Y.; Marra, A.; Malkoch, M.; Dondoni, A. Thiol-ene and thiol-yne-based synthesis of glycodendrimers as nanomolar inhibitors of wheat germ agglutinin. *J. Polym. Sci. Part A: Polym. Chem.* 2014, *52*, 2422–2433.

(105) Banger, A.; Sindram, J.; Otten, M.; Kania, J.; Wilms, D.; Strzelczyk, A.; Miletic, S.; Marlovits, T. C.; Karg, M.; Hartmann, L. Synthesis and self-assembly of amphiphilic precision glycomacromolecules. *Polym. Chem.* 2021, *12*, 4795–4802.

(106) Ting, S. R. S.; Min, E. H.; Escalé, P.; Save, M.; Billon, L.; Stenzel, M. H. Lectin Recognizable Biomaterials Synthesized via Nitroxide-Mediated Polymerization of a Methacryloyl Galactose Monomer. *Macromolecules* 2009, *42*, 9422–9434.

(107) Dai, X.-H.; Dong, C.-M.; Yan, D. Supramolecular and biomimetic polypseudorotaxane/glycopolymer biohybrids: synthesis, glucose-surfaced nanoparticles, and recognition with lectin. *The journal of physical chemistry. B* 2008, *112*, 3644–3652.

(108) Dong, C.-M.; Chaikof, E. L. Self-assembled nanostructures of a biomimetic glycopolymer–polypeptide triblock copolymer. *Colloid Polym Sci* 2005, *283*, 1366–1370.

(109) Kim, S.-H.; Goto, M.; Cho, C.-S.; Akaike, T. *Biotechnology Letters* 2000, *22*, 1049–1057.

(110) Sato, H.; Miura, Y.; Saito, N.; Kobayashi, K.; Takai, O. A micropatterned multifunctional carbohydrate display by an orthogonal self-assembling strategy. *Biomacromolecules* 2007, *8*, 753–756.

(111) Hulme, E. C.; Trevethick, M. A. Ligand binding assays at equilibrium: validation and interpretation. *British journal of pharmacology* 2010, *161*, 1219–1237.

(112) Abdouni, Y.; Yilmaz, G.; Monaco, A.; Aksakal, R.; Becer, C. R. Effect of Arm Number and Length of Star-Shaped Glycopolymers on Binding to Dendritic and Langerhans Cell Lectins. *Biomacromolecules* 2020, *21*, 3756–3764.

(113) Bertuzzi, S.; Gimeno, A.; Martinez-Castillo, A.; Lete, M. G.; Delgado, S.; Airoldi, C.; Rodrigues Tavares, M.; Bláhová, M.; Chytil, P.; Křen, V.*; et al.* Cross-Linking Effects Dictate the Preference of Galectins to Bind LacNAc-Decorated HPMA Copolymers. *International journal of molecular sciences* 2021, *22*.

(114) Tanaka, T.; Matsuura, A.; Aso, Y.; Ohara, H. Aqueous One-pot Synthesis of Glycopolymers by Glycosidase-catalyzed Glycomonomer Synthesis Using 4,6-Dimetoxy Triazinyl Glycoside Followed by Radical Polymerization. *Journal of applied glycoscience* 2020, *67*, 119–127.

(115) Kruger, A. G.; Brucks, S. D.; Yan, T.; Cárcarmo-Oyarce, G.; Wei, Y.; Wen, D. H.; Carvalho, D. R.; Hore, M. J. A.; Ribbeck, K.; Schrock, R. R.*; et al.* Stereochemical Control Yields Mucin Mimetic Polymers. *ACS central science* 2021, *7*, 624–630.

(116) Takara, M.; Toyoshima, M.; Seto, H.; Hoshino, Y.; Miura, Y. Polymer-modified gold nanoparticles via RAFT polymerization: a detailed study for a biosensing application. *Polym. Chem.* 2014, *5*, 931–939.

(117) Freichel, T.; Eierhoff, S.; Snyder, N. L.; Hartmann, L. Toward Orthogonal Preparation of Sequence-Defined Monodisperse Heteromultivalent Glycomacromolecules on Solid Support Using Staudinger Ligation and Copper-Catalyzed Click Reactions. *The Journal of organic chemistry* 2017, *82*, 9400–9409.

(118) Ponader, D.; Wojcik, F.; Beceren-Braun, F.; Dernedde, J.; Hartmann, L. Sequence-defined glycopolymer segments presenting mannose: synthesis and lectin binding affinity. *Biomacromolecules* 2012, *13*, 1845–1852.

(119) Wojcik, F.; Mosca, S.; Hartmann, L. Solid-phase synthesis of asymmetrically branched sequence-defined poly/oligo(amidoamines). *The Journal of organic chemistry* 2012, *77*, 4226–4234.

(120) Freichel, T.; Heine, V.; Laaf, D.; Mackintosh, E. E.; Sarafova, S.; Elling, L.; Snyder, N. L.; Hartmann, L. Sequence-Defined Heteromultivalent Precision Glycomacromolecules Bearing Sulfonated/Sulfated Nonglycosidic Moieties Preferentially Bind Galectin-3 and Delay Wound Healing of a Galectin-3 Positive Tumor Cell Line in an In Vitro Wound Scratch Assay. *Macromolecular bioscience* 2020, *20*, e2000163.

(121) Lete, M. G.; Hoffmann, M.; Schomann, N.; Martínez-Castillo, A.; Peccati, F.; Konietzny, P. B.; Delgado, S.; Snyder, N. L.; Jiménez-Oses, G.; Abrescia, N. G. A.*; et al.* Molecular Recognition of Glycan-Bearing Glycomacromolecules Presented at Membrane Surfaces by Lectins: An NMR View. *ACS omega* 2023, *8*, 16883–16895.

(122) *Solid phase peptide synthesis. I. The synthesis of a tetrapeptide*, 1963.

(123) Jensen, K. J. Solid-phase peptide synthesis: an introduction. *Methods in molecular biology (Clifton, N.J.)* 2013, *1047*, 1–21.

(124) Isidro-Llobet, A.; Alvarez, M.; Albericio, F. Amino acid-protecting groups. *Chem. Rev.* 2009, *109*, 2455–2504.

(125) Grant, G. A. *Synthetic Peptides: A User's Guide (Advances in molecular biology): A User's Guide*; Oxford University Press, 2002.

(126) Chan, W. C. *Fmoc solid phase peptide synthesis: A practical approach*; Practical approach series 222; University Press: Oxford, 2004.

(127) Stewart, J. M. Cleavage methods following Boc-based solid-phase peptide synthesis. *Methods in Enzymology* 1997, *289*, 29–44.

(128) Carpino, L. A.; Han, G. Y. 9-Fluorenylmethoxycarbonyl amino-protecting group. *J. Org. Chem.* 1972, *37*, 3404–3409.

(129) Barany, G.; Albericio, F. Three-dimensional orthogonal protection scheme for solid-phase peptide synthesis under mild conditions. *J. Am. Chem. Soc.* 1985, *107*, 4936–4942.

(130) Coste, J.; Le-Nguyen, D.; Castro, B. PyBOP®: A new peptide coupling reagent devoid of toxic by-product. *Tetrahedron Letters* 1990, *31*, 205–208.

(131) Pedersen, S. L.; Tofteng, A. P.; Malik, L.; Jensen, K. J. Microwave heating in solid-phase peptide synthesis. *Chemical Society Reviews* 2012, *41*, 1826–1844.

(132) Hoose, A.; Vellacott, R.; Storch, M.; Freemont, P. S.; Ryadnov, M. G. DNA synthesis technologies to close the gene writing gap. *Nature reviews. Chemistry* 2023, *7*, 144–161.

(133) Hahm, H. S.; Schlegel, M. K.; Hurevich, M.; Eller, S.; Schuhmacher, F.; Hofmann, J.; Pagel, K.; Seeberger, P. H. Automated glycan assembly using the Glyconeer 2.1 synthesizer. *Proceedings of the National Academy of Sciences of the United States of America* 2017, *114*, E3385-E3389.

(134) Hill, S. A.; Gerke, C.; Hartmann, L. Recent Developments in Solid-Phase Strategies towards Synthetic, Sequence-Defined Macromolecules. *Chemistry, an Asian journal* 2018, *13*, 3611–3622.

(135) Neuhaus, K.; Wamhoff, E.-C.; Freichel, T.; Grafmüller, A.; Rademacher, C.; Hartmann, L. Asymmetrically Branched Precision Glycooligomers Targeting Langerin. *Biomacromolecules* 2019, *20*, 4088–4095.

(136) Mueller, L. K.; Baumruck, A. C.; Zhdanova, H.; Tietze, A. A. Challenges and Perspectives in Chemical Synthesis of Highly Hydrophobic Peptides. *Frontiers in bioengineering and biotechnology* 2020, *8*, 162.

(137) Banger, A.; Pasch, P.; Blawitzki, L.-C.; Weber, S.; Otten, M.; Monzel, C.; Schmidt, S.; Voskuhl, J.; Hartmann, L. Detection of Lectin Clustering in Self-Assembled, Glycan-Functionalized Amphiphiles by Aggregation-Induced Emission Luminophores. *Macro Chemistry & Physics* 2023, *224*.

(138) Löwe, M.; Kalacheva, M.; Boersma, A. J.; Kedrov, A. The more the merrier: effects of macromolecular crowding on the structure and dynamics of biological membranes. *The FEBS journal* 2020, *287*, 5039–5067.

(139) Honigfort, D. J.; Altman, M. O.; Gagneux, P.; Godula, K. Glycocalyx crowding with mucin mimetics strengthens binding of soluble and virus-associated lectins to host cell glycan receptors. *Proceedings of the National Academy of Sciences of the United States of America* 2021, *118*.

(140) Hudak, J. E.; Canham, S. M.; Bertozzi, C. R. Glycocalyx engineering reveals a Siglec-based mechanism for NK cell immunoevasion. *Nature chemical biology* 2014, *10*, 69–75.

(141) Stuhr-Hansen, N.; Madl, J.; Villringer, S.; Aili, U.; Römer, W.; Blixt, O. Synthesis of Cholesterol-Substituted Glycopeptides for Tailor-Made Glycocalyxification of Artificial Membrane Systems. *Chembiochem : a European journal of chemical biology* 2016, *17*, 1403–1406.

(142) Saxon, E.; Bertozzi, C. R. Chemical and biological strategies for engineering cell surface glycosylation. *Annual review of cell and developmental biology* 2001, *17*, 1–23.

(143) Griffin, M. E.; Hsieh-Wilson, L. C. Glycan Engineering for Cell and Developmental Biology. *Cell chemical biology* 2016, *23*, 108–121.

(144) Dube, D. H.; Bertozzi, C. R. Metabolic oligosaccharide engineering as a tool for glycobiology. *Current opinion in chemical biology* 2003, *7*, 616–625.

(145) Lopez Aguilar, A.; Briard, J. G.; Yang, L.; Ovryn, B.; Macauley, M. S.; Wu, P. Tools for Studying Glycans: Recent Advances in Chemoenzymatic Glycan Labeling. *ACS chemical biology* 2017, *12*, 611–621.

(146) Wiederschain, G. Y. Essentials of glycobiology. *Biochemistry Moscow* 2009, *74*, 1056.

(147) Critcher, M.; O'Leary, T.; Huang, M. L. Glycoengineering: scratching the surface. *The Biochemical journal* 2021, *478*, 703–719.

(148) Li, Y.; Wang, M.; Hong, S. Live-Cell Glycocalyx Engineering. *Chembiochem : a European journal of chemical biology* 2023, *24*, e202200707.

(149) Cohen, M.; Senaati, H. P.; Fisher, C. J.; Huang, M. L.; Gagneux, P.; Godula, K. Synthetic Mucus Nanobarriers for Identification of Glycan-Dependent Primary Influenza A Infection Inhibitors. *ACS central science* 2016, *2*, 710–714.

(150) Honigfort, D. J.; Zhang, M. H.; Verespy, S.; Godula, K. Engineering of spectator glycocalyx structures to evaluate molecular interactions at crowded cellular boundaries. *Faraday discussions* 2019, *219*, 138–153.

(151) Woods, E. C.; Yee, N. A.; Shen, J.; Bertozzi, C. R. Glycocalyx Engineering with a Recycling Glycopolymer that Increases Cell Survival In Vivo. *Angewandte Chemie (International ed. in English)* 2015, *54*, 15782–15788.

(152) van de Cauter, L.; van Buren, L.; Koenderink, G. H.; Ganzinger, K. A. Exploring Giant Unilamellar Vesicle Production for Artificial Cells - Current Challenges and Future Directions. *Small methods* 2023, *7*, e2300416.

(153) Omidvar, R.; Römer, W. Glycan-decorated protocells: novel features for rebuilding cellular processes. *Interface focus* 2019, *9*, 20180084.

(154) Castellana, E. T.; Cremer, P. S. Solid supported lipid bilayers: From biophysical studies to sensor design. *Surface science reports* 2006, *61*, 429–444.

(155) Johnson, S. J.; Bayerl, T. M.; McDermott, D. C.; Adam, G. W.; Rennie, A. R.; Thomas, R. K.; Sackmann, E. Structure of an adsorbed dimyristoylphosphatidylcholine bilayer measured with specular reflection of neutrons. *Biophysical journal* 1991, *59*, 289–294.

(156) Egawa, H.; Furusawa, K. Liposome Adhesion on Mica Surface Studied by Atomic Force Microscopy. *Langmuir : the ACS journal of surfaces and colloids* 1999, *15*, 1660–1666.

(157) Cremer, P. S.; Boxer, S. G. Formation and Spreading of Lipid Bilayers on Planar Glass Supports. *J. Phys. Chem. B* 1999, *103*, 2554–2559.

(158) Brian, A. A.; McConnell, H. M. Allogeneic stimulation of cytotoxic T cells by supported planar membranes. *Proceedings of the National Academy of Sciences of the United States of America* 1984, *81*, 6159–6163.

(159) McConnell, H. M.; Watts, T. H.; Weis, R. M.; Brian, A. A. Supported planar membranes in studies of cell-cell recognition in the immune system. *Biochimica et biophysica acta* 1986, *864*, 95–106.

(160) Tamm, L. K.; McConnell, H. M. Supported phospholipid bilayers. *Biophysical Journal* 1985, *47*, 105–113.

(161) Kalb, E.; Frey, S.; Tamm, L. K. Formation of supported planar bilayers by fusion of vesicles to supported phospholipid monolayers. *Biochimica et biophysica acta* 1992, *1103*, 307–316.

(162) Crane, J. M.; Kiessling, V.; Tamm, L. K. Measuring lipid asymmetry in planar supported bilayers by fluorescence interference contrast microscopy. *Langmuir : the ACS journal of surfaces and colloids* 2005, *21*, 1377–1388.

(163) Luchini, A.; Tidemand, F. G.; Johansen, N. T.; Campana, M.; Sotres, J.; Ploug, M.; Cárdenas, M.; Arleth, L. Peptide Disc Mediated Control of Membrane Protein Orientation in Supported Lipid Bilayers for Surface-Sensitive Investigations. *Analytical chemistry* 2020, *92*, 1081–1088.

(164) Attwood, S. J.; Choi, Y.; Leonenko, Z. Preparation of DOPC and DPPC Supported Planar Lipid Bilayers for Atomic Force Microscopy and Atomic Force Spectroscopy. *International journal of molecular sciences* 2013, *14*, 3514–3539.

(165) Athmakuri, K.; Padala, C.; Litt, J.; Cole, R.; Kumar, S.; Kane, R. S. Controlling DNA adsorption and diffusion on lipid bilayers by the formation of lipid domains. *Langmuir* 2010, *26*, 397–401.

(166) Goronzy, I. N.; Rawle, R. J.; Boxer, S. G.; Kasson, P. M. Cholesterol enhances influenza binding avidity by controlling nanoscale receptor clustering. *Chemical science* 2018, *9*, 2340–2347.

(167) Mann, D. A.; Kanai, M.; Maly, D. J.; Kiessling, L. L. Probing Low Affinity and Multivalent Interactions with Surface Plasmon Resonance: Ligands for Concanavalin A. *J. Am. Chem. Soc.* 1998, *120*, 10575–10582.

(168) Zhu, X.-Y.; Holtz, B.; Wang, Y.; Wang, L.-X.; Orndorff, P. E.; Guo, A. Quantitative glycomics from fluidic glycan microarrays. *Journal of the American Chemical Society* 2009, *131*, 13646–13650.

(169) Godula, K.; Umbel, M. L.; Rabuka, D.; Botyanszki, Z.; Bertozzi, C. R.; Parthasarathy, R. Control of the molecular orientation of membrane-anchored biomimetic glycopolymers. *Journal of the American Chemical Society* 2009, *131*, 10263–10268.

(170) Delaveris, C. S.; Webster, E. R.; Banik, S. M.; Boxer, S. G.; Bertozzi, C. R. Membrane-tethered mucin-like polypeptides sterically inhibit binding and slow fusion kinetics of influenza A virus. *Proceedings of the National Academy of Sciences of the United States of America* 2020, *117*, 12643–12650.

(171) Aigal, S.; Claudinon, J.; Römer, W. Plasma membrane reorganization: A glycolipid gateway for microbes. *Biochimica et biophysica acta* 2015, *1853*, 858–871.

(172) Reeves, J. P.; Dowben, R. M. Formation and properties of thin-walled phospholipid vesicles. *Journal of cellular physiology* 1969, *73*, 49–60.

(173) Witkowska, A.; Jablonski, L.; Jahn, R. A convenient protocol for generating giant unilamellar vesicles containing SNARE proteins using electroformation. *Scientific reports* 2018, *8*, 9422.

(174) Dimova, R.; Aranda, S.; Bezlyepkina, N.; Nikolov, V.; Riske, K. A.; Lipowsky, R. A practical guide to giant vesicles. Probing the membrane nanoregime via optical microscopy. *J. Phys.: Condens. Matter* 2006, *18*, S1151-76.

(175) Steinkühler, J.; Tillieux, P. de; Knorr, R. L.; Lipowsky, R.; Dimova, R. Charged giant unilamellar vesicles prepared by electroformation exhibit nanotubes and transbilayer lipid asymmetry. *Scientific reports* 2018, *8*, 11838.

(176) Kresse, K. M.; Xu, M.; Pazzi, J.; García-Ojeda, M.; Subramaniam, A. B. Novel Application of Cellulose Paper As a Platform for the Macromolecular Self-Assembly of Biomimetic Giant Liposomes. *ACS applied materials & interfaces* 2016, *8*, 32102–32107.

(177) Weinberger, A.; Tsai, F.-C.; Koenderink, G. H.; Schmidt, T. F.; Itri, R.; Meier, W.; Schmatko, T.; Schröder, A.; Marques, C. Gel-assisted formation of giant unilamellar vesicles. *Biophysical journal* 2013, *105*, 154–164.

(178) Pautot, S.; Frisken, B. J.; Weitz, D. A. Production of Unilamellar Vesicles Using an Inverted Emulsion. *Langmuir* 2003, *19*, 2870–2879.

(179) Karamdad, K.; Law, R. V.; Seddon, J. M.; Brooks, N. J.; Ces, O. Preparation and mechanical characterisation of giant unilamellar vesicles by a microfluidic method. *Lab on a chip* 2015, *15*, 557–562.

(180) Fenz, S. F.; Smith, A.-S.; Merkel, R.; Sengupta, K. Inter-membrane adhesion mediated by mobile linkers: Effect of receptor shortage. *Soft Matter* 2011, *7*, 952–962.

(181) Kahya, N.; Scherfeld, D.; Bacia, K.; Schwille, P. Lipid domain formation and dynamics in giant unilamellar vesicles explored by fluorescence correlation spectroscopy. *Journal of structural biology* 2004, *147*, 77–89.

(182) Dieluweit, S.; Csiszár, A.; Rubner, W.; Fleischhauer, J.; Houben, S.; Merkel, R. Mechanical properties of bare and protein-coated giant unilamellar phospholipid vesicles. A comparative study of micropipet aspiration and atomic force microscopy. *Langmuir* 2010, *26*, 11041–11049.

(183) Ewers, H.; Römer, W.; Smith, A. E.; Bacia, K.; Dmitrieff, S.; Chai, W.; Mancini, R.; Kartenbeck, J.; Chambon, V.; Berland, L.*; et al.* GM1 structure determines SV40-induced membrane invagination and infection. *Nature cell biology* 2010, *12*, 11-8; sup pp 1-12.

(184) Römer, W.; Berland, L.; Chambon, V.; Gaus, K.; Windschiegl, B.; Tenza, D.; Aly, M. R. E.; Fraisier, V.; Florent, J.-C.; Perrais, D.*; et al.* Shiga toxin induces tubular membrane invaginations for its uptake into cells. *Nature* 2007, *450*, 670–675.

(185) Vagianou, C.-D.; Stuhr-Hansen, N.; Moll, K.; Bovin, N.; Wahlgren, M.; Blixt, O. ABO Blood Group Antigen Decorated Giant Unilamellar Vesicles Exhibit Distinct Interactions with Plasmodium falciparum Infected Red Blood Cells. *ACS chemical biology* 2018, *13*, 2421–2426.

(186) Villringer, S.; Madl, J.; Sych, T.; Manner, C.; Imberty, A.; Römer, W. Lectin-mediated protocell crosslinking to mimic cell-cell junctions and adhesion. *Scientific reports* 2018, *8*, 1932.

(187) Domma, A. J.; Henderson, L. A.; Nurdin, J. A.; Kamil, J. P. Uncloaking the viral glycocalyx: How do viruses exploit glycoimmune checkpoints? *Advances in virus research* 2024, *119*, 63–110.

(188) Peerboom, N.; Block, S.; Altgärde, N.; Wahlsten, O.; Möller, S.; Schnabelrauch, M.; Trybala, E.; Bergström, T.; Bally, M. Binding Kinetics and Lateral Mobility of HSV-1 on End-Grafted Sulfated Glycosaminoglycans. *Biophysical journal* 2017, *113*, 1223–1234.

(189) Said, J. S.; Trybala, E.; Görander, S.; Ekblad, M.; Liljeqvist, J.-Å.; Jennische, E.; Lange, S.; Bergström, T. The Cholestanol-Conjugated Sulfated Oligosaccharide PG545 Disrupts the Lipid Envelope of Herpes Simplex Virus Particles. *Antimicrobial agents and chemotherapy* 2016, *60*, 1049–1057.

(190) Soria-Martinez, L.; Bauer, S.; Giesler, M.; Schelhaas, S.; Materlik, J.; Janus, K.; Pierzyna, P.; Becker, M.; Snyder, N. L.; Hartmann, L.*; et al.* Prophylactic Antiviral Activity of Sulfated Glycomimetic Oligomers and Polymers. *Journal of the American Chemical Society* 2020, *142*, 5252–5265.

(191) Liu, J.; Li, J.; Arnold, K.; Pawlinski, R.; Key, N. S. Using heparin molecules to manage COVID-2019. *Research and practice in thrombosis and haemostasis* 2020, *4*, 518–523.

(192) Kitagawa, K.; Aida, C.; Fujiwara, H.; Yagami, T.; Futaki, S.; Kogire, M.; Ida, J.; Inoue, K. Facile solid-phase synthesis of sulfated tyrosine-containing peptides: total synthesis of human big gastrin-II and cholecystokinin (CCK)-39. *J. Org. Chem.* 2001, *66*, 1–10.

(193) Hoffmann, M. Sequenz-definiert sulfatierte und sulfonierte Glykooligo(amidoamine) und deren Präsentation auf Membranen. dissertation, Heinrich Heine University, Duesseldorf, 2023.

(194) Hoffmann, M.; Snyder, N. L.; Hartmann, L. Glycosaminoglycan Mimetic Precision Glycomacromolecules with Sequence-Defined Sulfation and Rigidity Patterns. *Biomacromolecules* 2022, *23*, 4004–4014.

(195) Chang, Y.; Moore, P. S. Merkel cell carcinoma: a virus-induced human cancer. *Annual review of pathology* 2012, *7*, 123–144.

(196) Neu, U.; Woellner, K.; Gauglitz, G.; Stehle, T. Structural basis of GM1 ganglioside recognition by simian virus 40. *Proceedings of the National Academy of Sciences of the United States of America* 2008, *105*, 5219–5224.

(197) Campanero-Rhodes, M. A.; Smith, A.; Chai, W.; Sonnino, S.; Mauri, L.; Childs, R. A.; Zhang, Y.; Ewers, H.; Helenius, A.; Imberty, A.*; et al.* N-glycolyl GM1 ganglioside as a receptor for simian virus 40. *Journal of virology* 2007, *81*, 12846–12858.

(198) Becker, M.; Dominguez, M.; Greune, L.; Soria-Martinez, L.; Pfleiderer, M. M.; Schowalter, R.; Buck, C. B.; Blaum, B. S.; Schmidt, M. A.; Schelhaas, M. Infectious Entry of Merkel Cell Polyomavirus. *Journal of virology* 2019, *93*.

(199) Yu, L.; Majerciak, V.; Zheng, Z.-M. HPV16 and HPV18 Genome Structure, Expression, and Post-Transcriptional Regulation. *International journal of molecular sciences* 2022, *23*.

(200) Raff, A. B.; Woodham, A. W.; Raff, L. M.; Skeate, J. G.; Yan, L.; Da Silva, D. M.; Schelhaas, M.; Kast, W. M. The evolving field of human papillomavirus receptor research: a review of binding and entry. *Journal of virology* 2013, *87*, 6062–6072.

(201) Ichikawa, S.; Nakajo, N.; Sakiyama, H.; Hirabayashi, Y. A mouse B16 melanoma mutant deficient in glycolipids. *Proceedings of the National Academy of Sciences of the United States of America* 1994, *91*, 2703–2707.

(202) Houben, R.; Celikdemir, B.; Kervarrec, T.; Schrama, D. Merkel Cell Polyomavirus: Infection, Genome, Transcripts and Its Role in Development of Merkel Cell Carcinoma. *Cancers* 2023, *15*.